Quantitative Temperature & Formaldehyde Concentration Imaging for High-Pressure Turbulent Fuel Jet Ignition

By

Joshua M. Herzog

A document submitted in partial fulfillment of
the requirements for the degree of

Doctor of Philosophy
(Nuclear Engineering and Engineering Physics)

at the

UNIVERSITY OF WISCONSIN–MADISON

2020

Date of final examination: 12/02/2020

This dissertation is approved by the following members of the Final Oral Committee:
David A. Rothamer, Professor, Mechanical Engineering
Riccardo Bonazza, Professor, Engineering Physics
Oliver Schmitz, Professor, Engineering Physics
Jaal B. Ghandhi, Professor, Mechanical Engineering
Scott T. Sanders, Professor Mechanical Engineering

Acknowledgements

I'd like to start by thanking my advisor, Prof. David Rothamer, for taking me on as a student and putting up with me over the past six and a half years, and pushing me to become a better scientist. It goes without saying that Dave's guidance and willingness to teach were instrumental in all of my academic successes as a graduate student. I also want to thank Prof. Riccardo Bonnaza for his mentorship and the opportunity to work with him and his research group. I am also indebted to the other members of my committee: Prof. Jaal Ghandhi, Prof. Scott Sanders, and Prof. Oliver Schmitz.

I also gratefully acknowledge the support of the Army Research Office (Grant Number W911NF-19-1-0238) for sponsoring much of this work.

To all of my fellow and former students at the Engine Research Center and those in the Wisconsin Shock Tube Laboratory: thank you for everything. Especially Mike Groendyk, James Cherry, Keith Dahl, Andrea Shen, Tyler Strickland, Arthur Gilliam, and Eri Amezcua; thank you for the long coffee breaks at Aldo's, Tuesday night gaming sessions, and the innumerable other ways you all made the stress of grad school bearable. Our time spent together at the Terrace and the Sett provided me with many of my fondest memories of grad school. I am also grateful for your encouragement and deep scientific discussions. In particular, Dan Reese, Dustin Witkowski, Steve Sakai, Chris Noble, and Alex Ames; thank you all for listening to my scatterbrained ideas and helping me form them into legitimate scientific questions. I especially want to thank Dan and Dustin for helping me figure out how to survive grad school in my earlier years, and Mike for helping me get across the finish line.

I also want to thank my family for their love and support. I am forever grateful for the support and sacrifice of my parents; without them none of my achievements would have been possible. Finally, I would like to thank my wonderful wife Emily. Thank you for your unending support, friendship, and love; for putting up with me for all these years; and especially for moving all the way to Madison and taking on this adventure with me.

Abstract

Understanding the process of turbulent fuel jet ignition in engines is critical to improve engine designs. Unfortunately, there is much we do not understand about the ignition process, and current diagnostic methods are insufficient to improve our understanding of the coupling between temperature, velocity, and chemistry in high-pressure turbulent jet ignition. Here, a diagnostic approach is designed that can simultaneously measure temperature, velocity, and formaldehyde concentration in a turbulent fuel jet during low-temperature ignition in an optically-accessible engine. Particle image velocimetry (PIV), aerosol phosphor thermometry (APT), and formaldehyde planar laser-induced fluorescence (PLIF) are used in combination. A detailed characterization of formaldehyde photophysics is performed using spectral simulations and experimental data. Several thermographic phosphors are characterized in detail (including physical and luminescence properties), models are developed for phosphor signal intensity and APT performance, and a method is outlined and demonstrated to combine simultaneous APT techniques to increase the temperature measurement range. The APT methods are applied to atmospheric pressure heated jets to validate the performance estimates, and identify issues in their application. A thorough analysis of design considerations for particle-based techniques is also provided, and performance estimates are made for the combined diagnostic. It was found that the Ce:LuAG phosphor with 355-nm excitation can be most easily integrated with PIV and formaldehyde PLIF measurements, and has good performance characteristics over the 700-1000 K temperature range of interest, with ∼20 K estimated precision on average. Multiple scattering was found to impose a significant limitation on particle seeding density. Several phosphor materials and techniques were also found to be viable for temperature imaging well above 1000 K (Ce:$GdPO_4$, Eu:BAM, and Ce:CSSO). Performance predictions for formaldehyde suggest that detection limits are on the order of 100 ppm throughout much of the temperature and pressure range expected during ignition, and a ratiometric background correction approach was discussed to avoid interference from phosphor luminescence, or other broadband background sources. PIV is readily integrated into the APT measurement. The proposed approach is capable of simultaneous temperature, velocity, and formaldehyde concentration imaging of low-temperature ignition processes, and provides a significant step towards improving our understanding of high-pressure turbulent jet ignition.

Contents

List of Figures

List of Tables

Nomenclature

$\beta_{x,y}$	Sensitivity of variable x to variable y
χ	Species mole fraction
$\dot{\phi}''$	Photon flux (photons/time/area)
ϵ	Spectral fluorescence emission intensity
η	Efficiency
$\hat{\boldsymbol{\epsilon}}$	Electric field polarization unit vector
$\hat{\boldsymbol{n}}$	Electric field propagation direction unit vector
$\hat{R}$	Specific gas constant
$\|\Phi\rangle$	Vibrational eigenstate
$\|\psi\rangle$	Electronic eigenstate
$\|\Theta\rangle$	Rotational eigenstate
$\mathcal{D}$	Direction cosine operator
$\mathcal{F}_i$	Rotational energy of state i
$\mathcal{G}_i$	Vibrational energy of state i
$\mathcal{H}$	Hamiltonian operator
$\mathcal{L}$	Lineshape function
$\mathcal{T}_i$	Electronic energy of state i
μ	Viscosity
ν	Photon spatial frequency
Ω	Collection solid angle
ω	Photon angular frequency
Φ	Fluorescence quantum yield
ϕ''	Photon density or fluence (photons/area)
σ	Absorption cross-section

τ	Lifetime or time constant
$\vec{\boldsymbol{\mu}}$	Transition electric dipole moment operator
$\vec{\boldsymbol{A}}$	Magnetic vector potential
$\vec{\boldsymbol{B}}$	Magnetic field vector
$\vec{\boldsymbol{E}}$	Electric field vector
$\vec{\boldsymbol{M}}$	Transition magnetic dipole moment operator
$\vec{\boldsymbol{p}}$	Momentum operator
$\vec{\boldsymbol{R}}$	Atomic position operator
$\vec{\boldsymbol{r}}$	Electronic position operator
$\vec{\boldsymbol{s}}$	Spin operator
$\vec{\vec{\boldsymbol{Q}}}$	Transition electric quadrupole moment operator
ξ_T	Fractional temperature sensitivity
A	Area
a, b, c	Rotational constants
B	Background signal intensity (photons)
b_x	Bias indicator for variable x
c	Specific heat capacity
C_{nr}	Ratio of the radiative rate constant to the non-radiative attempt rate
d	Diameter
E	Energy
E''	Energy density or laser fluence (energy/area)
F	Population fraction
g	Gain, *e.g.*, for an intensified camera
I	Line intensity
J, K, M	Rotational quantum numbers
k	Thermal conductivity
k	Transition rate constant
m	Sample mass
N	Number of particles
n	Number density
p	Pressure
R	Signal ratio
S	Signal intensity (photons)

s_x	Precision index for variable x
T	Temperature
t	Time
u_x	Total uncertainty in variable x
V	Volume
v	Velocity
Z	Partition function
SBR	Signal to background ratio
SNR	Signal to noise ratio

Physical Constants

α	Fine structure constant ≈ 0.0073
$\hbar$	Reduced Planck constant $\approx 1.055 \times 10^{-34}$ J·s
$\tilde{R}$	Universal gas constant ≈ 8.314 J/K-mol
c	Speed of light $\approx 2.998 \times 10^{8}$ m/s
e	Electron charge magnitude $\approx 1.602 \times 10^{-19}$ C
k_B	Boltzmann constant $\approx 1.381 \times 10^{-23}$ J/K
m_e	Electron mass $\approx 9.109 \times 10^{-31}$ kg

Chapter 1

Introduction

One of the most crucial aspects of diesel combustion is the ignition of the turbulent fuel jets injected in-cylinder. The ignition process has a strong influence on engine performance and emissions formation, and a significant effort has been dedicated to studying the process of turbulent fuel jet ignition in diesel engines. Unfortunately, traditional experiments have been primarily limited to measurements of pressure, pollutant emissions, and chemiluminescence of certain UV-active species which provide little direct information on temperature and composition distributions [1, 2]. Knowledge of temperature, velocity, and species concentrations are needed to better understand the complex turbulence-chemistry interactions. To achieve this, improved diagnostics and diagnostic characterization are required to improve our understanding of high-pressure turbulent jet ignition.

A recent study [3] using combined schlieren and formaldehyde planar laser-induced fluorescence (PLIF) imaging suggests that low-temperature ignition in turbulent high-pressure spray flames originates immediately behind the penetrating spray head on the radial periphery. This is followed by a rapid appearance of low-temperature reactions throughout the jet head, ultimately leading to high-temperature ignition. This description has further been developed into a conceptual model for turbulent ignition in high-pressure spray flames [4]. However, due to limitations in diagnostic capabilities, little quantitative data is available to validate the model.

Spatially- and temporally-resolved, quantitative optical diagnostics, including aerosol phosphor thermometry (APT) and formaldehyde PLIF, provide an opportunity to study ignition phenomena in diesel engines in greater detail. Temperature and velocity fields can be measured in 2D using combined APT and particle image velocimetry (PIV), while formaldehyde concentration fields can be measured using PLIF separate or simultaneous with APT and PIV. This approach can potentially be performed at

high-speed providing the temperature, concentration, and velocity field information needed to validate the conceptual model of turbulent high-pressure fuel-jet ignition.

In this work, I aim to develop a combined diagnostic for simultaneous imaging of formaldehyde species concentration, temperature, and velocity for high-pressure fuel jet ignition experiments in an optically-accessible engine. This will be accomplished through characterization of formaldehyde PLIF spectroscopy parameters at engine-relevant conditions, characterization of several different APT techniques that could be used in the jet ignition experiments, demonstration of the new APT techniques at atmospheric conditions, and the design of a combined APT and formaldehyde PLIF experiment for assessing high-pressure turbulent fuel jet ignition in an optically accessible engine.

To that end, this work represents a significant step towards the design and application of a combined APT-PIV-PLIF diagnostic for diesel ignition, and is believed to be the first attempt to integrate APT and PLIF concentration measurements. A major focus of this work is on the design and characterization of several new APT diagnostics using a variety of phosphors, and aims to characterize the performance of these phosphor materials in detail. A signal model was developed to describe some of the complicated features observed in the characterization data including non-linearity with respect to laser energy. The model uses excited-state absorption to describe and explain these features. The signal model is used to analyze phosphor performance including biases due to uncertainties in laser fluence and reference temperature, and a framework for quantifying diagnostic performance is provided. APT measurements in several different scenarios (two electrically heated air jets, and an air jet heated by a concentric flat flame) are also provided and analyzed to demonstrate the APT techniques and validate performance predictions.

Likewise, formaldehyde photophysics are discussed and analyzed by combining theoretical models with data reported in literature. Absorption cross-sections at engine relevant conditions are determined using data taken at ambient conditions, combined with relatively simple spectroscopy theory. Fluorescence quantum yields are extrapolated from measurements made at elevated temperature and pressure in nitrogen (up to around 800 K and 10 bar) using a physics-based model previously reported in the literature. Finally, collection fractions and emission spectrum band shapes are measured directly and extrapolated to higher pressure and temperature using the same relatively simple spectroscopic models and theory. As will be shown, knowledge of the collection fraction of formaldehyde can be used for background correction in the formaldehyde PLIF imaging diagnostic.

In addition to photophysics, a detailed discussion of design considerations is provided. The discussion addresses issues primarily concerning tracer particle response and diagnostic intrusiveness. A thorough discussion and analysis of experimental biases stemming from the enclosed experimental geometry in

an internal combustion engine (*e.g.*, surface reflections and multiple scattering) is provided. As will be shown, multiple scattering can present a significant challenge for experiments at even low or moderate seeding densities. Additional factors including blackbody radiation from particles are discussed, but are negligible at the conditions expected for ignition.

Finally, the results of the characterization and design analysis are used to choose experimental parameters for a prototypical turbulent high-pressure fuel-jet ignition experiment in an optical engine. Using the selected parameters, temperature imaging and formaldehyde concentration imaging performance is estimated, and a recommendation is made regarding phosphor selection. A strategy for performing the APT and PLIF diagnostics simultaneously is discussed, and a method for formaldehyde background correction is provided and analyzed in detail. The impact of a gate delay and stretched laser pulse on the APT diagnostic are discussed, and detection limits for the formaldehyde PLIF diagnostic are estimated. This work uses several new phosphors including trivalent cerium (Ce^{3+}) and praseodymium (Pr^{3+}) individually doped into calcium scandium silicate ($Ce_3Sc_2Si_3O_{12}$, CSSO) or Ce:CSSO and Pr:CSSO, and trivalent cerium doped into gadolinium phosphate ($GdPO_4$) or Ce:$GdPO_4$. Several more well-known phosphors are characterized as well, including divalent europium (Eu^{2+}) doped into barium magnesium aluminate ($BaMgAl_{10}O_{17}$, BAM) or Eu:BAM, and Ce^{3+} and Pr^{3+} doped into lutetium aluminum garnet ($Lu_3Al_5O_{12}$, LuAG) or Ce:LuAG and Pr:LuAG. In addition, this work investigates phosphors in which two ions are doped into the same host (co-doped phosphors). As will be shown, the co-doped phosphors allow the experimenter to effectively combine two phosphors, such that multiple different measurements can be made simultaneously; the co-doped phosphors also provide new possibilities for APT, *e.g.*, by comparing the emission intensity of the two ions.

The remainder of this thesis is organized as follows. Chapter 2 discusses background relevant to temperature and concentration measurements for turbulent high-pressure fuel-jet ignition, and provides background on the APT and PLIF techniques. Chapters 3 and 4 detail the results of the formaldehyde and phosphor photophysical characterization portions of the work. In particular, a signal model is derived and discussed in detail for the investigated phosphors, and a model is provided for formaldehyde photophysical properties including absorption cross-section at 355 nm, fluorescence quantum yield, and collection fraction. Next, the results of several APT experiments are presented in Chapter 5 to demonstrate the application of the APT diagnostics, validate the performance predictions, and discuss some potential issues in the application of APT techniques. Chapter 6 discusses additional considerations for experimental design of APT experiments including tracer response, intrusiveness, and multiple scattering to address the concerns introduced in Chapter 5. All of the aforementioned work is used to design the combined APT-PLIF experiment in Chapter 7. An outline of the technique is provided, including a

ratiometric background correction approach for formaldehyde PLIF, and performance estimates for APT are provided along with estimates of formaldehyde PLIF detection limits. Finally, a recommendation regarding the APT technique selection and the integration approach is made. Chapter 8 summarizes the results and concludes the thesis. A brief, non-technical summary of this work was created for non-scientists with the support of the Wisconsin Initiative for Science Literacy (WISL) and is provided in Appendix A.

Chapter 2

Background

Accurate spatially-resolved thermometry, velocimetry, and species concentration measurements are necessary to gain insight into the details of the complex physical and chemical processes that play key roles in the ignition of fuels in diesel engines. Temperature and species concentrations largely control local reaction rates and also can be used to estimate the local combustion progress. Formaldehyde concentration in particular is strongly tied to low-temperature oxidation and ignition of hydrocarbon fuels [5], and concentration fields can and have been used qualitatively as a marker for derived properties such as flame location [6] and more generally as an indicator of combustion progress [7]. Velocity measurements are likewise important as velocity can control transport of species and thermal energy. For these reasons, simultaneous spatially- and temporally-resolved temperature, velocity, and formaldehyde concentration measurements are desired due to the information they can provide relating to ignition in internal combustion engines.

2.1 Overview of Ignition Diagnostics

In most engine applications, pressure and heat release are the primary diagnostics used to characterize ignition. Pressure or heat release measurements are the simplest and least intrusive form of ignition diagnostic as cylinder pressure is commonly measured in engine experiments. When properly corrected for time lag, this diagnostic can provide an accurate measurement of the ignition delay [8]. Unfortunately, methods based on a single pressure measurement alone cannot provide spatially-resolved information. Combustion detection has similarly been performed using block-mounted accelerometers [9] and even ionization sensors in-cylinder [10]. However, these suffer the same drawbacks in that they are not spatially resolved and only indirectly measure ignition timing.

Quantitative diagnostics for ignition in internal combustion engines are often performed optically in optically-accessible engines. Typical optical diagnostics for ignition studies include natural luminosity or chemiluminescence imaging [11, 12] and schlieren or shadowgraph imaging [8]. Natural luminosity or chemiluminescence imaging collects light emitted from luminescent species in-cylinder and does not require any external excitation. However, since the emitted light intensity depends solely on the in-cylinder conditions there is little opportunity to control or improve the performance of the diagnostic. Further, it is difficult to apply these diagnostics quantitatively; there is often significant emission of light from outside the object plane, and the emitting species are often not known or interferences are present. Conversely, schlieren and shadowgraph measurements are dependent only on density gradients in the medium and can be applied at any condition provided the density gradients are large enough. However, these techniques are path integrated and can be influenced by phenomena outside the object plane. Finally, since schlieren images are only dependent on density gradients, they can be difficult to interpret as ignition processes have been show to "soften" density gradients relative to non-reacting fuel jets [3].

2.2 Temperature and Concentration Measurements

Although temperature and concentration are clearly important in combustion applications, accurate measurements are still difficult to achieve in engines. A broad overview of temperature measurement techniques is given by Childs [13]. Although many devices and techniques exist for both temperature and species concentration measurements, most are not suitable for measurements of high-pressure fuel jet ignition. Thermocouples and other temperature probes are subject to multiple biases, including time response, and by nature are only capable of point measurements. Similarly, point techniques for concentration measurement such as photoionization mass spectrometry [14] and molecular beam mass spectrometry [15]) are invasive and cannot be performed *in situ*.

Laser absorption measurements can be performed *in situ* in a relatively non-intrusive manner and can provide accurate measurements even in non-equilibrium scenarios [16, 17]. Further, absorption spectroscopy can provide detailed species concentration [18] and temperature information. Although these diagnostics resolve some of the issues with probe or point measurements, they are usually path-integrated and don't provide spatially resolved measurements. Some work has been done to apply line-of-sight laser absorption techniques in a spatially-resolved manner using tomographic reconstruction by sweeping the test volume in space [19] or using multi-beam absorption [20]. However, tomography is still limited in spatial resolution if high time resolution is also required.

Similarly, laser scattering techniques such as Coherent Anti-Stokes Raman Spectroscopy (CARS) and spontaneous Raman spectroscopy can be applied at high speed, are viable at high temperature, provide temperature accuracy on the order of a few percent [21], and can be spatially-resolved (typically 1-D [22]). Although some imaging with CARS has been done [23], the extension to planar imaging is often difficult and demanding in terms of equipment because collected data must be wavelength-resolved in addition to spatially-resolved. Additionally, measurements at high-pressures (> 50 atm) with these techniques are not routinely or easily performed.

Fully spatially- and temporally-resolved molecular scattering-based measurements include spontaneous Raman scattering and Rayleigh scattering. Scattering-based imaging measurements directly measure the scattered light intensity which has spectral features that depend on species composition as well as temperature [24]. Rayleigh scattering is an elastic process, where light is scattered at the same wavelength as the excitation source, whereas Raman scattering is an inelastic process that results in wavelength-shifted radiation. Raman scattering typically has a small cross-section, on the order of 10^7 times smaller than fluorescence processes [25], making detection difficult and often resulting in low signal-to-noise ratios (SNRs). This is a significant limitation in engine and combustion applications as even trace amounts of fluorescent substances can interfere significantly with the measurement. Similarly, Rayleigh scattering techniques can suffer from interference due to surface scattering, as the scattered light is not wavelength shifted from the excitation source. This has been demonstrated to be problematic in enclosed environments such as engines where measurements must be taken in close proximity to scattering surfaces [26]. In general, background radiation is still the most severe limitation in the application of Rayleigh scattering techniques in engines [27].

In high-pressure and high-temperature experiments, Rayleigh scattering is not perfectly monochromatic. Temperature (or Doppler) broadening results in a small change in the wavelength of scattered light due to the relativistic Doppler effect; the thermally broadened Rayleigh line shape is a measurement of the speed distribution of the scattering particles [28]. Pressure broadening also occurs and is a result of Brillouin scattering from acoustic waves [29] and, collectively, the Rayleigh line-shape is a function of temperature and pressure. Filtered Rayleigh scattering (FRS) takes advantage of this broadening by allowing only a narrow portion of the Rayleigh line shape to be imaged. Since unshifted light corresponds to slow or stationary particles (or surfaces), rejecting light at the excitation laser wavelength can greatly reduce the background surface scattering contribution [30]. Similarly, collecting a narrow band away from the excitation peak selects only particles that are moving at a uniform speed, *e.g.*, in high-speed flows. FRS has also been applied quantitatively to measure temperature to within a few percent accuracy in flames [31] and has also been successfully applied to measure fuel vapor fraction in a constant

temperature liquid spray vaporization experiment (effectively rejecting droplet scattering) to around 8% [32]; however, FRS intensity is dependent on the local collision environment, temperature, scattering species, and number density, and thus requires a significant knowledge of the flow of interest to apply quantitatively on a single-shot basis. In principle, angle-resolved FRS measurements can be used to measure temperature, velocity, density, and pressure simultaneously (and has been demonstrated in an air jet with 5-10% uncertainty in each quantity; single-shot precision estimates were not provided) [33] although this method is difficult to apply in a spatially-resolved manner as angle-resolved measurements are required at each point, and requires some knowledge or assumption of the chemical composition and scattering cross-sections.

Planar laser-induced fluorescence (PLIF) diagnostics can provide high-speed, spatially and temporally resolved temperature and concentration field measurements. Laser-induced fluorescence cross sections are much larger than for Rayleigh and Raman scattering and the emitted light is often wavelength-shifted from the excitation wavelength, reducing the likelihood for interference. PLIF can be performed with either existing species or by seeding a molecular tracer into the flow. Seeded hydrocarbon molecular tracers, such as 3-pentanone, have been used successfully at low temperature as fuel tracers. However, hydrocarbon species are not stable at high temperatures as they may decompose and react in air [34]. Conversely, PLIF imaging of nascent molecular species such as OH and NO can provide a direct measurement of both species concentration and temperature at elevated temperatures, though imaging of OH is not possible at low temperatures due to lack of sufficient concentration. PLIF can provide spatially and temporally resolved field measurements, can be performed at high speed, and can provide both qualitative and quantitative temperature and concentration information simultaneously. Additionally, PLIF can be performed with many UV-active tracer species including formaldehyde. PLIF dependence on both temperature and species concentration can also be a drawback in that it may not be possible to apply PLIF quantitatively without additional temperature or concentration information.

Aerosol phosphor thermometry (APT), in which thermographic phosphor particles are seeded into the flow, has been used successfully for planar imaging measurements of temperature in engines and other turbulent environments [35, 36]. Thermographic phosphor particles are typically composed of an inert ceramic host doped with rare-earth ions. Since the particles are solid, they are usually insensitive to pressure and composition. Further, since they are chemically inert and do not exhibit significant pressure dependence, they are an ideal tracer for engine measurements. Prior to this work, thermographic phosphors were limited to a maximum temperature of less than 1000 K due to relatively low quenching temperatures [37], although it was suggested that high temperature precision is achievable above 1000 K using a co-doped or scattering-referenced technique [38].

The combination of aerosol phosphor thermometry with formaldehyde PLIF is an ideal diagnostic choice for low-temperature ignition. APT is able to provide precise spatially-resolved temperature measurements and simultaneous velocimetry. Formaldehyde has a sufficient fluorescence quantum yield and absorption cross-section for engine measurements, forms in reasonable concentrations during diesel ignition, and is strongly tied to the low-temperature ignition process. APT measurements can be used in combination with formaldehyde PLIF to provide a quantitative estimate of formaldehyde mole fraction throughout the fuel jet. Simultaneous, spatially-resolved velocity, temperature, and quantitative formaldehyde mole fraction can provide a more complete description of the ignition process that has not yet been obtained experimentally.

2.3 Planar Laser-Induced Fluorescence

Although PLIF can directly provide both temperature and species concentration measurements, it can still be difficult to apply quantitatively due to the dependence of the measured signal on multiple parameters. These parameters can include not only pressure and temperature, but also the concentration of species in the test volume; interactions of the excited molecule with other species can result in collisional quenching that can impact the amount of light emitted and potentially the emission spectrum. Insufficient information about the collisional environment and quenching processes can be a significant barrier to quantitative measurements. The remainder of this section will briefly describe the laser-induced fluorescence process.

A general expression for PLIF intensity, in the linear excitation limit, is given by

$$S_{LIF} = \frac{E_p''}{\hbar\omega_0} V n_{abs}(p,T)\, \sigma(\omega_0,p,T)\, \Phi(\omega;\omega_0,p,T,\vec{\chi}) \frac{\Omega}{4\pi}\, \eta, \tag{2.1}$$

where the detected signal S_{LIF} is the number of photons incident per pixel, n_{abs} is the absorbing species number density, V is the excitation volume, Ω is the collection solid angle, $\hbar$ is the reduced Planck constant, ω_0 is the excitation photon frequency, and E_p'' is the incident laser fluence. The factor η is an effective optical collection efficiency, and the fluorescence quantum yield (FQY, Φ) represents the fraction of excited molecules that radiate. This expression is adapted from Hanson, *et. al.* [39] for a single electronic transition.

Equation 2.1 is written assuming that the LIF excitation is linear in energy, or rather, only a small fraction of the ground state population is excited. If, on the other hand, a significant fraction of the population is in an excited electronic state, the total absorption rate and hence emission intensity would

necessarily decrease as fewer absorbing molecules are available. The LIF equation (Equation 2.1) can be generalized to a spectrally-resolved LIF signal by rewriting the FQY in terms of the radiative rate coefficients $k_{r,ij}$ and transition lineshape function $\phi(\omega;\omega_0,p,T)$. The spectrally-resolved LIF equation is written as

$$\begin{aligned}\frac{\partial}{\partial\omega}S_{LIF}(\omega) &= \frac{E_p''}{\hbar\omega_0}\, V\, n_{abs}(p,T)\, \sigma(\omega_0,p,T)\, \frac{\sum_{ij} F_i(\omega_0,p,T,\vec{\chi})\, k_{r,ij}\, \phi(\omega;\omega_0,p,T)}{\sum_{ij} F_i(\omega_0,p,T,\vec{\chi})\, k_{r,ij} + \sum_{il} Q_{il}}\, \frac{\Omega}{4\pi}\eta \\ &= \frac{E_p''}{\hbar\omega_0}\, V n_{abs}(p,T)\, \sigma(\omega_0,p,T)\, \Phi(\omega;\omega_0,p,T,\vec{\chi})\frac{\Omega}{4\pi}\,\eta.\end{aligned} \tag{2.2}$$

The partial derivative on the left hand side is used to denote that this is a differential signal with respect to the emission frequency. Here, F_i is the population fraction of the initial rovibronic state i, and the pressure (p), temperature (T), and emitted photon frequency (ω) dependencies are explicitly shown for each factor. The FQY is now spectrally resolved by definition. Integrating Equation 2.2 with respect to emission frequency (ω) yields exactly Equation 2.1. The parameter $\vec{\chi}$ that appears in the population distribution expressions represents the dependence on the local collisional environment, or more specifically the local mole fractions of all species. The population fractions (F_i) in Equation 2.2 are typically taken as the Boltzmann fraction (assuming thermodynamic equilibrium) but in general may have a more complicated functional form that is pressure dependent. The summations in Equation 2.2 are to be taken as the sum over all possible combinations of initial rovibronic states i and final rovibronic states j. Finally, Q_{il} represents the nonradiative deactivation rate from the initial state i through deactivation mechanism l; the total deactivation rate from state i sums over all of the deactivation pathways. The nonradiative deactivation rate is generally dependent on pressure, temperature, and species mole fractions.

Many initial rovibronic states may contribute to the PLIF signal since the initial population is often able to redistribute before the fluorescence process is complete. This complex behavior is encapsulated in the FQY, which in the general case is assumed to be dependent on excitation wavelength and the local thermodynamic state (pressure, temperature, and species mole-fractions).

2.3.1 Formaldehyde PLIF

Formaldehyde, being present naturally as an intermediate species in hydrocarbon combustion, is an ideal molecular tracer for partial fuel oxidation and ignition in hydrocarbon combustion applications. Concentrations on the order of 1% mole fraction have been measured [40] via mass spectrometry in flame experiments. Similar concentrations have been reported in engines, where formaldehyde generally

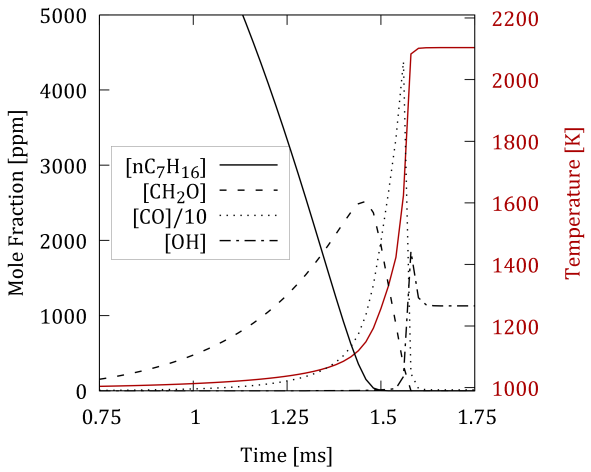

Figure 2.1: Calculated major species concentrations and temperature profile for a constant pressure reactor initially at 1000 K, 30 bar, using n-heptane in air at $\phi = 0.5$.

forms early through low-temperature reactions, and is very quickly consumed following high-temperature ignition [41].

To illustrate the relationship between formaldehyde and low-temperature ignition, the results of a chemical kinetics calculation for a constant pressure reactor at a typical injection condition of 30 bar and 1000 K are shown in Figure 2.1. Specifically, gas temperature and concentrations for several major species are plotted through the simulation. The calculation uses the LLNL n-heptane combustion mechanism [42, 43]. Formaldehyde begins to form as the fuel is consumed by low-temperature reactions, and is consumed during high-temperature ignition. For this condition, formaldehyde begins to form immediately and is almost completely consumed when the end-gas reaches 1500 K. In contrast, OH is first being formed in significant concentrations as CO is being consumed and the temperature exceeds 1500 K. OH formation begins following the peak temperature rise and it remains in significant concentrations indefinitely at the high temperatures following ignition. Therefore, OH is a good indicator of high-temperature regions, but does not provide information on the mechanism leading up to high-temperature ignition. Formaldehyde, in contrast, is an excellent marker for low-temperature chemistry.

Formaldehyde is also an attractive tracer molecule from a spectroscopic perspective due to its distinct absorption and emission spectrum. A sample absorption spectrum from HITRAN [44, 45] is shown in Figure 2.2, with the distinct spectral features called out, and the proposed 355 nm excitation wavelength shown as a vertical dashed blue line. The formaldehyde absorption and emission spectra have many distinguishable peaks corresponding to different vibrational bands. Emission bands fall in the wavelength range from 380 nm to 500 nm, with absorption bands below 380 nm [46]. Formaldehyde can be excited at 355 nm using the third harmonic of an Nd:YAG laser (as shown in Figure 2.2), and has a relatively

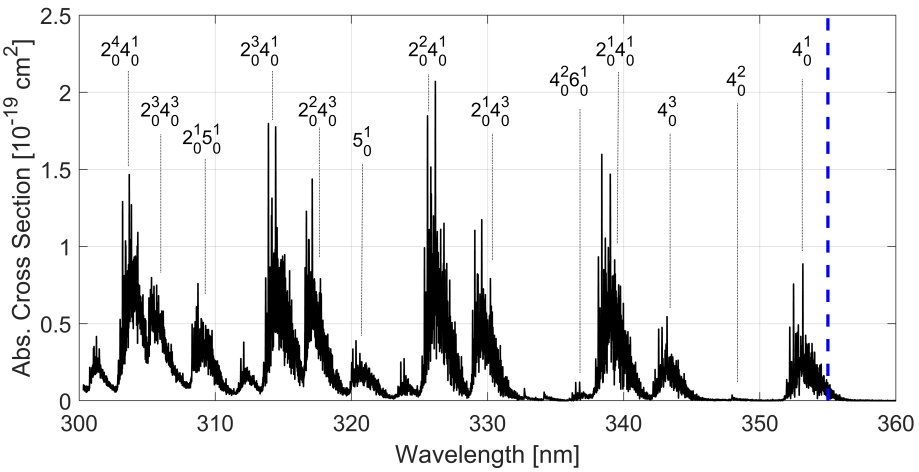

Figure 2.2: High resolution formaldehyde absorption spectra measured at 300 K, extrapolated to zero pressure. Data was taken from HITRAN [44, 45].

short lifetime on the order of 30-40 ns at atmospheric conditions, decreasing significantly as temperature and pressure increase [47, 48]. Although 355 nm excitation is not optimal as the absorption peak is closer to 353 nm, it has been used for qualitative formaldehyde concentration imaging in the past in both open flames and in engines [6, 49, 50]. Other formaldehyde PLIF studies have excited hot bands near 370 nm [51] or combination bands near 338 nm [52] to reduce temperature dependence and to increase total signal intensity, respectively. However, shorter wavelength excitation tends to result in decreased fluorescence lifetime as a result of increased predissociation through the closest triplet state and directly to H_2 + CO [50, 53] at higher energies. Currently, there is no complete dataset for formaldehyde absorption or fluorescence at elevated temperatures or pressures, and deactivation mechanisms are poorly understood. Specifically, rovibronic linestrengths (both vibrational and electronic components) for the absorption and fluorescence processes are not well known. Further, there is little information available relating to collisional behavior and quenching at engine-relevant conditions.

In sooting environments such as diesel engines, polycyclic aromatic hydrocarbons (PAHs) tend to interfere with formaldehyde emission, as PAHs have broadband absorption and emission spectra that can overlap significantly with formaldehyde. This issue, and potential solutions including combined on/off resonant imaging are discussed by Bakker, Maes, and Dam [54]. As a result of this interference it is much more difficult to make quantitative concentration measurements in sooting environments [55]. This is perhaps the most significant challenge in applying formaldehyde PLIF in diesel engines, as it is not necessarily clear what portion of the detected luminescence was emitted from formaldehyde.

A previous approach to quantitatively image formaldehyde PLIF in sooting environments was developed by Thering, *et al.*, [56] using difference-imaging with two wavelength bands. In this scheme,

two cameras are outfitted with filters designed to capture the fluorescence peaks in one channel, and the fluorescence minima in another channel. Since PAH fluorescence is expected to be broadband, these channels are subtracted and the broadband background is removed. One potential issue with this approach is that a significant portion of the formaldehyde emission exists in the off-peak channel, reducing signal level and signal-to-noise ratio of the measurements. Further, as will be shown in Chapter 3, the fraction of fluorescence intensity in the off-peak channel is temperature and pressure dependent resulting in a temperature- and pressure-dependent bias. The approach as proposed by Thering *et al.* [56] can eliminate the background signal from images, but alone is not suitable for quantitative formaldehyde mole fraction measurements due to these biases.

A more recent technique proposed to avoid bias from PAHs and other interfering species emission in formaldehyde PLIF measurements for diesel engines uses an on/off resonant excitation scheme [54]. The technique was applied successfully in a constant volume combustion chamber. The technique uses background subtraction of an average, off-resonance (*e.g.*, 350 nm) excitation image of interfering species emission where the formaldehyde absorption is expected to be negligible. The technique as implemented requires a separate experiment to estimate the time-averaged interfering emission, and is thus not suitable for single-shot, spatially- and temporally-resolved imaging. Taking near simultaneous interfering emission images would require a second tunable laser system and camera increasing the cost and complexity of the setup.

Like most fluorescent molecules, formaldehyde's absorption and emission spectrum exhibit a strong dependence on temperature. This is beneficial as the temperature dependence could be used for temperature measurement. On the other hand, significant temperature dependence can make quantitative concentration measurements much more difficult, particularly when background signals are present. The temperature dependence is likely the result of changes to the equilibrium rotational population distribution with temperature. Increasing temperature results in higher rotationally excited states becoming populated, and hence a broadening of the vibronic peaks.

Currently, highly accurate quantitative formaldehyde PLIF imaging in diesel engines has not been achieved due to uncertainties in spectral properties and interference from PAHs and other broadband sources. However, formaldehyde PLIF is routinely used qualitatively as an indicator of ignition [3, 57, 58].

2.4 Aerosol Phosphor Thermometry

Similar to molecular fluorescence, aerosol phosphor thermometry (APT) typically uses a laser or other light source to excite the phosphor to an excited electronic state. The phosphor then decays radiatively,

emitting a photon that is usually wavelength shifted from the excitation source. Phosphor emission can be described similar to molecular fluorescence with a few differences. First, since phosphors are composed of rare-earth ions doped into crystalline hosts, the absorption and emission are usually pressure independent, as the crystalline host is generally incompressible except at very high pressure. Further, phosphor emission is generally independent of the collisional environment as the ion is typically unable to interact with molecules outside of the host. Finally, APT techniques often operate outside the linear regime, such that phosphor emission intensity is not necessarily linearly proportional to excitation energy. Rather, there is typically a diminishing return in emission intensity with increasing laser energy. This can occur through several mechanisms. As excitation energy increases, the ground state population is depleted resulting in a nonlinear increase in signal with laser energy; this is typically the source of nonlinearity for molecular PLIF. More typically for phosphors, non-linearity can occur due to losses from the excited state, *e.g.*, due to excited-state absorption or through energy-transfer upconversion processes. Excited-state absorption (ESA), or photoionization of the excited state, is a relatively common effect in thermographic phosphors and solid-state laser materials (see *e.g.*, [59, 60]). As an example, Eu:BAM emission is nonlinear even for fluences as low as 10 mJ/cm^2 [61].

The luminescence signal, in photons incident per pixel, is given by the product of the number of phosphor particles N_p in a pixel volume V, the number of luminescence photons emitted per particle $S_{Lum,p}$, and the fraction of emitted photons collected $\Omega\eta/4\pi$, *i.e.*,

$$S_{Lum} = N_p S_{Lum,p} \frac{\Omega}{4\pi} \eta. \tag{2.3}$$

The number of luminescence photons emitted by a particle can be written as

$$S_{Lum,p} = N_{abs}(T)\Phi(\omega_0; T) \tag{2.4}$$

where N_{abs} is the number of photons absorbed by the ions in a particle into the desired upper state, and $\Phi(T)$ is the fluorescence quantum yield for emission from that state. Using these definitions and the particle number density (n_p) the collected luminescence signal can be written as

$$S_{Lum} = V n_p N_{abs}(\omega_0; T)\Phi(T) \frac{\Omega}{4\pi} \eta. \tag{2.5}$$

For the simplified case of excitation in the linear regime, assuming the laser fluence is uniform inside

the particles, the number of absorbed photons per particle can be written as

$$N_{abs} = \frac{E_p''}{\hbar\omega_0} N_{ion}\sigma(\omega_0; T) \tag{2.6}$$

where N_{ion} is the number of active ions per particle and $\sigma(\omega_0, T)$ is the ion absorption cross section at the laser frequency ω_0. The luminescence signal per pixel then becomes

$$S_{Lum} = \frac{E_p''}{\hbar\omega_0} V n_p N_{ion}\sigma(\omega_0; T)\Phi(T)\frac{\Omega}{4\pi}\eta. \tag{2.7}$$

This result is similar to that for linear LIF given by Equation 2.1 with the absorbing species number density replaced by the product of the particle seeding number density and the number of ions per particle.

Typically APT measurements use a two-color, single excitation wavelength ratiometric approach. This method has been performed in various scenarios with varying degrees of success. For example, Pr:YAG has been used with some success in in-cylinder studies [35] and in heated jet experiments [62]. Eu:BAM has been widely used for thermometry including in film cooling studies [63], in high-pressure cells [64], various heated jet geometries [65–67], and even in flame studies [68], with limited success. As another example, a relatively new tracer ZnO has also been characterized and applied using the ratiometric luminescence intensity ratio approach [69–71]. A more detailed review of phosphor thermometry is given by [72]. However, in all of these cases, gas-phase temperature measurements are limited to relatively low temperatures below 800 K. Two promising, recently proposed alternative techniques, co-doped APT [38] and scattering-referenced APT (SRAPT) [73], provide a possible solution for measurements at temperatures exceeding 1000 K.

The co-doped approach uses two different ions doped into the same host, where each ion has different quenching properties. Rather than measure changes in the emission spectrum shape, as with the LIR method, the entire emission of each ion is collected in a separate channel. The second ion adds another degree of freedom to the design process that can be used to further optimize the technique. The diagnostic sensitivity is controlled by the quenching behavior of the individual ions, and can be described mathematically in a straightforward manner following the analysis of [74].

Assuming a single exponential time decay for phosphor luminescence, and that the nonradiative rate follows an exponential dependence on the energy gap, the total emission intensity for either ion can be expressed as

$$S_{Lum} \propto \frac{N_{abs}}{1 + C_{nr} e^{-E/k_B T}}, \tag{2.8}$$

where N_{abs} is again the number of absorbed photons, $C_{nr} = {}^{k_{nr,0}}/_{k_r}$ is the ratio of the nonradiative transition attempt rate $k_{nr,0}$ to the radiative rate constant k_r. The final parameter in the equation is the characteristic energy gap for the deactivation process, E. The co-doped ratio is thus given by

$$R_{codoped} = \frac{S_{Lum,2}}{S_{Lum,1}} \propto \frac{N_{abs,2}}{N_{abs,1}} \frac{1 + C_{nr,1} e^{-E_1/k_B T}}{1 + C_{nr,2} e^{-E_2/k_B T}}. \tag{2.9}$$

The quantity ${}^{N_{abs,2}}/_{N_{abs,1}}$ is the ratio of emitted photons in the absence of quenching. The parameters E_1, E_2, $C_{nr,1}$, and $C_{nr,2}$ are determined by the selected ions and host, and can be chosen to optimize the temperature range and precision for a given experiment.

Alternatively, the SRAPT approach measures the ratio of the total phosphor emission intensity to the elastic scattering intensity. This is advantageous because all of the emitted light from the phosphor is captured. Further, since elastic scattering is likely already being captured for velocimetry, this technique reduces experimental complexity compared to the LIR method for simultaneous velocity and temperature measurements. The SRAPT technique can also be optimized for a specific temperature range by appropriate selection of quenching properties for host-ion combinations. Since the elastic scattering and phosphor emission do not have the same dependence on particle diameter, there is an additional random uncertainty related to the particle size distribution. However, even with this additional uncertainty the technique has been demonstrated to be capable of high-precision measurements at elevated temperatures [73]. Similar to the co-doped technique, the ratio can be expressed analytically with the additional assumption that scattering intensity is independent of temperature. The SRAPT ratio can be approximated as

$$R_{SRAPT} = \frac{S_{Lum,2}}{S_{sc}} \propto \frac{N_{abs,2}}{S_{sc}} \frac{1}{1 + C_{nr,2} e^{-E_2/k_B T}} \tag{2.10}$$

where the subscript "*sc*" is used to indicated the elastically scattered light. As before, the constant prefactor $({}^{N_{abs,2}}/_{S_{Mie}})$ is the ratio at absolute zero, such that the normalized ratio depends only on the quenching properties of the selected host and ion combination, $C_{nr,1}$ and E_1.

Chapter 3

Photophysical Characterization of Formaldehyde

In order to measure formaldehyde concentration quantitatively, it is imperative that we have a good understanding of the photophysical properties at the conditions where we're interested in making measurements. In particular, from the PLIF equation (Equation 2.1, and the spectrally-resolved version in Equation 2.2), the absorption cross-section and fluorescence quantum yield controls much of this behavior. Both quantities are generally temperature, pressure, and concentration dependent.

Some measurements of formaldehyde photophysical properties have been made (*e.g.*, in [45, 47]), although due to the molecule's complexity, many properties still are unknown. In particular, the temperature, pressure, and excitation wavelength dependence of the absorption cross-section at engine-relevant conditions is largely unknown, and few measurements have been made of fluorescence quantum yield at elevated temperature and pressure. This chapter will detail the results of recent investigations of formaldehyde photophysical parameters. This includes modeling work to predict properties (the absorption cross-section in particular), and experimental work where fluorescence emission bandshapes were measured at relevant conditions. The proposed combined APT/PLIF diagnostic uses a ratiometric formaldehyde imaging approach (this will be discussed in detail in Chapter 7), so ratiometric formaldehyde PLIF measurements will be presented and discussed as well.

Table 3.1: Engine hardware specifications

Parameter	Value	Unit
Effective Compression Ratio	12.0	-
Geometric Compression Ratio	13.9	-
Displacement	0.402	L
Bore	84.4	mm
Stroke	76.2	mm
Connecting rod length	144.8	mm
IVC/EVO/IVO/EVC	-164/164/347/375	CAD

3.1 Experimental Setup

Experimental formaldehyde PLIF characterization was performed in an optically accessible engine. The engine itself was designed in-house. The engine has a single cylinder, a centrally-located fuel injector, and is optically-accessible through the side of the piston for laser sheet access, and the top of the piston for imaging access. A UV-enhanced aluminum mirror is held at 45° to direct light transmitted from the piston window towards an optical table where imaging equipment is mounted. Engine geometry information is provided in Table 3.1, and a cross-sectional view of the engine is shown in Figure 3.1 with important features called out.

The PLIF investigation primarily focused on measuring formaldehyde emission spectra at various operating conditions. Formaldehyde was generated in the engine via low temperature ignition of n-heptane, while avoiding the onset of high-temperature ignition. This resulted in a narrow range of operating conditions where formaldehyde spectra could be measured. Once formed, the formaldehyde is excited with an ultraviolet laser sheet, and the resulting emission is captured via a spectrometer. The vast majority of the observed emission is believed to be from formaldehyde.

The optical setup is shown schematically in Figure 3.2. The laser source is a flash-lamp pumped Q-switched Nd:YAG laser operating at 10 Hz (Spectra Physics GCR-170). The third harmonic output at 355 nm is formed into a narrow sheet, approximately 2 cm wide and 0.5 mm thick, using three sheet forming optics. The sheet is formed primarily by a -100 mm focal length cylindrical lens followed by a 500-mm focal length spherical lens. A final 200-mm focal length cylindrical lens is used to correct for the distortions introduced by the curvature of the windows in the engines. The engine windows are made of UV-grade fused silica, but are not anti-reflection coated. At 355 nm, the estimated reflection coefficient per surface is 4%. A 361-nm longpass filter (Semrock Inc., BLP01-355R-50.8-D) was placed in front of the lens used to collect and focus light into the spectrometer to reject scattered laser light. The ICCD

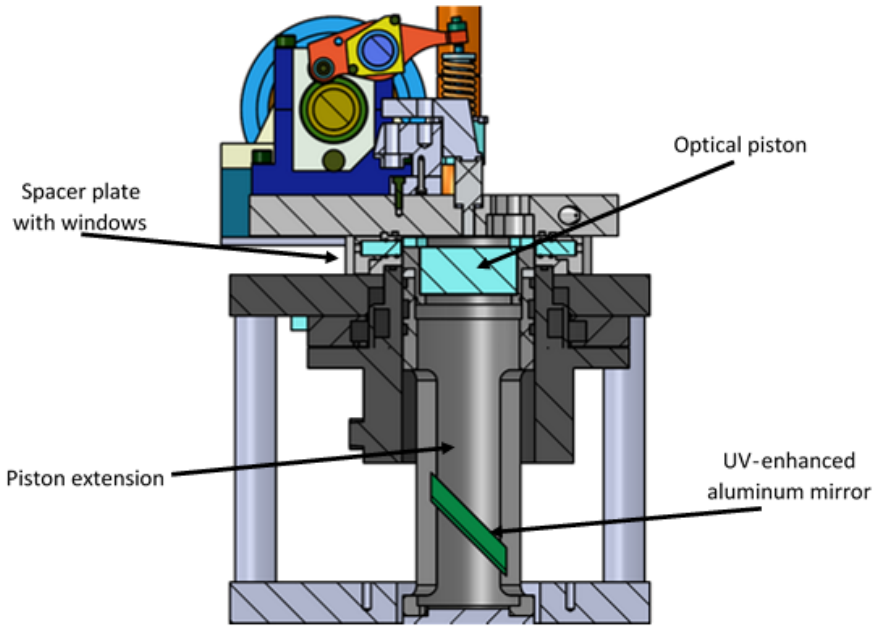

Figure 3.1: Cross-sectional view of the optical engine with features called out.

camera was gated on for 100 ns, starting approximately 20 ns before the arrival of the laser pulse.

The collection optics consist of a single 50-mm $f/1.2$ Nikon Nikkor lens used to focus light onto a 1-mm diameter fiber optic bundle that connects to the spectrometer entrance slit. On the slit end, the 19 fibers that compose the bundle are spread into a line along the length of the slit. The lens is focused to collect light originating in an approximately 6-mm diameter region in-cylinder positioned between the injector tip and the piston side window (through which the laser sheet exits the engine). The spectrometer (300-mm focal-length; Acton SP2300i) was outfitted with an intensified CCD camera (Princeton Instruments, PI-Max4 1024i-HB-FG-18-P46). The spectrometer used a diffraction grating with 1200 groove/mm and a 500 nm blaze wavelength. The spectral resolution for the 1200 groove/mm grating was measured to be 0.44 nm, as estimated from the full-width at half-maximum of a mercury vapor lamp spectral line (H-line, 404.7 nm).

A single spectral measurement is collected per cycle, and the data reported is an ensemble average over 200 measurements. Since the spectral resolution was relatively high, only a portion of the 380-500 nm range of the emission spectrum is collected in one measurement due to the limited size of the imaging sensor; six measurements are needed to cover the 380-500 nm range. The spectra are collected in portions and stitched together to form a single continuous measurement. In total, 1200 cycles or measurements are needed to measure the full emission spectrum at a given condition. All spectral measurements are corrected for relative spectral response using a quartz tungsten halogen lamp (Spectra Physics, Model 6319 20W QTH). A wavelength calibration is performed before collecting data using a mercury vapor

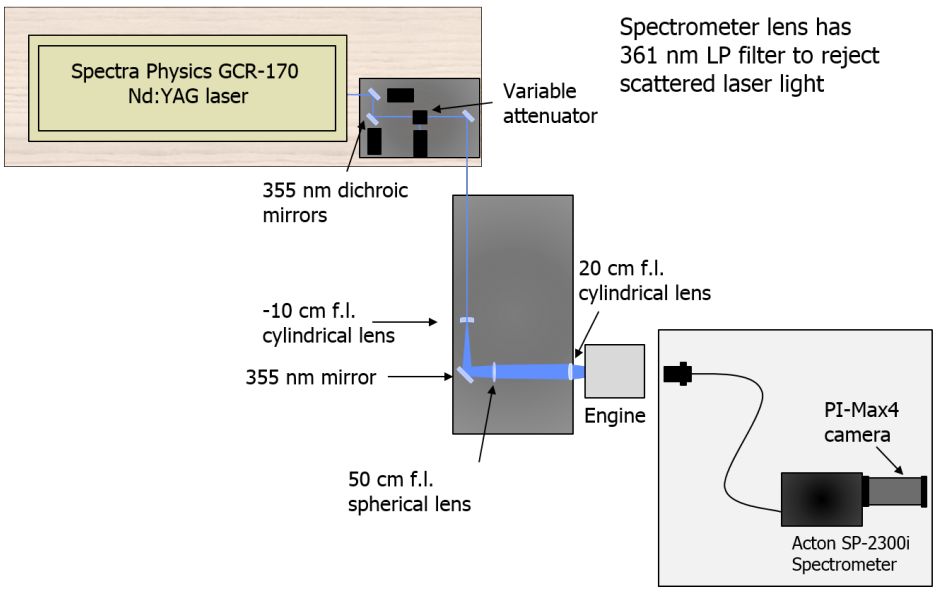

Figure 3.2: Experimental setup diagram for formaldehyde spectroscopy measurements

lamp.

3.1.1 PLIF Imaging Measurements

An additional set of imaging measurements were taken using a ratiometric technique based on the filter bands chosen by Thering *et al.* [56]. The spectrometer was replaced with two cameras separated by a beamsplitter (broadband 50% transmission/50% reflection). The experimental setup diagram is shown in Figure 3.3. Each camera has an 11-band formaldehyde imaging filter (Semrock Inc., FF01-CH2O) placed in front of it. One filter is held at normal incidence to the camera, and the other filter is held at a 15° angle of incidence. Changing the angle of incidence shifts the transmission bands of the filter. The normal incidence filter is setup to capture the peaks of the formaldehyde emission, while the tilted filter captures the valleys. The transmission bands of the filter, with a formaldehyde emission spectrum superimposed, are shown in Figure 3.4. These are the same filters used in [56], and are the filters that will be used for the proposed ratiometric background procedure that will be discussed in Chapter 7.

Both cameras are the same model (Princeton Instruments, PI-Max4 1024i-HB-FG-18-P46) and are outfitted with identical 85-mm Nikon Nikkor $f/1.4$ lenses. The PLIF images are formed into a ratio, which is related to temperature. Each image is flatfield corrected using the average image taken at a reference condition. The reference image is taken from an identical experiment at a known temperature and pressure. The flatfield-corrected PLIF images are then registered on an image-by-image basis to reduce the effect of camera shake resulting from engine vibrations. The images are resampled using

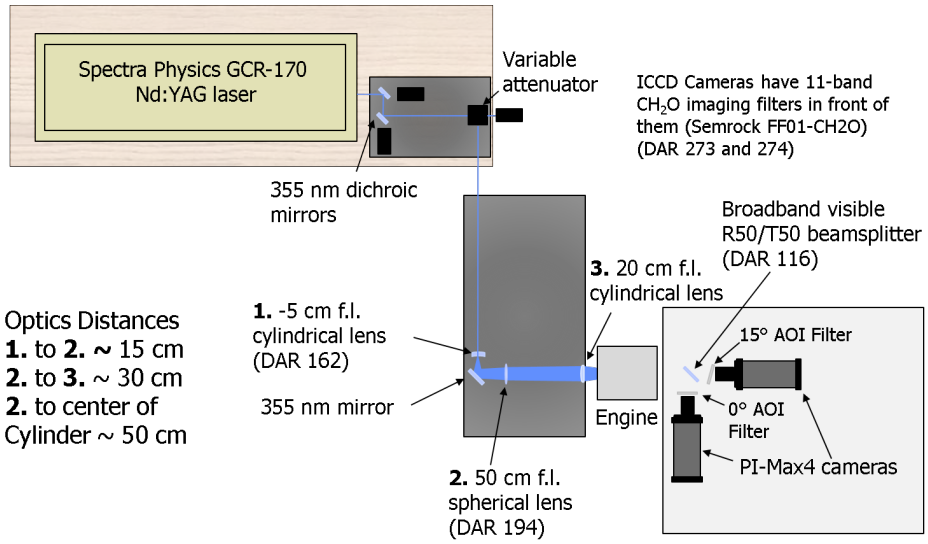

Figure 3.3: Experimental setup diagram for formaldehyde PLIF ratio imaging experiments.

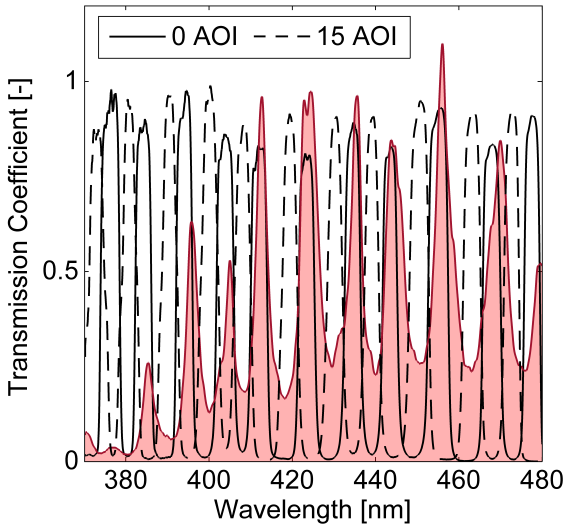

Figure 3.4: Transmission bands of the 11-band formaldehyde imaging filters. Transmission bands are shown in black curves; the formaldehyde spectrum is represented by the shaded red region.

a bicubic interpolation scheme. The ratio is then formed by dividing the two images on a per pixel basis. The known reference condition used for this data is 875 K and 30 bar. The temperature used in the calibration procedure was determined by isentropic compression of the air-fuel mixture, neglecting chemistry.

3.2 Spectral Modeling

Development of an effective diagnostic using PLIF naturally requires an understanding of the underlying physics that describes the absorption, energy transfer, and emission processes. To that end, this section outlines a spectral model for formaldehyde used to predict and describe the temperature- and pressure-dependence of formaldehyde spectroscopy to aid in the design of a formaldehyde imaging diagnostic. The spectral modeling results are used to estimate formaldehyde fluorescence properties and engine-relevant conditions.

The absorption cross-section and spontaneous emission intensities are calculated using a set of models in the Born-Oppenheimer approximation using the combined Franck-Condon Herzberg-Teller approach (these assumptions are discussed in detail and results are derived in Appendix B.1). Specifically, this assumes that electronic, nuclear vibrational, and nuclear rotational motions are separated with the exception of vibronic coupling which is included to first order. The full absorption cross section (σ) and spontaneous emission intensity (ϵ) per molecule are given by the sum over all possible transitions with transition frequency ω, weighted by the population fraction or probability for the initial state (F_i). These are given by

$$\sigma(\omega) = \frac{4\pi^2\alpha\omega}{3e^2}\sum_{ij} F_i(p,T)\ I_{ev}\ I_r\ \mathcal{L}(\omega;\omega_{ij},T,p) \tag{3.1a}$$

$$\epsilon(\omega) = \frac{4\hbar\omega^4\alpha}{3c^2e^2}\sum_{ij} F_i(p,T)\ I_{ev}\ I_r\ \mathcal{L}(\omega;\omega_{ij},T,p) \tag{3.1b}$$

where $\mathcal{L}(\omega)$ is the assumed lineshape function. The constants α and e are the fine structure constant and the electron charge, respectively; I_{ev} and I_r are the vibronic transition intensity factor (this can be thought of as the product of a Franck-Condon-like factor and a transition dipole moment; see Appendix B.1 for derivations), and the rotational transition intensity factor (also called the Honl-London factor [75]; see Appendix B.2 for derivations), respectively. Here the subscripts i and j represent the initial and final rovibronic states, respectively, and the sums are performed over every combination of rovibronic states. The population fraction F_i is the probability of a molecule being in state i and is temperature

and pressure dependent in general. For LIF emission, it is also dependent on the excitation wavelength. The lineshape function is also pressure and temperature dependent, and is centered at the most likely transition frequency $\hbar\omega_{ij} = E_j - E_i$.

For the results calculated here, the formaldehyde molecule is assumed to be an asymmetric rigid rotor, with five uncoupled harmonic oscillators and one anharmonic oscillator for the out of plane bending mode in the $\tilde{A}\ ^1A_2$ states, as this mode has been shown to be strongly anharmonic [76]. Although these approximations are not able to provide an accurate estimate of vibronic band intensities, they are believed to be sufficient to investigate the temperature and pressure trends of the absorption cross-section at fixed wavelength.

3.3 Absorption Cross-Section Estimates

Absorption cross-sections were estimated using the theory presented in Section 3.2 and Appendices B.2 and B.3, with spectroscopic data taken from both *ab initio* simulations and literature (the data set is tabulated in Appendix C). From Figure 2.2, the vibrational transition being excited at 355 nm is the 4_0^1 transition (v_m^n denotes a transition where vibrational mode v has n vibrational quanta in the excited $\tilde{A}\ ^1A_2$ state and m quanta in the ground $\tilde{X}\ ^1A_1$ state; $v = 4$ corresponds to the out-of-plane bending mode); this peak is relatively isolated from other vibronic transitions. As such, the shape of the peak is the result of many closely spaced rotational lines, with little or no interference from other vibronic transitions. The absorption cross-section band can then be written as

$$\sigma(\omega;T) = \frac{4\pi^2\alpha\omega}{3e^2} I_{ev} \frac{e^{-\mathcal{G}_{4_0}/k_BT}}{Z_v} \sum_{J'}\sum_{J''}\sum_{K'}\sum_{K''} \frac{e^{-\mathcal{F}_{J',K'}/k_BT}}{Z_r} I_r \delta(\omega - \mathcal{F}_{J'',K''} + \mathcal{F}_{J',K'}) \tag{3.2}$$

where $\mathcal{F}_{J,K}$ and G_{4_0} are the rotational and vibrational energies, and the symbols Z_v and Z_r represent the vibrational and rotational partition functions. In this notation, a single prime ($'$) denotes a quantum number of the initial ($\tilde{X}\ ^1A_1$) state, and a double prime ($''$) denotes the excited ($\tilde{A}\ ^1A_2$) state. Finally, since the transition dipole moment is zero at the equilibrium configuration, the vibronic transition strength I_{ev} is the product of the effective transition dipole moment squared, and the Franck-Condon factor for the transition. Specifically,

$$I_{ev} = \left|\frac{\partial\mu}{\partial q_4}\right|^2 \times |\,\langle \tilde{A}\ ^1A_2\ 4^1|q_4|\tilde{X}\ ^1A_1\ 4_0\rangle\,|^2 \tag{3.3a}$$

where

$$\left|\frac{\partial \mu}{\partial q_4}\right| = 0.17 \text{ Debye} \tag{3.3b}$$

and

$$|\langle \tilde{A}\ ^1A_2\ 4^1|q_4|\tilde{X}\ ^1A_1\ 4_0\rangle|^2 \approx |\langle 4^1|q|4_0\rangle|^2 \times |\langle 2^0|2_0\rangle|^2 \approx 6 \times 10^{-4}, \tag{3.3c}$$

where the Franck-Condon factors on the right hand side of Equation 3.3c are evaluated using the theory presented in Appendix B.3, using the harmonic approximation for all modes except the out-of-plane bending mode which uses a double-well potential (implemented as a Gaussian perturbation). The Franck-Condon factor is primarily controlled by the out-of-plane bending mode and the C-O stretching mode. This follows because the C-O bond is elongated and the out-of-plane bending mode undergoes a change in the shape of the potential energy surface upon excitation. The other four modes are largely unaffected. The photon frequency of the transition is approximately 28,312 cm^{-1} [77]. The vibrational partition function is calculated in the harmonic oscillator approximation as

$$Z_v = \prod_j \left(\frac{1}{1 - e^{-\hbar\omega_j/k_BT}}\right), \tag{3.4}$$

where ω_j is the vibrational frequency of mode v_j (there are six modes in total for formaldehyde). The rotational partition function is calculated in the rigid-rotor high-temperature limit as

$$Z_r = \frac{1}{2}\sqrt{\frac{\pi k_B^3 T^3}{\hbar^3 abc}}, \tag{3.5}$$

where a, b, and c are the spectroscopic rotational constants of the molecule in its initial state (tabulated in Table C.3).

A simulated absorption spectrum was calculated and is presented for comparison with experimental data in Figure 3.5. The simulated spectra in Figure 3.5 are divided by a factor of 3.5 to better match the experimental results from Chance 2011 [45]; the disagreement in magnitude is unsurprising because of the level of approximation required to calculate the spectrum (in particular the approximations used for the Franck-Condon factor calculation). Higher order rigid-rotor parameters are included in the calculation using data from [77]; in particular, the centrifugal distortion constants Δ_J, Δ_K, and Δ_{JK} are included. The transition dipole moment derivative used in the calculation is in entirely along the b axis. Pressure broadening with a width of 0.45 cm^{-1} (approximately corresponding to a pressure of 3 bar) is included to better match the data. Besides the difference in magnitude, many of the features of the absorption spectrum are captured well; one obvious exception is that some transitions near 355

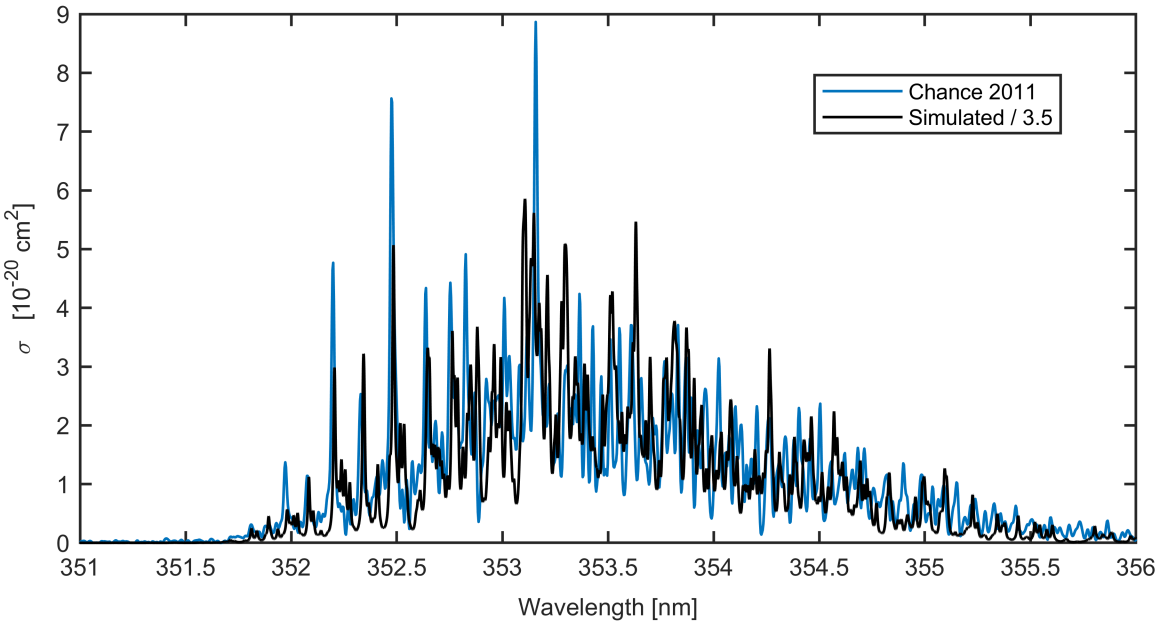

Figure 3.5: Comparison of measured and simulated absorption cross-sections of formaldehyde. The simulated spectra are divided by a factor of 3.5 to better match the measured value.

nm are shifted relative to the measured value. The theory presented captures the general trends of the absorption cross-section, but not the precise magnitude.

Several additional spectra are calculated to illustrate the temperature dependence of the absorption cross-section and are plotted in Figure 3.6 at a pressure of 30 bar, assuming the pressure broadening constant is 0.15 cm^{-1}/bar (consistent with the value reported by [78]; similar magnitudes were also reported by [79]). From the plot, the absorption cross-section at 355 nm increases slightly from 300 K to about 500 K or so before dropping monotonically due to the increasing partition function at higher temperatures.

Absorption spectra are available from [45] at 280 and 290 K, and can provide another estimate of temperature dependence (at least locally near 300 K). In the left of Figure 3.7, the absorption cross-section spectra at 280 and 300 K from [45] are divided by the spectrum at 290 K to show the relative change with temperature. Although there is a lot of high-frequency variation, cross-sections at excitation wavelengths near the peak (∼353 nm) clearly decrease with temperature, while at wavelengths away from the peak they increase. This is consistent with the simulation (shown in comparison with experimental data on the right side of Figure 3.7, where the data was filtered with a Lorentzian profile to simulate pressure broadening at 30 bar) where similar trends and magnitudes are observed, although the simulated P-branch appears to be shifted relative to the measurement.

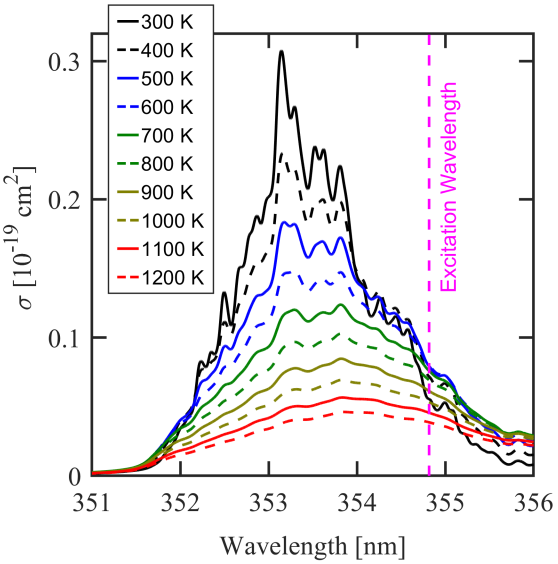

Figure 3.6: Calculated formaldehyde absorption cross-section at 30 bar from 300 to 1200 K. The simulation results were divided by a factor of 3.5 to match experimental data.

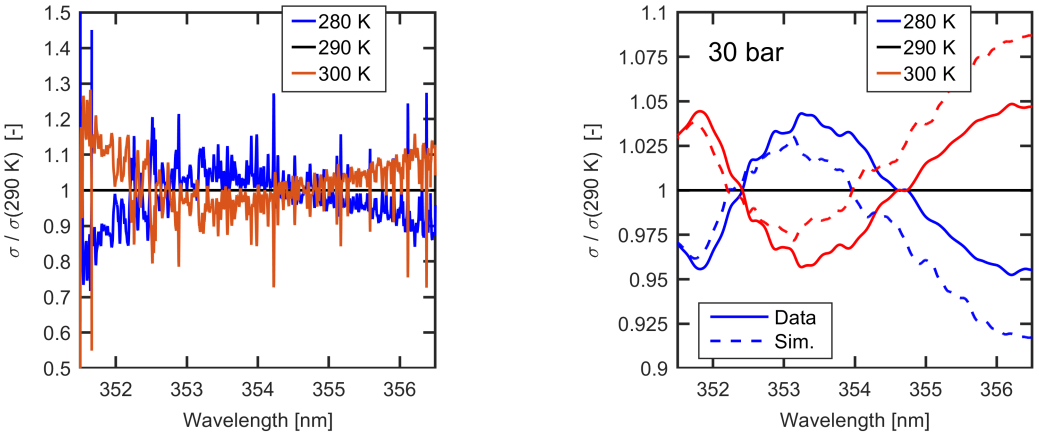

(a) Experimental data [44, 45]

(b) Comparison with simulation

Figure 3.7: Formaldehyde absorption cross-section at 280 and 300 K, normalized by the absorption spectrum at 290 K for experimental data.

Assuming only a single rotational transition is excited, the absorption cross-section can be normalized to its value at a reference condition, and written as

$$\frac{\sigma(T)}{\sigma(T_0)} = \frac{Z_v(T_0)}{Z_v(T)} \frac{Z_r(T_0)}{Z_r(T)} \exp\left(- \frac{F_{J',K'}}{k_B} \left(\frac{1}{T} - \frac{1}{T_0} \right) \right) \tag{3.6}$$

where the fact that we're exciting the vibrational ground state has been used and the vibrational population fraction is simply the inverse of the vibrational partition function (excluding the zero-point energy). In reality, multiple lines likely contribute to the absorption, particularly with an assumed laser line width of 1 cm^{-1}. (Line spacings are typically less than 1 cm^{-1}, as observed in [78].) However, the scaling depends only on the rotational energy level of the initial state, or the parameter $\mathcal{F}_{J',K'}$; the approximation is valid so long as the initial rotational states have similar energy levels. Or, more generally, $\mathcal{F}_{J',K'}$ could be temperature dependent to allow for excitation of multiple lines with slightly different initial energy levels as expected here. This approach, assuming only a single absorption transition is excited, has been applied for formaldehyde PLIF imaging correction before with parameters based on rigid asymmetric rotor models and theory [80].

The simulated absorption cross-sections as a function of temperature for the Nd:YAG 3rd harmonic (355 nm, or more precisely 28,184 cm^{-1}) are plotted in Figure 3.8a, normalized to their value at 300 K, with Equation 3.6 superimposed. In this plot, $\mathcal{F}_{J',K'}$ is a linear function of T, and was determined by a linear least squares fit to the simulation data. Equation 3.6 appears to describe the behavior of the absorption cross-section well, and there appears to be minimal pressure dependence. The fit result suggests the initial rotational energy level increases as temperature is increased. This is consistent with theory; as temperature increases, higher rotational levels are activated. Since rotational line strengths increase with the initial rotational quantum number J, it follows that the average energy of the initial state increases with temperature. Since the temperature dependence of the simulated spectra appear to be shifted relative to the measurements from [45], the analysis is repeated for the experimental data and the fit result is shown in Figure 3.8b. In the plot, the curves indicate the values predicted by Equation 3.6, and the experimental data points are taken from [45] after filtering to simulate a 30 bar pressure. The data from [45] appears to be represented well by Equation 3.6, but with a slightly lower parameter $\mathcal{F}_{J',K'} = 330$ cm^{-1}.

The simulation data shows that Equation 3.6 describes the temperature dependence of the absorption cross-section well. Pressure broadening does not appear to strongly affect the temperature trend. Using the experimental data from [45], the effective rotational energy level being excited at 290 K was found to be 330 cm^{-1}. For performance prediction calculations, the temperature dependence of the absorption

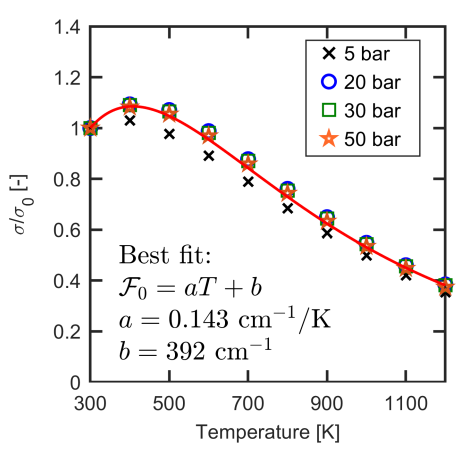

(a) Simulation data and best fit

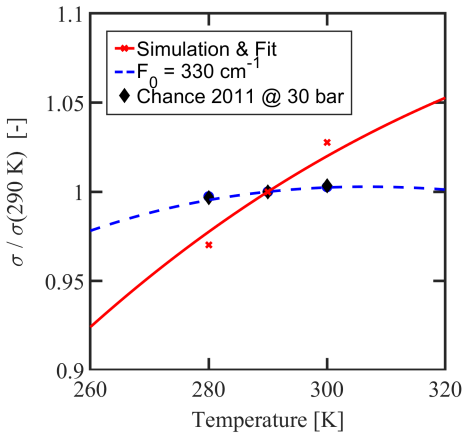

(b) Experimental data at 280-300 K, with simulation fit superimposed

Figure 3.8: Simulated temperature dependence of formaldehyde absorption cross-section at 355 nm. Absorption cross-sections are normalized to the value at 300 K. Solid lines are fits to Equation 3.6, and the best-fit initial energy $\mathcal{F}_0$ is used in place of $\mathcal{F}_{J',K'}$ in Equation 3.6. The simulation fit is compared to experimental data from 280-300 K in (b); although the simulation data fit did not include points at $T < 300$ K, the fit captures the low-temperature simulation results reasonably well (simulation results at 280, 290, and 300 K are included on the plot for comparison).

cross-section at the Nd:YAG 3rd harmonic wavelength is assumed to obey Equation 3.6 with $\mathcal{F}_{J',K'}$ being a linear function of temperature. The value of $\mathcal{F}_{J',K'}$ at 290 K is taken as 330 cm^{-1} (from the measured spectra [45]) and the slope of $\mathcal{F}_{J',K'}$ is taken as 0.143 cm^{-1}/K (from the simulation data). This combination is chosen because it represents a compromise between extrapolation of the 280-300 K data with a constant value of $\mathcal{F}_{J',K'}$ (which provides a lower limit on absorption cross-section) and the simulation data (which provides an upper limit). The resulting temperature dependence is plotted in the left panel of Figure 3.9 as a solid line, while the simulation fit and constant $\mathcal{F}_{J',K'}$ assumption are superimposed as dashed curves. From the plot, the absorption cross-section drops by almost a factor of 4 between 300 and 1200 K, although it may be slightly more or less depending on the values of $\mathcal{F}_{J',K'}$ chosen.

Unseeded flashlamp-pumped Nd:YAG lasers typically have line widths < 1 cm^{-1}, which is relatively large compared to the formaldehyde absorption cross-section linewidths. The large line width may have an impact on the absorption process. The absorption spectrum, with a Lorentzian fit to the absorption peak near the Nd:YAG third harmonic, is shown in the left of Figure 3.10 in relation to the laser line location. The spectrum is extrapolated to zero pressure (from [44, 45]), but is not fully rotationally-resolved. From the plot, the absorption peak is almost a perfect Lorentzian function, and the laser line lies almost directly on top of the peak (the shift is small compared to the assumed width of both peaks). Although this spectrum shows a smooth and broad peak, there is additional rotational structure that

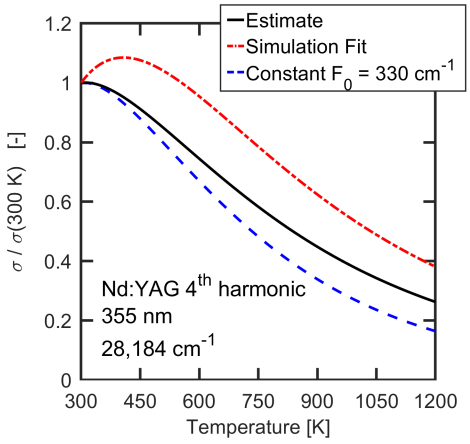

Figure 3.9: Assumed temperature dependence of the formaldehyde absorption cross-section at the Nd:YAG 3rd harmonic wavelength.

appears to be under-resolved (as observed in [78]). Assuming the laser line shape is also Lorentzian, the overlap integral (and hence total absorption cross-section) can be estimated at high pressure as

$$\sigma = \int_{\mathcal{R}} \frac{\sigma_{\max}\gamma_p^2}{(\nu-\nu_0)^2+\gamma_p^2} \cdot \frac{\gamma_L}{\pi} \frac{1}{(\nu-\nu_0)^2+\gamma_L^2}\, d\nu = \frac{\sigma_{\max}}{1+\frac{\gamma_L}{\gamma_p}} \tag{3.7}$$

where ν_0 is the location of the Lorentzian peak, γ_L and γ_p are the Lorentzian width parameters of the laser and absorption peaks, respectively, and $\sigma_{\max}$ is the maximum value of the absorption peak (1.604×10^{-20} cm^2). The laser line width is taken as 1 cm^{-1} and for simplicity the absorption peak width is taken as $\gamma_p = \gamma_p' p$ (where γ_p' is the pressure broadening coefficient of 0.15 cm^{-1}/bar and p is the pressure). This naturally ignores the complicated nature of the rotational structure, but at higher pressures the approximation should be valid. The pressure dependence of the absorption peak is calculated and plotted in the right of Figure 3.10. From the plot, accounting for the relatively large line width of the laser, there may be significant pressure dependence in the absorption cross-section at low pressures, but at typical engine pressures (above ~20 bar) the absorption cross-section has little dependence on pressure.

For performance estimation, Equation 3.6 will be used to estimate the absorption cross-sections at higher temperatures using the value $\mathcal{F}_{J',K'} = 330$ as determined from the low-temperature spectra. The 300 K absorption cross-section will be assumed to be pressure-dependent according to Equation 3.7 and the results plotted in Figure 3.10, and performance estimates will be restricted to pressures above ~ 20 bar.

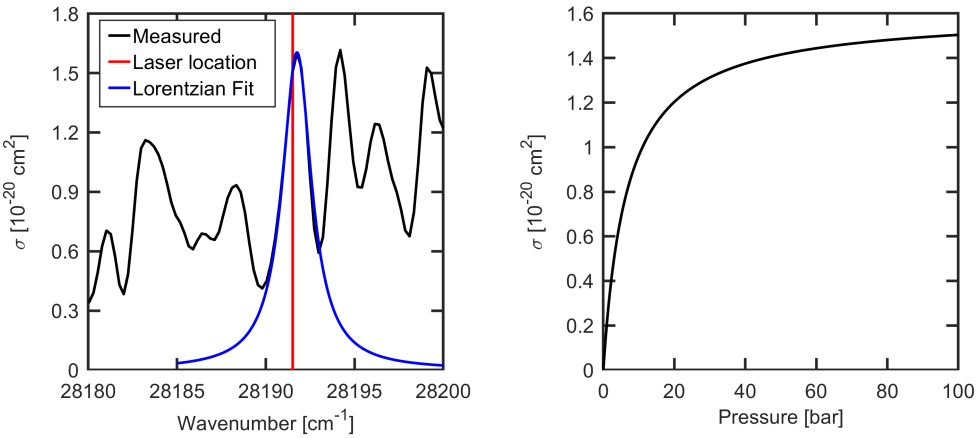

Figure 3.10: Left: formaldehyde absorption spectrum near the Nd:YAG 3rd harmonic (from [44, 45]) extrapolated to zero pressure. Right: calculated pressure dependence of the formaldehyde absorption cross-section at the Nd:YAG 3rd harmonic wavelength with an assumed laser line width of 1 cm^{-1}.

3.4 Fluorescence Quantum Yield Estimates

From the PLIF equation (Equation 2.2), the absorption cross-section, fluorescence quantum yield (FQY), and emission spectrum bandshape are all necessary to make a quantitative formaldehyde measurement. In this section, FQY values are discussed at conditions that are relevant for diagnostic performance prediction. The fluorescence quantum yield is equal to the fraction of electrons that deactivate radiatively after being excited. Specifically, it is given as

$$\Phi = \frac{k_r}{k_r + k_{nr}} = k_r \tau, \tag{3.8}$$

where the radiative rate k_r is defined in Equation 3.1b (divided by photon energy, $\hbar\omega$, to get the rate). Further, τ is the fluorescence lifetime (inverse of the total deactivation rate), and k_{nr} is the total non-radiative deactivation rate. The non-radiative rate can be a result of collisional quenching, intersystem crossing, or internal conversion. Internal conversion and intersystem crossing, and their associated rate constants, are discussed in Appendix B.4. Collisional quenching is more difficult to describe quantitatively so experimental results will be used to estimate lifetimes.

The radiative deactivation rate of formaldehyde from the 4^1 has been reported as $k_r \approx 435$ kHz ($\tau_r \approx 2.3$ µs) [81]. This value is consistent with theory and the spectroscopic parameters presented in this thesis (calculated $k_r \approx 340$ kHz). The nonradiative rate (at zero pressure; due to internal conversion and intersystem crossing) has been reported as 11.8 MHz ($\tau_{nr} \approx 85$ ns) [81]. The zero pressure fluorescence quantum yield is thus 0.035 using the observed rates, and the intrinsic lifetime of the excited state is about 82 ns. Estimates for diagnostic design calculations in Chapter 7 will use

$\tau_r = 2.3$ µs.

Collisional quenching is a signficant loss mechanism for formaldehyde fluorescence. Measurements of fluorescence lifetime have been made in several studies [47, 48] in nitrogen (although [48] also explores other gases including helium, oxygen, dimethyl-ether, and carbon dioxide). In particular, [48] developed a kinetic model describing collisional quenching, in which the effective decay rate (inverse fluorescence lifetime) can be written as

$$\tau^{-1} = k_f + (k_a + k_q)p - \frac{k_a k_b}{k_b p + k_p} p^2 \tag{3.9}$$

where p is the pressure of the bath gas, k_f is the decay rate of the excited state at zero pressure (based on the 82 ns lifetime, this would have the value of 12.3 MHz). The model assumes that electrons are transferred from the excited state $\tilde{A}$ to a collisionally excited state $\tilde{A}^\star$ with a rate k_a and reverse rate k_b. The collisionally excited state $\tilde{A}^\star$ deactivates spontaneously to the ground state $\tilde{X}$ with rate k_p. Direct collisional quenching from $\tilde{A}$ to $\tilde{X}$ occurs with rate k_q.

Although values for the rate constants are provided in [48], the fits are only performed at low pressures, up to around 1.5 bar. Further, there appears to be an error in the printed values. As such, the decay rate constants in nitrogen published in [47, 48] were fit to the model (Equation 3.9) using a 2D linear least squares algorithm. Temperature was included as the second dimension of the fit by making the k_a, k_b, and k_q parameters temperature dependent using an Arrhenius expression,

$$k_i = k_{i,0} e^{-\Theta_i / T} \tag{3.10}$$

as suggested in [48]. The resulting fit surface is shown below in the left of Figure 3.11, and the individual measurements are shown plotted against pressure on the right. From the plots, the model does indeed represent the results well, in particular matching those from [47] over much of the range. The results from [48] show more disagreement (in particular the Yamasaki 500 K data series), but also cover a smaller range and hence do not impact the fit results as much.

The best-fit parameters are tabulated in Table 3.2, along with the radiative rate from [81]. A few interesting features are observed in the parameters. First, k_f, the zero-presure rate, is almost a factor of 2 larger than the value found by [81]. As a result, the fit may not be representative of the low temperature and very low pressure behavior of formaldehyde. Additionally, the rate of collisional quenching from $\tilde{A} \rightarrow \tilde{X}$ is very low compared to the rate of quenching through the $\tilde{A}^\star$ state. The activation temperature of k_a is relatively large ($\Theta_a = 1950$ K $\rightarrow E_a \approx 1360$ cm^{-1}) and could correspond to activation of a number of formaldehyde's vibrational modes.

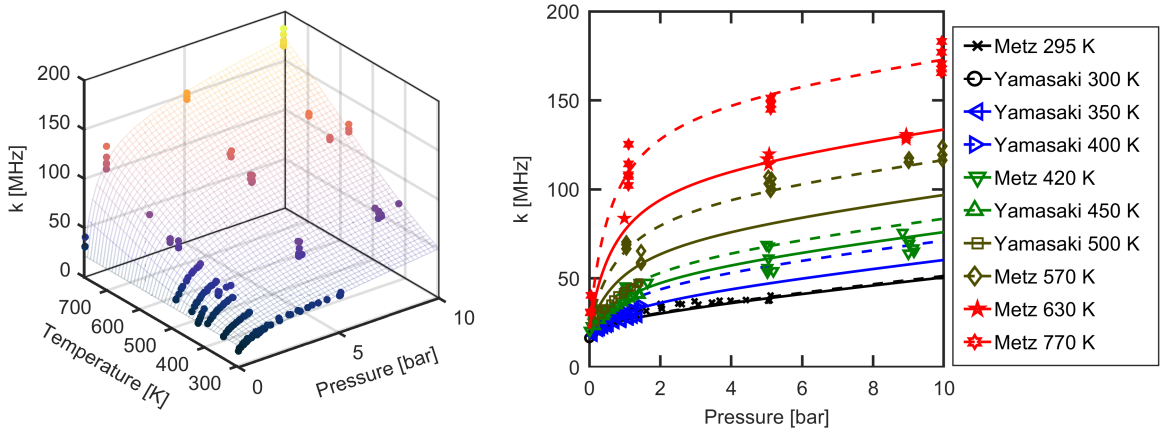

Figure 3.11: Measured formaldehyde fluorescence decay rates from the 4^1 vibrational state from Metz [47] and Yamasaki [48], with best-fit surface superimposed.

Table 3.2: Best-fit parameters for formaldehyde collisional quenching model. The radiative rate constant k_r is also included in the table for comparison, and is taken from [81].

Parameter	**Value**	**Units**
$k_{a,0}$	2718	MHz/bar
$k_{b,0}$	98.8	MHz/bar
$k_{q,0}$	3.2	MHz/bar
k_f	21.8	MHz
k_p	23.9	MHz
Θ_a	1953	K
Θ_b	716	K
Θ_q	121	K
k_r	0.45	MHz

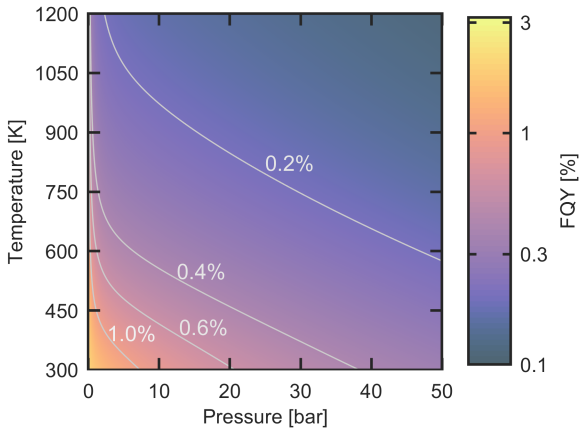

Figure 3.12: Calculated fluorescence quantum yield of formaldehyde in nitrogen as a function of temperature and pressure.

The fluorescence quantum yield of formaldehyde in nitrogen was calculated as a function of temperature and pressure using the model presented in Equation 3.9 and the best-fit parameters (listed in Table 3.2) and is plotted in Figure 3.12. At most, a couple percent quantum yield is possible at very low pressure and temperature. Above 10 bar, and above 800 K, the model is being extrapolated and may not be reliable. However, the extrapolation predicts a pressure dependence of approximately $\Phi \approx p^{-1}$, since at high pressure the deactivation rate becomes proportional to pressure. High pressure data is only available for nitrogen as a bath gas, so experiment design calculations will assume the bath gas is nitrogen for simplicity.

From the analysis and results presented by Yamasaki [48], oxygen in the high pressure limit quenches formaldehyde much more effectively than nitrogen. Specifically, Equation 3.9 in the high pressure limit becomes

$$\tau^{-1} = k_f + \frac{k_a}{k_b} k_p + k_q p, \tag{3.11}$$

and using the fit results from [48] at room temperature, the ratio k_a/k_b is approximately 4 times larger for oxygen than nitrogen, and k_q is approximately 7 times larger in oxygen than in nitrogen. On average, from pressures of 2 to 20 bar at room temperature, oxygen quenching is around 5 times as effective as nitrogen. Treating air as a mixture of nitrogen and oxygen (80% and 20%, respectively), the results from [48] can be used to show that the lifetime of formaldehyde in air is around 2.3 times smaller than the lifetime of formaldehyde in nitrogen at high pressures (on the order of 100 bar or larger total pressure) at 300 K. At 800 K, extrapolating based on the temperature fits for O_2, the lifetime of formaldehyde in air in the high pressure limit is reduced by around a factor of 3.5, and at 1000 K it is a factor of 4. Thus, for typical air mixtures at engine relevant pressures, the formaldehyde lifetime is approximately 25-30%

of the lifetime in nitrogen. This fact will be used later in Chapter 7 in regard to formaldehyde detection limits; specifically, the fits discussed in this chapter will be used to determine the FQY in nitrogen, then the fits from [48] will be used to apply a temperature and pressure dependent scaling to account for the presence of oxygen.

3.5 Fluorescence Bandshapes

In addition to fluorescence quantum yield and absorption cross-section, the fluorescence bandshapes are needed to estimate performance. In particular, bandshapes are needed to determine what fraction of fluorescence is collected, and to select appropriate filters for the imaging diagnostic. They are also needed to correct for background luminescence, as will be discussed in Chapter 7.

A series of formaldehyde emission spectra were taken in the optical engine. The experimental methods were described in Section 3.1. Nine spectra were measured at different conditions, with pressure from 1.5 to 53 bar, and temperatures from 370 to 740 K. For each measurement, the spectra were measured in 6 sets of 200 images. The 6 sets of measurements were needed to cover the emission wavelength range from 380 to 500 nm. For each set, the 200 images were averaged and background subtracted. The spectra were then concatenated after scaling and smoothing to produce a single continuous measurement. The results are shown in Figure 3.13, where the spectra were normalized by their integral over the 370 to 490 nm emission range. The spectra appear to broaden significantly at high temperature. The broadening is a result of increasing population in the higher rotational states, as suggested by the theory and results presented earlier in this chapter. There is additionally some pressure broadening that is visible; specifically, the 370 K case (at 4.6 bar) is actually broader than the 510 K (1.6 bar) case.

To augment the experimental data and extend the analysis outside of the limited pressure and temperature range that was feasible with engine experiments, a series of spectral simulations were performed using the data and theory presented in Appendices C, B.3, and B.2, and the theory presented earlier in this chapter. A sample spectrum is shown in Figure 3.14 in comparison with some experimental data (the simulation was filtered with a Lorentzian distribution with FWHM of ∼0.4 nm to better match the experimental resolution). Due to the complexity of the formaldehyde molecule, the calculation was cut off at $J = 50$ rotational levels, $v = 8$ vibrational levels for the out-of-plane bending and CO stretching modes and $v = 2$ vibrational levels in all other vibrational modes. Thirty-two levels were included in the anharmonic calculation for the out-of-plane bending mode. This simulation only includes cold bands, and hot bands involving the out-of-plane bending mode (*i.e.* $v = 0$ in the $\tilde{A}\ ^1A_2$ state for all modes except v_4). This is done to reduce the complexity of the calculation, and because it is not immediately

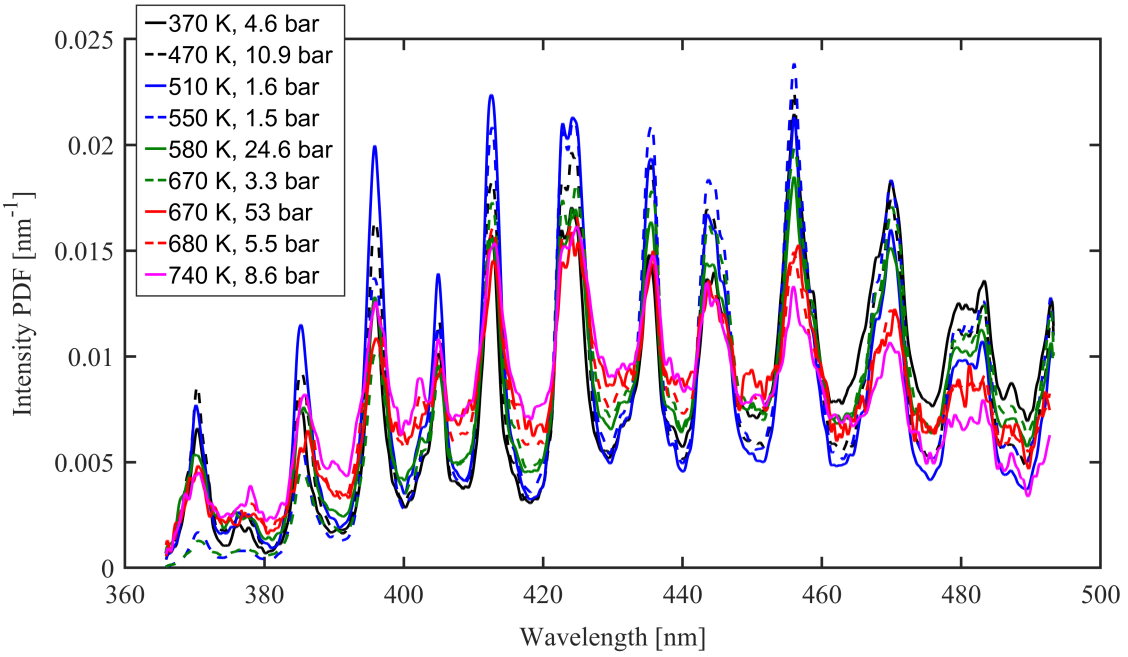

Figure 3.13: Measured formaldehyde emission spectra at engine-relevant conditions. Each spectrum is normalized by its integral.

clear whether vibrational equilibrium will be achieved in other modes before fluorescence occurs at higher pressures.

The calculated vibronic band strengths (*i.e.*, the relative height of different vibrational bands) do not match well with the experimental data. Specifically, the 2_1^0 progression appears to be underestimated, and the near-UV bands (< 400 nm) appear brighter than in the measured spectra. The discrepancy could be a result of ignoring hot bands (in particular, the 2_2^1 progression is excluded). Both effects also may be a result of error in the Franck-Condon calculation as anharmonic effects can be important at even relatively low excited vibrational states. The Morse oscillator has been shown to provide better agreement for transitions involving the C-O stretching mode [82]; the harmonic approximation tends to underestimate Franck-Condon factors (and hence transition intensities) for progressions with relatively large normal coordinate shifts. However, the relative shape, width, and location of the individual vibronic bands appears to match the measured spectra reasonably well.

The temperature and pressure dependence of the collection fraction is largely a result of increasing rotational population in higher rotational J states rather than a change in the vibrational population distribution. Thus, the temperature dependence results from changing vibrational band shapes, rather than changes in the intensity of vibrational peaks. As such, even with modest errors in the intensity of individual vibronic bands, the simulation is believed to be sufficient for estimating the temperature and

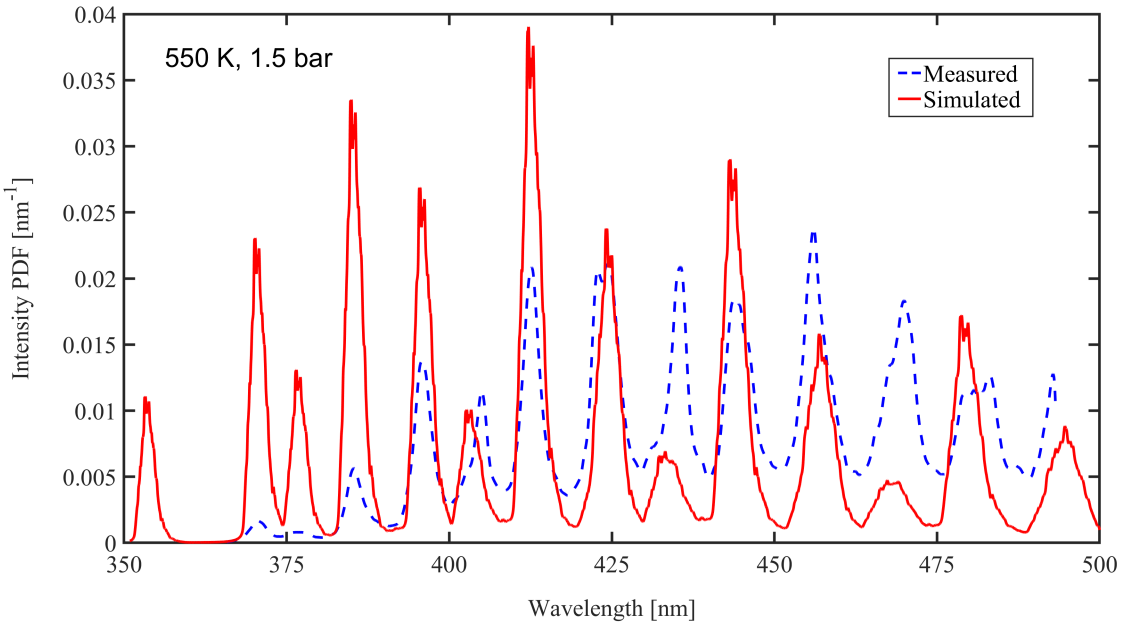

Figure 3.14: Calculated formaldehyde fluorescence spectrum compared with the measured spectrum at a similar condition. Both spectra are normalized by their integral.

pressure dependence of collection fractions and ratios.

A set of spectra were calculated at constant pressure and constant temperature to show the effect of just temperature or pressure on the spectrum; these spectra are plotted in Figure 3.15. From the plots, increasing temperature and pressure both tend to broaden the spectra, but do so in different ways. Increasing temperature populates higher rotational levels, such that transitions further away from the vibronic peak become more prominent at high temperatures; this fills in the gaps between vibronic bands as temperature increases, raising the local minima and lowering the local maxima of the spectrum. Pressure broadening causes individual rovibronic lines to broaden such that the individual lines blend together leading to a smoother and slightly broadened spectrum. Temperature clearly plays a dominant role in the broadening of the emission spectrum, while the impact of pressure is much weaker or even negligible at resolutions on the order of 1 nm; a factor of 10 change in pressure (10 bar to 100 bar) appears to have an almost negligible effect beyond smoothing some of the features. However, increasing temperature by a factor of 4 from 300 to 1200 K, the valleys between vibronic bands more than double in intensity at points, and the peak intensities drop by a factor of two in some cases.

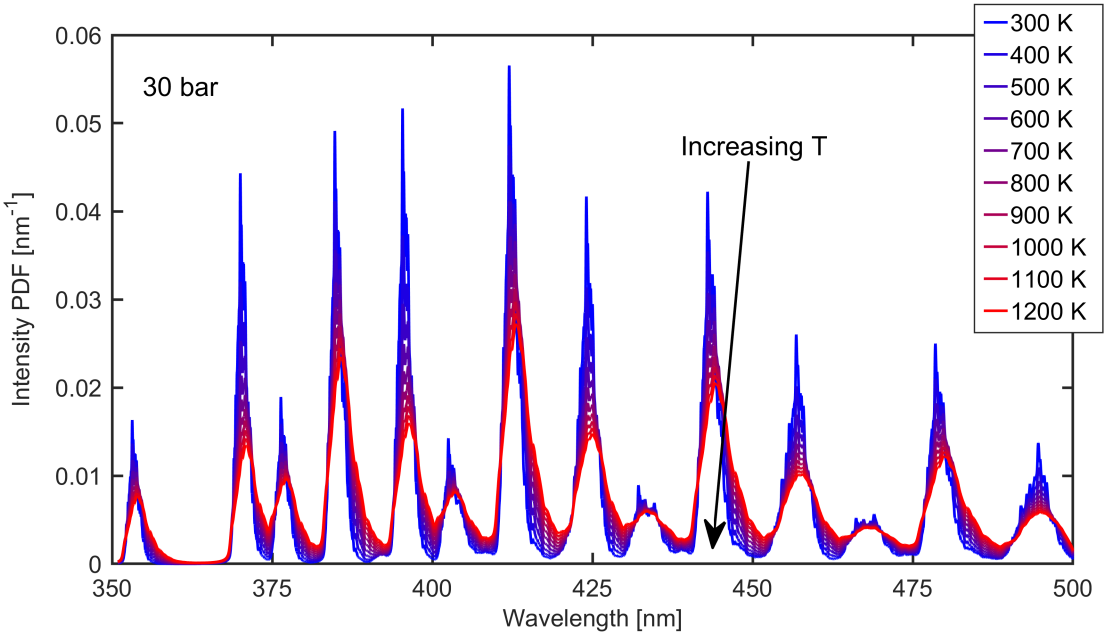

(a) Constant temperature

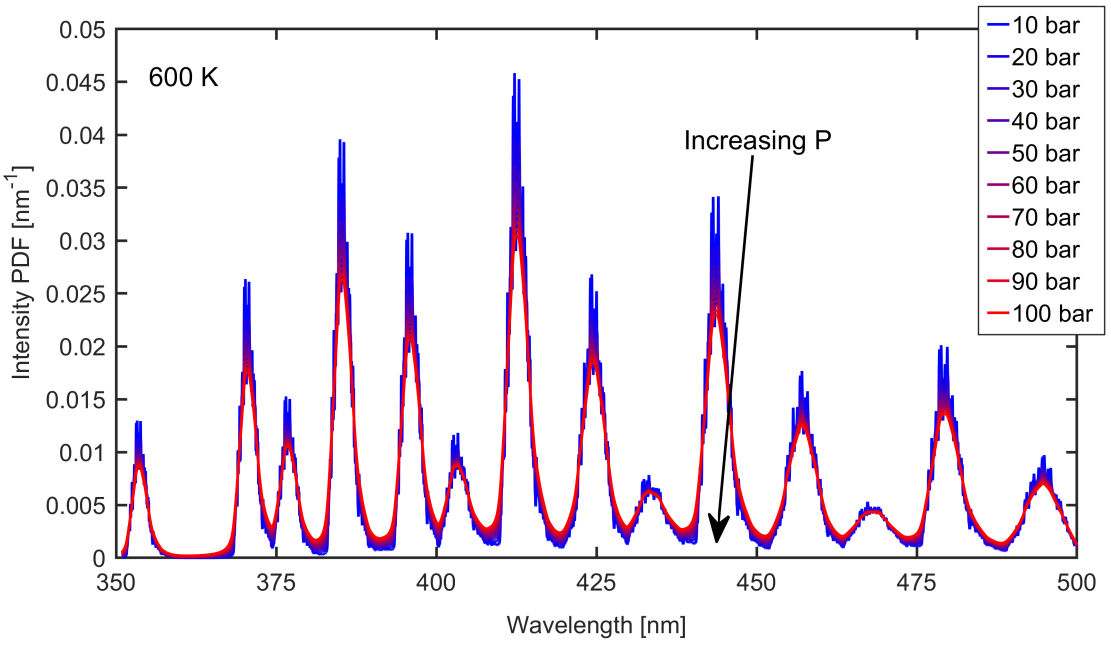

(b) Constant pressure

Figure 3.15: (a) Calculated formaldehyde fluorescence emission spectra at constant temperature (30 bar pressure) and (b) constant pressure (600 K temperature). No instrument function has been applied to the simulation results.

Table 3.3: Best-fit parameters for the formaldehyde collection fraction model.

Parameter	**Value**	**Units**
W	4	nm
w_0	2.42	nm
w_p	8.09×10^{-3}	nm/bar
w_T	2.33×10^{-3}	nm/K

3.5.1 Collection Fraction

A set of two identical thin-film interference filters (Semrock Inc., FF01-CH2O) will be used for ratiometric formaldehyde imaging. By changing the incidence angle of the filter, the transmission spectrum of the filter can be changed. Using 0 and 15 °AOI filters, the emission peaks and valleys can be collected [56]. The measured collection bands of the formaldehyde imaging filters at 0 and 15 °AOI are plotted in Figure 3.16. A sample formaldehyde emission spectrum is included on the bottom panel of Figure 3.16. The filter bands largely capture the peaks of the spectra at normal incidence, and the valleys when tilted at 15°. The collection bands are typically 4 nm wide.

The fraction of collected signal is calculated by integrating over the emission spectra, weighted by the collection bands. The normal incidence filter collects at most around 50% of the emitted light, while the tilted filter at most collects around 30% of the emitted light. At higher temperature and pressure, the tilted filter is expected to collect even more light. The calculated collection fraction in the normal incidence band S_1 is fit to the form:

$$S_1 = \mathrm{erf}\left(\frac{1}{2^{3/2}}\frac{W}{w_0 + w_p p + w_T T}\right) \tag{3.12}$$

where W, w_0, w_p and w_T are constants. This form is the analytical solution for a Gaussian lineshape with a square filter band (of width W) centered on the emission peak. The denominator inside the error function thus is an effective Gaussian width ($2^{3/2}$ times the width parameter σ). The band width is assumed to be 4 nm, while the remaining 3 parameters are fit. The results of the fit are tabulated in Table 3.3 and are shown graphically in Figure 3.17.

The simulated spectra are also used to calculate the collection fraction. Note that the fraction is only calculated over the 360 to 500 nm range, and the weak bands above 500 nm are excluded from the calculation. The results are plotted in Figure 3.18. The plots show an almost identical structure to Figure 3.17, which supports the model fit to the spectral measurements. However, the absolute magnitude is different because the simulated and measured spectra do not match exactly, particularly

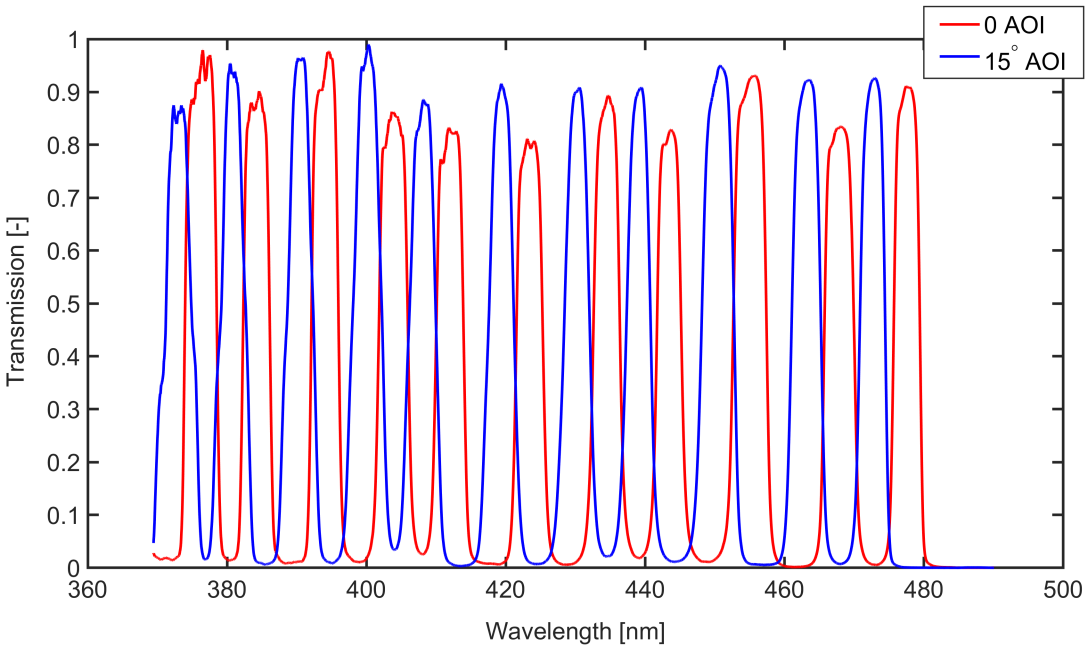

(a) Filter bands

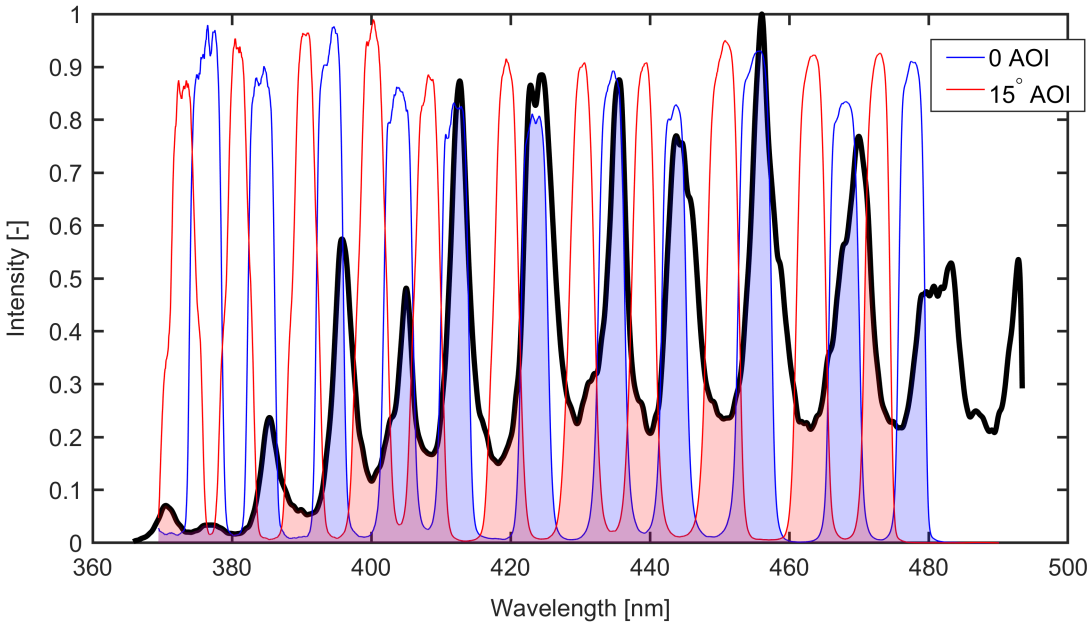

(b) Filters bands and emission spectrum

Figure 3.16: (a) Measured transmission of the formaldehyde imaging bands (Semrock Inc., FF01-CH2O) as a function of wavelength. Measurements are shown at 0 and 15 °AOI. (b) Filter transmission with sample spectrum overlaid. Shaded regions indicate the collected portion of the spectrum.

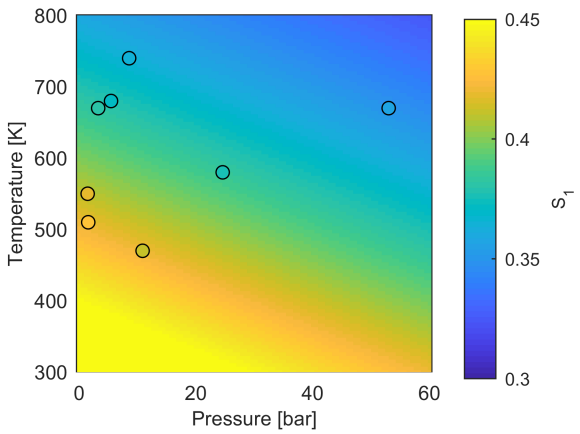

Figure 3.17: Calculated formaldehyde fluorescence collection fraction for both filters as a function of temperature and pressure. Points indicate measurements obtained from the measured emission spectra, while the shading indicates the best-fit value. One outlier (the 370 K, 4.6 bar point) was removed from this data set.

Table 3.4: Best-fit parameters for the formaldehyde collection fraction model based on simulated spectra.

Parameter	**Value**	**Units**
W	4	nm
w_0	2.3	nm
w_p	3.2×10^{-3}	nm/bar
w_T	1.5×10^{-3}	nm/K

in the baseline value at wavelengths above 400 nm. The best-fit parameters for use with Equation 3.12 are given in Table 3.4

3.6 Ratiometric Formaldehyde PLIF Imaging

Precise, quantitative measurements of formaldehyde concentration will be achieved using a ratiometric imaging technique. Since it was shown in Section 3.5 that the fraction of light collected in the normal incidence and tilted bands is dependent on both temperature and pressure, a calibration must be performed to determine the collection fraction and its sensitivity to temperature.

Ratiometric imaging measurements were performed in an engine using n-heptane low-temperature ignition to generate formaldehyde. Fuel was injected early in the compression stroke, and intake temperatures and pressures were limited to prevent the onset of high-temperature ignition. A ratio calibration at constant pressure was performed by sweeping intake temperature. The end-gas temperature is estimated from the isentropic compression of the air and fuel mixture (neglecting chemistry) from IVC to

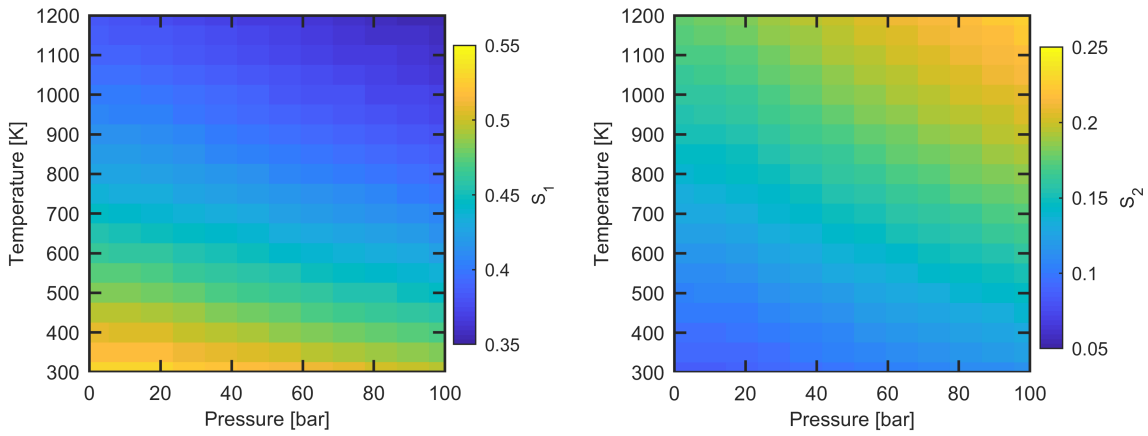

(a) Normal incidence filter S_1

(b) Tilted filter S_2

Figure 3.18: Calculated formaldehyde fluorescence collection fraction for normal incidence filter as a function of temperature and pressure from simulated emission spectra.

the constant image timing near TDC. The calibration was performed at a constant intake pressure of 1 bar, resulting in a calibration pressure of 32 bar. To calculate the ratio, two formaldehyde fluorescence images (one per camera and filter combination) are captured each cycle for 200 cycles. Each image is background subtracted and registered on a shot-to-shot basis to reduce the effect of camera motion. The raw ratio is calculated, and then a whitefield correction is applied using the average ratio image at a reference condition. The whitefield correction is typically assumed to be pressure dependent (*e.g.*, measurements taken at 30 bar use a whitefield image also taken at 30 bar) to account for pressure effects to first order. In this case, the reference condition was chosen as 875 K.

The measured ratio calibration function is shown in Figure 3.19. Since the calibration was performed over a relatively narrow temperature range, a linear fit describes the data well (*i.e.*, $R = aT + b$). The temperature sensitivity is

$$\xi_T = \frac{1}{R}\frac{\partial R}{\partial T} = \frac{1}{T-b} \approx 10^{-3}\ \mathrm{K}^{-1} \tag{3.13}$$

near 800-900 K. As a temperature diagnostic, the formaldehyde ratio has only modest temperature sensitivity. However, for the ratiometric background correction, lower temperature sensitivity is beneficial as it reduces the error in the background correction.

The ratio was also calculated from the simulation data, normalized by the value at 875 K as was done in the experimental data. The ratios are plotted in Figure 3.20, with the result of the linear *in situ* calibration superimposed. The results match well within the experimental uncertainty. The calibration, when whitefield corrected, is almost entirely independent of pressure. However, the absolute ratio does depend on pressure. The pressure dependence is shown in Figure 3.21, which plots the ratio normalized

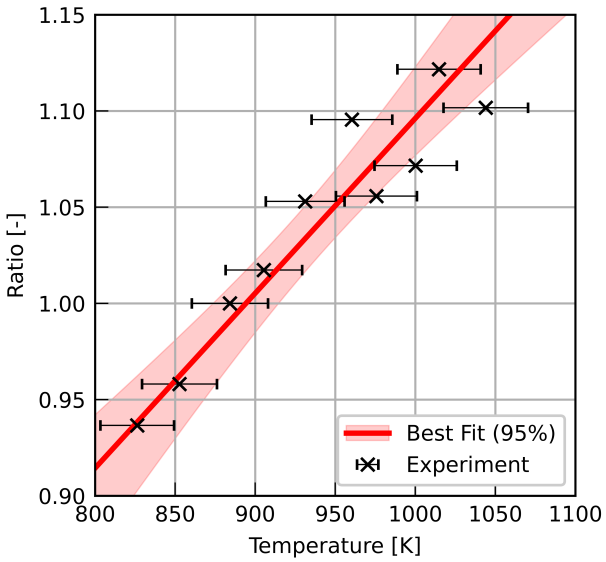

Figure 3.19: Measured formaldehyde ratio calibration function.

to its value at 875 K and 30 bar as a function of pressure; this plot is not whitefield corrected in the usual sense, and shows the impact of pressure on a measurement if the whitefield correction were not performed as described previously. From the plot, the uncorrected ratio has an approximately linear dependence on pressure.

The absolute luminescence intensity ratio for an experiment is needed for background correction as will be discussed in Chapter 7. The absolute ratio is determined from the ratio $R = S_2/S_1$, where S_2 and S_1 are the fractions of intensity collected in the two camera bands which were plotted in Figure 3.18 based on simulation data. For an experiment, ratio images are normalized to a reference condition, so the collection fractions at the reference condition must be known to apply the correction quantitatively. The absolute ratio is then simply the measured ratio multiplied by the known collection fraction ratio at the reference condition. A map of absolute ratio is plotted in Figure 3.22. Since the ratio is calculated as the intensity of the peaks normalized by the intensity of the valleys, the ratio is always below one. Additionally, the ratio increases monotonically with temperature and pressure, and appears almost linear in both temperature and pressure. The absolute value of the ratio at 875 K and 30 bar is 0.40 based on simulation data.

To simplify design calculations, the ratio was fit to the form

$$R = R_0 e^{a_p p + a_T T + a_{pT} pT + a_{T^2} T^2} \tag{3.14}$$

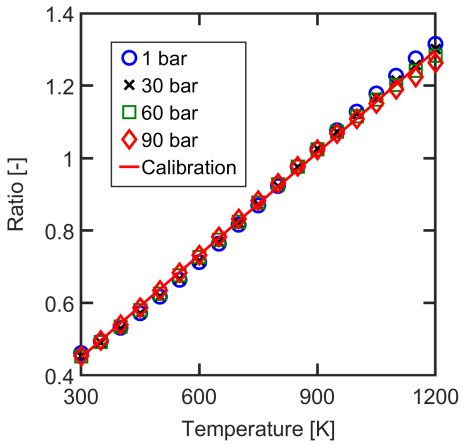

Figure 3.20: Simulated formaldehyde luminescence intensity ratio as a function of temperature and pressure. This calculation assumes a whitefield correction is taken at 875 K for each pressure series. The line labeled "calibration" is the same calibration curve fit to the experimental data and plotted in Figure 3.19.

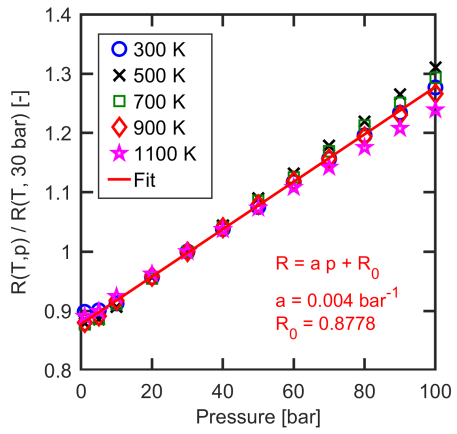

Figure 3.21: Simulated formaldehyde luminescence intensity ratio as a function of pressure, normalized to its value at 875 K and a constant pressure of 30 bar. This plot assumes that no whitefield correction is performed.

Table 3.5: Best fit parameters for absolute formaldehyde PLIF intensity ratio as a function of temperature and pressure.

Parameter	Value	Unit
R_0	0.0866	-
a_p	0.0044	bar^{-1}
a_T	0.0022	K^{-2}
a_{pT}	-8.297×10^{-7}	bar^{-1} K^{-1}
a_{T^2}	-6.652×10^{-7}	K^{-2}

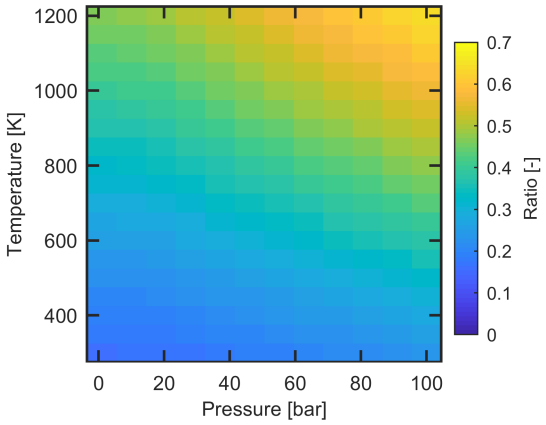

Figure 3.22: Calculated absolute formaldehyde PLIF intensity ratio as a function of temperature and pressure.

with an R^2 value of 0.999 for the fit; the fit parameters are tabulated in Table 3.5. This form additionally provides a simple expression for the temperature sensitivity:

$$\xi_T = a_T + a_{pT}p + 2a_{T^2}T, \tag{3.15}$$

which, over a small temperature range, is consistent with the results provided earlier in this section.

The ratio measurements, ratio temperature sensitivity, and fit information provided here will be used in Chapter 7 for performance estimation.

3.7 Conclusions

This chapter provided an overview of formaldehyde photophysics by combining experimental measurements and spectral simulations. Absorption cross-section at 355 nm, fluorescence quantum yield in nitrogen (and considerations for air), fluorescence collection fraction, and luminescence intensity ratio

were estimated for a range of engine relevant conditions, roughly from 300 to 1200 K, and 20 to 100 bar. These four quantities are instrumental for predicting diagnostic performance and for performing the proposed ratiometric background correction approach. This information will be used in Chapter 7 to make performance predictions.

Chapter 4

Photophysical Characterization of Phosphors

To design an APT diagnostic that is compatible with formaldehyde PLIF, we need to understand several aspects of diagnostic performance. Knowledge of the emission wavelength range and emission lifetime are necessary to identify phosphors and imaging techniques that can avoid interference from formaldehyde PLIF or other interferences (*e.g.*, by delayed gating or filtering by emission wavelength). Emission lifetime also can be indicative of luminescence quenching, which has a determining role in phosphor performance. Similar to formaldehyde PLIF, the performance of an aerosol phosphor thermometry technique is dependent largely on the tracer's emission intensity or brightness. For temperature measurements, temperature sensitivity (how quickly the brightness changes with temperature) also has a large impact on performance. Thus, temperature-dependent emission intensity is also critical to the design of an APT technique. Finally, APT relies on solid particles to discern information about the state of a surrounding fluid; particle size and heat capacity (or enthalpy) are instrumental in determining how well a particle is representative of the surrounding fluid, and in determining how flows are altered by adding solid phosphor particles.

The purpose of this chapter is to characterize and quantify these factors that are intrinsic to the phosphors being considered for the combined technique. This includes both particle physical properties and luminescence properties. This chapter details the results of several experiments that were performed to characterize phosphor properties. The chapter will begin with an overview of the phosphor compositions chosen for this study, including manufacturer supplied data. Particle physical properties are presented including particle size distributions, and heat capacity. Luminescence properties including emission life-

Table 4.1: Thermographic phosphor properties that are discussed in this chapter

Topic	Section
Physical properties	4.1
Emission spectra & lifetime measurements	4.4
Emission intensity measurements	4.5
Signal model	4.6
Performance model	4.7

time and emission spectra at elevated temperatures are shown, and a discussion of thermal quenching and phosphor electronic structure is provided. Measured phosphor signal intensities are provided in the aerosol phase.

The final two sections present in detail a phosphor signal intensity model, and a phosphor thermometry performance model. The signal model combines the lifetime and emission intensity data with particle size data to describe and predict phosphor emission intensity as a function of temperature and the excitation process. The performance model uses the signal model to predict APT precision and bias (from several sources) over a range of conditions. The estimates presented in this chapter are indicative of the performance expected and observed for heated jet and flame experiments that will be discussed in Chapter 5, and serve as a model for performance predictions for the combined formaldehyde PLIF & APT imaging technique that will be discussed in Chapter 7. This chapter is based primarily on the results reported in [83, 84]. For reference, Table 4.1 lists the topics that are discussed in this chapter.

4.1 Physical Properties

Several phosphor compositions are studied as potential candidates for APT imaging: Ce,Pr:LuAG, Ce:$GdPO_4$ (both raw, and after annealing at 1400 K for 20 minutes with a ramp rate of 300 K/hr), Ce:CSSO (raw and annealed), and Eu:BAM. Some preliminary characterization of Pr:CSSO (raw only) and Ce,Pr:CSSO (annealed only) is presented as well, but further characterization is needed before performance predictions are possible. Finally, analysis of Ce:LuAG excited at 355 nm is considered as well using data from a previous investigation by Witkowski and Rothamer [85]. Phosphor samples tested here were manufactured by Phosphor Technology Ltd., and have nominal properties as shown in Table 4.2, along with titanium dioxide, silicon dioxide, and aluminum oxide samples, which are often used and analyzed for high-speed PIV experiments [86], for comparison. This table also includes the calculated Dulong-Petit heat capacity for each material. Physical properties are largely independent of

Table 4.2: Comparison of phosphor particle compositions, manufacturer-specified volumetric-median particle diameter $\bar{d}$, density, and theoretical Dulong-Petit heat capacity.

Composition	Doping [%]	$\bar{d}$ [µm]	Density [kg/m^3]	$3N_Ak/m$ [kJ/kg-K]
Ce,Pr:LuAG ($Lu_3Al_5O_{12}$)	0.5 ea.	1.0	6700	0.59
Ce:$GdPO_4$	0.5	2.0	5990	0.59
Ce:CSSO ($Ca_3Sc_2Si_3O_{12}$)	0.5	1.3	3510	1.02
Eu:BAM ($BaMgAl_{10}O_{17}$)	0.5	1.8	3800	1.03
TiO_2	-	-	3780	0.94
SiO_2	-	-	2650	1.25
Al_2O_3	-	-	3990	1.22

doping ion and concentration (for relatively low doping concentrations), and thus only one representative measurement is provided per host tested. It is thus assumed that physical properties of singly doped Ce:LuAG or Pr:LuAG are identical to those of the co-doped Ce,Pr:LuAG, and likewise for the CSSO phosphors.

The mean particle size as provided by the manufacturer is insufficient for experiment design because it does not provide information about the distribution of particle sizes in the bulk powder or in the aerosol phase, the latter of which could depend on the seeding method. As such, particle size distributions (PSDs) are measured for several phosphors in the aerosol phase using an electrical low-pressure impactor (ELPI, Dekati). The ELPI contains 13 impactor stages, logarithmically spaced in cutoff diameter, and directly measures particle size histograms in a time-resolved fashion. Particle sizes are reported in terms of the Stokes diameter, which differs from the volume equivalent diameter only by the aerodynamic shape factor [87]. The measured (normalized) distributions are shown in Figure 4.1, and the moments are tabulated in Table 4.3 with the analytical moments of the log-normal distribution for comparison. For reference, the log-normal distribution has the PDF

$$f(x;\mu,s) = \frac{1}{xs\sqrt{2\pi}} e^{-\frac{(\ln x-\mu)^2}{2s^2}}, \tag{4.1}$$

where μ is the mean of the logarithm of the random variable, and s is the standard deviation of the logarithm of the random variable. Higher order moments up to m_6 are included in the table; these values will be used later as they are needed for the calculation of derived properties (*e.g.*, mean particle volume is proportional to m_3, while the variance in particle volume is proportional to m_6).

For APT, the specific heat capacity of the particles is additionally important as it determines thermal response time and thermal intrusiveness. Since the phosphors under consideration here are ceramic

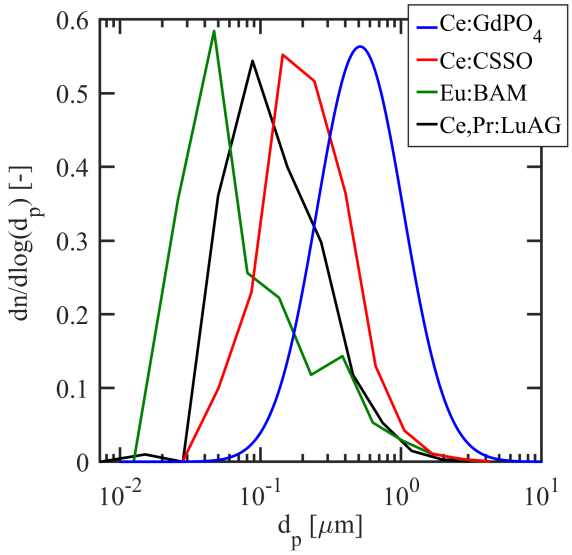

Figure 4.1: Estimated particle size distributions based on a log-normal fit to manufacturer data for Ce:$GdPO_4$, and ELPI measurements for the other phosphors.

Table 4.3: First six moments of each measured phosphor PSD. Ce:$GdPO_4$ values are based on a log-normal distribution that was fit to manufacturer provided PSDs. All other values are from ELPI measurements.

Composition	m_1 [μm]	m_2 [μm^2]	m_3 [μm^3]	m_4 [μm^4]	m_5 [μm^5]	m_6 [μm^6]
Ce,Pr:LuAG	0.36	0.28	0.37	0.68	1.53	3.90
Ce:$GdPO_4$	1.08	1.945	5.756	28.14	227	3009
Ce:CSSO	0.48	0.50	0.97	2.67	8.84	32.2
Eu:BAM	0.53	0.69	1.42	3.73	11.4	38.6
Log-normal	$e^{\mu+\frac{s^2}{2}}$	$e^{2\mu+2s^2}$	$e^{3\mu+\frac{9}{2}s^2}$	$e^{4\mu+8s^2}$	$e^{5\mu+\frac{25}{2}s^2}$	$e^{6\mu+18s^2}$

materials, they are insulators and, as a result, thermal energy is stored primarily in lattice vibrations as described by the Debye model for heat capacity [88]. The Debye heat capacity can be written as:

$$c_V = 9k\frac{N_A}{M}\left(\frac{T}{T_D}\right)^3 \int_0^{T_D/T} \frac{x^4 e^x}{(e^x-1)^2}\, dx, \tag{4.2}$$

where N_A is the Avogadro constant, k is the Boltzmann constant, M is the molecular weight of the solid, and n is the number of atoms in the unit cell (collectively, $kN_A/M = n\hat{R}$, where $\hat{R}$ is the specific gas constant of gas kinetic theory), and T_D is the Debye temerature, which is a property of the lattice. In the high-temperature limit ($T \gg T_D$), this reduces to the Dulong-Petit model, or

$$c_V = 3\frac{N_A k}{M} = 3n\hat{R}. \tag{4.3}$$

Measurements of specific heat capacity (performed by Dustin Witkowski) for several phosphors (Ce,Pr:LuAG, Ce:CSSO, and Ce:$GdPO_4$) were made from 300-600 K with a differential scanning calorimeter (PerkinElmer, 8000 DSC) at the Wisconsin Materials Research Science and Engineering Center. The results of the measurements, with fits to the Debye model, are shown in Figure 4.2. From the plot, the Debye model fits the shape of the curves very well. The theoretical Dulong-Petit capacities also fall well within the confidence interval of the fit (<1% difference); as such use of the Debye model for estimation of thermal properties is justified for similar phosphor compositions, including Eu:BAM. However, this method requires an estimate of the Debye temperature. For Eu:BAM, this is taken to be 1000 K (approximately that of Al_2O_3 [89]; BAM is structurally similar to Al_2O_3, and this approximation has been used before by other researchers [90]); for other phosphors, the Debye temperature could be measured directly or estimated from structural properties (see, *e.g.*, [91]).

4.2 Electronic Structure

The quenching behavior of each phosphor composition is directly related to its combined electronic and vibrational structure. Further, quenching processes can be observed by inspection of the phosphor's potential energy hypersurface. This can be done graphically through an electronic structure diagram [37], such as the Vacuum Referred Binding Energy (VRBE) diagram, which shows the location of electronic energy levels of the ion and host relative to the vacuum electron energy. Quenching occurs as a result of electron transfer from the excited $4f5d$ state to any other state (*e.g.*, ionization to the conduction band, or intersystem crossing to a vibrationally-excited $4f$ state) through a non-radiative process [92].

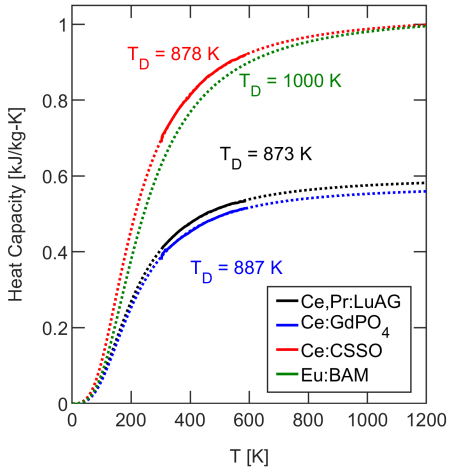

Figure 4.2: Measured and predicted heat capacities for each phosphor as a function of temperature. Solid lines indicate measured data, while dotted lines indicate fits to the Debye model for Ce,Pr:LuAG, Ce:CSSO, and Ce:$GdPO_4$. Measurements were not performed for Eu:BAM; instead, the theoretical Dulong-Petit value is used, and the Debye temperature is assumed to be ∼1000 K based on that of Al_2O_3 [89]

A VRBE diagram for the primary phosphors considered here was constructed using a recent theory presented by Dorenbos [93, 94], and is presented in Figure 4.3. For this diagram, lanthanide parameters are taken from [94], and host parameters from several sources [37, 95, 96]. Since little data is available for BAM, the band gap is taken as 7.3 eV (from [97]), and the Eu^{2+} $4f$ energy level is assumed to be -3.75 eV to match experimental quenching data from [74, 98]. The energy gap between the lowest $4f$ state and the excited $4f$ states is assumed to be unchanged from those of the free ion and are taken from [99]. $4f$ states with energies larger than the depressed $4f5d$ state are excluded, including all excited $4f$ levels in Eu^{2+}. The $4f$ and $4f5d$ energy levels are drawn in red and blue, respectively, with parabolic harmonic oscillator potential energy curves superimposed to illustrate the possibility of intersystem crossing. The $4f5d$ energy level is drawn including the Stokes shift, such that the transition energies are representative of an emission process.

From the diagram, two quenching mechanisms are observed. First, the intersection of the $4f$ and $5d$ PESs corresponds to intersystem crossing, which is characterized by a non-radiative vibronic transition to a $4f$ level. In most of the phosphors considered here, this occurs at energies above the bottom of the conduction band. However, for the Pr^{3+} doped phosphors, this occurs at lower energy levels, suggesting the Pr^{3+} doped phosphors quench via intersystem crossing. The second mechanism is ionization of the electron to the conduction band, which is evident in the Figure as the intersection of the blue $4f5d$ PES with the flat conduction band minimum. The Ce^{3+} doped phosphors and Eu:BAM appear to quench via

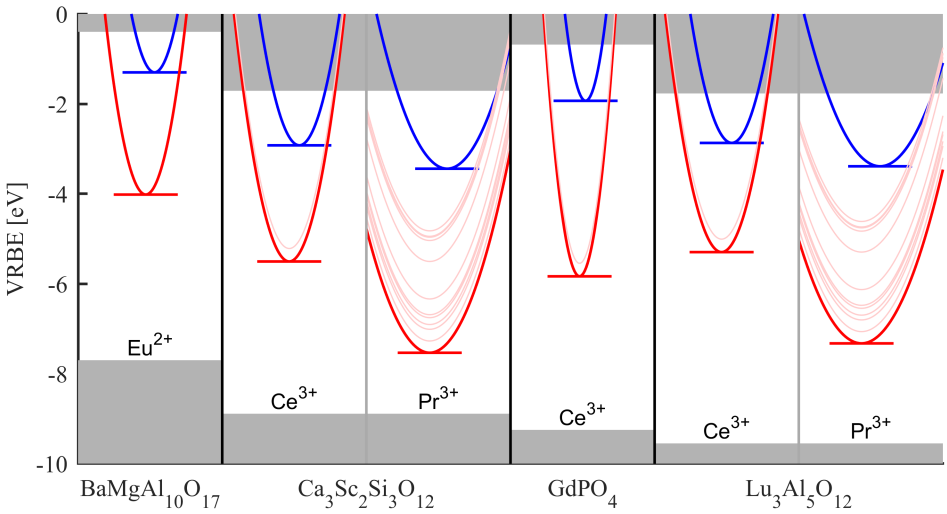

Figure 4.3: Vacuum-referred binding energy diagram for the tested phosphors. $4f$ levels are shown in red, and $5d$ levels in blue. Each energy level has a harmonic potential energy surface superimposed assuming the harmonic vibration frequency does not change between electronic states.

the conduction band. For simplicity, only the dominant (smallest energy-gap) mechanism is considered here. More generally, both mechanisms can influence the quenching behavior; the reader is referred to [92] for a detailed investigation of thermal quenching where both mechanisms are significant.

The quenching rate, or probability, for a given process decreases exponentially with increasing energy gap between the initial and final states. It has been shown previously [100] that quenching generally occurs through the process with the smallest energy gap, and that the quenching temperature is approximately proportional to the smallest energy gap. From Dorenbos [74], luminescence lifetime quenching can be explained most simply by the equation

$$k_{tot} = k_r + k_{nr,0} e^{-E/k_B T}, \tag{4.4}$$

where k_{tot} is the total deactivation rate (inverse lifetime), k_r is the radiative decay rate, $k_{nr,0}$ is the non-radiative attempt rate, and E is the characteristic energy gap of the decay mechanism. A derivation of this expression from first principles is provided at the end of Appendix B.4. For a 50% reduction in lifetime, Equation 4.4 can be solved for

$$T_{50} = \frac{E}{k_B \ln(k_{nr,0}/k_r)}. \tag{4.5}$$

In this expression, k_r is generally known from low-temperature time-resolved luminescence data and is

Table 4.4: Calculated quenching temperatures of selected phosphors based on energy-level diagram. The radiative lifetime of Pr:YAG and Ce:YAG are taken from [101] and Eu:BAM from [74]. Radiative lifetimes of other phosphors are estimated based on the material redshift. Non-radiative deactivation attempt rates are held constant for simplicity, since the actual phonon modes are unknown. Quenching temperatures are only calculated for phosphors that quench via the conduction band. The peak emission wavelength λ is also included in the table.

Phosphor	k_r [MHz]	$k_{nr,0}$ [THz]	E_{dc} [eV]	Mech.	T_{50} [K]	λ [nm]
Pr:LuAG	45.0	30	-	ISC	-	315
Ce:LuAG	16.7	30	1.100	CB	850	510
Pr:CSSO	50.5	30	-	ISC	-	300
Ce:CSSO	20.0	30	1.213	CB	1000	480
Ce:$GdPO_4$	69.1	30	1.250	CB	1200	320
Eu:BAM	1.1	30	0.902	CB	610	455
Pr:YAG	42.9	30	-	ISC	-	320
Ce:YAG	15.4	30	1.054	CB	840	525

host-dependent. The lifetime expression can be rewritten in terms of these parameters as

$$\tau^{-1} = k_r\left(1 + (C_{nr})^{1-\frac{T_{50}}{T}}\right), \tag{4.6}$$

where $C_{nr} = k_{nr,0}/k_r$ is a dimensionless parameter equal to the non-radiative attempt rate normalized by the radiative decay rate. The non-radiative deactivation rate is typically similar in magnitude to the largest phonon mode of the host [74], which is typically on the order of 30 THz (corresponding to 1000 cm^{-1} phonon energy). Table 4.4 lists some predicted values for several phosphors based on quenching to the conduction band. Note that the Pr^{3+} phosphors generally quench via intersystem crossing, which is dependent on vibrational parameters of the ground and excited states and is not easily predicted by this model, so those quenching temperatures are not included in the table.

From Table 4.4, a clear trend is evident in the Ce^{3+}-doped phosphors. Ce:YAG has the lowest quenching temperature, followed by Ce:LuAG, Ce:CSSO, and finally Ce:$GdPO_4$. For the same doping ion (Ce^{3+}), this trend is expected to be correct, but the quenching temperature results are not exact. In particular, this method overpredicts the Ce:YAG quenching temperature by around 70 K [37].

4.3 Furnace Characterization Experimental Setup

Initial spectroscopic characterization of phosphors is performed in a tube furnace (CM Furnaces, Rapid Temp Model 1720-12) up to 1500 K, as shown in the diagram in Figure 4.4. Bulk powder samples are

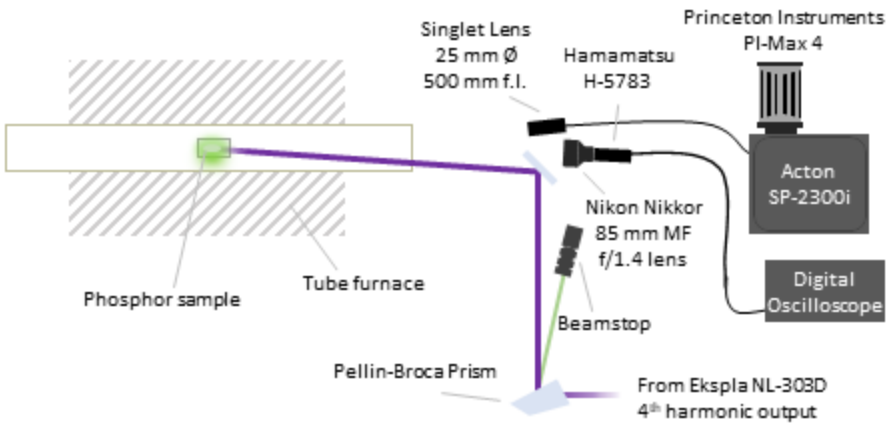

Figure 4.4: Experimental setup diagram for phosphor furnace characterization experiments.

placed in the furnace in an alumina dish that is angled upward towards the laser source and detector. Samples are excited at 10-Hz with either the 266-nm fourth-harmonic or 355-nm third-harmonic output of a Q-switched flashlamp-pumped Nd:YAG laser (Ekspla, NL 303D-10). No sheet forming optics are used; instead the beam is directed towards the sample at low fluence (<1 mJ/cm^2), and fluence is adjusted using a variable attenuator.

Spectrally-resolved emission measurements were taken with a spectrometer (Acton, SP2300i) using an intensified CCD camera (Princeton Instruments, PI-MAX4 1024i-HB-FG-18-P46) and a UV-rejection filter (Schott, WG-295). Temporally-resolved emission measurements were acquired with a photomultiplier tube (PMT) module (Hamamatsu, H-5783) outfitted with a UV-rejection filter (Schott WG-295). The estimated temporal resolution of the PMT is 0.7 ns based on the manufacturer-specified rise time; however, since the laser pulse duration is much longer than this (∼5 ns), the shortest lifetime measurable in this setup is closer to 5 ns. Additionally, the estimated spectral resolution is 2 nm, based on the measured full-width at half maximum of the H-line (404.7 nm emission) of a mercury vapor lamp.

Furnace temperature measurements are taken with a type-K thermocouple and reader (estimated 1% accuracy) placed in the furnace adjacent to the phosphor sample. Two additional type-B thermocouples installed in the furnace are measured simultaneously and are in good agreement (within 10 K) with the external thermocouple. Estimated temperature measurement uncertainty within the furnace is approximately 10 K.

4.4 Emission Spectra & Lifetime

Temperature measurement using APT relies strongly on the spectral properties of the phosphors. For example, phosphors must emit quickly (such that there is no significant tracer motion or change in the flow during the emission process), be easily excitable, emit at wavelengths that can be measured without significant background interference, and be sensitive to temperature. The emission spectra and lifetimes are thus critical for the design and characterization of an APT technique.

Measured room-temperature emission spectra are shown in Figure 4.5 for several phosphors. Emission spectra for Ce:LuAG at 355 nm excitation have been presented and analyzed in the literature previously [37] and are not repeated here. The Ce^{3+} ion in CSSO and LuAG emits betwee 500-600 nm and has little observable structure, while in $GdPO_4$ it emits with a center wavelength near 320 nm. The Pr^{3+} ion typically emits below 400 nm and exhibits two distinct peaks corresponding to emission to two different $4f$ energy levels. Pr^{3+} in LuAG emits near 320 nm, again with little structure. In Ce:CSSO and Ce,Pr:CSSO samples there is an additional blue/near-UV peak that does not correspond to Ce^{3+} or Pr^{3+} emission; this peak is instead due to emission from the CSSO host. The host emission largely overlaps the Pr^{3+} emission at room temperature before annealing, and obscures the shape of the Ce^{3+} emission band. After annealing, the host emission is reduced, but is not completely eliminated.

Time-resolved emission intensities are fit with a single-exponential decay to determine fluorescence lifetime, and are shown in the left of Figure 4.6. Lifetime data is only reported for the annealed Ce:CSSO, Ce:$GdPO_4$, and Ce,Pr:CSSO phosphors. Eu:BAM lifetimes were not measured directly in this work, and instead were taken from [102]. The measured signal per particle is displayed in the right hand side of Figure 4.6 for comparison, as measured in an atmospheric flame (see Section 5.3 for details). Although lifetime is inversely proportional to signal to first order, each phosphor exhibits some temperature dependence in the excitation process. As a result, the temperature dependence of the lifetime is not identical to the temperature dependence of the luminescence intensity.

The lifetimes for Ce:$GdPO_4$, Ce,Pr:CSSO, and Ce:CSSO are not monotonic with temperature, which may be a result of interfering host defect emission or indirect excitation of the $4f5d$ level. For $GdPO_4$, this is likely due to an indirect feeding mechanism or interaction with the Gd atom; there additionally appears to be a strong non-exponential character for this phosphor (particularly at elevated temperatures), and a temperature-dependent long lifetime component. For Ce:CSSO, host emission is directly evident and clearly dominant in the emission spectra. For Pr:CSSO, there is no evidence of host emission in the emission spectra. Comparing the singly-doped and co-doped CSSO phosphors, the lifetimes are largely in good agreement with the exception of possible interference from host emission. Additionally, the

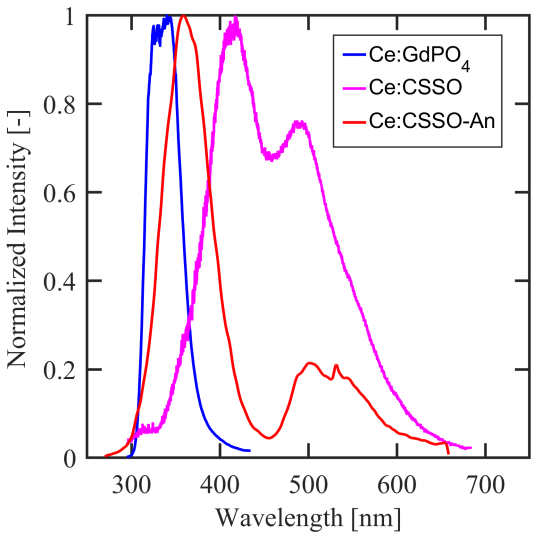

(a) Ce^{3+}-doped phoshors

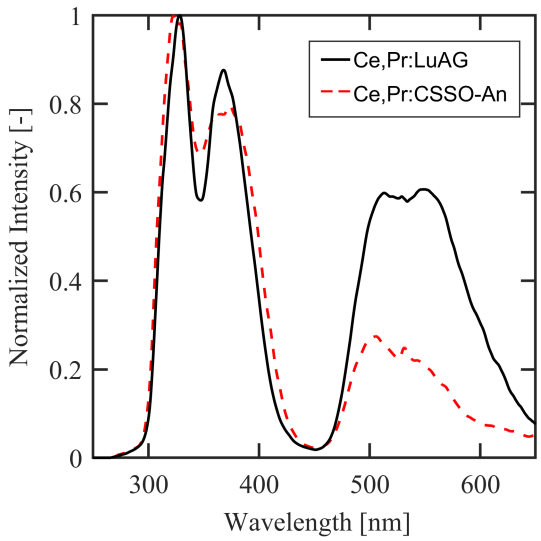

(b) Co-doped phoshors

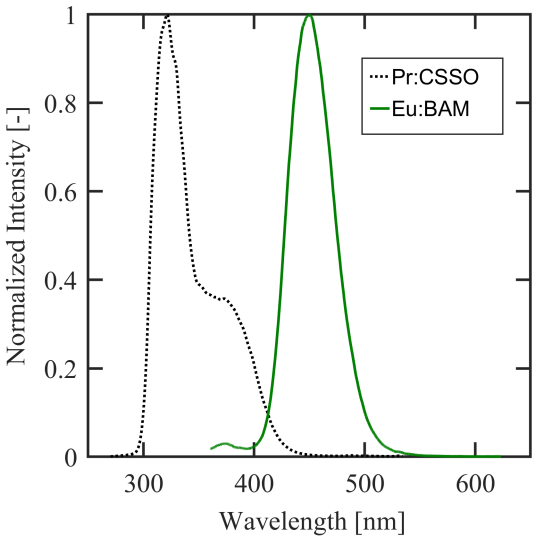

(c) Eu:BAM and Pr:CSSO

Figure 4.5: Experimental bulk powder emission spectra for several phosphors at 300 K at < 1 mJ/cm^2 fluence.

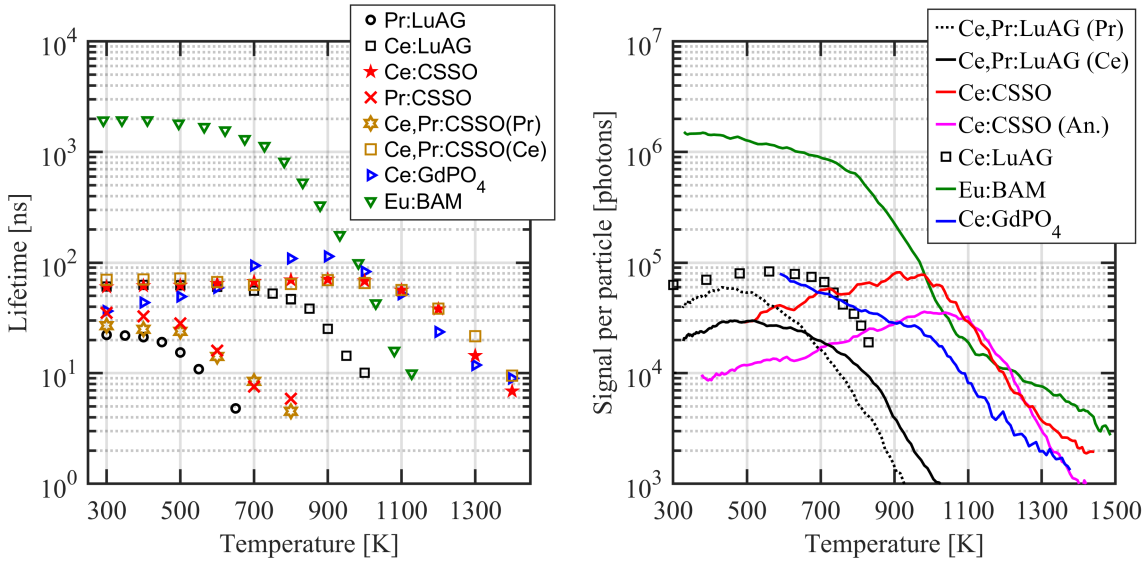

(a) Lifetime

(b) Signal intensity

Figure 4.6: Experimental emission lifetimes and intensities as a function of temperature. Lifetime was determined from a single exponential fit to measured time-resolved emission data. Measured signal per particle as a function of temperature was determined from aerosol data in a flame-heated jet for all phosphors except Eu:BAM and Ce:LuAG. Ce:LuAG data was adapted from [85]. Eu:BAM lifetime data is from [102], and the room-temperature signal per particle is taken from [36] and is scaled to the particle diameter and laser fluence used in the flame-heated jet experiment. All phosphors were excited using the Nd:YAG 4^{th} harmonic wavelength, except Eu:BAM and Ce:LuAG which used the Nd:YAG 3^{rd} harmonic.

Pr^{3+} in the co-doped phosphor at room temperature is reduced compared to the singly-doped value, indicating the possibility of energy transfer.

Temperature-dependent emission spectra and fluorescence decay curves are shown for Ce:CSSO, Pr:CSSO, and Ce:$GdPO_4$ in Figure 4.7 for the unannealed samples, and in Figure 4.8 for the annealed samples. As mentioned earlier, the Ce:CSSO phosphor exhibits evidence of host defect emission and indirect excitation processes in both the emission spectra and non-exponential luminescence decay. The host emission quenches at relatively low temperatures (it is almost immeasurable by 900 K), and is reduced significantly at all temperatures after annealing. This behavior is not evident in the Pr:CSSO phosphor. The Pr:CSSO spectra and decay curves change almost negligibly after annealing. Finally, Ce:$GdPO_4$ exhibits a significant slow component in the luminescence decay that is temperature dependent, resulting in the non-monotonic change in luminescence lifetime with temperature. The population dynamics of Ce:$GdPO_4$ are too complicated to be described with a single lifetime; thus, the reported lifetime is an average exponential lifetime that can be thought of as a weighted average of the different components.

4.5 Absolute Signal Intensities

Signal intensity versus temperature is shown in the right of Figure 4.6 for several of the phosphors. This plot is generated from flame data (see Section 5.3), where signal per particle is calculated based on manufacturer-provided camera properties and the estimated optical properties in Table 5.2. Specifically, the measured signal in counts on the camera S_{ADU} is related to signal-per-particle S_{pp} by the expression

$$S_{ADU} = g\frac{\Omega}{4\pi}\eta_{pc}\eta_{opt}S_{pp}nV \tag{4.7}$$

where g is the camera gain, Ω is the collection solid-angle, η_{pc} is the average photocathode quantum efficiency, η_{opt} is the average optical transmission, n is the particle seeding density (measured via Mie scattering), and V is the pixel volume in the object plane. Measurements of signal-per-particle at room temperature are made as well for a subset of phosphors; the results are provided in Table 4.5. The number of photons emitted per ion is also calculated at room temperature using the measured particle size distribution and doping percentages specified in Table 4.2. There is a relatively large uncertainty in the absolute signal measurements, estimated at a factor of 2, due to uncertainties in the scattering properties of the particles, and the transmission coefficients of lenses and optics. The Eu:BAM and Ce:LuAG (355 nm excitation) signal-per-particle values are not measured directly. Instead for Eu:BAM,

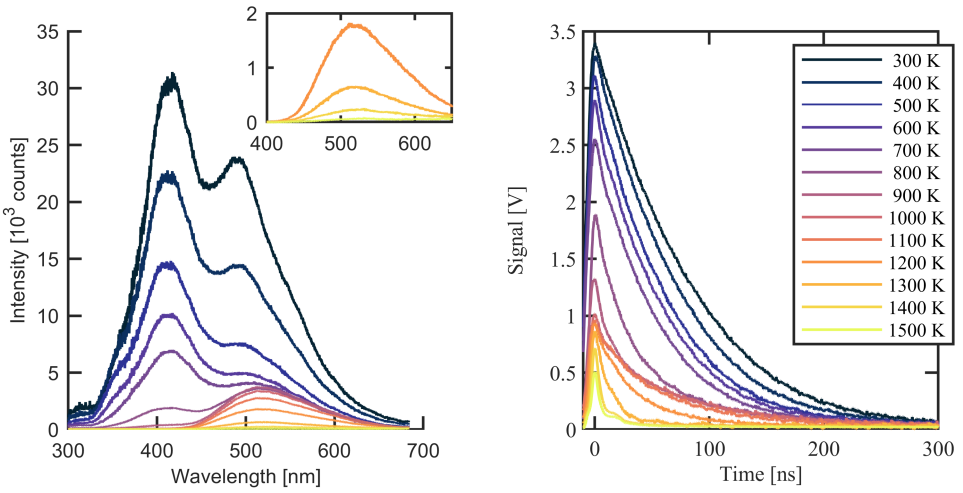

(a) Ce:CSSO

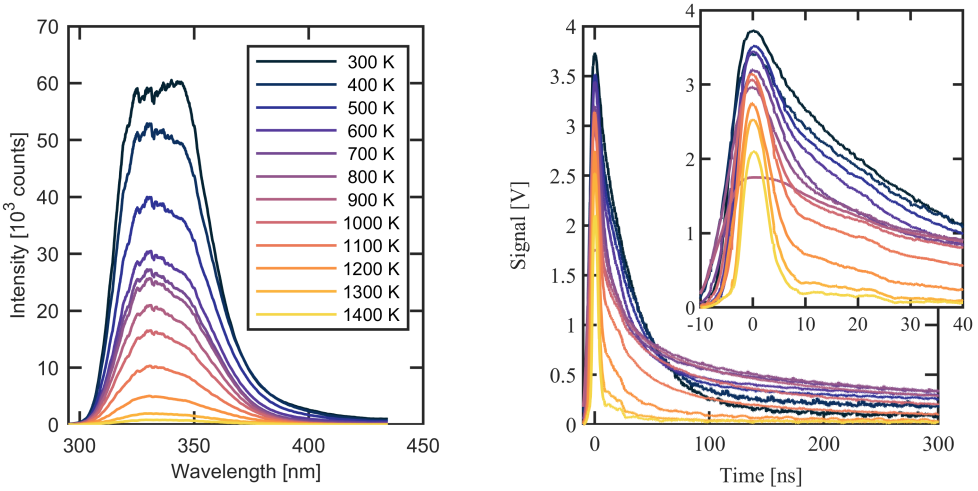

(b) $Ce:GdPO_4$

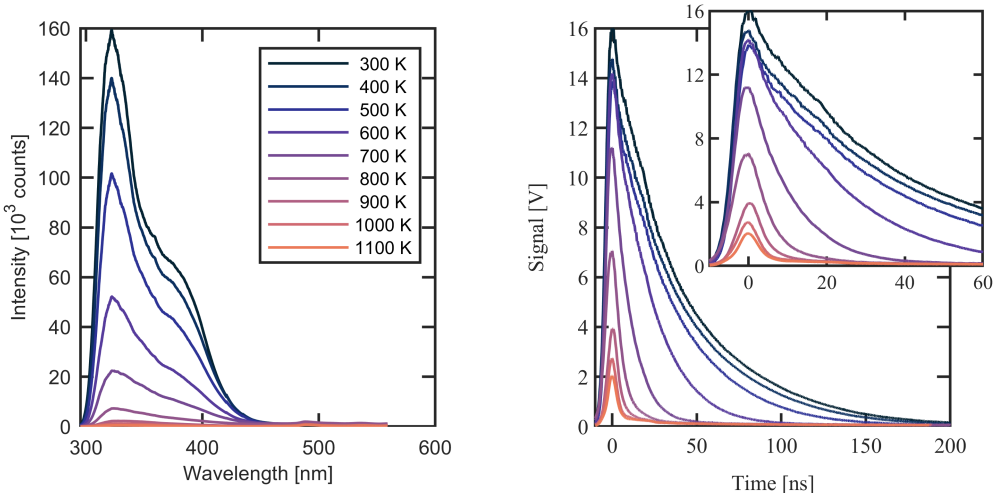

(c) Pr:CSSO

Figure 4.7: Temperature-dependent emission spectra (left) and fluorescence decay curves (right) for each phosphor. Pr:CSSO decay curves were corrected for PMT saturation with a saturation voltage of 4.6 V.

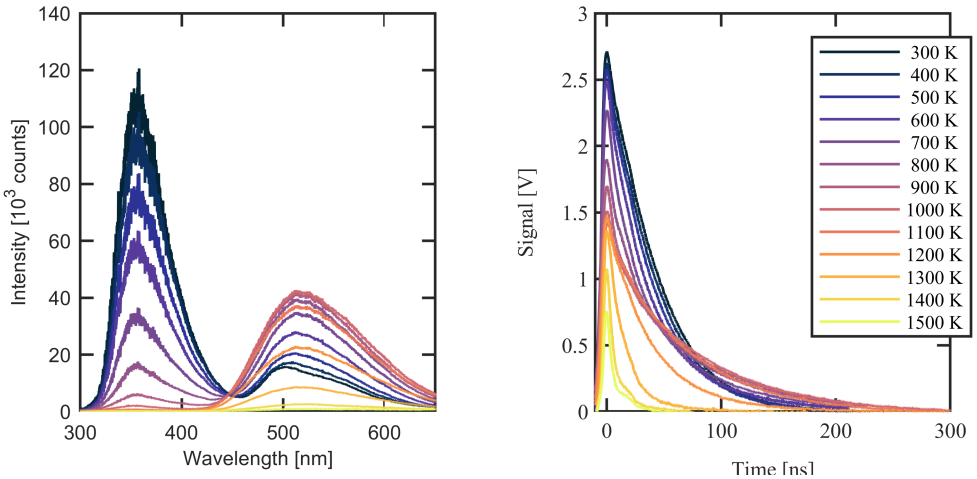

(a) Annealed Ce:CSSO

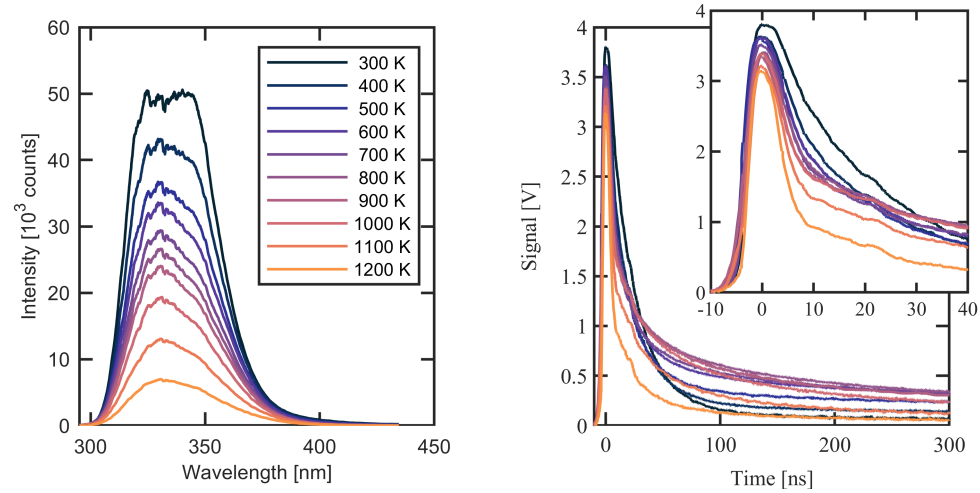

(b) Annealed Ce:$GdPO_4$

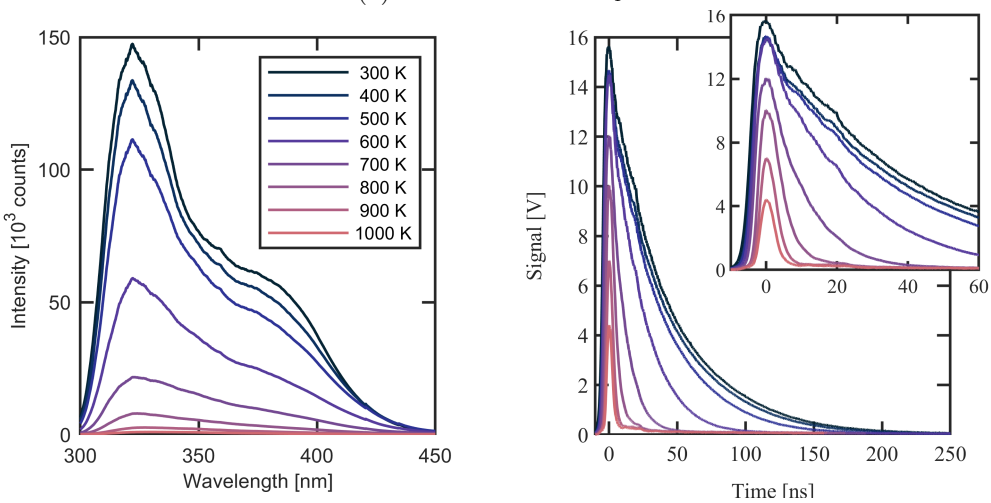

(c) Annealed Pr:CSSO

Figure 4.8: Temperature-dependent emission spectra (left) and fluorescence decay curves (right) for annealed phosphors. Pr:CSSO decay curves were corrected for PMT saturation with a saturation voltage of 4.6 V.

Table 4.5: Estimated signal levels for each phosphor at 295 K and average laser fluence of 30±2 mJ/cm^2. Host emission per ion (in parantheses) is calculated per Ce^{3+} ion. Eu:BAM is calculated using data from [36], and Ce:LuAG data is adapted from [85]. Here, λ_{ex} is the excitation wavelength and d_p is the volume-weighted mean particle diameter.

			Signal [photons]	
Band	λ_{ex} [µm]	d_p [µm]	per particle	per ion
Ce,Pr:LuAG (Ce^{3+})	266	0.72	1.6×10^4	3.8×10^{-4}
Ce,Pr:LuAG (Pr^{3+})	266	0.72	3.9×10^4	9.1×10^{-4}
Ce:CSSO (Ce^{3+})	266	0.99	3.0×10^4	3.5×10^{-4}
Ce:CSSO (Host)	266	0.99	8.5×10^4	(9.9×10^{-4})
Annealed Ce:CSSO (Ce^{3+})	266	0.99	1.0×10^4	1.2×10^{-4}
Annealed Ce:CSSO (Host)	266	0.99	1.7×10^4	(2.0×10^{-4})
Ce:$GdPO_4$ (Ce^{3+})	266	1.79	4.8×10^4	1.6×10^{-4}
Eu:BAM (Eu^{2+})	355	1.12	1.5×10^6	4.5×10^{-3}
Ce:LuAG (Ce^{3+})	355	0.99	6.3×10^4	1.7×10^{-3}

the room temperature value from [36] is scaled according to the relative signal intensity measurement made in the flame. For Ce:LuAG (355 nm excitation), data was taken from [85] and corrected for fluence and particle size.

Two obvious points can be made from the signal intensities in Figure 4.6. First, the signal quenching closely follows, but is not identical to, the lifetime quenching. In particular, there is some slow variation in signal at lower temperatures for most phosphors before the onset of quenching; this can potentially be attributed to changes in the absorption process rather than nonradiative processes. Second, Eu:BAM emits several orders of magnitude brighter than every other phosphor tested here, even after the onset of thermal quenching, which provides a significant advantage. From Table 4.5 Ce:LuAG at 355 nm excitation is also significantly brighter than most other garnet phosphors, but is still relatively dim compared to Eu:BAM on a per particle or per volume basis.

4.6 Signal Modeling & Linearity

The temperature imaging methods presented and discussed in this work are intensity-based, meaning that temperature is related to relative changes in signal-intensity or brightness. As such, a quantitative understanding of luminescence intensity is important to understand and design diagnostics. A general expression for the rate of photon emission per ion $\dot{S}$, on average, is

$$\dot{S} = n^\star k_r, \tag{4.8}$$

where $n^\star$ is the fraction of excited electrons, and k_r is the radiative deactivation rate. Assuming the excitation process is fast and the phosphor exhibits a perfectly exponential decay, this equation can be solved exactly. The total emitted signal per ion is $S = n^\star\Phi$, where $\Phi = k_r\tau$ is the fluorescence quantum yield (FQY) and τ is the lifetime of the excited state. The lifetime can be determined directly from time-resolved luminescence measurements (as is done here), and k_r is taken as the inverse of the lifetime in the low temperature limit. The remaining term, $n^\star$, is related to the excitation process and is highly fluence-dependent; this will be discussed next.

4.6.1 Fluence Dependence

The fraction of electrons excited is determined largely by the excitation laser fluence, and is a result of population dynamics. Many processes occur in complicated systems such as Ce,Pr:LuAG and the other phosphors under consideration here. Typical APT experiments, especially those considered here, operate at relatively low excitation and thus we are primarily concerned with low-intensity mechanisms such as ground-state absorption (GSA), spontaneous emission, and excited-state absorption (ESA). Recent investigations of Ce:LuAG and Ce:YAG have pointed to excited-state absorption (ESA) as a dominant low-intensity loss mechanism [103–105] for Pr- and Ce-doped garnets. The remainder of this section will focus on measurements and modeling of excitation and emission processes in phosphors, particularly including the ESA mechanism to explain several effects observed in phosphors including non-linearity with fluence and low signal-per-particle. This section is based primarily on [83, 84], where it was shown that ESA provides a consistent explanation for these effects in the Ce,Pr:LuAG phosphor, and rate-based modeling was used successfully as a method for diagnostic calibration.

The state of a system of independent ions can, to first order, be described by a series of coupled rate equations with two primary mechanisms: stimulated transitions (with rate proportional to excitation fluence rate) and spontaneous transitions (with a fixed rate for a given transition). Higher order processes that are proportional to the populations of two or more states, such as energy transfer upconversion, are ignored; these higher-order processes are not believed to be significant at the low doping concentrations and excitation fluences used in the APT experiments discussed here. The coupled system of rate equations can be written as

$$\dot{\vec{n}} = (\mathbf{A} + \mathbf{B}\dot{\phi}'')\vec{n} \tag{4.9}$$

where $\vec{n}$ is the population vector where each element n_i contains the fraction of the electrons that are currently in state i (here, $i = 0$ corresponds to the ground $4f$ state, $i = 1$ corresponds to the excited

$5d$ state, and $i = 2$ corresponds to the conduction band). A three-level model system is assumed for simplicity, but the analysis is valid for higher orders and other combinations of first-order processes. The entries in matrix $\mathbf{A}$ are the spontaneous transition rates between each state; similarly the entries in $\mathbf{B}$ are the absorption cross-sections for stimulated transitions between states. Finally, $\dot{\phi}''$ is the laser fluence rate (*i.e.*, the instantaneous time-derivative of laser fluence). The rate equation system (Equation 4.9) can be solved analytically and has the solution

$$\vec{n} = \exp(\mathbf{A}t + \mathbf{B}\phi'')\ \vec{n_0}, \tag{4.10}$$

where $\phi'' = \int \dot{\phi}'' dt$ is the cumulative fluence deposited up to time t, $\vec{n_0}$ is the initial population vector (typically taken as the ground state, $\vec{n_0} = |4f\rangle = \hat{e}_0$) and the equation is evaluated via matrix exponentiation. Several important points can be made from this solution. First, the excited population is a sum of exponentials with arguments that dependent on time, fluence, and products of t and ϕ'' to rational powers in general. Second, in the low-fluence limit, only a single exponential will dominate, such that the fluence curve will look like a single-exponential function. This is typical of many fluence curves for phosphors reported in the literature, as well as those shown here. For a more detailed discussion of this solution, please refer to the appendix in [83].

A simplified model can be used to capture the low signal-per-particle and non-linear excitation behavior of phosphors under the assumption that stimulated emission is negligible, and that any population excited to the conduction band does not return to either the $4f$ or $5d$ levels within the time scale of the excitation and emission process. In this case, the $\mathbf{A}$ and $\mathbf{B}$ matrices can be written as

$$\mathbf{A} = \begin{bmatrix} 0 & (k_r + k_{nr}) & 0 \\ 0 & -(k_r + k_{nr}) & 0 \\ 0 & 0 & 0 \end{bmatrix}, \tag{4.11}$$

and

$$\mathbf{B} = \begin{bmatrix} -\sigma_{12} & 0 & 0 \\ \sigma_{12} & -\sigma_{23} & 0 \\ 0 & \sigma_{23} & 0 \end{bmatrix}, \tag{4.12}$$

where $k_r + k_{nr} = \tau^{-1}$ is the temperature-dependent deactivation rate (inverse lifetime; individually k_r is the radiative rate and k_{nr} is the non-radiative rate), σ_{12} is the GSA cross-section, and σ_{23} is the ESA cross-section. For these values, the solution (Equation 4.10) can be written for each state without matrix exponentiation via eigendecomposition (see the appendix of [83]). The population of each level is given by

$$\vec{n} = \begin{bmatrix} \frac{e^{-\lambda_+}\lambda_-(\lambda_+ - \sigma_{23}\phi'') - e^{-\lambda_-}\lambda_+(\lambda_- - \sigma_{23}\phi'')}{\sigma_{23}\phi''(\lambda_+ - \lambda_-)} \\ \frac{\lambda_+\lambda_-}{\sigma_{23}\phi''(\lambda_+ - \lambda_-)}\left(e^{-\lambda_-} - e^{-\lambda_+}\right) \\ 1 + \frac{e^{-\lambda_+}\lambda_- - e^{-\lambda_-}\lambda_+}{\lambda_+ - \lambda_-}, \end{bmatrix} \tag{4.13}$$

where the eigenvalues $\lambda_\pm$ are given by

$$\lambda_\pm = \frac{(\sigma_{12} + \sigma_{23})\phi'' + (k_r + k_{nr})t}{2} \pm \frac{\sqrt{(\sigma_{12}\phi'' + \sigma_{23}\phi'' + (k_r + k_{nr})t)^2 - 4\sigma_{12}\sigma_{23}\phi''^2}}{2}. \tag{4.14}$$

Emitted signal intensity per unit time is equal to the product of the excited population and the radiative decay rate, or

$$\dot{S} = n^\star(t, \phi(t))k_r. \tag{4.15}$$

where $n^\star$ is the population of the excited state, given by the second entry in Equation 4.13. Note that the population model solution is not valid when the fluence rate is zero, but models the excitation process well up to that point. The model additionally works well for a simplified fluence profile, like a square wave, which is used later for simplicity. Assuming the laser pulse is short compared to the decay time and that the decay following excitation is exponential, Equation 4.15 can be integrated to find the total emitted intensity

$$S = n^\star(t_{pulse}, \phi)k_r\tau, \tag{4.16}$$

where t_{pulse} is the width of the laser pulse, and emission during the excitation process is neglected.

The analytical solution of the population model (Equations 4.13 and 4.15) was used for phosphor performance prediction with varying fluence, laser pulse widths, and integration durations; the results will be presented in Chapter 7. The short laser pulse approximation (Equation 4.16) was used for detailed characterization of the Ce,Pr:LuAG phosphor which will be discussed in the next section.

Detailed Investigation of Ce,Pr:LuAG

A detailed investigation of fluence-dependence in phosphor emission intensity for the Ce,Pr:LuAG phosphor was carried out in [83], where the three-level population model was fit to data and used to described observed trends. In this experiment, emitted signal intensity (per particle) was measured in a heated jet (please refer to Section 5.1.1 for experimental details) at different excitation laser fluences and temperatures. At each temperature, the fluence curves were divided by the measured luminescence lifetime such that the final value was proportional to the excited population fraction (under the assumption that $S = n^\star k_r\tau$). The population fraction measurements were then fit to the population model described by

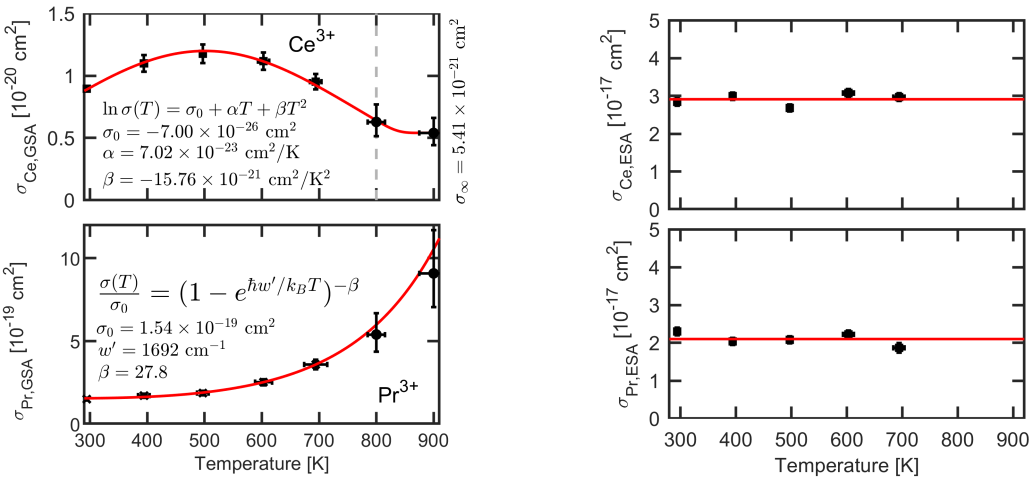

(a) GSA (b) ESA

Figure 4.9: Best-fit three-level model GSA and ESA cross-sections for Ce,Pr:LuAG.

Equation 4.10 via the ESA and GSA cross-section parameters (σ_{23} and σ_{12}, respectively). The ESA and GSA parameters were assumed to be temperature-dependent. Since GSA was shown to largely control the absolute scale of the excited population fraction, the room-temperature GSA values were set to be known values from literature. The resulting fit parameters are shown in Figure 4.9 and measured fluence curves in Figure 4.10. The fit parameter values at 800 and 900 K are determined from a single fluence measurement rather than fluence curves, as described in [84].

From Figure 4.10, the three-level model provides a consistent explanation for fluence non-linearity (large ESA cross-section) and signal increase with temperature prior to the onset of quenching (temperature dependent GSA cross-section). The model describes the data well. Further, predictions from the model are consistent with absolute signal estimates, with almost perfect agreement for Ce^{3+}, and a factor of 4 difference in Pr^{3+}. This agreement indicates the model is capturing most of the observed physics; the factor of 4 difference for Pr^{3+} is likely a result of temperature- and fluence-independent mechanisms like intra-ion energy transfer or concentration quenching, as discussed in [83].

Room-Temperature modeling Parameters for Ce:$GdPO_4$, Ce:CSSO, Ce:LuAG, and Eu:BAM

From the analysis of ESA and Ce,Pr:LuAG fluence data, the ESA cross-section appears to dominate the character of the fluence curve. An approximate solution where ESA is the dominant process (*e.g.*, due to poor excitation efficiency resulting from off-peak excitation, as is done here for all phosphors except Eu:BAM) shows that the exponential fluence scale is approximately the reciprocal of the ESA cross-section (see [83]). Further, from the Ce,Pr:LuAG data, the ESA cross-sections do not appear to

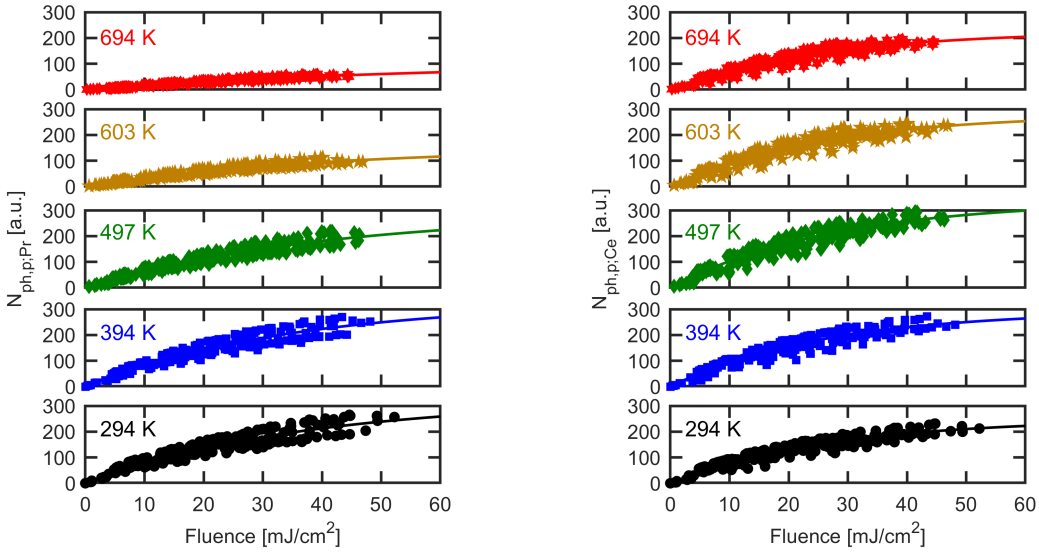

(a) Pr^{3+} (b) Ce^{3+}

Figure 4.10: Measured fluence curves for Ce,Pr:LuAG with three-level model fit superimposed for the Pr^{3+} emission and Ce^{3+} emission.

be temperature-dependent when accounting for spontaneous deactivation.

The ESA cross-sections for the other phosphors are estimated from the curvature of a signal intensity versus fluence curve. A measurement of signal as a function of laser fluence is shown in Figure 4.11 for Ce:$GdPO_4$, Ce:CSSO, and Eu:BAM from room temperature air jet measurements. These measurements were taken in the flame experiment described in Section 5.3 with the flame off. Fluence variation is a result of non-uniformity in the laser sheet, which varies from about 1 to 40 mJ/cm^2 for all phosphors. Signal is estimated as the measured intensity along the axis of the jet, corrected for the average seeding density profile based on elastic scattering measurements. For Eu:BAM, only 1 lifetime of emission is captured (2 microseconds), while for every other phosphor at least 3 lifetimes are captured. For comparison, data for the Ce,Pr:LuAG phosphor using the same experimental setup is included. Data for Ce:LuAG at 355 nm excitation is also included on the plot, but was taken from [85] and was not measured here in the jet.

ESA cross-sections are estimated from exponential fits to the fluence curves ($S \propto 1 - \exp(-\sigma\phi'')$, where σ is the absorption cross-section) and are summarized in Table 4.6. The fluence curves for Eu:BAM match reasonably well with results from [36, 106], and show saturation at very low fluences on the order of 10 mJ/cm^2 or less. Above this fluence, there is an increase in signal, but it is not captured by the fits in Figure 4.11 because the fluences are too high to be described by a single exponential (this could be caused in part by non-uniformity in the laser sheet profile). The ESA cross-section fit results for the Ce,Pr:LuAG phosphor in Table 4.6 match very closely but not exactly with those measured in Section

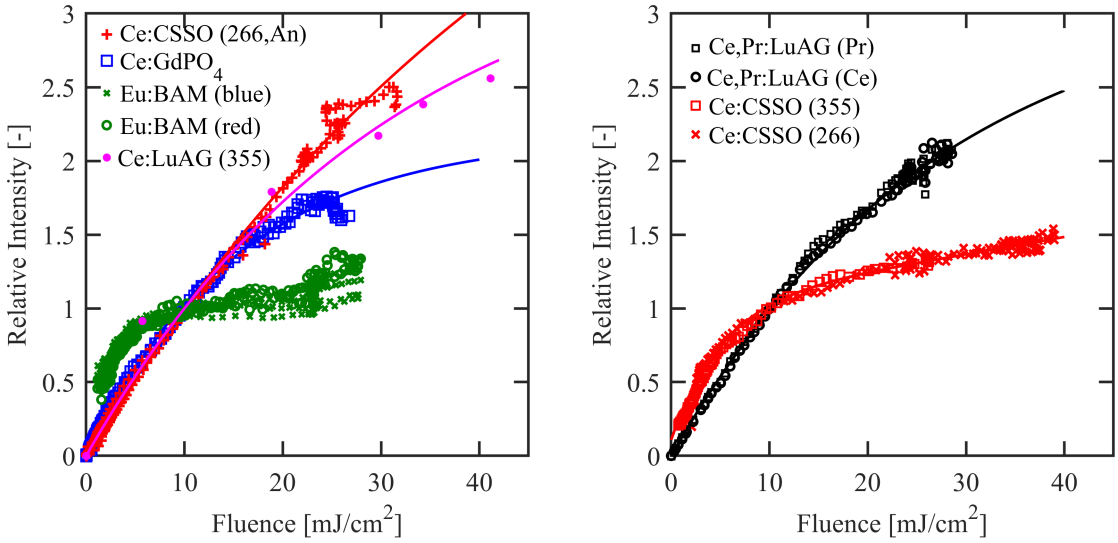

(a) Experimental fluence curves

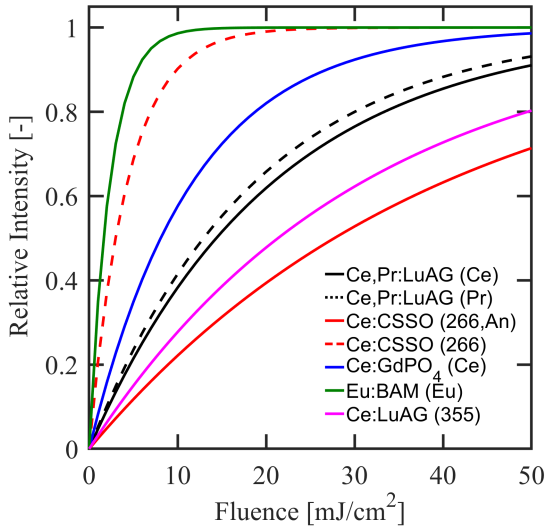

(b) Best-fit curves

Figure 4.11: (a): measured fluence curves normalized by the value at 10 mJ/cm^2 (∼6 ns laser pulse width) with best-fit superimposed, and (b): the best-fit curves normalized by their peak value. A single best-fit curve is shown for Eu:BAM in (b), using the average ESA cross-section value of 24×10^{-17} cm^2. The two Ce,Pr:LuAG data series lie almost directly on top of each other; as do the two raw Ce:CSSO series, and the two Eu:BAM series.

Table 4.6: Estimated ESA and GSA cross-sections at room-temperature. The red and blue Eu:BAM bands were averaged to provide a single measurement.

Phosphor (band)	λ_{ex} [nm]	σ_{ESA} [10^{-17} cm^2]	σ_{GSA} [10^{-19} cm^2]
Annealed Ce:CSSO (Ce^{3+})	266	1.4	0.04
Annealed Ce:CSSO (host)	266	1.6	0.07
Ce:CSSO (Ce^{3+})	266	13	0.46
Ce:CSSO (host)	266	7.2	0.79
Ce,Pr:LuAG (Ce^{3+})	266	2.7	0.15
Ce,Pr:LuAG (Pr^{3+})	266	3.0	0.42
Ce:$GdPO_4$ (Ce^{3+})	266	4.8	0.10
Eu:BAM	355	24	10.2
Ce:LuAG (Ce^{3+})	355	1.8	0.53

4.6.1. The difference between the two results is around 10-15%; this difference provides an estimate of the uncertainty in the fitting procedure.

Using the measured ESA cross-sections and estimated signal-per-ion, the GSA cross-section can be determined at room temperature. At room temperature, assuming the fluorescence quantum yield is 100%, the excited population fraction is identical to the signal-per-ion value. This follows from Equation 4.8, where the photon emission intensity is assumed to be exponential with rate constant k_r. Thus, the GSA cross-section is determined by equating the excited population fraction in Equation 4.13 to the phosphor signal per ion. The best-fit ESA and corresponding GSA cross-sections based on this procedure are tabulated in Table 4.6.

4.6.2 Integration and Excitation Duration

Up to this point, it has been assumed that the entire luminescence emission has been collected, and that the luminescence emission is slow compared to the excitation process. It is worthwhile to consider cases where only a portion of the emission is collected for experiment design. Further, at combustion-relevant temperatures, which are typically much higher than the onset of thermal quenching, it is also worthwhile to consider how signal is impacted by a slow excitation process to understand how laser pulse duration may impact signal generation.

Starting from Equation 4.8, the signal captured for an integration window from t_d to t_f (where t_d is

the gate delay after the laser pulse arrives) is

$$S = k_r \int_{t_d}^{t_f} n^\star(t')dt'. \tag{4.17}$$

Equation 4.13 describes the excited population fraction only during the excitation process. Immediately after the laser pulse ends at time t_p, when $\dot{\phi} = 0$, the population fraction is given instead by the simpler expression

$$\vec{n} = e^{\mathbf{A}(t-t_p)}\vec{n}(t_p), \tag{4.18}$$

where $\vec{n}(t_p)$ is the population vector evaluated immediately at the end of the laser pulse at time t_p. Although this solution looks similar to Equation 4.10, the exponential argument has a different structure (only 2 non-zero elements here compared to 4) which results in a significantly different form. Specifically for the proposed 3-level model system, the population of the excited $5d$ state is given by eigendecomposition as

$$n^\star(t) = n^\star(t_p)e^{-(k_r+k_{nr})(t-t_p)} \qquad t > t_p, \tag{4.19}$$

where $n^\star(t_p)$ is the population fraction in the excited $5d$ state after the laser pulse.

Substituting Equation 4.19 into Equation 4.17, collected signal is calculated in the three level model approximation as

$$S = k_r \int_{t_d}^{t_p} n^\star(t')\ dt' + \frac{k_r}{k_r + k_{nr}} n^\star(t_p)\left(1 - e^{-(k_r+k_{nr})(t-t_p)}\right). \tag{4.20}$$

In general, a numeric integration is performed for the first term. However, in the approximation that the laser pulse is very short compared to the emission time scale, light emitted during the excitation process is negligible and the collected signal can be approximated as

$$S = n_0^\star \frac{k_r}{k_r + k_{nr}}\left(1 - e^{-(k_r+k_{nr})(t-t_p)}\right). \tag{4.21}$$

Note that it has been implicitly assumed that the gate delay is shorter than the laser pulse width; if this is not the case, no light is collected during the excitation process and the remaining term in Equations 4.20 and 4.21 must be altered to include the correct integration limits. This approximation was used in [83], and is reasonable for fluorescence lifetimes long compared to the laser pulse duration; this requirement is satisfied for most phosphors used here except at temperatures significantly above T_{50}.

If instead the laser pulse is comparable or even long compared to the fluorescence decay time, then a significant portion of the signal is emitted during the excitation process. The exact solution could be found by numerically integrating Equation 4.13 in time, and multiplying by k_r. However, as all of the phosphors discussed here have ESA cross-sections much larger than the GSA cross-section, a significant simplification can be found (see the Appendix of [83]) and the excited population fraction during the laser pulse is approximately

$$n^\star(t) = \frac{\sigma_{12}\phi''(t)}{\sigma_{23}\phi''(t) + (k_r + k_{nr})t}\left(1 - e^{-\sigma_{23}\phi''(t) - (k_r+k_{nr})t}\right). \tag{4.22}$$

Now, making the assumption of a square-shaped laser pulse (*i.e.*, constant fluence rate; this may impact the results, but the impact is believed to be negligible for most phosphors and temperatures considered here where the laser pulse is short compared to the luminescence lifetime) and assuming there is no gate delay, the time-dependence cancels out of the exponential pre-factor and the integral can be carried out analytically, with the result

$$\begin{aligned} S &= \int_0^t k_r n^\star(t')dt' = \int_0^{t_p} k_r n^\star(t')dt' + \int_{t_p}^t k_r n^\star(t_p)e^{-(k_r+k_{nr})t'}dt' \\ &= k_r t_p \frac{\sigma_{12}\phi}{\sigma_{23}\phi'' + (k_r+k_{nr})t_p}\left[1 + \frac{e^{-\sigma_{23}\phi'' - (k_r+k_{nr})t_p}}{\sigma_{23}\phi'' + (k_r+k_{nr})t_p}\right. \\ &\qquad \left. + \frac{1 - e^{-(k_r+k_{nr})(t-t_p)} + e^{-\sigma_{23}\phi''}\left(e^{-(k_r+k_{nr})t} - e^{-(k_r+k_{nr})t_p}\right)}{(k_r+k_{nr})t_p}\right], \end{aligned} \tag{4.23}$$

where t_p is the laser pulse duration and t is the integration duration, starting from the arrival of the laser pulse. The last term inside the bracket in Equation 4.23 results from the emission after the laser pulse, while the first two terms correspond to emission during the excitation process. If the entire emission is collected ($t \to \infty$), then the result simplifies to

$$S = k_r t_p \frac{\sigma_{12}\phi}{\sigma_{23}\phi'' + (k_r+k_{nr})t_p}\left[1 + \frac{e^{-\sigma_{23}\phi'' - (k_r+k_{nr})t_p}}{\sigma_{23}\phi'' + (k_r+k_{nr})t_p} + \frac{1 - e^{-\sigma_{23}\phi''}e^{-(k_r+k_{nr})t_p}}{(k_r+k_{nr})t_p}\right]. \tag{4.24}$$

Finally, in the limit where the laser pulse is longer than the lifetime of the decay, $(k_r + k_{nr})t_p > 1$, and that the excitation is relatively weak, $\sigma_{23}\phi'' \ll (k_r + k_{nr})t_p$, the signal simplifies to

$$S \approx \sigma_{12}\phi'' \frac{k_r}{k_r + k_{nr}}. \tag{4.25}$$

There are a few points to note from this result. First, Equation 4.23 could be used to model signal intensity for any laser pulse duration without the need for numeric integration; this is important here

because APT will be used at temperatures where the lifetime is reduced by an order of magnitude or more from the room-temperature value. For some phosphors, *e.g.*, Pr:CSSO, this could result in lifetimes much shorter than the laser pulse duration. Next, in the limit of low excitation with a long laser pulse, the ESA cross-section no longer impacts the measured signal. Instead, electrons in the $5d$ level deactivate quickly before any significant portion can be pumped to the conduction band. Finally, the slow-excitation limit (Equation 4.25) represents a linear PLIF system; this expression is identical to that for a linear, 2-level system (see, *e.g.*, [39]). This not only simplifies the photophysics, but results in an increase in the effective fluorescence quantum yield - more light is emitted when the phosphor is excited slowly. This is advantageous for diagnostics, and the potential for improving diagnostic performance by stretching the laser pulse will be investigated in Chapter 7.

GSA Cross-sections at Elevated Temperatures

Relative signal per particle was measured for each phosphor in the flame (see Section 5.3 for experimental details) as a function of temperature as a SRAPT ratio. From the previous sections, both the ESA and GSA cross-sections at room temperature have been estimated from experimental data, and a detailed model was developed to describe emission intensity in terms of photophysical parameters and the duration and intensity of the laser pulse. Assuming the ESA cross-section is temperature-independent (consistent with the results of [83]), the GSA cross-section was fit at each temperature to the relative signal per particle according to Equation 4.20 using the exact solution of the population model (Equation 4.13). Since the GSA cross-section is proportional to signal intensity to first order, the room temperature value is needed as an anchor. Unlike in [83], it is not assumed that the laser pulse is short relative to the phosphor lifetime, and instead the signal is numerically integrated assuming the laser fluence rate is constant (*i.e.*, a square wave). This may have an impact on fit results particularly at high temperatures, but the impact is expected to be small throughout most of the temperature range considered here, particularly where excited state lifetimes are relatively long compared to the laser pulse duration. The integration duration is assumed to be large enough to capture all of the luminescence emission after the laser pulse ends (*i.e.*, $t \rightarrow \infty$).

The fit results are plotted in Figure 4.12, with fits to the measured luminescence lifetimes shown on the right. For Ce:$GdPO_4$, the Ce^{3+} lifetime is taken to be the fast component of the emission (around 15 ns at room temperature), rather than the average value shown in Figure 4.6. Ce:LuAG at 355 nm excitation is included by fitting the relative signal intensity data from [85], including the high-temperature furnace ratio data at 860 and 900 K to augment the aerosol calibration. The lifetimes

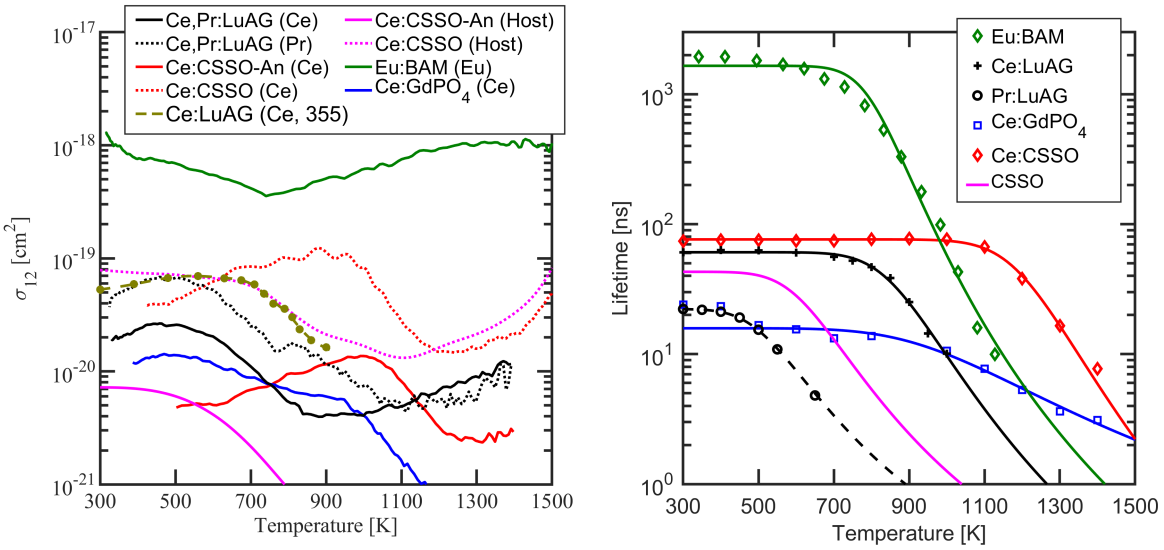

(a) GSA

(b) Lifetime fits

Figure 4.12: Estimated GSA cross-section for Ce:$GdPO_4$, Ce:CSSO, and Ce,Pr:LuAG at elevated temperatures, and the luminescence lifetime fits used to calculate the GSA cross-sections. The label "CSSO" represents the raw CSSO phosphor while "CSSO-An" is used for the annealed phosphor. The pink curve labelled "CSSO" represents the assumed CSSO host emission lifetime.

Table 4.7: Best-fit parameters for phosphor luminescence lifetime model described by Equation 4.26.

Phosphor	k_r [MHz]	$k_{nr,0}$ [GHz]	Θ [10^3 K]
Ce,Pr:LuAG (Ce^{3+})	16.45	9169	11.57
Ce,Pr:LuAG (Pr^{3+})	45.05	129.9	4.373
Ce:$GdPO_4$	63.26	44.63	7.0991
Ce:CSSO	13.1	835100	21.69
Eu:BAM	0.605	17000	13.83
Ce:CSSO (Host)	23.26	385.3	6.21

τ are fit to the form

$$\tau^{-1} = k_r + k_{nr,0} e^{-\Theta/T}, \tag{4.26}$$

where k_r is the radiative deactivation rate, $k_{nr,0}$ is the non-radiative deactivation attempt rate, and Θ is the activation temperature of the non-radiative deactivation mechanism. The parameters for the fits are summarized in Table 4.7.

The table and plots include fits for Ce:CSSO host emission under the assumption that the Ce^{3+} ions act as defect centers; *i.e.*, introduction of Ce^{3+} creates a substitutional defect where the number of absorbers is equal to the number of Ce^{3+} ions. This is a reasonable assumption as host emission appears to follow excitation of a $4f$ electron into the conduction band ($<$ 220 nm for Pr:CSSO [107], and at

355 and 266 nm here for Ce:CSSO and Ce,Pr:CSSO). Indeed, defects possibly resulting from charge or ionic radii mismatch between Pr^{3+} and Ca^{2+} have been suggested to be responsible for slow emission in Pr:CSSO [107] with similar properties as the host emission observed here.

Rather than directly measuring lifetime as a function of temperature, the shape of the quenching curve is taken from fits to the host SRAPT ratio vs. temperature calibration, and k_r is taken from the room temperature lifetime of 43 ns. The ground-state absorption cross section is then calculated in an identical manner to the other phosphors. It should be noted that the three level model was developed for $4f5d$ transitions in rare-earth doped phosphors, and may not be as representative of the host defect emission process. However, the model is believed to be suitable to describe the results for parameters similar to those used in this work (*e.g.*, 6 ns laser pulse, 10-50 mJ/cm^2 fluence).

The GSA cross-sections show a few interesting trends. First, several phosphors seem to have an increasing absorption cross-section (or at least only a slowly decreasing cross-section) at low temperature, and quickly decreasing absorption cross-section at intermediate to high temperatures. This trend is also visible in the Ce:LuAG data from [85]. The increase and subsequent decrease is consistent with harmonic oscillator theory. Consider an absorption peak due to a single electronic transition with vibrational structure superimposed. Exciting near the tail of the absorption peak excites higher vibrational states. As temperature increases, the equilibrium population fraction of these higher states increases until they are fully thermally-activated. Beyond this point, the increasing vibrational partition function causes the absorption cross-section to drop monotonically again (this is similar to the temperature dependence of the formaldehyde absorption cross-section discussed in Chapter 3).

At even higher temperature, most phosphors seem to exhibit a slight increase in absorption cross-section again. The cause of this increase is unclear, but a possible explanation is that it results from error in the assumed fluorescence quantum yield or lifetime fits. There additionally may be small errors resulting from camera non-linearity or other sensor effects. The low to moderate temperature behavior of the GSA cross-section is reasonable, and Ce,Pr:LuAG data matches well with previous measurements [83]. However, due to limitations in equipment and the physical model, there is likely some error at higher temperatures. Regardless of error in these individual components, the measured signal intensities (as well as those predicted by the model fit) are believed to be sufficient for the purposes of signal and performance estimation at similar conditions.

Both the annealed and unannealed Ce:CSSO phosphors' GSA cross-sections have a similar shape, but are scaled and slightly shifted relative to each other. In both cases, the cross-section seems to increase initially first before dropping off again more rapidly at higher temperatures. Likewise, the absorption cross-sections of both ions in Ce,Pr:LuAG seem to increase initially at a near exponential rate, tail off

above 700 K, and begin decreasing by 800 K. This contrasts slightly with the results from [84] at higher temperatures, but in that case, the very short lifetime was not accounted for. For several phosphors, particularly those that quench earlier, the lifetimes are extrapolated at higher temperatures and thus are not necessarily correct. This could influence the shape of the GSA cross-section measured here. However, the results of the signal model are still correct and representative of the signal data.

Signal per ion

Signal per ion is calculated using the best-fit GSA and ESA cross-sections and lifetime fit, presented in Table 4.7, for a 6 ns square-wave laser pulse for several fluence values using Equation 4.24. The results are shown in Figure 4.13. Saturation is evident for all phosphors, particularly Eu:BAM where there is little distinction between curves above 1 mJ/cm^2 except at high temperatures where the lifetime is similar to, or shorter than, the laser pulse duration. Predictions for Eu:BAM at high temperature further illustrate the model result that increasing spontaneous deactivation rates beyond the ESA absorption rate results in a more linear response with total fluence. This in turn leads to higher emitted signal per ion. In Figure 4.13, specifically for Eu:BAM, the initially saturated curves diverge at around 1000 K.

The calculated signal per ion for the Ce:CSSO host emission is plotted in Figure 4.14. The calculation is performed per Ce^{3+} ion, as the emission center and concentration are not known. This scaling does, however, provide a direct comparison in signal intensity between the Ce^{3+} and host emission bands. Both host emissions are relatively strong until around 600 K. In both cases, the host emission prior to quenching is brighter than the Ce^{3+} emission. However, once quenching begins near 600 K, the emission intensity drops quickly by an order of magnitude or more. By 900 K, the host emission in either sample is almost too weak to be observed.

Finally, the results for the Ce:LuAG phosphor with 355 nm excitation are plotted in Figure 4.15. Data was only available for Ce:LuAG up to 900 K, so a smaller temperature range (300-900 K) is considered for this case. The Ce:LuAG data from [85] was additionally taken at higher fluence so fluences up to 110 mJ/cm^2 (the highest fluence measured in [85]) are considered as well. Even at a more modest fluence of 30 mJ/cm^2, at 355 nm excitation the Ce:LuAG emission (per ion) is brighter than every other phosphor up to 900 K except perhaps Eu:BAM near 300 K.

With the lifetime and absorption cross-section data presented previously, the signal model predicts an increase in signal at very high temperatures for several phosphors (*e.g.*, above 1300 K in Ce,Pr:LuAG (Pr^{3+}) and Ce:CSSO (Host)). This is likely a result of experimental error, and thus these points have been removed from the plots.

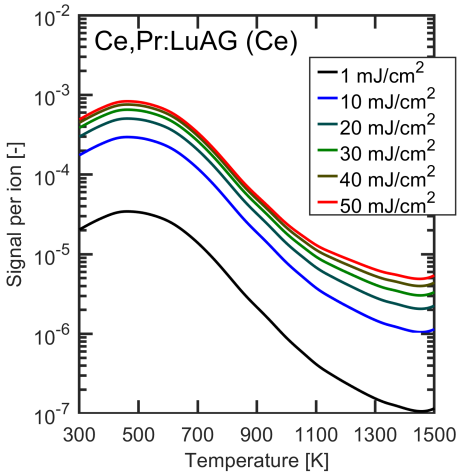

(a) Ce,Pr:LuAG (Ce^{3+})

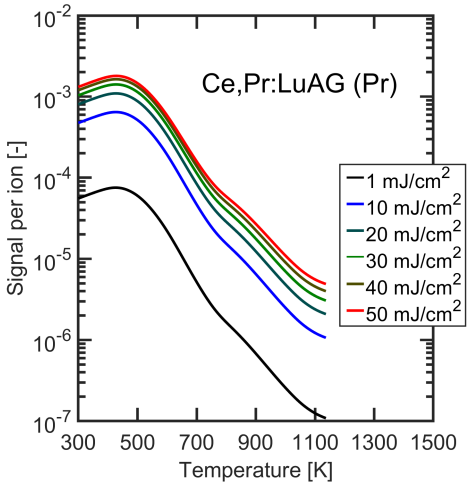

(b) Ce,Pr:LuAG (Pr^{3+})

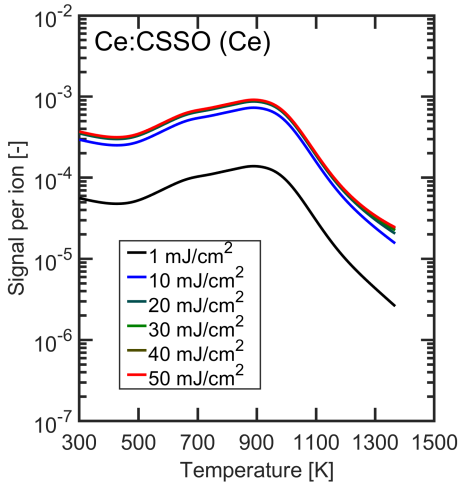

(c) Ce:CSSO (Ce^{3+})

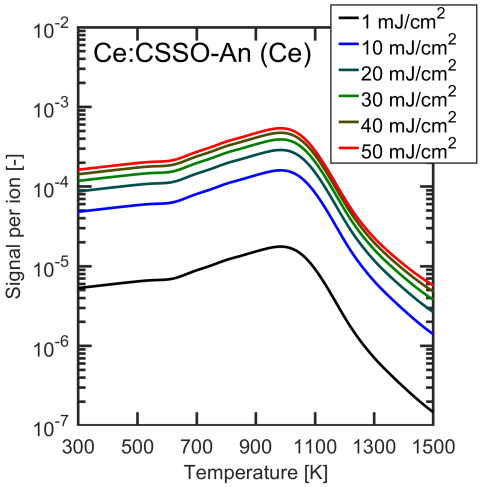

(d) Annealed Ce:CSSO (Ce^{3+})

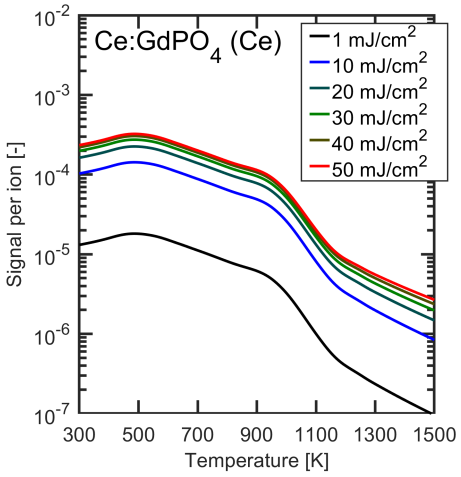

(e) $Ce:GdPO_4$ (Ce^{3+})

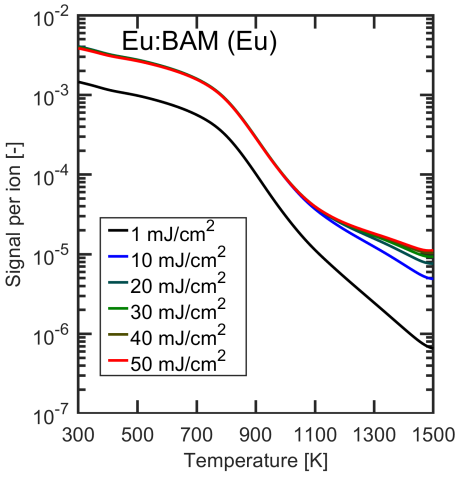

(f) Eu:BAM (Eu^{2+})

Figure 4.13: Signal per ion as a function of temperature and fluence for several phosphors. All phosphors are excited with a 6 ns (FWHM) laser pulse at 266 nm, except Eu:BAM which is excited at 355 nm.

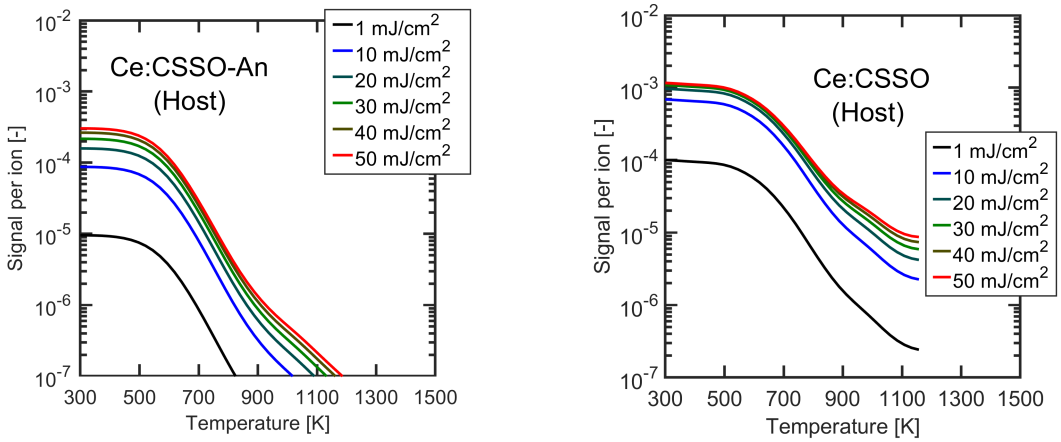

(a) Annealed Ce:CSSO host emission

(b) Raw Ce:CSSO host emission

Figure 4.14: Emitted signal per Ce^{3+} ion as a function of temperature and fluence for annealed and raw Ce:CSSO host emission.

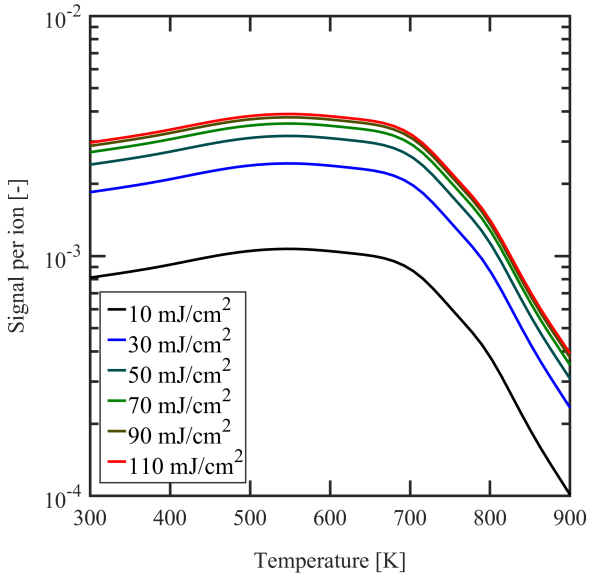

Figure 4.15: Emitted signal per Ce^{3+} ion as a function of temperature and fluence for the Ce:LuAG phosphor at 355 nm excitation.

4.7 APT Performance Modeling

The diagnostics considered in this study are intensity-based; temperature is related to the brightness or intensity of the measured signal. Thus, signal modeling results can be used to estimate diagnostic performance, including temperature precision and bias due to fluence uncertainty or background signals. These performance factors will be analyzed, discussed, and predicted in this section.

4.7.1 Definitions

For a ratiometric, intensity-based diagnostics, temperature is related to a signal ratio R, defined as the flatfield-corrected ratio of two signal measurements, or

$$R = \frac{S_2}{S_1}\frac{S_{1,ref}}{S_{2,ref}}, \tag{4.27}$$

where S_i represents the measured signal intensity in channel i, and the subscript ref indicates a reference or flatfield measurement. The flatfield measurement is needed to correct the ratio for differences in collection efficiency, and effectively sets the ratio to unity at the reference temperature. Temperature is related to this ratio by a calibration function, $T = T(R)$, that is often a complicated function of the ratio, as well as parameters like laser fluence, laser pulse duration or shape, and sensor integration duration.

For a known calibration function, the temperature precision is estimated from first-order uncertainty propagation as

$$s_T = \left|\frac{\partial T}{\partial R}\right| s_R = \frac{s_R}{R\xi_T}, \tag{4.28}$$

where ξ_T is the temperature sensitivity,

$$\xi_T = \frac{1}{R}\left|\frac{\partial R}{\partial T}\right|. \tag{4.29}$$

The temperature precision of the diagnostic then is determined by the calibration function and the ratio precision. The calibration function for an intensity-based technique like co-doped APT or SRAPT is largely intrinsic to the phosphor, as it is a direct measure of signal intensity per ion or per particle, and is thus largely independent of the collection optics (provided the majority of the emission is capture). However, the calibration function, like signal intensity, may depend on the excitation process (laser energy, pulse shape, and duration) as discussed in Section 4.6.

The ratio precision is also related to phosphor properties and the excitation process. From a first-

order uncertainty propagation, the ratio precision can be estimated as

$$\left(\frac{s_R}{R}\right)^2 = \left(\frac{s_{S_1}}{S_1}\right)^2 + \left(\frac{s_{S_1}}{S_2}\right)^2 - 2\rho_{S_1,S_2}\frac{s_{S_1}}{S_1}\frac{s_{S_2}}{S_2} \tag{4.30}$$

where s_x is the precision-index (or estimate of sample standard deviation) of the quantity x, and $\rho_{x,y}$ is the (normalized) correlation between variables x and y. For a shot-noise limited diagnostic, and signal measured in photons, the precision index of a signal measurement s_{S_i} is equal to the square-root of the signal. Further, the shot-noise is uncorrelated between the two measurements as it results from either photon emission or electron capture events, which are random, and hence $\rho_{S_1,S_2} = 0$. The ratio precision can then be written as

$$\frac{s_R}{R} = \sqrt{\alpha_1 S_1^{-1} + \alpha_2 S_2^{-1}}, \tag{4.31}$$

where the coefficients α_i are used to convert the arbitrary signal units of S_i into photons; these coefficients could additionally be used to include additional sources of noise, *e.g.*, added noise from the micro-channel plate of an intensifier, or thermal noise sources. Normalizing Equation 4.31 by its value at the reference condition,

$$\frac{s_R/R}{s_R/R(T_{ref})} = \sqrt{\frac{\alpha_1 S_1^{-1} + \alpha_2 S_2^{-1}}{\alpha_1 S_1^{-1}(T_{ref}) + \alpha_2 S_2^{-1}(T_{ref})}}, \tag{4.32}$$

and defining the new parameter

$$\alpha = \frac{\alpha_1 S_1^{-1}(T_{ref})}{\alpha_1 S_1^{-1}(T_{ref}) + \alpha_2 S_2^{-1}(T_{ref})} \tag{4.33}$$

which specifies the fraction of ratio noise resulting from S_1 ($0 \leq \alpha \leq 1$), Equation 4.31 can be rewritten in terms of the relative signal intensities as

$$\frac{s_R}{R} = \frac{s_R(T_{ref})}{R(T_{ref})}\sqrt{\alpha\frac{S_1(T_{ref})}{S_1} + (1-\alpha)\frac{S_2(T_{ref})}{S_2}}. \tag{4.34}$$

Normally the ratio function would be normalized to unity at the reference temperature, and hence $R(T_{ref}) = 1$, although this is not required and Equation 4.34 is valid in either case. Assuming the signal intensities captured on each sensor have the same magnitude (or SNR) at the reference temperature, then $\alpha = 0.5$, and both cameras contribute equally to the diagnostic precision. This expression ignores contributions from the flatfield correction, as the flatfield images are typically averaged over many measurements, reducing noise significantly. For SRAPT measurements (where scattering intensity is compared to luminescence intensity), there is an additional noise term resulting from the particle

size distribution as the ratio of scattered light to emitted light depends on diameter (luminescence is proportional to d_p^3 and scattering to $Q(d_p)d_p^2$, where $Q(d_p)$ is a scattering efficiency) [85]. This additional term will be referred to as "SRAPT uncertainty", and will be considered in detail in Chapter 6.

4.7.2 APT Ratio and Sensitivity

The ratio dependence on temperature for each phosphor characterized in the flame-heated jet in Section 4.6 for SRAPT are shown in Figure 4.16 for a range of fluences up to 50 mJ/cm^2 using the signal modeling results of Section 4.6, under the assumption that the ESA cross-section is constant with temperature. (Results for Ce:LuAG at 355 nm excitation are discussed later and shown in Figure 4.18.) More specifically, phosphor signal per ion is calculated using the signal model from approximately 300 to 1500 K, and 1 to 50 mJ/cm^2 (the temperature limits are reduced for some phosphors to avoid extrapolating to temperatures where no signal data was available). The SRAPT ratio is then calculated as the inverse of the signal intensity (per ion), and the ratio is normalized to unity at the reference temperature (300 K) for each fluence. This procedure assumes the elastic scattering intensity is independent of temperature.

From Figure 4.6, fluence has little impact on ratio until the onset of thermal quenching. When quenching is not dominant (*i.e.*, $\sigma_{23}\phi'' \gg (k_r + k_{nr})t_p$), the fluence dependence of the emitted signal does not change with temperature. Once thermal quenching becomes significant, spontaneous deactivation pulls electrons out of the excited state in competition with ESA, increasing the dependence of the ratio on laser fluence. This is observed in each phosphor when the lifetime becomes short enough that $\sigma_{23}\phi''$ and $(k_r + k_{nr})t_p$ are comparable in magnitude. Comparing the six phosphor compositions, increasing phosphor non-linearity (*i.e.,* increasing ESA cross-section) leads to an increase in fluence dependence of the ratio. Eu:BAM, having the largest ESA cross-section, exhibits the largest change in ratio when fluence is varied from 1 to 50 mJ/cm^2. Likewise, the annealed Ce:CSSO sample has the smallest ESA cross-section and exhibits the least fluence dependence.

The SRAPT ratio sensitivities are shown in Figure 4.17 for the same set of phosphors. Similar to the ratios, the sensitivity is constant with fluence until spontaneous deactivation becomes significant compared to the ESA process. Increasing fluence decreases sensitivity in general. The peak sensitivity of each phosphor is between 1 and 1.5%/K, with Ce,Pr:LuAG (Ce^{3+}SRAPT) the lowest at 1%/K. The shape of the sensitivity curves show some variation (with a period of a few hundred Kelvins) that is likely not physical; this variation is likely a result of noise influencing the smoothing spline fit to the GSA cross-section values used to generate the plot. However, the average sensitivity value is expected to be reasonably correct as the model results match the measured ratios well.

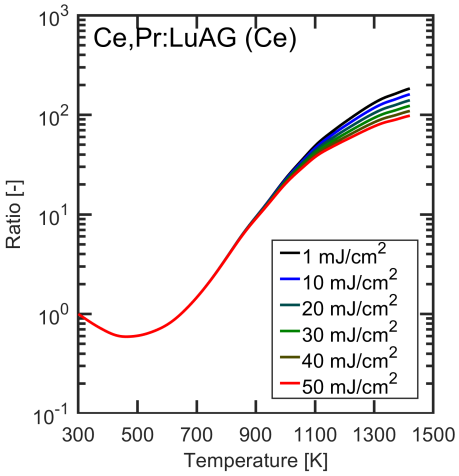

(a) Ce,Pr:LuAG (Ce^{3+})

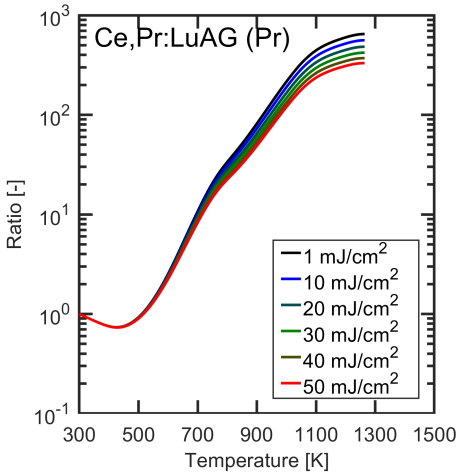

(b) Ce,Pr:LuAG (Pr^{3+})

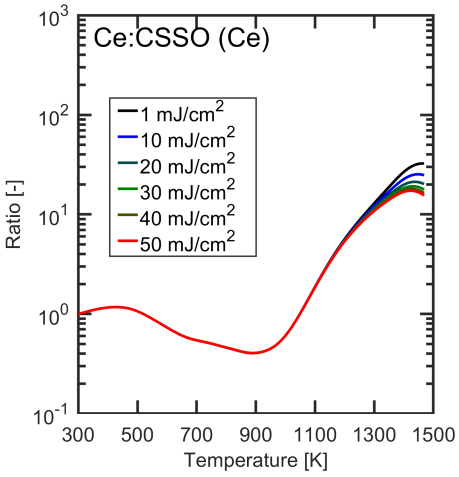

(c) Ce:CSSO (Ce^{3+})

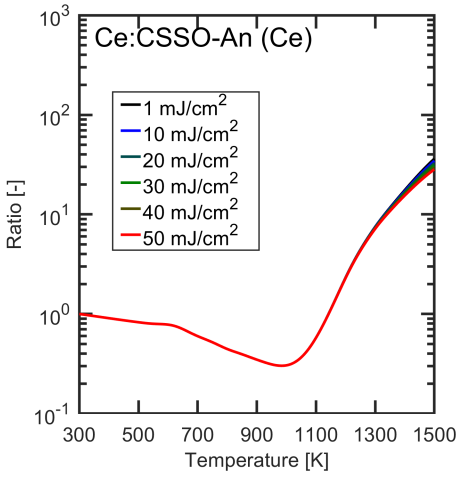

(d) Annealed Ce:CSSO (Ce^{3+})

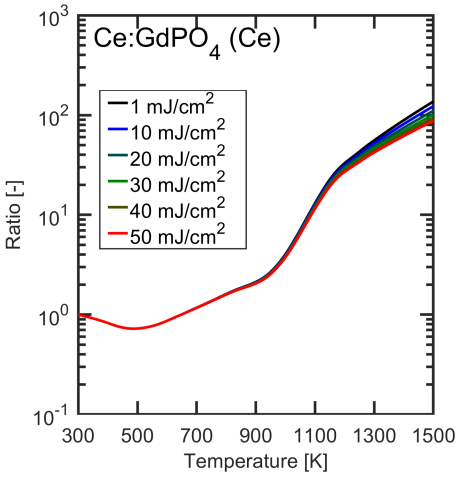

(e) $Ce:GdPO_4$ (Ce^{3+})

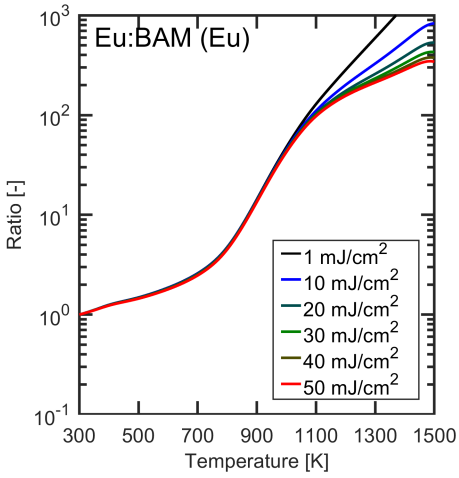

(f) Eu:BAM (Eu^{2+})

Figure 4.16: Ratio calibration functions for each phosphor at several fluences assuming constant ESA cross-section. Eu:BAM is excited at 355 nm, all other phosphors are excited at 266 nm. The laser pulse duration is assumed to be 6 ns for all cases.

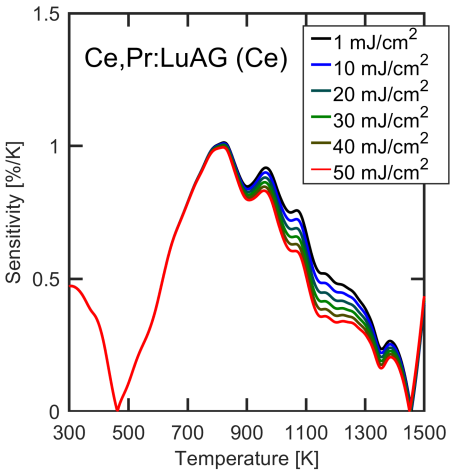

(a) Ce,Pr:LuAG (Ce^{3+})

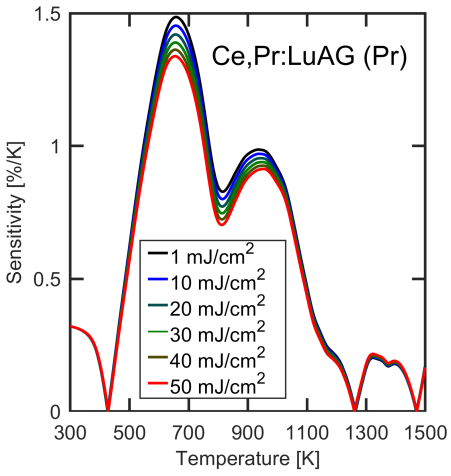

(b) Ce,Pr:LuAG (Pr^{3+})

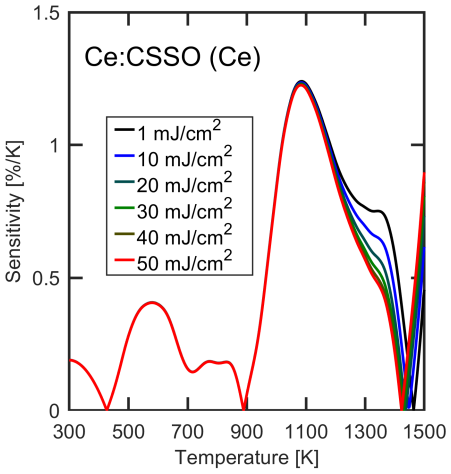

(c) Ce:CSSO (Ce^{3+})

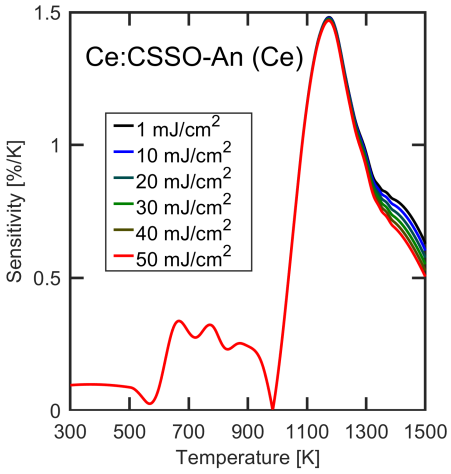

(d) Annealed Ce:CSSO (Ce^{3+})

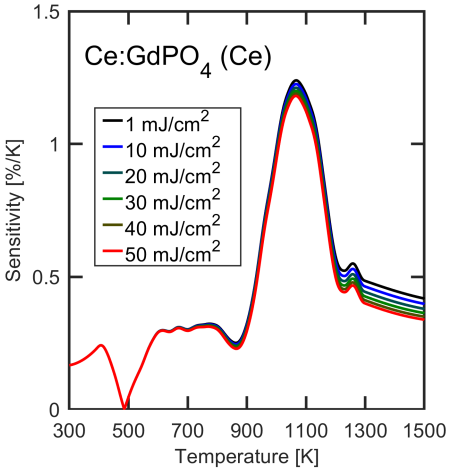

(e) $Ce:GdPO_4$ (Ce^{3+})

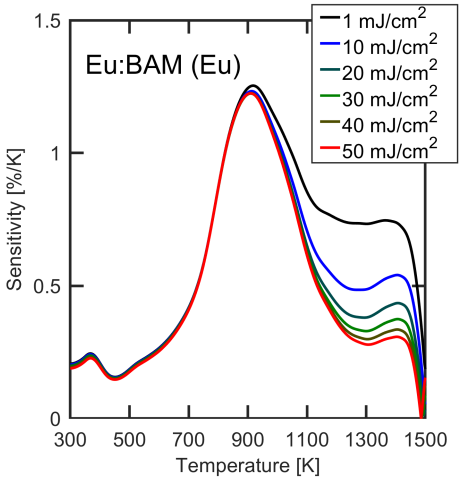

(f) Eu:BAM (Eu^{2+})

Figure 4.17: Ratio sensitivities calculated for each phosphor at several fluences assuming constant ESA cross-section. Eu:BAM is excited at 355 nm, all other phosphors are excited at 266 nm. The laser pulse duration is assumed to be 6 ns for all cases.

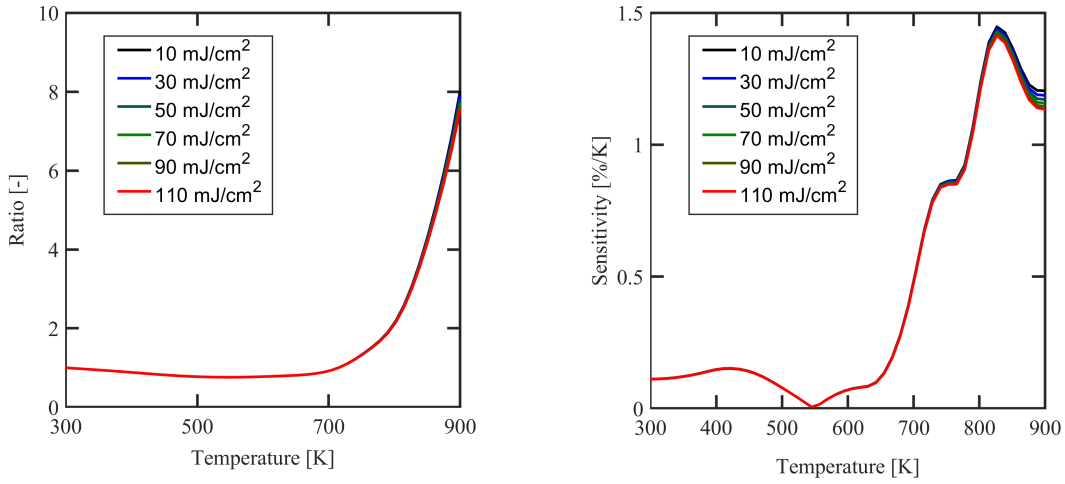

(a) Ratio (b) Sensitivity

Figure 4.18: Ratio and temperature-sensitivity for the Ce:LuAG SRAPT technique at 355 nm excitation with 355 nm excitation and 6 ns laser pulse duration at several fluences.

The ratio and sensitivity of the Ce:LuAG SRAPT technique with 355 nm excitation are shown in Figure 4.18. Similar to the other Ce^{3+}-doped phosphors, both ratio and temperature sensitivity are largely independent of fluence. There is even less fluence-dependence visible in the Ce:LuAG data in Figure 4.18 compared to the other phosphors as Ce:LuAG data is only presented up to temperatures of 900 K. Even at 900 K, the Ce^{3+} lifetime in LuAG is relatively long compared to the laser pulse duration so the weak fluence-dependence is expected. The Ce^{3+} SRAPT sensitivity has a peak value slightly below 1.5%/K near 800 K, similar to the Ce,Pr:LuAG phosphor, and above 800 K it appears the sensitivity is beginning to decrease again.

Co-doped and host-referenced ratios are effectively given by the ratio of the two SRAPT techniques for the two ions in the co-doped phosphor; likewise sensitivity is given as the difference between that of the two SRAPT techniques. The calculated ratio and sensitivity of the Ce,Pr:LuAG co-doped technique are provided in Figure 4.19 for several fluence values. Even for the co-doped technique, where in this case the ESA cross-sections are similar for the two ions and GSA cross-sections have similar temperature-dependence, the ratio is sensitive to fluence after the onset of quenching for at least one ion. The calculated temperature sensitivity shows a similar trend, where sensitivity is maximized at low fluence. The co-doped sensitivity for Ce,Pr:LuAG peaks just under 1%/K, making it the least-sensitive technique investigated so far here. However, since the co-doped method does not have an added ratio noise term resulting from the PSD, a reduction in sensitivity may be acceptable for many applications. Further, the co-doped technique can be used from about 400-700 K, whereas all other phosphors using SRAPT

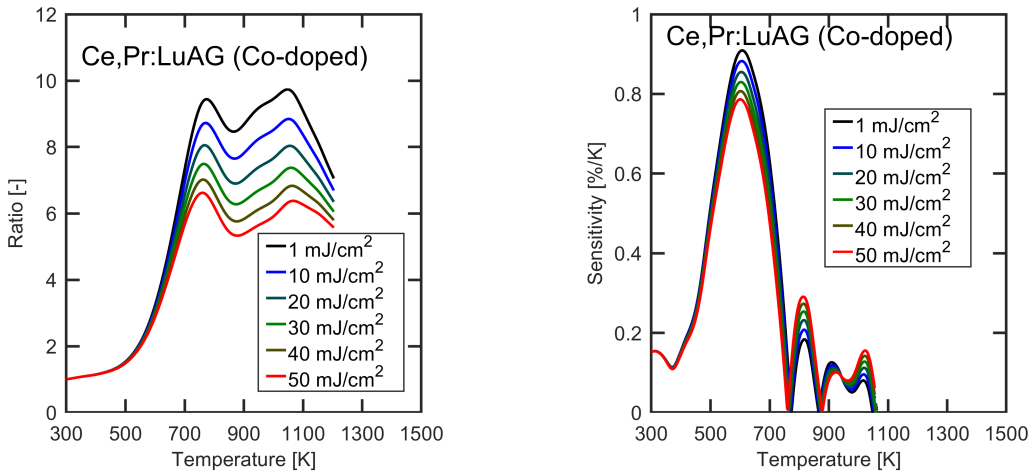

(a) Ratio

(b) Sensitivity

Figure 4.19: Ratio and temperature-sensitivity for the co-doped Ce,Pr:LuAG technique with 266 nm excitation and 6 ns laser pulse duration at several fluences.

(with the exception of Eu:BAM) are double-valued somewhere in this range.

Finally, the host-emission of Ce:CSSO (both annealed and unannealed) can be used as a diagnostic for both SRAPT (using the host emission as the temperature-dependent signal), and as a host-referenced APT technique. The calculated host-SRAPT ratio and sensitivity are plotted in Figure 4.20 for the annealed Ce:CSSO phosphor (top) and the unannealed phosphor (bottom). The host-SRAPT temperature sensitivity is actually quite high compared to several of the other phosphors, peaking near 2%/K for the annealed phosphor. The unannealed Ce:CSSO host-SRAPT diagnostic is usable from around 600 to 900 K, depending on collection efficiency. The annealed Ce:CSSO host-SRAPT technique appears to be viable from around 500 to 800 K; by 900 K, the host emission intensity is reduced by over a factor of 100 from the room temperature intensity and is likely too dim to provide a usable temperature measurement.

Similar to the co-doped Ce,Pr:LuAG technique, a host-referenced technique can be used with the Ce:CSSO phosphors that compares Ce^{3+} emission intensity to the host emission. As may be expected, the ratio calibration curves and temperature sensitivity of the host-referenced technique look very similar to the host-SRAPT technique for both cases, since Ce^{3+} quenching does not really begin until over 1100 K. There is a slight increase in sensitivity for the host-referenced technique due to the increase in Ce^{3+} absorption cross-section up to around 1000 K. However, near 1000-1100 K, there is a zero sensitivity point where the Ce^{3+} and host emission signal sensitivities are equal, and cancel each other out. The host-referenced technique may be capable of providing high quality temperature measurements at the lower end of the low-temperature ignition range (600-800 K).

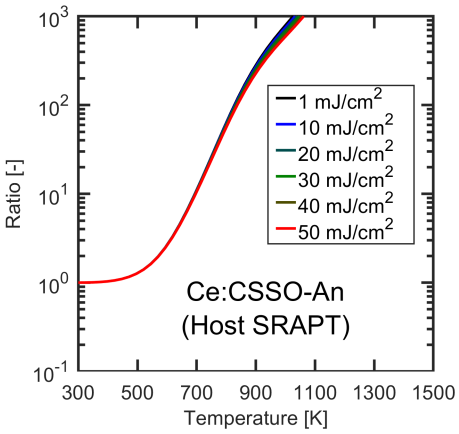

(a) Annealed Ce:CSSO Ratio

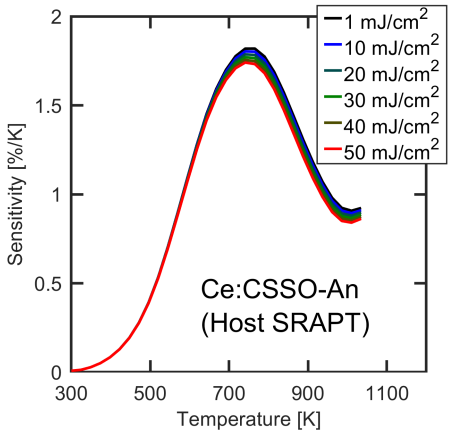

(b) Annealed Ce:CSSO Sensitivity

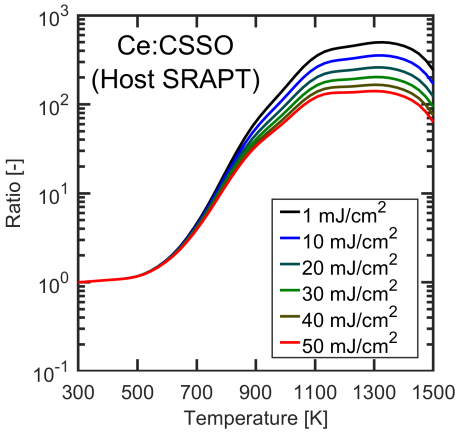

(c) Unannealed Ce:CSSO Ratio

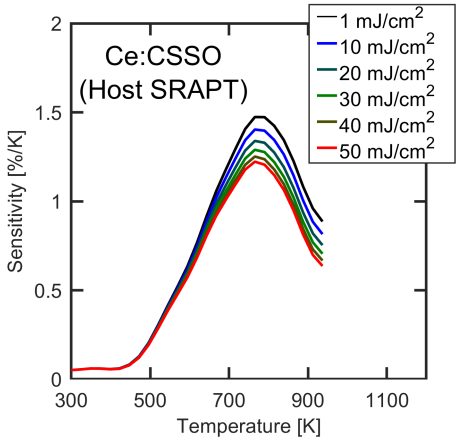

(d) Unannealed Ce:CSSO Sensitivity

Figure 4.20: Ratio and temperature-sensitivity for the annealed (top row) and unannealed (bottom row) Ce:CSSO host-SRAPT techniques with 266 nm excitation and 6 ns laser pulse duration at several fluences.

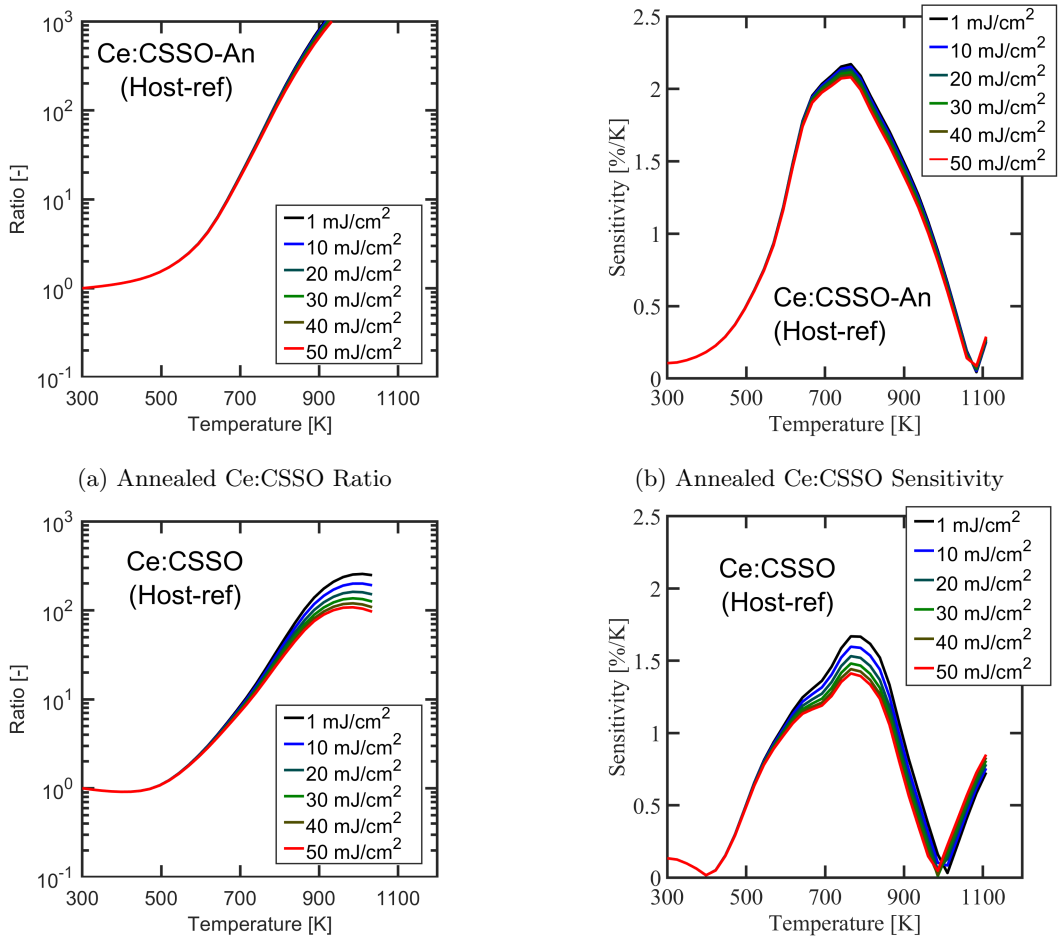

(a) Annealed Ce:CSSO Ratio

(b) Annealed Ce:CSSO Sensitivity

(c) Unannealed Ce:CSSO Ratio

(d) Unannealed Ce:CSSO Sensitivity

Figure 4.21: Ratio and temperature-sensitivity of the annealed (top row) and unannealed (bottom row) Ce:CSSO host-referenced APT techniques with 266 nm excitation and 6 ns laser pulse duration at several fluences.

Peak sensitivities of the co-doped, host-SRAPT, and host-referenced APT techniques again are around 1-2%/K. Interestingly, of all of the phosphors and techniques, the annealed Ce:CSSO host-SRAPT method has the largest temperature sensitivity sensitivity near 2%/K, and the co-doped Ce,Pr:LuAG technique actually has the lowest sensitivity peaking between 0.8 and 0.9 %/K. As with the SRAPT techniques that use $5d-4f$ emission, the host-referenced, co-doped, and host-SRAPT techniques' temperature sensitivity becomes fluence-dependent only after the onset of thermal quenching of at least one of the emission bands. Regardless of fluence, each of the host-SRAPT and host-referenced techniques peak in temperature sensitivity near 700-800 K, and have modest sensitivities over the 500-1000 K temperature range. The co-doped Ce,Pr:LuAG peaks in sensitivity near 500-600 K, and has modest sensitivity over the 400-700 K temperature range. In general, the techniques that rely on host and Pr^{3+} emission are not viable for temperature measurements beyond 900 or 1000 K.

4.7.3 Temperature Precision

Temperature precision was defined in Equation 4.28 as the precision with which a ratio measurement can be made, divided by the temperature sensitivity. Temperature sensitivity was discussed in Section 4.7.2. An expression for relative ratio precision was given in Equation 4.34. The relative ratio precision can be predicted from the signal modeling results. The relative ratio precision calculated for several of the SRAPT techniques are shown in Figure 4.22 with an assumed value of $\alpha = 0.5$, implying both the scattering signal and the luminescence signal contribute equally to the ratio noise at room-temperature. This is representative of typical heated jet SRAPT measurements where the additional SRAPT uncertainty is similar in magnitude to the luminescence shot-noise (*e.g.*, as in [85, 108]).

It is worth noting that with $\alpha = 0.5$ the ratio precision scales slower than $\sqrt{R}$ since the temperature-independent (Mie scattering) portion of the signal contributes a significant portion and is not temperature dependent. If the scattering measurement at room temperature has a negligible impact on the ratio precision (corresponding to $\alpha = 1$), then the ratio precision would scale exactly as $\sqrt{R}$ in the shot-noise limit. For simplicity, the remaining estimates in this section will ignore the SRAPT uncertainty term and use $\alpha = 1$; for performance predictions in Chapter 7, α will be calculated directly based on camera and phosphor properties.

The temperature precision is straightforward to calculate, and requires only an estimate of the ratio precision at room temperature. The ratio precision of the Ce,Pr:LuAG (Pr^{3+}) SRAPT technique at 300 K and a fluence of 20 mJ/cm^2 is assumed to be 10%, and all other precision values are scaled relative to Ce,Pr:LuAG (Pr^{3+}). The SRAPT noise is neglected (SRAPT noise will be discussed further

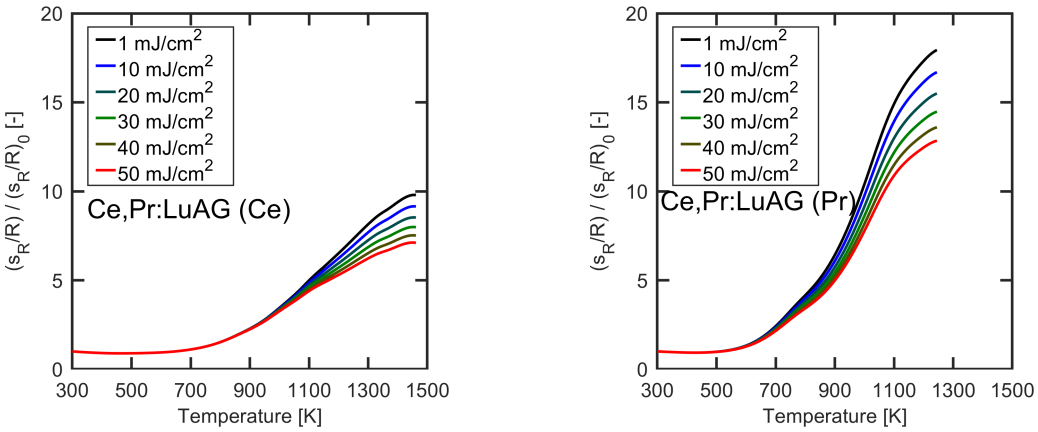

(a) Ce,Pr:LuAG (Ce^{3+})

(b) Ce,Pr:LuAG (Pr^{3+})

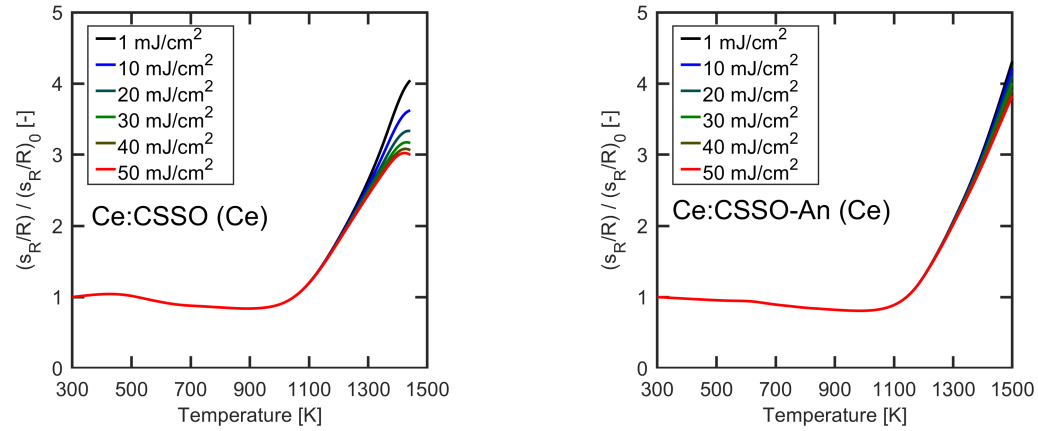

(c) Unannealed Ce:CSSO

(d) Ce:CSSO

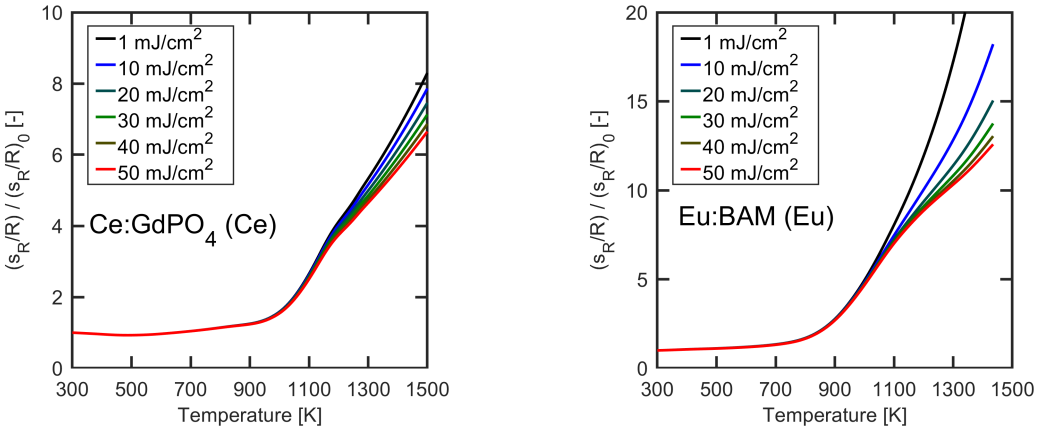

(e) $Ce:GdPO_4$

(f) Eu:BAM

Figure 4.22: Ratio precision indices calculated for several phosphors at several fluences assuming constant seeding density. Eu:BAM is excited at 355 nm, all other phosphors are excited at 266 nm. The laser pulse duration is assumed to be 6 ns for all cases.

in Chapter 6), and it is assumed that the scattering measurement has a negligible impact on precision as elastic scattering typically has a large cross-section relative to fluorescence processes (on the order of 10^6 times larger). The SRAPT ratio precision now scales as $s_R/R \propto \sqrt{R}$ since the scattering contribution is negligible ($\alpha = 1$ in Equation 4.34), and the ratio precision at room temperature scales with $\sqrt{S}$ where S is the signal emitted in photons per particle. Finally, it is assumed that the seeding density and particle diameter are constant for each phosphor. This calculation assumes the same volume of phosphor is added to the flow for each phosphor. The volumetric heat capacity of each phosphor material is the same to within ∼10% in the high-temperature (Dulong-Petit) limit. As a result, the temperature intrusiveness of each phosphor in this calculation is the same to within about 10%. The results for several of the SRAPT techniques are plotted in Figure 4.23.

As expected, increasing fluence tends to make measurements more precise, and measurements are most precise where both temperature sensitivity and signal intensity are high. The Eu:BAM phosphor has the best precision of any phosphor except perhaps Ce,Pr:LuAG (Pr^{3+}) near 600 K, and the Ce:CSSO phosphors at 1100 K. The Eu:BAM phosphor is about a factor of 10 brighter than Ce,Pr:LuAG (Pr^{3+}) for the same particle size; Eu:BAM's ratio precision is improved by about a factor of 3 over Ce,Pr:LuAG (Pr^{3+} SRAPT), and sensitivity after the onset of quenching is not significantly different between the two phosphors. For most phosphors the measurement becomes more precise as fluence is increased, although at the highest fluences near 50 mJ/cm^2 the precision index tends to approach a limiting value due to saturation. Eu:BAM is one exception; after the onset of quenching, precision initially improves with increasing fluence (*e.g.*, from 1 to 10 mJ/cm^2) but at higher fluences the gain in signal no longer balances the loss in temperature sensitivity and the precision index increases. For Eu:BAM, since the saturation is so severe, increasing fluence further provides no gain in signal and higher fluence actually results in worse temperature precision.

The same calculations were performed for the co-doped Ce,Pr:LuAG technique, the results of which are plotted in Figure 4.24. The same case is considered assuming that the Ce,Pr:LuAG (Pr^{3+}) emission intensity measurement has a relative precision of 10% at 20 mJ/cm^2 and room temperature, and the Ce^{3+}emission intensity precision is scaled assuming the detector is shot-noise limited. Comparing the results to those for the SRAPT techniques in Figure 4.23, the co-doped performance is very similar to both the $Ce^{3+}$and Pr^{3+}SRAPT techniques with the Ce,Pr:LuAG phosphor. The best-case precision is below ∼20 K from 500-650 K. The co-doped technique is improved over the Ce,Pr:LuAG SRAPT techniques below 500 K.

The calculation was also performed for the Ce:CSSO phosphors using the host-referenced and host SRAPT techniques, with results displayed in Figure 4.25. As before, the plots are scaled assuming a

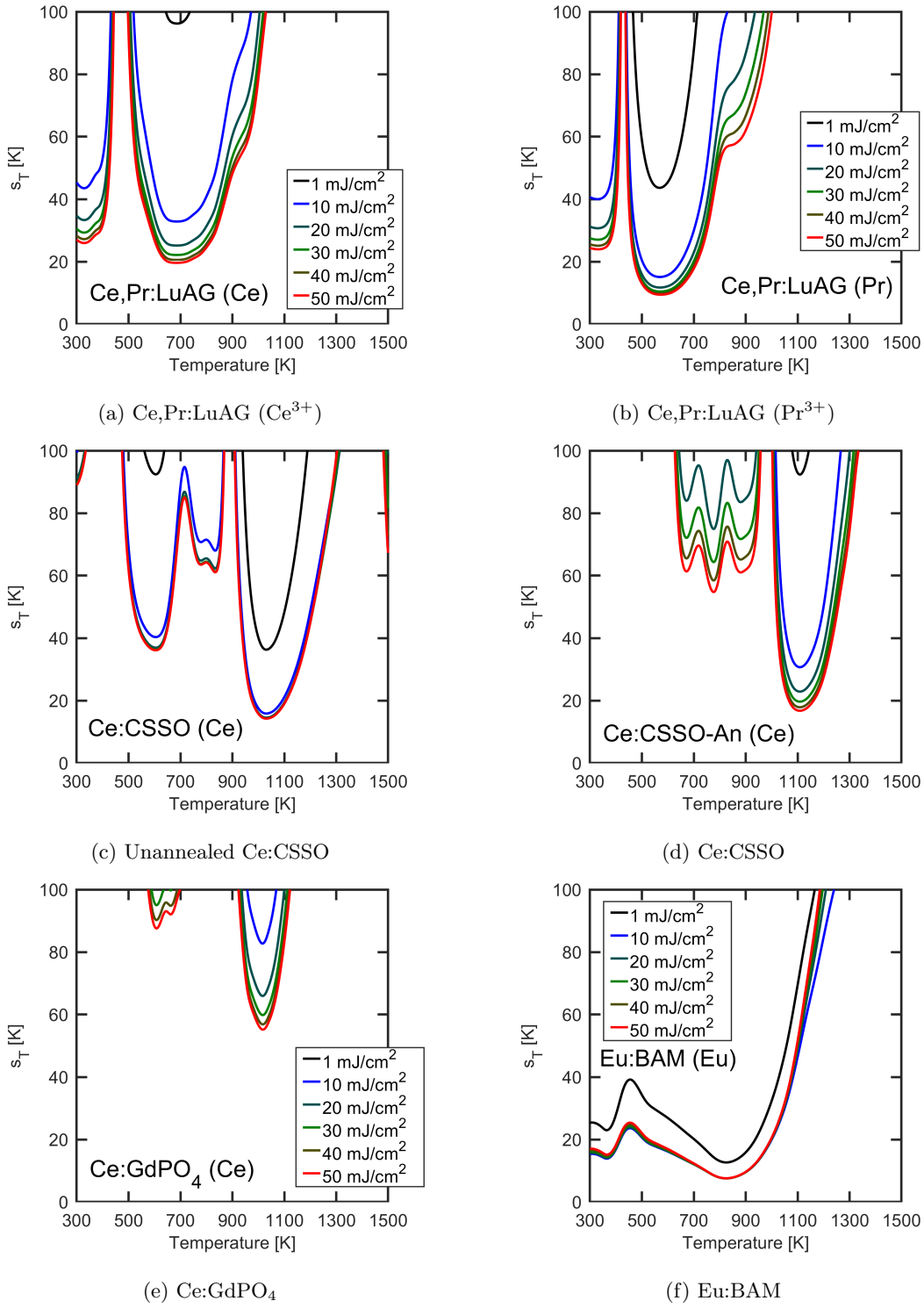

(a) Ce,Pr:LuAG (Ce^{3+})

(b) Ce,Pr:LuAG (Pr^{3+})

(c) Unannealed Ce:CSSO

(d) Ce:CSSO

(e) $Ce:GdPO_4$

(f) Eu:BAM

Figure 4.23: Temperature precision indices calculated for several phosphors at several fluences assuming constant seeding density and particle diameter. The room-temperature ratio precision is 10% for Ce,Pr:LuAG (Pr^{3+}) at 20 mJ/cm^2 laser fluence, and is assumed to scale with $\sqrt{S}$. Eu:BAM is excited at 355 nm, all other phosphors are excited at 266 nm. The laser pulse duration is assumed to be 6 ns for all cases.

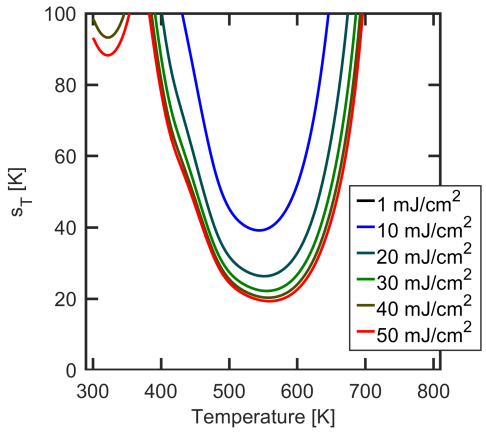

Figure 4.24: Calculated temperature precision of the co-doped Ce,Pr:LuAG technique assuming a 10% signal precision for the Pr^{3+} emission at 20 mJ/cm^2 fluence with 266 nm excitation and 6 ns laser pulse duration.

shot-noise limited detector setup such that Ce,Pr:LuAG (Pr^{3+}) has a signal intensity precision of 10% at 20 mJ/cm^2. The estimated performance host-referenced technique is a significant improvement over many of the other diagnostics in the 500-800 K temperature range, particularly for the unannealed phosphor.

Finally, the temperature precision calculations were performed for the Ce:LuAG phosphor with 355 nm excitation, and the results are displayed in Figure 4.26 assuming a shot-noise limited detector, scaled such that the signal intensity precision for Ce,Pr:LuAG Pr^{3+} emission is 10% at 300 K and 20 mJ/cm^2 fluence. The temperature precision of Ce:LuAG SRAPT at 355 nm excitation peaks near 800 K as expected from the sensitivity curve, and appears to be capable of a very precise measurement, and is second to only Eu:BAM in terms of temperature precision over the 700-1000 K temperature range.

The results of this analysis provide a few useful insights relating to diagnostic design. There is a trade-off between signal and sensitivity resulting from the phosphor non-linearity. If signal is not the limiting factor in the experiment, *e.g.*, if seeding density can be set to reach a target signal level, low fluence should be used to maximize temperature sensitivity and thus diagnostic precision. However, if seeding density is constrained to limit intrusiveness, some optimization procedure must be performed. If the phosphor seeding density is the limiting factor in the experiment, then high-fluence is preferable, although an optimization procedure may be needed to identify the laser fluence that minimizes temperature precision index depending on the phosphor.

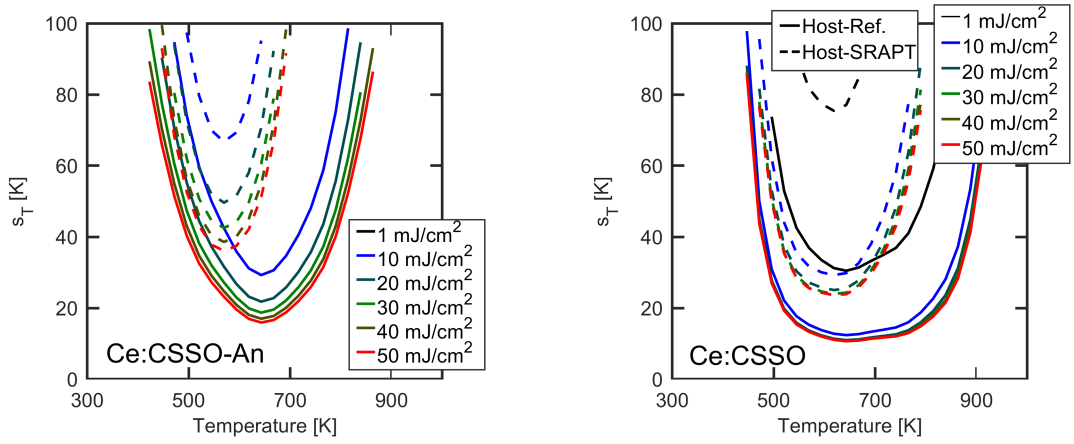

(a) Annealed Ce:CSSO

(b) Unannealed Ce:CSSO

Figure 4.25: Calculated temperature precision of the annealed and unannealed Ce:CSSO phosphors using the host-referenced APT and host SRAPT techniques with 266 nm excitation and 6 ns laser pulse duration at several fluences.

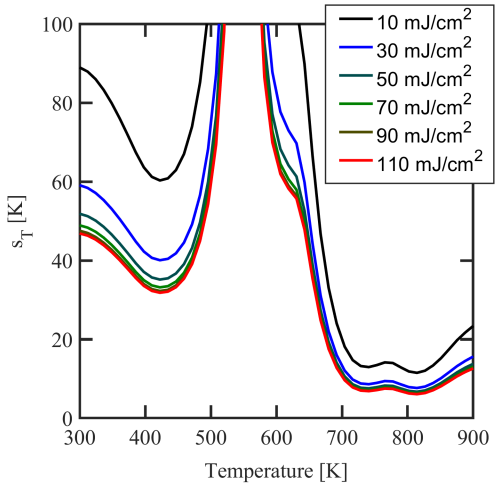

Figure 4.26: Calculated temperature precision of the Ce:LuAG SRAPT technique at constant seeding density with 355 nm excitation and 6 ns laser pulse duration at several fluences.

4.7.4 Combining Diagnostics

For co-doped phosphors, and Ce:CSSO where host emission can be measured, multiple diagnostics can be used simultaneously. Since each of these phosphors have two emission bands, two SRAPT techniques can be performed simultaneously with either co-doped APT (for Ce,Pr:LuAG) or host-referenced APT (for Ce:CSSO). These three measurements are made simultaneously using three detectors, and thus provide three independent measurements of temperature that can be combined to make a single improved temperature measurement using a weighted average approach.

The weighted average temperature is defined as

$$\bar{T} = \left(\sum_i T_i w_i\right) / \sum_i w_i, \tag{4.35}$$

where index i corresponds to the three techniques, T_i is the temperature measured by technique i, and w_i indicates the relative weighting of technique i. Assuming the uncertainties of each technique are uncorrelated, the temperature precision-index of the mean is given by

$$s_{\bar{T}}^2 = \frac{\sum_i s_{T_i}^2 w_i^2}{(\sum_i w_i)^2}. \tag{4.36}$$

From [109], the precision index (standard deviation) of the weighted average is minimized when

$$w_i = \frac{1}{s_T^2}, \tag{4.37}$$

or rather when the weight of a measurement is the inverse of its sample variance. The weighted average temperature variance is given by

$$\frac{1}{s_{\bar{T}}^2} = \sum_i \frac{1}{s_{T_i}^2}, \tag{4.38}$$

such that for N measurements of equal precision s_T, the weighted average precision $s_{\bar{T}}$ is given by $s_T/\sqrt{N}$, as expected for averaging N identical measurements.

For combining APT measurements, at best this results in about a 40% decrease in noise (or reduction by a factor of $\sqrt{3}$) if all three measurements have the same precision. However, the primary purpose of the weighted-average procedure is to intelligently combine the three measurements into a single measurement that covers a larger temperature range. This can be seen analytically as follows from the average

temperature sensitivity. The temperature precision of an individual measurement is given by

$$s_{T_i} = \frac{1}{\xi_{T_i}} \frac{s_{R_i}}{R_i}, \tag{4.39}$$

which is determined by the ratio precision, and the temperature sensitivity of the technique. The temperature precision of the combined technique can be defined analogously,

$$s_{\bar{T}} = \frac{1}{\xi_{\bar{T}}} \frac{s_{\bar{R}}}{\bar{R}}, \tag{4.40}$$

in terms of an average sensitivity $\xi_{\bar{T}}$, average ratio $\bar{R}$, and average ratio precision $s_{\bar{R}}$. Substituting Equation 4.38 into the temperature precision expression, and rewriting the individual temperature precision indices in terms of the relative weightings (using the temperature precision from Equation 4.39) results in

$$\frac{1}{s_{\bar{T}}^2} = \sum_i \xi_{T_i}^2 \frac{R_i^2}{s_{R_i}^2} = \xi_{\bar{T}}^2 \frac{\bar{R}^2}{s_{\bar{R}}^2}. \tag{4.41}$$

Defining the average ratio precision analogously to temperature precision,

$$\frac{\bar{R}^2}{s_{\bar{R}}^2} = \sum_i \frac{R_i^2}{s_{R_i}^2} = \sum_i \frac{w_i}{\xi_{T_i}^2}, \tag{4.42}$$

where the right-hand side follows from Equation 4.39, the average sensitivity becomes

$$\xi_{\bar{T}}^{-2} = \frac{\sum_i w_i \xi_{T_i}^{-2}}{\sum_i w_i}. \tag{4.43}$$

The average sensitivity is thus the inverse of the sum of the inverse-squared sensitivities of the individual techniques. Thus, the average sensitivity is always at least as large as the largest individual diagnostic sensitivity; the sensitivity of the average diagnostic is increased over that of a single diagnostic when multiple diagnostics have high temperature sensitivity.

As an example, the averaged temperature sensitivity and estimated temperature precision up to 1000 K for the Ce,Pr:LuAG phosphor (combining the Ce^{3+} SRAPT, Pr^{3+} SRAPT, and co-doped techniques) are shown in Figure 4.27. The temperature precision is calculated assuming the ratio measurement for each technique has a signal-to-noise ratio of 10 at 294 K. The average sensitivity is calculated from Equation 4.43, using signal modeling results from previous sections. The sensitivity plot has the relative weights of each technique, normalized such that the weights sum to 1, averaged over the 6 fluence values presented in the figure. From the plots, the Ce^{3+} SRAPT technique is dominant above 700 K, but also

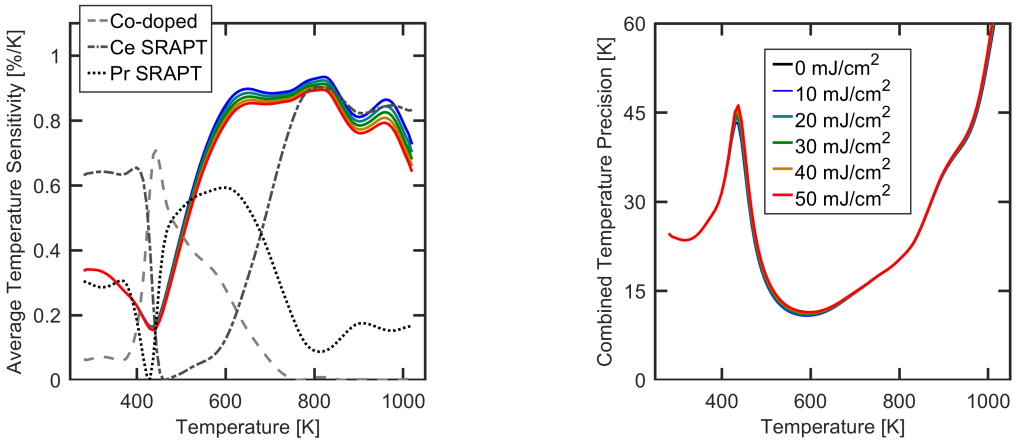

(a) Average sensitivity

(b) Precision

Figure 4.27: Temperature sensitivity and estimated temperature precision of the combined Ce,Pr:LuAG technique with 266 nm excitation (6 ns laser pulse duration) assuming each diagnostic has an initial ratio SNR of 10 at 294 K. Relative weightings for each technique are shown superimposed on the sensitivity plot (left), averaged over the 6 fluence values shown in the plot.

can be used below 400 K. The Pr^{3+} SRAPT technique is the dominant technique from about 500 to 700 K, while the co-doped technique performs best in a small window around 450 K. The effective sensitivity is at least 0.2%/K over the entire range.

4.7.5 Bias Estimation

From Equation 4.27, the ratio depends on the measured signal of each band at a reference condition. Assuming the laser pulse and integration durations are fixed, the ratio will depend parametrically on the laser fluence and temperature at the reference condition. More specifically, the ratio is a function

$$R = R(T; \phi'', T_0, \phi_0''), \tag{4.44}$$

with one independent variable (temperature T) and three parameters: laser fluence ϕ'', reference laser fluence ϕ_0'', and reference temperature T_0. For pulsed laser applications, the laser pulse and integration durations are typically constant to a good approximation. However, significant variation is possible in laser fluence due to thermal drift. Additionally, temperature may not be known accurately at a reference condition, for example, in an optically accessible engine. Uncertainties in any of these three parameters can potentially result in a significant bias in the measured temperature.

The effect of a bias in any of these three parameters (ϕ'', ϕ_0'', or T_0) can be estimated through a

first-order uncertainty propagation:

$$b_{T;x} \approx \frac{\partial T}{\partial x} b_x = \frac{\xi_x}{\xi_T} b_x, \tag{4.45}$$

where the variable x is used to stand in for any parameter that impacts the ratio, and the symbol b_x represents the bias in the quantity x. Likewise, ξ_x is the fractional sensitivity of the ratio to the quantity x, defined as

$$\xi_x = \frac{1}{R} \frac{\partial R}{\partial x}. \tag{4.46}$$

The bias (normalized by b_x) and sensitivity to x can be calculated directly from the ratio. The normalized temperature bias

$$\beta_{T;x} = \frac{x}{b_x} \frac{b_{T;x}}{T} = \frac{x}{T} \frac{\xi_x}{\xi_T}, \tag{4.47}$$

is plotted in Figures 4.28, 4.29, 4.30 for the fluence bias, reference temperature bias, and reference fluence bias, respectively.

As observed in Figure 4.28, a fluence bias has an almost negligible effect on the measurement. For this calculation, the fluence and the reference fluence are still assumed to be identical, and the corresponding temperature bias is a result of having the incorrect calibration function. At higher temperatures, where the ratio calibration function becomes fluence dependent, the fluence bias can become more significant as evident in the plots. The fluence bias additionally becomes significant where temperature sensitivity is low or zero, such as at the local extrema of the calibration function (*e.g.*, 550 K in Ce,Pr:LuAG Ce^{3+}SRAPT, or 900 K in Ce:CSSO Ce^{3+}SRAPT). In contrast, Figure 4.30 shows a large sensitivity to the reference fluence. For the reference fluence uncertainty, only the fluence in the reference condition is varied while the fluence for the measurement condition is held constant. This could result from, *e.g.*, thermal drift in the laser. Since the reference condition provides a constant scale factor to the measured ratio, a small uncertainty in the reference fluence can greatly impact the measurement. However, as the phosphors become saturated, the fluence bias diminishes as small increases in fluence have a diminishing impact on the emitted signal intensity. Similar to the fluence bias, the reference fluence bias peaks when temperature sensitivity is low or zero.

The bias resulting from uncertainty in reference temperature is largely independent of fluence. The shape of the curves in Figure 4.29 is determined by the inverse of the temperature sensitivity, while the magnitude scales with the temperature sensitivity at the reference temperature (here assumed to be 300 K). The normalized reference temperature bias is generally low (between 0 and 0.2) where each phosphor exhibits its peak temperature sensitivity. Like with fluence bias, the sensitivity is maximized where temperature sensitivity is low or zero.

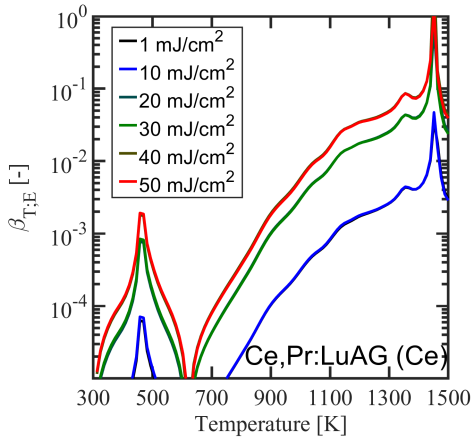

(a) Ce,Pr:LuAG (Ce^{3+})

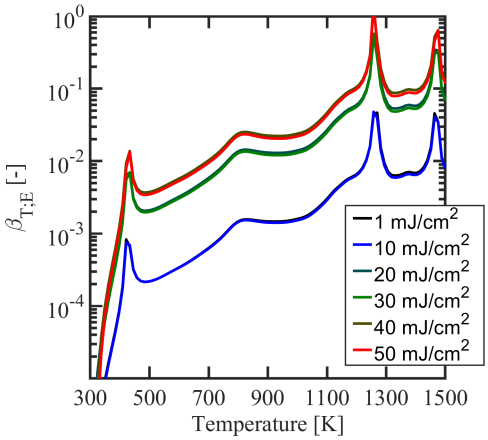

(b) Ce,Pr:LuAG (Pr^{3+})

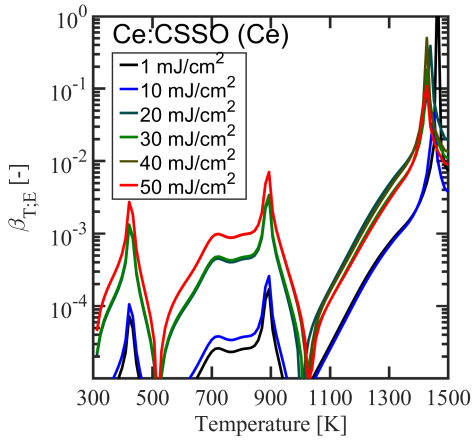

(c) Unannealed Ce:CSSO

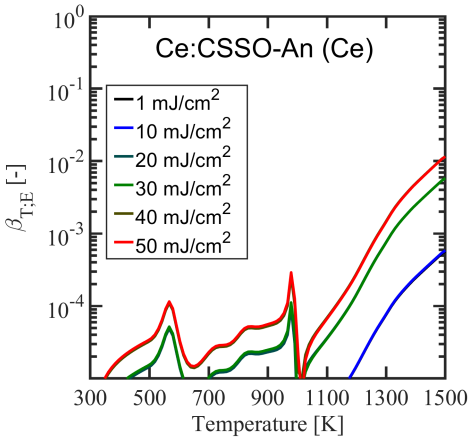

(d) Annealed Ce:CSSO

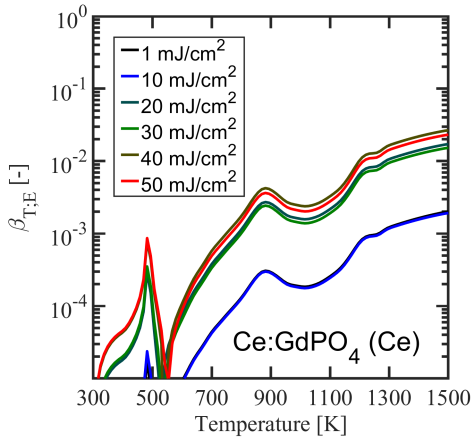

(e) $Ce:GdPO_4$

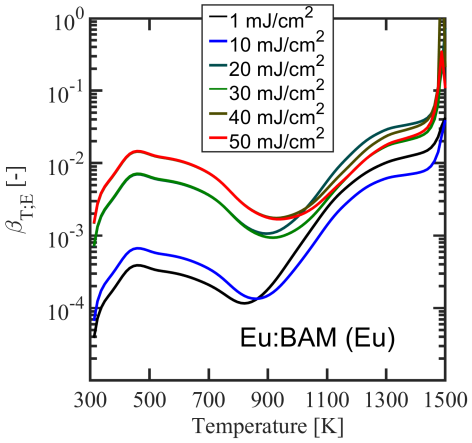

(f) Eu:BAM

Figure 4.28: Calculated sensitivity of SRAPT temperature measurements to laser fluence for several phosphors. Eu:BAM is excited at 355 nm, all other phosphors are excited at 266 nm. The laser pulse duration is assumed to be 6 ns for all cases.

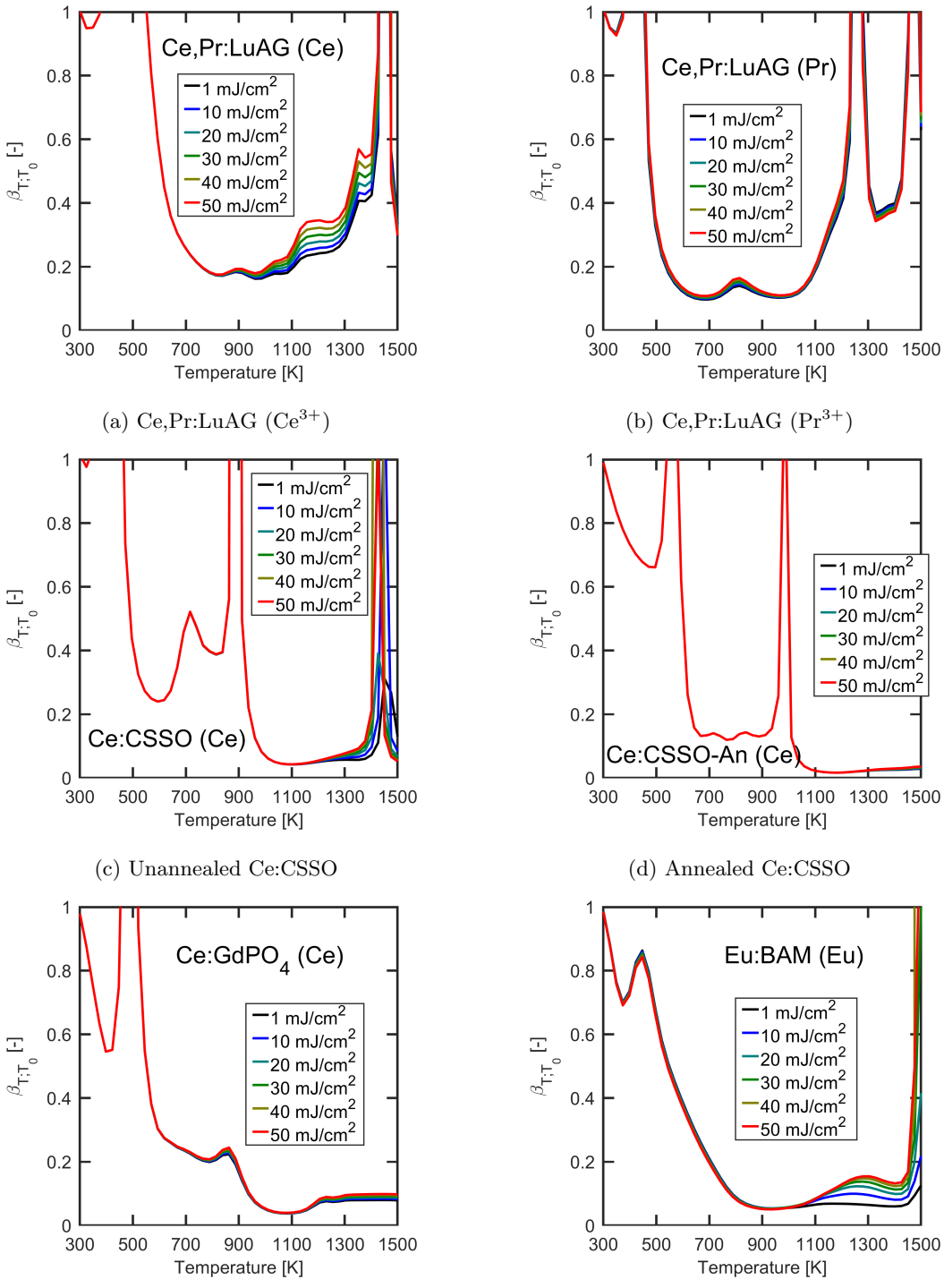

(a) Ce,Pr:LuAG (Ce^{3+})

(b) Ce,Pr:LuAG (Pr^{3+})

(c) Unannealed Ce:CSSO

(d) Annealed Ce:CSSO

(e) $Ce:GdPO_4$

(f) Eu:BAM

Figure 4.29: Calculated sensitivity of SRAPT temperature to reference temperature for several phosphors. Eu:BAM is excited at 355 nm, all other phosphors are excited at 266 nm. The laser pulse duration is assumed to be 6 ns for all cases.

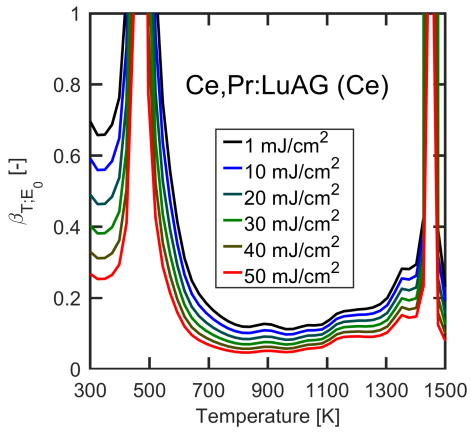

(a) Ce,Pr:LuAG (Ce^{3+})

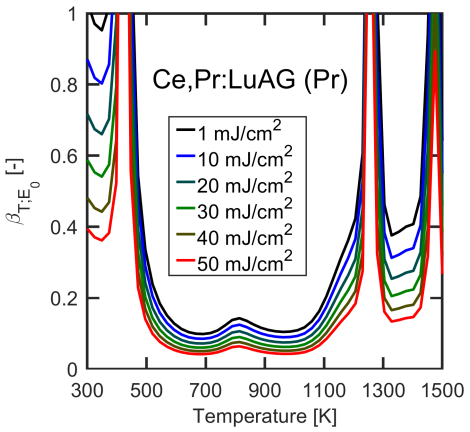

(b) Ce,Pr:LuAG (Pr^{3+})

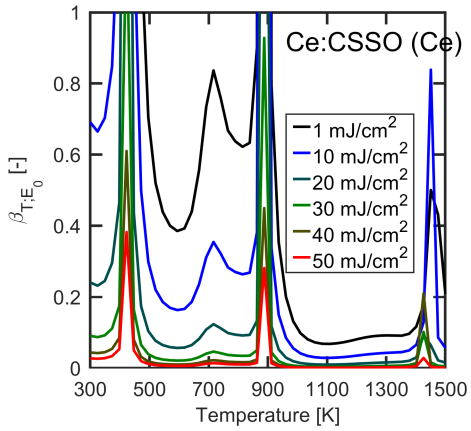

(c) Unannealed Ce:CSSO

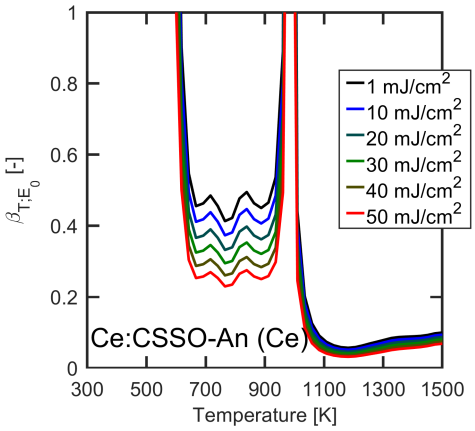

(d) Annealed Ce:CSSO

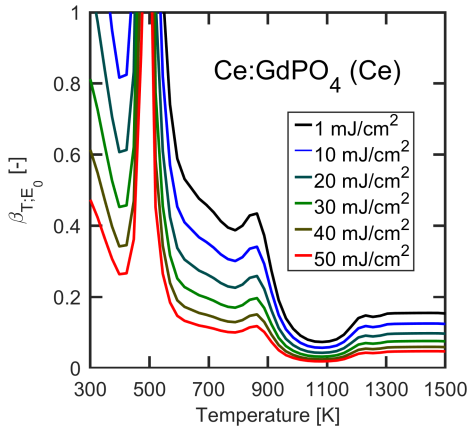

(e) $Ce:GdPO_4$

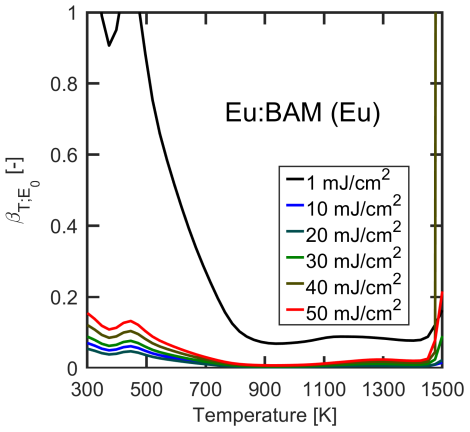

(f) Eu:BAM

Figure 4.30: Calculated sensitivity of SRAPT temperature measurements to reference laser fluence for several phosphors. Eu:BAM is excited at 355 nm, all other phosphors are excited at 266 nm. The laser pulse duration is assumed to be 6 ns for all cases.

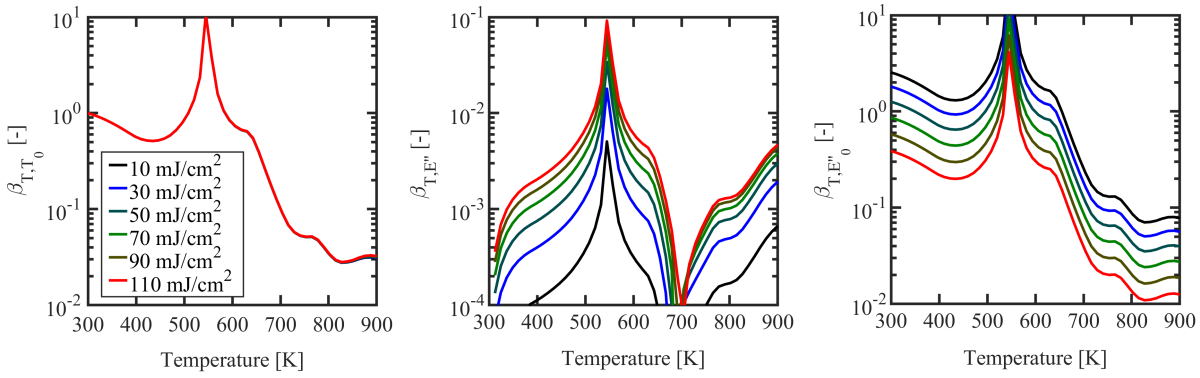

(a) $\beta_{T;T_0}$ (b) $\beta_{T;E''}$ (c) $\beta_{T;E''_0}$

Figure 4.31: Sensitivity of temperature measurements to reference temperature, fluence, and reference fluence for Ce:LuAG SRAPT at 355 nm excitation and 6 ns laser pulse duration.

Finally, the three normalized biases ($\beta_{T;T_0}$, $\beta_{T;E''}$, and $\beta_{T;E''_0}$) are plotted for the Ce:LuAG SRAPT technique at 355 nm excitation in Figure 4.31. As with the other phosphors, the temperature bias resulting from any of the sources considered is relatively small where the phosphor is sensitive to temperature, and becomes very large when the temperature sensitivity goes to zero at ~500 K. Both reference fluence and reference temperature uncertainty could have an impact on the measurement results, but as observed in the ratio curves in Figure 4.18, fluence has little impact on the ratio and sensitivity at the temperatures considered here.

This analysis additionally provides some insights for diagnostic design. Typically the reference condition is taken as room temperature, and the same fluence used for data collection ($E'' = E''_0$). Most of the phosphors used here are intended to have high temperature sensitivity at high temperatures; as a result most have little or no temperature sensitivity at 300 K. As such, to reduce error due to uncertainty in the reference temperature, it is advisable to choose the reference temperature at a point where the phosphor is insensitive to temperature. The same argument applies to laser fluence; using a fluence where the phosphor is insensitive to changes in fluence is advantageous to reduce uncertainty. Increasing fluence tends to both decrease temperature sensitivity (increasing s_T) and decrease fluence sensitivity (decreasing $b_{T,\phi''}$) as a result of saturation. An optimization procedure is needed to minimize the total temperature uncertainty, $u_T^2 = s_T^2 + b_{T,\phi''}^2$.

4.8 Conclusions

This chapter described the results of several phosphor characterization experiments including furnace measurements (where bulk powder samples were analyzed), and heated jet and flame measurements.

Analysis of bulk powder samples were used to investigate quenching at high-temperatures in phosphors, primarily through analysis of fluorescence decay curves. Furnace measurements additionally provided emission spectrum bandshapes. Aerosol (heated jet) measurements were used to estimate absolute emission intensities on a per particle basis at different excitation laser fluences. This data was used later in the chapter to develop a signal model (based on population dynamics) to describe the fluence and temperature dependence of the observed signal trends. The signal model makes up a significant portion of a performance prediction model (including the combination of several diagnostics performed simultaneously) which was also derived and discussed in detail in this chapter.

Some preliminary performance and signal estimates for a variety of phosphors were presented and discussed in this chapter in a way that was intended to be independent of the experimental setup details. In particular, trends in signal, temperature sensitivity, and temperature measurement precision were discussed for different phosphors and measurement techniques. Many of the phosphors and techniques appear to be capable of similar peak performance for the same level of intrusiveness (in terms of heat capacity added to the flow), but significant differences were observed in the range at which precise measurements can be made. Finally, potential sources of bias were analyzed and presented for each phosphor and technique. The signal and performance model (and associated data) will be used in Chapter 7 to perform detailed performance predictions that account for equipment limitations, and to recommend a particular phosphor and technique for the proposed measurements.

Chapter 5

Aerosol Phosphor Thermometry Imaging Demonstration

A significant amount of effort went into APT characterization and calibration that was presented in Chapter 4 in an effort to design an improved APT diagnostic that can be used simultaneously with formaldehyde PLIF. In this chapter, the results of the APT characterization and calibration were used to demonstrate the use of several phosphors and techniques. These results show the potential thermometry performance (including precision and temperature range) that can be achieved using the selected phosphors and techniques, demonstrate the use of the phosphor signal model for diagnostic calibration, and validate many of the performance modeling results of Section 4.7. Additionally, the demonstration results highlight some additional issues that need to be considered for diagnostic design, including the impact of multiple scattering and other biases from background sources.

Two experiments were performed and are discussed in this chapter. First, the Ce,Pr:LuAG phosphor was applied to an electrically heated air jet, and measurements were made using the Ce^{3+} SRAPT, Pr^{3+} SRAPT, and co-doped APT techniques. Measurements were made up to 800 K in a uniform temperature jet to assess temperature measurement performance, and measurements up to 900 K were made in a non-uniform temperature field to demonstrate the combination of the co-doped and SRAPT diagnostics. Next, the Ce,Pr:LuAG, Ce:CSSO, Ce:$GdPO_4$, and Eu:BAM phosphors were used in an air jet heated via mixing with the products of a methane-air flat flame. The flame-heated jet results are used primarily to demonstrate the temperature range of the different thermometry techniques. The results shown in this chapter are primarily from [83, 84, 108], with some results that have not yet been published.

5.1 Ce,Pr:LuAG Heated Jet Imaging

The first experiment that will be discussed is a heated air jet that was investigated using the Ce,Pr:LuAG phosphor. The jet was operated in two different configurations, one where a uniform temperature field was achieved from 300 to 800 K in increments of 100 K, and another configuration where a non-uniform temperature profile was established with a cold jet center around 550 K and a hot edge near 900 K. This range conveniently spans much of the usable range of the Ce,Pr:LuAG phosphor. The experimental setup information, including an estimate of optical parameters, is given in Section 5.1.1. In both configurations, the jet was operated at a constant air mass flow rate (1 scfm) which results in a mean exit velocity of 1.7 m/s at room temperature. The flow in the tube is not turbulent; the room-temperature Reynolds number in the tube was ∼2000. As the jet is heated, the exit velocity increases (proportional to T) and the Reynolds number drops (reaching ∼1300 at 600 K and 1000 at 800 K). The increase in temperature causes the jet to contract, and is particularly noticeable above 600 K.

For each experiment, three temperature measurements are taken simultaneously using the three cameras: Ce^{3+} SRAPT, Pr^{3+} SRAPT, and Ce-Pr co-doped APT. The Ce^{3+} SRAPT ratio is formed between the Ce^{3+} emission intensity and the Mie scattering images, the Pr^{3+} SRAPT ratio is formed between the Pr^{3+} emission intensity and the Mie scattering images, and the Ce-Pr co-doped APT ratio is formed between the Ce^{3+} and Pr^{3+} emission intensity images. The three measurements are made simultaneously such that at each laser pulse, three unique temperature field measurements are obtained. The three measurements are then combined into a single weighted-average measurement using manufacturer-provided camera noise properties on a single-shot basis. The remainder of this section will present the results of each individual temperature diagnostic, as well as the weighted-average measurement, for the uniform and non-uniform temperature field measurements. The data shown here is taken at an average fluence of around 33 mJ/cm^2; the actual calibration procedure accounts for fluence variation as measured via Mie scattering.

5.1.1 Experimental Setup

The second experimental setup used for phosphor characterization is a heated air jet. The experiment consists of a ceramic tube, 19-mm inside diameter, with particle seeder, heaters, and insulation. Dry air flows through the tube at a constant mass flow rate (28.3 slpm; fed by a compressed air line). A portion of the air is split off and passed through a particle seeder which adds phosphor particles to the flow. The seeded air is heated by a series of electric heaters. The end of the ceramic tube is open to the atmosphere.

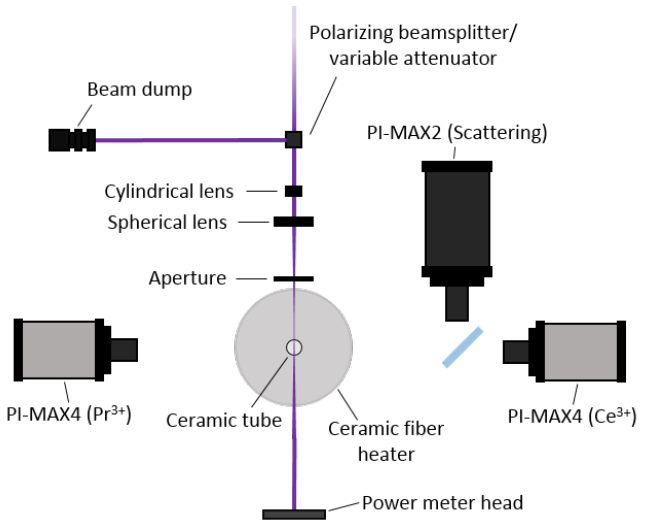

Figure 5.1: Experimental setup diagram for seeded jet characterization and validation experiments.

The air jet was heated using an inline 6-kW electric heater (Sylvania, 038825) followed by a 1.8-kW annular vacuum-formed ceramic-fiber heater (Thermcraft Inc. Fibercraft, VF-180-2-24-V) before exiting from the 19-mm ID ceramic tube. The total air flow rate of the jet was 28.3 slpm. Particles were seeded into the jet upstream of the heaters using a a fluidized bed aerosol generator (TSI, Model 3400A) with an inlet air pressure of 240 kPa gauge. Jet exit temperature and horizontal temperature profiles were measured with a bare wire type-K thermocouple (0.01" wire dia., and 0.021" bead dia.) and thermocouple reader (Omega, Omegaette HH308) with an estimated combined uncertainty of 1%. No corrections were applied to the measurements here because they were estimated to be less than 10 K for the highest temperature cases.

The heated jet optical layout is shown in Figure 5.1. The optical setup is relatively straightforward; luminescence emitted by the phosphor is collected on two cameras, while scattered laser light is collected on a third. The cameras are placed on either side of the jet to maximize collection efficiency. The Ce^{3+} camera and scattering camera are placed on the same side of the jet, with a dichroic beamsplitter used to separate the Ce^{3+} emission from the scattered laser light.

Both Pr^{3+} and Ce^{3+} emission was imaged using an intensified CCD camera (ICCD) (Princeton Instruments, PI-MAX4 1024i-HB-FG-18-P46) with a Gen. III HBf intensifier. Scattering signal was also imaged onto an ICCD camera (Princeton Instruments, PI-MAX2 7489-0022). The Ce^{3+} and scattering cameras were placed on the opposite side of the jet from the Pr^{3+} camera. The Ce^{3+} emission and scattering signal were directed to their respective cameras using dichroic beamsplitter (Semrock Inc., FF01-347). The filter bands used for each camera, along with derived parameters including collection solid angle Ω, are listed in Table 5.1.

Table 5.1: Equipment and estimated collection efficiency for scattering and fluorescence emission cameras. A dichroic beamsplitter (Semrock Inc. FF347-Di01) is additionally used and included in the collection efficiency calculation, but not explicitly listed in the table.

Signal	Camera	Lens	Filters	$\eta_{PC}\eta_{opt}$ [-]	$\Omega/4\pi$ [-]
Ce^{3+}	PI-Max 4	Nikon Nikkor 85-mm (f/1.4)	Schott Glass WG295 Asahi Spectra ZVL0470	0.37	2.5×10^{-3}
Pr^{3+}	PI-Max 4	Sodern Cerco 45-mm (f/1.8)	Schott WG-295 Semrock FF01-267 Melles Griot O3SWP604	0.18	1.5×10^{-3}
Scat.	PI-Max 2	Nikon Nikkor UV 105-mm (f/4.5)	Asahi Spectra ZUS0300 Schott WG-280	0.02	2.5×10^{-4}

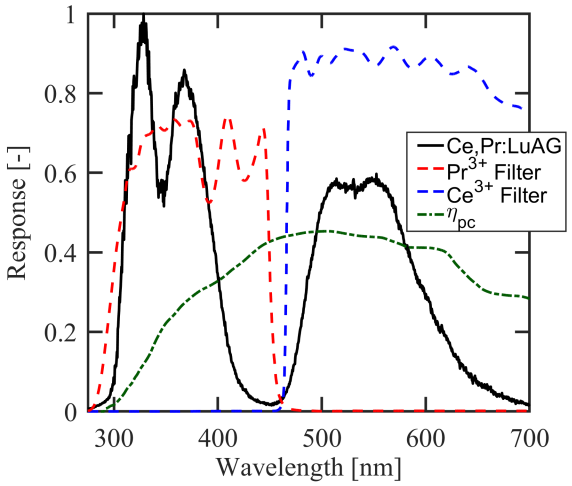

Figure 5.2: Room temperature emission spectrum (solid black curves), with camera collection bands superimposed (dashed curves).

Transmission spectra for the emission collection bands, PI-Max 4 photocathode quantum efficiency, and room temperature emission spectra are shown in Figure 5.2. These transmission bands include an estimated spectral response for the lenses (with data for the Nikon lens from [110], and an estimated 85% transmission for the Sodern Cerco lens based on manufactuer data). From the plot, the filter and camera combinations clearly limit the Pr^{3+} band to 300-450 nm, and the Ce^{3+} to 450-700 nm, effectively capturing radiation from a single ion.

The phosphor was excited at 10 Hz using the 266-nm fourth-harmonic output of a Q-switched, flashlamp-pumped Nd:YAG laser (Ekspla, NL 303D-10). The laser sheet was formed using a -75-mm focal length cylindrical lens, followed by a 200-mm focal length spherical lens. The laser sheet 5-95% thickness was measured to be 0.9 ± 0.1 mm using the scanning knife edge technique at the center of

the jet, and was approximately 20 mm tall. The peak laser intensity in the sheet was estimated to be approximately 50% larger than the average. The laser sheet is focused at the front edge of the jet to avoid breakdown within the jet. The edges of the laser sheet were clipped to remove the low-intensity tails.

Seeding densities are estimated by extinction; a separate experiment was performed where seeding density was varied by sweeping seeder feed rate at constant laser energy. Optical extinction at 532-nm is measured using a set of photodiodes, and is taken simultaneously with Mie scattering imaging. The extinction and scattering data are used to generate a linear calibration between number density (based on Mie theory and the measured optical extinction) and average Mie scattering intensity. This calibration is then applied to the scattering images used for APT, after correcting for the laser profile.

A demonstration experiment is also performed in the same jet after generating a non-uniform horizontal temperature profile. This is done by heating the jet core to around 500 K using the inline heater and heating the circumference of the jet to 900 K using the cylindrical heater. This generated a smoothly varying radial temperature profile with a hot edge, heating the interior of the jet via thermal conduction. The resulting temperatures range from 550 to 900 K. Horizontal temperature profiles were measured using the same type-K thermocouple and reader, and again are not corrected for conduction, convection, or radiation biases.

5.1.2 Signal and Ratio Calibration

The calibration used for the Ce,Pr:LuAG heated jet measurements is based on the signal modeling results presented in Chapter 4. In short, a series of fluence curves (measuring signal per particle as a function fluence) were taken at temperatures from 300 to 700 K in 100 K increments. The resulting data was fit to a signal model, which was discussed in Section 4.6. In this case, a simplified model was used where $S = n^{\star} k_r \tau$, ignoring any emitted light during the laser pulse. This is equivalent to the assumption that the laser pulse duration is short compared to the luminescence decay time (this corresponds specifically to Equation 4.21). This assumption is valid for the majority of the range over which the data was collected. The relative signal intensity for the two ions of the Ce,Pr:LuAG phosphor are plotted in Figure 5.3 at several fluences, with the model result superimposed.

From Figure 5.3, both Pr^{3+} and Ce^{3+} show an initial increase in signal with temperature, with signal peaking at 400 and 500 K, respectively. Additionally, the saturation behavior is evident; doubling the fluence from 15 to 30 mJ/cm^2 results in less than twice the emitted signal intensity. The lack of linear signal dependence on fluence is observed as a non-uniform scale between subsequent curves.

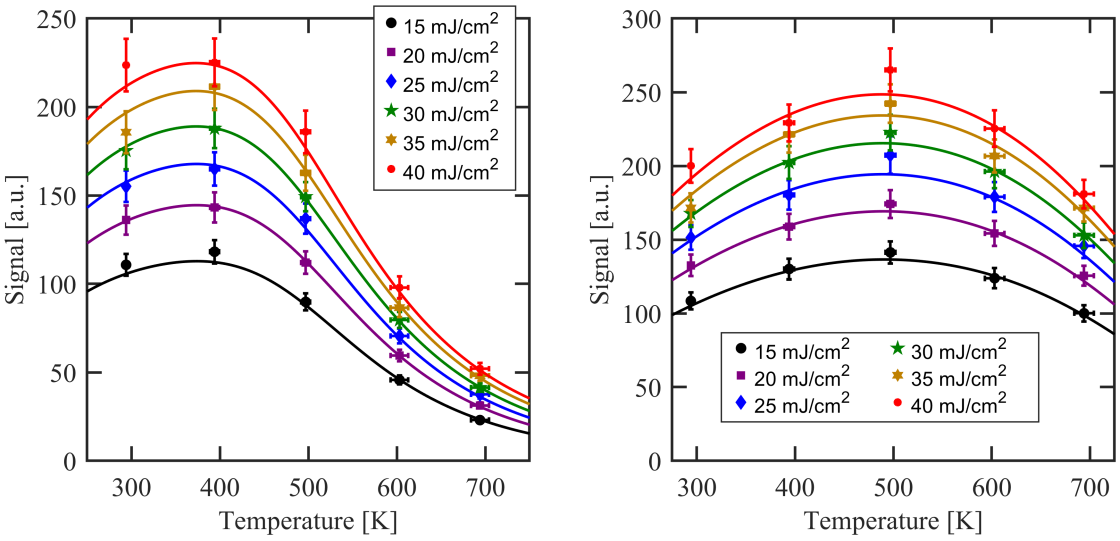

(a) Pr^{3+} (b) Ce^{3+}

Figure 5.3: Relative signal intensity of Pr^{3+} and Ce^{3+} in Ce,Pr:LuAG at several different fluences. Data points are measurements averaged over a fluence range of ± 2 mJ/cm^2, while solid curves are evaluated from fits to the signal model presented in Section 4.6.

The measured ratios, along with those calculated from the signal modeling results, are shown in Figure 5.4 for each of the three techniques. Clearly the signal modeling results represent the measured ratios well, and the analysis and observations from Section 4.6 are confirmed here. Specifically, the calibration functions are independent of fluence until thermal quenching becomes significant, and the phosphor linearity changes. This is observed in the data here primarily for the co-doped technique where ratio values are reduced as fluence increases.

5.1.3 Data Analysis Procedure

The calibration is applied to temperature imaging as follows. Raw images are first background subtracted and registered. The images are then converted to ratio measurements according to Equation 4.27. The reference measurements are taken as an average over 200 images at the 294 K condition. The average laser fluence is estimated at every point in the image based on the Mie scattering measurements, and a unique calibration function based on the local laser fluence is generated for each point. To calculate temperature, the unique calibration function ($R(T)$) is inverted at every point on the image domain for each single-shot ratio image. If more than one temperature exists for a given value of the ratio for a given technique, the results of the other two techniques are used to determine the correct root. An automated signal threshold was applied to the Mie scattering images using Otsu's method [111] to mask

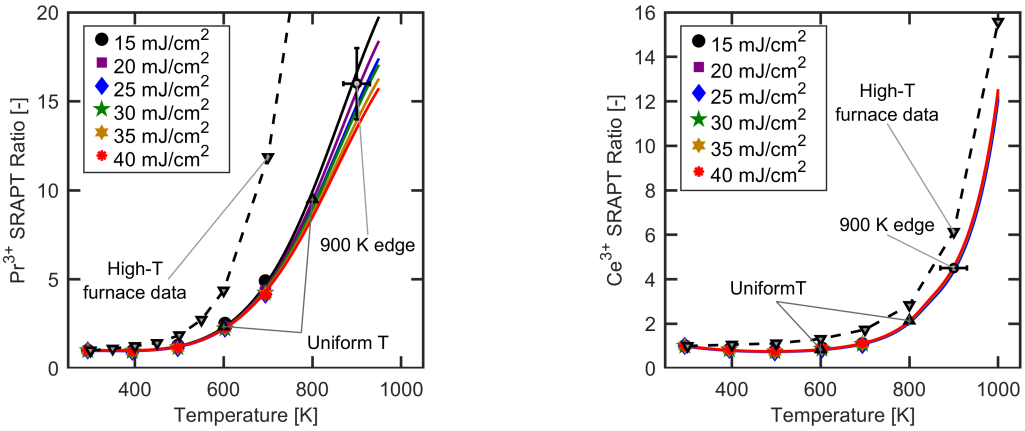

(a) Pr^{3+} SRAPT

(b) Ce^{3+} SRAPT

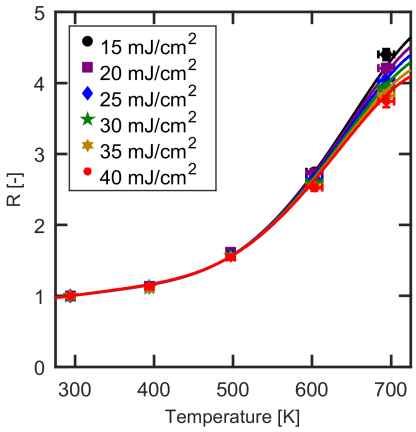

(c) Co-doped

Figure 5.4: Ratio calibration for Ce,Pr:LuAG heated jet measurements at several different fluence values. Points indicate measurements averaged over ± 2 mJ/cm^2, while curves are calculated from signal modeling results presented in Section 4.6. High-temperature furnace data from [37] ("High-T Furnace Data") and several additional high-temperature, 25 mJ/cm^2 fluence heated jet measurements (discussed in [84]; "Uniform T" and "900 K edge") are included for comparison.

data where signal density or laser energy is low.

Fluence is calculated on a per-row basis from the 294 K average Mie-scattering image assuming that on average the phosphor mass flow rate is constant. Laser scattering intensity is proportional to both number density and fluence. The shape of the fluence profile is thus estimated as being identical to the average scattering-intensity profile integrated over the jet width. The integration is done to account for jet spreading. The fluence is then determined by normalizing the fluence profile such that it integrates to the total laser energy. For the measurements shown in the following sections, the laser energy varied by about 3% as the jet was heated. This variation was measured and accounted for when determining temperature.

Since three measurements are made simultaneously, a combined measurement based on the weighted average (as described in Section 4.7.4) was calculated as well. The weighted-average temperature is calculated as follows. For each pixel and each technique, a temperature precision is estimated based on the local laser fluence, measured temperature, calibration function (based on signal model results from Section 4.6), and measured camera noise properties (detailed in Appendix E). Using the calculated temperature precision, a relative weight is assigned to each pixel of each technique ($w_i = 1/s_{T,i}^2$), and the weighted average temperature is calculated.

5.1.4 Ratio Precision

Before showing imaging results, it is instructive to look at the measured ratio precision. From 4.7, the ratio precision can be thought of as a fundamental measure of performance; it is a measure of the quality of the imaging experiment and the brightness of the phosphors. The temperature precision is simply the ratio precision scaled by the temperature sensitivity of the diagnostic. The ratio precision, measured as the spatial coefficient of variation of the ratio in the center 2.5 mm wide by 5 mm tall rectangle in the jet, is shown as a function of seeding density in Figure 5.5. Each point in the plot indicates a separate temperature image, and the seeding density is calculated as the average value (based on scattering intensity) within the same rectangular region.

The ratio precision measurements show several interesting trends. First, for both SRAPT techniques, the ratio precision approaches 7-8% at the highest seeding densities and lowest temperatures (before quenching becomes significant; 300 K). For the co-doped technique, the ratio precision approaches 5%. The higher ratio uncertainty for SRAPT may be a result of added SRAPT uncertainty from the poly-dispersed particle size distribution, and is discussed in Section 6.6. In the absence of quenching, the ratio precision is otherwise independent of temperature. This is evident in the Ce^{3+} SRAPT data, where

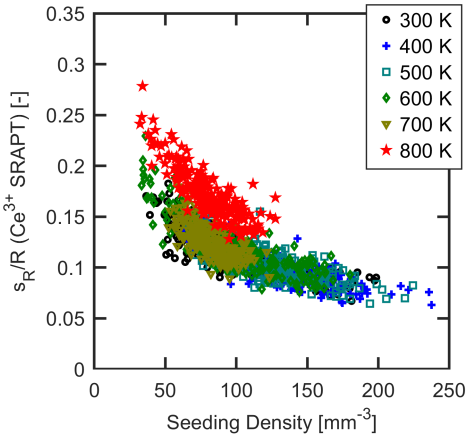

(a) Ce^{3+} SRAPT

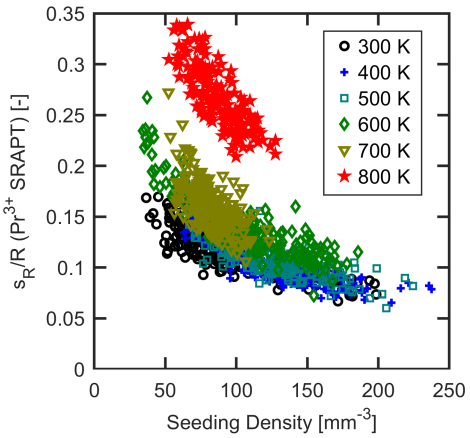

(b) Pr^{3+} SRAPT

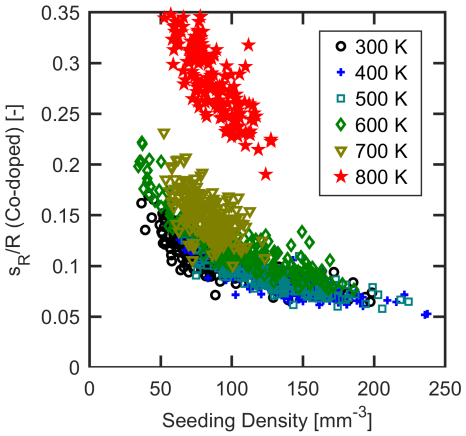

(c) Co-doped APT

Figure 5.5: Measured ratio precision as a function of seeding density for Ce,Pr:LuAG in a heated air jet from 300 to 800 K.

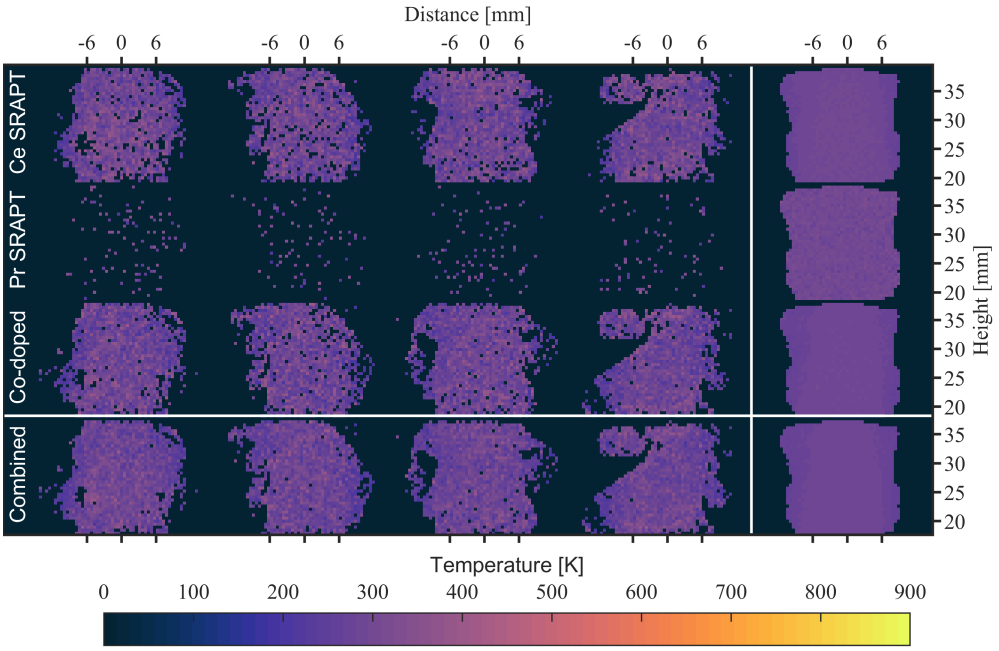

Figure 5.6: Series of single-shot (first four columns) and average of 200 images (rightmost column) for each diagnostic using the Ce,Pr:LuAG phosphor at a mean jet temperature of 300 K. The Ce^{3+} SRAPT, Pr^{3+} SRAPT, and co-doped techniques are shown in the first three rows, with the weighted average diagnostic in the bottom row.

there is no discernible trend in temperature until 800 K, where the signal intensity has dropped by about a factor of 2 (increasing the noise of the luminescence band by a factor of $\sim \sqrt{2}$). Similar behavior is observed for Pr^{3+} SRAPT, except quenching occurs earlier. From the plots, a signal-to-noise ratio of 10 at room temperature is typical of the measurements, and the precision estimates made in Section 4.7 are directly comparable to the results shown here.

5.1.5 Uniform Heated Jet Imaging Results

A series of single-shot images for each technique, the single-shot weighted average measurements, and the average temperature fields for a set of 200 images for each diagnostic are shown in Figures 5.6, 5.8, 5.7, 5.9, 5.10, and 5.11 for mean jet temperatures of 300, 400, 500, 600, 700, and 800 K, respectively, at a mean fluence of 33 mJ/cm^2. In the temperature images, a clear boundary generally exists between the seeded jet and the unseeded ambient air. The seeded region is largely at a uniform temperature but tends too cool off near the edges of the jet due to mixing with the surrounding cold air at 300 K. This is particularly noticeable in the hottest images.

The room temperature images are shown in Figure 5.6. Since only the jet is seeded, measurements are only made inside the jet itself and a sharp boundary is observed between the seeded jet and the

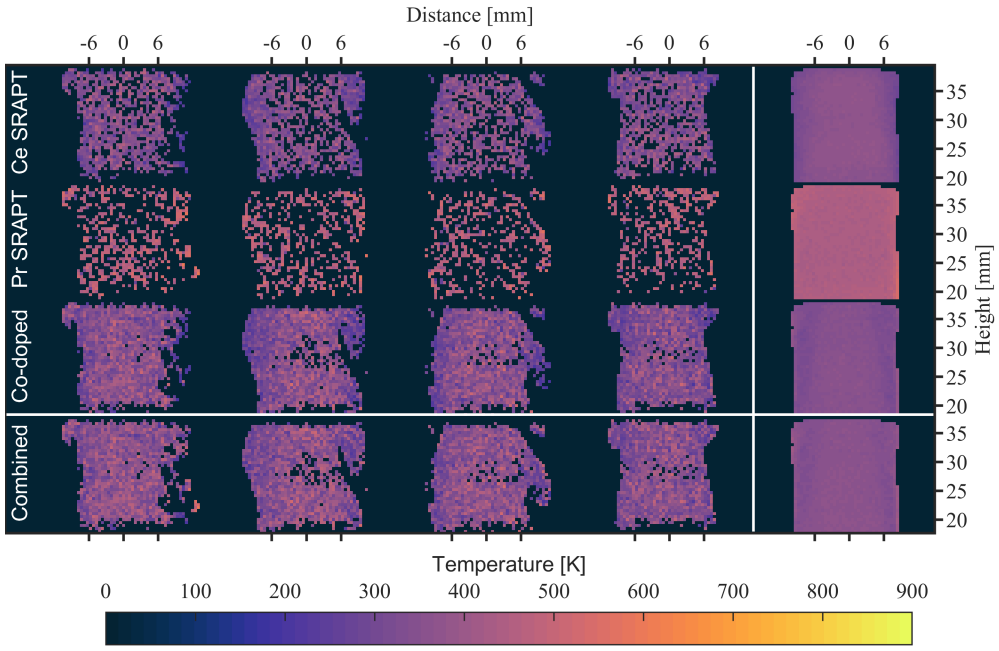

Figure 5.7: Series of single-shot (first four columns) and average of 200 images (rightmost column) for each diagnostic using the Ce,Pr:LuAG phosphor at a mean jet temperature of 400 K. The Ce^{3+} SRAPT, Pr^{3+} SRAPT, and co-doped techniques are shown in the first three rows, with the weighted average diagnostic in the bottom row.

surrounding air with which the jet is mixing. The images clearly show slices of an unstable jet with significant structure. Each of the techniques except Pr^{3+} SRAPT has some sensitivity at 300 K, and as a result a temperature measurement can be made at 300 K. The temperature sensitivity at 300 K is due to temperature-dependence of the absorption process, and is thus very weak, particularly for Pr^{3+} SRAPT. No measurement is possible for Pr^{3+} SRAPT because 300 K is near the local minimum of the calibration function; as a result, noise or a slight bias in the ratio measurement is enough to push the measured ratios outside of the range of the calibration function.

Images of the first elevated temperature field at 400 K are shown in Figure 5.7. Again, only the jet is seeded so a sharp boundary is present between the seeded jet and unseeded ambient air. At 400 K, none of the Ce,Pr:LuAG APT techniques are very sensitive, resulting in a lot of noise in the temperature maps. Additionally, many of the measurements are empty (shown as 0 K on the figures). Since the ratio function has a minimum value for each technique (typically below 1 for SRAPT since signal increases initially with temperature before quenching for both Ce^{3+} and Pr^{3+}; equal to 1 for co-doped), and at 400 K very little quenching has occurred yet, noise pushes many of the measurements outside the range of the calibration function. There is additionally some calibration bias in fitting the signal model that, due to the low temperature sensitivity at 400 K, may result in a 10-20 K error. This bias is evident

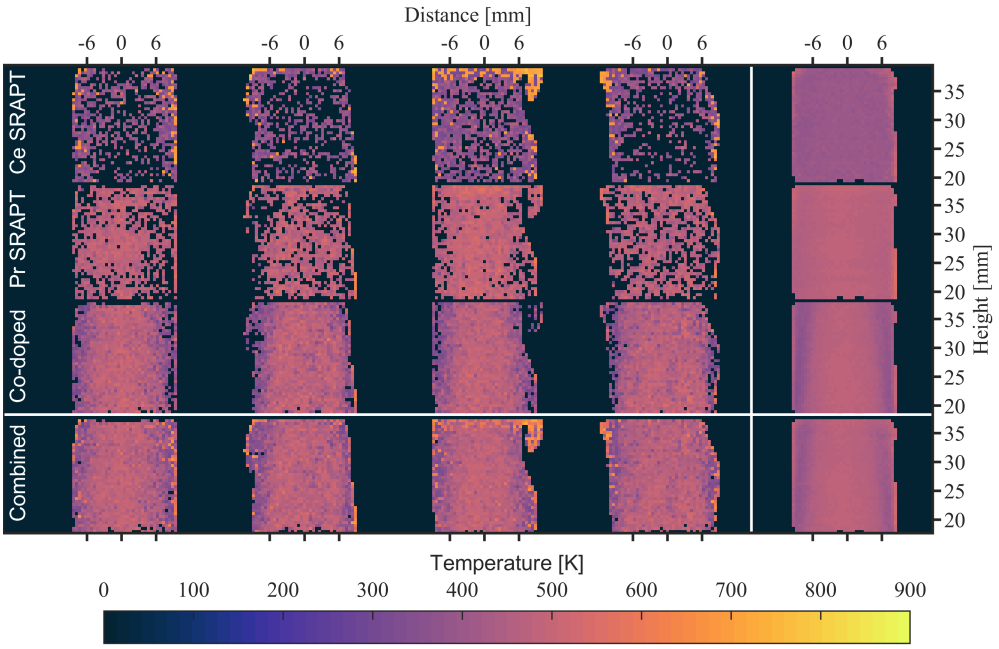

Figure 5.8: Series of single-shot (first four columns) and average of 200 images (rightmost column) for each diagnostic using the Ce,Pr:LuAG phosphor at a mean jet temperature of 500 K. The Ce^{3+} SRAPT, Pr^{3+} SRAPT, and co-doped techniques are shown in the first three rows, with the weighted average diagnostic in the bottom row.

in particular for the Pr^{3+} SRAPT technique which is noticeably hotter than the other measurements. However, the measurements from the other techniques are still 10-20 K low.

The 500 K measurements, shown in Figure 5.8 similarly are noisy, and the Ce^{3+} SRAPT measurement in particular has many empty measurements. The Ce^{3+} SRAPT technique has a local minimum in its calibration function near 500 K, such that noise takes many of the ratio measurements outside of the calibration function range. However, the Pr^{3+} SRAPT and co-doped techniques still perform reasonably well here. Due to low sensitivity, there is still some calibration bias at 500 K, and each technique differs from the thermocouple measurement by about 5 K. The edges of some Ce^{3+} SRAPT images are much hotter than expected; this appears to be a result of the software binning process where pixels with few or no phosphor particles are included in the average (this may also be influenced by registration error). Since the co-doped and Pr^{3+} also do not provide a good measurement on the low-seeding density edges at this temperature, the Ce^{3+} measurement is weighted higher for the combined technique. However, the erroneous Ce^{3+} SRAPT measurements appear to have little impact on average.

At 600 K, shown in Figure 5.9, the Pr^{3+} SRAPT and co-doped techniques work very well, and fill in the temperature map throughout the entire imaging region. However, the Ce^{3+} SRAPT technique still has low sensitivity, and the resulting temperature map is noisy. At 600 K, the jet edge temperature is

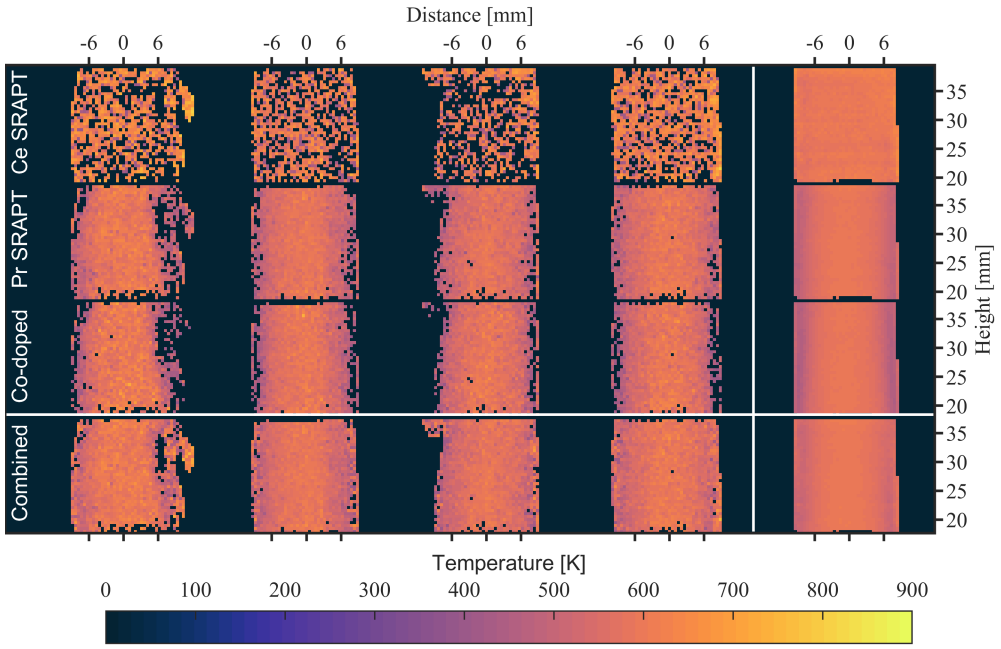

Figure 5.9: Series of single-shot (first four columns) and average of 200 images (rightmost column) for each diagnostic using the Ce,Pr:LuAG phosphor at a mean jet temperature of 600 K. The Ce^{3+} SRAPT, Pr^{3+} SRAPT, and co-doped techniques are shown in the first three rows, with the weighted average diagnostic in the bottom row.

clearly colder than the jet core temperature due to thermal conduction into the surrounding cold air. All of the techniques except Ce^{3+} SRAPT are able to detect this cooling.

At 700 K, shown in Figure 5.10, the co-doped measurement is noisy and many measurements are empty because the co-doped ratio sensitivity is starting to drop as the calibration curve approaches a local maximum between 700 and 800 K. Above 700 K, the application of the co-doped technique with Ce,Pr:LuAG is not recommended. In contrast, Pr^{3+} quenching is significant at 700 K such that the Pr^{3+} SRAPT sensitivity is high, but signal intensity is beginning to drop; this results in a reasonably precise measurement. The Ce^{3+} ion is just beginning to quench at 700 K such that temperature sensitivity is relatively low still, but a reasonable measurement is possible. 700 K is the lowest temperature where Ce^{3+} SRAPT should be used based on the results presented here.

The images taken at 800 K mean jet temperature are shown in Figure 5.11. From the single-shot images, the Ce^{3+} SRAPT and Pr^{3+} SRAPT techniques appear to work very well. In both cases, few if any measurements are empty as both techniques have high sensitivity at 800 K. The Pr^{3+} SRAPT technique is noticeably noisier than the Ce^{3+} SRAPT technique; this is because the Pr^{3+} emission intensity is reduced by an order of magnitude or more at 800 K, while the Ce^{3+} emission is only reduced by about a factor of 2. Both measurements are capable of capturing the decrease in temperature at the

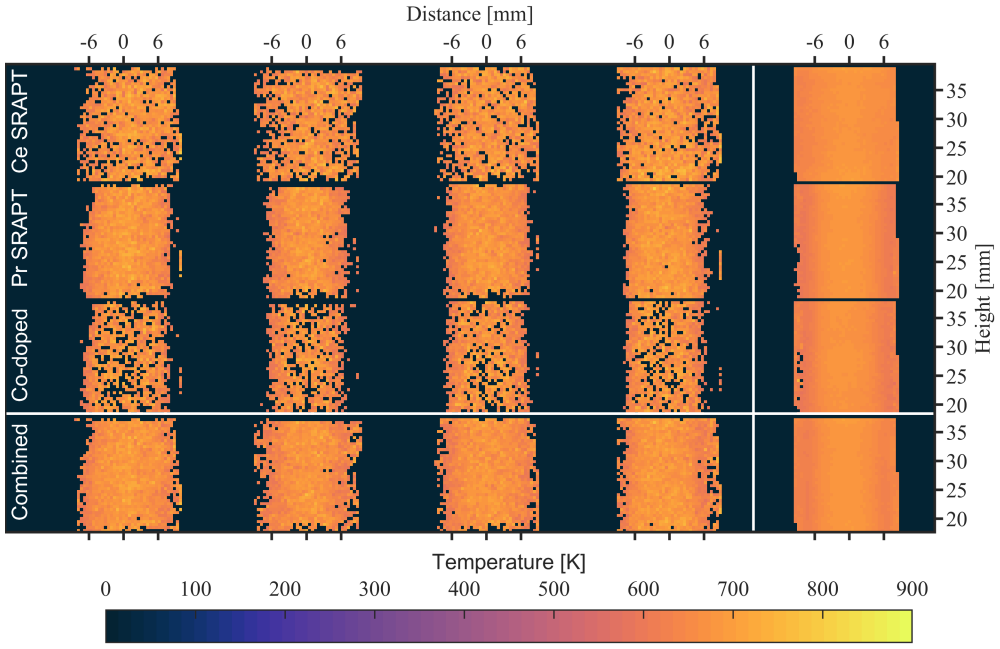

Figure 5.10: Series of single-shot (first four columns) and average of 200 images (rightmost column) for each diagnostic using the Ce,Pr:LuAG phosphor at a mean jet temperature of 700 K. The Ce^{3+} SRAPT, Pr^{3+} SRAPT, and co-doped techniques are shown in the first three rows, with the weighted average diagnostic in the bottom row.

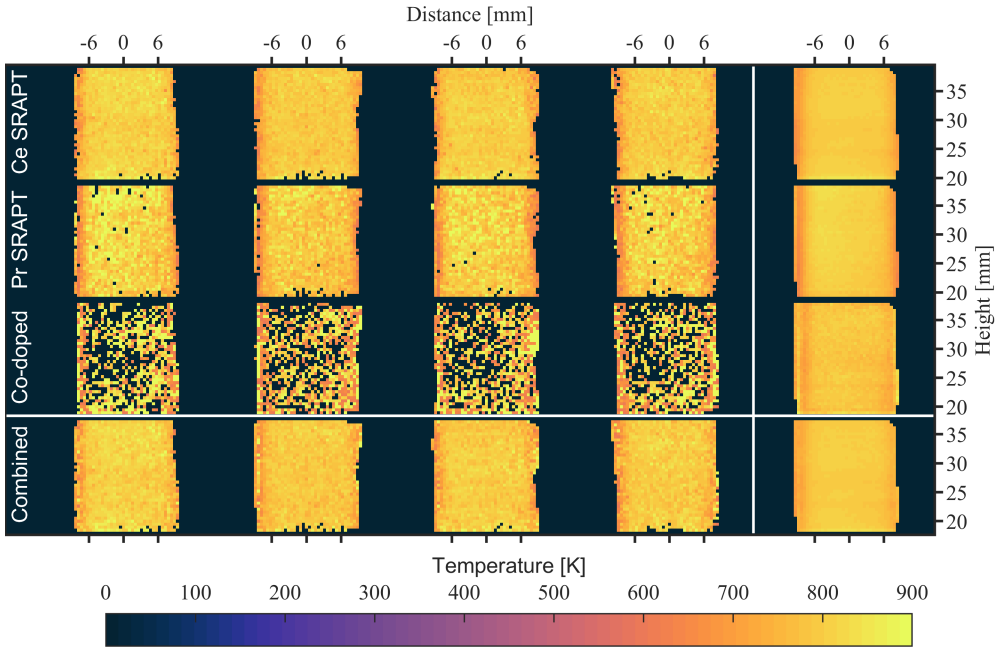

Figure 5.11: Series of single-shot (first four columns) and average of 200 images (rightmost column) for each diagnostic using the Ce,Pr:LuAG phosphor at a mean jet temperature of 800 K. The Ce^{3+} SRAPT, Pr^{3+} SRAPT, and co-doped techniques are shown in the first three rows, with the weighted average diagnostic in the bottom row.

jet edge due to thermal conduction. It is worth noting that the co-doped measurement is noisy, but still possible to use at 800 K. Although the co-doped calibration function has a local maximum between 700 and 800 K, and is thus not a monotonic function of temperature, it is possible to discern which branch of the calibration curve to use based on the simultaneous measurement of the Pr^{3+} SRAPT and Ce^{3+} SRAPT ratios. However, near the local maximum the sensitivity is very low or zero, such that measurements can be very noisy and are more strongly affected by biases in the reference condition.

For all of the measurements presented so far, the weighted average generally takes the best of the measurements, and can be interpreted as a method to combine diagnostics. Since only three measurements are being averaged, at most a 40% reduction in noise is possible if each measurement has the same quality and they are weighted perfectly. From the single-shot image stacks shown in Figures 5.6 to 5.11, typically there is one technique that performs best at any given temperature; as a result little noise reduction is achieved. However, the primary benefit of the weighted average method is that continuous temperature measurements are achievable throughout a larger temperature range, from 300 to 800 K in this case.

The horizontal temperature profiles, averaged over a height of 1.5 mm at a location approximately 20±3 mm above the jet exit, are shown in Figure 5.12. The figure shows two plots: on the left a comparison of the different techniques are shown at 300, 600, and 800 K; the weighted average temperature profiles at each mean jet temperature are shown on the right. From the figure, all techniques including the weighted average appear to capture the jet exit temperature well, except for the Ce^{3+} SRAPT technique at 600 K, which overestimates the temperature by about 20 K near the edges. At 800 K, the phosphor temperature profiles appear flatter than the profile measured with the thermocouple. In this case, the APT measurement is likely correct since the thermocouple is subject to conduction bias that was not corrected in this analysis. Additionally, the plot on the right shows that the temperature measurements at 400, 500, and 700 K are slightly below the expected value, on the order of 10 K for the 500 and 700 K cases. At 400 K the disagreement is closer to 35 K; however, all three diagnostics have very poor sensitivity near 400 K, so this is not surprising. At 500 and 700 K, the error is likely a result of calibration bias caused by an imperfect fit to the calibration data. At 600 K, the Ce^{3+} SRAPT technique does not perform well due to its low temperature sensitivity; however, the weighted averaging method correctly determines the temperature despite the error. A similar effect is observed near the left edge of the jet (-7.5 mm) at 800 K; here the co-doped technique erroneously returns a temperature much hotter than expected, but the weighted average is still reasonable.

Temperature precision was also estimated using the spatial standard deviation within a 2.5 mm square box in the center of the jet images for each technique. The results are plotted in Figure 5.13 for

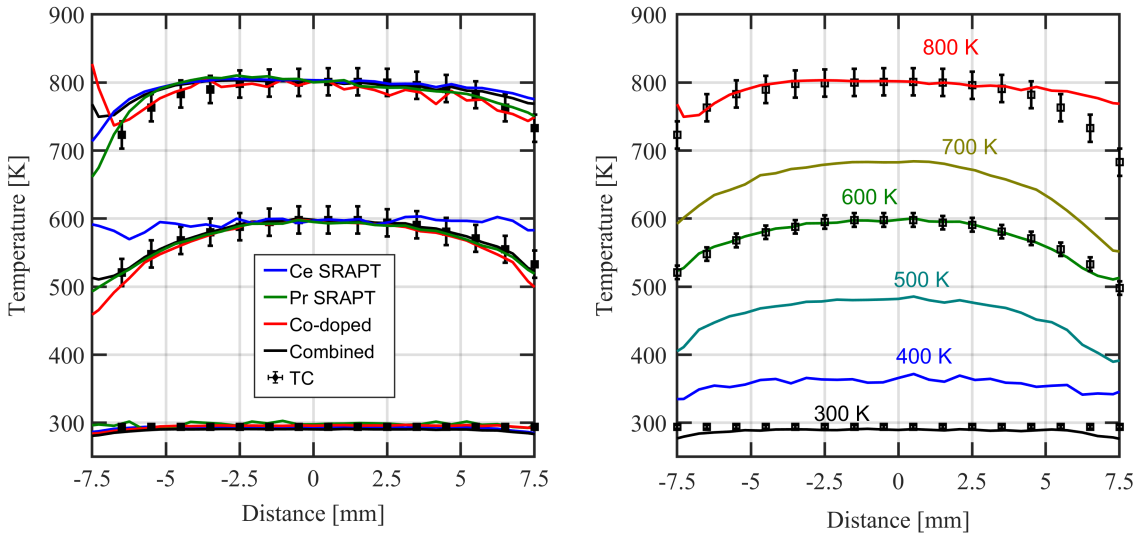

(a) Comparison of techniques at 300, 600, and 800 K (b) Weighted average measurement from 300 to 800 K

Figure 5.12: Horizontal temperature profiles from the uniform heated jet using the Ce,Pr:LuAG phosphor. In both plots, the symbols indicate thermocouple measurements with estimated error bands, while curves indicate the APT results.

both the individual and combined techniques as a function of seeding density. As expected, increasing seeding density generally decreases the temperature precision index, with $s_T \propto 1/\sqrt{n}$ in the shot-noise limit. The weighted average precision is clearly the best-case precision. However, there is generally little noise reduction as a result of the averaging process. Instead, the weighted average effectively chooses the best technique for a given temperature. One exception to this is the 300 K case, where the temperature precision of the combined technique is slightly improved over all of the individual measurements. There is additionally a slight improvement in temperature precision for the 500, 600, and 700 K cases on average (between 5 and 10% of the best individual precision), but the effect is almost too small to be seen in the figure. At 400 and 800 K, there is no measurable improvement in precision.

The best-case single-shot temperature precision is approximately 20-25 K at a mean temperature of 800 K, largely from the Ce^{3+} technique. Similarly, using the Pr^{3+} technique at 600 K, a single-shot temperature precision of 15-20 K is achievable. These results are consistent with the precision estimates from Section 4.7, specifically the estimated precision of the combined technique plotted in Figure 4.27. With an initial signal-to-noise ratio of 10 at room temperature, temperature precision was estimated to be ~15 K and ~20 K at mean temperatures of 600 and 800 K, respectively.

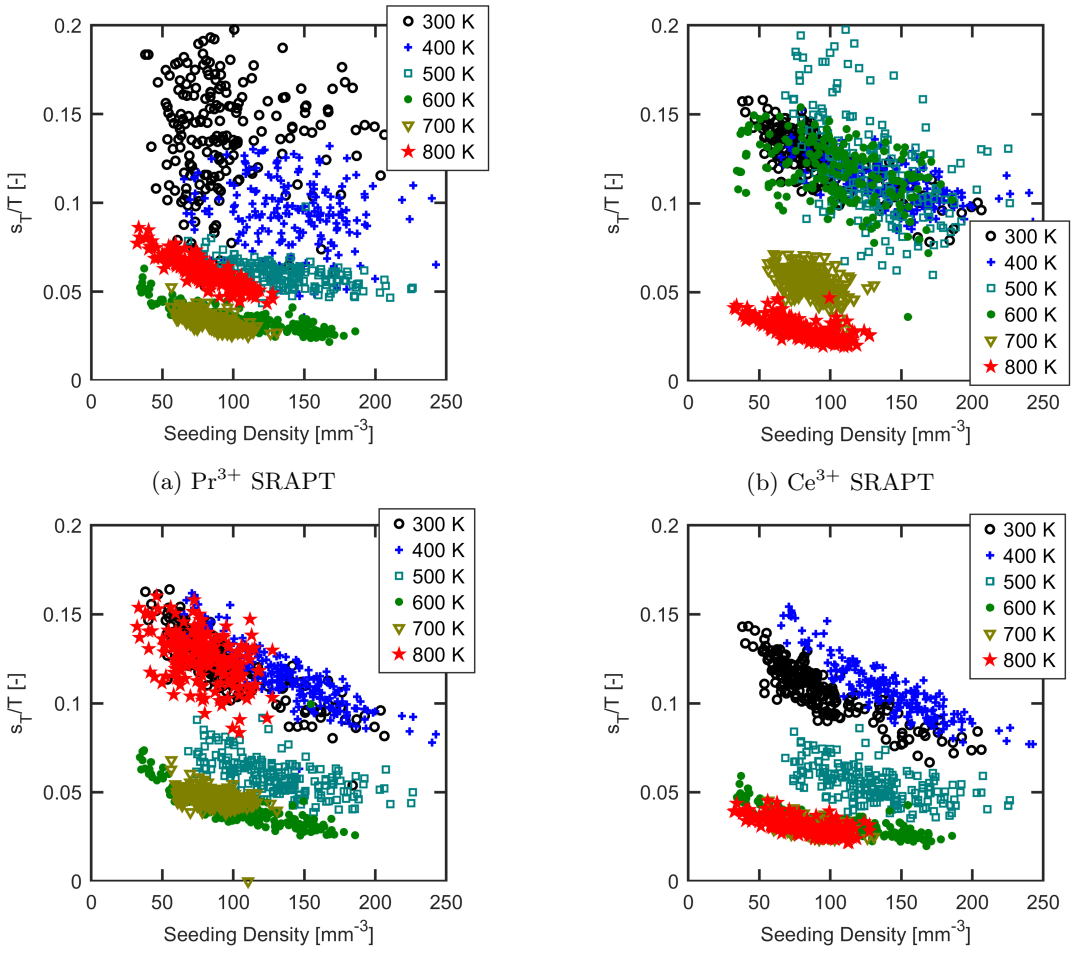

(a) Pr^{3+} SRAPT

(b) Ce^{3+} SRAPT

(c) Co-doped

(d) Combined

Figure 5.13: Measured temperature precision for the various Ce,Pr:LuAG techniques from 300 to 800 K, and a mean fluence of 33 mJ/cm^2 in the heated jet experiment.

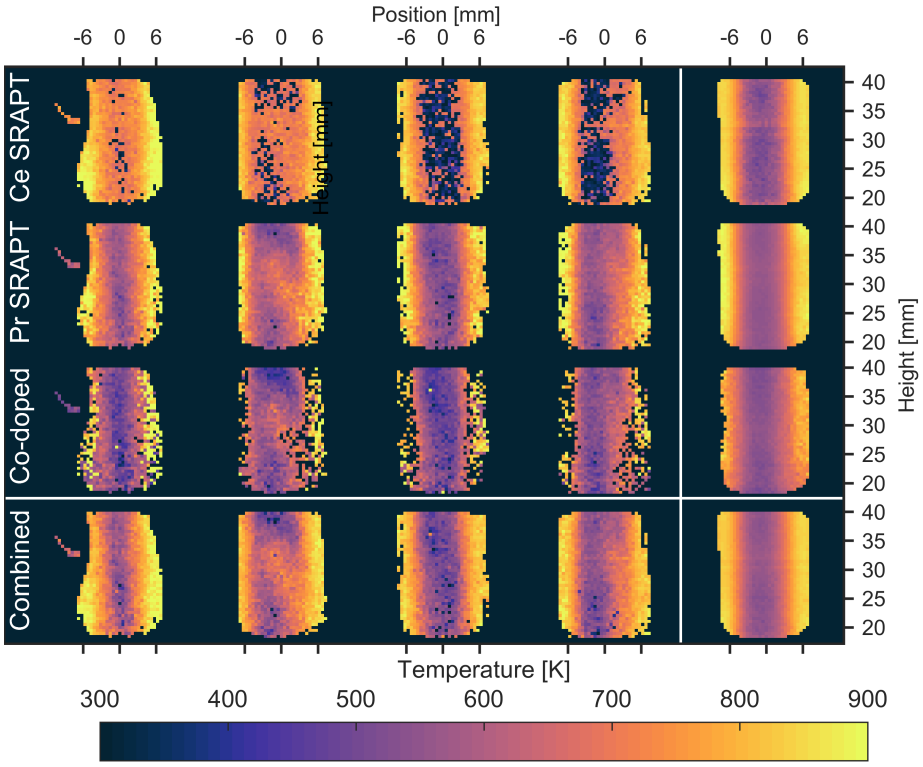

Figure 5.14: Series of single-shot (first four columns) and average of 200 images (rightmost column) for each diagnostic using the Ce,Pr:LuAG phosphor for the non-uniform heated air jet condition. The Ce^{3+} SRAPT, Pr^{3+} SRAPT, and co-doped techniques are shown in the first three rows, with the weighted average diagnostic in the bottom row.

5.1.6 Non-uniform Heated Jet Results

Non-uniform heated jet measurements are performed in an identical fashion to the uniform jet case, except the heaters are run in such a way that the jet maintains a cold core at around 550 K, whereas the jet edges reach a temperature of around 900 K. This provides a temperature field that covers the majority of the usable temperature range of the Ce,Pr:LuAG phosphor. A series of single-shot images for each technique, along with averages over a stack of 200 images, and the single-shot and averaged combined-diagnostic measurements are shown in Figure 5.14.

In general, each diagnostic captures at least a portion of the heated jet in Figure 5.14. Pr^{3+} SRAPT performs the best as it provides a reasonable measurement throughout almost the entire domain. The co-doped technique fails at higher temperatures as the jet edge is at a temperature above which the co-doped calibration function reaches a local maximum. Measurements are still possible in this region, but the uncertainty is much larger, and noise can result in a significant number of measurements outside the domain of the co-doped calibration function. The Ce^{3+} SRAPT technique is perhaps the most interesting case; all of the single-shot measurements at the jet core are erroneous. However, averaging

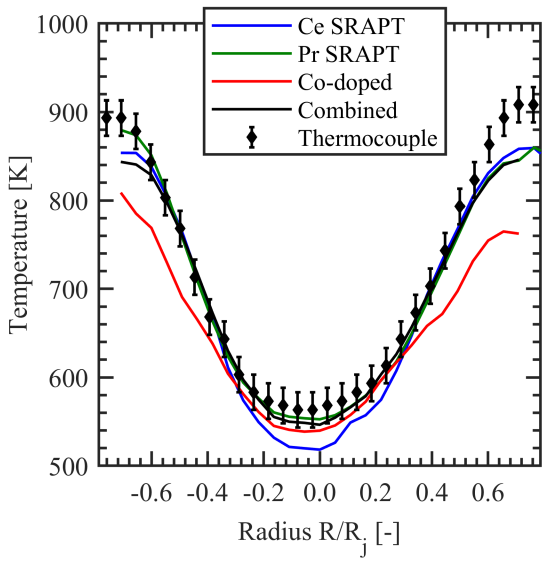

Figure 5.15: Horizontal temperature profiles from the non-uniform heated jet using the Ce,Pr:LuAG phosphor.The data points indicate thermocouple measurements with estimated error bands, while curves indicate the APT results.

over the 200 measurements still provides a reasonable picture of the average temperature. Since the Ce^{3+} SRAPT calibration function has a local minimum near 550 K, the single-shot measurements alternately select points that are either hotter or colder than the true temperature due to noise or small temperature fluctuations within the jet. The measured temperature distribution is bimodal, but the average value is correct.

The average behaviors can be seen better in Figure 5.15, which shows the average horizontal temperature profile measured with the Ce,Pr:LuAG phosphor (averaged over a 1.5 mm vertical region, 20±3 mm above the jet exit), along with a temperature profile measured using a bare-wire type K thermocouple. From the plot, the Pr^{3+} SRAPT technique appears to capture the temperature profile entirely, up to near 900 K where the seeded region of the jet ends. In contrast, the Ce^{3+} SRAPT technique does not accurately capture the low temperature behavior near 550 K exactly; however, as the diagnostic has zero temperature sensitivity at a point near 550 K, the modest 40 K error is somewhat surprising. The co-doped technique fails to capture the jet temperature profile at high temperatures, generally above 650 K. Similar to Ce^{3+} SRAPT at 550 K, the co-doped technique has a local maximum in the ratio near 750 K, and the temperature sensitivity drops quickly in this temperature range.

The ability to make temperature measurements even at these zero sensitivity points (750 K for the co-doped technique and 550 K for the Ce^{3+} SRAPT technique) is evidence of the utility of combining diagnostics. Combining diagnostics in this fashion can extend the temperature range of a phosphor. The

weighted average temperature, shown in Figure 5.15, matches the thermocouple profile very well except at the very edge of the seeded region of the jet where all of the techniques are erroneous due to the loss of seeding density. Figure 5.15 seems to suggest the upper temperature limit of the technique is around 900 K. However, this is likely an underestimate as in this case the measurement fails when seeding density is lost at the edge of the jet, rather than loss of signal through thermal quenching. From Section 4.6, an upper limit is estimated as closer to 1000 K, but depends greatly on the required temperature precision for the measurements.

5.2 APT Flame-Heated Jet Imaging

APT imaging experiments were performed with a variety of phosphors (including Ce,Pr:LuAG, Ce:CSSO, Eu:BAM, and Ce:$GdPO_4$) in an air jet heated by mixing with the products of a concentric methane-air flat flame. The details of the experimental setup are provided in 5.3. In this experiment, the flame and jet configuration is fixed, and several different phosphor compositions are used to image the jet. The jet provides a temperature range of approximately 300 - 1600 K vertically along the jet centerline. Temperature variation of the air jet is achieved through mixing with products of the surrounding methane-air flame.

Some of the phosphors used here can provide multiple measurements. In particular three measurements are possible with Ce,Pr:LuAG (exactly as in the heated jet measurements). Three measurements are also made simultaneously with Ce:CSSO; Ce^{3+} SRAPT, host emission SRAPT, and a host-referenced technique that compares Ce^{3+} emission to host emission. The host-referenced method is similar to the co-doped method except emission in the second band results from host defects rather than an additional ion. Host-referenced thermometry has been suggested recently based on characterization of the Sm:TiO_2 phosphor [112]. The remaining phosphors, Ce:$GdPO_4$ and Eu:BAM, have only SRAPT as an option since only one emission peak exists. Eu:BAM SRAPT can additionally be performed using a luminescence intensity ratio method, although it is primarily used at lower temperatures; an additional experiment using Eu:BAM in this manner was performed and is described here as well.

Temperature was also measured using two bare-wire type-R thermocouples with bead diameters of 0.0762 and 0.127 mm. Three horizontal thermoocouple sweeps were acquired at heights of 19, 36, and 47 mm above the burner surface using the 0.127 mm bead, and a vertical sweep was acquired along the axis of the jet starting at 40 mm above the burner surface using the 0.0762 mm thermocouple. The horizontal measurements were corrected for conduction and radiation using the theory and data presented in [113]. The correction was carried out using temperature derivatives calculated directly from the thermocouple

sweeps. The radiation correction magnitude was found to be between 10 and 60 K (for gas temperatures of 1050 and 1600 K, respectively). The conduction error magnitude varied from 200 to less than 15 K (for gas temperatures of 600 and 1000 K, respectively). The vertical sweeps were corrected for radiation but not conduction, as the conduction error at these locations is believed to be less than 15 K.

For temperatures below 1000 K (corresponding to less than 40 mm above the burner surface), the Ce,Pr:LuAG APT measurement is used to calibrate the other phosphors. At these locations the conduction bias in the thermocouple was estimated to be on the order of 200 K or larger; the Ce,Pr:LuAG phosphor measurement was calibrated *ex situ* and believed to be more accurate in this portion of the jet. The Ce,Pr:LuAG calibration is taken from the heated jet data in Section 5.1. The same collection optics are used for both measurements, except for the beamsplitters (see Sections 5.1.1 and 5.3 for equipment details). Since the Ce,Pr:LuAG uses a physics-based model for calibration, and the flatfield correction removes any non-spectrally-dependent differences in collection efficiency, the slight differences in equipment are not believed to have an impact on the result.

The seeding densities used in these experiments were selected such that, at most, the flow's heat capacity is increased by 1% (approximately corresponding to a drop in temperature of 1%). This was deemed acceptable given that other sources of bias present in the measurements have similar or greater magnitude.

5.3 Experimental Setup

The heated jet experiment described in Section 5.1.1 is limited to a maximum temperature of about 900 K. To achieve higher temperatures, several phosphor compositions are tested instead in a cold jet mixed with the products of a methane-air flat flame. This flame setup provides a slowly-varying, non-uniform temperature that can be used for diagnostic demonstration.

The experiment makes use of a flat-flame burner with a center tube (Holthuis and Associates, center tube burner). The burner consists of a 60-mm outer diameter porous plug, with a 12-mm inner diameter tube that allows a central co-flow. Air and methane are mixed upstream of the burner at a fixed equivalence ratio ($\Phi \approx 1.15$) with flow rates (49.3 ± 0.2 slpm air, and 5.6 ± 0.1 slpm methane). This forms a premixed methane-air flame on the outer annular ring of the burner where a porous plug allows the fuel-air mixture to escape at a uniform velocity. Air is fed through the center tube (12 mm inner diameter) at a constant mass flow rate of 2 slpm. Before entering and exiting the burner, the compressed air is passed through a particle seeder which adds phosphor particles to the flow exiting the center tube.

The surrounding flame heats the air jet mostly by thermal conduction. This gives the seeded region of

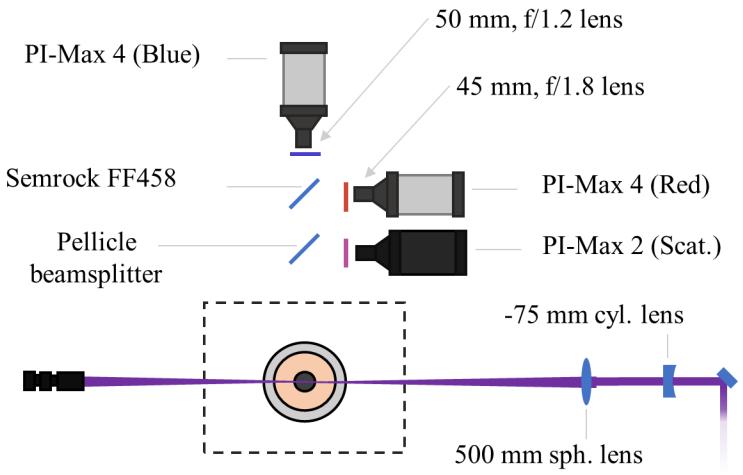

Figure 5.16: Experimental setup diagram for the flame-heated jet demonstration experiments.

the jet the appearance of a diffusion flame. Because the jet is heated this way, seeding densities decrease at higher temperatures as the gas expands making it difficult to observe the highest temperatures in the jet.

The optical setup is shown schematically in Figure 5.16. The optical setup consists of two intensified CCD cameras (Princeton Instruments, PI-MAX4 1024i-HB-FG-18-P46) with Gen. III HBf intensifiers for the emission measurements, and a third ICCD camera (Princeton Instruments, PI-MAX2 7489-0022) was used to capture elastically scattered laser light. In all cases, a Pellicle beamsplitter (with an assumed 8% broadband reflection coefficient based on manufacturer specifications) reflected a portion of the scattered and emitted light to the scattering camera. The transmitted light was split between the emission cameras using a dichroic beamsplitter with a 458-nm cutoff wavelength (Semrock Inc., FF01-458-Di02) for all cases except Eu:BAM SRAPT where only a single luminescence camera was used. Two sets of luminescence filters were used, one for Eu:BAM SRAPT termed “Lum” and another set referred to as the “Red” and “Blue” bands which were used for all other luminescence measurements. Similarly, three sets of scattering collection optics were used, one for Eu:BAM SRAPT which uses a UV camera lens, and one each for 266-nm and 355-nm scattering (each consisting of a UV-grade fused silica singlet spherical lens) for all other measurements.

The filter combinations are listed in Table 5.2, with some derived properties including collection efficiency estimates based on measured room temperature emission spectra. The top portion of the table provides data for the luminescence collection bands for each phosphor (“Red” and “Blue” bands are used for each phosphor, while “Lum” is only used for Eu:BAM SRAPT). The bottom portion tabulates the optics and efficiency of the three scattering measurements. The estimated collection efficiencies include

Table 5.2: Equipment and estimated collection efficiency for scattering and luminescence cameras in flame experiment. Phosphors using 266-nm excitation are shown in the top portion, and Eu:BAM at 355-nm excitation is in the bottom. The dichroic beamsplitter (Semrock Inc., FF458-Di02) is included in the collection efficiency calculation for the Red and Blue bands. Superscripts a, b, c, d, and e indicate phosphors Ce,Pr:LuAG, Ce:CSSO, annealed Ce:CSSO, Ce:$GdPO_4$, and Eu:BAM, respectively.

Band	Camera	Lens	Filters	$\eta_{PC}\eta_{opt}$ [-]	$\Omega/4\pi$ [-]
Red	PI-Max 4	Nikon Nikkor	Reynard R00944	0.341^a	9×10^{-4}
		50-mm (f/1.2)	Asahi Spectra ZVL0470	0.316^b	
				0.341^c	
				0.099^e	
Blue	PI-Max 4	Sodern Cerco	Schott WG-295	0.144^a	4×10^{-4}
		45-mm (f/1.8)	Melles Griot O3SWP604	0.215^b	
				0.180^c	
				0.113^d	
				0.141^e	
Lum	PI-Max 4	Nikon Nikkor	Semrock BLP01-355R	0.308^e	4×10^{-4}
		50-mm (f/1.2)	Asahi Spectra ZVS0490		
266 Scat.	PI-Max 2	UV Singlet Lens	Edmund 39-320	0.012^{abcd}	1×10^{-7}
		100-mm (f/90)			
355 Scat.	PI-Max 2	UV Singlet Lens	Edmund 67-893	0.016^{ce}	1×10^{-7}
		100-mm (f/90)			
SRAPT	PI-Max 2	Sodern Cerco	Edmund 67-893	0.015^e	6×10^{-7}
Scat.		45-mm (f/32)			

the lens transmission, taken as 90% for the singlet lens, and 85% for the Sodern Cerco lens (based on manufacturer data). Absolute spectral response data for the Nikon Nikkor lenses from [110] was included in the calculation. The f-number and collection solid angle listed for the "SRAPT Scat." band in Table 5.2 is based on the smallest aperture available with the Sodern Cerco 45-mm lens; this value only approximates the experimental conditions because the lens does not have fixed f-stops. Since the unannealed Ce:CSSO Ce^{3+} and host emission overlap appreciably, the collection efficiency estimate for this phosphor is calculated assuming all emitted light at wavelengths longer than 460 nm is due to Ce^{3+} luminescence, while wavelengths shorter than 460 nm are due to host emission.

In addition to the data in Table 5.2, the transmission bands, PI-Max 4 spectral response, and room temperature phosphor emission spectra are shown in Figure 5.17 for both the 266-nm excitation and 355-nm excitation phosphors. The transmission band calculation again includes the lens transmission. From the plot, the 460-nm cutoff effectively separates the emission of the Ce^{3+} and Pr^{3+} ions in Ce,Pr:LuAG;

however, for Ce:CSSO, the host emission somewhat overlaps the Ce^{3+} emission. The overlap is reduced following annealing of the phosphor (see [83]), and at elevated temperatures after the host emission has quenched significantly.

Phosphor particles were seeded into the co-flow jet using a fluidized bed aerosol generator (TSI, Model 3400A) at an inlet air pressure of 350 kPa gauge. Air flow rate to the seeder was measured with a digital mass flow meter (Alicat, M-50SLPM-D) and held at 2.0 ± 0.1 slpm. Air flow rates for room temperature imaging without the flame were varied between 10 and 15 slpm to achieve a range of seeding densities and flow patterns suitable for whitefield correction.

Seeding density estimates are made from the absolute Mie scattering intensity images. The signal per particle measurements from the heated jet setup using Ce,Pr:LuAG (Section 5.1.1) were used, in combination with the estimated optical and experimental parameters (see Tables 5.1 and 5.2), to convert absolute luminescence signal intensity images to number density images at room temperature. The data is then used to generate a (linear) calibration between the Mie scattering intensity image and the local number density. Finally, the Mie scattering calibration is scaled by the scattering cross-section predicted by Mie scattering theory to estimate number density for other phosphors in addition to Ce,Pr:LuAG.

5.3.1 Data Analysis Procedure

The calibration function used in this experiment was determined *in situ* and does not directly account for fluence variation. (The *in situ* calibration data was used to generate the signal model results in Section 4.6.) The analysis procedure is otherwise almost identical to the heated jet imaging results. Raw images are first background subtracted, image registration is performed, and the images are converted to ratio measurements according to Equation 4.27. A whitefield image set is taken without the flame, and averaged over 200 images. The ratio images are then normalized by the whitefield ratio image. Finally, a 2x2 moving average filter was applied to reduce noise. The estimated spatial resolution is 1.12 line pairs per millimeter based on a binned and filtered image of a 1951 USAF resolution test chart (MIL-STD-150A). To calculate temperature, the calibration function is numerically solved at every point in the image domain using the whitefield-corrected ratio as input. In general, the ratio calibration is not a monotonic function of temperature, and thus multiple roots exist. For phosphors where multiple diagnostics are carried out simultaneously, the simultaneous measurements are used to determine which root of the calibration function is correct. Otherwise, the highest temperature root is taken.

To remove the influence of noise and background each signal image is thresholded, requiring at least 1000 counts of scattering intensity and 200 counts of luminescence intensity to keep a measurement; this

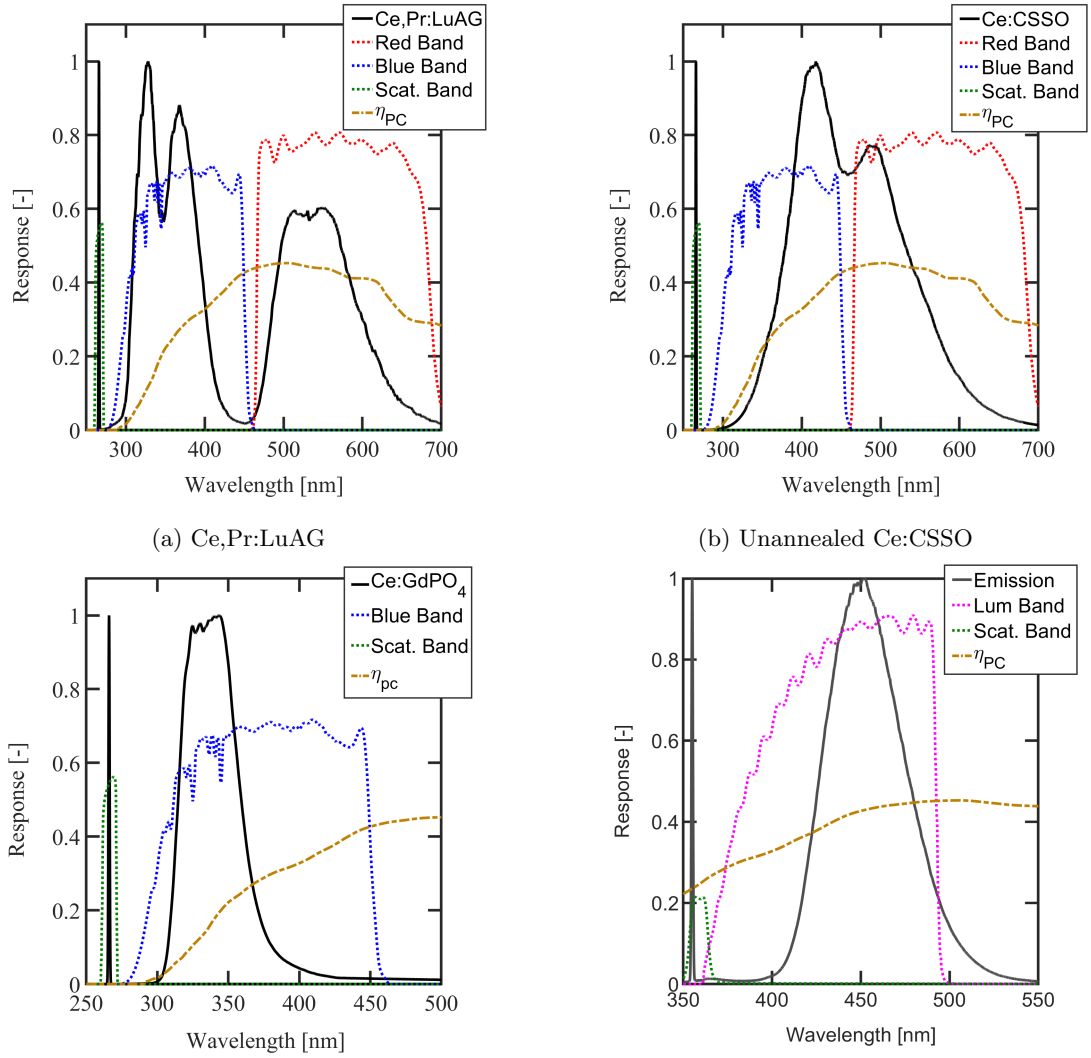

(a) Ce,Pr:LuAG

(b) Unannealed Ce:CSSO

(c) Ce:GdPO$_4$

(d) Eu:BAM

Figure 5.17: Room temperature emission spectra of each phosphor with collection bands and photocathode quantum efficiency of luminescence camera superimposed. The 8% reflection assumed for the pellicle beamsplitter is not included for the Scat. bands for clarity.

intensity roughly corresponds to the point above which the luminescence cameras are linear to within ∼5-10% (see Appendix E). When calculating the average image, a region is masked if 20% or more of the single-shot measurements did not meet the thresholding criteria at the same location. For Ce:$GdPO_4$ and Ce,Pr:LuAG (Pr^{3+} SRAPT), the threshold was moved up to 50%; in both cases the single-shot measurements are sparse (meaning that many pixels are empty because the measurements are out of range) and the flame was oscillatory. This prevents too much of the imaging domain from being masked.

5.3.2 Ratio Precision

Similar to the heated jet data, the ratio precision provides a measure of the imaging quality of the experiment. The ratio precision is calculated over a rectangular region (approximately 10 mm × 8 mm) from images of the jet at 300 K with the flame turned off. The measured precision is shown in Figure 5.18. As before, each data point represents a single image. Seeding density is calculated based on Mie scattering intensity, and is averaged over the rectangular region; ratio precision is calculated as the coefficient of variation (sample standard deviation divided by the mean).

For Ce,Pr;LuAG and annealed Ce:CSSO, the co-doped and host-referenced (respectively) ratio precision are significantly improved over the SRAPT precision. This is likely indicative of the additional SRAPT error term. However, for the unannealed Ce:CSSO the SRAPT and host-referenced ratio precisions are similar. Unannealed Ce:CSSO was run at much higher seeding densities, which could greatly reduce the SRAPT error. For Eu:BAM, the spectral luminescence intensity ratio method also has the best ratio precision. However, the signal intensities for Eu:BAM (both scattering and luminescence) are sufficiently high that intensifier saturation may reduce the apparent noise. Note that the ratio precision estimates here are not corrected for camera non-linearity, but the imaging results and calibration functions are.

5.3.3 Calibration Functions

For each phosphor, the calibration function is generated by comparing the mean measured ratio to the thermocouple temperature along the vertical centerline. The data is fit using a modified Arrhenius-like expression with the form:

$$R = \frac{R_0 + C_{NR} e^{-\Theta/k_B T}}{1 + \epsilon_1 T + \epsilon_2 T^2}. \tag{5.1}$$

The numerator of the function is the usual Arrhenius like term describing thermal quenching (see Section 2.4), modified to allow the ratio to go to a value of R_0 at $T \to 0$. The denominator is a polynomial that aims to describe changes in the absorption cross-section to first order. The measured ratios and

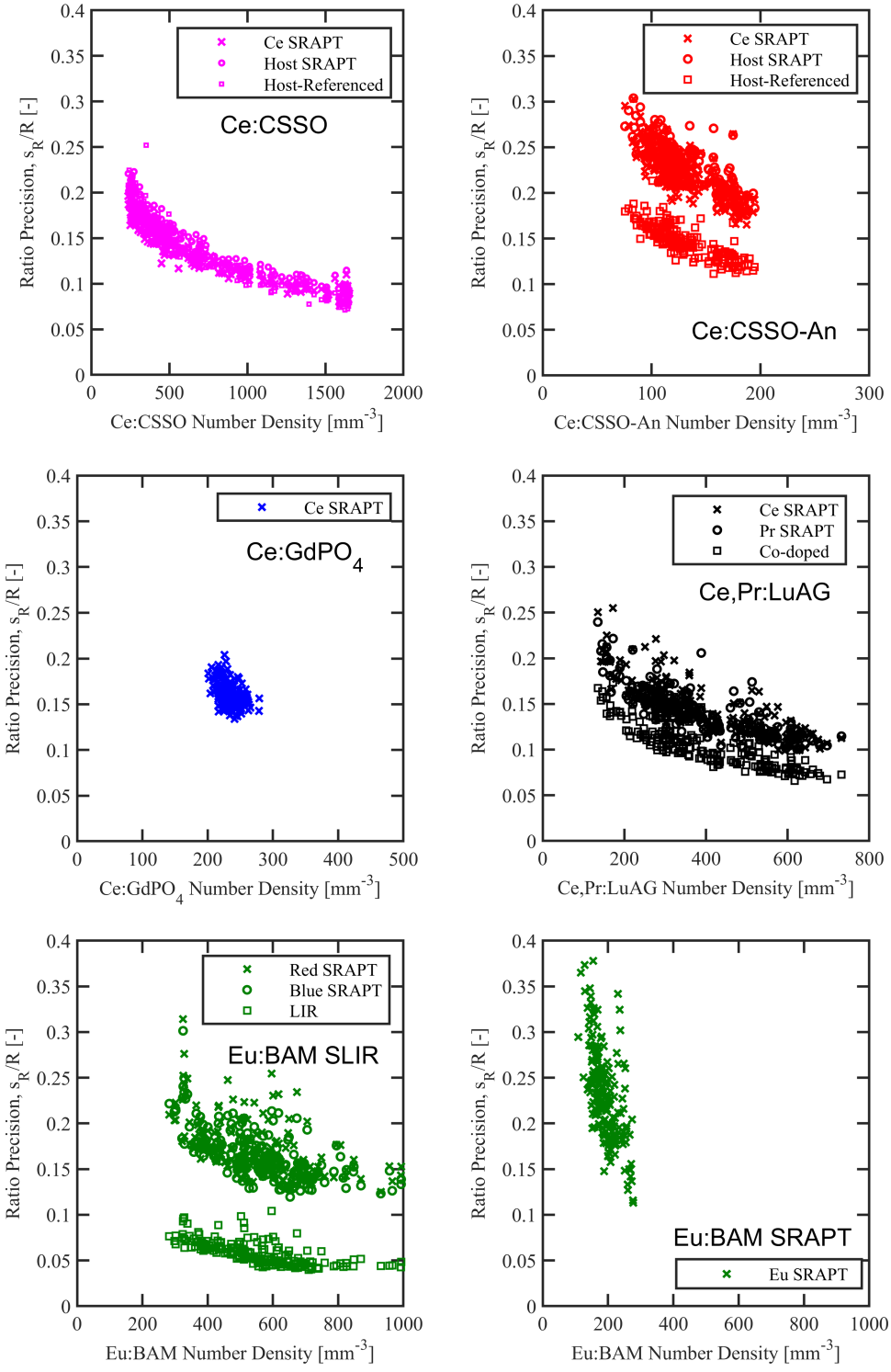

Figure 5.18: Measured ratio precision for each phosphor and diagnostic taken in the flame experiment

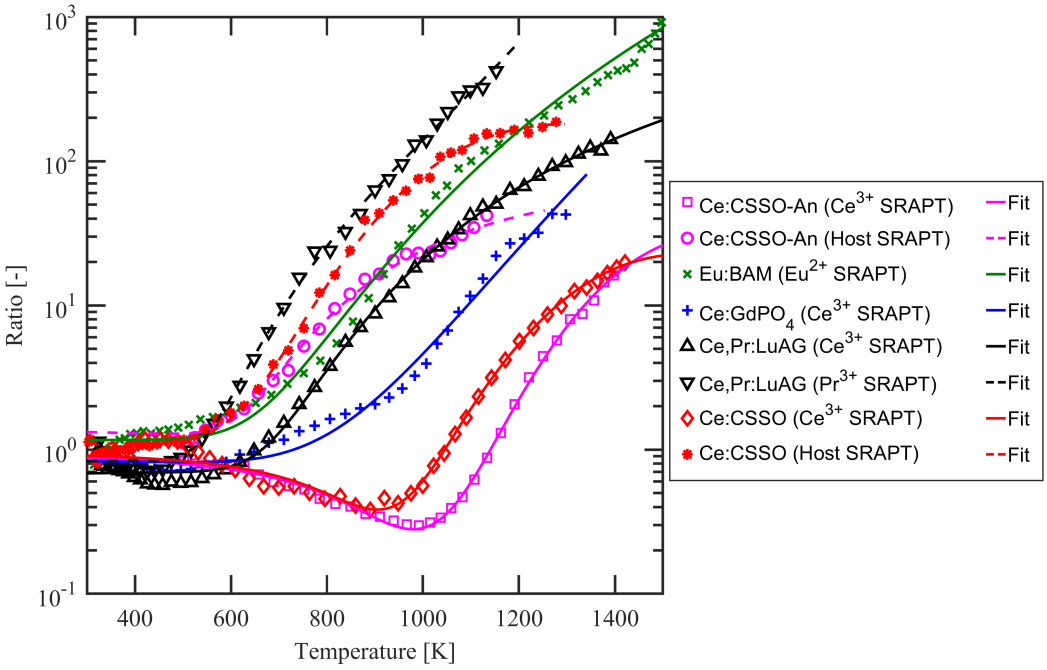

Figure 5.19: Measured and best-fit ratios for each SRAPT diagnostic characterized and used in the flame experiment. Only every third data point is shown in the plot for clarity.

comparison with the fits are shown in Figure 5.19, and the fit parameters are tabulated in Table 5.3. Note that the original Ce,Pr:LuAG calibration and fluence model are used for the Ce,Pr:LuAG data as described in Section 5.1; the data provided in the table and figure are fit to the same model for comparison but an *in situ* calibration is not used for Ce,Pr:LuAG.

The fits in Figure 5.19 capture the data well, with a few notable exceptions. In particular, the fit for Eu:BAM and Ce:$GdPO_4$ deviate from the data slightly throughout much of the data series. These phosphors both exhibit several inflection points in the calibration curves and the form of the fit function cannot capture all of them exactly. However, as will be shown in the temperature imaging results, this error does not significantly impact the temperature measurement at temperatures above $\sim$ 700 K for Ce:$GdPO_4$ and $\sim$ 900 K for Eu:BAM. The temperature imaging results are only shown above 700 K for Ce:$GdPO_4$ and 900 K for Eu:BAM SRAPT as a result. The fits for the CSSO phosphors and for Ce,Pr:LuAG capture the behavior very well, except near 300 K where the fits do not go precisely to unity as expected. This may be due to a background signal that was not adequately removed by the background subtraction process, *e.g.*, from multiple scattering or reflections from nearby optics. Table 5.3 has two entries for Eu:BAM. The entry labeled "Low Fluence" is at a fluence of below 3 mJ/cm^2 near the limit where Eu:BAM is linear; this does appear to have an impact on the data, and is consistent with the ratios calculated in Section 4.6.

Table 5.3: Best-fit ratio calibrations for flame temperature-imaging experiments.

Signal	C_{NR} [-]	R_0 [-]	Θ [K]	ϵ_1 [K^{-1}]	ϵ_2 [K^{-2}]
Annealed CSSO (Ce^{3+} SRAPT)	1.1039×10^{4}	0.9338	13718	-1.8×10^{-3}	8.836×10^{-7}
Annealed CSSO (Host SRAPT)	6.1427×10^{6}	1.4259	9703	9.1213×10^{-4}	-4.878×10^{-8}
Eu:BAM (Eu^{2+} SRAPT)	3.457×10^{5}	0.7	9873	-1.436×10^{-3}	9.226×10^{-7}
Eu:BAM (Eu^{2+} SRAPT) (low $\dot{\phi}''$)	1.645×10^{4}	1.1536	6770	-2.128×10^{-4}	4.0484×10^{-8}
Ce:$GdPO_4$ (Ce^{3+} SRAPT)	1000	0.8572	6471	-5.769×10^{-4}	1.5059×10^{-7}
Ce,Pr:LuAG (Ce^{3+} SRAPT)	8.134×10^{5}	0.659	9758	3.556×10^{-4}	-8.154×10^{-8}
Ce,Pr:LuAG (Pr^{3+} SRAPT)	1.919×10^{7}	0.7866	9472	1.3×10^{-3}	-8.696×10^{-7}
CSSO (Ce^{3+} SRAPT)	9.9×10^{3}	0.9536	12829	-2.0×10^{-3}	1.039×10^{-6}
CSSO (Host SRAPT)	2.501×10^{4}	1.0794	6704	-8.18×10^{-4}	6.042×10^{-7}

The calibration functions for the luminescence intensity ratio diagnostics (host-referenced Ce:CSSO, co-doped Ce,Pr:LuAG, and Eu:BAM spectral LIR methods) are likewise shown in Figure 5.20. Since these ratios are not easily related to simple signal intensity or quenching models, they are fit to a double exponential instead for simplicity. The ratios are reasonably well represented, but some deviation is evident particularly for the unannealed Ce:CSSO samples. The double exponential function is also insufficient for representing the Ce,Pr:LuAG co-doped APT ratio, as it reaches a local maximum near 750-800 K; the double-exponential fit is only valid up to ∼650-700 K. Comparing the Ce,Pr:LuAG co-doped ratio to the results of Sections 5.1, the co-doped ratios measured in the flame are consistent with those measured in the heated jet. As with the Ce,Pr:LuAG SRAPT techniques, the heated jet calibration is used for the remainder of this discussion.

5.3.4 Flame Imaging Results

The diagnostics were applied to image a jet heated by mixing with the products of an atmospheric methane-air flat flame, which is pictured in Figure 5.21. In the picture, the flat flame is parallel to the surface of the porous plug surrounding the central 12-mm diameter tube. Room-temperature air seeded with phosphor particles exits from the tube and mixes with the products of the flat flame.

A set of mean temperature images for the 200 image sets are shown in Figures 5.22 and 5.23. For each phosphor, imaging data needed for each diagnostic approach are acquired simultaneously (*e.g.,* for Ce,Pr:LuAG, Ce^{3+} luminescence, Pr^{3+} luminescence, and elastic scattering intensity are measured simultaneously) using up to 3 cameras. This results in three simultaneous images for Ce,Pr:LuAG and both Ce:CSSO phosphor samples, but only one temperature image for Ce:$GdPO_4$ and Eu:BAM (SRAPT and SLIR methods are performed separately since different filter combinations are used). The optical

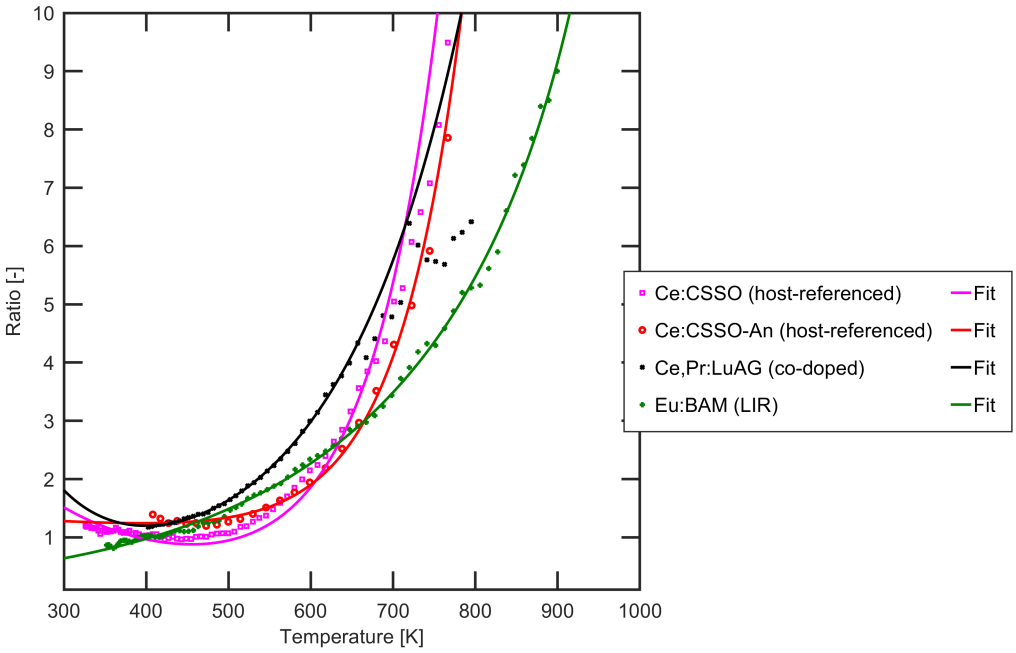

Figure 5.20: Measured and best-fit ratio calibration functions for the luminescence intensity ratio diagnostics

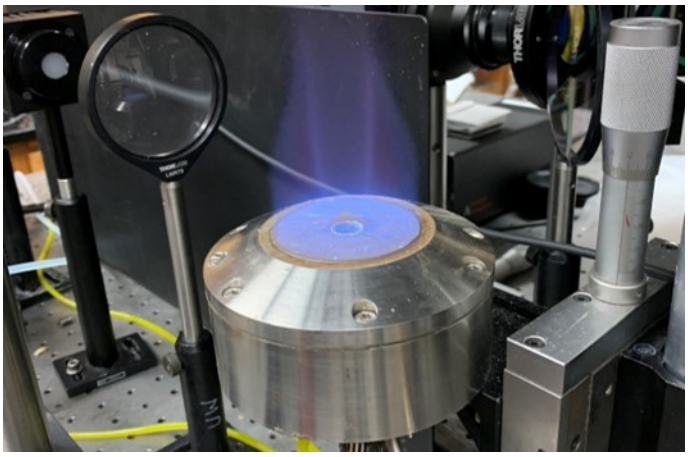

Figure 5.21: Picture of burner configuration for flame-heated jet experiments.

layout was shown in Figure 5.16 in Section 5.3.

The images show a cold jet core in the bottom center of the image that is heated as it mixes with the products of the surrounding flat flame. The velocity of the combustion products is not perfectly matched with the jet velocity ($\sim$ 0.3 m/s for the seeded air jet, and $\sim$ 2.2 m/s for the hot combustion products assuming the combustion products reach 2000 K and the average molecular weight is that of nitrogen). Higher above the burner surface, more time is allowed for the flame to heat the jet, which results in a temperature field that looks similar to a diffusion flame. However, only the cold air is seeded, and thus an abrupt cutoff is apparent at the outer boundary of the air jet. Signal measurements (and hence temperature measurements) outside of this region are likely erroneous and may be a result of background radiation from the flame. The bottom of the image for all images shown in this chapter is approximately 17 mm above the burner surface.

From the plots, each technique and phosphor clearly is capable of imaging in a different temperature range. On the low end, the Ce,Pr:LuAG co-doped technique covers 400 to 700 K; Ce:CSSO (both annealed and unannealed) host-referenced APT and host SRAPT both cover a range from 400 to approximately 800 K. In most of the images, the cold jet core is not visible because most of the phosphors used in this study do not have significant temperature dependence near room temperature. One exception is the Ce,Pr:LuAG phosphor, where the co-doped technique works well down to around 400 K or less. Another exception is for Eu:BAM SLIR method where temperatures down to around 400 K are measureable. The Ce^{3+} SRAPT technique can also be used with Ce:CSSO (both annealed and unannealed) at relatively low temperatures as there is a small amount of temperature sensitivity due to changes in the absorption cross-section with temperature; however, this does not provide a good measurement because the sensitivity is relatively low and because the calibration function is double valued for some temperatures making it impossible to determine the correct root without more information.

From the images, the Eu:BAM SRAPT phosphor reaches the highest temperatures, although the Ce:CSSO phosphor is very close as well (both annealed and unannealed). The unannealed Ce:CSSO phosphor provides a less noisy measurement due to higher signal intensities, but temperature sensitivity is shifted slightly; the unannealed phosphor begins quenching at a slightly colder temperature. Ce:$GdPO_4$ additionally covers much of the temperature range from 800 to 1300 K, but has a weak emission resulting in low signal-to-noise ratios. The Ce,Pr:LuAG phosphor covers the range from 300 to 1000 K very well, and the images here suggest that measurements up to almost 1100 K may be possible with improved high-temperature calibration data.

There are a few noticeable differences between the different phosphors and techniques. Each technique does not perform well near the edge of its usable temperature range. In particular, Ce,Pr:LuAG

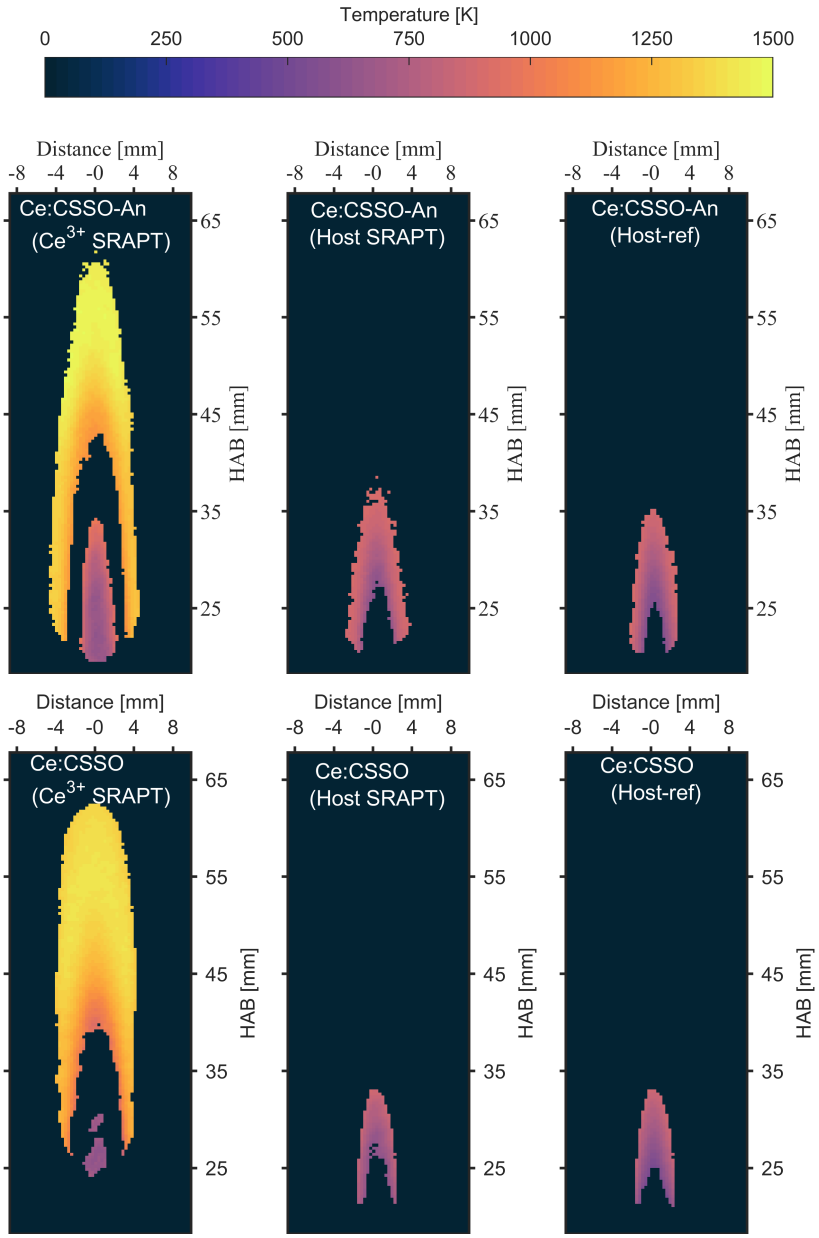

Figure 5.22: Average temperature images for each technique measured in the flame-heated jet with Ce:CSSO and annealed Ce:CSSO. Averages are taken over 200 images, and regions where signal is below the threshold are masked. The annealed Ce:CSSO phosphor is shown in the top row, followed by the unannealed Ce:CSSO phosphor on the bottom row.

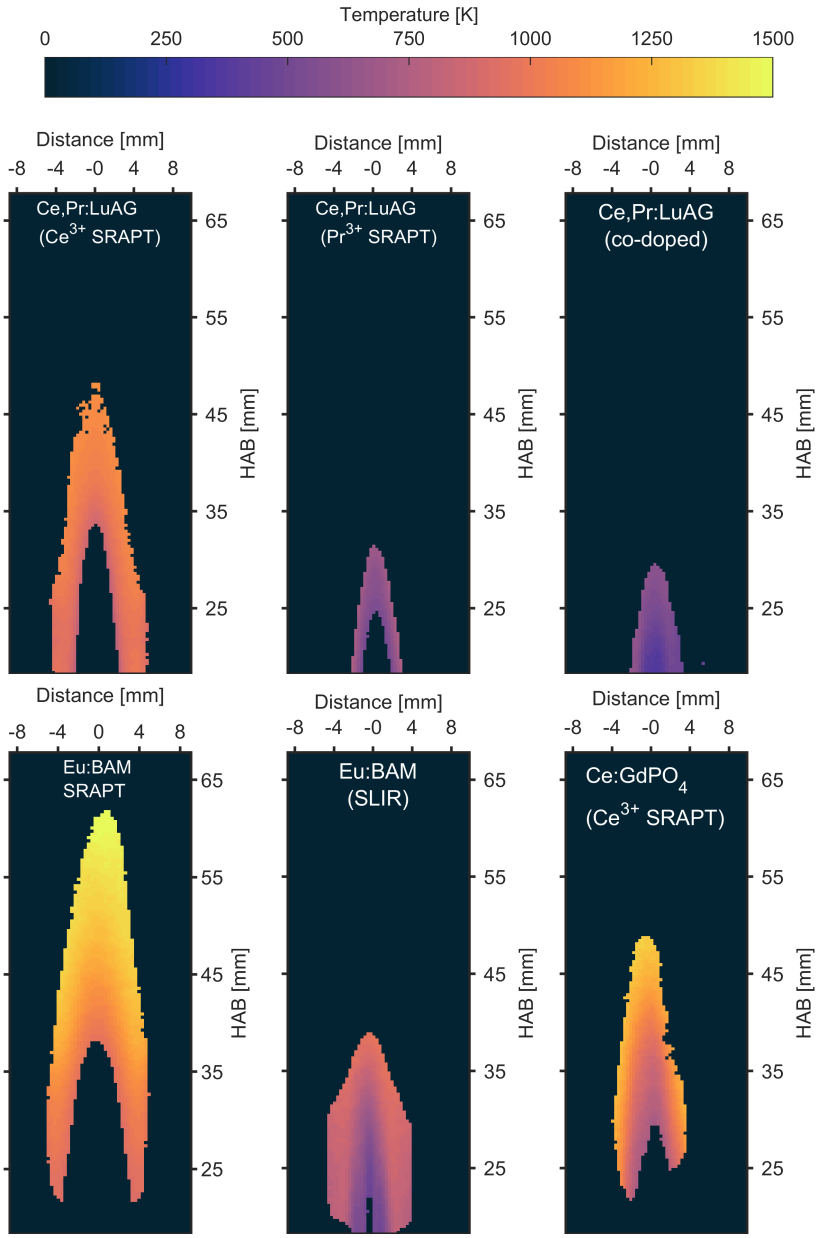

Figure 5.23: Average temperature images for each technique measured in the flame-heated jet with Ce,Pr:LuAG, Eu:BAM, and Ce:$GdPO_4$. Averages are taken over 200 images, and regions where signal is below the threshold are masked. The Ce,Pr:LuAG phosphor is shown in the first row. Eu:BAM (SRAPT and SLIR) and Ce:$GdPO_4$ are shown in the bottom row.

(Ce^{3+} SRAPT) underpredicts temperatures near and above 1000 K, while the Eu:BAM SLIR measurement appears to underpredict temperatures above ∼600 K. For Ce,Pr:LuAG, this is largely a result of calibration bias since the technique was not calibrated above 1000 K. For Eu:BAM SLIR, particularly near the hot edges of the jet (horizontal distances ∼ 4 mm at ∼25 mm HAB), this may be a result of multiple scattering. High seeding density and very low emission intensity per particle at the jet edge, combined with close proximity to the bright jet core, make the edge susceptible to bias from multiple scattering. Light emitted at the cold jet core is scattered from the hot particles at the edge before being detected by the camera, making it appear that the scattered light was emitted by the hot particles near the edge. Since the emission intensity is so low at the hot jet edge, the scattered light can significantly bias the measurement and lower the measured ratio. It should be noted that there is some less obvious discrepancy between the other techniques as well, mostly likely a result of calibration bias and a slight unsteadiness in the flame.

Single-shot images are shown in Figures 5.24, 5.25, 5.26, and 5.27 for Ce,Pr:LuAG, annealed Ce:CSSO, unannealed Ce:CSSO, and the remaining phosphors (Eu:BAM and Ce:$GdPO_4$), respectively. For each figure, 9 representative single-shot images are chosen; the same image is used for each technique for phosphors that provide multiple simultaneous measurements.

The Ce,Pr:LuAG images are shown in Figure 5.24. From shot-to-shot, the jet appears relatively stable, at least at the lower temperatures evident in the figure. The co-doped technique covers the cold part of the jet well and is the only technique that can make a measurement on the interior of the jet down to 300 K. The Pr^{3+} SRAPT technique captures a small layer of the jet after it has been heated to around 600 K; the measurements are no longer viable above 800 K. The Ce^{3+} SRAPT technique covers the largest area, and begins measuring around 800 K and continues up to around 1100 K, as extrapolated by the lower temperature calibration. The measurements are only calibrated below 1000 K, so hotter measurements may be erroneous. However, the presence of hotter measurements that have not been removed by the automated thresholding procedure suggests that the Ce^{3+} SRAPT technique with the Ce,Pr:LuAG phosphor could be used up to higher temperatures. Here, each SRAPT technique is only used at or above the onset of thermal quenching (roughly at $T > T_{50}$), although in principle measurements can be made at colder temperatures by taking advantage of the temperature-dependent absorption process.

Single-shot images from the annealed Ce:CSSO measurements are shown in Figure 5.25. Similar to Ce,Pr:LuAG, the Ce^{3+} technique covers the highest temperature range, while the host SRAPT and host-referenced APT technique fill in gaps in the colder center of the jet. The Ce^{3+} SRAPT measurement does have a portion of the colder jet center filled in, although it appears to be biased hot.

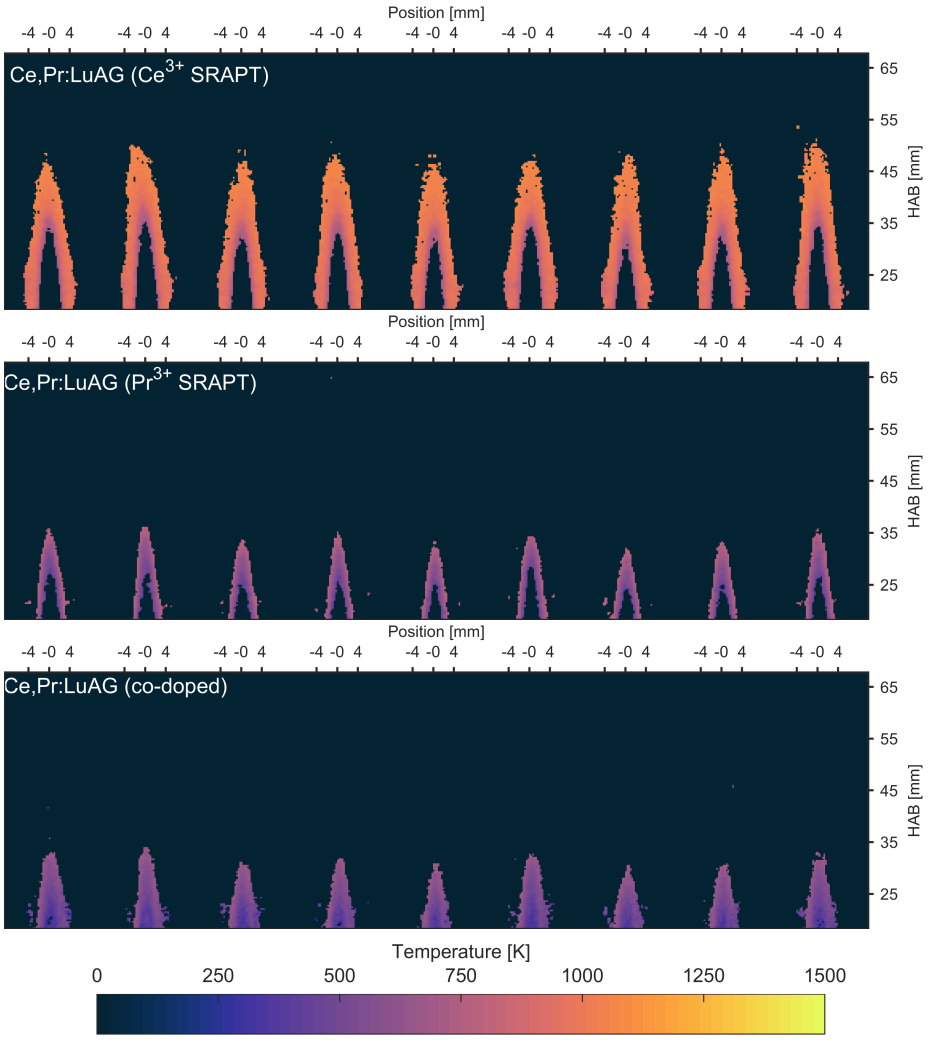

Figure 5.24: Single-shot images for Ce,Pr:LuAG flame-heated jet temperature measurements. Each row shows a single technique. From top to bottom: Ce^{3+} SRAPT, Pr^{3+} SRAPT, and Ce^{3+}-Pr^{3+} co-doped APT.

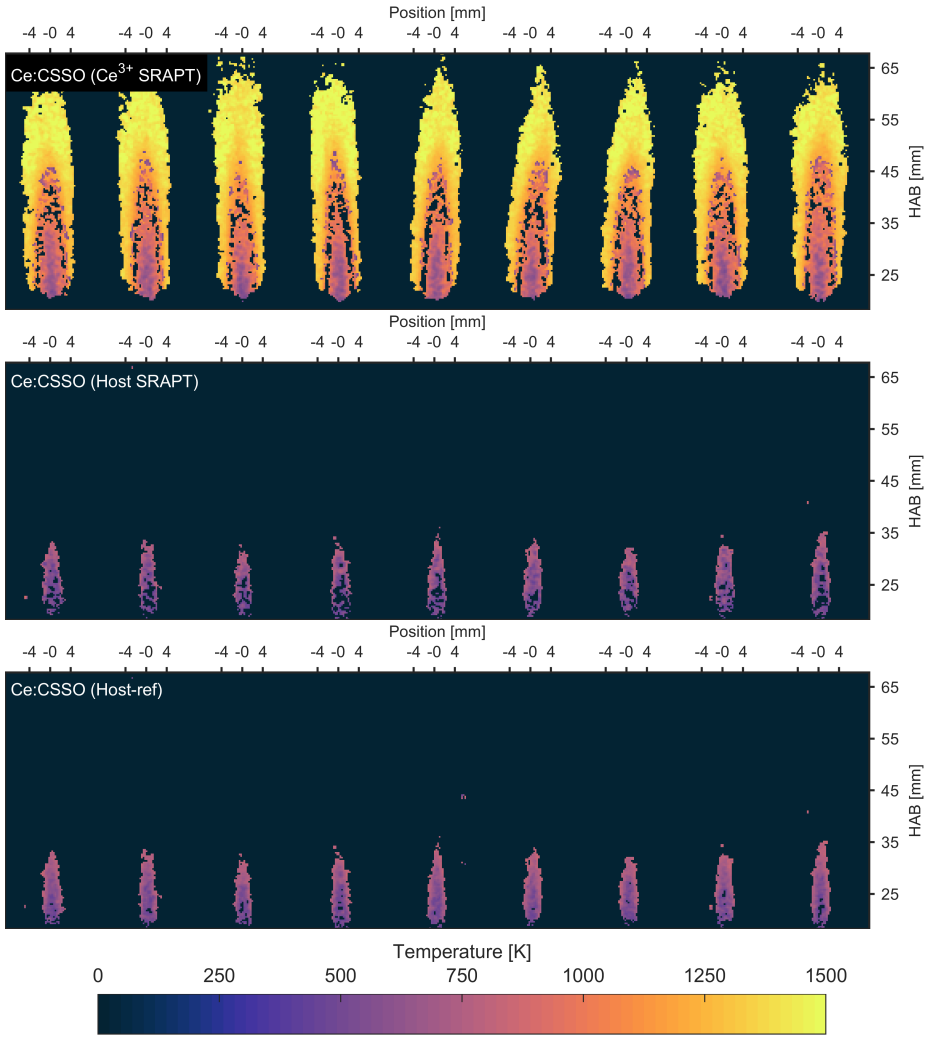

Figure 5.25: Single-shot images for annealed Ce:CSSO flame-heated jet temperature measurements. Each row shows a single technique. From top to bottom: Ce^{3+} SRAPT, host SRAPT, and host-referenced APT.

The Ce^{3+} SRAPT calibration function for Ce:CSSO is double valued; initially the ratio drops due to an increasing absorption cross-section with temperature, followed by thermal quenching which leads to an abrupt increase in the ratio. Some cold temperature measurements are available where the host emission is used to determine which branch of the calibration function is correct. However, this only works for a few measurements near the jet core. Once the host emission is completely quenched, the high-temperature branch of the Ce^{3+} calibration is used instead. As a result, the entire temperature range where no host emission is visible but the Ce^{3+} SRAPT calibration function is still double-valued (approximately 800-1050 K) is biased hot. There is additionally a thin band of temperatures around 1000 K where measurements are not possible with the Ce^{3+} SRAPT technique. This occurs because the calibration function reaches a local minimum (the increasing absorption cross-section negates the onset of quenching), so the sensitivity goes to zero. As a result, any noise in the measurement results in a relatively large measurement error such that no measurements are observed in this temperature range; this manifests as a small layer within the jet where the temperature is undefined (these points are masked in the images shown here).

The unannealed Ce:CSSO measurements are shown in Figure 5.26. Similar to the annealed Ce:CSSO phosphor, the Ce^{3+} measurements cover the largest area, with the host SRAPT and host-referenced APT measurements covering a smaller portion of the jet core. As with the annealed phosphor, the Ce^{3+} SRAPT technique is double valued below 1000 K, resulting in a similar band where temperature measurements are not possible. There are two primary differences between the unannealed and annealed Ce:CSSO. First, the unannealed Ce:CSSO begins quenching at a slightly colder temperature than the annealed Ce:CSSO. Second, the unannealed Ce:CSSO is much brighter at low temperatures (but not after the host emission has quenched). Both of these effects are likely a result of interfering host emission or host feeding, and alter the temperature sensitivity and thus the performance of the technique. The results here suggest that the host SRAPT and host-referenced APT measurements cover a larger portion of the jet for the unannealed Ce:CSSO compared to the annealed Ce:CSSO, likely due to the increased low-temperature emission intensity.

Finally, the Eu:BAM and Ce:$GdPO_4$ phosphors are shown in Figure 5.27, with Eu:BAM SRAPT on top, Eu:BAM SLIR in the middle, and Ce:$GdPO_4$ SRAPT on bottom. The Eu:BAM phosphor covers a very similar range to the Ce:CSSO phosphors; Eu:BAM SRAPT's effective range is from 900 to 1500 K, and the SLIR method can potentially provide a measurement from 400-1000 K. It is possible that with an improved calibration function fit, measurements could be possible at an even larger temperature range. This additionally demonstrates that given an appropriate optical setup, combined SLIR and SRAPT measurements with Eu:BAM may be possible covering the range from 400 K to 1500 K. How-

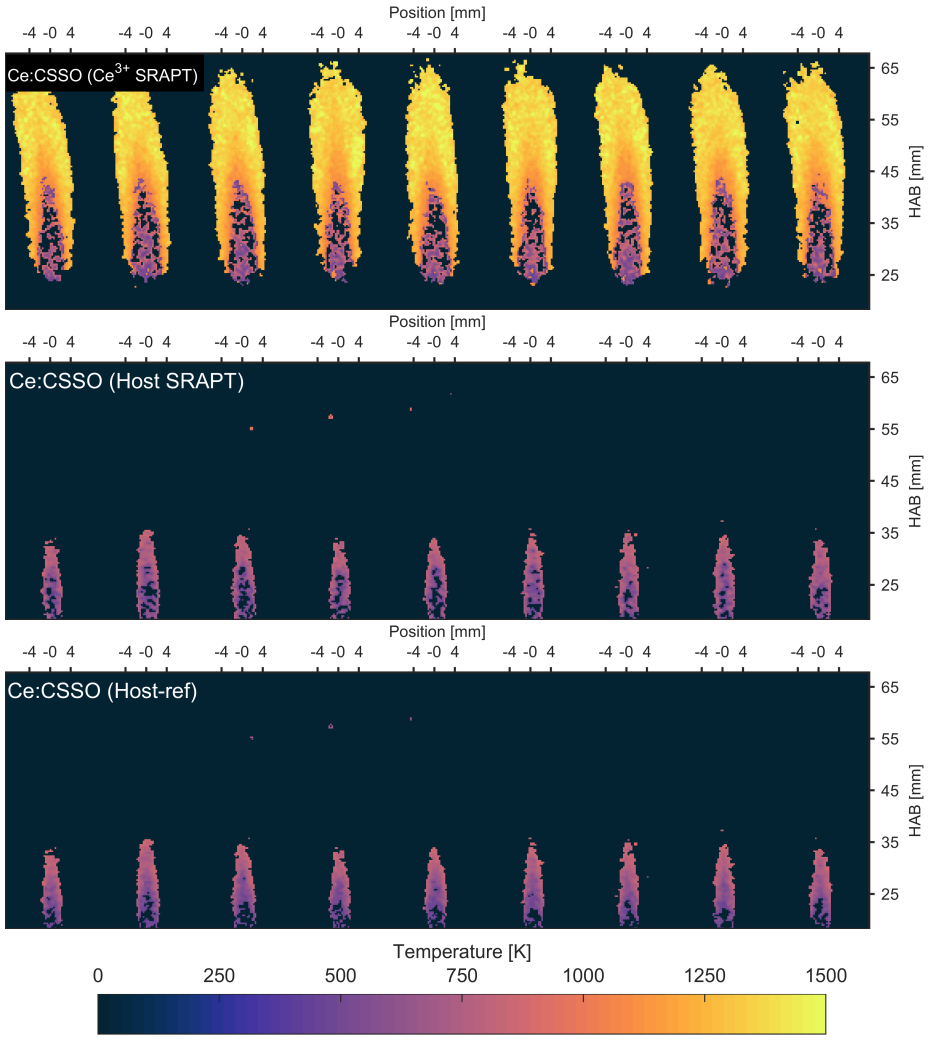

Figure 5.26: Single-shot images for unannealed Ce:CSSO flame-heated jet temperature measurements. Each row shows a single technique. From top to bottom: Ce^{3+} SRAPT, host SRAPT, and host-referenced APT.

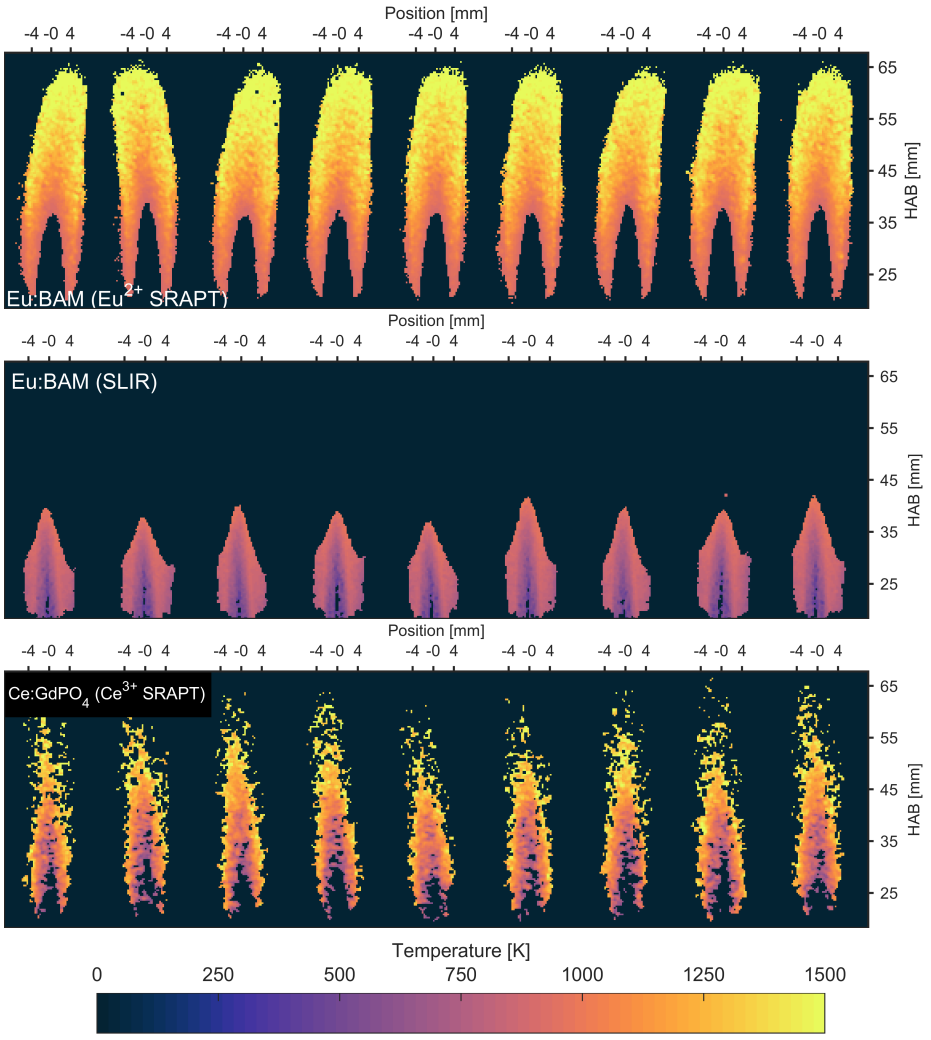

Figure 5.27: Single-shot image stacks for Eu:BAM SRAPT (top), Eu:BAM SLIR (middle) and Ce:$GdPO_4$ SRAPT (bottom).

ever, the SLIR setup requires relatively narrow collection bands that may not be feasible in low signal environments. Finally, since Eu:BAM is so bright, the measurement signal to noise ratio is improved over the Ce:CSSO phosphors. Ce:$GdPO_4$ covers a temperature range from around 800 to 1300 K, but, due to low emission intensity, the temperature images are very noisy.

Comparing the single-shot images, a few trends are evident. First, Eu:BAM appears to be influenced strongly by multiple scattering. This is particularly apparent in the Eu:BAM SLIR image sets, where the edge at ±4 mm (horizontal from center) is much cooler than the value measured by every other technique. As with the mean image, this is likely a result of multiple scattering. The other phosphors do not appear to be influenced nearly as much by multiple scattering, although this is unsurprising as the other phosphors do not exhibit the same range of emission intensity per particle as Eu:BAM. Eu:BAM at room temperature is significantly brighter (on a per particle basis) than any other phosphor considered here, but above 1000 K the signal intensity is reduced by two orders of magnitude. The large usable dynamic range of the Eu:BAM emission intensity may partly explain why multiple scattering appears to influence Eu:BAM results more than other phosphors; none of the other phosphors are bright enough such that ratios of over 100 can be measured. The Ce:$GdPO_4$ and annealed Ce:CSSO phosphors both appear noisy and irregular compared to the results for Ce,Pr:LuAG, raw Ce:CSSO, and Eu:BAM. Ce:$GdPO_4$ and annealed Ce:CSSO have the weakest emission intensity per particle, so this is an expected result as the signal to noise ratio is expected to be low when compared with the brighter phosphors (see Figure 5.18).

The vertical temperature profiles, calculated as the median of the stack of 200 images, are shown in Figure 5.28. The median is used here to better represent the variability in the data. In particular, the Ce:CSSO phosphors near 1000 K are strongly bimodal due to the double-valued calibration function for Ce^{3+} SRAPT. This is evident in the median profile (although not in the mean profile) as a plateau in the measured temperature in between two linear regions (at 1100 K with the annealed Ce:CSSO Ce^{3+} SRAPT technique). In general, each diagnostic matches the temperature measured by the thermocouple reasonably well, except at the low and high temperature limits where the calibration function is not valid. For Eu:BAM, the limits of the measurement are from 900 to 1500 K. For the two Ce:CSSO phosphors, the upper limit is around 1400-1500 K. Both Ce:CSSO phosphor measurements vary significantly at around 1000 K; this is because the calibration function is not monotonic, and it is not possible to determine which root is correct. As a result, the measurements are biased towards the assumed root (the high-temperature root), and measurements in the range of 850-1100 K may be erroneous. However, the unannealed Ce:CSSO phosphor, with a slightly lower quenching temperature, performs better in this region because the Ce^{3+} SRAPT technique can be used at slightly colder temperatures.

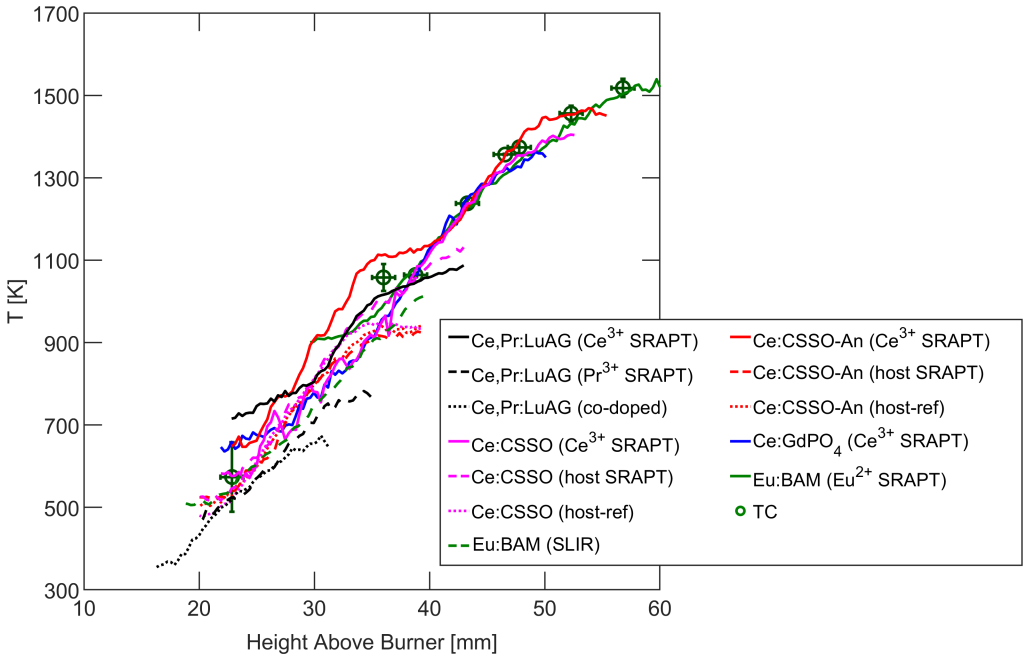

Figure 5.28: Vertical temperature profiles for each phosphor and technique measured in the flame. Thermocouple measurements are superimposed.

The thermocouple profiles on the plot use data from both beads. In particular, the data point at 36 mm above the burner appears hotter than the surrounding measurements would suggest. The 36 mm HAB data point was taken with the larger wire and bead, and as a result may be biased slightly hot; the magnitude of the conduction error typically increases with bead diameter [113], and since the jet core is colder than the jet edge the thermocouple is biased hot (radiation was found to be negligible at this location).

The horizontal profiles, taken at three locations above the burner (24, 36, and 47 mm), are shown in Figure 5.29. The results are largely similar to the vertical profiles; most diagnostics match the profiles reasonably well (at least at temperatures where the diagnostics are sensitive), although the APT measurements consistently report colder temperatures at 36 mm HAB. The 36 mm HAB thermocouple measurement sweep may be biased hot due to conduction along the wire; although a correction was applied, it is likely that the correction was insufficient to remove all of the temperature bias. There is additionally some visible error in both Ce:CSSO Ce^{3+} SRAPT diagnostics near 1000 K due to the double-valued nature of the calibration function, but it is less obvious than in the vertical profiles.

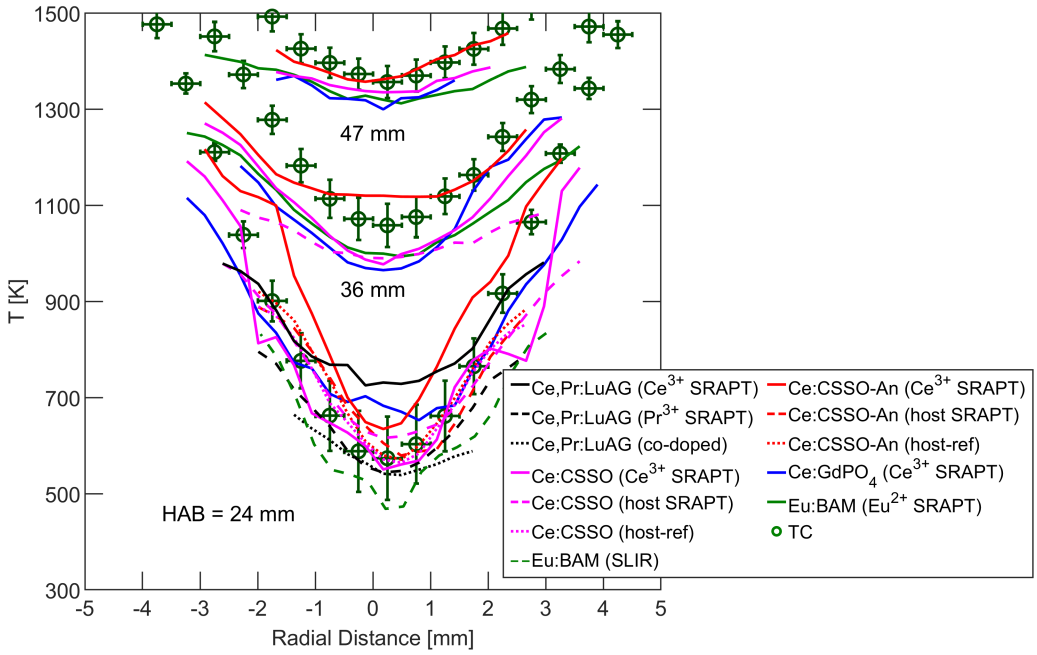

Figure 5.29: Horizontal temperature profiles for each phosphor and technique measured in the flame. Thermocouple measurements are superimposed. The horizontal sweeps were performed with the larger thermocouple bead, and may be biased slightly hot.

5.3.5 Combined Diagnostics

So far, each technique is used individually with each phosphor resulting in multiple simultaneous measurements for the Ce:CSSO and Ce,Pr:LuAG phosphors. However, a single representative measurement can be obtained from the three individual measurements using the weighted average approach discussed in detail in Section 4.7.4. The weighted average method is used exactly as described previously for the Ce,Pr:LuAG phosphor. However, for the Ce:CSSO phosphors, this is not always possible; since host emission quenches at low temperatures and Ce^{3+} emission does not begin quenching until over 1000 K, there are no overlapping regions where multiple diagnostics can be used simultaneously. Instead, the host-referenced diagnostic is used everywhere there is sufficient host emission signal and the host-referenced ratio is within range of the calibration function. Any points that are outside the range of the calibration function due to noise, but still have sufficient host emission signal, use the host SRAPT diagnostic. Finally, the remaining points are filled in with the Ce^{3+} SRAPT technique, but only at measured temperatures above 1000 K.

Mean temperatures images, averaged over the 200 images, are shown in Figure 5.30 for the combined diagnostics. From the images, both Ce:CSSO phosphors are largely able to capture the range from 500 to 1500 K, although there is some difficulty capturing the region between 900 and 1100 K. Ce,Pr:LuAG

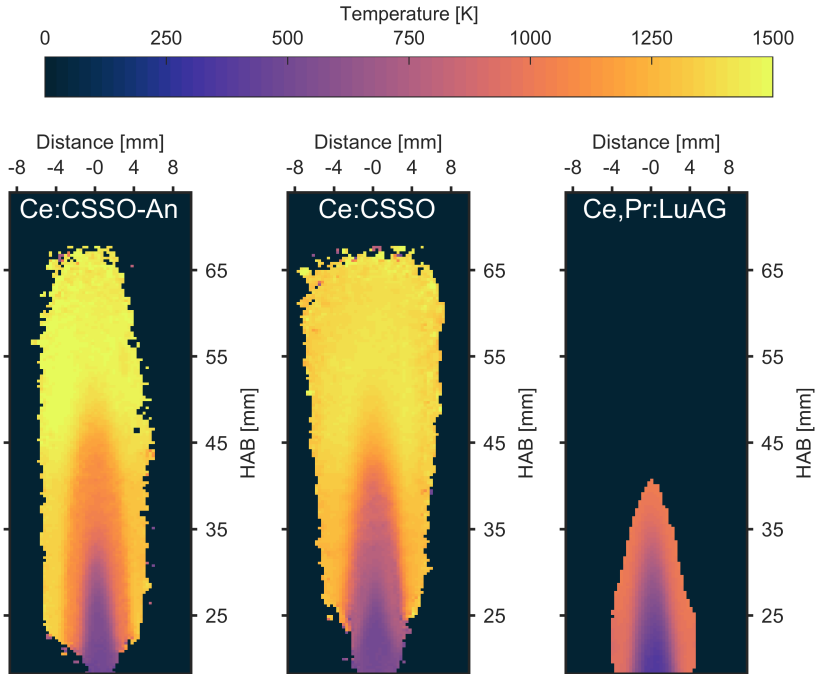

Figure 5.30: Average temperature images for the combined diagnostic using Ce,Pr:LuAG, Ce:CSSO, and annealed Ce:CSSO taken in the flame. Averages are taken over 200 images, and regions where signal is below the threshold are masked. The bottom of the images corresponds to 17 mm above the burner surface.

works well up to 1000 K. The unannealed Ce:CSSO phosphor shows the largest area of the flame, but may be insufficiently masked as the edges appear cooler than expected.

The three combined measurements disagree slightly, particularly at the jet edges where the seeding density is low, and at temperatures where the individual diagnostics perform poorly. Specifically, the Ce,Pr:LuAG measurement tails off at temperatures approaching 1000 K (such that regions where the jet temperature is expected to be over 1000 K appear uniform); as with the Ce,Pr:LuAG Ce^{3+} technique, this is likely because of calibration error above 1000 K. It is also possible that the jet edges are influenced by multiple scattering, similar to Eu:BAM SLIR. Both Ce:CSSO techniques appear to capture the jet behavior well. However, the annealed Ce:CSSO measurement between 700 and 1100 K appears to be influenced strongly by the double-valued nature of the annealed Ce:CSSO Ce^{3+} SRAPT ratio, and does not match the other diagnostics well in this range. The unannealed Ce:CSSO phosphor does not appear to have this issue. Both Ce:CSSO phosphors are erroneous at low temperatures (below ~500 K). Overall, the raw Ce:CSSO phosphor appears to be the least bias over its usable range (~500-1400 K).

Single-shot images for the combined techniques are shown in Figure 5.31. The images look similar to the single shot images for the individual technique, but only show regions where the diagnostics work well. For the Ce:CSSO phosphors, there is a gap around 900 to 1100 K where no diagnostic works well.

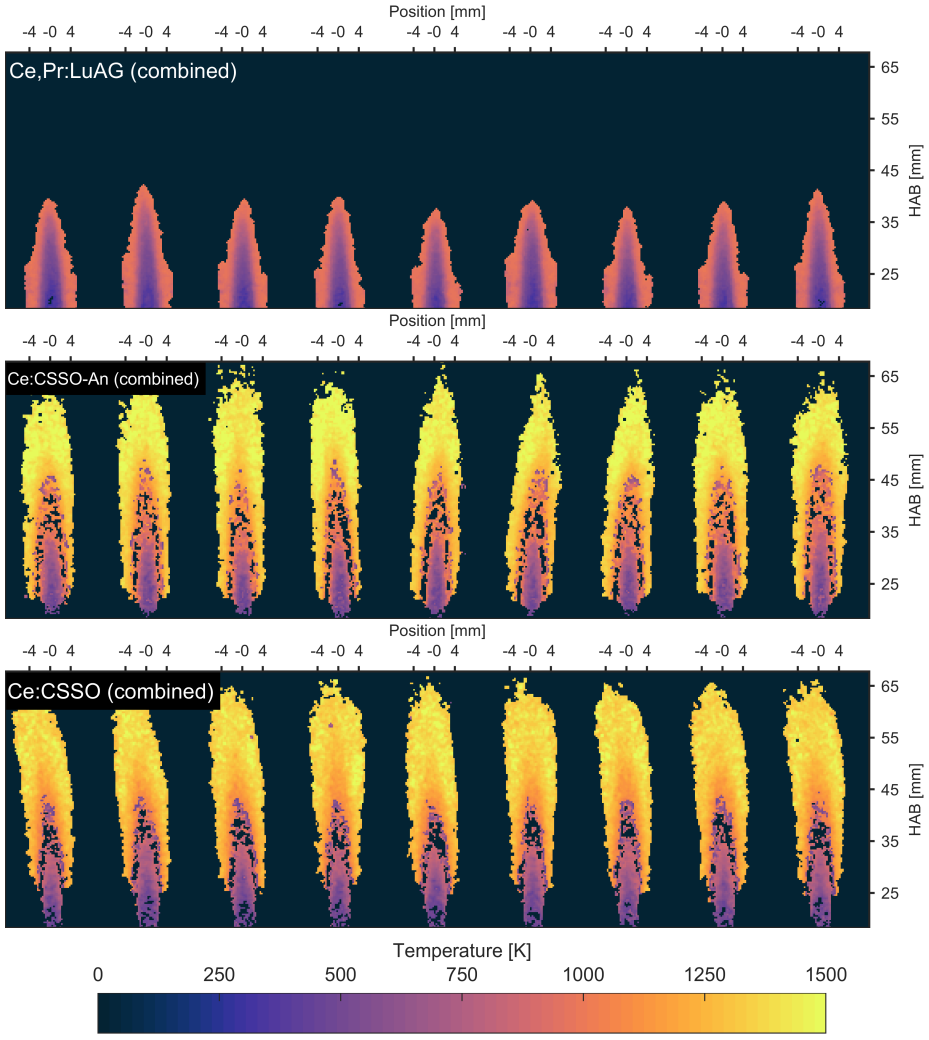

Figure 5.31: Single-shot image stacks for the combined diagnostics using Ce,Pr:LuAG, Ce:CSSO, and annealed Ce:CSSO. From top to bottom: Ce,Pr:LuAG, annealed Ce:CSSO, and unannealed Ce:CSSO.

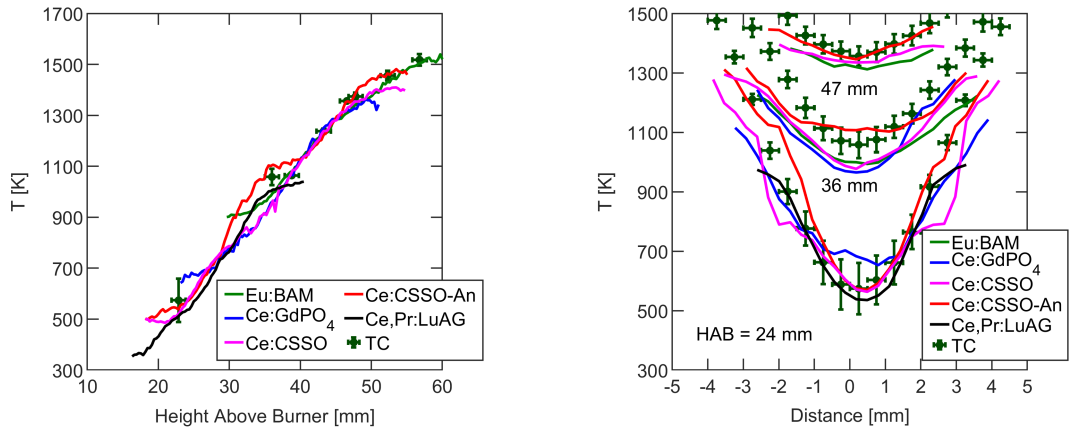

(a) Vertical

(b) Horizontal

Figure 5.32: Vertical and horizontal temperature profiles for each phosphor using combined techniques if available. Eu:BAM and Ce:$GdPO_4$ are included, but these phosphors only use a single SRAPT technique.

Finally, the horizontal and vertical temperature profiles are shown in Figure 5.32. In both plots, the Eu:BAM and Ce:$GdPO_4$ phosphor are included, so the performance of the various phosphors can be compared directly. From the figure, even though the individual techniques for Ce,Pr:LuAG and the Ce:CSSO phosphors do not capture the shape of the temperature profiles well on their own, the combined measurements match the thermocouple measurements very well. In particular, both Ce:CSSO phosphors have a continuous temperature measurement throughout the 900-1100 K region where the Ce^{3+} SRAPT technique is double valued, although the annealed phosphor still does not match the expected temperature perfectly in this range. However, the unannealed phosphor, having a slightly lower quenching temperature, matches the thermocouple profiles much better.

5.4 Conclusions

Two APT demonstration experiments were performed to validate the phosphor characterization, performance estimates, and design information discussed in Chapter 4. The first experiment, an electrically-heated jet demonstration using the Ce,Pr:LuAG phosphor, successfully demonstrated the use of the phosphor signal-modeling results for fluence-dependent calibration. APT performance was also estimated to validate performance modeling results discussed in Section 4.7, and diagnostic combination using the weighted average approach described in Section 4.7.4 was demonstrated. The second experiment was performed in a flame-heated jet to reach temperatures up to ~1500 K to validate the quenching behaviors of the different phosphors, and to demonstrate their use for APT.

The results verify temperature trends and performance estimates from Section 4.7; in particular, Ce,Pr:LuAG was shown to be able to cover the temperature range from 300 to at least 1000 K (provided a suitable calibration were provided above 1000 K), and Ce:CSSO (both annealed and raw) are capable of temperature imaging up to almost 1500 K. Eu:BAM similarly is competitive with the Ce:CSSO phosphors at temperatures above 1200 K (as predicted in Section 4.7) due to its high signal intensity, even though it quenches at much lower temperatures ($T_{50} \approx 600$ K for Eu:BAM compared to ≈ 1200 K for Ce:CSSO).

These results additionally highlight some features that should be considered in the design of new diagnostics. In particular, multiple scattering appears to be a potential source of bias for Eu:BAM (and possibly Ce,Pr:LuAG) and should be considered in the design of new experiments. Further, seeding density can strongly impact performance and careful consideration should be made in selecting an appropriate amount of phosphor. Finally, additional background sources and other signal biases may have a strong impact on temperature measurements, so experiment design should focus on avoiding or eliminating potential signal biases.

Chapter 6

Design Considerations for Particle-Based Techniques

Detailed information relating to phosphor photophysics was discussed in Chapter 4. However, photophysics is only partly responsible for diagnostic performance. In addition, since solid particles are being probed to measure temperature or velocity, it is equally important that the particle temperature and velocity are representative of that of the surrounding fluid. We are thus concerned with the response of a tracer particle to disturbances in the flow and temperature fields. Beyond that, seeding solid particle into the flow can alter the flow characteristics, and so we are equally interested in the intrusiveness of the diagnostic. The first two sections of this chapter will focus on characterizing tracer particle response and intrusiveness based on these considerations.

In addition to particle response and intrusiveness, signal biases (such as those resulting from multiply-scattered light) can bias temperature measurements as was discussed in Chapter 5. Some potential sources of signal bias in an optical engine are surface scattering, multiple scattering from particles, and blackbody radiation from particles. Careful experimental design considerations should be made to avoid or reduce the impact of these sources. To that end, each of these effects are investigated in this chapter to aid in the design and selection of an appropriate APT technique for high-pressure turbulent fuel jet ignition.

Finally, as was noted in Section 4.7.1 and observed in demonstration data in Section 5.1.4, SRAPT techniques have an additional uncertainty term resulting from the particle size distribution. The final section of this chapter will discuss this source of uncertainty in detail. For convenience, the issues considered in this chapter are listed in Table 6.1.

Table 6.1: List of design considerations for aerosol phosphor thermometry techniques

Topic	**Section**
Tracer particle response	6.1
Intrusiveness	6.2
Multiple scattering - signal bias	6.3.2
Multiple scattering - laser sheet spreading	6.3.3
Multiple scattering - imaging resolution	6.3.4
Engine head reflections	6.4
Phosphor blackbody radiation	6.5
PSD contribution to SRAPT uncertainty	6.6

6.1 Tracer Particle Response

To quantitatively apply particle-based diagnostics, the particle velocity and temperature need to be representative of the local flow conditions. However, since particles have inertia, they must undergo acceleration and heat transfer before they equilibrate. As such, the equilibration time is an important parameter for experiment design. This section will characterize the thermal and momentum response properties of the phosphor materials under consideration for APT. The analysis focuses on simpler estimates for design, such as lumped capacity models, but also will investigate the effect of convection and transient processes on particle response. For simplicity of analysis, particles are assumed to be spherical, and, due to the small particle size, the assumption of low Reynolds number is made and justified [61]. It is further assumed that the flow is incompressible.

6.1.1 Momentum Response

Momentum response analysis typically begins with the Stokes flow and Stokes drag approximation, which provides the simplest expression for drag on a spherical particle at low Reynolds number. Under this assumption, the mathematics of the velocity field and particle dynamics are greatly simplified. The Stokes drag force and particle velocity profile in a uniform flow is given by (see, *e.g.*, [114] for a derivation and discussion)

$$F_D = \frac{\pi d_p^3 \rho_p}{6} \dot{v_p} = -3\pi\mu d_p v_p \qquad \Longrightarrow \qquad \frac{v_p}{v_{p,0}} = \exp\left(-\frac{18\mu}{\rho_p d_p^2} t\right), \tag{6.1}$$

where on the right-hand side it has been assumed the fluid velocity is constant, resulting in an exponential velocity decay. The time constant is a property of the particle and fluid (independent of velocity profile),

and has the value

$$\tau_v = \frac{\rho_p d_p^2}{18\mu}. \tag{6.2}$$

Since the dynamics depend on particle diameter-squared, the area-weighted particle diameter ($d^2 \rightarrow m_2$ in the notation of Section 4.1) is used here for this calculation. This time scale represents how much time it takes a particle to react to changes in the flow field. The flow field, or fluid velocity profile, from the Stokes solution is given by

$$\frac{v_r}{v_p} = -\cos\theta\left(1 - \frac{3d_p}{4r} + \frac{d_p^3}{16r^3}\right) \tag{6.3a}$$

$$\frac{v_\theta}{v_p} = \sin\theta\left(1 - \frac{3d_p}{8r} - \frac{d_p^3}{32r^3}\right) \tag{6.3b}$$

where r is the distance from the particle. The velocity field disturbance is relatively long-range, decaying only $\propto r^{-1}$. The velocity profile is critical to analyzing the forced convection of phosphor particles and will be used in later discussions. The fluid velocity disturbance is also of interest in analyzing diagnostic intrusiveness and will be discussed further in later sections.

Particle rotation can additionally influence the velocity field, and thus potentially the convection process. In the Stokes flow assumption, particle torque is similarly proportional to rotation rate and thus rotational velocity follows a similar exponential decay. For a solid sphere, the rotation time constant is smaller than the velocity time constant:

$$I\dot{\omega} = \pi\mu\omega \qquad \Longrightarrow \qquad \tau_r = -\frac{\rho_p d_p^2}{60\mu} \tag{6.4}$$

where $I = m_p d_p^2/10$ is the particle moment of inertia. Rotational equilibration is thus much faster than velocity equilibration. Further, the impact of rotation on the fluid velocity field decays proportional to r^{-2} and is thus much shorter range [114]. Since particle orientation is not expected to impact the diagnostic significantly, rotational equilibration is fast, and the impact of rotation on the flow field is restricted to the region near the particle, rotation will not be considered further as it relates to particle relaxation.

The Stokes model was used to estimate response time scales using Equation 6.1, and the results are listed in Table 6.2 for the particles considered here in air at 1000 K. The calculation is repeated for a hypothetical 1-µm diameter particle for comparison. Since the velocity decay is exponential, several calculations are provided for different levels of equilibration. At 3τ, the particle is equilibrated to 95% of the velocity difference; it takes 6.9τ to equilibrate 99.9% of the initial difference. From the table, the phosphor samples with the particle size distributions measured here typically require 10's of µs

Table 6.2: Tracer particle velocity response times calculated from Equation 6.2 in air at 1000 K for the particle size distributions listed in Table 4.3. The table includes the measured area-weighted mean diameter $\bar{d}_A$ of the particles. Assuming an ideal gas and constant particle properties, the response times are independent of pressure and scale with the inverse-square-root of temperature. Values in parenthesis indicate the response time of a perfect 1.0 µm diameter sphere.

		Velocity Response Time [µs]		
Composition	$\bar{d}_A$ [µm]	95% (3τ)	99% (4.6τ)	99.9% (6.9τ)
Ce,Pr:LuAG	0.53 (1.0)	7.2 (25.8)	11.1 (39.5)	16.7 (59.3)
Ce:$GdPO_4$	1.39 (1.0)	44.8 (23.0)	68.8 (35.3)	103.2 (53.0)
Ce:CSSO	0.71 (1.0)	6.8 (13.5)	10.4 (20.7)	15.5 (31.0)
Eu:BAM	0.83 (1.0)	10.1 (14.6)	15.5 (22.5)	23.2 (33.7)

to equilibrate; for sub-10 µs response times, particle diameters significantly smaller than 1.0 µm are required. For reference, the moments of the particle size distributions that these results are based on are listed in Table 4.3.

The effect of particle shape on momentum relaxation is typically described by a shape factor χ which relates the real drag force to that on a spherical particle with an equivalent diameter. The Cunningham slip correction factor, $C_c(d_P)$, is needed to account for non-continuum effects if the particle is in the slip or transitional flow regimes, and is based on the particle Knudsen number ($\mathrm{Kn} = 2\lambda/d_p$ where λ is the mean free path of the flow). See [87] for more detailed background on particle science, [115] for a detailed investigation of shape factor for irregularly shaped particles and agglomerates, and [116] for a discussion of the Cunningham slip correction factor. In general, the shape factor acts to increase the particle drag, while the Cunningham slip correction factor reduces the drag force. The actual drag force including these corrections can be written as

$$F_D = -\frac{3\pi\mu\chi d_p}{C_c(d_p)} v_p \qquad \Longrightarrow \qquad \frac{v_p}{v_{p,0}} = \exp\left(-\frac{\chi}{C_c(d_p)}\frac{18\mu}{\rho_p d_p^2} t\right), \tag{6.5}$$

with the new time constant

$$\tau_v = \frac{C_c(d_p)}{\chi}\frac{\rho_p d_p^2}{18\mu} \tag{6.6}$$

such that the particle response time is scaled by the factor $C_c(d_p)/\chi$. The Cunningham slip correction factor is given by [116]

$$C(d_p) = 1 + \alpha\mathrm{Kn} + \beta\mathrm{Kn}\exp(-\gamma/\mathrm{Kn}) \tag{6.7}$$

where α, β, and γ are fluid-dependent parameters. For air, $\alpha \approx 1.207$, $\beta \approx 0.440$, and $\gamma \approx 0.78$ [116]. For sufficiently dense gases, $\mathrm{Kn} \to 0$ and $C_c(d_p) \to 1$. The Cunningham correction factor is plotted

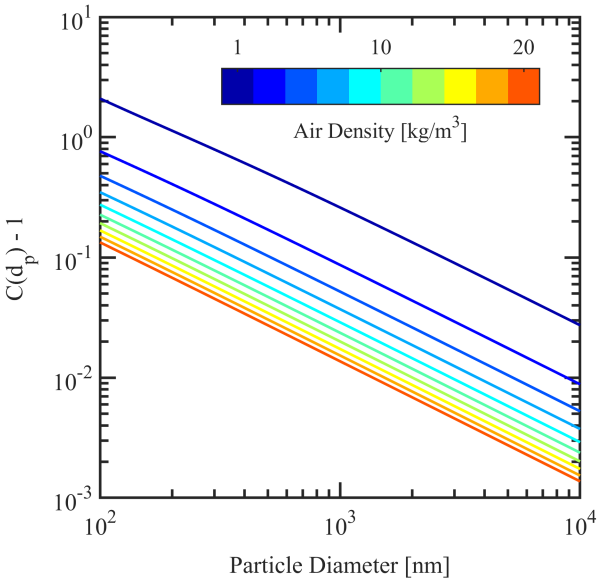

Figure 6.1: Cunningham slip correction factor in air for various gas densities and particle diameters.

for a range of particle sizes in air at several different conditions in Figure 6.1. Note that to first order, the mean free path is a function of density only ($\lambda \propto \rho^{-1}$), and is otherwise independent of pressure and temperature. This plot provides a low-density correction to time response estimates; for a 1.0 µm particle diameter, the correction is required (for 1% accuracy in response time) if the air density is below about 10 kg/m^3. The correction is usually required at atmospheric pressure, but only for temperatures above ∼1000 K at a pressure of 30 bar. To first order, $C_c(d_p) - 1 \propto 1/d_p$ which is evident in Figure 6.1. The Cunningham correction is necessary for particles smaller than ∼ 1 µm diameter at any reasonable density, and will be used for experimental design considerations in later sections of this thesis.

The shape factor is more difficult to quantify as it depends on the geometry of the particle. The shape factor also is dependent on the flow regime, but for the moderate shape factors expected here ($1 < \chi < 1.5$) the dependence on flow regime is only modest [87]. For regularly-shaped aspheric particles (*e.g.*, ellipsoid, cone, or disk), it can be determined theoretically [117]. A useful estimate of shape factor for slightly aspheric particles is that of an ellipsoid. The shape factor for an ellipsoid is plotted in Figure 6.2. For low to modest aspect ratios ($0.5 < E < 2$) averaged over orientation, $1 < \chi < 1.1$.

The particles typically used for APT and PIV techniques are usually not spherical or ellipsoidal, and instead are somewhat irregularly shaped, as seen in the sample SEM image ∼300 nm Pr:YAG phosphor particles in Figure 6.3. The particles in this image do appear to have a relatively small aspect ratio, which suggests a relatively small shape factor ($1 < \chi < 1.1$) according to the theoretical ellipsoid

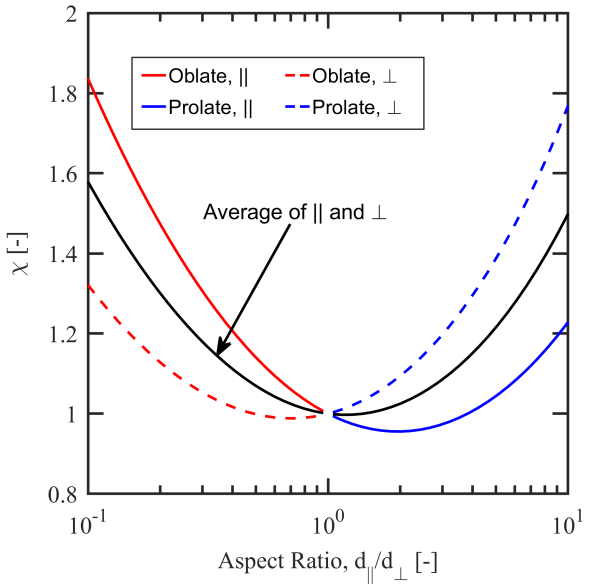

Figure 6.2: Shape factor for ellipsoidal particle as a function of diameter aspect ratio.

shape factor presented earlier. These values are also reasonably consistent with measurements of various agglomerated spheres and other irregularly shaped particulates (*e.g.*, NaCl cubes) [115]. Further, the ellipsoid approximation for shape factor has been used successfully for irregularly shaped particles [118]. Although the actual shape factor is unknown, values of the shape factor for spheroids and cubes provide a range of possible values. Based on the theory and measurements discussed here, the shape factor is assumed to be 1.07 (based on an ellipsoid with average aspect ratio of 0.5 or 2.0), with an uncertainty of 10%.

High Concentration Effects

Until now, only single isolated particles were considered. This is typically a reasonable assumption as low seeding densities are used for most diagnostic applications. However, since the velocity field disturbance in Stokes flow is relatively long range ($\propto r^{-1}$), even a small number of particles can influence the surrounding velocity profile and alter the fluid drag. A theoretical analysis of drag on a cloud of spherical particles was conducted by Tam [119], accounting for the particle size distribution of the aerosol, and another correction for the Stokes drag, $\kappa = F_{D,actual}/F_D$, was found as

$$\kappa = 1 + \frac{\varrho d_p}{2} + \frac{\varrho^2 d_p^2}{12} \tag{6.8}$$

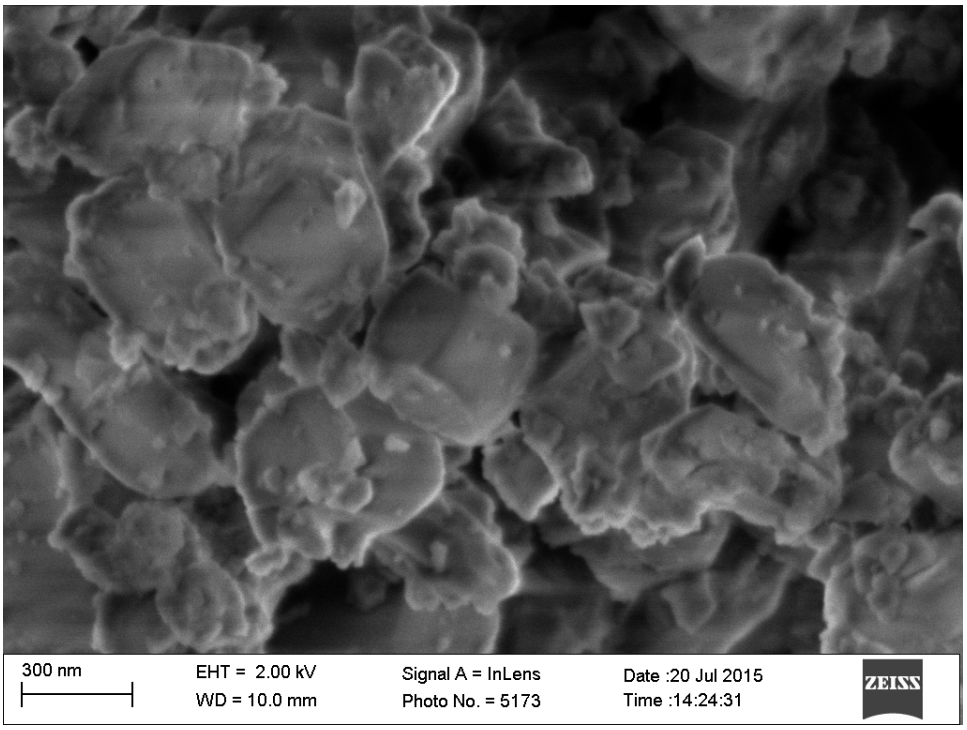

Figure 6.3: Sample SEM image of 300 nm Pr:YAG phosphor particles.

where

$$\varrho = \frac{12\pi n m_2 + \sqrt{144\pi^2 n^2 m_2^2 + 12\pi n m_1 (64 - 2\pi n m_3)}}{16 - 3\pi n m_3/2} \tag{6.9}$$

and $m_i = \bar{d_p^i}$ represents the i-th moment of the normalized PSD, and n is the total number density. A simpler expression can be obtained assuming all particles have the same diameter, d_p, as

$$\kappa = \frac{16 + 2\pi n d_p^3 + 2\sqrt{48\pi n d_p^3 - 3\pi^2 n^2 d_p^6}}{(4 - 6\pi n d_p^3)^2}. \tag{6.10}$$

The value $\kappa - 1$ is plotted in Figure 6.4 as a function of seeding density for the four particles specified above, and for an ideal 1.0 µm particle. From the plot, even at high seeding densities of several thousand per cubic millimeter, the effect is negligible and alters the momentum time constant by less than 1%.

The final momentum relaxation time scale, including all of the effects considered so far (including κ for completeness), is given by

$$\tau_v = \frac{C_c}{\kappa\chi} \frac{\rho_p d_p^2}{18\mu}. \tag{6.11}$$

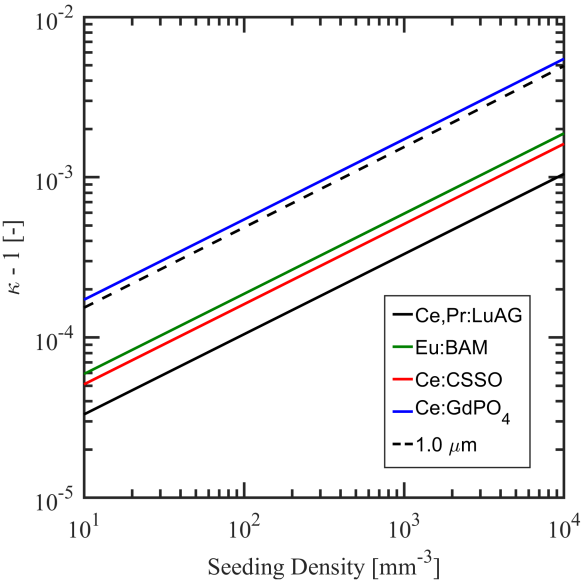

Figure 6.4: Effect of seeding density on particle momentum relaxation time.

Relaxation Length Scale

So far, much effort has been focused on calculation of the time scale of momentum relaxation. Another measure can be derived from the Stokes flow assumptions that instead relates relaxation to displacement for a constant velocity flow field. This has the added benefit that relaxation can be compared to imaging resolution; if, *e.g.*, the relaxation length scale is smaller than the image resolution, the momentum relaxation process should have no impact on the measurement. Likewise, if the relaxation length scale is long, the relaxation length scale determines the effective measurement resolution. Further, since PIV relies on the motion of tracer particles between successive frames, displacement of the particle relative to the fluid will result in a velocity measurement error.

The position-space solution (*i.e.*, the displacement of the particle relative to the fluid) can be derived simply by integrating the right-hand side of Equation 6.1, rewritten in terms of the momentum time constant τ_v, as

$$x_p = L_v\left(1 - e^{-t/\tau_v}\right), \tag{6.12}$$

where x_p is the particle displacement, and $L_v = v_{p,0}\tau_v$ is the momentum length scale. Solving 6.12 for time, and substituting the result into Equation 6.1 results in

$$\frac{v_p}{v_{p,0}} = 1 - \frac{x}{L_v}, \tag{6.13}$$

such that the particle is displaced exactly a distance of L_v relative to the motion of the flow following a disturbance. Thus, this displacement is precisely the displacement error as measured by PIV in the Stokes flow limit (assuming the interframe delay is at least $\sim 3\tau_v$). There are two drawbacks of this estimate. First, to estimate the response length, a measure of the initial velocity difference is required which is not possible without detailed knowledge of the fluid dynamics of the experiment. Second, this estimate is only valid for a constant velocity flow field, and is hence invalid for most flows of interest. However, an upper bound on displacement could be estimated using the average local flow velocity. For example, a 10 µs response time following a 100 m/s impulsive velocity disturbance would result in a maximum displacement of 1 mm relative to the motion of the fluid. Particle displacement in response to a velocity disturbance will be considered in Chapter 7 to aid in the selection of an appropriate particle size for the combined diagnostic; however, estimates in Chapter 7 will additionally consider the case of a nonuniform flow specific to the flows under investigation in the proposed engine experiments.

6.1.2 Velocity Response in an Unsteady Flow

So far, much of the analysis has focused on determining the time scale of a particle. Using the time scale, one can easily quantify how quickly a particle responds to a step change in flow properties. In reality, we're typically interested in more complex flow behaviors. Here, a simple estimate of particle response to an unsteady flow is presented.

For simplicity, we consider the one-dimensional motion of a particle under a periodic excitation; this scenario is intended to represent, *e.g.*, a turbulent eddy. The fluid velocity along the particle's path is assumed to be of the form

$$v(t) = \bar{v} + v' \cos(\omega t). \tag{6.14}$$

where the mean (Reynolds-averaged) velocity of the flow is $\bar{v}$, and the turbulence intensity at frequency ω is $I = v'/\bar{v}$. In the Stokes limit the one-dimensional equation of motion is given by

$$\frac{\partial v_p}{\partial t} + \frac{v_p}{\tau_v} = \frac{v(t)}{\tau_v}. \tag{6.15}$$

which is identical to the Stokes equation of motion for a non-zero fluid velocity in one-dimension where the constants have been replaced with the single parameter τ_v (see Section 3.2.3 of [120] for a more detailed discussion and derivation of this equation of motion in three-dimensions). Solving the equation

at late times where $t \gg \tau$, the slip velocity ($v_{slip} = v_p - v(t)$) is given by

$$v_{slip} = \frac{\omega\tau_v v'}{1+(\omega\tau_v)^2}\Big[\sin(\omega t) - \omega\tau_v \cos(\omega t)\Big]. \tag{6.16}$$

The slip velocity magnitude is generally of order v' or larger at $\omega\tau_v \approx 1$ or larger. In the low frequency limit (*i.e.*, when the particle response time is short compared to the time scale of the disturbance), the particle experiences little slip. When the response time is very long, the particle motion is completely out of phase with the flow and the slip velocity is on average v'. In the latter case, the particle cannot trace the flow at all. The RMS slip velocity (averaged over the period $2\pi/\omega$) is given by

$$\langle v_{slip}\rangle = \frac{\omega\tau_v}{\sqrt{1+(\omega\tau_v)^2}}\frac{v'}{\sqrt{2}}. \tag{6.17}$$

Choosing the response times $\omega\tau_v = 1$ results in a 50% velocity slip. To more faithfully represent velocity fluctuations at frequency scale ω within 10% accuracy it is required that $\omega\tau_v < 1/7$; or for 1% slip or less, $\omega\tau_v < 1/70$.

Direct numerical simulations of a shear layer by Samimy and Lele [121] directly calculated RMS velocity tracing error in an oscillating flow field and found similar behaviors. In particular it was found that at small $\omega\tau_v$ the RMS slip velocity is approximately linear in $\omega\tau_v$ and levels off as $\omega\tau_v \to 1$. At $\omega\tau_v \ll 1$ the particle motion was very similar to that of the flow, at $\omega\tau_v$ near unity significant deviation was observed, and finally at $\omega\tau_v \gg 1$ the velocity fluctuations appeared to have little impact on the particle motion and consequently the slip velocity was equal to the fluctuating velocity. For turbulent motion, they additionally found that $\omega\tau_v > 0.05$ grossly misrepresented flow features, consistent with this analysis.

To better illustrate the frequency behavior of the particle response, the transfer function for the particle motion is calculated using the Laplace transform. Specifically, the Laplace transform of the particle's equation of motion is given by

$$s\hat{v_p} + \frac{\hat{v_p}}{\tau_v} = \hat{v} \qquad \Longrightarrow \qquad H \equiv \left|\frac{\hat{v_p}}{\hat{v}}\right| = \frac{1}{s\tau_v + 1}. \tag{6.18}$$

The transfer function H is calculated and plotted as a function of the Laplace frequency variable s in Figure 6.5. At small frequencies, very little slip is evident, neglecting the initial exponential decay to the mean velocity. At higher velocities, the particle is clearly unable to trace the velocity fluctuations; at $s\tau_v = 1$ the transfer function magnitude is 50%, and drops quickly above this point. Since turbulent fluctuations do not need to be resolved in the present study, and instead primarily linear motion is

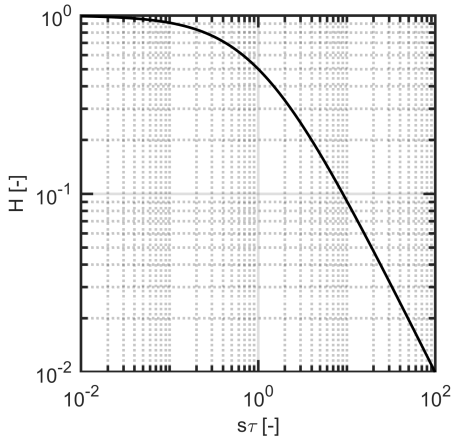

Figure 6.5: Velocity transfer function H for a particle in Stokes flow as a function of the frequency parameter $s\tau$.

expected at the integral length scales, $\omega_L \tau_v = 1$ is likely sufficient for the current investigation, where ω_L is the largest integral scale frequency.

For reference, the range of turbulent frequencies in a given experiment are bounded by the integral scale frequency ω_L (*i.e.*, the highest frequency containing macroscopic fluid motion) and the Kolmogorov frequency ω_η (the frequency associated with turbulent dissipation), and the scales are related by the Reynolds number Re_L via $\omega_L/\omega_\eta = \sqrt{\mathrm{Re}_L}$ [122]. For a typical turbulent fuel jet (exit velocity $u_j = 500$ m/s, jet diameter $d_j = 150$ µm, and $\mathrm{Re} \approx 10^4$), at a distance of 1 cm from the virtual origin, the integral frequency scale is around 50 kHz and the Kolmogorov frequency is on the order of 5 MHz. Thus, a choice of response time $\tau_v = 5$ µs would be a reasonable choice to capture most if not all of the integral scale motions, but would be incapable of resolving the majority of the turbulent motions.

Although this is a very simple analysis, this frequency response behavior has been verified computationally in turbulence studies [123]. In particular, the particle energy spectra were found to be scaled relative to the turbulence spectra by the factor H, as given by Equation 6.18.

6.1.3 Thermal Response

Tracer particle thermal response is generally more difficult to describe as it is often coupled to the velocity field. The most straightforward analysis is derived via the lumped capacity model, where a simple energy balances gives

$$m_p c_p \dot{T}_p = -h A_p (T_p - T_\infty) \qquad \Longrightarrow \qquad \frac{T_p - T_\infty}{T_{p,0} - T_\infty} = \exp\left(-\frac{6h}{\rho_p c_p d_p} t \right) = \exp\left(-\frac{12 k_f}{\rho_p c_p d_p^2} t \right), \quad (6.19)$$

Table 6.3: Tracer particle thermal response times calculated from the lumped capacity model in air at 1000 K. Assuming an ideal gas and constant particle properties, the response times are independent of pressure and scale with the inverse square-root of temperature. For simplicity, particle specific heat capacities are taken at the high-temperature (Dulong-Petit) limit. Values in parenthesis indicate the response time of a perfect 1 µm diameter sphere.

	Thermal Response Time [µs]		
Composition	95% (3τ)	99% (4.6τ)	99.9% (6.9τ)
Ce,Pr:LuAG	4.1 (14.6)	6.3 (22.4)	9.4 (33.6)
Ce:$GdPO_4$	25.4 (13.1)	38.9 (20.0)	58.4 (30.0)
Ce:CSSO	6.6 (13.2)	10.1 (20.3)	15.2 (30.4)
Eu:BAM	10.0 (14.5)	15.3 (22.2)	22.9 (33.2)

where on the far right, it is assumed that the flow velocity is zero (*i.e.*, pure conduction). Pure conduction is typically used as a worst-case response time, as convection generally acts to increase the heat transfer coefficient. This is additionally a good model for situations where the flow is not isothermal, but acceleration is negligible. This method was applied successfully by Fond [61], and it was observed that lumped capacity calculations agree reasonably well with a finite-difference conduction calculation (based on the work of [124]) at the 95% temperature equilibration time.

The thermal response times for each of the phosphor compositions considered here are listed in Table 6.3, and compared with those of a 1.0 µm particle of the same composition. From the table, it is evident that at the high-temperature limit, particle material has little impact on the response time; this is because the product $\rho_p c_p$ in the Dulong-Petit limit is dependent only on atomic number density of the crystal, which does not vary significantly for solids.

The lumped capacity model works well for particles in pure conduction when the volumetric heat capacity of the surrounding fluid is negligible compared to that of the particle (*i.e.*, $\rho_f c_f / \rho_p c_p \to 0$). However, even for the case where $\rho_f c_f / \rho_p c_p = 10^{-3}$ (*e.g.*, a solid ceramic particle in atmospheric air) the transient nature of the temperature relaxation process can still impact the temperature response estimate [124]. In this case, assuming constant properties, for the particle to equilibrate within 1% requires about 15% longer than predicted by the lumped capacity model (4.6τ for lumped capacity, compared to 4.9τ for the transient case, where $\tau = \rho_p c_p d_p^2 / 12 k_f$ is the particle relaxation time; this follows from the results presented in [124]). The transient nature of the heat transfer problem may need to be considered in cases where the fluid heat capacity is relatively high (*e.g.*, $\rho_f c_f / \rho_p c_p > 10^{-3}$) or when a very high degree of equilibration is required (*e.g.*, 99% or better).

6.1.4 Combined Thermal and Momentum Response

A more rigorous analysis of particle thermal response thus should account for the transient nature of the problem, and convection if necessary. The energy transport equation for the surrounding fluid in spherical coordinates (assuming no dependence on θ, consistent with the Stokes' flow result) can be written as (adapted from Appendix F of [125], for variable thermal conductivity, and no dependence on the polar angle)

$$\rho c\frac{\partial T}{\partial t}+\rho c v_r\frac{\partial T}{\partial r}+\rho c\frac{v_\phi}{r}\frac{\partial T}{\partial \phi}=\left(k\frac{\partial}{\partial r}+\frac{2k}{r}+\frac{\partial k}{\partial T}\frac{\partial T}{\partial r}\right)\frac{\partial T}{\partial r}+\left(\frac{k}{r^2}\frac{\partial}{\partial \phi}+\frac{1}{r^2}\frac{\partial k}{\partial T}\frac{\partial T}{\partial \phi}+\frac{k\cot\phi}{r^2}\right)\frac{\partial T}{\partial \phi}$$
$$+\mu\left[2\left(\frac{v_r}{r}+\frac{v_\phi\cot\phi}{r}\right)^2+\left(\frac{\partial v_\phi}{\partial r}-\frac{v_\phi}{r}+\frac{1}{r}\frac{\partial v_r}{\partial \phi}\right)^2\right], \tag{6.20}$$

where the fluid subscript (f) has been dropped for simplicity, the flow field is assumed to be incompressible in accordance with the Stokes flow solution, and the thermal conductivity of the fluid is assumed to depend only on temperature. Fluid viscosity μ is also assumed to be constant in order to satisfy the Stokes' flow assumption. To satisfy the continuity equation, density must be constant. Further, the heat capacity of the fluid depends only on temperature. The energy equation can be normalized and written as

$$\frac{\partial \Theta}{\partial \tau}+\frac{\mathrm{Pe}}{2}v\left(v_r^\star\frac{\partial \Theta}{\partial z}+\frac{v_\phi^\star}{z}\frac{\partial \Theta}{\partial \phi}\right)=\hat{\alpha}\left[\left(\frac{\partial}{\partial z}+\frac{2}{z}+\hat{k}\frac{\partial \Theta}{\partial z}\right)\frac{\partial \Theta}{\partial z}+\frac{1}{z^2}\left(\frac{\partial}{\partial \phi}+\cot\phi+\hat{k}\frac{\partial \Theta}{\partial \phi}\right)\frac{\partial \Theta}{\partial \phi}\right]$$
$$+\mathrm{Ec}\ \mathrm{Pr}\ \frac{v^2}{\hat{c}}\left[\frac{2}{z^2}\left(v_r^\star+v_\phi^\star\cot\phi\right)^2+\left(\frac{\partial v_\phi^\star}{\partial z}-\frac{v_\phi^\star}{z}+\frac{1}{z}\frac{\partial v_r^\star}{\partial \phi}\right)^2\right]. \tag{6.21}$$

In this expression, the normalized quantities are

$$\begin{aligned}
\Theta &= \tfrac{T-T_\infty}{T_{p,0}-T_\infty} && \text{Normalized temperature}\\
v &= \tfrac{v_p}{v_{p,0}} && \text{Normalized particle velocity}\\
v_r^\star &= \tfrac{v_r}{v_p} && \text{Radial Stokes velocity profile}\\
v_\phi^\star &= \tfrac{v_\theta}{v_p} && \text{Azimuthal Stokes velocity profile}\\
z &= \tfrac{r}{r_p} && \text{Normalized radial coordinate}\\
\tau &= t\tfrac{\alpha(T_\infty)}{r_p^2} && \text{Normalized time}\\
\hat{k} &= \tfrac{T_{p,0}-T_\infty}{k}\tfrac{\partial k}{\partial T} && \text{Normalized thermal conductivity derivative}\\
\hat{c} &= \tfrac{c(T)}{c(T_\infty)} && \text{Normalized specific heat capacity}\\
\hat{\alpha} &= \tfrac{\alpha(T)}{\alpha(T_\infty)} && \text{Normalized thermal diffusivity,}
\end{aligned}$$

and the dimensionless numbers are

$$\begin{aligned}
\mathrm{Ec} &= \tfrac{v_{p,0}^2}{c(T_\infty)}\tfrac{1}{T_{p,0}-T_\infty} && \text{Particle Eckert number}\\
\mathrm{Pe} &= 2\tfrac{v_{p,0}r_p}{\alpha(T_\infty)} && \text{Particle Peclet number}\\
\mathrm{Pr} &= \tfrac{\mu}{\rho\alpha(T_\infty)} && \text{Fluid Prandtl number,}
\end{aligned}$$

where α is the fluid thermal diffusivity. The temperature response of the particle can then be calculated from an energy balance at the fluid-particle interface. Specifically, the heat flux out of the particle is equal to the heat flux entering the adjacent fluid element, or

$$\rho_p\frac{\pi d_p^3}{6}c_p\dot{T}_p = -\iint q''(\mathbf{r})\,r^2\sin\phi\,d\theta\,d\phi\bigg|_{r=r_p} \implies \frac{\partial\Theta_p}{\partial\tau} = -\frac{3}{2}\frac{\rho c}{\rho_p c_p}\int d\phi\sin\phi\frac{\partial\Theta}{\partial z}\bigg|_{z=1}. \tag{6.22}$$

This approach is coupled with velocity response, where the particle velocity obeys a similar differential equation

$$\rho_p\frac{\pi d_p^3}{6}\dot{v_p} = -F_D, \tag{6.23}$$

where F_D is the drag force on the particle. Assuming Stokes drag ($F_D = 3\pi\mu d_p v_p$), the velocity response is

$$v = \frac{v_p}{v_{p,0}} = \exp\left[-\frac{18\mu}{\rho_p d_p^2}t\right] = \exp\left[-\frac{9}{2}\,\mathrm{Pr}\,\frac{\rho}{\rho_p}\,\tau\right], \tag{6.24}$$

where Pr and τ are the same Prandtl number and dimensionless time used in the energy equation. This equation also shows a convenient relationship between thermal and momentum relaxation time scales,

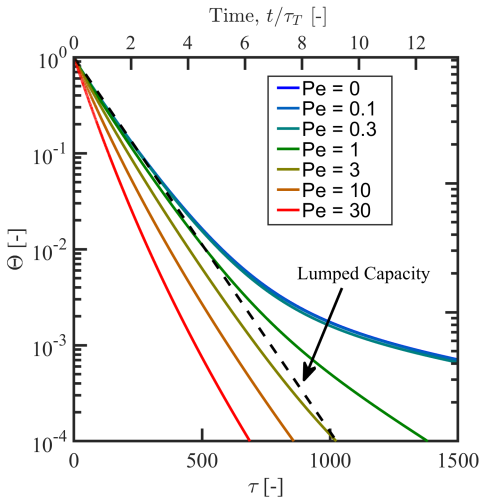

Figure 6.6: Calculated temperature response for a spherical particle at Pr = 0.7, ρ_p/ρ = 650, and $(c\rho)/(c_p\rho_p) = 350$ for several Pe values. These values are representative of Ce,Pr:LuAG at 30 bar, 1000 K.

via

$$\frac{\tau}{\tau_v} = \frac{9}{2}\mathrm{Pr}\frac{\rho}{\rho_p} \implies \frac{\tau_T}{\tau_v} = \frac{3}{2}\mathrm{Pr}\frac{c_p}{c}, \tag{6.25}$$

which suggests that the thermal response time will be shorter than the momentum response time for fluids with $c/c_p > {}^3\!/_2\mathrm{Pr}$. For solid particles entrained in air, this is usually satisfied.

From this analysis, three parameters are necessary to characterize the combined response if viscous dissipation is ignored. The Peclet number, the volumetric heat capacity ratio $(c\rho)/(c_p\rho_p)$, and the product of the Prandtl number with the density ratio Pr ρ/ρ_p. For most gases, Pr $\approx$ 1, and the density ratio is on the order of 0.001 to 0.01. The volumetric heat capacity ratio is similar in magnitude to the density ratio. The Peclet number depends on the relative velocity, but an upper bound is estimated here as 30 (roughly corresponding to a 1.0 µm diameter particle at 100 m/s slip velocity in air at 1000 K and 30 bar). A representative set of calculations of the convection model were run and temperature decay profiles are shown in Figure 6.6 for an assumed Pr = 0.7, $\rho_p/\rho = 650$, $(c_p\rho_p)/(c\rho) = 350$, and a variable Peclet number. For simplicity, the material properties are held constant. These conditions correspond approximately to Ce,Pr:LuAG in air at 1000 K and 30 bar. For the materials under consideration the volumetric heat capacity is relatively constant; only the density ratio changes appreciably for different phosphors.

There are a few interesting points to note from Figure 6.6. First, the lumped capacity response is not always the most conservative estimate of tracer response. For low Pe, transient convection (and conduction for Pe = 0) actually predict a slower decay late in the equilibration process. For large tem-

perature gradients or very precise measurements, where 99% or better equilibration is required (e.g., immediately following shock compression), or for cases with a more modest volumetric heat capacity ratio (say $\rho_p/\rho < 100$, or experiments with liquid flows), lumped capacity estimates can significantly underestimate the result. This may be a larger issue for liquid flows, but for aerosol measurements the lumped capacity model appears to be sufficient (within 20% at 95% relaxation) for design purposes. Further, since τ_T is usually smaller than τ_v (see Equation 6.25), velocity relaxation is typically the limiting factor for tracer particle response and thermal relaxation may not need to be considered separately.

It is worth noting that the coupling between momentum and thermal response is independent of length scale. Or, put more simply, the dimensionless solution presented here is independent of particle size. In particular, the scale factor between the thermal and momentum time constants is not dependent on particle size. The dimensionless time value τ is dependent on particle diameter, but particle diameter is only needed to connect the dimensionless solution to a physical time. This is advantageous as only a single calculation needs to be run for a given material and fluid condition to determine the shape of the response curve $\Theta(\tau)$. An appropriate particle size can thus be selected from a single calculation.

6.2 Intrusiveness

Analysis of tracer particle intrusiveness should similarly consider potential effects on the velocity and temperature of the gas. In combustion environments, chemical reactivity can additionally impact the flow of interest. Intrusiveness can be characterized in a relatively straightforward way; introducing particles to the flow can alter the temperature and velocity of the mixture, effectively biasing the measurement.

Analysis of the temperature and velocity bias resulting from seeding particles into the flow is analyzed as follows. It is assumed that the initial (unseeded) flow is uniform in temperature and velocity, with values of T_0 and v_0, respectively. The unseeded fluid has an initial density of ρ_0 and specific enthalpy of h_0. Phosphor particles are assumed to be introduced to the flow at a different temperature ($T_{p,0}$ with enthalpy $m_p h_{p,0}$ per particle), at zero velocity. Assuming the mixing occurs at constant pressure, the enthalpy, mass, and momentum density of the mixture are then given by

$$\rho h + n m_p h_p = \rho_0 h_0 + n m_p h_{p,0}, \tag{6.26}$$

$$\rho = \rho_0 \frac{T_0}{T}, \tag{6.27}$$

and

$$(\rho + n m_p) v = \rho_0 v_0. \tag{6.28}$$

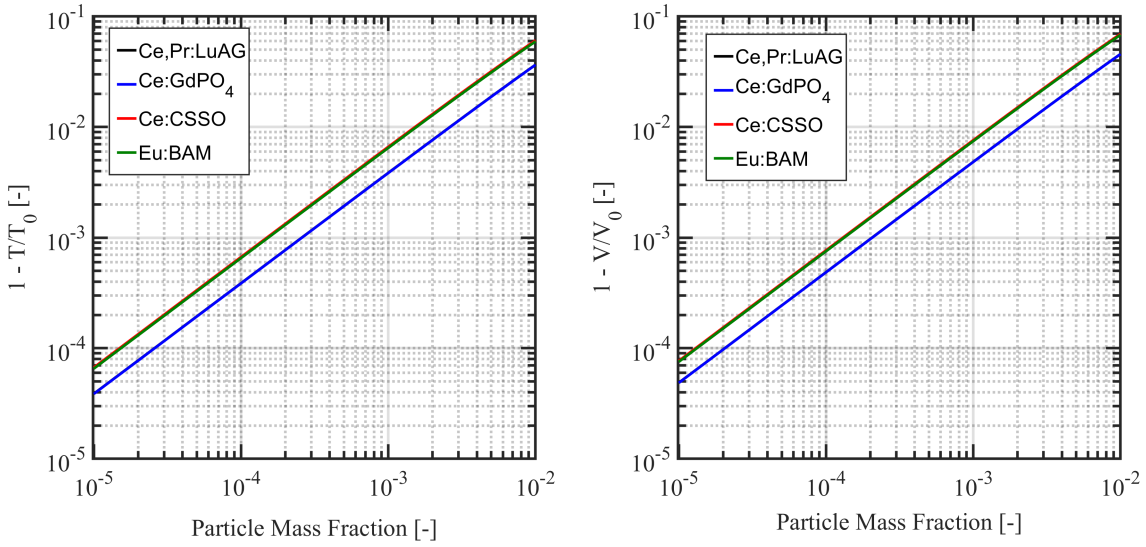

(a) Temperature

(b) Velocity

Figure 6.7: Estimated change in temperature and velocity resulting from particle seeding as a function of seeding density. The initial air temperature is 1000 K, and the initial particle temperature is 300 K.

It is assumed that the particle volume fraction is negligibly small. After equilibration, the particles will have the same velocity and temperature as the gas. Equations 6.26, 6.27, and 6.28 must be solved simultaneously to find the equilibrium conditions.

Figure 6.7 shows the fractional change in temperature and velocity (for air at 30 bar, 1000 K; shown as $1 - T/T_0$ and $1 - v/v_0$, respectively) for each of the four particle compositions under investigation as a function of added mass fraction (nm_p/ρ_0). The specific heat capacity of $GdPO_4$ and LuAG is smaller than that of BAM and CSSO, and as a result the relative change in velocity and temperature is smaller for the same amount of mass added. From these plots, velocity is impacted more strongly than temperature; this is because the flow mass density increases more than the specific heat capacity with the addition of phosphor particles. The relative change in temperature and velocity of the flow effectively places an upper limit on seeding density, and is determined by accuracy requirements. For CSSO and BAM at 1% accuracy, the particle mass fraction should be less than ~0.15%; for $GdPO_4$ and LuAG, the limit is ~0.2%. Both limits are based on the change in velocity, as velocity is impacted more strongly than temperature. This analysis will be repeated in Chapter 7 to determine upper limits on seeding density for the combined experiment.

6.3 Multiple Scattering

By seeding many particles (per unit volume) in a region significantly larger than the volume of the laser sheet, the region surrounding the laser sheet in APT measurements can become a highly scattering turbid medium where the single-scattering assumption may no longer be valid. Multiple scattering refers to the collective effect of light interactions (scattering events) with small particles throughout the domain of the experiment. The effects of multiple scattering have been observed and discussed in many phosphor applications (*e.g.*, [64, 67, 126, 127]); the effects on measurement quality and magnitude of multiple scattering thus need to be considered for experiment design.

In addition to intrusivness, multiple scattering provides another (potentially more strict) upper limit on seeding density in an experiment. The impact of multiple scattering will be assessed here in three ways to provide an upper limit on seeding density. The first effect (effect #1) is that multiple scattering can change the amount of light incident on a detector. From a zero order analysis (Beer-Lambert's law), the light collected on a detector is equal to the amount of emitted light, minus the fraction of emitted light that is attenuated by scattering or absorption between the source and sensor. This results in a small reduction in signal. However, perhaps more importantly, the light scattered in the zero order analysis continues to propagate, and can potentially be collected on a nearby detector after additional scattering events. The additional light collected on the sensor very likely originates somewhere outside of the collection volume, and thus biases the measurement. In this case, it is necessary to identify a seeding density level where the signal bias has a negligible impact on the measurement compared to the required temperature uncertainty.

The second effect of multiple scattering (effect #2) is to reduce the spatial resolution by increasing the observed size of image features, and blurring boundaries between features. It is necessary to ensure the seeding density is sufficiently low such that the features at the target length scale are not sufficiently obscured.

The final effect (effect #3) is that propagation through multiply scattering media can result in an increased laser beam divergence, increasing the thickness and altering the shape of the laser sheet. Thus it is also important to ensure the laser sheet thickness is not increased substantially beyond the resolution requirement. Divergence of the laser sheet can also impact the measurement in other ways, for example by reducing the local laser fluence and changing the beam profile.

Recent studies on phosphor thermometry have identified three primary mechanisms through which multiple scattering can affect a measurement [67]:

1. Luminescence emission from the laser sheet is multiply scattered before being collected on the

image sensor,

2. Incident laser light is scattered from the laser sheet, then excites luminescence outside of the laser sheet which is collected on the image sensor, and

3. Incident laser light is scattered from the laser sheet, then excites luminescence outside of the laser sheet which is multiply scattered before being collected on the image sensor.

These mechanisms are related to the three effects of multiple scattering described in the previous paragraph as follows. A change in measured intensity (effect #1) is the result of luminescence emission that is multiply scattered before being collected (mechanism #1). The analysis and result is identical for scattered laser light as well, *e.g.*, for the SRAPT technique. Luminescence that is excited outside of the laser sheet (mechanism #2) is a result of broadening and other changes to the laser sheet profile (effect #3). The final mechanism, luminescence generated from multiply scattered laser light that is again multiply scattered before being detected, is a higher order scattering process that is captured by both effects #1 and #3; specifically, multiple scattering causes laser sheet divergence (effect #3) which excites luminescence that propagates through many scattering events before being detected (effect #1, with a different source distribution). The remainder of this section will focus on estimating the magnitude of the increase in signal, increase in laser sheet thickness, and loss of spatial resolution resulting from multiple scattering.

6.3.1 Overview of Multiple Scattering Theory

The physics of light propagation in turbid or scattering media has been studied extensively in fields such as biomedical optics, where the diffusion-like behavior of photon transport can have significant implications for imaging diagnostics and even cancer treatment [128]. Multiple scattering similarly has implications for atmospheric science and astronomy, where, *e.g.*, attenuation and reflection of light within a scattering medium is of interest in studying planetary atmospheres [129]. In the field of combustion diagnostics, a significant effort has been put into specifically the reduction of signal corruption via multiple scattering using structured laser illumination planar imaging (SLIPI) [130]. Less effort has been devoted to quantifying the effect of multiple scattering on diagnostic performance. Detailed computational studies of the effects of multiple scattering on imaging results have been performed in fuel sprays [131], although the computational methods are not suitable for diagnostic design. Some effects of multiple scattering have been observed in APT experiments [64, 65], and SLIPI has been applied with some success to combat these effects [126, 127]. In this section, a brief overview of multiple scattering theory

and techniques will be provided and applied in an effort to predict the impact of multiple scattering on APT performance.

Multiple scattering calculation techniques can be divided into two classes: deterministic and stochastic. Deterministic techniques aim to solve the radiative transfer equation, which describes the ensemble-averaged transport of photons within a turbid medium. Because of the complexity of the radiative transfer equation, deterministic methods can be very difficult to solve particularly for complex geometries ([132] provides a review of some analytical methods, illustrating the complexity of the problem). Stochastic methods typically make use of the Monte Carlo method, whereby many "photon packets" are propagated through randomized collision events to estimate the radiation intensity field solution (*e.g.,* [133]). The Monte Carlo method is exact (in that no approximations are made in the solution), but statistical - the result is an ensemble average of discrete random events. The Monte Carlo method for photon transport has been used successfully for making detailed predictions in combustion diagnostic applications [131]. However, in this case, detailed information about fuel spray properties, combustion chamber geometry, and optical properties were required, making the technique more appropriate for detailed computational studies rather than providing insight for experiment design. For the purpose of experiment design, we will focus primarily on deterministic methods to predict the impact of multiple scattering on diagnostic performance. The remainder of this section will focus on application of different techniques to estimate the impact of multiple scattering as it relates to incident light intensity, laser sheet thickness, and imaging resolution. Appendix D contains additional considerations regarding multiple scattering, including an analytical solution for isotropic first-order scattering (Section D.1) and a discussion of scattering phase functions (Section D.2).

6.3.2 Incident Light Intensity

The change in incident light intensity leaving the experiment domain is estimated via solution of the radiative transfer equation (RTE), primarily following the approach of Van de Hulst using the Method of Successive Orders [134]. For simplicity, the geometry is assumed to be a uniformly seeded cylinder that is infinitely wide, with apertures on the top and bottom that are perfectly transparent. This is representative of measurements that will be made in the optical engine (where the bottom aperture is the piston window and the top aperture is a non-reflecting flat head), but likely overestimates the effect of multiple scattering in an open flow such as an air jet. The idea is simple: starting from the light source (*e.g.*, a laser sheet), determine where the light propagates before scattering. The map of scattering locations (or local energy deposition) forms a new distributed "source" for the first-order

scattering solution. The calculation is repeated to determine the location to where the singly-scattered light propagates before scattering again. This procedure is repeated up to some scattering order N, and the total light intensity at a given location (*e.g.*, the piston window) is given by the sum of the intensities from each individual scattering order term. In this way, the zero order solution corresponding to the incident light after Beer-Lambert attenuation can be compared directly to the contribution of multiply-scattered light summed over all higher orders. Mathematically, the local source function J_l of scattering order l is related to the the previous ($l-1$ order) scattering radiance or specific intensity I_{l-1} by [134] (Chapter 4, Display 4.4)

$$J_l(\tau', \mu, \phi) = \frac{a(\tau')}{4\pi} \int_{-1}^{1} d\mu' \int_{0}^{2\pi} d\phi' \; \Phi(\tau', \cos\alpha) I_{l-1}(\tau', \mu', \phi'), \tag{6.29}$$

where $\mu = \cos\theta$ is the scattering angle, ϕ is the azimuthal angle, and τ' is the optical depth or distance along the cylinder axis normalized by the extinction coefficient ($\tau' = n\sigma_e z$, where n is scatterer number density and σ_e is the extinction cross-section). The albedo $a(\tau) = \sigma_s(\tau)/\sigma_e(\tau))$ is the ratio of the scattering to extinction probabilities and is allowed to be variable depending on depth. The albedo is necessary to determine the fraction of deposited light that is scattered again at a given location. This formulation assumes the problem is one-dimensional; the source is dependent only on the axial dimension of the cylinder, and the cylinder radius is large compared to the height. The function Φ is the scattering phase function, and $\cos\alpha$ is the cosine of the relative scattering angle, which is given by

$$\cos\alpha = \mu\mu' + \sqrt{1-\mu^2}\sqrt{1-\mu'^2}\cos\left(\phi - \phi'\right). \tag{6.30}$$

The energy deposition is directional (*i.e.*, its a vector quantity), and includes anisotropy via the phase function. The source function J_l thus is an expression of the l-times scattered light intensity at a depth τ' into the cylinder that is propagating in the direction determined by (μ, ϕ). Similarly, the local intensity I_l can be expressed from the lth order source function as

$$I_l(\tau', \mu, \phi) = \begin{cases} \int_0^{\tau'} J_l(\tau'', \mu, \phi) e^{(\tau''-\tau')/\mu} \frac{d\tau''}{|\mu|} & \mu > 0 \\ \int_{\tau_0}^{\tau'} J_l(\tau'', \mu, \phi) e^{(\tau''-\tau')/\mu} \frac{d\tau''}{|\mu|} & \mu < 0 \end{cases} \tag{6.31}$$

where the integral is taken over the height of the cylinder (with total optical depth τ), and the brackets $|x|$ indicate the absolute value of the quantity x. τ' again is the optical depth into the cylinder ($0 \leq \tau' \leq \tau$), and τ'' is a dummy variable for integration over τ'. The conditional expression ensures that radiation propagating in one direction is not contributing to the energy deposition on the opposite side of the

source. At $\mu = 0$, the specific intensity is equal to the source function. From the equation, the incident intensity of a given scattering order is simply the Beer-Lambert attenuated source function intensity of the same order.

One useful simplification arises from considering an isotropic source function, *e.g.*, for luminescence emission of phosphors. If the source function is independent of ϕ, then from Equation 6.31, the next higher order specific intensity function is also independent of ϕ, and so on for all orders, regardless of the anisotropy of the scattering process. However, anisotropic scattering can alter the μ dependence of J_l and I_l. The Henyey-Greenstein phase function [135] is a convenient descriptor of anisotropy for multiple scattering calculations, and has the form

$$\Phi(\cos\alpha) = \frac{1 - g^2}{(1 + g^2 - 2g\cos\alpha)^{3/2}}, \tag{6.32}$$

where g is the scattering anisotropy parameter, or the average value of $\cos\alpha$, and α is the scattering angle.

The relative intensity contribution of each scattering order at the exit aperture is determined by numerically performing the integrals in Equations 6.29 and 6.31 at each scattering order until the solution is converged. This process models the engine as a perfect cylinder, where the radius is large compared to the height. The laser sheet is assumed to create a light source that is infinitely thin within the cylinder, and the sheet is assumed to take up the entire cylinder cross-sectional area. For luminescence, this results in a problem that is independent of the azimuthal angle ϕ; for simplicity, this assumption is applied to scattered laser light as well. This assumption would be identical to the case in which the laser sheet propagates radially inward from all angles, rather than propagating horizontally across the cylinder. Optical properties are assumed to be uniform throughout the cylinder. Finally, the top and bottom surfaces are assumed to be perfectly transparent. In reality, due to reflections, the effect of multiple scattering could be increased slightly, as light reflected from the head has additional opportunity to interact with particles before exiting through the piston window. The assumed geometry is shown in Figure 6.8.

With these approximations, the Method of Successive Orders calculation as written can be applied directly. Specifically, the result depends on the optical thickness of the cylinder τ, the albedo of the particles $a \approx 1$, and the scattering anisotropy parameter g. Finally, the location of the source sheet within the cylinder τ_s additionally may have a small effect. The intensity of the radiation source is unimportant as scattering is a linear process. Since the scattering is assumed to be independent of the

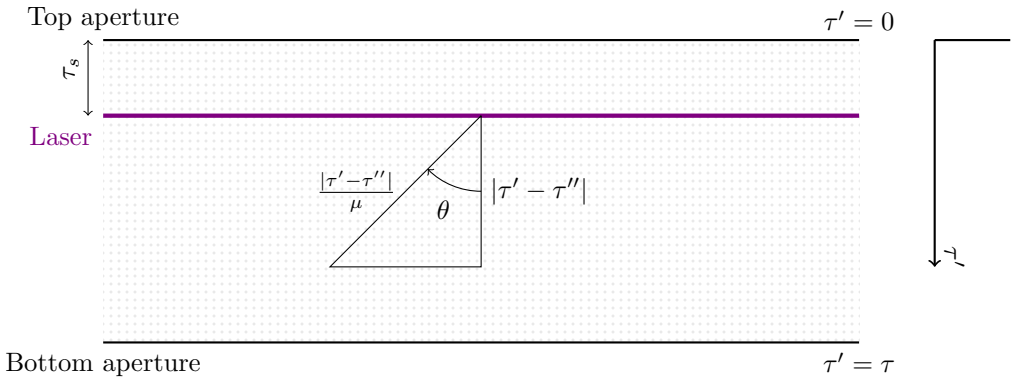

Figure 6.8: Diagram of assumed geometry for multiple scattering calculations in a cylinder. The calculation assumes the top and bottom apertures are perfectly transmissive.

azimuthal angle, Equation 6.29 can be rewritten as

$$J_l(\tau', \mu, \phi) = \frac{a(\tau')}{4\pi} \int_{-1}^{1} d\mu' I_{l-1}(\tau', \mu') \int_0^{2\pi} d\phi' \; \Phi(\tau', \cos\alpha) = \frac{a(\tau')}{4\pi} \int_{-1}^{1} d\mu' I_{l-1}(\tau', \mu') f(\tau', \mu, \mu'), \tag{6.33}$$

where $\cos\alpha$ is given by Equation 6.30 and ϕ is taken to be any arbitrary value, *e.g.,* 0. Thus, the integral over ϕ' produces a map

$$f(\tau', \mu, \mu') = \int_0^{2\pi} d\phi' \; \Phi(\tau', \cos\alpha) \tag{6.34}$$

between the incident and exiting scattering directions μ' and μ, which depends on the scattering phase function. For an isotropic phase function, this map is a constant and equal to 2π. For an anisotropic phase function, *e.g.,* the Henyey-Greenstein phase function, the map depends on the average scattering anisotropy g. Using the Henyey-Greenstein phase function, the map $f(\mu, \mu')$ is plotted for $g = 0.2$, $g = 0.5$, and $g = 0.8$ in Figure 6.9 to illustrate the effect of anisotropy. For moderate anisotropy (*e.g.*, $g = 0.2$), the calculation is largely unaffected as the map $f(\mu, \mu')$ is largely unchanged from the isotropic case. However, as anisotropy is increased towards $g = 1$, the scattering angle is less likely to change following a scattering event, such that at $g = 0.8$ the probability of a particle maintaining its current angle (or undergoing a very small deflection) is several orders of magnitude larger than the probability of a particle having a significant change in direction. Practically, this indicates that multiply scattered light from a highly anisotropic scattering process is much more likely to originate on or near the line of sight of the detector, particularly at lower scattering orders.

Any luminescence that is scattered before being collected biases the measurement and is considered "multiply-scattered" light. For Mie scattering images, the incident laser light must be scattered once before it can be detected, and any additional scattering biases the measurement and is considered

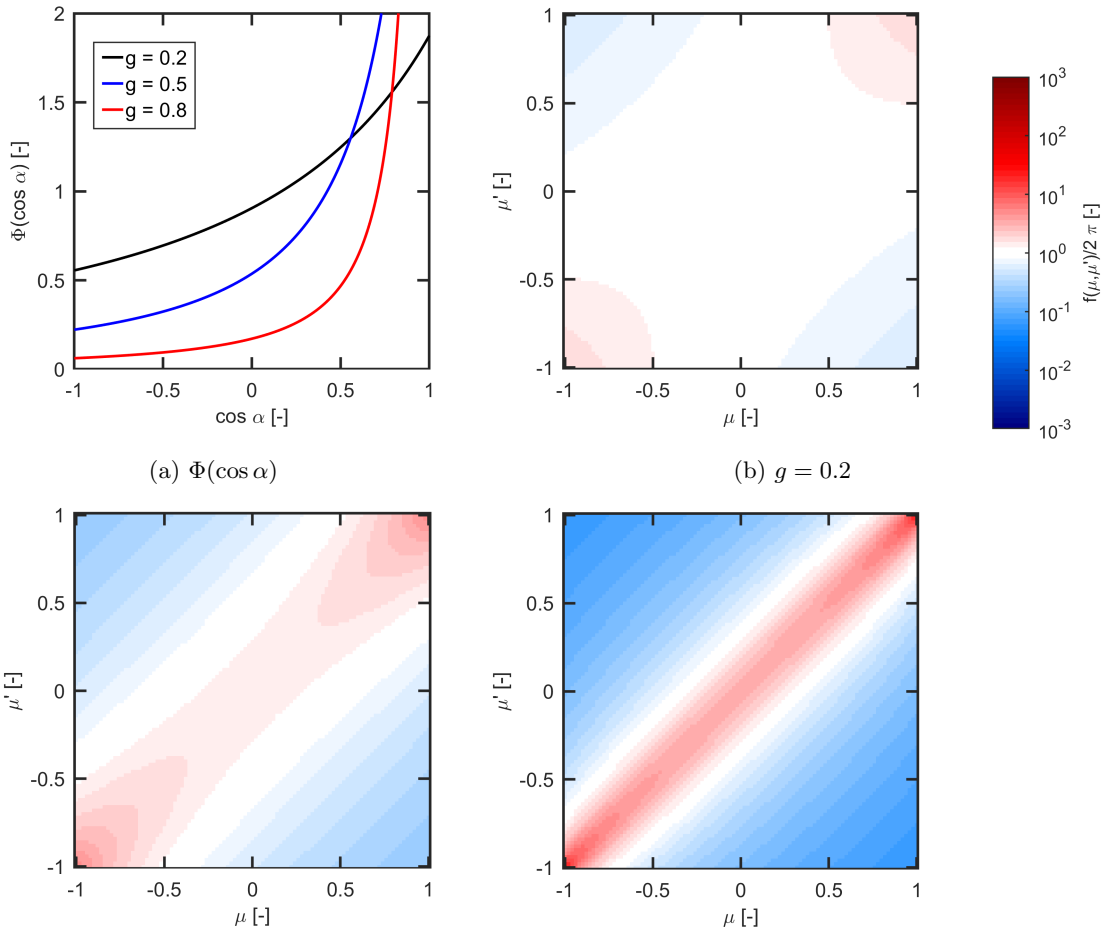

(a) $\Phi(\cos\alpha)$ (b) $g = 0.2$

(c) $g = 0.5$ (d) $g = 0.8$

Figure 6.9: Scattering phase function Φ and $f(\mu, \mu')$ map for $g = 0.2$, 0.5, and 0.8 calculated using the Henyey-Greenstein function.

"multiply-scattered". For the purposes of the remaining discussion, the initial scattering of the incident laser light is ignored and the initial source sheet distribution is assumed to be identical to that of the luminescence measurement. Thus, for the remainder of this section, all "scattered" light (first and higher scattering orders) is undesirable and biases both measurements; only the zero-order non-scattered light is desired.

The relative contribution of multiply-scattered light exiting the cylinder at normal incidence will be used to assess the impact of multiple scattering. The relative contribution here is defined as the ratio of multiply scattered light intensity to the zero-order non-scattered light intensity, or

$$\frac{\Delta I}{I} = \frac{\sum_{l>0} I_l(\tau, 1)}{I_0(\tau, 1)} \tag{6.35}$$

where the result is assumed to be independent of the azimuthal angle by symmetry, and τ corresponds to the exit aperture depth. The quantity $\Delta I/I$ represents the relative bias in the signal measurement. The numerator represents the collected light that has been scattered at least one time (and likely does not originate from the intended collection volume). The denominator represents the portion of the source light that reaches the sensor without having been scattered, and includes attenuation (via the Beer-Lambert law) due to scattering; the denominator represents the expected or desired signal.

This calculation is a direct measure of the fraction of light that likely originated outside of the intended collection volume; this provides a relative measure of signal bias resulting from multiple scattering. A plot of this value for several values of the scattering anisotropy parameter g as a function of optical thickness τ_0 is shown in Figure 6.10. From the plot, the behavior at low optical thickness is independent of scattering anisotropy and is described well by a power law fit in optical thickness. The effect of increasing anisotropy (such that $|g| \to 1$) is to increase the scattering order. As scattering anisotropy increases, it takes an increasing number of scattering events for the radiation originating far away from the source to be turned such that it leaves the cylinder at normal incidence. However, from the calculation, the amount of additional light exiting the cylinder is unaffected by anisotropy. At higher scattering anisotropy, the additional light tends to originate further away from the measurement volume. In reality, since the cylinder is not infinitely wide and the cylinder walls are not perfectly reflective, this is likely an overestimate particularly at large values of g. It should be noted that the mean free path for a given optical thickness $\tau = n\sigma H$ (for cylinder height H) is given by $\lambda = 1/(n\sigma) = H/\tau$; thus, the mean free path for a 1% optical thickness is 100 times larger than the physical thickness of the cylinder. ($\tau = 0.01$ corresponds to $\sim$650 mm^{-3} for a 1 µm diameter particle with scattering efficiency of 2 and a 1 cm depth.) As a result, even for the first order scattering contribution, the additional observed light

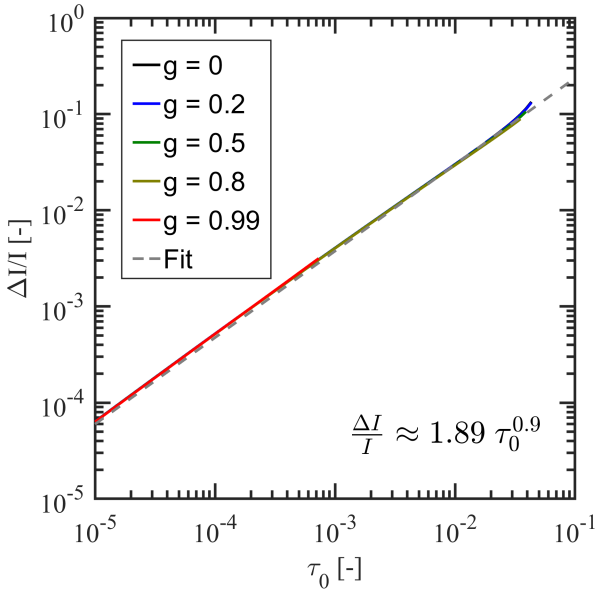

Figure 6.10: Estimated signal bias as a function of optical thickness for several values of anisotropy. The laser sheet location is in the center of the cylinder. ΔI refers to scattered light that is collected, and I refers to the amount of non-scattered light that is collected.

could originate from anywhere in the cylinder with similar probability.

Multiple scattering effects additionally may depend on location (height) of the laser sheet or source within the cylinder. In Figure 6.10, the laser sheet is assumed to be in the middle of the cylinder. A similar calculation was performed for isotropic scattering where the laser sheet location was varied between 10 and 90% of the cylinder height, and the results are plotted in Figure 6.11. Laser sheet location has very little impact the intensity increase, although appears to be maximized when the laser sheet is in the center of the cylinder. This result is not very surprising; moving the location of the laser sheet only weakly impacts the total amount of luminescence that is deposited (or scattered) throughout the cylinder, and more scattering occurs when the sheet is centered. This follows because most energy is deposited (or scattered) near the source sheet, and the average distance between the laser sheet and each potential scattering location in the cylinder is minimized when the sheet is centered.

Finally, the increase in intensity is plotted as a function of scattering anisotropy for several fixed values of optical thickness in Figure 6.12, with the laser sheet in the center of the cylinder. As observed in Figure 6.10, anisotropy has little effect on the end result; the primary effect of anisotropy is to change the typical scattering order and, correspondingly, the distance from which the multiply scattered light originated from in-cylinder. However, at the largest optical thicknesses, some variation is evident. A small reduction in intensity is observed for moderate scattering anisotropy compared with the isotropic

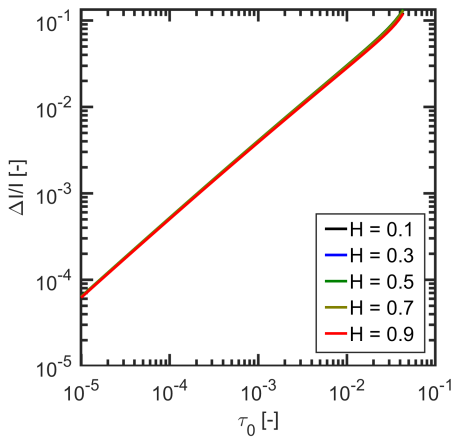

Figure 6.11: Estimated signal bias as a function of optical thickness and laser sheet location. ΔI refers to scattered light that is collected, and I refers to the amount of non-scattered light that is collected.

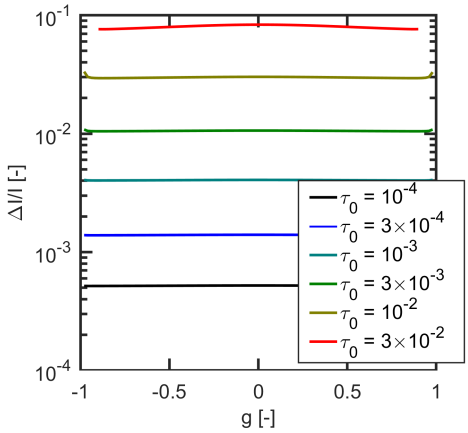

Figure 6.12: Estimated signal bias as a function of scattering anisotropy for several optical thicknesses. ΔI refers to scattered light that is collected, and I refers to the amount of non-scattered light that is collected.

case. However, the difference is only on the order of 5-10% of the isotropic value for $\tau = 0.03$, and for $\tau \leq 0.01$ only 2.5% or less. At very high anisotropy the intensity contribution from multiply scattered light increases again.

Interestingly, for $\tau_0 < 0.1$, I_1/I_0 is in fact several times larger than τ_0 at the relatively low τ_0 values considered here. Notably, at $\tau_0 = 0.01$, $I_1/I_0 \approx 0.03$. This is a non-intuitive result as only a fraction of light equal to $1 - e^{-\tau_s} \approx \tau_s$ that exits the chamber at normal-incidence is initially scattered. However, this fraction corresponds only to the light that is emitted at normal incidence; the source is assumed to be isotropic such that light propagates with equal probability in all directions. Light that is emitted at non-normal incidence must travel a much longer distance before escaping the cylinder (the optical distance is τ_s/μ for light emitted in direction μ), and is more likely to scatter. Scattered light is thus

more likely to exit the cylinder at normal incidence, as it represents the shortest path out of the cylinder. Multiple scattering does not change the total amount of light leaving the cylinder, but instead causes the angular distribution to become weighted closer to normal incidence. In short, light that is emitted from phosphor particles at non-normal incidence contributes significantly to the scattered light exiting the cylinder at normal incidence, contributing to a possible measurement bias.

6.3.3 Laser Sheet Thickness

Laser sheet thickness, as a measurement of spatial resolution, can be severely impacted by multiple scattering. Many expressions have been provided for laser pulse broadening as a result of multiple Mie-like scattering events. However, most solutions are either approximate or computationally intensive [136]. As a result, many different measures of beam spreading exist (see [136] for a good overview of some small-angle scattering solutions for beam spreading). The solutions for beam radius R generally have the form

$$\frac{R^2}{z^2} = \beta \langle \theta^2 \rangle n \sigma_s z, \tag{6.36}$$

where $\langle \theta^2 \rangle$ is the second moment of the scattering phase function (as discussed in Appendix D.2), and n is again the particle number density. The factor β is a dimensionless value that depends on the approximations used in the derivation. A value of $\beta = 1/16$ was reported using a path integral approach [137]. Similarly, values of $\beta = 1/12$ and $\beta = 1/3$ have been reported using different approaches by [138] and [136], respectively.

From Section D.2, typical values of $\langle \theta^2 \rangle$ are around 0.4. Choosing $z = 4$ cm (approximately half of the engine bore for the proposed experiment), and 1 µm diameter particles (with assumed scattering efficiency of 2) at a seeding density of 300 mm^{-3}, the optical thickness $\tau = n\sigma_s z \approx 0.02$. In this case, the beam radius is between 0.9 mm (for $\beta = 1/16$) and 2.0 mm (for $\beta = 1/3$). For comparison, a 6 mm diameter laser beam focused with a 500 mm focal length lens can spread between 0.5 mm (for $M^2 = 10$, where M^2 is the laser beam quality factor) and 1.1 mm (for $M^2 = 50$) over the same distance from the focal point. This is potentially a significant effect that can be comparable to far field beam spreading; more precise estimates will be given in Chapter 7.

6.3.4 Imaging Resolution

The final effect of multiple scattering considered here is the impact on imaging resolution. Similar to the analysis of laser beam spreading, any image formed that passes through an optically dense turbid medium will likely be distorted, and can be analyzed in the small-angle scattering approximation. An

analysis of this sort was carried out by [139], where the modulation transfer function (MTF) of a turbid system (excluding the imaging system itself) was derived as

$$\text{MTF} = \exp\left[-\kappa z + \kappa z \frac{w}{2\sqrt{\pi} f} \text{erf}\left(\frac{\pi f}{w} \right) \right] \tag{6.37}$$

where f is the angular resolution (in cycles/rad), $\kappa = n\sigma_s$ is the scattering coefficient, z is the distance through which a ray of light must pass, and w is Gaussian width of the scattering phase function (in [139] it was assumed the phase function was Gaussian). Based on fits to the Henyey-Greenstein phase function, [139] found that $w = 2.3$, 4.7, and 7.6 rad^{-1} for $g = 0.6$, 0.8, and 0.9, respectively. The total system MTF is given as a product of the MTF of the lens system, and the scattering MTF.

For an assumed object-plane distance of 0.5 m, and an assumed lower limit on imaging resolution of 2.0 line pairs per mm, the required angular frequency is $f > 1000$ cycles per radian. Thus, $\pi f / w \gg 1$, so we can take the high-frequency limit as $M \approx \exp(-\kappa z)$. Setting $\kappa z = \tau/2$ corresponding to the laser sheet being in the middle of the cylinder where τ is the optical thickness of the cylinder, MTF $\approx \exp(-\tau/2)$. For any reasonable value of τ on the order of $10^{-2} - 10^{-1}$, MTF ≈ 1.

A reasonable estimate of resolution limit f_{res} is given by the frequency at which the MTF is reduced by a factor of two, or the frequency below which 50% or more of the contrast variation is faithfully captured. For small optical thicknesses less than ~ 0.5, very little impact on imaging resolution is expected. For this reason, the effect of multiple scattering on imaging resolution will not be considered further.

6.4 Reflection Analysis

The measurements proposed here are to be performed in an enclosed environment, near solid surfaces. This poses an additional challenge compared to open environments such as flames. Surfaces close to the laser sheet can reflect light. The reflected light can bias the measured intensity on a camera, and can potentially alter the effective collection solid angle and hence the spatial resolution of the measurement. This section will outline some analysis to estimate the impact of surface reflections on diagnostic performance.

As with multiple scattering, this analysis will assume the engine head is described well by a flat surface, that the laser sheet is much wider and longer than the distance between the laser sheet and engine head, and that the distance between the reflecting surface and the laser sheet (h) is small compared to the object plane distance (d_o). This geometry is shown in Figure 6.13. From the diagram, specularly

reflected light is focused on the sensor and originates from near the intended collection volume. Diffusely reflected light originates from every point on the laser sheet (blue dotted lines), and is slightly out of focus since the origin of diffuse rays is outside the object plane. The remainder of this section will analyze the intensity of reflected light, and the potential impact to spatial resolution (estimated as the distance between the origin of the reflected light and the intended collection volume).

Reflected light intensity depends only on the reflection coefficients (R_S and R_D for specular and diffuse reflections, respectively), and the light intensity incident on the reflecting surface. Because of the symmetry involved in the problem, every point along the reflecting surface is identical, so only a single point need be considered. Assuming the light sources in the laser sheet are isotropic with uniform intensity, the amount of light incident on the reflecting surface at any point can be calculated as

$$\phi'' = \int d^2r \frac{\phi_0''(\vec{\boldsymbol{r}})}{4\pi r^2} \tag{6.38}$$

where ϕ'' is the emission intensity per unit laser sheet area (or photon flux), the subscript 0 represents the light originating from the laser sheet, d^2r is the surface area element in the laser sheet plane, r is the relative position vector, and $r = |\vec{\boldsymbol{r}}|$ is the magnitude of the relative position vector. This equation effectively represents the sum of all the contributions from every part of the laser sheet, where the light from the laser sheet is emitted isotropically and decays in intensity $\propto r^{-2}$. Since emission intensity is assumed to be constant throughout the laser sheet, the integral can be rewritten as

$$\phi'' = \frac{\phi_0''}{4\pi} \int \rho \, d\rho \, d\varphi \, \frac{1}{\rho^2 + h^2} \tag{6.39}$$

where cylindrical coordinates are used with radius ρ and polar angle ϕ. The axial distance z is equal to the distance between the laser sheet and engine head, h. Defining the incidence angle θ as the angle between the $\hat{z}$-axis and the incident light ray, the total amount of light incident at any point on the reflecting wall is

$$\phi'' = \frac{\phi_0''}{4\pi} \int d\theta \, d\varphi \, \frac{\tan(\theta)}{1 + \cos^2(\theta)} \implies \frac{\partial \phi''}{\partial \Omega} = \frac{\phi_0''}{4\pi} \frac{1}{\cos(\theta) + \cos^3(\theta)} \tag{6.40}$$

where on the right side the angular distribution of intensity is taken as the derivative with respect to solid angle $d\Omega = \sin(\theta) \, d\theta \, d\varphi$.

For a specular reflection, the reflected ray exits with the same angle, and with intensity scaled by the specular reflection coefficient R_s. The reflected light acts as a new source with an angular-resolved intensity distribution given by Equation 6.40 that can be collected on the detector. For sufficiently small

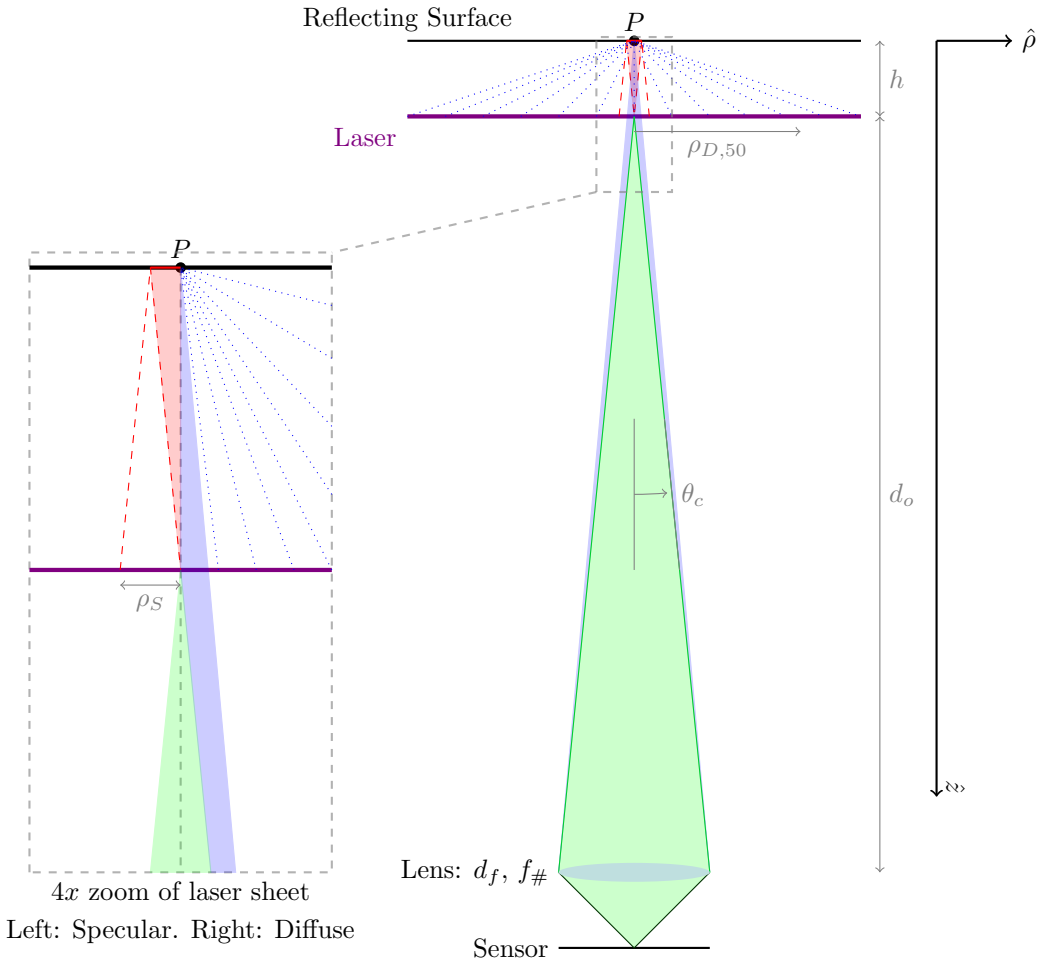

Figure 6.13: Diagram of assumed geometry for reflection analysis near a flat surface. Both the laser sheet and the reflected surface act as distributed sources. Green lines and shaded areas represent light collected directly from the source. The shaded red region indicates the range of specularly-reflected rays that can be collected by the lens, while the red dashed lines indicate the paths of the extreme rays that are collected. Blue dotted lines indicate the rays that are diffusely reflected from the cylinder head, while the blue shaded region indicates the range of diffusely-reflected rays that are captured by the lens. This diagram is not drawn to scale.

collection solid angles, $\cos(\theta) \approx 1$ and the amount of specularly-reflected light collected by the lens ($S_{R,s}$) is

$$S_{R,s} = \int d\Omega \, \frac{\phi_0''}{4\pi} \frac{R_s}{\cos(\theta) + \cos^3(\theta)} \approx R_s \frac{\phi_0''}{2} \frac{\Omega}{4\pi} \tag{6.41}$$

where R_s is the specular reflection coefficient and Ω is the collection solid-angle. Compared to the light collected directly from a point in the laser sheet, with intensity $S_0 \approx \phi_0'' \Omega / 4\pi$, specularly-reflected light contributes a relative intensity of

$$\frac{S_{R,s}}{S_0} \approx \frac{R_s}{2}. \tag{6.42}$$

Perhaps more importantly, the distance over which the specularly reflected light originates can be calculated directly from the intensity distribution function. For a given cone half-angle θ_c or collection solid-angle Ω ($\theta_c^2 \approx \Omega/\pi$), the source location extends to a distance of

$$\rho_S \approx 2h \tan\theta_c = h \frac{d_f}{f_\# d_o}. \tag{6.43}$$

The factor of 2 appears because the light propagates horizontally a distance $h \tan\theta_c$ both before and after reflecting off the wall, before being collected by the lens. On the right hand side, the expression is rewritten using the lens focal length d_f, lens f-number $f_\#$, and object plane distance d_o. For typical values of $f_\# = 1.4$, $d_f = 85$ mm, and $d_o = 1000$ mm, $\tan\theta_c \approx 0.03$. Thus, for a laser sheet that is within 0.5 cm of a specularly-reflecting surface, reflected light originates within ~0.3 mm of the intended imaging location. It should be noted that this is an upper bound; specularly reflected light will originate no further than a distance of ρ_S from the intended collection volume.

Diffuse reflectors are slightly more complicated. In particular, the calculation must be performed in two steps. The total amount of light diffusely reflected from a point on the reflecting surface is

$$\phi'' = R_d \frac{\phi_0''}{4\pi} \int_0^{2\pi} \int_0^{\pi/2} d\theta \, d\varphi \frac{\tan\theta}{1 + \cos^2(\theta)} \cos(\theta) = R_d \frac{\pi}{8} \phi_0''. \tag{6.44}$$

The incident intensity distribution is the same as that calculated in Equation 6.40, but a factor of $\cos(\theta)$ is included in the integrand according to the Lambertian reflector assumption; light incident at an angle θ is reflected with intensity proportional to $\cos(\theta)$.

The amount of diffusely reflected light collected by the lens is estimated as the total reflection intensity (the right hand side of Equation 6.44) multiplied by the fraction of solid-angle subtended by the lens. For a Lambertian reflector, the angular distribution (with respect to the viewer) is proportional to the cosine of the viewing angle, such that the total solid-angle over which light is reflected is π steradians.

Thus, assuming a sufficiently small collection solid-angle, the amount of diffusely-reflected light collected by the lens is given by

$$S_{R,d} = R_d \phi_0'' \frac{\pi}{8} \int \frac{d\Omega \cos(\theta)}{\pi} \approx R_d \frac{\phi_0''}{8} \Omega. \tag{6.45}$$

A diffuse reflector can provide more reflected light than a specular reflector for the same reflection coefficient (for an infinitely large source sheet), and

$$\frac{S_{R,d}}{S_0} \approx R_d \frac{\pi}{2}. \tag{6.46}$$

Finally, since there is no sharp distance cut-off as with specular reflections, the average distance from which the diffusely-reflected light originates is estimated here as the angle below which 50% of reflected light originates. Mathematically, this is given by θ_{50} via

$$\frac{4}{\pi} \int_0^{\theta_{50}} d\theta \, \frac{\sin\theta}{1 + \cos^2\theta} = \frac{1}{2}, \tag{6.47}$$

with the solution $\cos\theta_{50} = \sqrt{2} - 1$, or $\theta_{50} \approx 1.144$ radians. The estimated horizontal distance is then $\rho_{D,50} = h \tan\theta_{50} \approx 2.2h$, or approximately 2.2 times the distance between the laser sheet and the reflecting surface.

Based on this analysis, both specular and diffuse reflections can result in similar biases in measured intensity. For specular reflections, only light very near the intended imaging location is reflected and captured; depending on the required imaging resolution, this may not negatively impact the measurement. For diffuse reflections, light throughout the cylinder (more than twice the distance from the laser sheet to the wall) can reach the sensor, and result in a significant bias in the measured signal (and hence temperature). However, the intensity of diffuse reflections are dependent on the extent of the illuminated region and are likely significantly overestimated here as the laser sheet is not infinitely large. Specular reflections may be preferable as they can result in an increase in fluorescence intensity (up to a 50% increase for a perfect reflector), and without a significant impact on spatial resolution for sufficiently small collection solid angles. However, this is likely not practical, and the better solution may be to reduce the diffuse reflection coefficient as much as possible, *e.g.*, through the application of high emissivity paints.

Use of a high-emissivity paint, with at most 3% diffuse reflection coefficient, is likely necessary to make the impact of surface reflections negligible. For an infinitely wide source sheet this results in a 5% increase in signal intensity, but this is likely an overestimate. For a more reasonable source sheet radius equal to h (the distance between the source sheet and the engine head), the diffuse reflection intensity is reduced by a factor of 4-5 (for a total of $\sim 1\%$; this can be seen by changing the upper integration

limit on θ to $\pi/4$ and carrying out the integral). For Chapter 7, it will be assumed that a coating is applied to the engine head with diffuse reflection coefficient $\leq 3\%$, and as a result surface reflections have a negligible impact on diagnostic performance.

6.5 Phosphor Blackbody Radiation

As solid particles, thermographic phosphors will emit blackbody radiation at optical wavelengths when sufficiently hot, which can interfere with the APT signal. The total emission intensity per particle per unit radiation frequency, $\partial\dot{S}/\partial\omega$, is given by the product of the Planck function $\mathcal{P}_e$ [140]

$$\mathcal{P}_e = \frac{\hbar\omega^3}{4\pi^3 c^2}\left[e^{\frac{\hbar\omega}{k_B T}} - 1\right]^{-1}, \tag{6.48}$$

the particle surface area $\pi d_{p,A}^2$, and the solid-angle of a Lambertian emitter π, normalized by the photon energy $\hbar\omega$, resulting in

$$\frac{\partial\dot{S}}{\partial\omega} = \frac{\omega^2}{4\pi^2 c^2}\ \pi d_{p,A}^2\ \left[e^{\frac{\hbar\omega}{k_B T}} - 1\right]^{-1}, \tag{6.49}$$

where $\dot{S}$ represents the total number of emitted photons per unit time, and again $d_{p,A}$ is the surface area-weighted mean particle diameter. Integrating over the entire spectrum results in

$$\dot{S} = \frac{k_B^3 T^3}{2\pi^2 c^2 \hbar^3}\pi d_{p,A}^2\ \zeta(3), \tag{6.50}$$

which is similar to the Stefan-Boltzmann formula, but represents emitted photon flux rather than emitted power. Here, $\zeta(3)$ is Apéry's constant (~ 1.202) and $\zeta(z)$ is the Riemann zeta function. For a typical phosphor particle diameter of 1 µm, and an exposure of 1 µs, the blackbody signal per particle is approximately 2.2×10^7 photons. The vast majority of this radiation is infrared thus motivating shorter wavelength diagnostics. Figure 6.14 plots the number of visible photons per particle for the hypothetical particle as a function of temperature on the left hand side, with the normalized photon emission spectrum on the right. From the plots, for low temperature ignition studies, blackbody radiation per particle is expected to be negligible if wavelengths longer than 700 nm are rejected. The expected background intensity per particle for each phosphor composition considered here is calculated and displayed in Table 6.4 for comparison.

Comparing the blackbody signal per particle to the luminescence signal per particle based on the signal modeling results (presented in Section 4.6) suggests that blackbody radiation isn't important until about 1550 K; at this temperature, the estimated blackbody intensity per particle is 10% of the

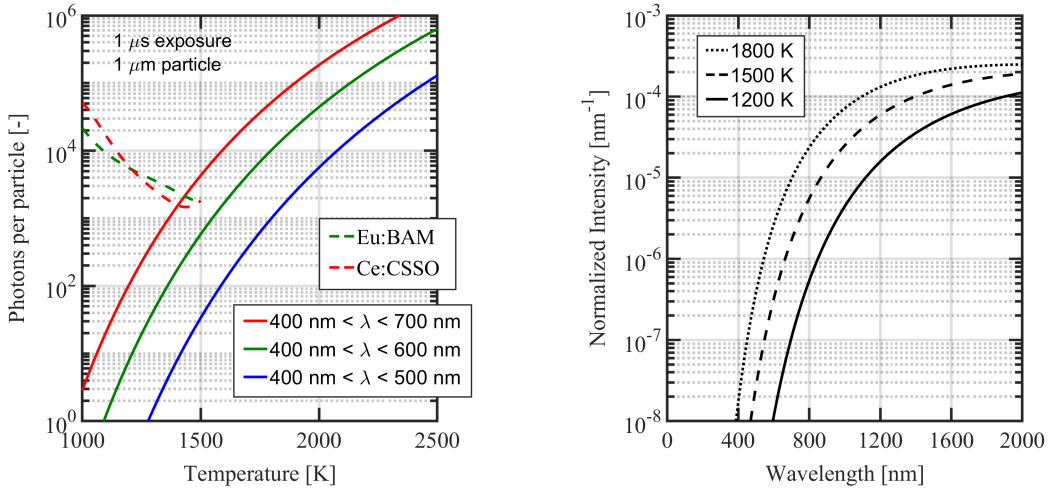

(a) Intensity versus temperature

(b) Blackbody spectrum

Figure 6.14: Blackbody optical radiation intensity as a function of temperature, and normalized blackbody spectra at optical and near infrared wavelengths. (a) includes plots of the phosphor signal per particle for Eu:BAM and unannealed Ce:CSSO at 30 mJ/cm^2 (6 ns laser pulse, 355 nm excitation for Eu:BAM, 266 nm excitation for Ce:CSSO) for the same particle size using the results of Section 4.6, for comparison.

Table 6.4: Calculated blackbody intensity per particle for each phosphor. Assumed collection bands and integration duration are shown in the table, corresponding to the phosphor's emission spectrum. In the table, $\dot{S}$ is the photon emission rate and S is the total number of photons emitted over the exposure period.

	900 K		1200 K		1500 K		Wavelength	Exposure
Phosphor	$\dot{S}$ [s^{-1}]	S [-]	$\dot{S}$ [s^{-1}]	S [-]	$\dot{S}$ [s^{-1}]	S [-]	[nm]	τ_{exp} [μs]
Ce,Pr:LuAG	2.8×10^{4}	0	1.2×10^{7}	5.8	4.6×10^{8}	230	450-700	0.5
Ce:$GdPO_4$	2.1×10^{-2}	0	620	0	3.1×10^{5}	0	300-400	0.2
Ce:CSSO	5.0×10^{4}	0	2.1×10^{7}	10	8.1×10^{8}	410	450-700	0.5
Eu:BAM	280	0	5.4×10^{5}	1	5.4×10^{7}	110	400-550	2.0

luminescence per particle for annealed Ce:CSSO at a fluence of 30 mJ/cm^2 and a 6 ns laser pulse. However, this comparison is an underestimate as the collected background signal depends on geometry as well. For scattering and luminescence signals, light is collected only within the laser sheet, which produces a well-defined collection volume. However, for blackbody radiation, particles out of plane can have a significant contribution as well, significantly increasing the collection volume.

The contribution of blackbody emission outside of the focal plane is estimated as follows. The fraction of light collected by a lens from any point source within this volume is given by

$$\frac{\Omega}{4\pi} = \frac{d_f^2}{16 f_\#^2 d_o^2}, \tag{6.51}$$

where $f_\#$ is the lens f-number, d_f is the focal length, and d_o is the object plane distance. For a typical experimental setup (*e.g.,* $f_\# = 1.4$, $d_f = 85$ mm, $d_o = 500$ mm), the collected solid angle fraction is 9×10^{-4}. From Equation 6.51, a 10% change in the object distance would result in about a 20% change in collection efficiency.

Light originating from outside the focal plane has a different magnification than light originating within the focal plane or laser sheet. This tends to spread the source over a larger region (or more pixels) in the image plane. Assuming the phosphor seeding density is uniform throughout the cylinder volume, and that the cylinder height h is small compared to the object plane distance d_o (as expected for the high-temperature cases considered here near TDC, where $h \approx 1$ cm and $d_o \approx 50 - 100$ cm), this spreading to first order does not alter the amount of incident light on a pixel. Since the cylinder height is small, only modest variation in focus is expected throughout the cylinder, and the amount of light captured per pixel is not impacted by the focus variation. The effect of the imperfect focus is to blur blackbody radiation (similar to the application of a Gaussian filter to an image) and spread it out over several pixels, but the total intensity is unchanged. If the blackbody source distribution is reasonably uniform, then the imaged blackbody radiation is also uniform and has the same intensity. For this reason, focus does not need to be considered when estimating background blackbody radiation. Instead, for a given pixel, contributions from out of plane are estimated by integrating over the cylinder height. The effective collection volume is thus a rectangular box, where collection efficiency is non-uniform in the depth direction.

Based on this analysis, and the signal modeling results of Section 4.6, blackbody radiation starts to become significant (SBR<10) near 1150-1200 K for annealed Ce:CSSO at 50 mJ/cm^2, 450-700 nm collection bands, and a 200 ns exposure. This calculation also assumes a 0.3 mm wide laser sheet, a 7 mm engine cylinder height, and a 550 nm diameter particle. Annealed Ce:CSSO represents the case where

blackbody radiation is expected to be most significant as it is viable at high-temperatures but has a weak emission compared to Eu:BAM, Ce:LuAG at 355 nm excitation, and unannealed Ce:CSSO. The particle diameter, laser sheet thickness, and cylinder height are chosen to be comparable to the experimental setup described in Chapter 7. Since the temperature range under consideration here is primarily below 1200 K, blackbody radiation is not a significant source of error and will not be considered further. However, this analysis does suggest that blackbody radiation may have impacted the temperature measurements presented in Section 5.2, particularly at high temperatures with the dimmer phosphor samples.

6.6 PSD Contributions to SRAPT Ratio Precision

Equation 4.31 assumes that the only sources of uncertainty in the ratio measurement are due to noise in the measurement of luminescence and scattering intensities. However, since the measured signal depends on diameter-cubed for luminescence, but closer to diameter squared for scattering, the ratio must have some dependence on particle diameter. Written to explicitly contain this dependence, including the change in scattering efficiency with diameter, the ratio is

$$R_{SRAPT} = \frac{S_{p,scat}}{S_{p,lum}} \frac{\langle d^3 \rangle}{\langle Q(d) d^2 \rangle} \frac{\sum_i Q(d_i) d_i^2}{\sum_i d_i^3}, \tag{6.52}$$

where $S_{p,scat}$ and $S_{p,lum}$ are the scattering and luminescence signal per particle for the average particle size, angle brackets $\langle \cdot \rangle$ represent the population average quantity (*i.e.*, $\langle d^i \rangle$ is the i-th moment of the PSD), d_i is the diameter of each particle i in the sample, $Q(z)$ is the scattering efficiency at diameter z, and the sums are performed over the N particles in the collection volume. The uncertainty analysis summarized in Equation 4.31 describes the contributions from the signal per particle ratio (the first factor on the right-hand side of Equation 6.52); this contribution is unchanged and will be neglected in the remaining analysis. The middle factor in Equation 6.52 (ratio of the mean cubed diameter to the mean squared diameter weighted by scattering efficiency) has no dispersion as it is the average over the population. The factor on the far right of Equation 6.52 represents the random sampling of particles from the PSD, and is the source of the added SRAPT uncertainty.

The first-order uncertainty propagation for the SRAPT ratio (Equation 6.52), neglecting the camera noise terms discussed previously, is

$$N\left(\frac{s_{R,PSD}}{R}\right)^2 = \left(\frac{s_{Q(d)d^2}}{\langle Q(d)d^2 \rangle}\right)^2 + \left(\frac{s_{d^3}}{\langle d^3 \rangle}\right)^2 - 2\frac{s_{Q(d)d^2,d^3}}{\langle Q(d)d^2 \rangle \langle d^3 \rangle}, \tag{6.53}$$

where the sums have been replaced with the factor N on the left hand side, which indicates the number of particles being sampled in the collection volume (*i.e.*, we're averaging the dispersion of N randomly selected particles). Thus, the right hand side corresponds to the variance introduced by a single particle, which is reduced by the factor N when averaging or summing over N particles in the collection volume. The symbol $s_{x,y}$ is the covariance of the variables x and y.

The precision indices are determined from the PSD. The moments of the PSD that are independent of scattering efficiency are given by the following definitions:

$$\langle d^2 \rangle = E[d^2] = m_2 \tag{6.54}$$

$$\langle d^3 \rangle = E[d^3] = m_3 \tag{6.55}$$

$$s^2_{d^2} = E[(d^2 - \langle d^2 \rangle)^2] = m_4 - m_2^2 \tag{6.56}$$

$$s^2_{d^3} = E[(d^3 - \langle d^3 \rangle)^2] = m_6 - m_3^2 \tag{6.57}$$

$$s_{d^2,d^3} = E[(d^2 - \langle d^2 \rangle)(d^3 - \langle d^3 \rangle)] = m_5 - m_2 m_3. \tag{6.58}$$

The relevant moments that depend on scattering efficiency are given by the following definitions:

$$\langle Q(d)d^2 \rangle = E[Q(d)d^2] = q_{1,2} \tag{6.59}$$

$$s^2_{Q(d)d^2} = E[(Q(d)d^2 - \langle Q(d)d^2 \rangle)^2] = q_{2,4} - q_{1,2}^2 \tag{6.60}$$

$$s_{Q(d)d^2,d^3} = E[(Q(d)d^2 - \langle Q(d)d^2 \rangle)(d^3 - \langle d^3 \rangle)] = q_{1,5} - q_{1,2} m_3. \tag{6.61}$$

Here, $E[x]$ is the expected value of event x, and as before the moments of the PSD are defined by

$$m_i = \langle d^i \rangle, \tag{6.62}$$

and now the scattering efficiency-weighted moments are defined as

$$q_{i,j} = \langle Q(d)^i d^j \rangle. \tag{6.63}$$

The SRAPT uncertainty resulting from particle sampling, including the Mie scattering efficiency, can then be written as

$$\frac{s_{R,PSD}}{R} = \sqrt{N^{-1}} \sqrt{\frac{q_{2,4}}{q_{1,2}^2} + \frac{m_6}{m_3^2} - 2\frac{q_{1,5}}{q_{1,2} m_3}} = \frac{k_Q}{\sqrt{N}}, \tag{6.64}$$

where k_Q is the magnitude of the SRAPT uncertainty for a single particle. The SRAPT uncertainty is

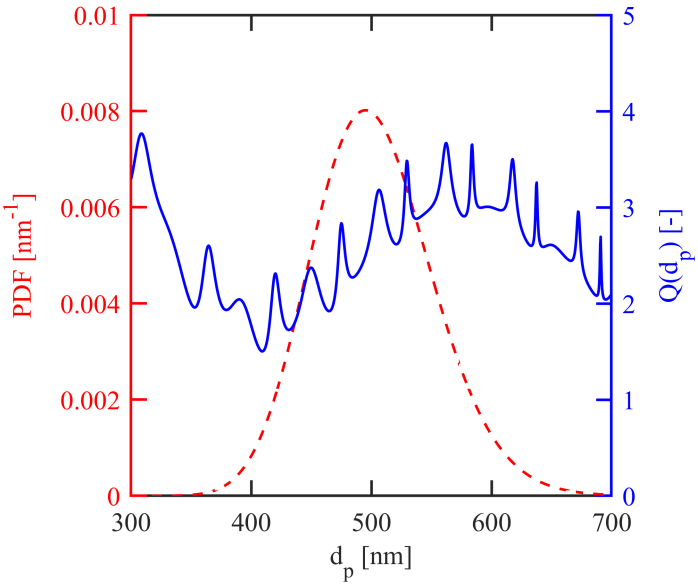

Quantity	Value	Units
m_2	2.5×10^{-4}	µm^2
m_3	1.3×10^{-4}	µm^3
m_4	6.8×10^{-5}	µm^4
m_5	3.5×10^{-5}	µm^5
m_6	1.9×10^{-5}	µm^6
$q_{1,2}$	6.8×10^{-4}	µm^2
$q_{2,4}$	5.2×10^{-4}	µm^4
$q_{1,5}$	9.8×10^{-5}	µm^5
k_Q	3.9	-
k	3.3	-

Figure 6.15: Sample particle size distribution and Mie scattering efficiency (assuming an index of refraction of 1.8) as a function of particle diameter (left) with calculated moments and SRAPT uncertainty constant (right).

thus inversely proportional to the square-root of the number of particles being imaged or sampled (or the seeding density) with a scale factor that depends on the PSD and scattering efficiency model. For comparison, neglecting the scattering efficiency would simply replace the moments in the expression by taking $q_{i,j} \rightarrow m_j$; this new scaling parameter that neglects scattering efficiency is labeled k (this follows from Equation 6.63 if $Q(d_p)$ is assumed constant).

A sample calculation was performed for a log-normally distributed particle diameter with a count median diameter of 500 nm and width parameter $s = 0.1$ (resulting in a 117 nm FWHM). The calculated PDF and scattering efficiency at each diameter (assuming 266 nm laser light) are plotted in Figure 6.15, with PSD moments and SRAPT uncertainty magnitude tabulated on the right. From the plot and moments shown in Figure 6.15, the Mie scattering efficiency is characterized by high frequency oscillations compared to the width of the PSD; these oscillations do not contribute significantly to the calculated moments. Since the PSD is relatively wide, the variation in scattering efficiency has a modest impact on the SRAPT uncertainty, and the calculated k and k_Q values are within 20%. At higher values of the scattering parameter $x = \pi d_p/\lambda >\sim 10$, corresponding to slightly larger micron-scale particles, the low-frequency dependence of $Q(d_p)$ on d_p is reduced, such that $k \rightarrow k_Q$.

The scaling parameter k was calculated for each phosphor studied here, using the PSDs measured in Section 4.1 and are tabulated in Table 6.5. The table also includes a few representative values calculated

Table 6.5: Estimated SRAPT uncertainty due to particle seeding for each phosphor. The parameter k is a property of the PSD; the estimated ratio precision values assume a 1.0 mm^3 pixel volume. PSD moments were reported in Table 4.3.

		s_R/R [-]			
Phosphor	k [-]	100 mm^{-3}	500 mm^{-3}	1000 mm^{-3}	2000 mm^{-3}
Ce,Pr:LuAG	2.8	0.28	0.13	0.09	0.06
Ce:$GdPO_4$	7.6	0.76	0.34	0.24	0.17
Ce:CSSO	2.9	0.29	0.13	0.09	0.06
Eu:BAM	1.9	0.19	0.09	0.06	0.04

for a cubic measurement volume with side length of 1 mm (or $V = 1$ mm^3), neglecting the scattering efficiency. For comparison, a log-normal distribution with parameters μ and s has a SRAPT uncertainty constant k given by

$$k = \sqrt{e^{4s^2} + e^{9s^2} - e^{6s^2}}. \tag{6.65}$$

No closed form expression for k_Q exists for spherical particles in general.

Perhaps the most important result from this analysis is that the SRAPT uncertainty is inversely proportional to the square-root of the number of particles being sampled, and is otherwise dependent only on the PSD and the scattering efficiency of the particles. Since the scattering efficiency appears to have only a small impact on the result, the measured PSDs are relatively low-resolution, and non-spherical particles are used (and hence the Mie scattering efficiency is only approximate), scattering efficiency is neglected for the remaining discussion and experiment design presented in Chapter 7. This appears to be a reasonable approximation for particles on the order of 500 nm or larger.

This phenomenon was observed experimentally in the room temperature air jet (see Section 5.3 for experimental details) using the Eu:BAM phosphor. The SRAPT method was used to determine the SRAPT ratio precision, then the LIR method was used to determine the LIR ratio precision. The camera lens apertures were adjusted such that the same signal intensity was captured between the two configurations, such that the results are directly comparable. The measured signals and ratio precision estimates are shown in Figure 6.16. The data was not corrected for linearity, and there is clearly some non-linearity in the response at high signal levels (above 10,000 counts for the LIR band); however, the nonlinearity is not significant below 5,000 counts; ratio precision is compared in this range.

From Figure 6.16, at a scattering intensity of 5,000 counts, the magnitude of the additional SRAPT uncertainty term is about 0.2 to 0.3. Using the measured PSD and theory proposed (*i.e.*, Equation 6.64 and $k = 1.9$), this corresponds to about 90 particles in the collection volume, or a seeding density of

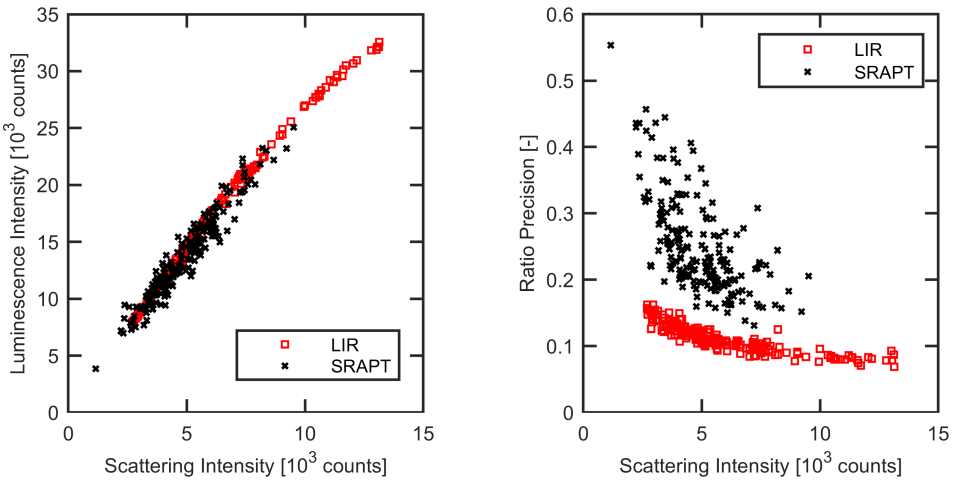

Figure 6.16: Comparison of SRAPT and LIR signal intensities (left) and ratio precision (right) for Eu:BAM.

around $\sim$ 200 mm^{-3} (0.1 mm^3 volume, with a 2x2 moving average filter). This is consistent with the seeding density estimated from Eu:BAM signal intensity of $\sim$150 mm^{-3}. The SRAPT uncertainty is clearly a real, measurable effect, and the magnitude agrees reasonably well with the theory discussed here. This estimate will be used to estimate the contribution of the SRAPT uncertainty for experiment design calculations in Chapter 7.

6.7 Conclusions

This chapter discussed in detail multiple effects that impact temperature and signal measurements due to solid particles dispersed in a gas flow. In particular, tracer particle dynamics and tracer response were considered (both momentum and temperature response), and a relatively simple theory was selected to estimate particle response times and select particle sizes based on the highest integral frequency scale that is of interest for the measurement. Diagnostic intrusiveness was also considered based on a simple theory where it is assumed cold, stagnant particles are introduced to the flow that then equilibrate, reducing the flow momentum and temperature (but increasing density). Both of these effects will be applied in Chapter 7 for a specific set of requirements for low-temerature ignition of a diesel jet.

A significant amount of effort went into the analysis of multiple scattering effects. By seeding solid particles into the flow, light (both emitted and scattered) no longer propagates unimpeded through the air mixture, and this can bias the measurement. The largest impact was found to be multiply-scattered light that exits the cylinder at normal incidence (and hence is collected by any imaging system) and biases the intensity measurement. A relationship was found between seeding density (more specifically

Table 6.6: Relative importance of design considerations for aerosol phosphor thermometry techniques. The column "Significant?" indicates whether the topic needs to be considered in detail in more detail in Chapter 7

Topic	**Section**	**Significant?**
Tracer particle response	6.1	Yes
Intrusiveness	6.2	Yes
Multiple scattering - signal bias	6.3.2	Yes
Multiple scattering - laser sheet spreading	6.3.3	Yes
Multiple scattering - imaging resolution	6.3.4	No
Engine head reflections	6.4	No (if $R_d < 3\%$)
Phosphor blackbody radiation	6.5	No (for T $<$ 1200 K)
PSD contribution to SRAPT uncertainty	6.6	Yes

the optical depth in the cylinder) and signal bias. Additionally, the impact of multiple scattering on laser sheet thickness and imaging resolution were discussed. Each of these effects will be considered for experiment design in Chapter 7.

Reflections off the engine head were analyzed and discussed, and it was found that they could potentially be significant, particularly for a diffusely-reflecting head. However, treating the engine head with high-emissivity (low-reflectance; $R_d \leq 3\%$) paint may be sufficient to make reflections negligible. For this reason, reflections will not be considered in detail for design purposes. Similarly, the possibility of particle blackbody radiation was analyzed and discussed, where it was found that blackbody radiation is likely unimportant below 1200 K (or hotter for some of the brighter phosphors). Blackbody radiation will thus not be considered as a significant bias in Chapter 7. Finally, the effect of the particle size distribution on SRAPT imaging was considered in detail, and a theory was proposed to describe the observed effects, and will be used to estimate SRAPT uncertainty contributions for experiment design in Chapter 7. The design considerations discussed in this chapter are summarized again in Table 6.6 with some basic conclusions regarding their relative importance to the design process.

Chapter 7

Combined APT/PLIF Experiment Design and Implementation

The earlier chapters in this thesis focus on development of APT and formaldehyde PLIF individually. The primary goal of this work is to design a strategy in which both diagnostics can be performed simultaneously. This is challenging for several reasons. Formaldehyde emission is relatively broadband from around 350 to over 500 nm, similar to the emission range of many thermographic phosphor materials. Removing or avoiding background radiation on either diagnostic is necessary for an accurate and precise measurement. Further, formaldehyde is excited typically at 355 nm while many of the phosphors under investigation here are excited at 266 nm. Shorter wavelength excitation of formaldehyde can lead to significant reduction in fluorescence quantum yield and excitation below 300 nm is likely not suitable. Excitation spectra shown in [81] suggest emission intensity is at least an order of magnitude lower when exciting at 290 nm compared to 355 nm excitation, although it is not clear how this changes at elevated temperature and pressure.

This chapter will outline a combined diagnostic approach, and discuss some possible solutions to the aforementioned challenges. Temperature precision and resolution requirements will be defined based on the physics under investigation in the engine, and APT performance predictions will be made for several diagnostic approaches. Formaldehyde PLIF diagnostic performance will be discussed, in particular focusing on detection limits; the impact of the temperature measurement accuracy and precision on the formaldehyde concentration imaging results will be assessed as well. Finally, a recommendation for phosphor and simultaneous formaldehyde imaging strategy will be made, along with a discussion of potential issues that remain to be addressed, and potential changes in equipment that could improve

diagnostic performance.

7.1 Brief Description of the Combined Diagnostic

A combined diagnostic for simultaneous temperature, velocity, and formaldehyde concentration is proposed using aerosol phosphor thermometry (APT) with particle image velocimetry (PIV) and formaldehyde planar laser-induced fluorescence (PLIF). Phosphor particles will be seeded into the air flow entering the engine, while formaldehyde is formed in-cylinder by low-temperature reactions during ignition. Ultra-violet laser light will be used to excite luminescence from formaldehyde and the phosphor particles; ultra-violet laser light scattered from the phosphor particles will be needed for PIV. Either 4 or 5 cameras will be used to image the various light sources; if only a single APT diagnostic is used (*e.g.*, Eu:BAM SRAPT only) then 2 cameras are used to capture light needed for APT, otherwise 3 cameras are needed for APT to perform the combined co-doped/host-referenced APT and SRAPT measurements. The proposed formaldehyde PLIF diagnostic requires two cameras separated by a beamsplitter. One of the formaldehyde imaging cameras captures the peaks of the formaldehyde emission, and another captures the valleys or local minima. The optical setup is discussed in more detail in Section 7.1.1. Since multiple diagnostics are being performed simultaneously, the emitted or scattered light from either formaldehyde PLIF or APT can act as a background signal for the other diagnostic.

The formaldehyde measurements are expected to be biased due to broadband background radiation, either from the phosphor particles, or from other interfering species such as polycyclic aromatic hydrocarbons (PAHs). To remove this background, a ratiometric imaging approach is proposed in which two cameras for formaldehyde imaging will image different portions of the emission spectrum, one on-peak and one off-peak. This will be accomplished using the 11-band formaldehyde imaging filters as discussed in Sections 3.1 and 3.6. The ratio of the two images is used to infer the background intensity. The proposed approach for background subtraction extends the approach suggested by Thering *et al.* [56], where emission was collected using the same two multi-band filters but a direct frame subtraction was applied. The approach in [56] is limited in that a significant portion of formaldehyde emission exists in the off-peak band, and the fraction is both temperature and pressure dependent. The proposed approach is intended to provide a quantitative measurement by accounting for the temperature and pressure dependence of the intensity ratio.

Table 7.1: Engine hardware specifications

Parameter	Value	Unit
Effective Compression Ratio	12.0	-
Geometric Compression Ratio	13.9	-
Displacement	0.402	L
Bore	84.4	mm
Stroke	76.2	mm
Connecting rod length	144.8	mm
IVC/EVO/IVO/EVC	-164/164/347/375	CAD

7.1.1 Proposed Experimental Setup

The proposed experiment is intended to be performed in an optically-accessible engine at the University of Wisconsin-Madison. The same engine as discussed in Section 3.1 will be used with slight modifications to the piston; geometry information is repeated in Table 7.1 for convenience. A cross-sectional diagram of the engine (with the modified piston) is also shown in Figure 7.1.

Most of the details of the engine geometry are not necessary for predicting diagnostic performance, with the exception of volume which determines the pressure, temperature, and seeding density at each crank angle; all of the information necessary to calculate cylinder volume is provided in Table 7.1. Additionally, as was be discussed in Chapters 6 and 7, the height of the cylinder is important in determining certain aspects of diagnostic performance. The cylinder height (specifically, the distance between the piston surface and cylinder head) is calculated and plotted as a function of crank angle in Figure 7.2. At TDC, when height is minimized, the cylinder height is approximately 10 mm.

All of the engine optics are custom manufactured using UV-grade fused silica. The piston and spacer plate side windows for the proposed experiments are both UV anti-reflection (AR) coated (on both sides of the optics) to maximize transmission of the laser sheet into and out of the engine, and to avoid distortions and stray light inside the engine. (Optics used in Section 3.1 were not UV-AR coated.) The piston and spacer plate windows both have a lensing effect on the laser sheet as it enters the cylinder, so a custom lens was designed to correct the laser sheet for this effect. An experimental setup diagram showing the laser source and optics relative to the engine is shown in Figure 7.3.

In this experiment, five cameras are used: three for APT, and two for formaldehyde PLIF. Depending on the selected APT technique or techniques, only two APT cameras may be used. A series of beamsplitters are used to separate the formaldehyde emission from the phosphor emission and scattering signal, and to guide the formaldehyde, phosphor, and scattering signals to the appropriate sensor. Specific

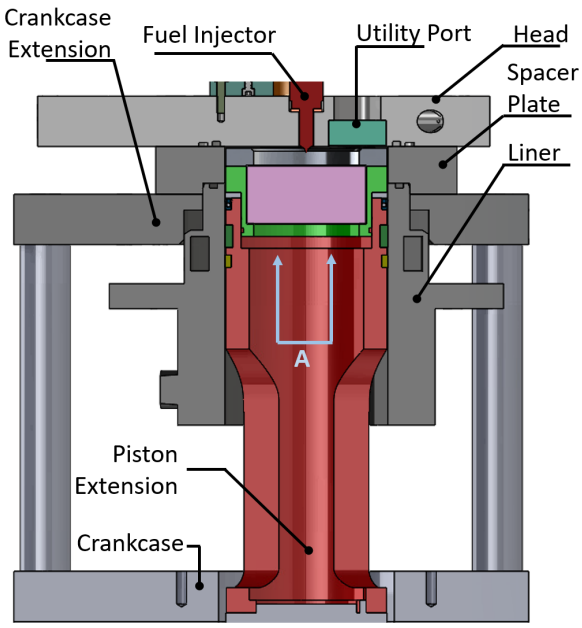

Figure 7.1: Annotated diagram of engine (side view). Diagram was produced by Michael Groendyk. The piston and spacer plate side windows are not shown in this diagram.

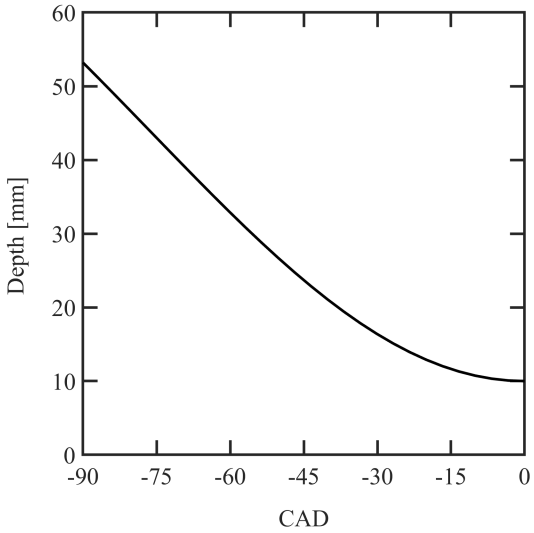

Figure 7.2: Height of cylinder in optical engine as a function of crank angle

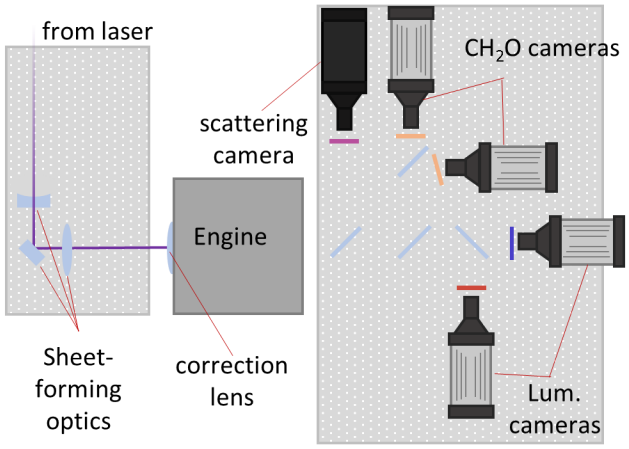

Figure 7.3: Experimental setup diagram for proposed engine experiments

equipment information (*e.g.*, beamsplitter models) is not provided here as this is beyond the scope of the design work presented in Chapter 7. The formaldehyde PLIF imaging approach makes use of two 11-band interference filters designed to capture formaldehyde fluorescence setup such that one camera captures the peaks of the emission spectrum, and the other camera captures the valleys or minima. The transmission spectra of the filters are shifted by changing the angle of incidence (AOI) of the filter. At 0° AOI the emission peaks are captured, and at 15° AOI the valleys of the emission spectrum are captured. The transmission spectrum of the filters was measured and is plotted in Figure 3.4, with the formaldehyde emission spectrum superimposed.

For the purposes of experiment design, it is assumed that a Nikon Nikkor 85 mm manual focus $f/1.4$ lens is used, that there is at least 500 mm separation distance between the lens and object plane; performance estimates will primarily use intensified CCD cameras (these are discussed in detail in Appendix E). The lens is chosen to maximize the f-number while still retaining a focal length long enough to provide the required magnification. The beamsplitters and collection optics, besides the formaldehyde imaging filters, are not specified as they will be determined using the results presented later in this chapter.

7.2 The Ignition Environment & Target Conditions

The combined formaldehyde PLIF and APT imaging diagnostic is intended to be used for high-pressure turbulent fuel jet ignition imaging in optically-accessible compression-ignition engines. The temperature range under consideration is typically from 600-1200 K, and pressure from 30 to 100 bar. The selected pressure range is typical of diesel engines near TDC before ignition (corresponding to a 1 to 3 bar intake

pressure, with a compression ratio of ∼13); the selected temperature range roughly brackets the 800 to 1000 K cool-flame temperature range observed by Dahms *et al.* in a series of homogeneous reactor configuration calculations [4], while allowing for both hotter and colder injection conditions. During engine operation, the air in the cylinder is compressed, then liquid fuel is injected into the engine at high pressure. The injected liquid fuel atomizes and entrains air, causing vaporization and heating of the fuel followed by ignition. Measurements are intended to image the fuel jet throughout the later part of the entrainment and heating processes, and during the ignition process. Temperature precision and spatial resolution requirements are derived from this picture and are discussed in the remainder of this section. The specification of these quantities is required as they serve as objectives for the diagnostic design.

7.2.1 Diagnostic Design Goals

The primary purpose of this work is to develop a diagnostic that can be used to validate and develop a deeper understanding of the mechanism for high-pressure turbulent fuel jet ignition, largely motivated by the simulation work of Dahms *et al.* [4] and Krisman *et al.* [141]. Briefly, high-pressure fuel jet ignition is believed to begin with low-temperature ignition on the hot lean radial periphery which causes a cool-flame wave to propagate inwards to the fuel-rich jet core, significantly decreasing the ignition delay of the colder, fuel-rich regions (relative to that of a homogeneous mixture). This process is strongly influenced by turbulence-chemistry interactions.

To validate and develop deeper understanding of this mechanism, simultaneous temperature, velocity, and formaldehyde concentration measurements are needed to observe the onset of low-temperature ignition and cool-flame wave propagation at length scales where the majority of energy and momentum transport occurs. These measurements will enable initial investigation of turbulence-chemistry interactions at integral length scales. Temperature precision, spatial and temporal resolution, and formaldehyde detection limits must be chosen carefully to capture the large-scale physics and chemistry needed to fully characterize the ignition process. Turbulence scales (*i.e.*, scales smaller than the smallest integral scale) do not need to be resolved as the majority of energy and anisotropy is contained near the integral length scales [122]. Temperature precision must be sufficient that low-temperature ignition and temperature wave propagation can be observed. The following sections will discuss in detail the resolution and temperature precision required to make these measurements.

7.2.2 Temperature Uncertainty Requirements

Temperature impacts the physics and chemistry of the ignition process in many ways, so identifying a requirement for measurement uncertainty is challenging. Two requirements will be discussed here. First, a temperature uncertainty required from a chemical kinetics standpoint, which would be required to relate temperature measurements to chemical kinetics models with any degree of certainty. Being the smaller value, the chemical kinetic temperature uncertainty requirement is a target value, but not necessarily required for this experiment. The second uncertainty requirement is based on temperature changes throughout the ignition process, and thus acts as a minimum uncertainty needed to identify the location and timing of an ignition event in-cylinder. The two criteria are discussed in the following paragraphs, starting with the limit based on chemical kinetics.

From chemical kinetics, a typical expression describing the chemical reaction rate for combustion is given by the modified Arrhenius expression as [142]

$$k = AT^n e^{-E/k_B T}. \tag{7.1}$$

From first order uncertainty propagation, the uncertainty in the rate coefficient due to temperature uncertainty can be written as

$$\frac{u_k}{k} \approx \left| n + \frac{E}{k_B T} \right| \frac{u_T}{T}. \tag{7.2}$$

Here, the symbol u_x indicates the uncertainty in the parameter x. The factor multiplying the fractional temperature uncertainty in Equation 7.2 is the sensitivity of the rate constant k to temperature T, and depends on the temperature exponent n, as well as the energy gap E for the reaction. Typically, n is between -1 and 1, with $n = 0$ corresponding to the usual form of the Arrhenius equation. Energy gaps vary significantly based on the reaction. Several reactions and their corresponding modified Arrhenius parameters are shown in Table 7.2. The data shown in Table 7.2 is taken from the Lawrence Livermore National Laboratory's (LLNL) n-heptane combustion kinetic mechanism, version 3.1 [42, 43].

Low-temperature reactions are shown in the top portion of the table. Specifically, hydrogen abstraction from fuel by molecular oxygen ($RH + O_2 \longrightarrow R + HO_2$), hydrogen abstraction from fuel by the hydroxyl radical ($RH + OH \longrightarrow R + H_2O$), and the formation of hydroperoxyalkyl radicals from the alkylperoxy radical ($ROO \longrightarrow QOOH$). Here RH is a fuel molecule (n-heptane, C_7H_{16}), and R represents the associated alkyl radical (C_7H_{15}). These three reaction classes are thought to be important in the initiation of low-temperature autoignition in alkanes [143], and are considered here (specifically for n-heptane) to be representative of low-temperature ignition reactions. Since multiple R and Q isomers

exist for the same fuel species, only a single representative reaction is listed in the table. The bottom portion of the table shows several high-temperature reactions for comparison.

Table 7.2: Arrhenius parameters for several important combustion reactions and calculated temperature sensitivity of the reaction rate constant at 1000 K based on data from the LLNL n-heptane mechanism.

Reaction	n [-]	E/k_B [K]	$\lvert n + E/(k_B T)\rvert$ [-]
$C_7H_{16} + O_2 \longrightarrow C_7H_{15} + HO_2$	0	26570	26.57
$C_7H_{16} + OH \longrightarrow C_7H_{15} + H_2O$	1.8	480	2.28
$C_7H_{15}OO \longrightarrow C_7H_{14}OOH$	0	13310	13.31
$H + O_2 \longrightarrow OH + O$	-0.406	8353	7.95
$CO + OH \longrightarrow CO_2 + H$	1.89	-583	1.31
$O + H_2 \longrightarrow OH + H$	2.67	3166	5.84
$OH + H_2 \longrightarrow H_2O + H$	1.5	1726	3.23
$O + H_2O \longrightarrow OH + OH$	2.02	6743	8.76

The sensitivity of the rate constant to temperature can easily vary from 1 to well over 10 at 1000 K. The sensitivity is effectively a measure of how significant a temperature uncertainty is to the final calculated result; for example, if the temperature sensitivity is 5, then a 1% temperature error corresponds to a 5% error in the rate coefficient. Currently, the most certain rate coefficient measurements are for the $H + O_2 \longleftrightarrow OH + O$ reaction, with an estimated uncertainty of 15% (it has further been suggested that 15% uncertainty may not be sufficient for combustion simulation) [144]. If we choose 15% as an upper limit for uncertainty of the rate coefficient, and conservatively estimate its sensitivity to temperature as 10, then a 1.5% temperature uncertainty is required to have any confidence in the rate constant measurement assuming that there are no additional sources of uncertainty besides temperature. Since there are additional sources of uncertainty to consider that are potentially of similar magnitude, a more reasonable upper bound on temperature uncertainty is 1%.

From a chemical kinetics standpoint, we thus aim to have less than 1% temperature uncertainty in order to relate any measured quantities to chemical kinetics, *e.g.*, for validation of models. A target temperature uncertainty limit is thus 1% for the experiment. However, this requirement is more strict than needed solely to characterize the ignition process. Instead, to characterize the low-temperature ignition process, at minimum we must determine the time and location at which low-temperature ignition occurs. Another, less stringent, limit will be derived in the following paragraphs that is sufficient to determine the location and timing of ignition for typical compression ignition engine conditions.

Since high-pressure turbulent fuel jet ignition is believed to begin on the hot (low equivalence ratio) radial periphery (which then results in the propagation of a cold-flame wave), the chemistry at the initial

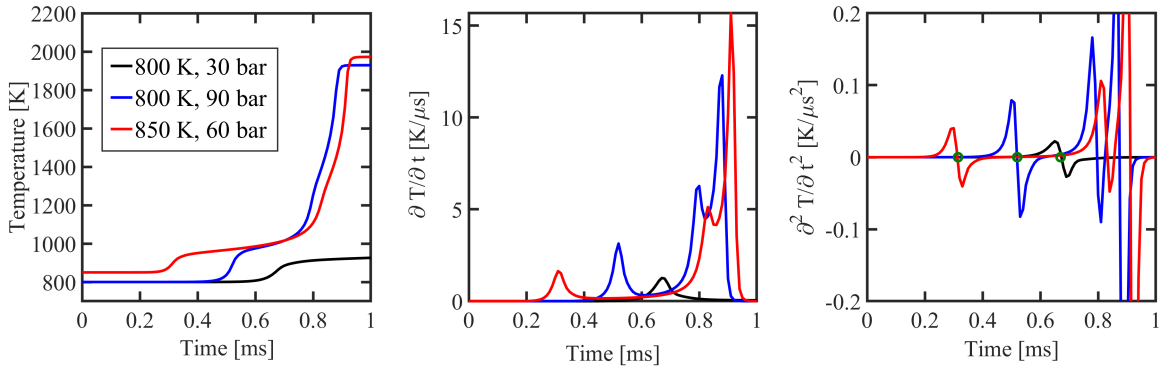

(a) T (b) dT/dt (c) d^2T/dt^2

Figure 7.4: Temperature profiles, temperature rise rates, and temperature curvatures for an equivalence ratio of 0.5, n-heptane/air mixture at constant pressure for several initial conditions.

point of low-temperature ignition can be approximated reasonably well using a homogeneous reactor. In fact, [4] showed that at low equivalence ratios typical of the onset of low-temperature ignition at early times ignition delays determined by the homogeneous reactor model match well with the inhomogeneous case. Thus, the initial temperature increase following low-temperature ignition can be approximated using a homogeneous reactor model, at least on the radial periphery. Several sample temperature profiles at constant pressure, with calculated temperature rise rates, are shown for a stoichiometric mixture of air and n-heptane at constant pressure in Figure 7.4 for three initial conditions. The initial conditions are chosen to be representative of the lean periphery of the fuel jet (800-850 K, equivalence ratio 0.5, and 30-90 bar pressures).

There are a few points from Figure 7.4 worth noting. First, each case exhibits clear low-temperature ignition. This occurs around 0.3 ms into the simulation for the 850 K case, 0.5 ms for the 800 K & 90 bar case, and 0.7 ms for the 800 K & 30 bar case. The temperature at the point of low-temperature ignition (based on the peak temperature rise rate) is around 850-900 K for each case. Low-temperature ignition is clear in the temperature rise rate, appearing as a distinct local maximum. The temperature at the low-temperature ignition point is similar for the three cases; however, the temperature increase varies from 100 K to 200 K in these three cases.

To correctly identify low-temperature ignition, a temperature diagnostic must resolve the temperature change associated with low-temperature ignition. Specifically, the temperature uncertainty must be less than 50% of the temperature increase resulting from low-temperature ignition. The remainder of this analysis will thus aim to estimate the temperature increase following low-temperature ignition for typical fuels and conditions, and subsequently the minimum temperature precision required for an ignition diagnostic.

To make this estimate, a series of 0D chemical kinetics calculations were run using the LLNL n-heptane combustion mechanism [42, 43] at constant pressure, with variable pressure, initial temperature, and initial fuel mole fraction. The initial temperature range was taken to be from 700 to 850 K, equivalence ratio from 0.5 to 2.0, and pressure of 30 to 90 bar. The equivalence ratio range was chosen to span a wide range of the most reactive (shortest homogeneous ignition delay) fuel-air mixture conditions. The temperature range corresponds to the range of adiabatic fuel-air mixture temperatures expected for 900 K air for the chosen equivalence ratio range; the pressure range is consistent with the peak pressures observed in the optical engine with 1 to 3 bar intake pressure. For each condition, high-temperature ignition is identified as the time at which the temperature derivative reaches its maximum value, and the low-temperature ignition time is identified as the time at which the absolute value of the second derivative of temperature is minimized preceding high-temperature ignition (note that in Figure 7.4c, the curvature becomes negative after the onset of low-temperature ignition); this corresponds to the peak temperature rise rate if there is distinct low-temperature ignition. The temperature jump from low-temperature ignition is taken as the temperature difference in temperature between low-temperature ignition, and the initial temperature of the gas mixture.

The calculated temperature jumps are plotted in Figure 7.5. In general, increasing equivalence ratio and pressure increases low-temperature heat release, but only up to a point. At the 725 K initial temperature, equivalence ratios near 2 at 80-90 bar have no measurable distinct low-temperature ignition event; the curvature of the temperature rise rate is monotonic. At lower pressures and equivalence ratios, low-temperature ignition is obvious and temperature increases on the order of 200 K are common. For higher initial temperatures, above 800 K, the temperature jump decreases significantly and is typically on the order of 50 to 100 K. Higher initial temperature also shifts the threshold for no distinct low-temperature to higher pressures and equivalence ratios.

We're primarily interested in imaging ignition events in high-pressure fuel jets, which typically start on the outer periphery and travel inward [3]. In these locations, the fuel-air mixture could be relatively hot and at low equivalence ratio. Thus, an acceptable diagnostic should be able to resolve the expected temperature change at any of these locations. The minimum temperature change where distinct low-temperature ignition occurs is around 50 K. As such, we require about 25 K precision, or around 3% precision at mean temperatures of 800 K.

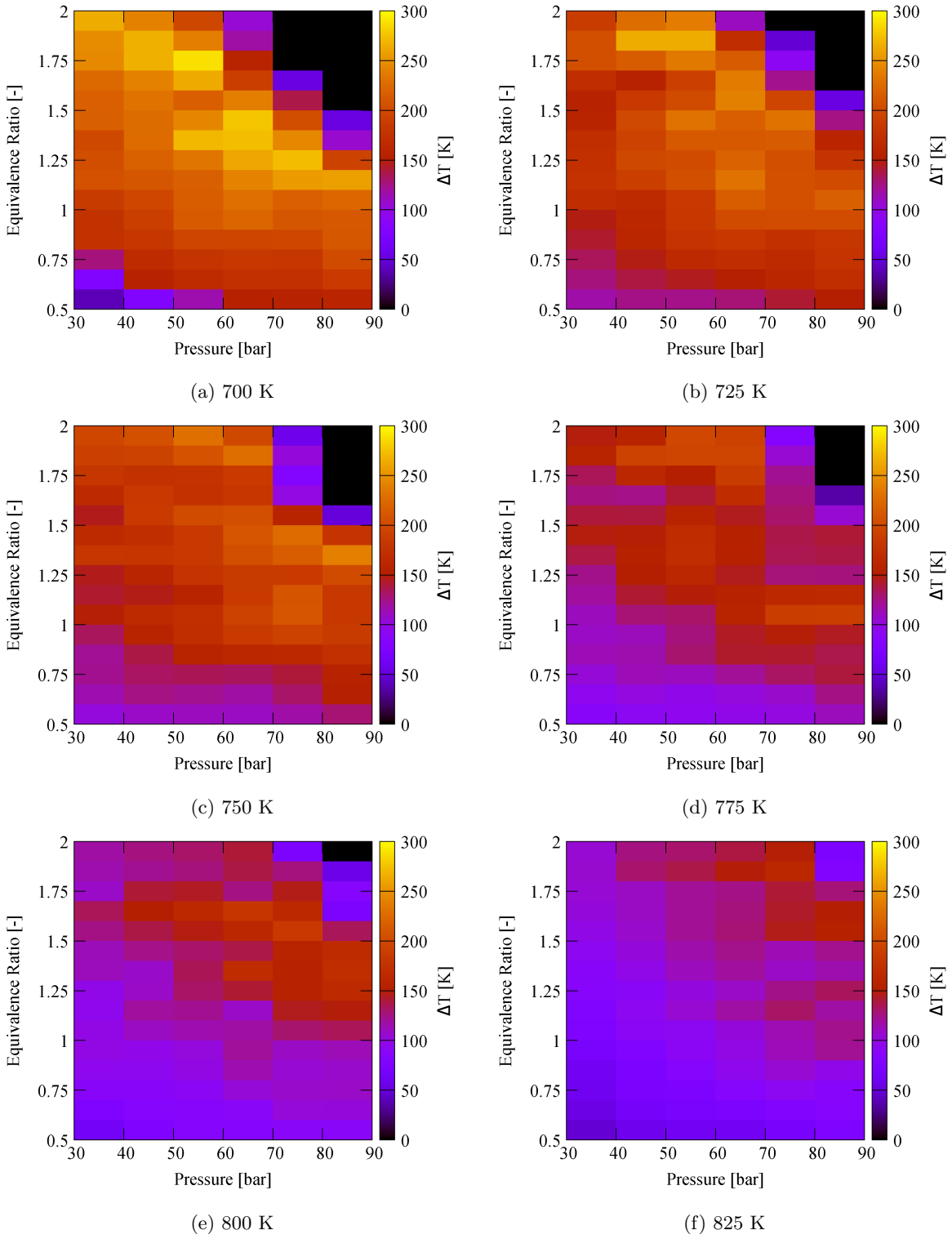

(a) 700 K

(b) 725 K

(c) 750 K

(d) 775 K

(e) 800 K

(f) 825 K

Figure 7.5: Calculated temperature jump at low-temperature ignition for n-heptane in air at several equivalence ratios, pressures, and initial temperatures.

7.2.3 Resolution Requirements

A significant challenge for understanding the diesel process ignition is the coupling between transport processes, turbulence, and chemistry. This results in highly non-uniform behaviors, including temperature and composition stratification leading to localized low-temperature ignition events on the radial periphery of the fuel jet [3]. To adequately observe the ignition process in high-pressure turbulent fuel jets, it is imperative that the diagnostic have sufficient spatial resolution to capture, at minimum, the smallest integral length scale of the turbulent fuel jet.

Motion at the integral turbulent length scales is typically anisotropic and is responsible for the bulk of transport processes in turbulent flows [122]. As energy is transferred to smaller turbulence scales via the energy cascade, directional bias and anisotropy information is lost such that turbulence at inertial and Kolmogorov scales is statistically "universal". Although turbulence does affect the ignition process below the integral length scale, the majority of effects that are dependent on the physical geometry or system (*i.e.*, all effects that are not "universal" turbulence effects) are evident only at integral length scales; thus we require a spatial resolution sufficient to measure the smallest integral length scale.

A diesel jet behaves similarly to a turbulent gas jet [145], and can thus be described well through some relatively simple analysis [122]. In particular, turbulent jets have a universal (constant) spreading rate $\beta = \partial r_{1/2}/\partial z \approx 0.1$, where $r_{1/2}$ is the radial coordinate of the jet at which the mean velocity is reduced to 50% of its peak value, and z is the axial coordinate. Taking the jet radius to be the distance R at which the velocity profile goes to 5% of its peak value ($R \approx 2.25 r_{1/2}$, from Figure 5.15 of [122]), then $R \approx 2.25\beta(z - z_0)$ and the universal turbulent jet half-angle is $\theta = \arctan(2.25\beta) \approx 12°$. The cone full angle of 24° is consistent with measurements of diesel sprays [146].

From turbulent jet theory, the smallest integral length scale is the lateral scale L_{22} defined by the lateral velocity autocorrelation function [122], which has a length of approximately $L_{22} \approx 0.3 r_{1/2}$. Thus, the smallest length scale that must be observed depends on the location within the turbulent jet where measurements are desired. For thermometry, measurements are needed at or downstream of the point of ignition. Using the lift-off length H as the imaging location, the spatial resolution required is $L_{22} \approx 0.3\beta H$.

A required time scale can be estimated from either the integral jet time scale, or from considering the displacement of a fluid parcel during a time Δt and relating it back to the spatial resolution. The integral jet time scale is given by $\tau_0 = r_{1/2}/u_0 = \beta(z - z_0)^2/(B\ d_j\ u_j)$ [122], where d_j is the jet orifice diameter, B is a universal empirical constant ($B = 5.8$ [122]), and u_j is the jet exit velocity.

The temporal resolution required to limit the displacement of a fluid parcel to a distance of $z - z_0$

Table 7.3: Estimated length and time scales for turbulent jet with typical high pressure fuel jet injection parameters

Scale	**Symbol**	**Value**	**Units**
Jet orifice dia.	d_j	140	µm
Lift-off length	H	1	cm
Injection pressure	p	350	bar
Fuel density	ρ	680	kg/m^3
Jet exit velocity	u_j	320	m/s
Jet radius	R	2.1	mm
50% velocity radius	$r_{1/2}$	0.9	mm
Lateral integral scale	L_{22}	280	µm
Jet exit time scale	$\tau_j = d_j/u_j$	440	ns
Jet time scale	τ_0	36	µs
Displacement time scale	$\tau_{L_{22}}$	11	µs

can be estimated in a similar fashion. From the mean axial centerline velocity expression for a turbulent jet [122],

$$u_0 = \frac{u_j B d_j}{z - z_0}, \tag{7.3}$$

the displacement over a time interval Δt can be found via integration as

$$\Delta z = \sqrt{2u_j B d_j (t + \Delta t)} - \sqrt{2u_j B d_j t} = \sqrt{2u_j B d_j (t + \Delta t)} - z(t), \tag{7.4}$$

or

$$\frac{z}{z_0} = \sqrt{\frac{t}{t_0}} \tag{7.5}$$

where z_0 and t_0 determine the initial location of the particle or fluid parcel.

Calculated scales and resolution requirements for a typical jet orifice diameter of 140 µm and exit velocity of 320 m/s (based on a 350 bar injection pressure for n-heptane; $u_j = \sqrt{2p/\rho}$), and lift-off length of 1 cm are shown in Table 7.3. From the table, the typical length scale is less than 0.3 mm. The jet time scale is on the order of 30 microseconds. However, to maintain the spatial resolution requirement, the temporal resolution must be better than ∼10 µs.

Lift-off Length & Resolution Estimate

From 2001 to 2006, Siebers *et al.* developed a correlation between lift-off length H, in-cylinder conditions, and injector properties [147–149] as

$$H = CT^{-3.74}\rho^{-0.85}d_j^{0.34}u_j Z_{st}^{-1}, \tag{7.6}$$

where T is the ambient air temperature [K], ρ is the ambient air density [kg/m^3], d_j is the jet orifice diameter [µm], u_j is the jet exit velocity [m/s], and Z_{st} [-] is the stoichiometric fuel mass fraction. With these units, Pickett *et al.* report the value of the proportionality constant as $C = 7.04 \times 10^8$ based on experiments using several different fuel compositions including n-heptane and #2 diesel [149].

Estimates of lift-off length and required spatial resolution are calculated using Equation 7.6. The stoichiometric mass fraction (Z_{st}) is 0.062 for n-heptane and 0.062-0.064 for #2 diesel fuel in air at 21% O_2 [147, 149]. Injector orifice diameter will be assumed to be 140 µm, which is representative of a typical automotive diesel fuel injector and is a size used routinely in optical engine experiments. Finally, a jet orifice velocity u_j of 320 m/s (again based on a 350 bar injection pressure with n-heptane) will be used as this is representative of typical automotive diesel fuel injectors, and has been used frequently in optical engine experiments. The remaining parameters, temperature and density, are a function of the engine operating conditions. Specifically, temperature and density depend on the intake conditions and engine geometry.

Figure 7.6 shows the required resolution plotted against intake pressure at three different initial air temperatures. The intake pressure is assumed to be equal to the pressure at IVC, and the IVC air temperature is assumed to be constant at 350 K, equal to the engine coolant temperature. Further, it is assumed that fuel is injected at TDC; TDC conditions are calculated assuming an isentropic compression from IVC with a constant specific heat ratio. For this calculation, the compression ratio from IVC to TDC is 11.85, and the specific heat ratio of air is assumed to be 1.38 (the average value between 350, 1 bar and 900 K, 30 bar). From the plot, at elevated temperature and pressure, resolution requirements could be as strict as 0.1 mm or less to properly resolve the smallest features. However, for modest intake pressures and temperatures (350-400 K, and 0.5-2 bar), resolving features at a scale of 0.3 mm is sufficient; these values are consistent with the predicted values in Table 7.3.

For an intake condition of 1 bar and 350 K, the required resolution is around 0.6 mm. Based on this analysis, the required pixel size will be taken as a 0.3 mm cube based on the Nyquist-Shannon sampling theorem; *i.e.*, the measurement bandwidth should be double the signal bandwidth to guarantee perfect reconstruction [150]. (It is also worth noting that using optical flow techniques, PIV can provide

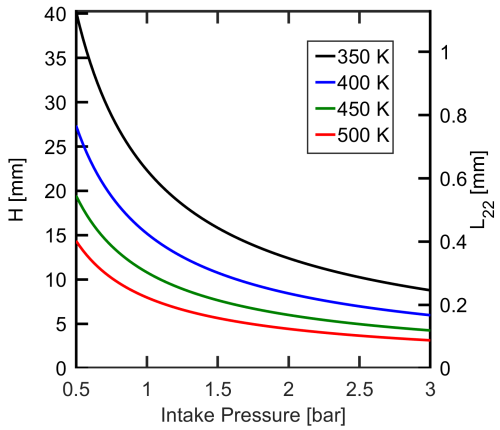

Figure 7.6: Calculated lift-off lengths (left axis) and smallest integral length scale (L_{22}; right axis) for a diesel jet during engine experiments as a function of intake pressure.

velocity measurements at spatial resolutions comparable to that of the imaging system [151].) The 0.6 mm resolution is sufficient to resolve all integral scale features for atmospheric intake conditions, and is reasonable for modest intake conditions up to 400 K at relatively low pressures as well. Signal intensity, and hence measurement precision, depends also implicitly on spatial resolution. For larger pixel sizes, more light is collected on a pixel increasing the measurement precision. As will be shown in the following sections, the 0.3 mm object plane pixel size provides a good trade-off between precision and resolution.

7.3 Parameter Space for Experiment Design

The previous sections described the basic implementation of the combined diagnostic, and estimated the resolution and temperature precision required to detect the onset of low-temperature ignition. There are still several choices that must be made regarding the combined diagnostic, including whether to use a delayed gating approach and which phosphor and technique should be used for thermometry. Additionally, for a given phosphor, many parameters are needed to characterize thermometry performance. Some parameters, including engine geometry, are fixed; Table 7.4 lists some of the optical parameters that are assumed to be fixed here. Although the APT diagnostic and formaldehyde PLIF diagnostic will likely use different optical equipment, they are assumed to have the same optical parameters for simplicity. Note that the optical, collection, and quantum efficiency parameters are only important for luminescence and formaldehyde fluorescence measurements, as scattering is assumed to be bright enough to saturate the sensor regardless of these efficiencies. PIV is assumed to be performed using the scattered UV laser light imaged by the APT scattering camera; the scattering camera is assumed to be software binned for APT measurements, while the unbinned images are used directly for PIV. Further considerations for

Table 7.4: Fixed optical parameters used for experiment design calculations.

Parameter	Value	Unit
Laser sheet thickness	0.3	mm
Pixel length	0.3	mm
Pixel volume	0.027	mm^3
Lens $f/\#$	1.4	-
Object plane dist.	0.6	m
$\Omega/4\pi$	6.4×10^{-5}	-
Collection half-angle	50	mrad
Sensor quantum eff.	0.4	-
Optical eff.	0.75	-
Max. integration duration	2	µs
Laser pulse duration	6	ns

PIV will be provided in the following sections.

The parameters in Table 7.4 are based on the PI-Max 4 camera characterized in Appendix E. In reality, the optical and sensor quantum efficiencies will vary based on the phosphor wavelength; the numbers provided are reasonable for visible emission (Eu:BAM, Ce^{3+} emission for all phosphors except Ce:$GdPO_4$, and formaldehyde fluorescence), but the efficiencies are a slight overestimate for UV emission (Ce:$GdPO_4$, Ce:CSSO host emission, and Pr^{3+} emission from Ce,Pr:LuAG).

The design space consists of the following parameters: laser energy (or fluence), particle seeding density, mean particle diameter, width of the particle size distribution, and camera gate delay. Only the laser fluence impacts the formaldehyde measurement; the remaining parameters only impact the thermometry measurement. Seeding density can have a strong impact on PIV, and at least 15 particles per interrogation region are recommended [152]. Based on the required spatial resolution, this places a lower seeding density limit at ~550 mm^3, which is consistent with typical APT seeding densities (*e.g.*, in [106, 108]). As will be shown in the following sections, the ideal seeding density for APT exceeds the lower limit needed for PIV, so the remainder of the discussion will focus on APT limits. Laser fluence will be treated as a free parameter for the performance estimates.

Excitation laser pulse duration could additionally be considered a free parameter if a different laser system was used. However, the fixed 6 ns laser pulse will be assumed for the performance estimates. The effect of laser pulse duration on performance will be discussed later.

7.4 APT Seeding Density & Size Limits

In the previous section (Section 7.2), physical arguments from chemical kinetics and turbulence were used to find a required spatial resolution and temperature precision necessary to identify ignition processes throughout a diesel fuel jet. To summarize, it was found that a object plane pixel size of approximately 0.3 mm and a temperature precision of 25 K (3%) are required to adequately observe the low-temperature ignition process. In this section, the spatial resolution and temperature precision requirements will be used to identify limits on seeding density and particle size.

Seeding density and particle size have several effects on diagnostic performance including total signal intensity, intrusiveness, and particle response or relaxation. These effects depend only on seeding density and particle size, and have been described in Chapters 4 and 6. Multiple scattering additionally is strongly impacted by particle size and seeding density, as discussed in Section 6.3, and will be considered as well.

Although phosphor luminescence intensity depends only on the mass of phosphor seeded into the flow, particle diameter impacts the measurement as well. The ratio of luminescence intensity to scattering intensity and scattering biases increases with increasing particle diameter. Using larger particles thus minimizes the impact of scattered luminescence. Increasing particle diameter also increases the particle response time. The problem of particle size and seeding density selection is reduced to maximizing both values under the constraint that the effects of intrusiveness, particle response, and multiple scattering are acceptable. Tracer particle response will be used to set an upper limit on particle diameter, while intrusiveness and multiple scattering will both be used to provide an upper limit on seeding density at fixed particle size.

7.4.1 Particle Response

Tracer particle response was investigated in detail in Section 4. Here, an upper limit on particle size will be determined that is compatible with the required spatial resolution and temperature precision. The primary effect of tracer particle response is to reduce measurement resolution. If the response time of a particle is too large, the particle is able to move between multiple measurement locations before equilibrating, potentially biasing each measurement. To address this, we require the particle response times to be sufficiently low that, on average, the particle does not leave the measurement volume before it has equilibrated.

Visualizing the fuel spray as a turbulent jet, turbulence theory predicts the displacement of a fluid element starting at the virtual origin of jet according to Equation 7.4. Solving for the time step Δt

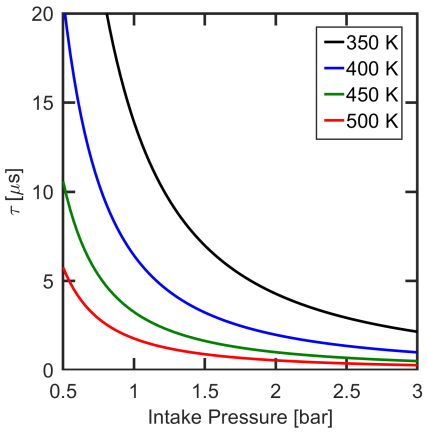

Figure 7.7: Maximum allowed particle time response as a function of engine intake conditions.

corresponding to a displacement Δz of a particle starting at the lift-off length H results in

$$\Delta t = \frac{(H + \Delta z)^2 - H^2}{2Bd_j u_j}. \tag{7.7}$$

This result calculates the time it takes for a particle or fluid parcel to move a distance Δz downstream from the lift-off location $z = H$.

To have a negligible impact on the imaging measurement, we require the allowed displacement to be half of the required spatial resolution. For a minimum lift-off length of 1 cm, and spatial resolution of 0.3 mm, the required time response is ∼5 µs. This assumes the jet orifice diameter is 140 µm and the jet exit velocity is 320 m/s.

The required time response can also be calculated as a function of lift-off length (and hence engine intake conditions) by relating the displacement to the length scale L_{22}: $\Delta z = L_{22}/2 \approx 0.15\beta H$, and the time response requirement is then

$$\Delta t = \frac{H^2}{2Bd_j u_j} 0.15\beta(1 + 0.3\beta). \tag{7.8}$$

The required time response Δt is calculated according to this expression and is plotted in Figure 7.7 as a function of engine intake conditions. From the plot, a 5 µs response time is sufficient for moderate intake conditions, but is likely not sufficient at elevated intake temperatures and pressure. For the prototypical diesel ignition experiment considered here, 5 µs will be taken as the target particle response time.

Particle response characteristics were discussed in detail in Section 6.1, including the calculation of both momentum and thermal relaxation time scales. The momentum relaxation length scale is described well by Stokes drag, with small corrections for the effects of high seeding density, non-spherical particle

shapes, and non-continuum effects to first order. The maximum particle diameter can be calculated directly by rearranging Equation 6.2 to solve for d_p, leading to

$$d_p = \sqrt{\frac{18\mu}{\rho_p}\frac{\lambda\xi}{C}\frac{\tau}{f}}, \tag{7.9}$$

where μ is the fluid viscosity, ρ_p is the particle density, λ is a dimensionless factor to account for high seeding densities, C is the Cunningham slip correction factor, and ξ is the shape factor. For the purposes of this calculation, the shape factor is held constant at 1.07 (typical of the values discussed in Section 6.1), and the Cunningham correction factor is calculated assuming the working fluid is air. At the high densities typical of engine experiments, the Cunningham correction factor is generally small, on the order of a couple percent larger than unity. The effect of seeding density is also very small even for large diameter particles; at 10^6 mm^{-3}, only a couple percent change in response time is expected. Thus, velocity response is analyzed at two conditions, $n = 0$ and $n = 10^6$ mm^{-3}. Finally, the factor f represents the degree to which the particle's velocity has relaxed. For 95% relaxation, $f = 3$.

Transient thermal response analysis, including convection, was carried out as well in Section 6.1. Thermal response is more complicated as it is coupled to the velocity response, as shown in Figure 6.6. Without more detailed information about the temperature and velocity along the particle's path, the lumped capacity response provides a good estimate of temperature equilibration time (up to 95% equilibration), even at Peclet numbers of order 1.

For the purpose of experiment design, 95% equilibration is sufficient and any error associated with incomplete equilibration is small compared to the required temperature precision. The required particle diameter for a given thermal response time from the lumped capacity model is

$$d_p = \sqrt{\frac{12k}{\rho_p c_p}\frac{\tau}{f}}, \tag{7.10}$$

where k is the fluid thermal conductivity, $\rho_p c_p$ is the particle's volumetric heat capacity, and again f is the dimensionless parameter corresponding to the degree of relaxation required (here $f = 3$, for 95% relaxation).

The maximum diameters, based on both velocity and temperature, are calculated for each phosphor particle in air (at 600 K, 30 bar) using the Dulong-Petit heat capacity for each phosphor in Table 7.5. The Dulong-Petit heat capacity is the largest heat capacity the solid can have at any temperature, and increasing gas temperature tends to increase the allowable particle diameter; thus, this combination of parameters provides a conservative estimate of response time. Similarly, Figure 7.8 plots the instanta-

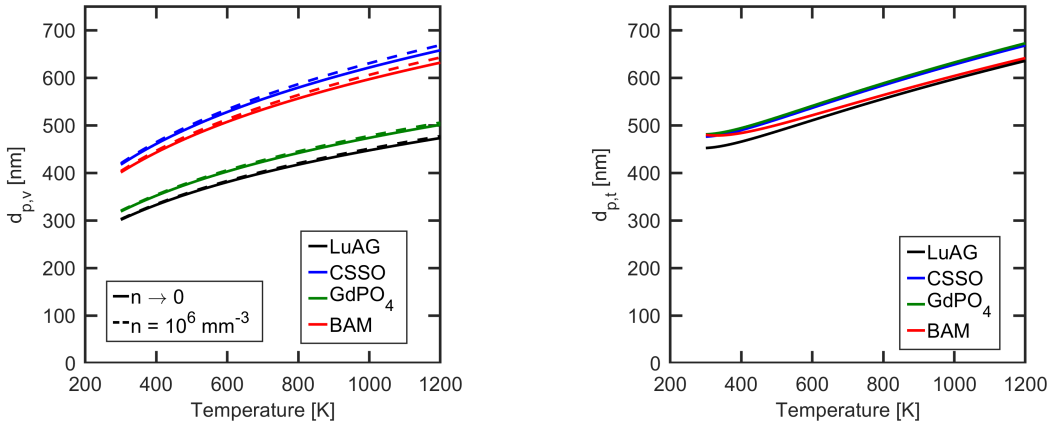

(a) Velocity

(b) Temperature

Figure 7.8: Instantaneous maximum particle diameter for each host material as a function of temperature at 30 bar based on temperature and velocity response

Table 7.5: Calculated upper limit on particle diameter in 600 K, 30 bar air. Particle heat capacity is taken in the Dulong-Petit (high-temperature) limit. Diameter based on velocity response is taken at zero seeding density, with the value at $n = 10^6$ mm^{-3} shown in parentheses.

Phosphor	$d_{p;v}$ [nm]	$d_{p;T}$ [nm]
LuAG	381 (383)	510
CSSO	528 (533)	540
$GdPO_4$	403 (406)	540
BAM	507 (513)	520

neous required diameter for each phosphor at a range of relevant temperatures. In the plots, the Debye model and best fit parameters provided in Table 4.2 and Figure 4.2 are used to calculate particle heat capacity, while air viscosity and thermal conductivity are calculated using the data and fitting parameters provide in [153]. In general, thermal conductivity and viscosity vary $\propto \sqrt{T}/\Omega(T)$ for a dilute gas following the Chapmann-Enskog theory, where the collision integral $\Omega(T)$ is a slowly-varying function of temperature and density. To first order, however, particle diameters scale with $T^{1/4}$ at relatively low densities, with some dependence on fluid properties.

From the plots in Figure 7.8, the higher density particles (LuAG and $GdPO_4$) are limited primarily by their velocity response, while the lower density particles respond much more quickly to velocity gradients and are hence limited by thermal response. Since the volumetric heat capacities of each phosphor are so similar, there is little difference in the thermal response of each particle. At higher temperatures, larger particles are acceptable because thermal conductivity and viscosity are increased. The limit on particle diameter thus should be determined at the coldest temperature where measurements should be made.

Here, 600 K is chosen as an approximate lower limit for investigation. From Table 7.5, the required diameters vary slightly with each particle, but are around 500 nm for the low density particles that are limited by temperature response (CSSO and BAM) and 400 nm for the higher density particles that are limited by velocity response (LuAG and $GdPO_4$). The response times estimated here are sufficient to adequately observe most motions at the integral length scales under consideration here; the 50% frequency response at $\omega\tau = 1$ is sufficient since turbulent motions do not need to be resolved.

7.4.2 Intrusiveness

Diagnostic intrusiveness was characterized in detail in Section 4. Here, upper limits on particle seeding density are determined to avoid significant changes to fluid temperature and momentum. An upper limit of 1% change in temperature is imposed such that the intrusiveness is negligible compared to the temperature precision. As the intrusiveness depends only on the total mass of phosphor added to the flow, and is not dependent on particle size, the calculation will be performed at the largest feasible particle size, determined in Section 7.4.1 (400 nm for LuAG and $GdPO_4$, and 500 nm for CSSO and BAM). Larger particles are advantageous as luminescence intensity is proportional to d^3, while scattering effects scale as d^2 in the intermediate to large particle size region ($x = \pi d_p/\lambda \geq 1$, where λ is the light wavelength), such that the ratio of luminescence intensity to scattering coefficient increases with d (ignoring high-frequency variation in the scattering efficiency). In contrast, changing seeding density alone has no impact on this ratio.

The relative change in temperature following the addition of phosphor particles was discussed in Section 6.2 for the particle size distributions used in previous phosphor experiments. Solving Equations 6.26, 6.27, and 6.28 for number density based on both temperature change (n_T) and velocity change (n_v) we find

$$n_T = \frac{\rho_0}{m_p} \frac{h\frac{T_0}{T} - h_0}{h_p - h_{p,0}} \tag{7.11}$$

and

$$n_v = \frac{\rho_0}{m_p} \left(\frac{v_0}{v} - \frac{T_0}{T} \right). \tag{7.12}$$

where as before, ρ is the fluid density, h is specific enthalpy, T is temperature, m_p is average particle mass, and the subscripts 0 stands for the initial condition (before seeding). For Equation 7.12, T is determined by Equations 6.26, 6.27, and 6.28.

Maximum allowable number densities were calculated according to Equations 7.12 and 7.11 and are presented in Table 7.6 at 1200 K and 30 bar, corresponding to the lowest air densities under consideration

Table 7.6: Calculated seeding density limits for each phosphor in air at 1200 K 30 bar (10.45 kg/m^3 air density) using the Dulong-Petit phosphor heat capacity.

Host	d_p [μm]	m_p[fg]	c_p [J/kg-K]	n_V [mm^{-3}]	n_T [mm^{-3}]
LuAG	381	196	590	1.1×10^5	1.4×10^5
CSSO	528	271	1020	5.1×10^4	5.9×10^4
$GdPO_4$	403	205	590	1.1×10^5	1.3×10^5
BAM	507	259	1030	5.4×10^4	6.3×10^4

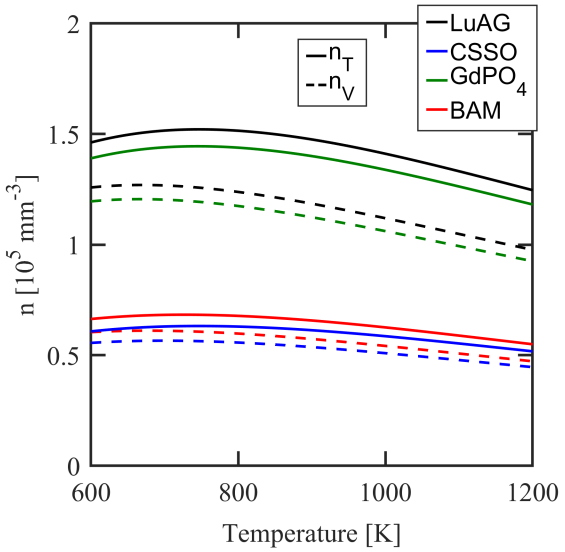

Figure 7.9: Calculated upper limit on seeding density as a function of temperature for air at 30 bar for each phosphor host material.

here. The 1% seeding density limits are additionally calculated and plotted in Figure 7.9 for a range of temperatures at 30 bar in air. In both cases, the instantaneous particle heat capacity is used from the Debye model. In both the table and the plot, the limiting diameter calculated in Section 7.4.1 is assumed for each particle.

From Figure 7.9 and Table 7.6, intrusiveness does not impose a strong limit on seeding density. Considering both temperature and velocity, very high seeding densities are feasible on the order of $10^2 - 10^3$ times larger than what was used in the experiments reported in Chapter 5. This follows because of the high air densities and relatively small particle diameters under consideration here.

7.4.3 Multiple Scattering Limits

The theory and design considerations related to multiple scattering were discussed in detail in Section 6.3. In particular, three impacts of multiple scattering were identified. First, multiple scattering can

cause signal migration, where the signal measured on a sensor is increased due to random scattering events. The increase in signal is erroneous, in that the light likely originated outside of the collection volume and is not representative of the non-scattered light that is collected directly. Second, multiple scattering can cause an increase in the width of the laser beam or sheet, decreasing the effective spatial resolution. Finally, since light must pass through the turbid medium to be imaged, multiple scattering can reduce the resolution of the measurement.

In this section, a limit on seeding density is determined based on estimates of signal migration combined with consideration of the thermographic phosphor temperature sensitivity and signal ratios at conditions expected inside the engine. In particular, an upper limit on seeding density (or rather, optical thickness) is calculated such that the maximum temperature bias is less than 1%, making it negligible compared to the required temperature precision. From this value, the impacts of multiple scattering on spatial resolution (in terms of laser sheet thickness and imaging resolution) are estimated.

Limit on Optical Thickness

An upper limit on seeding density can be estimated from the temperature uncertainty requirement. To ensure a 2.5% temperature uncertainty is possible, the multiple scattering intensity is limited to a 1% increase on a given pixel. This value is chosen to ensure that the temperature bias is small compared to the required temperature precision. The temperature bias resulting from a signal bias can be estimated from first-order uncertainty propagation as

$$\frac{b_T}{T} = \left(\frac{R}{T}\frac{\partial T}{\partial R}\right)\frac{b_S}{S}, \tag{7.13}$$

where b_x is the bias in quantity x. This calculation assumes that only a single camera is biased significantly from multiple scattering, or that the multiple scattering bias is uncorrelated between the two cameras. The magnitude of signal bias for a homogeneous environment was estimated in Section 6.3. The erroneous signal measured at any location originates, on average, from every point inside the cylinder with similar probability. Thus, the signal bias magnitude b_S is evaluated at the mean temperature inside the engine. However, the signal measured at any given pixel is dependent on the local temperature. Taking this into account the temperature bias can be written as

$$\frac{b_T}{T} = \left(\frac{R}{T}\frac{\partial T}{\partial R}\right)\frac{b_S(\langle T\rangle)}{S(T)} = \left(\frac{R}{T}\frac{\partial T}{\partial R}\right)\frac{b_S(\langle T\rangle)}{S(\langle T\rangle)}\frac{R(T)}{R(\langle T\rangle)}. \tag{7.14}$$

The quantity $b_S(\langle T\rangle)/S(\langle T\rangle)$ is the relative signal increase from multiple scattering as defined previously, where for simplicity the engine is assumed to be at temperature $\langle T\rangle$. The quantity $R(T)/R(\langle T\rangle)$ measures the relative intensity of the signal at a given temperature to that at the average temperature in the cylinder. If a measurement is made at a point where the ratio is large (and signal very low) compared to the average value in the engine, the temperature bias is increased. In contrast, if the engine is hot on average and a measurement is made in a cold region, the multiply scattered "hot" light has a much smaller impact relative to the brighter "cold" light.

An estimate of the impact of temperature non-uniformity can be found from simple models of luminescence lifetime quenching. From Equation 4.4, normalized by the room temperature value, the ratio can be estimated as

$$R \approx 1 + C_{NR} e^{-\Theta/T}, \tag{7.15}$$

where C_{NR} is the nonradiative attempt rate (around 10^6, based on data in Table 4.4), and $\Theta = E/k_B$ is the characteristic temperature of the deactivation process (for a 1 eV energy gap, $\Theta = 11,600$ K). From this model, the sensitivity of temperature to multiple scattering intensity is

$$\left(\frac{R}{T}\frac{\partial T}{\partial R}\right)\frac{R(T)}{R(\langle T\rangle)} = \frac{T e^{\Theta/T}}{\Theta C_{NR}}\frac{(1 + C_{NR}e^{-\Theta/T})^2}{1 + C_{NR}e^{-\Theta/\langle T\rangle}}. \tag{7.16}$$

At and above the onset of quenching (around $T/\Theta \approx 0.05$), where temperature measurements are first possible, this sensitivity to multiple scattering is generally minimized. For $C_{NR} = 10^6$ and $\bar{T}/T \approx 0.8$, this sensitivity is generally near or below 1 at all temperatures. Two plots of the multiple scattering sensitivity as defined by Equation 7.16 are shown in Figure 7.10. From the Figure, the sensitivity of the temperature bias to multiple scattering intensity is at most ~1 for moderate temperature fluctuations of up to ~20%. This means that a 1% multiple scattering signal bias results in at most a 1% temperature bias, and thus 1% multiple scattering signal bias is used to determine the upper limit on optical thickness.

For the purposes of experiment design, the upper limit on τ_0 will be taken as 0.01, which corresponds conservatively to $\Delta I/I \approx 0.03$, using the correlation provided in Figure 6.10. The upper limits on seeding density imposed by limiting signal migration as discussed in this section are calculated using the particle diameters determined in Section 7.4.1, and the optical engine cylinder height at TDC is estimated at 10 mm. The estimates are provided in Table 7.7. Two results are shown, one using the Mie scattering cross-section and one using a constant scattering efficiency of two. Since a range of particle sizes are necessarily used due to an imperfect particle size distribution, and the Mie scattering efficiency is a highly oscillatory function of particle diameter, the constant scattering efficiency of two provides an additional

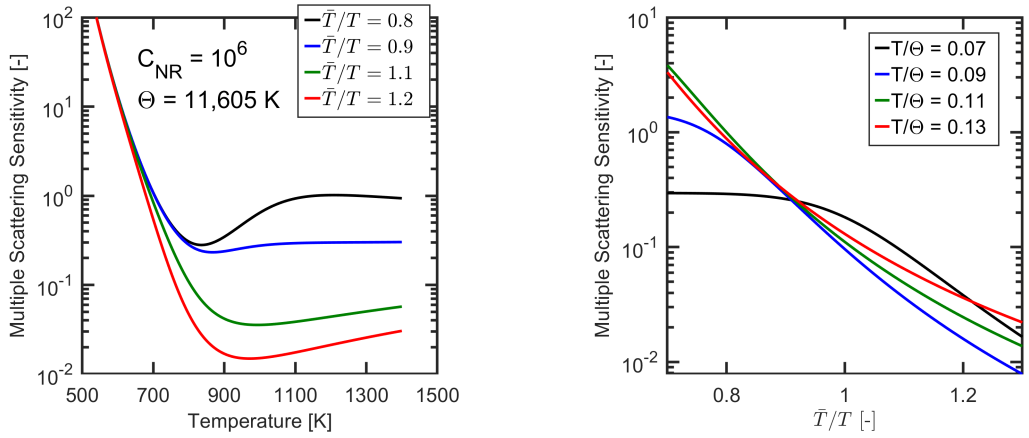

(a) Sensitivity versus local temperature

(b) Sensitivity versus mean temperature

Figure 7.10: Calculated sensitivity of temperature to multiple scattering intensity for different operating conditions and temperature non-uniformity. (a) Sensitivity as a function of local temperature for several mean temperature values. (b): Sensitivity as a function of normalized mean temperature for several local temperature values. For all cases, the non-radiative attempt rate $C_{NR} = 10^6$, consistent with data reported here.

Table 7.7: Calculated seeding density limits for each phosphor based on multiply scattered light intensity. Optical thickness is chosen as $\tau_0 = 0.01$, and particle diameters are based on the results of Section 7.4.1. Scattering efficiency is calculated based on the selected particle diameter d_p.

Host	$\boldsymbol{d_p}$ **[nm]**	$\boldsymbol{Q_{Mie(d_p)}}$ **[-]**	$\boldsymbol{n_{Q=2}}$ **[mm^{-3}]**	$\boldsymbol{n_{Mie}}$ **[mm^{-3}]**
LuAG	381	2.0	4300	4500
CSSO	528	3.1	2200	1500
$GdPO_4$	403	1.7	3900	4500
BAM	507	2.2	2500	2200

estimate of number density that is less susceptible to uncertainty in particle physical properties.

The seeding density limits imposed by multiple scattering are significantly more strict than those imposed by intrusiveness, and are independent of pressure. The requirements provided by this estimate are reasonable; measurements have been made successfully using APT at similar or lower seeding densities [83]. Note that these seeding density limits (particularly given the small particle sizes) are also sufficiently strict that the effect of particle seeding on the local velocity profile is negligible, as discussed at the end of Section 6.2.

Laser Sheet Thickness

For simplicity, and as an upper bound, the laser sheet thickness is estimated using Equation 6.36 with $\alpha = 1/3$ (corresponding to the solution by [136]) as a conservative estimate after propagating across the

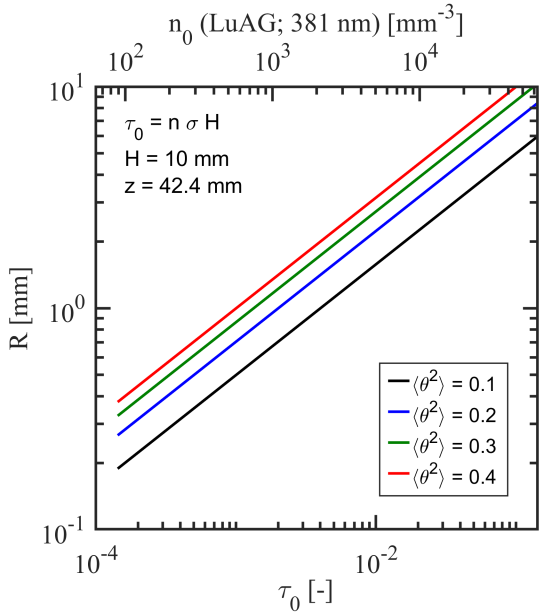

Figure 7.11: Calculated laser sheet beam spread at the center of the cylinder due to multiple scattering. The optical thickness τ_0 on the bottom axis corresponds to the same definition (based on cylinder height) used in Section 7.4.3. Beam thickness is calculated after propagating across half the bore, at $z = 42.4$ mm.

radius of the cylinder. The optical thickness ($\tau_0 = n\sigma H$; the same quantity used in Section 7.4.3) is used as the independent variable because it is independent of particle size and composition; the corresponding seeding density for a 381 nm LuAG particle is shown on the top axis. The optical thickness is calculated assuming the height of the cylinder is 10 mm (corresponding to the optical engine cylinder at TDC). The multiply-scattered laser beam shape is Gaussian. The approximate Gaussian width of the beam is $R = z\sqrt{\alpha n \sigma z \langle\theta^2\rangle}$, and the 5-95% width is thus approximately $4R$. The calculated beam spread function width R is plotted in Figure 7.11 for a range of cylinder optical thickness values. Several values of $\langle\theta^2\rangle$ are included. From the plot, a thickness of over 1 mm is possible even for low seeding densities and optical thickness values, and for strongly forward scattering particles. To achieve laser sheet thickness of 0.3 mm across the entire field of view, it may be necessary to devise a strategy to reduce beam divergence, *e.g.*, by using a slightly converging laser sheet.

7.5 APT Performance

In the previous sections, the optimum particle diameter and maximum number density were determined for each phosphor for the target temperature precision of 2.5% and spatial resolution of 0.6 mm (the best case pixel size to achieve this resolution is 0.3 mm), determined from turbulent gas jet theory and

chemical kinetics considerations. Using those results, diagnostic performance is estimated and presented here for several APT techniques for an assumed experimental geometry (details are provided in Section 7.1.1; for simplicity formaldehyde collection optics are not included here). The calculations also make some assumptions about the equipment used in the experiment, and in particular the intensified CCD cameras; sensor characterization information is provided in Appendix E, and the noise factor is assumed to be 2.0 at maximum gain. The filter set used to capture the luminescence emission can also have an impact on the quality of the measurement; for simplicity, each phosphor is assumed to have filters sufficient for a 30% combined photocathode and optical efficiency. This corresponds to around 80% filter transmission efficiency over the entire emission spectrum of each phosphor, and is assumed to be independent of temperature.

All of this information is now used to estimate achievable temperature precision with each phosphor. There are 4 important parameters that have not been specified yet: laser pulse duration, total laser fluence, integration duration, and gate delay. For the initial estimate, laser fluence will be considered a free parameter and several values will be used. Laser pulse duration will be held constant at 6 ns, integration duration will be long enough to capture the entire emission at room temperature, and there will be no gate delay. This is representative of an ideal case with no significant background radiation to avoid from formaldehyde or other sources. Additional considerations will be made later for less ideal conditions, and alternative excitation sources.

To estimate temperature precision, the following procedure is used. First, the air conditions at IVC are specified (here, 1 bar and 350 K), along with the intake seeding density. The intake seeding density is calculated from the estimated upper limit on optical thickness from multiple scattering (note that optical thickness is a constant throughout the compression stroke regardless of whether fuel is added or not; from Section 6.3, only the optical thickness controls the amount of multiple scattering). The compression stroke is assumed to be isentropic, and the new temperature and cylinder volume is calculated as a function of crank angle. At each point, the luminescence signal measured on each camera is calculated based on the specified parameters, signal modeling results of Section 4.6, instantaneous seeding density, and particle size. For SRAPT techniques, scattering signal is assumed to be bright enough to saturate the sensor at the highest density point, and signal levels at other conditions are simply scaled by the seeding density. For each camera, a signal-to-noise ratio is determined based on characterization data presented in Appendix E. These values are used to calculated the ratio precision, and the additional SRAPT error (see Section 6.6) is modeled and included assuming a log-normal PSD with a 15% width ($s = 0.15$). A flatfield correction is assumed to be performed at the lowest temperature (350 K) using 200 images, and this is included in the ratio precision estimate. Temperature precision

is calculated using the theory provided in Section 4.7. Temperature measurement bias is estimated as well using a 5% shot-to-shot variation in laser energy, and a 2% long-term laser energy drift (*i.e.*, a 2% difference in fluence between the flatfield data and the measurement). Both of these values are consistent with the Ekspla NL303-D-10 laser at 266 nm operation.

This calculation is repeated starting at the conditions calculated for TDC, and assuming volume is constant with temperature swept from 600 to 1200 K to simulate possible conditions during injection and ignition. In this case, the seeding density is constant, but is reduced by 4% to simulate the addition of fuel (4% fuel mole fraction corresponds to an equivalence ratio of just over 2 for n-heptane). Since low-temperature chemistry is believed to begin near the lean, hot edge, this represents a conservative estimate of seeding density.

7.5.1 SRAPT Performance

The temperature precision and bias estimates are provided for Ce:LuAG (Ce^{3+}) SRAPT (355 nm excitation) and Eu:BAM (Eu^{2+}) SRAPT (355 nm excitation) in Figure 7.12, and for the Ce:CSSO Ce^{3+} SRAPT and host SRAPT techniques (unannealed only; 266 nm excitation) in Figure 7.13. The Ce,Pr:LuAG (Ce^{3+} SRAPT, 266 nm excitation) technique is also shown in Figure 7.12 for comparison with Ce:LuAG. The other phosphors are excluded because the estimated temperature precision indices are much too large to be feasible options.

The SRAPT performance estimates show that Eu:BAM can provide a reasonable measurement throughout much of the compression stroke and at TDC for the assumed constant pressure combustion from 800 to over 1000 K; a precision of ∼20 K or better is possible near 800-1000 K. Extrapolating to higher fluences suggests that performance decreases at higher fluence. While sensitivity does decrease in general for Eu:BAM with increasing fluence, Eu:BAM is completely saturated according to the 3-level model at 10 mJ/cm^2 and hence extrapolating beyond this point may provide inaccurate results. For Ce:LuAG (Ce^{3+} SRAPT), similar 20 K precision may be possible at sufficiently high fluence, and there is evidence that Ce:LuAG at 355 nm excitation does not saturate until $>$ 50 mJ/cm^2 [85], possibly providing an improvement in performance. Ce:LuAG performance appears to suffer significantly beyond 1000 K, and in particular biases become significant or even dominant due to the large multiple scattering bias. Ce,Pr:LuAG has similar trends in performance, but is generally worse throughout most of the temperature range; this is likely a result of poor excitation efficiency of Ce^{3+} at 266 nm. Ce,Pr:LuAG could be improved by increasing seeding density as the multiple scattering bias is relatively small compared to the temperature precision near 1000 K. However, for measurements above 800 K, Ce:LuAG at 355 nm

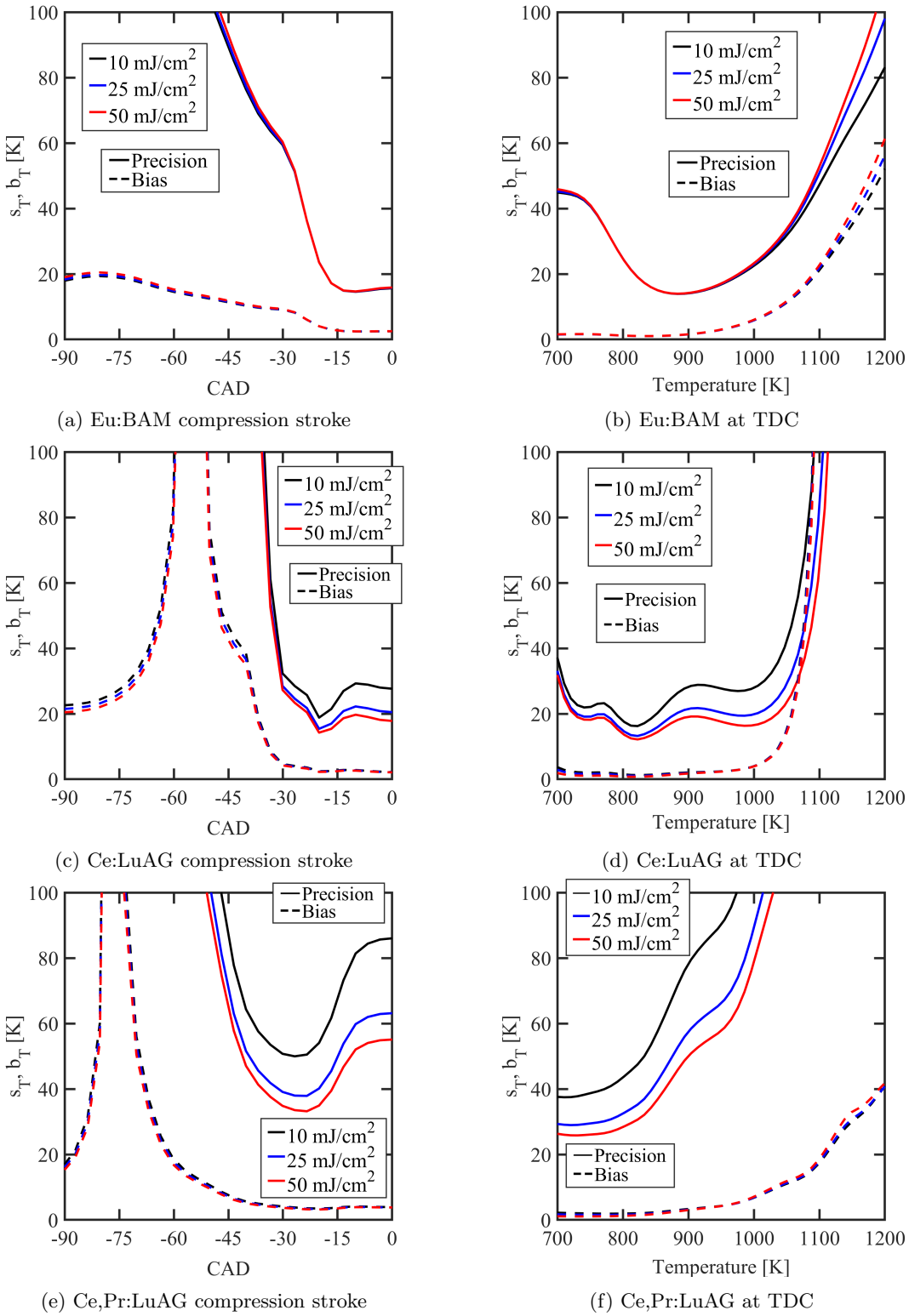

(a) Eu:BAM compression stroke

(b) Eu:BAM at TDC

(c) Ce:LuAG compression stroke

(d) Ce:LuAG at TDC

(e) Ce,Pr:LuAG compression stroke

(f) Ce,Pr:LuAG at TDC

Figure 7.12: Estimated performance for Eu:BAM Eu^{2+} SRAPT (355 nm excitation), Ce:LuAG (355 nm excitation) and Ce,Pr:LuAG Ce^{3+} SRAPT (266 nm excitation) in the optical engine during the compression stroke and at constant pressure at TDC. Pressure is calculated assuming isentropic compression from atmospheric pressure, 350 K air intake, and is approximately 32 bar for the constant pressure case. The laser pulse duration is 6 ns.

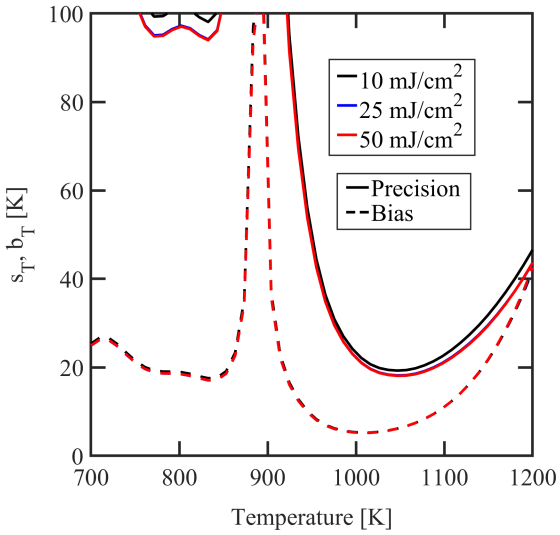

(a) Ce:CSSO Ce^{3+} SRAPT at TDC

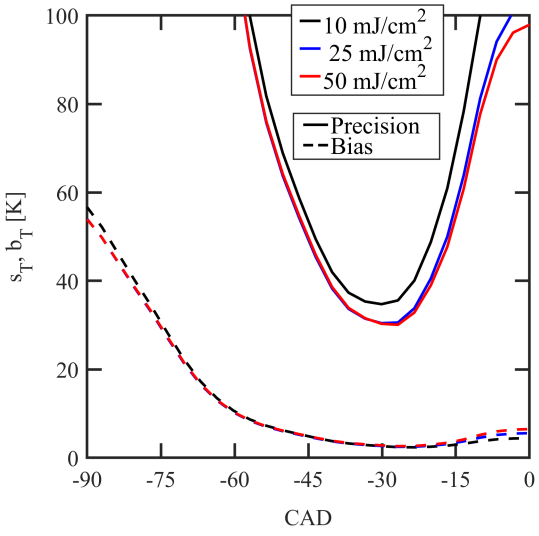

(b) Ce:CSSO host SRAPT compression stroke

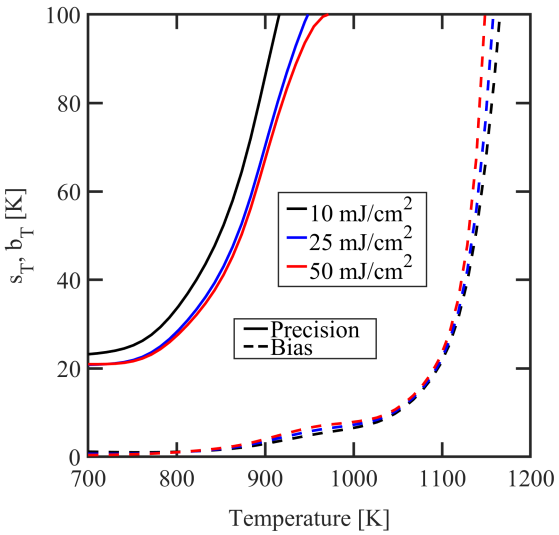

(c) Ce:CSSO host SRAPT at TDC

Figure 7.13: Estimated performance for Ce:CSSO Ce^{3+} SRAPT (top row) and host SRAPT (bottom row) in the optical engine. For Ce^{3+} SRAPT, performance is only shown for the constant pressure combustion case because the technique does not work well below 900 K. For host-SRAPT, performance is shown for both the constant pressure and compression stroke cases. Pressure is calculated assuming isentropic compression from an initial atmospheric pressure, 350 K air intake, and is approximately 32 bar for the constant pressure case. Calculations are performed at 266 nm excitation with a 6 ns laser pulse duration.

excitation and Eu:BAM are superior to Ce,Pr:LuAG for this application.

The CSSO phosphor unsurprisingly works well at high temperature; although no performance information is included during the compression stroke since the phosphor does not work well until at least 900 K. The Ce:CSSO Ce^{3+} SRAPT technique is expected to have a temperature precision of better than 20 K between 1000 and 1100 K, and slightly worse precision at higher temperatures. One of the most significant features of the raw Ce:CSSO sample is that even at 1200 K, temperature precision better and bias of less than 40 K is possible. The host SRAPT is also a viable option at lower temperatures providing at best 30 K precision from 700-800 K. As noted in Chapter 5, there is a sensitivity gap such that continuous measurements may not be possible with high precision from 850 to 950 K.

Each of the plots in Figures 7.12 and 7.13 additionally shows the estimated temperature bias magnitude as dashed lines. The bias contains a contribution from shot-to-shot variation in laser energy (5%) and long-term laser energy drift (2%) based on manufacturer specifications of the Ekspla NL-303D-10 laser, and a 5 K systematic uncertainty in the temperature at IVC (where the whitefield correction is assumed to be performed). The plot additionally contains the multiple scattering bias calculated according to Equation 7.14. The multiple scattering bias is generally the dominant term, particularly at high temperatures. From the plots, the bias is relatively small compared to the single-shot precision throughout most of the temperature range but becomes significant near each phosphor's upper temperature limit; this is expected since measurement of the hot phosphor particles (which emit only weakly) are impacted more strongly by the "cold", bright background radiation. The constant pressure combustion case assumes $\langle T \rangle \approx 940$ K, which is the estimated air temperature at TDC; this may slightly underestimate the multiple scattering bias.

The estimated bias is similar in magnitude, but smaller than the temperature precision requirement in general; at lower temperatures, the bias is much lower than the required precision. It is thus possible to increase the seeding density without increasing the bias indicator above 25 K for a subset of the target temperature range. Increasing seeding density (effectively reducing the precision index but increasing the bias indicator) may be beneficial for dimmer phosphors like Ce,Pr:LuAG where the Ce^{3+} emission only reaches around 5,000 counts at 700 K for the fired condition, and 50 mJ/cm^2. This is not the case for Ce:LuAG, where the bias is already comparable to the estimated precision near 1000 K. Instead, the bias for Ce:LuAG could be reduced by slightly lowering seeding density, although this would also impact the precision. At these same conditions, however, the Eu:BAM emission is almost bright enough to saturate the camera (over 30,000 counts) and would benefit little from increased seeding density. For comparison, the Ce:CSSO Ce^{3+} emission is around 10,000 counts at this condition, and Ce:CSSO host emission is around 5,000 counts.

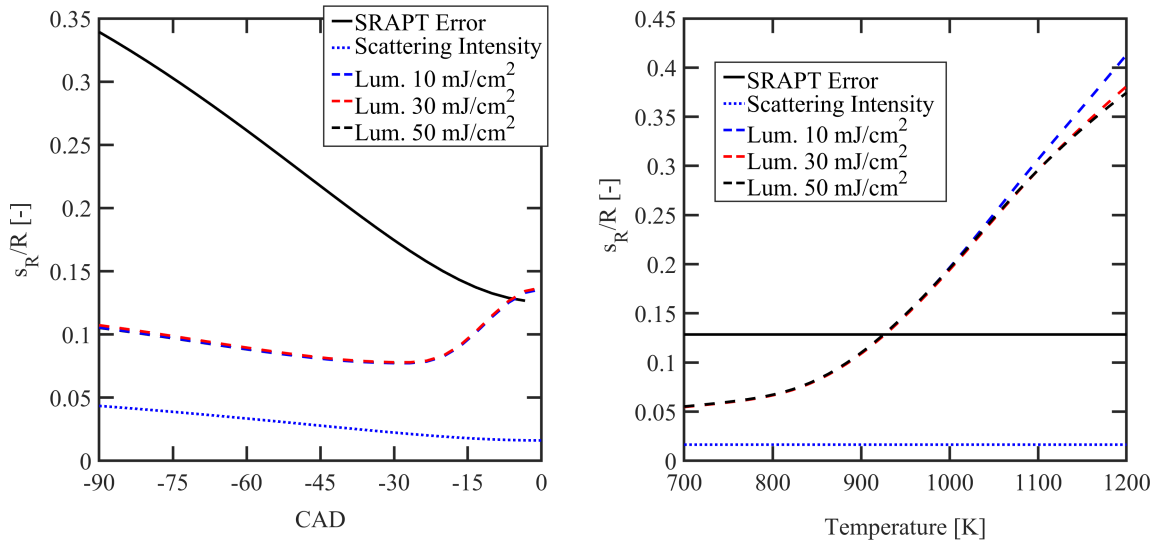

(a) Compression stroke

(b) Constant pressure

Figure 7.14: Calculated sources of ratio noise for Eu:BAM SRAPT technique for the compression stroke and constant pressure combustion cases.

It is instructive to outline the different primary sources of noise in the diagnostic. For this purpose, Eu:BAM will be used as an example although for all of the SRAPT measurements presented in Figures 7.12 and 7.13 the behaviours are similar. The primary sources of noise in the ratio measurement can be attributed to camera noise (two measurements, 1 per camera) and additional noise in the SRAPT measurement. These noise sources are plotted as a function of temperature (for the constant pressure calculation) and crank angle (for the compression stroke calculation) in Figure 7.14. From the plots, the added SRAPT error is relatively large and similar in magnitude to the signal precision in the luminescence band. The SRAPT error is particularly large early in the compression stroke because of the low seeding density. Because the scattering signal is so bright, it contributes very little to the total ratio precision (about 2% at the highest seeding densities). Instead, the precision is dominated by the shot-noise of the luminescence measurement and the noise resulting from the particle size distribution. At the highest temperatures, and especially for the dimmer phosphors, the measurement precision is dominated by the noise in the luminescence intensity measurement.

7.5.2 Co-doped and combined performance

The co-doped technique using the Ce,Pr:LuAG and Ce:CSSO phosphors are intended to cover an intermediate temperature range and extend the range at which measurements can be obtained. For Ce,Pr:LuAG, combining co-doped and SRAPT measurements has been shown to provide a continuous

measurement from 300 to 1000 K. Similarly, measurements with Ce:CSSO phosphor provide a possibility for temperature imaging up to over 1200 K by combining the host-referenced and SRAPT approaches. As such, this section will discuss performance that can be achieved using the co-doped Ce,Pr:LuAG phosphor and the singly-doped Ce:CSSO phosphor using a combination of SRAPT, co-doped APT (for Ce,Pr:LuAG) and host-referenced APT (using Ce:CSSO) approaches.

For analysis, temperature imaging performance is calculated in an identical fashion to the SRAPT performance estimates. The performance of each technique is determined individually, then a combined temperature precision is calculated using a weighted average as described in Section 4.7.4. Temperature biases are included in the calculation and plots, but are not included in the weighting of the diagnostics. Instead, the temperature biases are included as an upper limit on the potential bias that could be expected; including temperature bias in the weighted average procedure would likely have a negligible impact on the result as the temperature biases of the individual techniques are very small compared to the temperature precision on a single-shot basis, except at the highest temperatures.

The calculated diagnostic performance is shown in Figure 7.15 for both phosphors, and for both the compression stroke and the assumed constant pressure combustion scenario starting at TDC. The performance of both phosphors is relatively good throughout different portions of the compression process. Ce,Pr:LuAG performs best at lower temperatures; however, this is balanced by the low seeding density in the earlier portion of the compression stroke so measurements with any phosphor are not really possible until -75 CAD. The Ce:CSSO phosphor actually appears to perform well over the entire temperature range, specifically at TDC during the assumed constant pressure combustion event. The host-referenced and host-SRAPT techniques together give better than 30 K precision up to ∼850 K, then the Ce^{3+} SRAPT dominates above 950 K again providing better than 30 K precision from at least 1000 to almost 1150 K. By combining techniques appropriately, the gap from 850 to 950 K fills in slightly as well, resulting in ∼80 K precision at worst between 850 and 950 K. Increasing fluence has the effect of generally increasing signal intensity and decreasing temperature sensitivity; both of these effects are actually beneficial in reducing the temperature gap of Ce:CSSO from 850 to 950 K, increasing signal measurement precision. It is possible that at higher fluences the temperature gap may be reduced even further.

It is additionally instructive to consider the sources of noise in the co-doped temperature measurement. From the discussion of SRAPT, it was clear that there were two significant sources of noise: the luminescence intensity measurement and the particle size distribution. In co-doped APT and host-referenced APT, there is no noise from the particle size distribution. However, since both signals are luminescence measurements, both signal bands are relatively weak and thus subject to a significant

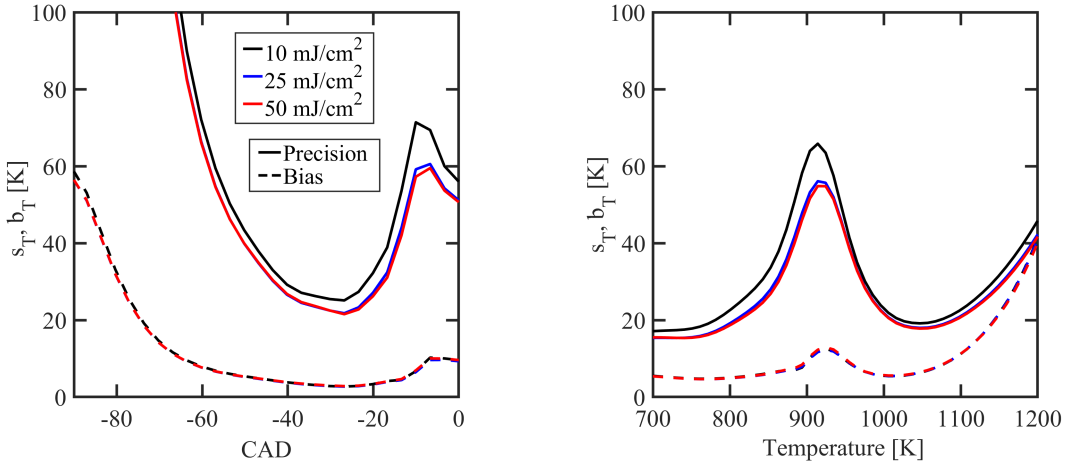

(a) Ce:CSSO compression stroke

(b) Ce:CSSO TDC

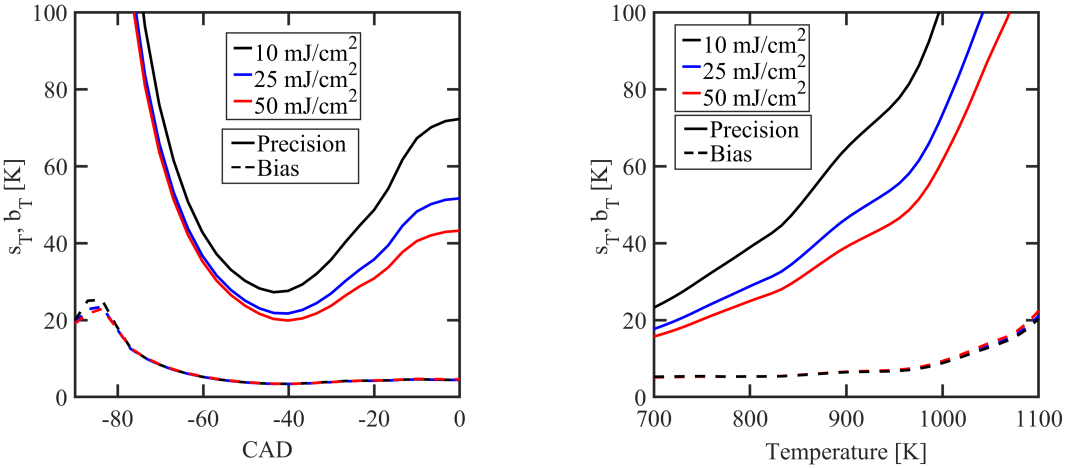

(c) Ce,Pr:LuAG compression stroke

(d) Ce,Pr:LuAG TDC

Figure 7.15: Estimated performance for Ce:CSSO (top row) and Ce,Pr:LuAG (bottom row) combined techniques in the optical engine during the compression stroke (left) and at constant pressure at TDC (right). Pressure is calculated assuming isentropic compression from an initial atmospheric pressure, 350 K air intake, and is approximately 32 bar for the constant pressure case. All calculations assume a 6 ns duration laser pulse and 266 nm excitation.

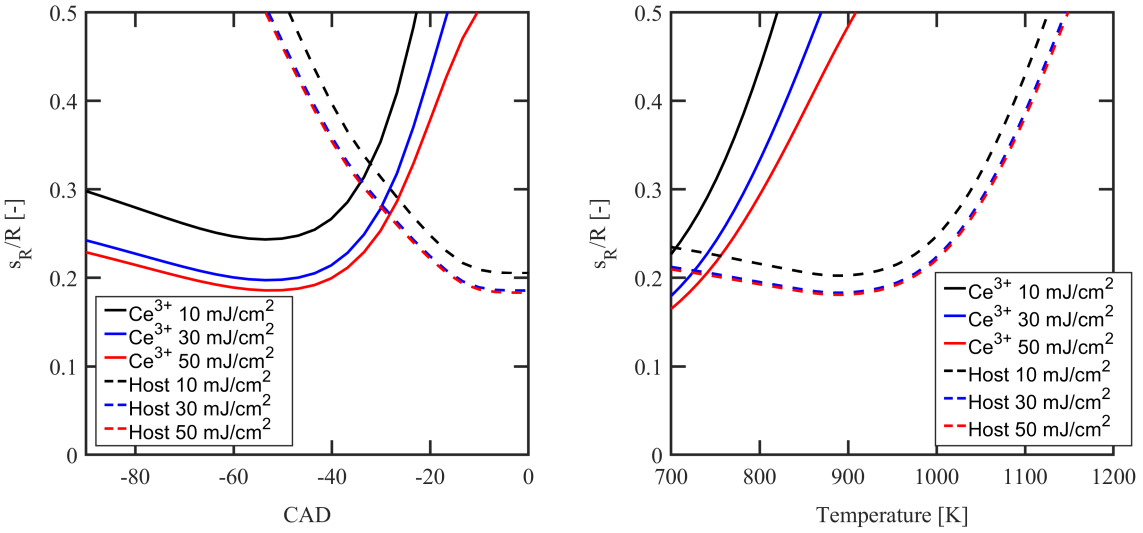

(a) Compression stroke

(b) Constant pressure

Figure 7.16: Calculated noise sources for the Ce:CSSO host-referenced technique for the compression stroke and the constant pressure combustion calculation.

amount of noise. From Figure 7.14, the PSD noise was similar in magnitude to the luminescence noise at moderate temperatures. It can thus be concluded that in switching to co-doped APT, the PSD noise term is replaced by a second luminescence noise term of similar magnitude, and the total ratio precision is not altered significantly. However, the two luminescence terms are both temperature dependent whereas the PSD noise is not. As an example, the noise terms for the host-referenced Ce:CSSO technique are shown in Figure 7.16. At low temperatures, where the host-referenced technique is viable, the noise components are similar and the host-referenced technique performs similarly to the SRAPT techniques.

7.5.3 Equipment Effects

A best-case temperature precision can be estimated for the case where a perfect sensor is used, with a gain factor of unity, zero read noise, and perfect efficiency. This represents a theoretical perfect detector, and as such, also represents the most precise measurement that is possible. Performance estimates are provided for the Ce:LuAG (355 nm excitation) technique and the combined unannealed Ce:CSSO technique using the assumed perfect sensors. Since scattering is so bright compared to luminescence, the contribution of the scattering signal is negligible. The precision and bias estimates are plotted below in Figure 7.17. Clearly a large performance improvement is possible, on the order of a factor of 2 or better, with precision indices lower than 10 K in some ranges. Throughout most of the range, the bias indicator is at or below 10 K; as before, increasing seeding density can improve temperature precision

($\propto n^{-0.5}$) at the cost of increasing the bias (dominated by multiple scattering; $\propto n^{0.9}$).

7.5.4 Reflection Analysis

An analysis of reflections from a surface near a laser sheet or source was carried out in Section 6.4. Using the assumed optical parameters, specifically the collection half-angle of 50 mrad and assuming the laser sheet is centered in the cylinder at TDC (such that the distance between the sheet and the head is 5 mm), light originating from a given location within the laser sheet after reflection off the cylinder head is collected from within a distance of ∼0.5 mm, which is very close to the acceptable spatial resolution limits. If the engine head is polished, the reflectance at best could be as high as perhaps 60%, such that a 30% increase in signal is possible with a very small loss in spatial resolution; this could potentially improve diagnostic precision by up to 10-15%, assuming the diagnostic is shot-noise limited, and that the ratio precision is limited by the luminescence measurement.

For diffuse reflection, this is not the case; since the laser sheet is 5 mm from the reflecting surface, diffuse light is collected from as far as 10 mm or more. It is thus necessary to reduce diffuse reflections as much as possible. This can be done with high-temperature paint, such as the Tempil Pyromark 1200 or Tempil Pyromark 2500 paint manufactured by Markal, which has a reported emissivity of 97% (or reflectively of around 3%) for near UV wavelengths and is suitable for high-temperature and combustion applications. Although this meets the maximum reflection coefficient discussed in Section 6.4, diffuse reflections may still be a problem and can potentially bias the temperature imaging result. Additional experiments may be needed to verify the reflection coefficients and angular distribution of reflected light in the engine to further reduce the impact of surface reflections.

7.5.5 APT Gate Delay

Earlier in this chapter, interference between diagnostics has been discussed as a potential bias in the formaldehyde PLIF measurement due to phosphor radiation at similar wavelengths. However, the formaldehyde PLIF measurement is just as likely to interfere with the APT measurement, particularly if they use the same excitation wavelengths and collection bands. One potential method to avoid interference in the APT diagnostics is to delay gating of the intensifier, such that light is only captured after the bulk of the formaldehyde emission is complete (this method naturally requires the use of intensified cameras as other systems are not capable of shuttering or gating on a nanosecond time scale). The formaldehyde lifetime depends on temperature and pressure; at 770 K and 10 bar, it was measured at about 6 ns in nitrogen [47]. From Chapter 3, extrapolating to 1000 K and 30 bar puts the lifetime

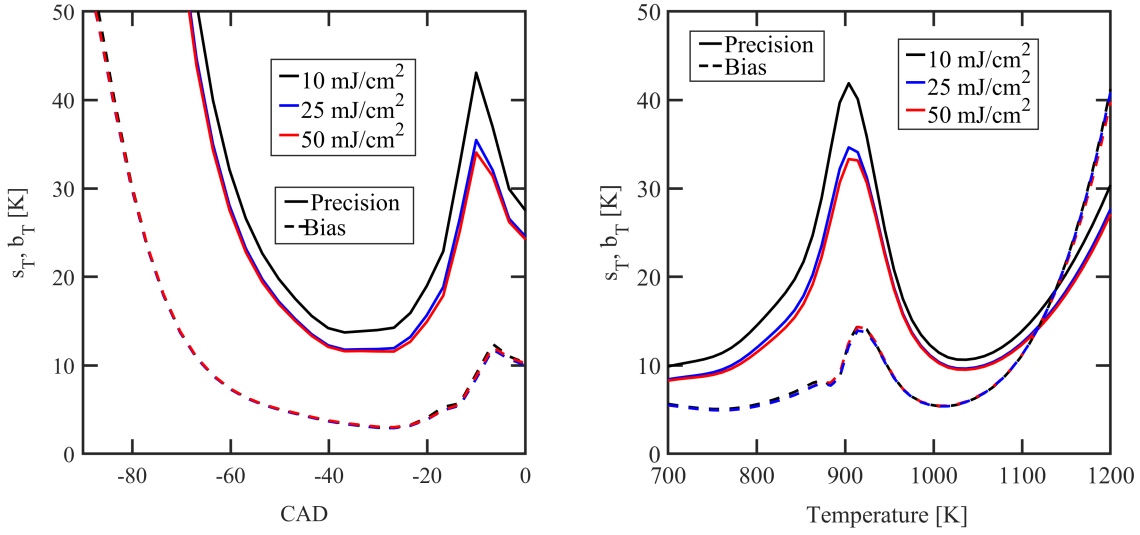

(a) Ce:CSSO compression stroke

(b) Ce:CSSO TDC

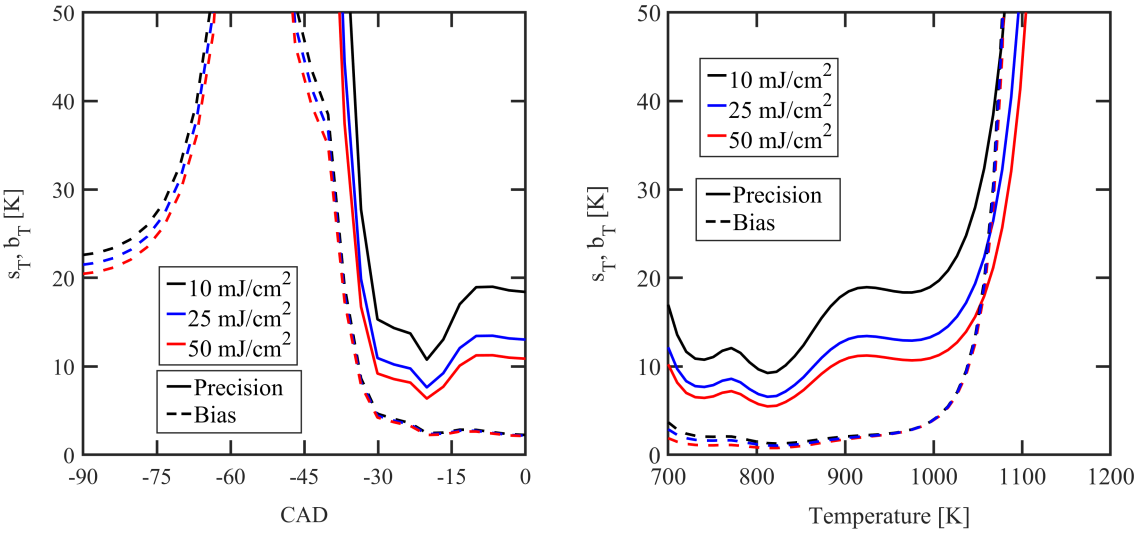

(c) Ce:LuAG compression stroke

(d) Ce:LuAG TDC

Figure 7.17: Calculated temperature precision and bias for the unannealed combined Ce:CSSO (top row) and Ce:LuAG (355 nm excitation) SRAPT techniques (bottom row) for a perfect image sensor and optics for the compression stroke (left column) and constant pressure at TDC (right column).

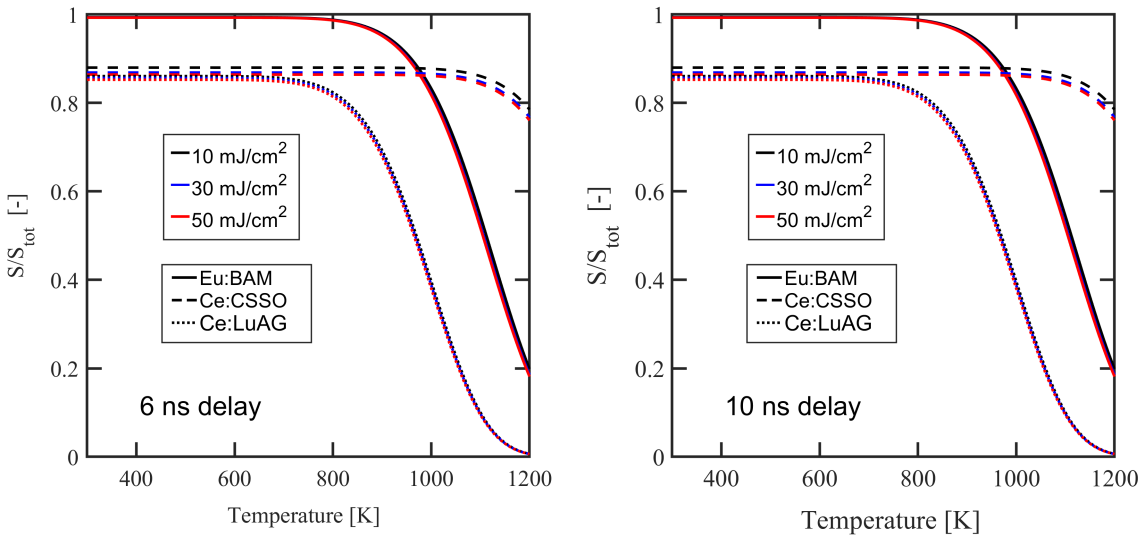

(a) 6 ns

(b) 10 ns

Figure 7.18: Calculated signal intensity of Eu:BAM and Ce:CSSO after a 6 ns and 10 ns gate delay. The signal intensities are normalized to their value with zero gate delay.

closer to 3 ns, and in air (assuming 20% oxygen, 80% nitrogen mole fractions) the lifetime is ∼1.0 ns. Ideally, gating should be delayed by at least 2.5 lifetimes beyond the laser pulse width to ensure no formaldehyde emission is captured; including the 6 ns laser pulse and 3 formaldehyde lifetimes, gating should therefore be delayed by a total of 9 ns.

The effect of a gate delay on emitted signal intensity was described using the three level model in Section 4.6. Mathematically, Equation 4.8 is integrated starting at time $t = t_d$ where t_d is the gate delay. The upper integration limit is unaffected. The signal incorporating a gate delay was calculated for Eu:BAM and Ce:CSSO (luminescence bands only), and is plotted in Figure 7.18 normalized by the value with no gate delay. Two gate delays are shown, 6 ns and 10 ns. The shorter gate delay corresponds to only the laser pulse, while the longer delay corresponds to at least 2.5 formaldehyde lifetimes in air at any temperature and pressure combination above 700 K and 30 bar.

For Eu:BAM, the delayed gating approach is feasible up to over 1000 K when the Eu:BAM lifetime drops quickly and becomes shorter than or comparable to the gate delay. Ce:CSSO similarly is not strongly affected even at high temperatures due to its high quenching temperature; however, Ce:CSSO exhibits around a 10-20% loss in signal intensity because its room-temperature lifetime is only around 70 ns. Similarly, Ce:LuAG exhibits a modest loss in signal at lower temperatures, around 10-20% but much of the signal is still collected until around 900 K when the lifetime is reduced.

The delayed gating approach is feasible for Eu:BAM without significant loss of signal, at least up

to 1000 K. This is advantageous because the formaldehyde and Eu:BAM emission bands overlap significantly, and they are excited at the same wavelength. For Ce:CSSO, delayed gating is possible even at temperatures over 1000 K, but there will be a small impact on performance (on the order of 10% increase in noise, or less); delayed gating also is possible with Ce:LuAG up to modest temperatures (at least 900 K). The delayed gating approach would result in an additional factor of 2 reduction in emission intensity (or $\sim \sqrt{2}$ reduction in precision) because a broadband beamsplitter is needed to image the phosphor and formaldehyde luminescence simultaneously.

For CSSO host emission and Pr^{3+} emission from either LuAG or CSSO, the phosphor lifetimes are likely too short to be able to delay several formaldehyde lifetimes beyond the laser pulse duration and still capture a significant portion of the signal at elevated temperatures (*e.g.*, Pr:CSSO has a lifetime of only a few nanoseconds at 700 K). However, each of these signals are deeper in the UV. Background rejection can be achieved instead by restricting the collection bands to less than 370 nm; although restricting the collection bands in this way could reduce collection efficiency by up to a factor of 2, resulting in up to 40% increase in noise.

7.5.6 266nm-355nm Laser Co-propagation

So far, very little has been said about the excitation wavelength used for the experiments. Formaldehyde excitation implicitly assumes 355 nm here, and phosphor excitation was performed and characterized at either 355 nm (for Eu:BAM, or singly-doped Ce:LuAG) or 266 nm (for all other phosphors). Clearly, if any phosphor except Eu:BAM or Ce:LuAG were selected, then two laser sheets must be co-propagated. Using two laser sheets simultaneously has several impacts on diagnostic performance relating to background radiation. These impacts will be discussed here briefly.

The first impact to be discussed is the excitation of formaldehyde at 266 nm. Formaldehyde does indeed absorb light weakly at 266 nm, corresponding to the $\tilde{X}\ ^1A_1 \rightarrow \tilde{A}\ ^1A_2 5_0^6$ vibronic band (following the progression labeled in [77]). However, excitation at shorter wavelengths greatly increases the probability of photodissociation [154] at low pressures, and the fluorescence lifetime and quantum yield is reduced by several orders of magnitude [81]. In fact, fluorescence excitation spectra at low pressure show negligible emission at below 310 nm excitation [81]. This suggests that the 266 nm excitation should have a weak or even negligible impact on the formaldehyde PLIF measurement. It is, however, not clear whether fluorescence excited at 266 nm is more likely to occur at high pressure, *e.g.*, due to the collisional quenching of the photodissociation process.

Many of the phosphor samples, in particular those doped with Ce^{3+}, are likely to absorb at 355 nm

as well. Vibrational relaxation in solids tends to be very fast (i.e., the excited population distribution approaches an equilibrium distribution quickly upon excitation) such that the emission spectrum and properties are largely independent of excitation wavelength. Thus, diagnostic performance is expected to be largely unaffected if 355 and 266 nm laser light is co-propagated; however, the effective laser fluence and ground-state absorption cross-sections are likely different, which may slightly alter the emission intensity and temperature sensitivity. Further characterization may be needed if a co-propagation approach with overlapping laser sheets is used.

Co-propagation also has the added benefit that the excitation laser pulses could be separated by a small gap in time on the order of 100 nanoseconds. Rather than imposing a gate delay on the APT cameras, the two measurements could be separated such that each emission is captured entirely, largely avoiding formaldehyde fluorescence in the APT measurements, and only capturing the 266 nm excitation of the phosphor. This could also reduce or avoid completely the background in the formaldehyde PLIF measurements that originates from the phosphor particles. However, it is not clear whether formaldehyde will emit strongly when excited at 266 nm at engine-relevant pressures.

7.5.7 Laser Pulse Duration

Laser pulse duration can additionally impact the performance results. So far, experiments and much of the analysis was restricted to a fixed laser pulse duration of 6 ns, characteristic of many Nd:YAG laser systems including the Ekspla NL303D-10. However, by stretching the laser pulse for a constant total fluence, a higher signal intensity can be achieved for many of the phosphors considered here. In particular, the slow excitation limit derived in Section 4.6 suggests that for a sufficiently slow excitation, the phosphor response is linear (per Equation 4.25). This is achieved by limiting the peak fluence rates such that ESA becomes negligible during the excitation process. Although actually achieving the linear limit may require laser pulses that are too long for many combustion and engine experiments, modest increases in signal intensity can still be achieved by relatively small increases in the laser pulse duration. This can *e.g.*, be achieved by using a pulse stretcher.

The effect of laser pulse duration on signal intensity for the Eu:BAM and Ce:CSSO luminescence emission is calculated and plotted in Figure 7.19. The values in the plot are calculated for a total fluence of 30 mJ/cm^2 and are normalized to the previously assumed 6 ns laser pulse duration. The plot shows a clear increase in intensity with increasing laser pulse duration for a fixed amount of laser energy or fluence. By exciting more slowly, fewer electrons are absorbed into the conduction band via ESA and thus the effective fluorescence quantum yield is higher. The effect is only significant when the laser pulse

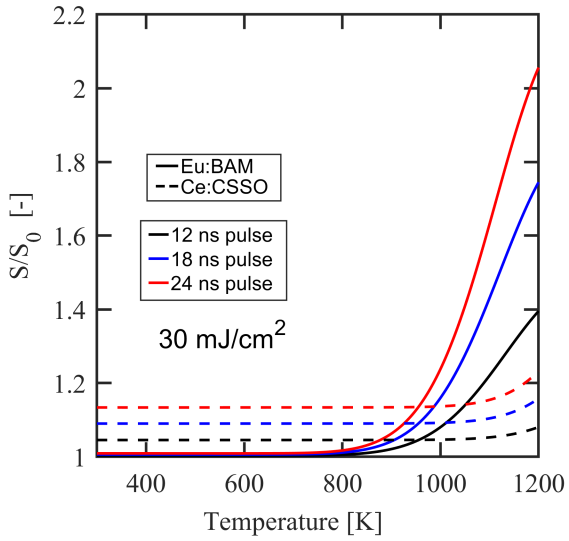

Figure 7.19: Effect of laser pulse duration at constant fluence of phosphor luminescence. Signal is calculated at constant fluence of 30 mJ/cm^2 for a variable laser pulse duration, and is normalized to its value with a 6 ns laser pulse width. The laser pulse is assumed to be a square wave for simplicity.

is long compared to the luminescence lifetime; thus, there is little change for Eu:BAM until thermal quenching reduces the lifetime to 10s of nanoseconds or less. Since the Ce:CSSO lifetime is relatively short even at room temperature, there is some increase in signal for Ce:CSSO at any temperature.

Combined Gate Delay and Laser Pulse Shaping

When using a gate delay approach to avoid background fluorescence, a shorter laser pulse is actually beneficial for a fixed laser fluence. To avoid formaldehyde fluorescence, all light emitted during the excitation process must be rejected. By increasing the laser pulse width, the fraction of light emitted before gating the intensifier is increased significantly, resulting in a larger loss. To illustrate this effect, signal intensity is plotted in Figure 7.20 as a function of laser pulse duration (at constant fluence) where gating starts 5 ns after the laser pulse ends. A minimum of 4 ns delay is required to reject most of the formaldehyde emission at 700 K, 30 bar; 5 ns is used here for a conservative estimate. Stretching the laser pulse increases signal by shifting the majority of the emission to occur during the excitation process; excluding light emitted during the laser pulse thus eliminates this benefit. Instead, for the delayed gating approach, it is beneficial to reduce the laser pulse duration as much as possible.

From Figure 7.20, combining a very short laser pulse (0.1 ns) with a 5 ns gate delay is a feasible approach for rejecting background with both the Eu:BAM phosphor (up to ~1100 K) and Ce:LuAG (up to ~1000 K) with only a factor of two loss in signal intensity.

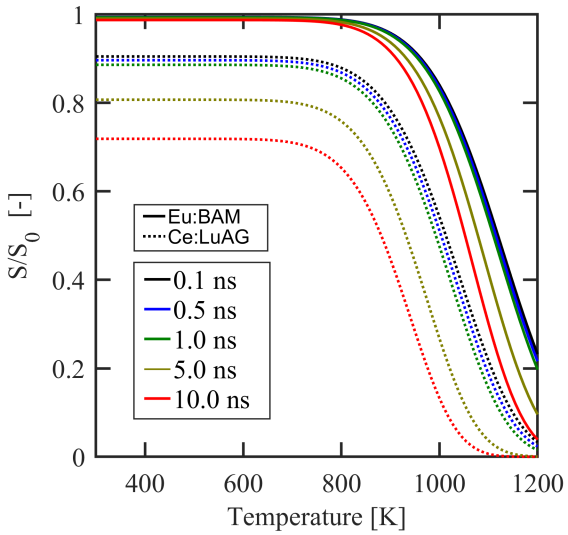

Figure 7.20: Calculated signal intensity for Ce:LuAG (dotted) and Eu:BAM (solid) for a variable laser pulse duration, and gate delay of 5 ns following the laser pulse.

7.6 APT Diagnostic Selection and Integration

Analysis of APT diagnostic performance in Section 7.5 shows the three best approaches for APT in the engine are the combined Ce:CSSO diagnostic, the Ce:LuAG (355 nm excitation) SRAPT diagnostic, and the Eu:BAM SRAPT diagnostic. Eu:BAM SRAPT covers the 700 to 1100 K range with high precision, and in particular better than 30 K precision from 800 to over 1000 K. The Ce:LuAG SRAPT measurement can provide around 20 K precision from 700 to over 1000 K, while the combined Ce:CSSO diagnostic can similarly provide better than 30 K precision from below 700 K to 1200 K, with a small performance gap from 850-950 K where the precision index increases. For each phosphor, the estimated bias limits are relatively small, on the order of 10 K or less except at the highest temperatures for Eu:BAM and Ce:LuAG. Increasing laser fluence likely improves diagnostic performance except Eu:BAM, where at high temperatures the short laser pulse duration results in significant ESA losses. However, because Eu:BAM is saturated at below 10 mJ/cm^2, the signal model does not accurately capture the slow increase in intensity with increasing fluence observed in Eu:BAM [36] at high fluences. Stretching the laser pulse for Ce:CSSO may be beneficial in increasing the emission intensity without altering the temperature sensitivity of the diagnostics.

Both Eu:BAM and Ce:CSSO phosphors emit between 400 and 500 nm, while Ce:LuAG emits from 450 to 650 nm. For Eu:BAM and Ce:CSSO, a broadband beamsplitter will be needed to split the image between the formaldehyde and APT cameras. For Ce:LuAG a dichroic beamsplitter could be used with

a cutoff near 480-500 nm; this would result in a small reduction in Ce:LuAG signal intensity, on the order of 5-10%.

Both Eu:BAM and Ce:LuAG SRAPT readily integrate with the formaldehyde PLIF diagnostic as the same excitation wavelength is used for both Eu:BAM and formaldehyde. For Eu:BAM a delayed gating approach is required, while for Ce:LuAG, interference can be avoided by collecting only wavelengths longer than 500 nm. The formaldehyde PLIF imaging system should be gated from the start of the laser pulse to at least 2.5 lifetimes after the laser pulse, or at least 4 ns after the laser pulse. The Eu:BAM SRAPT diagnostic should begin gating approximately 2.5 formaldehyde lifetimes after the laser pulse. For temperatures below ∼1000 K, this should have a negligible impact on Eu:BAM SRAPT performance. Above 1000 K, the temperature sensitivity and signal intensity of the diagnostic will both likely be impacted, and performance will likely suffer.

Integration of the Ce:CSSO APT diagnostic is more complicated and requires two lasers. For simplicity, and to avoid interference between the two measurements, it is recommended that the 355 and 266 nm lasers be co-propagated but separated in time by about 200 ns, and the 355 nm laser pulse come first; this is sufficient that any excitation of the phosphor will have decayed before the 266 nm laser pulse arrives, and that no photodissociation of formaldehyde is triggered before performing the measurement. However, the Ce:CSSO APT diagnostic is advantageous in that it can cover the upper end of the low-temperature ignition range and reach temperatures up to perhaps 1400 K.

Overall, the Ce:LuAG SRAPT diagnostic is recommended for its simplicity as it meets the performance requirements with the simplest experimental setup and approach.

7.7 Formaldehyde Detection Limits

From the LIF equation (Equation 2.1) and the parameters determined in Chapter 3, estimates of formaldehyde imaging performance can be made. Performance estimates will largely assume the same optical parameters from Table 7.4; however, the optical efficiency is reduced by 50% to account for the broadband beamsplitter required for the two formaldehyde cameras. Because the formaldehyde emission is so fast, the entire emission is collected. Some background radiation is collected from phosphor luminescence, PAHs, and other interfering molecules. This background signal will be removed via the ratiometric technique discussed in Section 7.1. In this section, the formaldehyde detection limits (*i.e.*, the formaldehyde concentration at which the formaldehyde PLIF signal-to-noise ratio is unity) will be determined neglecting these background processes. Then, the added noise due to the temperature-dependent background correction will be calculated, assuming a fixed 50 K temperature precision.

The LIF equation is repeated here for reference:

$$S_{LIF} = \frac{E''}{\hbar\omega_0} V n \sigma \Phi \frac{\Omega}{4\pi} \eta. \tag{7.17}$$

The collection fraction η and fluorescence quantum yield Φ are both pressure- and temperature-dependent. The absorption cross-section is additionally temperature dependent, but the pressure dependence is weak above 10 bar (based on the analysis in Chapter 3).

For simplicity, an ideal intensified CCD (ICCD) sensor will be assumed. In particular, there is assumed to be no read noise, dark noise, or other thermal noise sources; the sensor is assumed to have a gain sufficiently high that these sources are negligible. This is representative of a high-end ICCD camera; typical quantum efficiencies are as high as 50%. Typical ICCD noise factors at high gain for Gen II intensifiers are 1.6-2.2 and 3.5 to 4.2 for Gen III filmed intensifiers [155]; a value of 2.5 will be assumed for this analysis as conservative estimate for the Gen III filmless intensifiers which should have similar noise factors to Gen II devices. Thus, for a required signal-to-noise ratio of 1,

$$\text{SNR} \approx \frac{\sqrt{S_{LIF}}}{\sqrt{F}} = 1 \qquad \Longrightarrow \qquad S_{LIF} = F = 2.5, \tag{7.18}$$

and approximately 2.5 photons need to be captured on average.

The number density of formaldehyde n needed to generate a given number of photons on a detector S_{LIF} can be found by solving the LIF equation (Equation 7.17) for number density, or

$$n = S_{LIF,\text{min}} \frac{\hbar\omega_0}{E''} \frac{4\pi}{\Omega} \frac{1}{V\sigma\Phi\eta}. \tag{7.19}$$

From Chapter 3, around 40% of the emitted light is captured by the normal incidence filter, and the FQY of formaldehyde in air is large compared to the FQY in nitrogen; these effects are both accounted for in the analysis. There is an additional assumed optical efficiency of 75% (for a total of 37.5% including the beamsplitter) from Table 7.4. The solution of this equation is plotted as a function of temperature at 30, 60, and 90 bar pressure and 100 mJ/cm^2 laser fluence at 355 nm in Figure 7.21. Concentrations lower than 100 ppm can be measured throughout much of the low-temperature ignition range, although at higher temperatures the detection limits increase significantly. Increasing pressure decreases the detection limits (in terms of mole fraction) because the fluorescence quantum yield decays more slowly than $\propto p^{-1}$ at the low-temperature ignition conditions, but number density increases proportionally to p.

Initial formaldehyde formation is likely to occur at temperatures below 800 K based on diesel jet

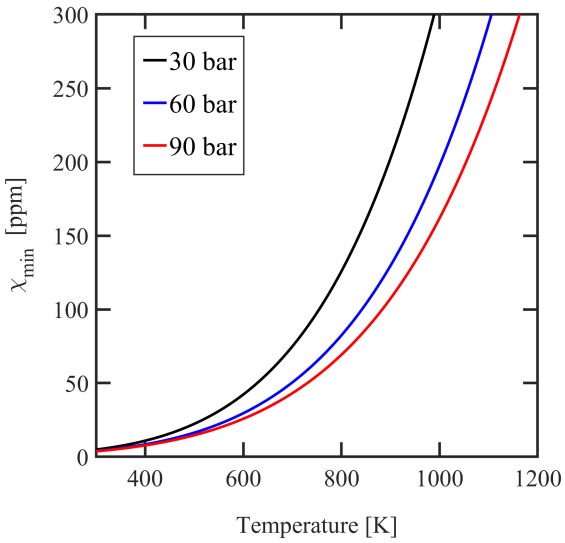

Figure 7.21: Calculated formaldehyde PLIF detection limits at 100 mJ/cm^2 for the ideal ICCD camera. Detection limits are defined as the concentration at which the measured signal-to-noise ratio is 1.

experiments performed by Idicheria *et al.* [57]. Formaldehyde concentrations are believed to form on the order of 1000 ppm or larger (up to ~10,000 ppm) at these temperatures during low-temperature ignition based on simulation results (*e.g.*, [156]) using n-heptane as a surrogate. Thus, the detection limits are suitable for capturing formaldehyde formation during low-temperature ignition. Note that the detection limits assume a constant laser fluence of 100 mJ/cm^2 that is representative of a typical experiment; it is possible that higher fluences could be used to lower the detection limits if necessary.

7.7.1 Ratiometric Formaldehyde PLIF Background Correction

Formaldehyde PLIF measurements are expected to be biased due to a broadband background signal, either from overlapping phosphor emission or from luminescence excited from PAHs or other compounds in the engine. The ratiometric imaging approach adopted here allows for the reduction or elimination of this bias as follows. The measured (biased) formaldehyde PLIF ratio R' can be written as

$$R' = \frac{S_2 + B_2}{S_1 + B_1} = R\frac{1 + \mathrm{SBR}_2^{-1}}{1 + \mathrm{SBR}_2^{-1}\frac{R}{R_B}}, \tag{7.20}$$

where S_i and B_i are signal and background intensity measured in band i, $\mathrm{SBR}_2 = S_2/B_2$ is the signal to background ratio, $R = S_2/S_1$ is the actual signal ratio of camera 2, and $R_B = B_2/B_1$ is the ratio of the background signals. R_B is the background ratio which is simply the ratio of the collection efficiencies of the two formaldehyde cameras for a perfectly uniform broadband background. Solving for the signal to

background ratio,

$$\mathrm{SBR}^{-1} = \frac{R - R'}{R' - R_B}\frac{R_B}{R} \qquad \Longrightarrow \qquad S_2 = (S_2 + B_2)\frac{R}{R'}\frac{R' - R_B}{R - R_B}. \tag{7.21}$$

The corrected signal on camera 1 is likewise given by

$$S_1 = (S_1 + B_1)\frac{R' - R_B}{R - R_B}, \tag{7.22}$$

where the quantity $S_i + B_i$ is the total signal measured in camera i.

The unbiased ratio is calibrated to temperature and pressure (see Section 3.6). The temperature measurement from the APT diagnostic is used to determine the unbiased ratio R using the formaldehyde PLIF ratio calibration function.

The uncertainty in the APT diagnostic naturally propagates into the formaldehyde background correction. Using a first order uncertainty propagation, the uncertainty in the background signal (in channel 1 - collecting the peaks of the emission) is given by

$$\frac{s_{S_1}}{S_1} \approx \left|\frac{R}{R - R_B}\xi_T\right| s_T, \tag{7.23}$$

where ξ_T is the fractional temperature sensitivity of the formaldehyde ratio, and s_T is the temperature precision of the temperature diagnostic. This expression blows up when $R \to R_B$; if the background ratio is equal to the actual ratio, the ratio is not biased and it becomes impossible to determine the value of the bias signals B_1 and B_2.

7.7.2 Temperature Error

For a quantitative formaldehyde concentration imaging technique, the temperature field measured from the APT technique is used to determine the formaldehyde PLIF intensity ratio in the absence of background signals. Using the known ratio, the fraction of signal due to background can be calculated from the measured ratio. This analysis was performed in Section 7.1, and the relative signal precision (and hence concentration precision) resulting from uncertainty in the temperature measurement was calculated as

$$\frac{s_{S_1}}{S_1} = \frac{s_\chi}{\chi} = \frac{1}{\mathrm{SNR}_1} \approx \left|\frac{R}{R - R_B}\xi_T\right| s_T \tag{7.24}$$

where s_x is the precision in quantity x, R is the actual signal ratio at the measured temperature, R_B is the ratio of the background signals, and ξ_T is the formaldehyde PLIF ratio temperature sensitivity.

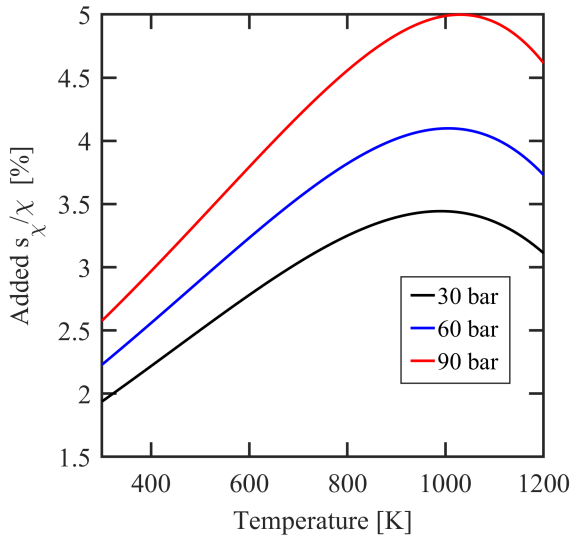

Figure 7.22: Calculated noise in formaldehyde concentration measurement resulting from a 50 K temperature precision.

For the calculations presented here, it is assumed that the background ratio R_B is equal to 1; this follows from having a broadband (uniform spectral distribution) background, and equal collection efficiency between cameras. The ratio R and sensitivity ξ_T were determined in Section 3.6; the ratio is approximately a linear function of temperature. Finally, the temperature precision will be taken as 50 K (providing a conservative estimate) for simplicity. No flatfield correction was used in deriving this expression, so the ratio in Equation 7.24 is an absolute intensity ratio and is not normalized to unity at a reference condition. All of the data needed to calculate the remaining quantities, R and ξ_T, were presented in detail in Chapter 3 using both experimental and simulation data.

The calculated noise as a result of the temperature precision s_T of 50 K is plotted in Figure 7.22. From the plot, the added noise is small, but increases with pressure and temperature. As pressure and temperature increase, the ratio approaches unity as the peaks spread out. However, over the range of conditions relevant to ignition, the ratio is still sufficiently far from unity that this added noise term is relatively small. At worst, for a 50 K temperature precision, the noise in the corrected concentration has an added contribution of 0.05, or 5% of the measured value. Since this value is significantly smaller than unity, it has a negligible impact on the detection limits.

7.7.3 Nonuniform Oxygen Concentrations

Since measurements are performed in a non-uniform reacting environment, the local oxygen concentration can vary from approximately 20% (very low equivalence ratio) to potentially 0% in very fuel-rich

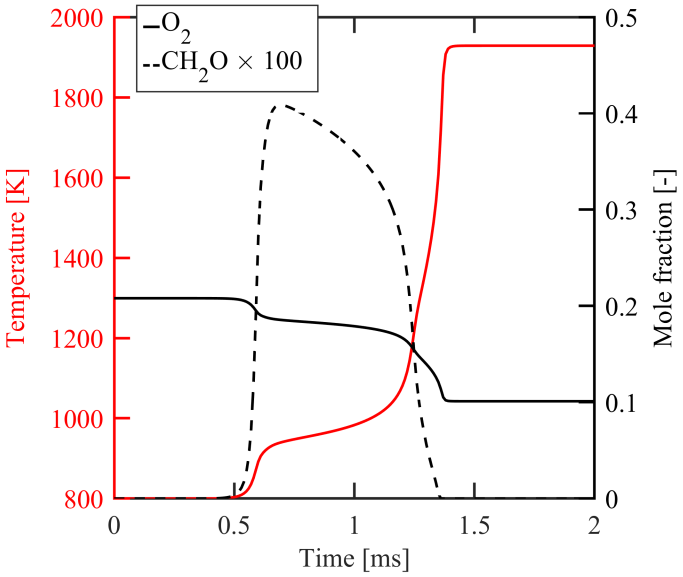

Figure 7.23: Simulated oxygen and formaldehyde mole fractions and temperature in a homogeneous reactor at 800 K, 50 bar.

locations, or in the combustion products. More realistically, during low-temperature ignition, oxygen concentrations could vary by closer to a factor of 2. As an example, a constant-pressure homogeneous reactor calculation was run using n-heptane with an initial equivalence ratio of 0.5, initial temperature of 800 K, and pressure of 50 bar; this case is intended to be representative of low-temperature ignition on the lean fuel jet periphery at a moderate intake condition of 50 bar and 350 K (this is similar to the condiitons used in Figure 7.4). The oxygen mole fraction and temperatures are plotted as a function of time in Figure 7.23.

From Figure 7.23, oxygen mole fraction changes by around 15% during low-temperature ignition (from $t = 0$ to $t = 1$ ms); for larger fuel concentrations the change is expected to be larger; an upper bound is chosen here as a factor of 2 during low-temperature ignition. Since the quenching behavior of oxygen is very different from that of nitrogen (from [48], oxygen quenches formaldehyde fluorescence about 7 times more than nitrogen at 300 K in the high pressure limit), this variation in oxygen concentration can greatly impact the measurement by changing the FQY. The uncertainty in the signal or mole fraction estimate due to uncertainty in the FQY can be estimated via uncertainty propagation as

$$s_{S_{LIF}} \approx \left|\frac{\partial S_{LIF}}{\partial \Phi}\right| s_\Phi \qquad \Longrightarrow \qquad \frac{s_{S_{LIF}}}{S_{LIF}} = \frac{s_\Phi}{\Phi}. \tag{7.25}$$

For a nitrogen-oxygen mixture, the formaldehyde fluorescence decay rate (inverse lifetime) is determined using the mole-fraction weighted model parameters of pure oxygen and nitrogen. The relative

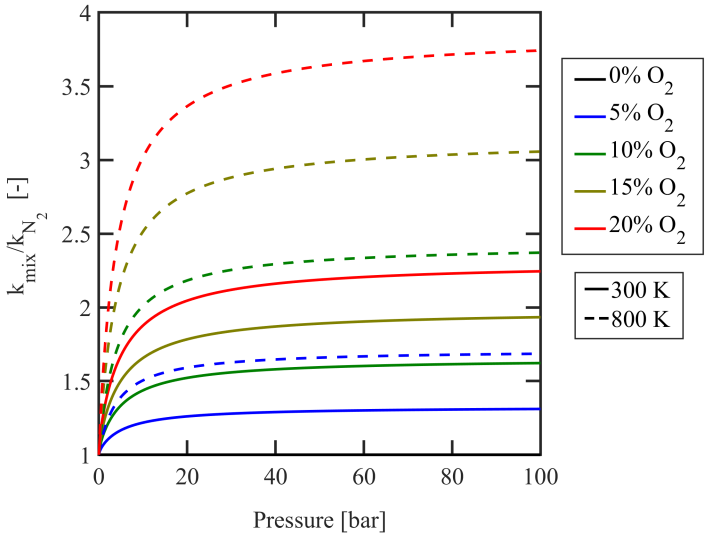

Figure 7.24: Fluorescence decay rate of formaldehyde in nitrogen-oxygen mixtures as a function of pressure, referenced to the decay rate in pure nitrogen. Calculation is performed using the model and parameters from [48].

change in fluorescence decay rate (and hence FQY) with oxygen concentration as a function of pressure (referenced to the lifetime in pure nitrogen) is plotted in Figure 7.24 at bath gas temperatures of 300 and 800 K using model parameters from [48].

Reducing the oxygen concentration from 20% to 10% (and maintaining the balance with nitrogen) at 800 K increases the FQY by around 50%. Thus, assuming the remaining species have quenching behavior similar to that of nitrogen, nonuniformity in the oxygen concentration (when uncorrected) adds no more than 50% uncertainty to the measurement. This increases the detection limits by ∼10%.

7.8 Particle Image Velocimetry Integration

To integrate particle velocimetry measurements, it is recommended to use the APT elastic scattering camera for PIV imaging. This camera should be an ICCD camera with UV lens to collect the 355 nm elastically-scattered laser light, and requires frame transfer capability on the CCD sensor such that two images can be taken sequentially. The first image is used for SRAPT, while the image pair together is used for PIV. The Princeton Instruments PI-Max 2 camera (characterized in Appendix E) has this capability, and has its peak photocathode quantum efficiency at UV lengths, making it a suitable choice. Alternatively, a high-speed CMOS camera with a sub-microsecond minimum exposure could be used instead; the Phantom V1840 has a minimum exposure of ∼500 ns and a quantum efficiency of ∼20% at 355 nm, and would be a suitable choice.

For typical PIV processing, particle discplacement should be approximately 25% of the interrogation region size (typically taken as 32 pixels). The mean velocity of the turbulent jet along the centerline at the liftoff location is (from the turbulent jet theory discussed in Section 7.2.3

$$u(z) = \frac{u_j B d_j}{z - z_0} \approx \frac{u_j B d_j}{H}. \tag{7.26}$$

Using the design injection pressure of 350 bar, orifice diameter of 140 µm, and 1 cm lift-off length, the mean centerline velocity at H is approximately 26 m/s. For the given pixel length of 0.3 mm, and a 32x32 pixel interrogation region, the appropriate interframe delay is approximately 90 µs (or $\sim$ 10 kHz frame rate). This interframe delay is sufficiently long that no interference is expected in either the APT or PLIF measurement due to the second laser pulse, and is achievable with both the Phantom V1840 and the PI-Max 2. Higher injection pressures will require shorter interframe delays.

Using the same camera for PIV and APT has some drawbacks. In particular, ICCD cameras and (to a lesser degree) high-speed CMOS cameras typically have lower spatial resolution and pixel densities than conventional high-resolution PIV cameras. Since 32 pixel square interrogation regions are typically used for PIV processing, resulting in usually no more than one measurement in an 8 or 16 pixel region, velocity resolution with typical PIV processing is lower than required here. Optical flow techniques provide a possible method to achieve high-spatial resolution, similar to that of the image sensor [151]. In particular, [151] reported accuracy on the order of 0.5 pixel/frame (corresponding to $\sim$1.6 m/s or $\sim$6% for the proposed parameters) using a conventional double-pulsed technique. Additionally, it may be possible to increase the velocity resolution by software binning the scattering measurements for APT rather than hardware binning.

7.9 Proposed Experimental Setup & Conclusions

It is recommended that Ce:LuAG SRAPT with 355-nm excitation be used for APT based on the results of the previous sections, and that PIV be performed using the same detector that is used for elastic scattering imaging of the SRAPT technique. The Mie scattering camera could be either a high-speed CMOS camera or an ICCD camera. The luminescence camera will likely need to be an ICCD camera, although a high-speed CMOS camera with sufficient sensitivity and quantum efficiency may be possible as well. The formaldehyde PLIF technique will be performed using two separate ICCD detectors, separated by a beam splitter; ICCD cameras are required due to the low signal levels (and relatively large detection limits) estimated for formaldehyde. The proposed optical layout is shown in Figure 7.25, with optics

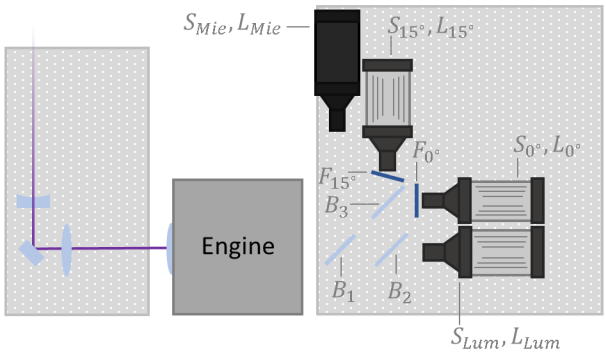

Figure 7.25: Optical layout of the proposed APT, formaldehyde PLIF, and PIV diagnostic. The optics specifications for each element are listed in Table 7.8.

Table 7.8: Required equipment for the proposed APT, formaldehyde PLIF, and PIV diagnostic.

Label	**Type**	**Specifications**
S_{Mie}	ICCD camera (or high-speed CMOS)	$< 90\mu s$ frame transfer, $\leq$ 50 µm binned pixel
S_{Lum}	ICCD camera (or high-speed CMOS)	$\geq$ 0.4 QE, $\leq$ 50 µm binned pixel
$S_{0°}$	ICCD camera	$\geq$ 0.4 QE, $\leq$ 50 µm binned pixel
$S_{15°}$	ICCD camera	$\geq$ 0.4 QE, $\leq$ 50 µm binned pixel
L_{Mie}	Camera lens	105-mm f.l., UV-transmissive
L_{Lum}	Camera lens	f/1.4, 85-mm f.l.
$L_{0°}$	Camera lens	f/1.4, 85-mm f.l.
$L_{15°}$	Camera lens	f/1.4, 85-mm f.l.
B_1	dichroic beamsplitter	Reflect $\leq$ 360 nm
B_2	dichroic beamsplitter	Reflect $\leq$ 490 nm
B_3	broadband beamsplitter	50% reflection, 50% transmission
$F_{0°}$	formaldehyde imaging filter, 0° AOI.	Semrock Inc., FF01-CH2O
$F_{15°}$	formaldehyde imaging filter, 15° AOI.	Semrock Inc., FF01-CH2O

specifications listed in Table 7.8. In addition to the optics explicitly listed in Table 7.8, each camera will additionally require a bandpass filter. The bands are listed in Table 7.9. Note that the specification for each ICCD camera requires $\leq$ 50 µm binned pixel; since the assumed magnification is -0.165, a 50 µm binned pixel is required to achieve the proposed collection volume (*e.g.*, 4x4 binning with a 12.5 µm physical pixel size).

The proposed approach requires the Ce:LuAG phosphor doped at 0.5% with a mean particle diameter of ∼400 nm, and a log-normal distribution width parameter of 0.15, corresponding to a 140 nm FWHM, or typical particle diameters from 330 to 470 nm. Maximum seeding densities at TDC should be on the order of 4500 mm^{-3}. Performance predictions were made using a laser fluence of 50 mJ/cm^2 for APT and

Table 7.9: Required imaging bands for the proposed 4-camera APT, PIV, formaldehyde PLIF technique.

Sensor	**Minimum [nm]**	**Maximum [nm]**
S_{Mie}	350	360
S_{Lum}	490	650
S_{0°	380	480
S_{15°	380	480

100 mJ/cm^2 for formaldehyde PLIF; both techniques can be performed at fluences of over 100 mJ/cm^2.

Performance estimates for the technique suggest that better than ∼30 K temperature precision is possible between 700 and 1000 K (-30 CAD to 0 CAD), and temperature biases less than ∼5 K in this range. Above 1000 K, performance appears to decrease significantly, although this temperature range is extrapolated using furnace data and may not be representative of the aerosol luminescence intensity above 1000 K. Formaldehyde PLIF detection limits are estimated to be less than 100 ppm at 800 K throughout the 30 to 100 bar pressure range, but increase significantly at higher temperatures.

7.9.1 Possible Improvements & Future Work

Several possible improvements in the approach are possible with future investigation. First, the impact of excitation wavelength on the phosphors under consideration has not been considered in depth. From a simple harmonic oscillator model, it is apparent that exciting closer to the electronic $4f5d$ transition energy can result in an increased absorption cross-section at low temperature, and can significantly alter the temperature dependence of the ground-state absorption process. Further, altering the excitation wavelength can impact the excited-state absorption cross-section. It is not immediately apparent how ESA cross-sections will change with excitation wavelength. It is possible that small adjustments in excitation wavelength can be used to increase emission intensity and alter phosphor linearity that could be taken advantage of in future APT work.

Additionally, this work was limited to phosphors that have been identified previously as being potential candidates for APT due to their high quenching temperatures. Other phosphors such as Ce,Pr:CSSO have been discussed, but more information is needed in the aerosol phase before detailed performance predictions can be made. Additionally, each phosphor investigated here used a fixed doping concentration. Concentration quenching is a complex process by which emission intensity is reduced as doping concentration increases through electron transfer between nearby ions [157]; this process is also likely temperature dependent. Doping concentration provides another parameter that could be optimized to increase diagnostic performance.

Some equipment changes may be possible to increase performance. In particular, the intensifier noise factor is assumed to be 2.5 and the detector quantum efficiency is assumed to be 0.4, which are both typical of Gen III. image intensifiers; this results in an SNR that is three times smaller than that of a perfect sensor in the shot-noise limit. Significant gains in performance may be possible with improved image sensors; however, the performance predicted here is typical of ICCD sensors that are currently available. Other (non-intensified) sensors may be suitable for the APT measurement if sufficiently sensitive and fast systems are available; for formaldehyde PLIF, an intensified camera is likely necessary due to the low signal levels and short exposure durations.

Chapter 8

Conclusions

Improved temperature, species concentration, and velocimetry diagnostics, along with improved diagnostic characterization, are required to improve our understanding of high-pressure turbulent jet ignition. In this work, an approach for simultaneous thermometry, velocimetry, and formaldehyde concentration imaging was proposed and designed. The proposed diagnostic makes use of various aerosol phosphor thermometry techniques for temperature imaging and simultaneous velocimetry via the particle image velocimetry method with scattered UV laser-light. Formaldehyde planar laser-induced fluorescence is proposed to be used simultaneously with the thermometry diagnostic. The simultaneous temperature measurement enables background correction of the formaldehyde concentration imaging technique, and quantitative correction for temperature-dependent spectroscopic parameters. Simultaneous measurement of temperature, velocity, and formaldehyde concentration can provide new insight in the mechanism of turbulent jet ignition; for example, by enabling direct measurement and investigation of thermal transport ($\boldsymbol{\nabla} \cdot \vec{\boldsymbol{u}}T$) and its relationship to combustion progress or chemistry via the formaldehyde mole fraction.

The work presented in this thesis focuses on the fundamentals needed to design the combined technique: design and analysis of aerosol phosphor thermometry techniques, demonstration of aerosol phosphor thermometry, and analysis of formaldehyde laser-induced fluorescence. These studies provided the results and analysis needed to design a diagnostic approach that combines both formaldehyde laser induced fluorescence and aerosol phosphor thermometry. This work additionally provided a thorough investigation of experimental factors that must be considered in the design of APT techniques; in particular, tracer particle response, seeded particle intrusiveness, and multiple scattering. Based on these factors, a recommendation regarding choice of APT diagnostic and formaldehyde PLIF integration strat-

egy was made, and estimates of integrated diagnostic performance were provided.

Investigation of phosphor photophysics and aerosol phosphor thermometry focused on two areas: phosphor signal modeling, and APT performance modeling. A model for phosphor photophysics including excited-state absorption at low excitation fluences was developed and was found to be consistent with the behaviors observed in many phosphors, such as strong non-linearity at low excitation fluence. Excited state absorption (ESA) refers to the ionization (or more generally, the further excitation) of electrons from the excited state to, *e.g.*, the conduction band. Effectively, ESA reduces the fluorescence quantum yield of a phosphor by providing a new mechanism by which the initially excited state can be deactivated. The developed signal model accounts for ESA and the ground-state absorption (GSA) process using temperature-dependent absorption cross-sections, that were fit to measured signal intensities from measurements of phosphor particles seeded into an air jet and heated via mixing with the products of a flame. This was done for several phosphor compositions including Eu:BAM, Ce:CSSO, Ce,Pr:LuAG and Ce:$GdPO_4$. The signal model results were combined with a detailed uncertainty analysis to investigate phosphor performance (in terms of temperature uncertainty) including contributions from intrinsic photon shot noise, camera or detector sources, and biases stemming from uncertainties in experimental conditions. Additionally, a model for temperature uncertainty due to contributions from the particle size distribution of the phosphor was described and used in performance estimates.

The aforementioned signal model provides a convenient calibration function for both the co-doped and scattering-referenced APT (SRAPT) techniques, as they are intensity based. Using the fluence-dependent calibration function for the Ce,Pr:LuAG phosphor, high-precision co-doped APT was demonstrated from 400 to almost 900 K in a heated air jet. By accounting for fluence effects in the calibration function, diagnostic performance was improved at higher temperatures, where the calibration function becomes sensitive to fluence. Further, combination of simultaneous APT measurements (*e.g.*, Ce^{3+} SRAPT, Pr^{3+} SRAPT, and Ce^{3+}-Pr^{3+} co-doped APT) was demonstrated on a single-shot basis using a weighted average approach that was also analyzed in detail. By combining multiple single-shot measurements, the single-shot temperature range was greatly improved over a single diagnostic; the weighted-average approach effectively chooses the best diagnostic to use at a given frame and pixel location. Finally, demonstrations of several phosphors and techniques were performed in an air jet heated by mixing with the products of a methane-air flame. Several of the phosphors, all of which were selected for their high quenching temperatures, were shown to be capable of providing reasonable temperature precision at temperatures of at least 1000 K (for Ce,Pr:LuAG) and up to 1200 K (for Ce:$GdPO^4$) and at least 1400 K (for Eu:BAM and Ce:CSSO). These results represent a significant improvement in the temperature limit of APT; prior to this work, the highest reported APT measurements with reasonable

precision were less than 1000 K [68]. Further, the results validate the approach of phosphor (or more specifically, host and ion) selection via the analysis of thermal quenching and the E_{dc} parameter (the energy gap between the excited $5d$ level and the host conduction band minimum).

Following characterization of phosphor photophysics and performance, a variety of experimental effects were investigated in an effort to aid the design of APT experiments. In particular, much effort was dedicated to investigating tracer particle response, intrusiveness, and optical effects resulting from the enclosed experimental environment. Tracer response was investigated under the Stokes flow assumption, where the coupling between velocity and temperature was considered. Velocity relaxation appears to be well-represented by the Stokes flow assumption with appropriate corrections for non-sphericity and non-continuum flow effects. On the other hand, simple lumped capacitance estimates of temperature response were found to be insufficient for cases in which the fluid has a large heat capacity. However, for most cases involving solid particles suspended in the gas phase (provided 95% relaxation is sufficient) the lumped capacity temperature response estimate under pure conduction is sufficient for Peclet numbers of order 1 or below. Tracer particle response provides an upper limit on particle diameter for a given experiment.

Tracer intrusiveness was investigated as well, primarily in terms of added heat capacity and mass density to the flow. For the high pressures encountered in engines, this form of intrusiveness was found to be largely insignificant in experiment design. Instead, seeding density limits are chosen to limit the amount of multiple scattering. Multiple scattering analysis was performed for an idealized engine geometry where, based on a theoretical model for phosphor photophysics that is representative of most high-quenching phosphors used for thermometry, it was found that the optical thickness of the engine $\tau = n\sigma z$ should be at most 0.5%. This value is required to limit the temperature bias (assuming 20% temperature fluctuations throughout the engine) to no more than 1% of the absolute temperature. This limits the maximum seeding density at TDC to around 2000-3000 mm^{-3} (for $\sim$ 500 nm diameter particles). Finally, reflection analysis suggests that reflections can provide a significant signal bias, on the order of $R/2$ (where R is the reflection coefficient). Specular reflections tend to originate near the imaging location and may not significantly impact the spatial resolution. Diffuse reflections, however, lead to light transport across the entire cylinder and as such may present a significant signal bias if not properly prevented.

Some investigation of formaldehyde photophysics was performed and presented, primarily using spectroscopy theory and simulation. The temperature dependence of the absorption cross-section at a fixed wavelength (Nd:YAG 3rd harmonic) and pressure were determined both via spectral simulation using the asymmetric rotor model, and described more generally using a temperature-dependent population factor.

It was found that at 355 nm, the absorption cross-section increases slightly before decaying with increasing temperature; the estimates suggest that the cross-section decreases by only a factor of 3-5 from 300 to 1200 K. Fluorescence quantum yield (FQY) is estimated from measurements of fluorescence lifetime, and extrapolated to higher pressures and temperatures using a curve fit to a collisional quenching model. The FQY estimates are generally equal to or larger than 0.1% at all conditions that were investigated for this study in nitrogen; the FQY is reduced by a factor 2-4 (depending on temperature and pressure) when the bath gas is air. Finally, estimates of collection fraction (and luminescence intensity ratio) for the filter combination proposed for the quantitative background correction were made from measured spectra, and compared to the results of a Herzberg-Teller-style fluorescence bandshape simulation. The measured values are in good agreement with the simulations, and a simple model was provided for the collection fraction and ratio as a function of temperature and pressure. To a good approximation, the measured and simulated ratios are linearly proportional to temperature. The temperature sensitivity of the formaldehyde luminescence intensity ratio using the chosen bands is relatively low, on the order of 10^{-3} K^{-1}, which is beneficial for the proposed background correction procedure.

The phosphor photophysics model and calculation results were used to estimate performance in the engine during the compression stroke, assuming a constant pressure combustion event at TDC. The calculation was performed for an assumed set of intensified CCD cameras and again for a perfect sensor for comparison. Temperature precision of better than 30 K throughout much of the low-temperature ignition range using either Ce:LuAG, Eu:BAM or Ce:CSSO, with biases that typically are small compared to the temperature precision except at the highest temperatures. Overall, Ce:LuAG (355 nm excitation) SRAPT is recommended for thermometry as it provides continuous 30 K or better temperature precision from 700 to over 1000 K at TDC (with bias less than 5 K at the same conditions), and is easily integrated with formaldehyde PLIF and PIV. The calculations were repeated for a perfect sensor to provide a limit on temperature precision. Finally, detection limits were calculated for the formaldehyde PLIF portion of the experiment; detection limits are typically below 100 ppm at temperatures below 800 K, for a 100 mJ/cm^2 laser fluence (detection limits are inversely proportional to laser fluence). At higher temperatures the detection limits increase, while with increasing pressure the detection limits decrease. For a 50 K temperature precision from APT, an added noise of up to 5% is estimated in the formaldehyde PLIF measurements due to the temperature-dependent background procedure.

The results discussed here also motivate several new avenues of research to improve performance of the combined diagnostic. Phosphor signal modeling shows the relative importance of absorption transitions for the phosphor. Altering excitation wavelength can potentially increase the ground-state absorption cross-section (and alter its temperature dependence); excitation wavelength also can impact

the excited state absorption cross-section. Several other factors that require more detailed experimental investigation include changes in doping concentration, and excitation laser pulse duration. Other phosphor compositions, such as Ce,Pr:CSSO, could potentially be used as well, but more detailed characterization in the aerosol phase is necessary. Regarding formaldehyde PLIF, experimental validation of fluorescence lifetime at combustion relevant conditions (in both air and nitrogen) is required to validate the performance estimates. Both fluorescence lifetime and absorption cross-section estimates should be validated as well to accurately correct formaldehyde PLIF images for quantitative imaging.

The key findings of this work are summarized below.

- A phosphor signal model accounting for excited state absorption, excitation laser fluence, and excitation laser pulse duration was developed
- Several phosphors and APT techniques were demonstrated in a flame-heated jet, extending the upper temperature limit of APT from below 1000 K to at least 1400 K
- Developed and demonstrated a method to combine simultaneous APT diagnostics using a single phosphor
- Design considerations for particle-based techniques were discussed in detail, and multiple-scattering was found to have the most significant impact on APT measurements at engine-relevant conditions
- A ratiometric background correction approach for formaldehyde PLIF (using the simultaneous APT measurement) was derived, and performance considerations were discussed
- Formaldehyde PLIF and APT performance were estimated at engine relevant conditions using a variety of modeling results

Appendix A

Overview for Non-Scientists

I have written this chapter of my thesis to communicate my research with as wide of an audience as possible, and not just scientists. Scientific research should be conducted to benefit all of society; as such it is imperative that scientists communicate their findings with others. Scientific communication is especially important as scientific research becomes more specialized, and the communication barrier between the sciences and the humanities [158] remains or even grows. Naturally, the inability to communicate is a significant challenge to overcome in solving the various problems of the world. Communication is all the more important when political and economic decisions are being made in response to questions that are inherently scientific, in particular those regarding climate change and energy policy. Thanks to the Wisconsin Initiative for Science Literacy (WISL) at UW-Madison for the opportunity and platform to present my research to a non-science audience, and for sponsoring and supporting the creation of this chapter.

A.1 Introduction

Climate change is widely recognized by scientists and non-scientists alike as one of the most important challenges for our generation. The American Physical Society (APS) has even released the following statement in 2007 [159]:

> The evidence is incontrovertible: Global warming is occurring.
>
> If no mitigating actions are taken, significant disruptions in the Earth's physical and ecological systems, social systems, security and human health are likely to occur. We must reduce emissions of greenhouse gases beginning now.

To provide some context for this statement, scientists, let alone major scientific associations, rarely if ever make direct statements like this. Scientific writing typically leaves room for the unknown; scientists understand that no measurement is perfect, and that there is always room for error. That makes the APS' statement all the more significant: even in 2007, scientists accepted human causes of global warming as an indisputable fact. Our understanding of human impacts on climate change has evolved significantly since then, and in 2018 scientists for the first time identified extreme weather events that could only have occurred as a result of human influences on climate change [160]. Clearly, the problem of global warming and climate change is significant, and we're already seeing some of its initial impacts.

Global warming is a problem, but what do we do about it? To answer that, we need to know something about its causes. Global warming is usually described as the result of greenhouse gases, which trap infrared light that would otherwise escape Earth's atmosphere. The trapped radiation is ultimately absorbed again at the Earth's surface, heating the planet. A major source of greenhouse gases is combustion engines, which in the US produce around 30% of greenhouse gas emissions. Combustion engines are used in our cars and trucks, in planes, in power plants, and in industrial settings for a wide variety of tasks; they are even used to power recreational equipment like jet skis and snowmobiles. It has been suggested by combustion scientists that we can potentially reduce greenhouse gas emissions from combustion engines by 50% [161] simply by improving fuel efficiency, potentially going a long way toward reducing the impacts of climate change. Development of other technologies could decrease emissions even further.

Unfortunately, we can't just stop using combustion engines. Much of our economy, food and water supply, and essential services rely on combustion engines; alternatives do not exist (and may not for many years) that can act as a drop-in replacement. Instead, it is important that we continue to work on improving the technology that we do have as one step towards reducing carbon emissions. Unfortunately, scientists do not have a good understanding of much of the chemistry and physics that drives engine performance and emissions formation. Developing this understanding is critical for making better engines, and for shifting to more advanced engine designs or fuels. My research over the past 6 years has focused on developing tools that allow scientists to understand what is happening inside engines. The specific tools I develop are called optical diagnostics, which largely employ cameras and lasers to make measurements inside engines. Advanced optical diagnostics let us capture an immense amount of information in a very short time that is not accessible in traditional experiments. For the remainder of this chapter, I will discuss my contribution to the development of optical diagnostics for combustion engines. In particular, my research focuses not only on development of specific tools, but also aims to answer the question how do I choose or design a tool for a specific combustion experiment. I'll start

with a short motivation for my work, and discuss why better tools are needed. Next, I'll provide a brief description of the optical diagnostics I've been working on these past six years. Then, I'll discuss some background information that is important to diagnostics, namely quantum mechanics, and outline some of our research results that specifically focus on the physics of optical diagnostics. Finally, I'll discuss some specifics of engines, and how we design diagnostics to make measurements in engines.

A.2 Global Warming & Other Impacts of Carbon Emissions

Before jumping into the specifics of my research, I want to outline some of the physics involved in global warming. Global warming serves as both the very high-level personal motivation for my work in combustion, but also is an excellent example of some of the physical concepts that come into play for optical diagnostics. In fact, the diagnostics I've spent my academic career developing and designing operate on the same principle by which the Earth is heated: absorption and emission of radiation. The remainder of this section contains a brief overview of global warming; a more complete description with many additional details is provided by the American Chemical Society in their climate science toolkit [162].

Temperature is a measure of how much energy an object has stored; as an object absorbs more energy, its temperature will increase. When we think about the temperature of an object, say the Earth, what we're really interested in is the energy balance: where does energy come from, and where does it go? If we consider Earth as a whole, the vast majority of energy available on Earth comes from the Sun. The Sun itself is a large hot ball of gas, mostly hydrogen. Since the Sun is so hot, it behaves similar to an incandescent light bulb: it radiates a significant amount of heat in addition to light. The Earth is a large nearly spherical rock with a thin atmosphere surrounding it. A small portion of the radiation emitted from the Sun reaches Earth and can be absorbed (heating the Earth), or reflected. Even though the Earth is very cold compared to the Sun, the Earth will also emit radiation; this is how Earth maintains its temperature. A diagram of the Earth-Sun system is shown in Figure A.1 with some of these processes shown schematically. All of these competing processes collectively determine the temperature of Earth.

If Earth had no atmosphere, the average surface temperature would be around 0°F. But, as it stands, only around 60% of energy emitted from Earth escapes, and the surface temperature on average is closer to 60°F. This is a result of the greenhouse effect. A large portion of the radiation emitted from Earth is absorbed by the greenhouse gases and clouds in the atmosphere and ultimately emitted back towards the Earth. Much of the re-emitted radiation is absorbed at Earth's surface, increasing the planet's temperature. As we add more greenhouse gases to the atmosphere, less radiation escapes (*i.e.*, more

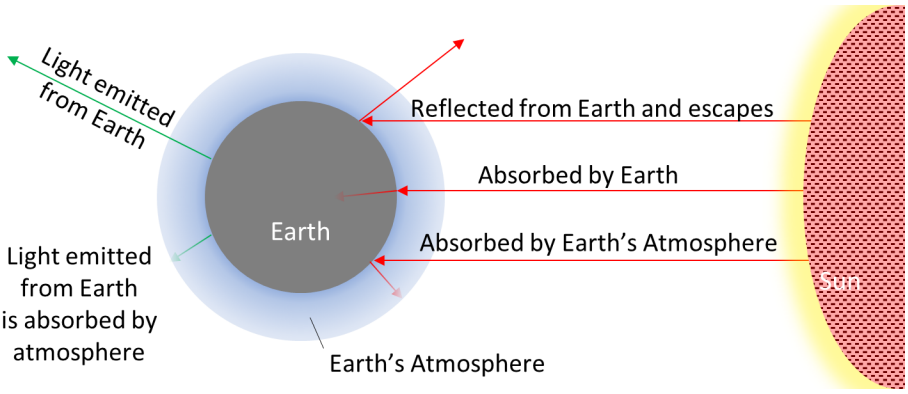

Figure A.1: Diagram of Earth-Sun system showing the different paths radiation can take as arrows.

radiation is reabsorbed at Earth's surface), further increasing the temperature. As Earth warms, the problem gets worse: the polar ice caps slowly melt reducing Earth's ability to reflect Solar radiation. The warmer Earth also raises the temperature of the atmosphere, allowing it to hold more water vapor (water vapor being the largest contributor to the greenhouse effect). There are also changes that can act to decrease the greenhouse effect as Earth warms, like the formation of more clouds (resulting from the additional water vapor) that reflect Solar radiation. However, in total, the greenhouse effect tends to become more severe at higher temperatures, and changes in carbon dioxide emissions tend to have a large impact.

The IPCC estimates that doubling the amount of carbon dioxide in the atmosphere will increase Earth's surface temperature by an additional 3-8°F . This may not seem like a significant change; Madison, WI experiences typical temperature swings from 40 to 60°F routinely each day in Spring. It's really important, however, to realize what this temperature increase really means. Imagine having a cup of boiling water in one hand, and a small ice cube in the other. The average temperature of these two objects (*i.e.*, the temperature of the water if I were to put the ice cube in and let it melt) is relatively high, say 195°F. If I replace the ice cube with liquid water at the same temperature, the average temperature of the two objects increases to around 200°F. By replacing ice with liquid water, the average temperature of the system increases by only 5°F, and the temperature of the two individual objects hasn't changed, but we obviously no longer have any ice. This is illustrated in Figure A.2. On Earth, a primary effect of global warming is to shrink the polar regions in much the same way that the ice cube melts and is replaced with liquid water in our example. The slight temperature increase is only a symptom of a larger issue: the balance between cold and hot regions on the planet is disrupted, particularly in the form of melting polar ice caps and shrinking regions of cold polar air. Smaller polar air regions tend to be less stable and move more frequently to lower latitudes, leading to more extreme

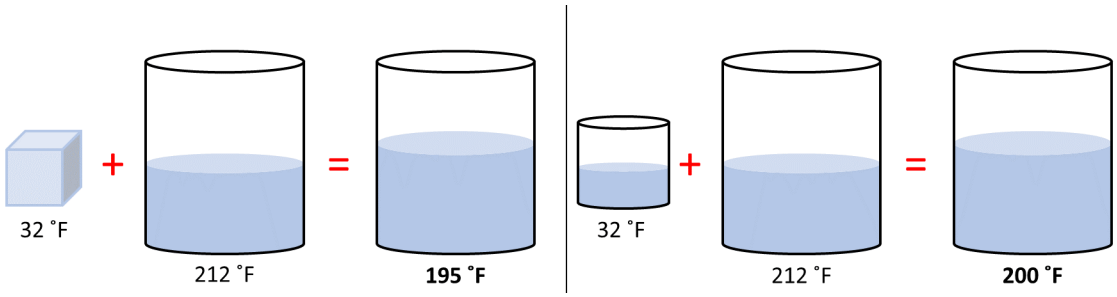

Figure A.2: Illustration of water and ice mixing. Left: an ice cube is added to a cup of boiling water, which melts, resulting in an average temperature of 195°F. Right: liquid water (with the same initial temperature) is added instead of ice, resulting in an average temperature of 200°F.

weather events. Beyond this, increased greenhouse gas concentrations in the atmosphere already are having significant impacts on temperature, ocean acidity, and rising sea levels, all of which can have profound impacts on human and natural systems.

Figure A.3 shows a simple diagram of Earth's atmospheric carbon cycle, which shows some of the ways carbon is stored on Earth. From the diagram, burning fossil fuels adds carbon to the atmosphere which can eventually move into the ocean, into the soil, or into plant matter. Burning any fuel adds carbon to the atmosphere, but fossil fuels specifically add "old" carbon, or carbon that has been stored underground for millions of years. Since it takes millions of years for plant matter to decompose into oil again, "old" carbon is not "recycled" back to its original state, and adds more carbon overall. With new technologies, we focus on "renewable" fuels where the carbon is recycled back to its original state, and only briefly affects the environment as the carbon moves from the atmosphere into the biosphere (or plant matter) again. We also hope to develop improved engines that are more efficient, so less carbon is released overall. In both cases, scientists need better tools to understand the chemistry and physics that happens inside engines.

Internal combustion engines (like those used in cars and trucks) have been around for over a hundred years; one may naively assume we know everything there is to know about combustion, but this is far from the truth. Early engines were developed from the simple understanding that a fuel burns after it is compressed and heated. In fact, we are still very far from having a thorough understanding of the physics and chemistry at play; scientists are only recently beginning to understand the coupled physics and chemistry of the fuel and air mixture inside an engine. This understanding is becoming more critical to engine design now because we're interested in increasing efficiency and using alternative "carbon neutral" fuels to fight climate change. Alternative fuels can behave very differently from more traditional fuels like gasoline and diesel; we need to understand the physics and chemistry at play to be able to use alternative fuels effectively. We also need this understanding to make engines more efficient.

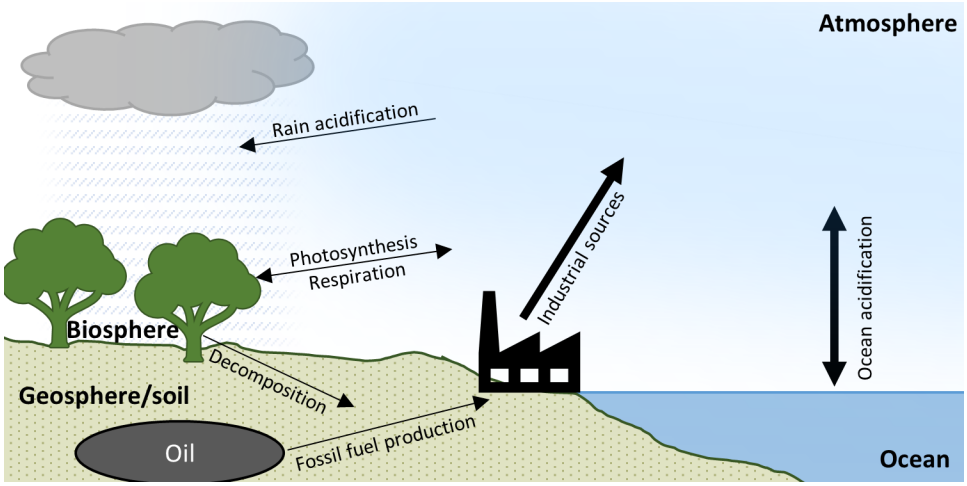

Figure A.3: Illustration of a portion of the atmospheric carbon cycle showing several of the ways carbon enters and exits our atmosphere. Some important processes are not drawn, including interaction with Earth's geosphere (*i.e.*, soil) and other human sources (*e.g.*, agriculture).

Every gallon of gasoline contains around 5 pounds of carbon, and burning a gallon of gasoline produces about 18 pounds of carbon dioxide gas. Developing tools and performing experiments to learn about the detailed physics and chemistry of combustion in engines is necessary to make more efficient engines (ultimately burning less fuel), and to design engines to better use alternative fuels.

A.3 Optical Diagnostics & Aerosol Phosphor Thermometry

The discussion of global warming in the previous section not only describes my motivation for studying combustion, but also serves as an excellent example of how light and matter interact. In that discussion, the Sun, since it is very hot, emits radiation in the form of heat and light. The Earth absorbs and reflects some of that radiation. Greenhouse gases in the atmosphere absorb a small fraction of the radiation as well. This is the same principle on which optical diagnostics operate. Using optical diagnostics, we aim to measure temperature or other parameters by exciting an object (*e.g.*, by shining a light on it until it absorbs light), and measuring the light that comes out with a camera. This process of light absorption and emission is illustrated in Figure A.4. Imagine shining a flashlight into a box with a cloud of particles. The light is initially white, meaning it is composed of all colors with equal brightness. If the particles are luminescent, meaning they can absorb and emit light, particles will absorb some of this light, but only certain colors are absorbed. The remaining light passes through the particles. After the particles absorb some light, they can re-emit with a different color. Usually the emitted light is red-shifted, meaning the emitted light contains more red light than the absorbed light.

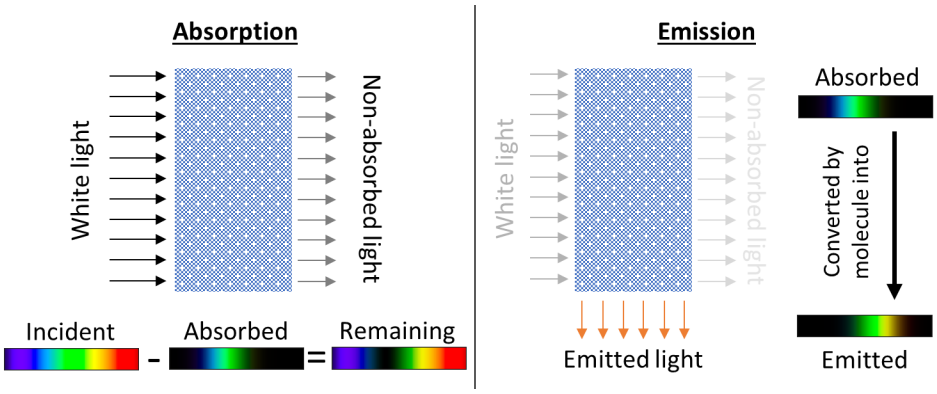

Figure A.4: Illustration of white light interacting with an absorbing material. Only certain frequencies (colors) of light are absorbed and the rest are unaffected. The material later emits light at a different frequency. Note the emitted light is "red-shifted" with respect to the absorbed light.

The technique we're interested in here is called laser-induced fluorescence. Laser-induced means that we're using a laser to provide light for our particles to absorb, and fluorescence is the scientific term for light that is emitted from a molecule quickly. This is identical to how glow-in-the-dark toys work. Imagine a glow-in-the-dark ball. The ball is initially outside during the day and absorbs light from the Sun. Then, moving it indoors into a dark room, the ball glows dimly as it re-emits some of the light it absorbed earlier. For optical diagnostics, we replace the Sun with a laser, and instead of toys we are looking at molecules or tracer particles smaller than a grain of sand. (We call them tracer particles because they are meant to trace the motion of the fluid flow.) The molecules or particles we're interested in also re-emit the light they absorbed over a very small fraction of a second (less than 1 millionth of a second typically), while glow-in-the-dark toys emit lightly slowly over hours.

Over the last six years, I have worked to improve our understanding of the physics of these tracer particles so we can make better optical diagnostic tools for engines. This work has focused on trying to answer the following questions:

- How does temperature affect how a molecule or particle absorbs and emits light?
- What parameters are important for designing or choosing a particular optical diagnostic tool?
- Can we predict how well an optical diagnostic will work?

The last bullet point is perhaps the most important. Not only do we need to develop these experimental techniques, but we really need to understand how well they work. Every experiment and every measurement has some error or uncertainty associated with it. To design or choose an experimental method we need to know what this uncertainty or error is, and we need to know whether a tool is capable of answering our scientific questions.

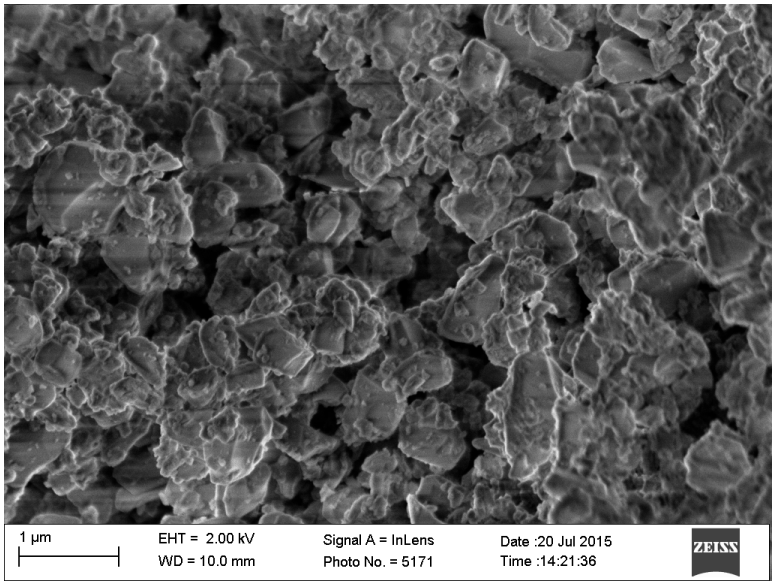

Figure A.5: Scanning electron microscope image of a phosphor sample

The questions posed above are very broad. In my thesis, I focus on a specific subset of the problem, where I investigate solid tracer particles called thermographic phosphors (thermographic meaning that some properties change as temperature changes, and phosphor meaning the particles can absorb and emit light), and focus on the design of a temperature measurement tool for the air and fuel mixture inside of a diesel engine just before the fuel ignites. The technique of using thermographic phosphor particles to measure gas temperatures is called aerosol phosphor thermometry. In practice, we put these phosphor particles into the engine suspended in air (similar to how dust can be suspended in air) and we shine a laser on them. Similar to the glow-in-the-dark ball or the Earth, the particles absorb some of the laser light and reflect some of it. The light that is absorbed is later emitted again with a different color, and we observe and measure the emitted light by taking pictures with scientific cameras. By looking at the color (or frequency) of the emitted light, and the brightness of the emitted light, we can determine the temperature of the particle.

The particles themselves are very small, usually less than a micrometer in diameter (1 thousand micrometers is equal to a millimeter); a microscope image of a phosphor sample is shown in Figure A.5. The particles in this image are made of a garnet (similar, but not identical to the gemstone garnet), but some of the atoms are pulled out and replaced with praseodymium ions. The praseodymium ions are what gives the particle its ability to absorb and emit light. This is only one example though; many different materials (and ions) can be used to make a phosphor, and a major challenge of this work is to find the best material for a given experiment.

A.4 Quantum Mechanics and Phosphor Photophysics

We aim to measure temperature with these tracer molecules or particles by taking advantage of their absorption and emission properties. What does temperature have to do with absorption and emission of light? To answer this question, we need to delve into the field of physics that describes the atom: quantum mechanics. You might be wondering, what does quantum mechanics have to do with combustion measurements? Quantum mechanics is the theory that describes what happens when light interacts with matter.

More specifically, quantum mechanics is the theory that describes how matter (including electrons and atoms or molecules) interact at very small scales (at distances around a billionth of a meter). In popular science, quantum mechanics typically evokes images of a thought experiment by Erwin Schrodinger about a cat in a box that may or may not be dead. Schrodinger suggests that the cat is both dead and alive (the cat's life being controlled by an atomic process), and that the ambiguity is only resolved when one 'measures' or observes the cat. From a practical standpoint, this can be misleading. This would imply quantum mechanics is a theory about what we don't (or can't) know or understand. A more approachable and useful description is that quantum mechanics is a theory of probability; it tells us how likely certain events are. This is a key part of the Copenhagen interpretation of quantum mechanics. In this interpretation Schrodinger's thought experiment does not pose a problem; the outcome is determined long before a conscious observer opens the box [163], with both outcomes equally likely.

Quantum mechanics, however, cannot tell us what will happen, only what may happen. As an example, consider the Moon orbiting Earth. Classical mechanics can tell us the precise path that the Moon will take around Earth. An electron orbits an atom in much the same way (mathematically speaking), but quantum mechanics cannot tell us the electron's precise path. Instead, it tells us the probability with which the electron will be at any given location. This comparison is shown in Figure A.6. This feature makes quantum mechanics unintuitive, even to experts in the field.

Besides telling us something about how electrons orbit atoms, quantum mechanics is necessary to understand the details of optical diagnostics, and especially how objects absorb and emit light. If we consider again an electron orbiting an atom, this system can absorb light. Light, being a wave, pushes on the electron in orbit. If the light has the appropriate frequency (or color), making it resonant with the electron, the electron can be pushed into a different orbit (similar to how an opera singer can cause a glass to vibrate by singing at the glass' resonant frequency). This pulls some energy out of the light field, and gives it to the electron. Emission, or the "glow" in glow-in-the-dark, is the reverse process; after the opera singer stops singing, the glass still "rings", producing sound. Similarly, after absorbing

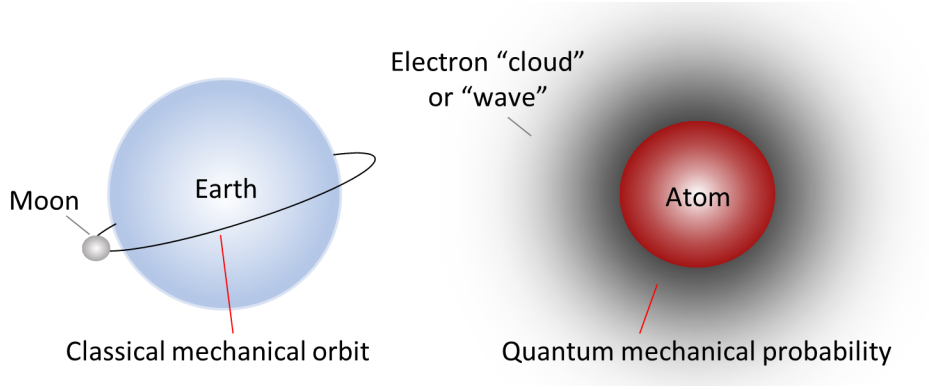

Figure A.6: Illustration of the Moon orbiting Earth (left) and an electron orbiting an atom (right). The dark cloud or fog surrounding the atom indicates the likelihood of an electron being at that location. Near the center of the atom, the cloud is very dark and dense, indicating electrons are more likely to be near the center.

light and moving to a new orbit, an electron will fall back down to its original orbit and in doing so will create a small burst of light. Each of these processes (absorption and emission of light, as well as the resonating glass) are illustrated in Figure A.7. As an aside, if the frequency of light is too high, the electron can actually be ripped away from the atom, similar to how an opera singer can shatter a glass by singing loudly at the glass' resonant frequency. This is of course not desirable, because light cannot be emitted if the electron is ripped away from the atom, as a broken glass cannot produce sound.

As I mentioned, quantum mechanics is a theory of probability. To make a diagnostic, we need to know the probability that a molecule or phosphor particle will absorb light, and the probability that it will re-emit that light. But why am I discussing probabilities? If we're trying to make measurements, don't we need to know more than just a probability that a particle will emit light? The answer is statistics. Statistics provides a link between the quantum mechanics (the physics of a single atom) and the behaviors we observe in real life (composed of many, many atoms). When we have a large number of atoms absorbing and emitting light, the law of large numbers effectively says we can interpret the probability as a fraction. Going back to Schrodinger's Cat, if we perform this thought experiment 1 million times, statistics would tell us to expect to get each result one half million times.

A.4.1 Phosphor Emission Probability

Let's go back to the question of the probability of absorbing and emitting light. More specifically, we're interested in understanding the photophysics (or the luminescent properties) of different phosphor materials. We can gain some insight into these questions through some simple experiments where we heat a sample of phosphor particles (remember, a phosphor particle is a small piece of material, like a grain

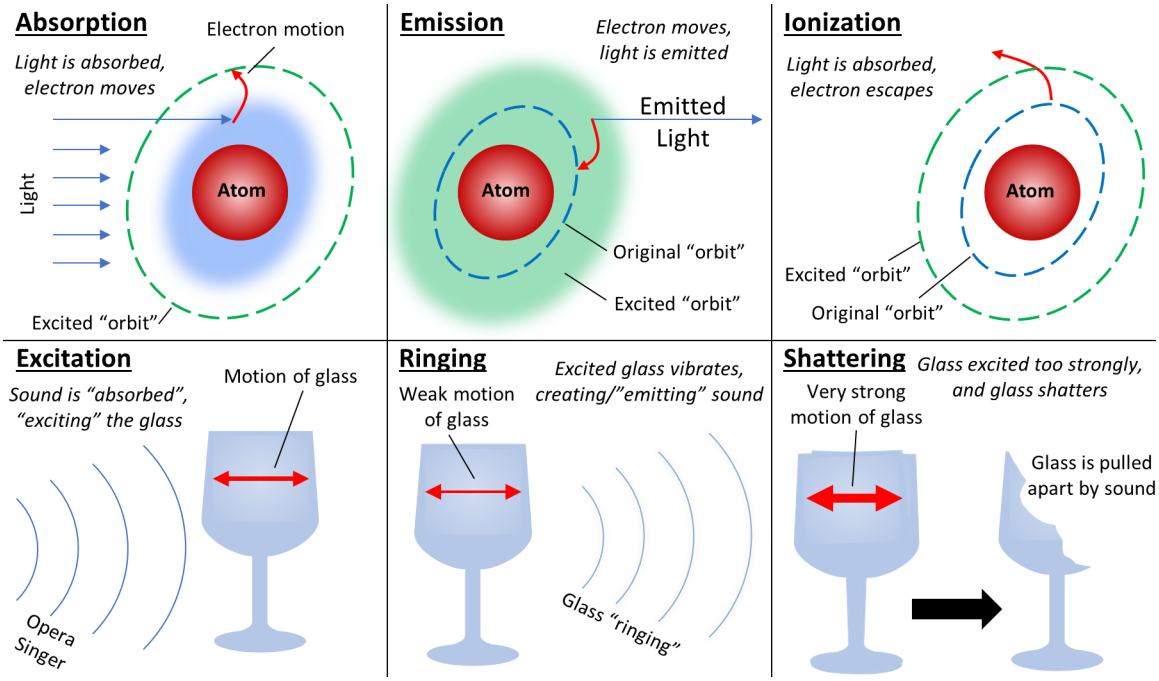

Figure A.7: Illustration of absorption and emission of light by an atom (top) in comparison with the excitation of a wine glass by an opera singer's voice (bottom). Red arrows indicate the motion of electrons (in the case of the atom) and the glass (for the wine glass example). Electrons are shown as shaded blue or green clouds around the atom, and the empty orbits are shown as dashed curves.

of sand, that can absorb and emit light) to a known temperature, excite it with a laser, and measure the color and intensity (brightness) of their emission. The brightness is a measure of the probability with which a phosphor will absorb and emit light. A series of panels showing the color content and brightness of the emission for a phosphor sample at different temperatures is shown in Figure A.8.

All of the phosphor materials we investigated for thermometry show an interesting trend: the brightness of the emission drops quickly as temperature is increased, but only above some threshold temperature. This suggests that colder particles are more likely to emit light. This phenomenon is called thermal quenching. Imagine our phosphor particle is made up of two billiard balls connected by an elastic band. As we increase the temperature, the billiard balls tend to move faster and pull harder on the elastic band (temperature is a measure of the average speed of the atoms that make up an object). Occasionally the two billiard balls will collide, and the faster they move, the more frequently these collisions will occur. Now, imagine one of the billiard balls absorbs some light and gains some energy. Each collision between the billiard balls provides an opportunity for that extra energy to be transferred to the other billiard ball. Depending on how the energy is transferred, it may not be available to be re-emitted as light. Put simply, after an electron absorbs energy from light, it can either emit a burst of light, or the electron can be pushed back into its original orbit by collisions with other atoms. Since collisions are more likely

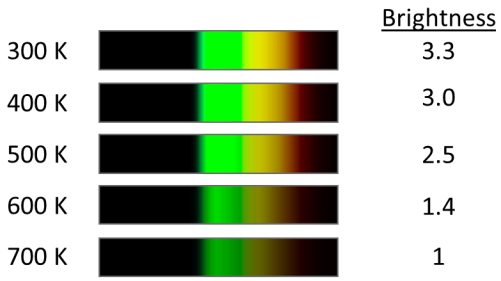

Figure A.8: Color content and brightness of a phosphor sample as it is heated from room temperature (300 K) to 700 K (or 800°F). The "brightness" value next to each panel measures the relative brightness of the emission, compared to the value at 700 K. For example, the phosphor is 3.3 times brighter at room temperature than it is at 700 K.

to occur at higher temperature, less light is emitted as temperature increases. Thermal quenching is the most important mechanism controlling a phosphor's capability for temperature measurement.

Using all of this information, we designed a temperature measurement tool or diagnostic that takes advantage of thermal quenching. We directly measure the brightness of the phosphor particles with a camera, and using our knowledge of the phosphor's thermal quenching, we can find the temperature of the phosphor particle. Since thermal quenching only happens above a threshold temperature, we can only use this technique above that threshold temperature.

Thermal quenching is a double-edged sword. As every photographer knows, the darker an object is, the more difficult it is to photograph, and the noisier or grainier the images tend to be. This makes it more difficult to measure temperature; we need the phosphor to be dim at high temperatures, but it also must be bright enough that we can get a good photograph. Thermal quenching is a property of the phosphor material, so our only option is to find materials with an appropriate threshold temperature. The threshold temperature sets the temperature range where we can make measurements. One additional significant outcome of this work is the identification of several phosphor materials that can be used from around 1350-2250°F, hundreds of degrees hotter than any other aerosol phosphor thermometry measurement has been made.

A.4.2 Particle Absorption Probability

So far, I've mostly discussed the physics of light emission and how it affects our temperature measurements. Absorption of light is an important part of the process as well. A phosphor can only emit as much light as it has absorbed, so if we want a phosphor to be bright (which is required to make a good measurement) we need the phosphor to be able to absorb light with high probability. The probability of an electron absorbing light depends on the frequency of the light. The closer the light frequency is to

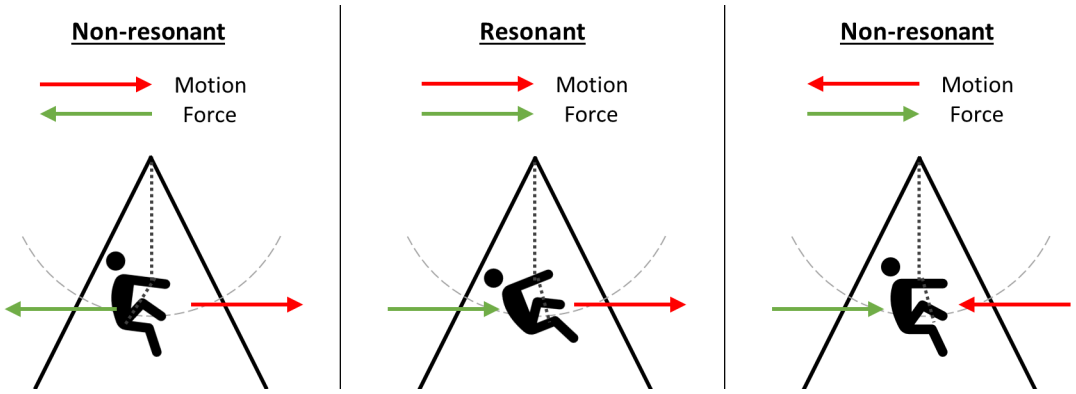

Figure A.9: Illustration of person on a swing. On the left and right, the person is moving forward, but pushing against the motion, and is non-resonant. In the middle, the person pushes with the motion of the swing, causing resonance.

the resonant frequency, the higher the probability of absorption, just like the opera singer and the glass.

What exactly is resonance though, and why does this matter? When talking about structures (the wine glass, for example), every object has a natural resonant frequency at which it tends to vibrate (for the wine glass, it's typically around 500-1,000 Hz, or roughly between the musical notes B_4 and B_5). For example, a pendulum on a clock has a natural frequency of 1 revolution per second; this allows it to precisely count seconds – every revolution of the pendulum marks another second passed. If we push on an object at the same frequency, the object will tend to move faster and faster – *i.e.*, the motion caused by pushing an object at its natural frequency is amplified. This amplification is called resonance. As an example, imagine sitting on a swing. If you push forward while the swing is moving forward, you start to swing faster and higher. If you push against the swing, or push at the wrong time, you tend to slow down. Pushing only during the forward motion of the swing is equivalent to exciting the swing at its natural frequency. This is illustrated in Figure A.9; pushing with the motion of the swing causes resonance and an amplification of the motion, while pushing against the swing does not.

Molecules behave in much the same way. The resonant frequency of a molecule depends on how the electrons are arranged around its constituent atoms (*i.e.*, the shape of electron cloud around the atom in Figure A.7), just as the resonant frequency of the wine glass depends on the glass' shape, and the resonance frequency of the swing depends on the chain length. When a molecule is excited near its resonant frequency, the electrons are able to move much more quickly – the effect of the laser is amplified when it is resonant with the molecule. Since the electrons are able to interact with the laser more efficiently, the probability with which the phosphor absorbs light increases near the resonant frequency.

In this work we showed that we can make better temperature measurements by using lasers with

frequencies closer to the resonant frequency of the phosphor. Using lasers close to the resonant frequency of the phosphor greatly increases the probability that the phosphor will absorb light, which in turn makes the phosphor's emission brighter. We also were able to estimate how the absorption probability changes with temperature for a few different phosphor materials, and have started looking into how temperature influences the phosphor's resonant frequency.

In addition to frequency, several other factors can affect the probability with which a phosphor particle can absorb light. These factors include how bright the laser light is and how long the particles are exposed to the light. Using quantum mechanics and statistics, I developed a model describing how these two factors influence the probability with which light is absorbed. There are a couple conclusions we form from the model. First, perhaps counter-intuitively, the brighter the light is, the lower the probability with which it is absorbed. We generally call this process a non-linear excitation. Similar to how an opera singer shatters a glass, a laser can excite a system so strongly that the electron is pulled entirely out of the system. Once the electron is pulled out, it is not able to emit light so it doesn't contribute to measurement. The second conclusion is that exposing particles to light for a longer period is advantageous. We want to supply a specific amount of light to a particle. If we apply that light very quickly, the particle will see a very bright flash. If we apply the same amount of light over a longer period, the flash will be weaker. Since the phosphors exhibit non-linear excitation, the weaker flash allows the particles to absorb more light. To summarize, a large portion of my work was dedicated to understanding the physics of phosphors, which relies strongly on quantum mechanics. In this section, I've outlined some of the basics of the theories, and discussed what we learned.

A.5 The Combustion Environment & Designing a Diagnostic

The tools I'm primarily interested in designing are to be used in engines. We fill the engine with a cloud of tiny phosphor particles, and replace some of the metal engine parts with glass. With this configuration, we can shine a laser into the engine, and place a camera on the other side to photograph the particles as they "glow". A diagram of the engine pieces, along with a picture of the optical-engine piston and head is shown in Figure A.10. Relative to the diagram, the camera would be pointing up into the piston window, looking at the fuel jet.

The diagram shows a small box with a diffuse-looking cone entering from the left. The cone represents a diesel fuel jet, or a stream of liquid fuel that breaks up into droplets, and then vaporizes. The diesel jet is actually very similar to a garden hose. Normally when you open the valve on a garden hose, you see a stream of liquid. But, if you partially cover the hose exit, that stream transforms into a more diffuse

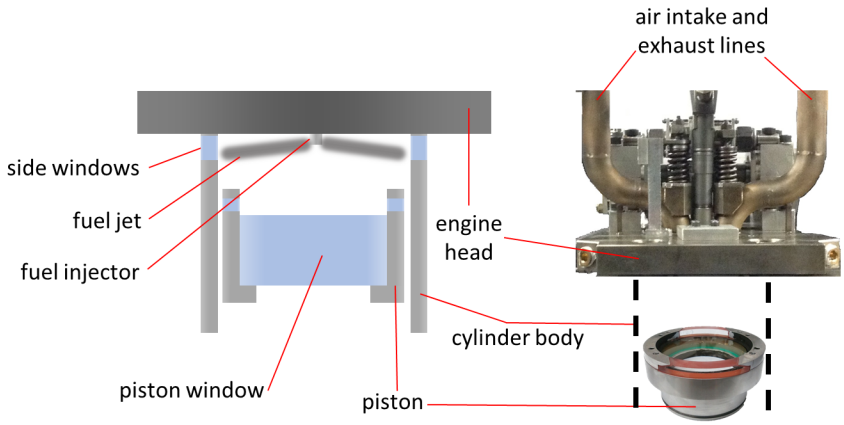

Figure A.10: Diagram and photograph of optically-accessible engine. The images on the right only show the piston (bottom) and engine head (top), which are featured in the diagram on the left.

spray. In the latter case, the liquid jet is moving so fast, friction between the water and surrounding air causes the jet to break apart into droplets. For this project, we're interested in looking primarily at the physics and chemistry of this fuel jet.

The experiment hopefully seems pretty straightforward, but we still have a few questions to answer. Namely:

- How big should the particles be?
- How many particles should we put in the engine?

And of course,

- Which phosphor material should we use?

There are a few secondary questions that are considered in my thesis as well (mostly related to specifics of the laser that is used to excite the phosphor particles) that I won't discuss further here. The last question, which phosphor material should we use, is the hardest question to answer, and for that reason I'll discuss it last.

A.5.1 Particle Size Requirements

Let's consider the first question, how big should the particles be, and try to develop some physical intuition about the problem. There are really two competing issues with particle size. First, the amount of light a particle can emit depends on particle size. When discussing light emission earlier, I talked about electrons absorbing and emitting light. Only the electrons in the particle can absorb or emit light.

In fact, only a handful of electrons in a phosphor particle can be resonant with the laser, so only a very small fraction of them can absorb and emit light. By making the particle larger, we're adding more and more electrons, some of which can absorb and emit light. Thus, by increasing the particle size, we can get more light out of the phosphor. Remember, to have a good measurement, we need to have as much light as possible emitted from the phosphor.

The second issue of particle size is slightly more complicated. Imagine a cloud of dust, or even the air in a dusty room. If the air is still, one can see dust particles slowly falling and collecting on the floor. If there is a breeze, one might see the dust particles moving along with the air. Gravity always pulls the particles down, while friction (usually called drag in a fluid) pushes against any motion of the particle. In fact, friction or drag tries to push the particle in the direction the air is moving. If the particle is moving at exactly the same speed and direction the air is moving, there is no drag or friction on the particle.

The particle motion can have a major impact on measurements we make using phosphors. When we use particle-based diagnostics like aerosol phosphor thermometry, we're really measuring the temperature of the particle, not the temperature of the gas. But of course, we really want to know the gas temperature; we need to ensure that the particle is representative of the gas. This means the particle needs to move along with the gas and have the same temperature. We are thus concerned with how quickly a particle responds to a change in temperature or velocity. We can estimate the time it takes for a particle to respond to a change in temperature or velocity; in both cases, the response time increases as particle size increases.

We want to have a large particle to get as much light as possible, but we also need the particle to be small enough to respond quickly to changes in temperature or velocity. The simplest solution is to choose the particle size to be just small enough that they can respond to any changes we expect in the fuel jet. The fuel jet itself is turbulent which, put simply, means that the motion of any individual fuel droplet is random and chaotic. Although this sounds like it should only complicate things, it actually simplifies them: all turbulent jets look alike on average, and scientists know a lot about turbulent jets.

Using this information, I estimate that particles must respond to changes in either velocity or temperature within about 5 microseconds (1 second is equal to 1 million microseconds). If I require a 5 microsecond response time, then the particle diameters must be less than 500 nanometers (1 meter is equal to 1 billion nanometers). Since we want to use the largest particles we can, we should use particles that are 500 nanometers in diameter.

A.5.2 Particle Seeding Density Limits

The second question, how many particles should we use, is a slightly more complicated question. The number of particles we use matters for a couple reasons. When we photograph particles, we never are looking for an individual particle (*i.e.*, we don't see an image of a single sphere). We usually have particles that are so small that they take up less than 1 pixel of the picture. In fact, we may use so many particles that we have 100 or more of them squeezed into a single pixel in the image, so the pictures we take look more like clouds than images of individual particles. We want to have as many particles as we can because every particle we add gives us more emitted light. There are some downsides as well; since we have solid particles suspended in a gas, adding more particles can actually slow down or cool the gas in the engine. This means the particles are intrusive, and could actually change how the diesel fuel jet burns in an unknown way. Having many particles can also impact the quality of our photographs, through a process called multiple scattering. In my thesis I've identified multiple scattering as being the most important factor in determining how many particles should be used.

Multiple scattering (or maybe just scattering) is actually closely related to another popular science discussion, why is the sky blue? As a child I remember seeing this question asked and answered in a public service announcement sponsored in part by Girl Scouts of the United States of America. In the announcement, a young child asks her father why is the sky blue? Dissatisfied with his answer, she answers the question instead. To paraphrase, she states that since blue is the shortest visible wavelength (or highest visible frequency), blue light is diffused by oxygen and nitrogen in Earth's atmosphere up to 10 times more than other colors.

I would alter only one word in her answer: rather than being diffused, I would say light is scattered, meaning that when light strikes a molecule (say, nitrogen or oxygen) it is deflected randomly. Blue light is indeed scattered many times more than red light in Earth's atmosphere. Thus, when we look away from the Sun, we see blue because we're seeing only light that is scattered towards us (most of which is blue light). When looking at the Sun, it appears yellow because we only see light that hasn't been scattered.

We have answered the question why is the sky blue using the concept of scattering. My follow-up question now is why are clouds white? Clouds, similar to air, are made up of particles that scatter light with one significant difference. Air is made up of tiny molecules that do not scatter light very strongly. Clouds, on the other hand, are typically made up of water droplets that are much larger than a molecule. These larger particles are much more likely to scatter light regardless of color; in fact, light will be scattered many times before exiting the cloud again. This is illustrated in Figure A.11. Since

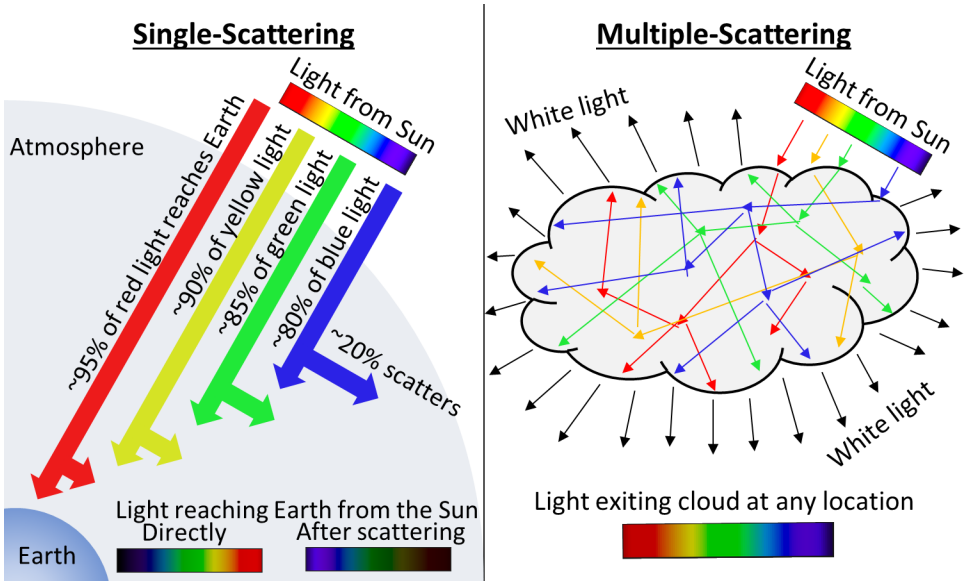

Figure A.11: Illustration of single scattering in Earth's atmosphere, in contrast with multiple scattering in a cloud.

light is randomly scattered so many times, any light that exits the cloud is white.

Multiple scattering can happen in optical diagnostics as well. Instead of clouds of water droplets, we have clouds of phosphor particles that scatter light efficiently. This means that any light emitted inside the engine from phosphor particles can scatter off of other phosphor particles before we can photograph it. It can also scatter off droplets of liquid fuel. This can make the images appear fuzzy, as though we were taking a photograph of the Sun through a thin cloud or haze. Multiple scattering can also make some regions appear brighter or darker than they should appear, similar to the apparent glow or halo when viewing the Sun through a cloud or haze.

In my thesis I developed a model to estimate how multiple scattering can affect our measurements. It turns out that even for very few particles in the engine, our measurements can be severely impacted. The most important impact is that parts of the phosphor "cloud" appear brighter than they should, similar to how the Sun illuminates an entire cloud, and not just the portion of the cloud that obstructs one's view of the Sun.

There are other impacts from multiple scattering as well. We excite laser particles using a laser beam that is formed into a narrow sheet. Imagine this as a laser pointer where instead of a "dot", the light forms a thin line. Multiple scattering makes this beam spread out, so instead of a thin line, we might see a thick line or even a rectangle. This same effect happens with laser pointers. Although lasers tend to diverge slightly even without multiple scattering (*i.e.*, the "dot" is larger when you are shining the laser from further away), the shape of the laser pointer beam can be distorted when it passes through

clouds or even air at long distances.

To avoid large experimental errors, I found that we need to have a relatively small number of particles in the engine. A single pixel in a photograph should have no more than around 50 particles. Although this number may seem large, the particles themselves are very small. In fact, the particles we use here are about 10 times smaller in diameter than the water droplets that make up many clouds (which in turn are about 1,000 times smaller than raindrops).

A.5.3 Precision Requirements and Phosphor Selection

The last question we need to answer in designing an experiment using aerosol phosphor thermometry is which phosphor should I use? To be able to answer that, we need to understand the benefits different phosphor materials can bring to an experiment. Of the materials we've identified, there are two properties that really control how well they can measure temperature: the phosphor brightness, and the phosphor quenching temperature.

From the previous section, thermal quenching is the phenomenon where phosphors emit less light at higher temperatures. We need to have thermal quenching to be able to measure temperature – if the phosphor's brightness doesn't change, we can't determine its temperature. But, if there is too much thermal quenching, the phosphor won't be bright enough to photograph. We want to choose a phosphor that begins to quench at temperatures slightly colder than the temperatures we're trying to measure. In this case, we want to measure at temperatures where diesel fuel starts to burn. This is typically around 800°F at the coldest. We have identified several possible phosphors that have thermal quenching temperatures around 800°F.

Phosphor brightness depends on other things besides thermal quenching. At cold temperatures (room temperature or colder) thermal quenching does not happen at all in most phosphors. Instead, the phosphor's brightness is partially intrinsic to the phosphor, and partially controlled by the laser frequency (or color) used to excite it.

Choosing a phosphor is very difficult because of these complexities. I approach this problem by determining how precise a temperature measurement needs to be, then determining which phosphors are capable of providing that precision.

So how good of a measurement do we need? Diesel ignition is controlled by chemistry. If we have a mixture of air and fuel that is hot enough to burn, chemical reactions will cause the fuel to break apart and combine with oxygen in the air. This chemical reaction releases heat and raises the temperature of the gas. Some mixtures of fuel and air, typical of diesel engines, will actually burn in two steps; one

at low-temperature and one at high-temperature. The low-temperature step happens first and heats the gas by about 200°F or less. By considering this temperature increase, I estimate that we need to measure temperature to within 2.5% or about 50°F of its true value. This may sound pretty simple; after all, most digital thermometers can measure within 2°F, and medical grade thermometers even less. But thermometers are very different devices – a thermometer is large (several millimeters or more in diameter) and measures slowly. It can take several seconds or even minutes to get a measurement. We use thermographic phosphors because we can measure things very fast (within less than a microsecond, or more than 100,000 times faster than the blink of an eye) and in small spaces (phosphor particles are less than a micrometer in diameter, or about 100 times smaller than the thickness of a human hair). Beyond that, we're interested in measuring temperatures at 1700°F or higher, and no traditional thermometer is capable of that.

Now that we know what our temperature precision should be, we predict the temperature precision we can achieve using each of the phosphor materials. This is a mathematically-intensive process, and a large portion of my thesis is dedicated to doing just this. It turns out that several of the phosphors we investigated can meet our criterion, but each at a different range of temperatures. There is no single phosphor that can cover every scenario we'd like to measure.

In this case, we choose phosphor materials by trying to predict how well each material will work for our application, then choosing the one that appears to work best. But this isn't always possible, especially when there are a lot of possible materials to choose from. Instead we rely on more general observations about phosphor performance. Some general observations we've found from this work are:

- Our best performance typically comes from phosphors that are intrinsically bright, or by using lasers with frequencies near the phosphor's resonant frequency
- We are usually only able to measure temperatures slightly hotter than the phosphor's quenching temperature

But perhaps the most important lesson is simply that designing a diagnostic or experiment is not a simple task. Many factors come into play, and many of the aspects of diagnostic performance are coupled to each other.

A.6 Conclusions

Throughout this chapter, I've outlined my work investigating, improving, and designing optical diagnostic methods primarily using aerosol phosphor thermometry. My work focused on understanding the

optical properties (or photophysics) of these materials and tried to understand the physics of light absorption and emission in these materials. I discussed this throughout Section 4. The second goal of my work was to outline a framework for experiment design, design a diagnostic using that framework, and estimate the diagnostic's performance. I discussed this in Section 5. Some of the highlights of my work that I discussed or mentioned in this chapter include:

- Characterized several new phosphor materials that could be used for aerosol phosphor thermometry
- Improved our understanding of, and developed a model for, absorption and emission of light in phosphors
- Demonstrated temperature imaging experiments using aerosol phosphor thermometry at over 1500°F in an atmospheric flame
- Characterized the effects of tracer particle response and multiple scattering on diagnostic performance
- Developed a framework for the design of aerosol phosphor thermometry diagnostics
- Developed a performance prediction model for aerosol phosphor thermometry diagnostics
- Designed a diagnostic approach that could be used to investigate ignition in diesel engines

As with any scientific work, new problems and questions arise in the course of conducting research. In this case, I spent a lot of time investigating the impacts of different effects like multiple scattering on the performance of my diagnostic, and I formed conclusions from that analysis. Future work needs to experimentally validate both the models I developed, and the conclusions I formed. Some other things that need to be done in the future include:

- Perform the diagnostic in an engine
- Measure the absorption and emission properties of additional phosphors identified in this work
- Validate the phosphor absorption model for a wider range of conditions

Overall, this work presents a significant step forward in understanding, designing, and applying experimental techniques that use aerosol phosphor thermometry.

Appendix B

Molecular Spectroscopy Theory

B.1 Overview

Formaldehyde is assumed to obey the Born-Oppenheimer principle, which roughly states that the molecular and electronic motions within the molecule are independent. Neglecting spin, this allows the Hamiltonian operator two be written as [164]

$$\mathcal{H} = \mathcal{H}_e + \mathcal{H}_v + \mathcal{H}_r, \tag{B.1}$$

with energy eigenstates defined by

$$\begin{aligned} &\mathcal{H}_e \left|\psi_i\right\rangle = \mathcal{T}_i \left|\psi_i\right\rangle \qquad \mathcal{H}_v \left|\Phi_i\right\rangle = \mathcal{G}_i \left|\Phi_i\right\rangle \qquad \mathcal{H}_r \left|\Theta_i\right\rangle = \mathcal{F}_i \left|\Theta_i\right\rangle \\ &\quad \implies \mathcal{H} \left|\psi_i\right\rangle \left|\Phi_i\right\rangle \left|\Theta_i\right\rangle = (\mathcal{T}_i + \mathcal{G}_i + \mathcal{F}_i) \left|\psi_i\right\rangle \left|\Phi_i\right\rangle \left|\Theta_i\right\rangle = E_i \left|\psi_i\right\rangle \left|\Phi_i\right\rangle \left|\Theta_i\right\rangle . \end{aligned} \tag{B.2}$$

The eigenkets $|\chi_i\rangle$, $|\Phi_i\rangle$, and $|\Theta_i\rangle$ are eigenstates of the electronic, vibrational, and rotational Hamiltonians, respectively. The energies associated with the electronic, vibrational, and rotational eigenstates are given by $\mathcal{T}_i$, $\mathcal{G}_i$, and $\mathcal{F}_i$, respectively. The subscript i is used to denote any unique single combination of electronic, vibrational, and rotational eigenstates or quantum numbers.

Absorption and emission of radiation corresponds to transitions between different eigenstates, and is characterized by a rate constant. The transition rate, or intensity, between any two states i and j can be determined from Fermi's Golden Rule [165]. For photophysical processes, transitions occur due to a coupling between the electric field generated by the charge distribution in the molecule and an external field. The interaction Hamiltonian ($\mathcal{H}'$) in this case is given by the potential energy of the

electromagnetic interaction as

$$\begin{aligned}\mathcal{H}' &= -\frac{e}{m_e}\vec{\boldsymbol{p}}\cdot\vec{\boldsymbol{A}} - \frac{e}{m_e}\vec{\boldsymbol{s}}\cdot\vec{\boldsymbol{B}} \\ &\approx -\frac{eA_0}{m_e}\hat{\boldsymbol{\epsilon}}\cdot\vec{\boldsymbol{p}} - i\frac{e\omega A_0}{m_e c}(\hat{\boldsymbol{n}}\cdot\vec{\boldsymbol{r}})(\hat{\boldsymbol{\epsilon}}\cdot\vec{\boldsymbol{p}}) - i\frac{e\omega A_0}{m_e c}(\hat{\boldsymbol{n}}\times\hat{\boldsymbol{\epsilon}})\cdot\hat{\boldsymbol{s}}\end{aligned} \tag{B.3}$$

where $\vec{\boldsymbol{p}}$ is the momentum operator of an individual interacting particle, $\vec{\boldsymbol{r}}$ is the electron position operator, and $\vec{\boldsymbol{A}}$ is the magnetic vector potential of the electromagnetic field. The second term in the first line is due to interaction between the electron spin and the magnetic field, where $\vec{\boldsymbol{s}}$ is the spin operator and $\vec{\boldsymbol{B}}$ is the magnetic field vector. The scalar properties e, m_e, and c, are the electron charge, electron mass, and speed of light, respectively. Excitation is assumed to be a monochromatic plane wave (propagating in the direction $\hat{\boldsymbol{n}}$ with polarization direction $\hat{\boldsymbol{\epsilon}}$, magnetic vector potential magnitude A_0, and frequency ω), and the simplification on the second line makes use of a multipole expansion assuming the radiation wavelength is large compared to the atomic or molecular scale [166]. This expression explicitly ignores contributes on the order of A^2 and higher. The approximation explicitly includes the electric dipole, electric quadrupole, and magnetic dipole terms*.

Equation B.3 can be rewritten using commutation relations to separate the interaction Hamiltonian into parts that depend only parametrically on molecular geometry (*i.e.*, multipole moments), and pieces that depend on molecular orientation relative to the perturbing field (*i.e.*, a rotational contribution). Specifically, $(\hat{\boldsymbol{\epsilon}}\cdot\vec{\boldsymbol{p}}) = im_e\omega(\hat{\boldsymbol{\epsilon}}\cdot\vec{\boldsymbol{r}}) = im_e\omega r\mathcal{D}$ (where $\mathcal{D}$ is the direction cosine operator). Similar procedures can be used to rewrite the other three terms, resulting in

$$\begin{aligned}\mathcal{H}' &= -iA_0\omega(\hat{\boldsymbol{\epsilon}}\cdot\vec{\boldsymbol{\mu}}) - i\frac{A_0\omega^2}{2c}(\hat{\boldsymbol{\epsilon}}\cdot\vec{\vec{\boldsymbol{Q}}}\cdot\hat{\boldsymbol{n}}) - i\frac{A_0\omega}{2m_e c}(\hat{\boldsymbol{\epsilon}}\cdot\vec{\boldsymbol{M}}) \\ &= -iA_0\omega\mu\mathcal{D} - i\frac{A_0\omega^2}{2c}Q\mathcal{D} - i\frac{A_0\omega}{2m_e c}M\mathcal{D}\end{aligned} \tag{B.4}$$

where $\vec{\boldsymbol{\mu}} = \sum e\vec{\boldsymbol{x}}$ is the total electric dipole moment operator, $\vec{\vec{\boldsymbol{Q}}} = \sum e(\vec{\boldsymbol{x}}\vec{\boldsymbol{x}} - r^2\delta_{ij}/3)^\dagger$ is the total electric quadrupole moment operator, and $\vec{\boldsymbol{M}} = \sum e(\vec{\boldsymbol{L}} + 2\vec{\boldsymbol{s}})$ is the total magnetic dipole moment operator. The sums are performed over each electron and ion in the molecule.

Fermi's golden rule can now be used to define a transition rate k_{ij} from state i to state j, given by

$$\begin{aligned}k_{ij} &= \frac{2\pi}{\hbar}\left|\langle\Theta_i|\langle\Phi_i|\langle\psi_i|\mathcal{H}'|\psi_j\rangle|\Phi_j\rangle|\Theta_j\rangle\right|^2\delta(E_i - E_j \pm \hbar\omega) \\ &= \frac{2\pi A_0^2\omega^2}{\hbar}\left|\langle\psi_i|\mu + \frac{\omega}{2c}Q + \frac{1}{2m_e c}M|\psi_j\rangle\right|^2\left|\langle\Theta_i|\mathcal{D}|\Theta_j\rangle\right|^2\left|\langle\Phi_i|\Phi_j\rangle\right|^2\delta(E_i - E_j \pm \hbar\omega)\end{aligned} \tag{B.5}$$

*For formaldehyde, the electric dipole term is dominant, but all three components are included for completeness

†Here, $r^2 = \sum_k x_k x_k$ is subtracted to make $\vec{\vec{\boldsymbol{Q}}}$ traceless.

where the sign on $\hbar\omega$ inside the δ-function determines whether this is an absorption or emission process.

The rate constant expression (Equation B.5) is clearly separated into electronic, vibrational, and rotational components. As written, the directional dependence of the multipole operators is removed by averaging over all orientations, and absorbing the direction cosine from the dot product into the rotational component. Note that the transition moment operators still have some directional dependence in that they are tensors; the rotational component implicitly depends on direction of the electromagnetic wave relative to the transition moments. There is no dependence on the vibrational coordinates to first order. Defining I_e, I_v, and I_r as the electronic, vibrational, and rotational line intensities, the simplified expression is

$$k_{ij} = \frac{2\pi}{\hbar}|\vec{\boldsymbol{E}}|^2 I_e I_v I_r \delta(E_i - E_j \pm \hbar\omega). \tag{B.6}$$

The electric field intensity $|\vec{\boldsymbol{E}}| = \omega A_0$ is the electric field strength associated with the vector potential A_0 in the plane wave approximation. The calculation is performed at the equilibrium geometry of the initial state j. For absorption, the molecular properties are taken at the ground state, and the electric field intensity is determined by the laser energy. For fluorescence, the equilibrium geometry is at the excited state, and electric field intensity is related to the availability of electromagnetic modes in the medium.

So far it has been assumed that the dipole operator is independent of the nuclear motion. This assumption is typically referred to as the Condon approximation, and forms the theoretical basis of the Franck-Condon approach. However, this is in general not true; in particular, formaldehyde's dipole operator has a strong nuclear coordinate dependence through coupling with the out-of-plane bending mode [167]. Since the multipole operators include a contribution from the atomic charge distribution, nuclear motion can instantaneously create a transition moment; *e.g.*, the dipole moment is $\vec{\boldsymbol{\mu}} = \sum_i e\vec{\mathbf{r_i}} - \sum_I eZ_I\vec{\mathbf{R_I}}$, and thus depends on the instantaneous configuration. In this expression, Z_I is the atomic number of atom I, and $\vec{\boldsymbol{R}}_I$ is the position operator of atom I. Since the nuclei move continuously, the electronic and vibrational transition intensity can no longer be separated exactly, and instead a series expansion in $\vec{\boldsymbol{R}}_I$ is used[168].

The rate constant using Fermi's golden rule can now be expressed to second order as

$$\begin{aligned} k_{ij} &= \frac{2\pi}{\hbar}|\tilde{\mathbf{E}}|^2 \Bigg| \langle\psi_i|\mu_0 + \frac{\omega Q_0}{2c} + \frac{M_0}{2m_e c}|\psi_j\rangle \langle\Phi_i|\Phi_j\rangle \\ &\qquad + \sum_l \left(\frac{\partial \langle\psi_i|\mu + \frac{\omega Q}{2c} + \frac{M}{2m_e c}|\psi_j\rangle}{\partial q_l} \right)_{\mathbf{q_0}} \langle\Phi_i|q_l|\Phi_j\rangle \Bigg|^2 I_r \delta(E_i - E_j \pm \hbar\omega) \\ &= \frac{2\pi}{\hbar}|\tilde{\mathbf{E}}|^2 I_{ev} I_r \delta(E_i - E_j \pm \hbar\omega), \end{aligned} \tag{B.7}$$

where the new symbol I_{ev} represents the coupled vibronic transition intensity in the combined Franck-Condon Herzberg-Teller method. The nuclear position operator q_l is written in dimensionless normal-mode coordinates, as opposed to Cartesian coordinates (denoted as x_l), such that q_l represents a dimensionless displacement of the nucleus in the direction of normal mode vector l.

The δ-function in the rate constant expressions is a result of energy uncertainty under the assumption that the transition is infinitely slow [166]. In reality, the transition lifetime is finite which results in a distribution of finite width. This effect is typically referred to as lifetime or natural broadening, and the width can be estimated from the time-energy uncertainty relation. Unlike most uncertainty relations, the time-energy uncertainty relation ($\Delta E = \hbar/\Delta t$) does not suggest a finite precision with which energy or time can be measured. Instead this is simply a result of quantum dynamics that a transition occurring in a finite time is not perfectly sharp [169]. The energy distribution of the transition can be further widened due to collision broadening and temperature broadening. As a result this Dirac-δ function is replaced with a pressure and temperature dependent lineshape function.

From the preceding discussion, transition intensity (like energy) can be separated into products of the electronic, vibrational, and rotational transitional intensities if the Franck-Condon approximation is satisfied, or vibronic and rotational factors in the Herzberg-Teller scheme. These behaviors collectively result in what is known as the *Energy-Intensity Model* [164]. Following this model, a complete spectrum can be written as a sum of individual transition lines, where each line is characterized by a transition energy, a transition strength, and a lineshape function. With this formulation, the single molecule absorption cross-section (σ_{ij}, with units of length squared) and emission intensity (ϵ_{ij}, with units of energy per unit time per unit frequency) can be written as

$$\sigma_{ij}(\omega) = \frac{4\pi^2\alpha\omega}{3e^2} I_{ev} I_r \delta(\omega_{ij} - \omega) \tag{B.8a}$$

and

$$\epsilon_{ij}(\omega) = \frac{4\hbar\omega^4\alpha}{3c^2e^2} I_{ev} I_r \delta(\omega_{ij} - \omega), \tag{B.8b}$$

where the dimensionless number α is the fine structure constant, and a factor of three is included in the denominator to generalize the plane-wave assumption [170]. These definitions correspond exactly with those given by [171], though here the equations are expressed in SI units.

Equation B.8a is found by using the definition of absorption cross section and dividing the rate-constant expression (Equation B.7) by the energy flux of the applied electromagnetic field. The single molecule fluorescence power (Equation B.8b) is simply the product of Equation B.7 with the photon energy ($\hbar\omega$), and the electric field strength rewritten in terms of the photonic density of states in free

space[‡]. More generally, Equation B.8b can be scaled by the inverse of the index of refraction of the surrounding medium, n^{-1}, to account for non-vacuum effects to first order [172].

The full absorption cross section and spontaneous emission intensity per molecule are given by the sum over all lines, weighted by the population fraction or probability for the initial state (as stated in Chapter 3). These are given by

$$\sigma(\omega) = \frac{4\pi^2\alpha\omega}{3e^2}\sum_{ij} F_i(p,T)\ I_{ev}\ I_r\ \mathcal{L}(\omega;\omega_{ij},T,p) \tag{B.9a}$$

$$\epsilon(\omega) = \frac{4\hbar\omega^4\alpha}{3c^2e^2}\sum_{ij} F_i(p,T)\ I_{ev}\ I_r\ \mathcal{L}(\omega;\omega_{ij},T,p) \tag{B.9b}$$

where $\mathcal{L}(\omega)$ is the assumed lineshape function. Here the subscripts i and j again represent the initial and final rovibronic state, respectively, and the sums are performed over every combination of rovibronic states. The population fraction F_i is the probability of a molecule being in state i and is temperature and pressure dependent in general. For LIF emission, it is also dependent on the excitation wavelength. The lineshape function is also pressure and temperature dependent, and is centered at the most likely transition frequency $\hbar\omega_{ij} = E_j - E_i$.

Due to the complexity of polyatomic molecules, as well as the lack of information relating to more complex formulations for formaldehyde, the remaining analysis assumes that the formaldehyde molecule is adequately described as an uncoupled anharmonic oscillator and asymmetric rotor. Anharmonicity must be considered for the out of plane bending mode in the $\tilde{A}\ ^1A_2$ states, as it has been shown to be strongly anharmonic, instead being represented by a symmetric double well potential [76]. Appendix C outlines the results of several *ab initio* calculations that were used to estimate spectral properties including transition dipole moments and derivatives.

B.2 The Rigid Rotor

The asymmetric rotor was first described in depth by King, Hainer, and Cross in a series of papers beginning in 1943 [173–179]. Due to the complexity of the asymmetric rotor problem, the solutions do not lend themselves to a closed form solution for quantum numbers $j > 3$, and can be difficult to compute exactly. Books (e.g., [180]) with tables of linestrengths as a function of the asymmetry parameter, κ, have been published. The analysis by King, Hainer, and Cross instead employs a variational method in which the energy eigenvalues and eigenkets are determined exactly using the symmetric rotor as a basis

[‡] $|E_0|^2 = 2u/\epsilon_0$, and $u = \hbar\omega N(\omega)$, where $N(\omega) = \hbar\omega^3/\pi^2c^3$ is the photonic density of states in free space

set. The analysis begins with the rotational Hamiltonian, which is assumed to be uncoupled from the vibrational Hamiltonian, expressed as [181]

$$\mathcal{H}_r = \hbar^{-2}[a\mathcal{P}_a^2 + \mathcal{P}_b^2 + c\mathcal{P}_c^2] = \hbar^{-2}[a\mathcal{P}^2 + (b-a)\mathcal{P}_b^2 + (c-a)\mathcal{P}_c^2] \tag{B.10}$$

Where $\mathcal{P}_i$ is the angular momentum operator along the ith principal axis, and a, b, and c are the spectroscopic rotational constants defined by $a = \hbar^2/2I_a$, and so on for b and c. This Hamiltonian is exactly Watson's rotation-vibration Hamiltonian with the vibrational and ro-vibrational terms excluded [182] (vibrational terms will be considered in Section B.3). The spectroscopic rotational constants are ordered such that $a \geq b \geq c$.

Solutions can be found as a linear combination of the symmetric rotor wavefunctions, denoted by quantum numbers J, K, and M, corresponding to the $\mathcal{P}^2$, $\mathcal{P}_c$, and $\mathcal{P}_z$ operators, respectively. This was first described by Wang [183] in an effort to determine the energy levels and wavefunctions of the asymmetric top, though line intensities were first calculated using this formulation in the completely asymmetric case by Cross, Hainer and King [174]. For reference, the symmetric rotor Hamiltonian and angular momentum operators operators have the following properties:

$$\mathcal{H}_r \left|JKM\right\rangle = \mathcal{F}_{JKM} \left|JKM\right\rangle \tag{B.11a}$$

$$\mathcal{P}^2 \left|JKM\right\rangle = \hbar^2 J(J+1) \left|JKM\right\rangle \tag{B.11b}$$

$$\mathcal{P}_c \left|JKM\right\rangle = \hbar K \left|JKM\right\rangle \tag{B.11c}$$

$$\mathcal{P}_z \left|JKM\right\rangle = \hbar M \left|JKM\right\rangle . \tag{B.11d}$$

The $|JKM\rangle$ eigenstates are used as a basis for the determining the asymmetric rotor energy levels and transition strengths. From King, Hainer, and Cross [173], the energy levels of the asymmetric rotor are given by

$$\mathcal{F}_{J,\tau} = \frac{a+c}{2} J(J+1) + \frac{a-c}{2} E_\tau(\kappa), \tag{B.12a}$$

where

$$\kappa = \frac{2b-a-c}{a-c}. \tag{B.12b}$$

The energy eigenvalues are now labeled by two quantum numbers, J and τ, where κ is an asymmetry parameter. The K eigenvalue is no longer used since the $\mathcal{P}_c$ operator no longer commutes with the

Hamiltonian, and thus does not form mutual eigenstates. Instead, the quantum number τ is used which in the limiting prolate and oblate symmetric rotor cases becomes identical to K. The quantum number J corresponds to the total angular momentum operator, $\mathcal{P}^2$, and is the same quantum number that appears for the symmetric rotor. This is a result of the total angular momentum being dependent only on the sum of the rotor moments of inertia ($\mathcal{P}^2 = \mathcal{P}_a^2 + \mathcal{P}_b^2 + \mathcal{P}_c^2$), and commuting with the Hamiltonian operator. The second term is a contribution due to the asymmetry of the molecule. Note that each $|J\tau\rangle$ state has $2J+1$ degeneracy, as with the symmetric rotor. Further, τ takes on the values $\{-J,\ -J+1,\ \cdots,\ J-1,\ J\}$, similar to K for the symmetric rotor.

The values of $E_\tau(\kappa)$ are found by diagonalizing the Hamiltonian matrix, or rather the asymmetric $E_\tau(\kappa)$ matrix, in the symmetric rotor basis. The Hamiltonian matrix is constructed by applying the asymmetric Hamiltonian operator to the symmetric rotor eigenkets, resulting in

$$\begin{aligned}\langle J'K'M'|E_\tau(\kappa)|JKM\rangle =& \frac{\sqrt{J(J+1)-(K+1)(K+2)}\sqrt{J(J+1)-K(K+1)}}{2}\delta_{K,K'+2} \\ &+\frac{\sqrt{J(J+1)-(K+1)(K+2)}\sqrt{J(J+1)-K(K+1)}}{2}\delta_{K+2,K'} \\ &+\kappa K^2\delta_{K,K'}.\end{aligned} \tag{B.13}$$

Calculation of the transition strength of a rotational transition for an asymmetric rotor is described in detail by Wollrab [184], largely following the methods of Cross [174]. The rotational transition strength is calculated from the matrix elements of the direction cosine between the initial and final rotational states. This represents the transformation between the space-fixed electric field frame and the principal frame of the molecule, and assumes the principal axes directions do not change between the initial and final states. This is generally not a good approximation for UV transitions, and corrections will be discussed later. Mathematically, the rotational transition strength is

$$I_r = |\langle J\tau|\mathcal{D}|J'\tau'\rangle|^2 = \sum_{F,M,M'} |\langle J\tau M|\mathcal{D}_{Fg}|J'\tau'M'\rangle|^2. \tag{B.14}$$

where the sum is taken over all degenerate eigenstates M and M', and F is summed over all three spatial dimensions $\hat{x}$, $\hat{y}$, and $\hat{z}$. Here, the direction cosine operator has been explicitly written as the transformation between from the molecule-fixed g axes to the radiation field fixed F axes.

Averaging over all spatial orientations, the sum over F is replaced by selecting a single direction, here $\hat{z}$, and multiplying by three. The direction cosine operator is written in the symmetric rotor basis, and transformed to the asymmetric rotor basis. This is achieved by applying the same transformation to the

symmetric rotor direction cosines that diagonalizes the asymmetric Hamiltonian submatrix, $E(\kappa)$. One additional step is required to transform the symmetric rotor direction cosines into a basis set belonging to the same symmetry group of the asymmetric rotor. This transformation was described first by Wang [183] in detail, and hence is referred to as the Wang transformation. The symbols T and X are used to describe the transformation diagonalizing the Hamiltonian, and the Wang transformation, respectively.

The Wang transformation and asymmetry transformation are defined by

$$X = \frac{1}{\sqrt{2}} \times \begin{bmatrix} -\mathbb{1}_{\mathbf{J}} & \mathbf{0}_{\mathbf{J},\mathbf{1}} & \mathbb{J}_{\mathbf{J}} \\ \mathbf{0}_{\mathbf{1},\mathbf{J}} & \sqrt{2} & \mathbf{0}_{\mathbf{1},\mathbf{J}} \\ \mathbb{J}_{\mathbf{J}} & \mathbf{0}_{\mathbf{J},\mathbf{1}} & \mathbb{1}_{\mathbf{J}} \end{bmatrix} \tag{B.15}$$

and

$$T^{\dagger} H_{K',K''} T = E_{\tau}(\kappa), \tag{B.16}$$

where the matrix $\mathbb{1}$ is the identity matrix, $\mathbb{J}$ is the exchange matrix, and $\mathbf{0}_{\mathbf{n},\mathbf{m}}$ is the n by m matrix of zeros. The transformations X and T are diagonal with respect to J, and hence only operate on the K states (transforming them to the τ basis), allowing the line strength equation to be rewritten as

$$I_r = 3|\left\langle J|\mathcal{D}_{Zg}|J'\right\rangle|^2 \times |\left\langle J\tau|\mathcal{D}^A_{Zg}|J'\tau'\right\rangle|^2 \times \sum_{M,M'} |\left\langle JM|\mathcal{D}_{Zg}|J'M'\right\rangle|^2 \tag{B.17}$$

where $\mathcal{D}^A_{Zg} = (T')^{\dagger}(X')^{\dagger} \left\langle JK|\mathcal{D}_{Zg}|J'K'\right\rangle XT$ is the direction cosine operator transformed from the symmetric rotor basis to the asymmetric rotor basis. As defined in Equation B.16, T is a projection operator that transforms the K states into the τ states, while X operates only on the K states. The prime ($'$) is used to identify the initial state.

	R	Q	P
$\langle JK\|\mathcal{D}_{Fz}\|J'K\rangle$	$2\sqrt{(J+K+1)(J-K+1)}$	$2K$	$-2\sqrt{J^2-K^2}$
$\langle JK\|\mathcal{D}_{Fy}\|J'K\pm1\rangle$ $= i\langle JK\|\mathcal{D}_{Fx}\|JK\pm1\rangle$	$\mp\sqrt{(J\pm K+1)(J\pm K+2)}$	$\mp\sqrt{(J\mp K)(J\pm K+1)}$	$\sqrt{(J\mp K)(J\mp K-1)}$
$\langle J\|\mathcal{D}_{Fg}\|J'\rangle^2$	$[16(J+1)^2(2J+1)(2J+3)]^{-1}$	$[16J^2(J+1)^2]^{-1}$	$[16J^2(4J^2-1)]^{-1}$
$\langle JM\|\mathcal{D}_{Zg}\|J'M\rangle^2$	$4(J+M+1)(J-M+1)$	$4M^2$	$4(J^2-M^2)$
$\langle JM\|\mathcal{D}_{Yg}\|J'M\pm1\rangle^2$ $= -\langle JM\|\mathcal{D}_{Xg}\|J'M\pm1\rangle^2$	$(J\pm M+1)(J\pm M+2)$	$(J\mp M)(J\pm M+1)$	$(J\mp M)(J\mp M-1)$

Table B.1: Direction cosine matrix elements in symmetric rotor basis set. R, Q, and P represent the R-, Q-, and P-branch transitions corresponding to $J' = J+1$, $J' = J$, and $J' = J-1$, respectively.

The final requirement to calculate the linestrengths is the direction cosine matrix elements between the symmetric rotor states. For reference, these are listed in Table B.1. From the table, the first two terms of Equation B.17 are independent of K and can be simplified as they are not acted upon by T and X. In particular, the sum can be evaluated and the final expression simplified to

$$3\left\langle J|\mathcal{D}_{Zg}|J'\right\rangle^2 \sum_{M,M'} \left\langle JM|\mathcal{D}_{Zg}|J'M'\right\rangle^2 = \begin{cases} \frac{1}{4(J+1)} & J' = J+1 \text{ (R-branch)} \\ \frac{2J+1}{4J(J+1)} & J' = J \text{ (Q-branch)} \\ \frac{1}{4J} & J' = J-1 \text{ (P-branch).} \end{cases} \tag{B.18}$$

After evaluating the line strength matrices, the selection rules must be applied. So far, the quantum number τ has been used to label each of the $2J+1$ states of the asymmetric rotor. However, they are better labeled using two quantum numbers, K_a and K_c. These quantum numbers are defined as the values of the quantum number K of the symmetric rotor, transformed into the asymmetric rotor basis used here (*i.e.*, using the Wang transform) for the prolate and oblate rotors, respectively. In particular, the asymmetric label $\tau = K_a - K_c$. These quantum numbers, and their relationship to τ, are discussed in detail in [173] and [185]. Note that these quantum numbers form the same basis as τ. From [174] and [185], the following selection rules apply:

$$\Delta K_a = 0, \pm 2, \pm 4... \qquad \Delta K_c = \pm 1, \pm 3... \qquad \vec{\mu} \parallel \hat{a} \tag{B.19}$$

$$\Delta K_a = \pm 1, \pm 3... \qquad \Delta K_c = \pm 1, \pm 3... \qquad \vec{\mu} \parallel \hat{b} \tag{B.20}$$

$$\Delta K_a = \pm 1, \pm 3... \qquad \Delta K_c = 0, \pm 2, \pm 4... \qquad \vec{\mu} \parallel \hat{c} \tag{B.21}$$

where the notation $\vec{\mu} \parallel \hat{x}$ means the transition moment lies along the direction $\hat{x}$. In general, the transition moment may have non-zero components along each axis, and then all transitions (except those where ΔK_a and ΔK_c are both zero or even) are allowed and should be scaled by the appropriate component of the transition moment. For formaldehyde, the transition moment for $\tilde{X}\ ^1A_1 \leftrightarrow \tilde{A}\ ^1A_2$ lies primarily along the $\hat{b}$ axis, resulting from vibronic coupling with the out-of-plane bending mode.

Axis-Switching

The axis-switching effect appears in electronic molecular transitions where geometry of the excited state differs from that of the ground state. Specifically, the principal axes are rotated upon excitation due to change in the electronic charge distribution [186]. Mathematically, this requires that a rotation be applied to the initial (or final) state, $\mathcal{D}^J_{M',M}$, where the superscript J indicates there is a dependence on

the total angular momentum quantum number. The subscripts indicate the initial and final M and M' quantum numbers. The rotational line strength is now written as

$$I_r = 3|\langle J|\mathcal{D}_{Zg}|J'\rangle|^2 \times |\langle J\tau|\mathcal{D}^A_{Zg}|J'\tau'\rangle|^2 \times \sum_{M,M'} |\langle JM|\mathcal{D}^J_{M',M}\mathcal{D}_{Zg}|J'M'\rangle|^2. \tag{B.22}$$

The $\mathcal{D}^J_{M',M}$ operator specifically is the Wigner D-matrix with non-zero Euler angles α, β, and γ, and can be written as [166]

$$\mathcal{D}^J_{M',M} = e^{-i(M'\alpha+M\beta)}d^J_{m',m} \tag{B.23}$$

where $d^J_{m',m}$ is a function of only the angle β, and the exponential in M' and M has an arbitrary effect on the calculation as it only alters the phase of the matrix element. The 'reduced' matrix element $d^J_{m',m}$ has an explicit formula derived by Wigner that is a power series in trigonometric functions of $\beta/2$. This formula is not repeated here. The matrix element $d^J_{m',m}$ can also be written in terms of Jacobi polynomials and the spin-weighted spherical harmonics. In terms of the Jacobi polynomials, the reduced rotation operator is [187]

$$d^J_{M',M}(\beta) = \sqrt{\frac{(J+M)!(J-M)!}{(J+M')!(J-M')!}}\sin(\beta/2)^{M-M'}\cos(\beta/2)^{M+M'}P^{(M-M',M+M')}_{J-M}\big(\cos(\beta)\big), \tag{B.24}$$

where $P^{(a,b)}_n(x)$ is the Jacobi polynomial.

B.3 The Harmonic Oscillator

The harmonic oscillator model in quantum mechanics is of great theoretical interest due to its widespread appearance in quantum mechanics and theoretical simplicity. Although higher-order potentials, such as the Morse oscillator, may describe molecular vibrations more accurately, they are sufficiently complex that calculations of matrix elements are difficult and often approximate by nature (see, *e.g.*, [188]). In contrast, Franck-Condon type overlap integrals and nuclear position matrix elements can be calculated in a straightforward manner for the harmonic potential. Further, expressions for coupled harmonic oscillator matrix elements and Franck-Condon factors have been developed both approximately and exactly [189, 190]. Finally, for many vibrational and vibronic transitions of interest, particularly for formaldehyde, only relatively low vibrational states (up to about $v = 4$) are apparent in fluorescence spectra in combustion environments [50]; this is advantageous as the harmonic oscillator model tends to

perform well compared to experiment at low quantum numbers.

To first order, any molecular potential is harmonic [191]. This can be shown as follows using an unspecified Hamiltonian for n particles, expanded in terms of the particle positions as

$$\mathcal{H}_v = \mathcal{T}_v + \mathcal{V}_v = \frac{\dot{\mathbf{x}}^T \mathbf{M} \dot{\mathbf{x}}}{2} + \mathbf{x}^T \mathbf{K} \mathbf{x} + \mathcal{O}(\boldsymbol{x}^3), \tag{B.25}$$

where $\mathbf{x}$ is the vector of particle positions, $\mathbf{M}$ is a diagonal mass matrix, and $\mathbf{K}$ is the Hessian matrix of the potential, which is used to approximate the actual potential. The superscript T (^{T}) is used here to denote the matrix transpose of classical quantities.

The constant and linear terms in the potential vanish necessarily (*i.e.*, $\frac{\partial \mathcal{V}}{\partial x_i} = V(\mathbf{0}) = 0$) to enforce the equilibrium condition, such that the first non-zero term is quadratic. The cubic terms are generally not zero but are ignored, along with higher order terms, for simplicity.

The atomic position vector $\mathbf{x}$ has length $3n$, and the mass and spring-constant matrices $\mathbf{M}$ and $\mathbf{K}$ are $3n$ by $3n$, where n is the number of atoms in the molecule. This results from the $3n$ total nuclear degrees of freedom. The position vector and mass matrix are explicitly given by

$$\mathbf{x} = [x_1, y_1, z_1, ..., x_n, y_n, z_n]^T \tag{B.26a}$$

and

$$\mathbf{M}_{i,j} = m_i \delta_{i,j}. \tag{B.26b}$$

The Hamiltonian can be rewritten in terms of mass-weighted normal coordinates to simplify the expression, leading to

$$\mathcal{H}_v = \frac{\dot{\mathbf{Q}'}^T \dot{\mathbf{Q}'}}{2} + \mathbf{Q'}^T \mathbf{W} \mathbf{Q'}, \tag{B.27}$$

where the mass-weighted atomic coordinates are defined by $\boldsymbol{Q'} = \boldsymbol{M}^{\frac{1}{2}} \boldsymbol{x}$. The harmonic frequencies can be identified as the non-diagonal matrix $\mathbf{W}$, defined by

$$\mathbf{W} = \mathbf{M}^{\frac{1}{2}} \mathbf{K} \mathbf{M}^{\frac{1}{2}}. \tag{B.28}$$

Next, a system of normal coordinates is defined in which the harmonic potential is diagonal. This is done via eigendecomposition with the eigenvector matrix $\mathbf{L}$, defined by

$$\mathbf{L}^{-1} \mathbf{W} \mathbf{L} \equiv \hbar^2 \mathbf{\Gamma}^2 \implies \Gamma_{i,j} = \frac{\omega_i}{\hbar} \delta_{i,j}, \tag{B.29}$$

where $\mathbf{\Gamma}$ is the (diagonal) reduced frequency matrix. The $\mathbf{L}$ matrix of normal-mode vectors transform the Hamiltonian into normal mode coordinates $\mathbf{Q} \equiv \mathbf{L}\mathbf{Q}'$, resulting in the final Hamiltonian

$$\mathcal{H}_v = \dot{\mathbf{Q}}^T\dot{\mathbf{Q}} + \frac{\mathbf{Q}^T\hbar^2\mathbf{\Gamma}^2\mathbf{Q}}{2} = \sum_j \left(\dot{Q}_j^2 + \frac{\omega_j^2 Q_j^2}{2}\right) = \sum_j \mathcal{H}_{v,j} \tag{B.30}$$

In this coordinate system, the Hamiltonian becomes a sum over $N = 3n - 6$ ($3n - 5$ for diatomics) independent harmonic oscillators, where 6 of the $3n$ modes (or 5 for diatomics) correspond to rotation and translation and are thus excluded from the $\boldsymbol{L}$ matrix. Since the Hamiltonian is completely uncoupled (*i.e.,* no cross-terms), the energy eigenvalues are calculated by summing over the $3n-6$ one-dimensional harmonic oscillator energies.

Rewritten in dimensionless normal coordinates (using $q_i = \sqrt{\omega_i/\hbar}Q_i$) the Hamiltonian is

$$\mathcal{H}_v = \sum_j \frac{\hbar\omega_j}{2}\left(-\frac{\partial^2}{\partial q_j^2} + q_j^2\right). \tag{B.31}$$

where the equation is now written in the quantum mechanical limit where the time derivative terms are replaced with the corresponding momentum operators.

The total vibrational energy is given by the sum of the individual energies for each of the N vibrational modes, or

$$\mathcal{H}_v \left|\Phi_i\right\rangle = \sum_j \hbar\omega_j \left(v_j + \frac{1}{2}\right)\left|\Phi_i\right\rangle = \mathcal{G}_i \left|\Phi\right\rangle. \tag{B.32}$$

The vibrational line strength in the Franck-Condon approximation is given by the overlap of the vibrational eigenstates between the initial and final states of the transition. Specifically,

$$I_v = |\left\langle v_1' \cdots v_N' | v_1'' \cdots v_N''\right\rangle|^2 = \left| \int_{\mathbb{R}^N} d^N\vec{\boldsymbol{q}}'' \left\langle v_1' \cdots v_N' | \vec{\boldsymbol{q}}''\right\rangle \left\langle \vec{\boldsymbol{q}}'' | v_1'' \cdots v_N''\right\rangle \right|^2, \tag{B.33}$$

where the vibrational eigenstate is explicitly labeled by each of the vibrational quantum numbers v_j, and the final and initial states are denoted by a single and double prime ($'$ and $''$), respectively. The integration variable $\vec{\boldsymbol{q}}''$ is the position vector in the normal mode coordinate system of the initial state and hence is a length N vector.

Calculation of the overlap integrals clearly requires a relationship between the ground and excited state normal coordinate system. Typically a linear transformation is used. This transformation was first proposed by Duschinsky in 1937 [192], and is routinely used due to its simplicity, even though in general the actual transformation is not linear [193]. Note also that this method does not work if the

excited state and ground state differ in the total number of vibrational normal modes, such as for a bent to linear transition, and in that case alternative methods are required [189]. The transformation is typically written as

$$\vec{q}' = \mathbf{J}\vec{q}'' + \mathbf{K} \tag{B.34}$$

where $\mathbf{J}$ is the Duschinsky matrix, which can be described as a rotation in the N dimensional normal mode space, and $\mathbf{K}$ is the normal coordinate shift between the two geometries, which is closely related to the Huang-Rhys parameter and Stokes shift. In the limit that there is no normal mode mixing (*i.e.,* $\boldsymbol{J}$ is diagonal), the N-dimensional system is completely uncoupled, and the vibrational transition intensity for a transition is given by the product of the transition intensities for the N one-dimensional shifted oscillators.

The overlap integrals for even an uncoupled harmonic oscillator cannot be written in closed form. Instead, they are typically solved recursively by exploiting the recursive properties of Hermite polynomials [194]. The derivation of these recursion relations is straightforward but tedious, particularly in the general case including the effect of Duschinsky mixing. Islampour *et. al.* [190], derives a general expression for these overlap integrals as follows using the Hermite polynomial generating functions

$$\begin{aligned}\langle \mathbf{v}'|\mathbf{v}''\rangle =& I_0\left[\prod_{j=1}^{N}\frac{(-1)^{v_j''+v_j'}}{\sqrt{v_j''!v_j'!}}\right]e^{\boldsymbol{\sigma}''^{\dagger}\mathbf{A}\boldsymbol{\sigma}''+\boldsymbol{\sigma}'\mathbf{B}\boldsymbol{\sigma}'^{\dagger}-\boldsymbol{\sigma}''^{\dagger}\mathbf{C}\boldsymbol{\sigma}'} \\ &\times\frac{\partial^{v_1''+\cdots+v_N''+v_1'+\cdots+v_N'}}{\partial\sigma_1'^{v_1'}\cdots\partial\sigma_N'^{v_N'}\partial\sigma_1''^{v_1''}\cdots\partial\sigma_N''^{v_N''}}e^{-\boldsymbol{\sigma}''^{\dagger}\mathbf{A}\boldsymbol{\sigma}''-\boldsymbol{\sigma}'^{\dagger}\mathbf{B}\boldsymbol{\sigma}'+\boldsymbol{\sigma}''^{\dagger}\mathbf{C}\boldsymbol{\sigma}'}\end{aligned} \tag{B.35}$$

where $\mathbf{A}$, $\mathbf{B}$, and $\mathbf{C}$ are matrices defined by the harmonic oscillator strengths and Duschinsky rotation matrix. The dimensionless vector $\boldsymbol{\sigma}$ describes the shift parameter (in mass-weighted normal coordinates), $\mathbf{K}$. Finally, I_0 is the overlap integral of the ground states, $I_0 = \langle \mathbf{0}|\mathbf{0}\rangle$.

This expression can be written more compactly by defining the block matrix $\mathbf{M}$ and block vector $\boldsymbol{\sigma}$

$$\mathbf{M} = \begin{bmatrix} -\mathbf{A} & \mathbf{C} \\ \mathbf{0} & -\mathbf{B} \end{bmatrix} \qquad \boldsymbol{\sigma} = \begin{bmatrix} \boldsymbol{\sigma}'' \\ \boldsymbol{\sigma}' \end{bmatrix}. \tag{B.36}$$

Equation B.35 can now be written as

$$\langle \mathbf{v}'|\mathbf{v}''\rangle = I_0\left[\prod_{j=1}^{N}\frac{(-1)^{v_j''+v_j'}}{\sqrt{v_j''!v_j'!}}\right]e^{\boldsymbol{\sigma}^{\dagger}\mathbf{M}\boldsymbol{\sigma}}\frac{\partial^{v_1''+\cdots+v_N''+v_1'+\cdots+v_N'}}{\partial\sigma_1^{v_1'}\cdots\partial\sigma_{2N}^{v_N'}\partial\sigma_1^{v_1''}\cdots\partial\sigma_N^{v_N''}}e^{-\boldsymbol{\sigma}^{\dagger}\mathbf{M}\boldsymbol{\sigma}}. \tag{B.37}$$

A recursion relation can be derived from this expression (see appendix B.5). The recursion relation is

$$\langle v_1 \cdots v_k + 1 \cdots v_{2n} \rangle = \sqrt{\frac{1}{v_k + 1}} (\mathbf{T}\boldsymbol{\sigma})_k \langle v_1 \cdots v_k \cdots v_{2n} \rangle + \sum_{j=1}^{2n} \sqrt{\frac{v_j}{v_k + 1}} \mathbf{T}_{j,k} \langle v_1 \cdots v_j - 1 \cdots v_{2n} \rangle \quad \text{(B.38)}$$

where the notation $\langle v_1 \cdots v_k + 1 \cdots v_{2n} \rangle$ is used to represent the Franck-Condon factor where any index k is incremented by one. Since this formulation is independent of whether the incremented quantum number belongs to the excited or ground state, the typical bra-ket notation is dropped.

The matrix $\mathbf{T}$ is a square block matrix composed of 4 matrices, individually of rank N, and is defined by

$$\begin{aligned} \mathbf{T} = \mathbf{M} + \mathbf{M}^\dagger &= \begin{bmatrix} 2\mathbf{A} & \mathbf{C} \\ \mathbf{C}^\dagger & 2\mathbf{B} \end{bmatrix} = \begin{bmatrix} \mathbb{1} - 2\boldsymbol{\Gamma}''^{\frac{1}{2}} \mathbf{G}^{-1} \boldsymbol{\Gamma}''^{\frac{1}{2}} & 2\boldsymbol{\Gamma}''^{\frac{1}{2}} \mathbf{G}^{-1} \mathbf{J}^\dagger \boldsymbol{\Gamma}'^{\frac{1}{2}} \\ 2\boldsymbol{\Gamma}'^{\frac{1}{2}} \mathbf{J} \mathbf{G}^{-1} \boldsymbol{\Gamma}''^{\frac{1}{2}} & \mathbb{1} - 2\boldsymbol{\Gamma}'^{\frac{1}{2}} \mathbf{J} \mathbf{G}^{-1} \mathbf{J}^\dagger \boldsymbol{\Gamma}'^{\frac{1}{2}} \end{bmatrix} \\ &= \mathbb{1} - 2 \begin{bmatrix} \boldsymbol{\Gamma}''^{\frac{1}{2}} \\ \boldsymbol{\Gamma}'^{\frac{1}{2}} \end{bmatrix} \mathbf{G}^{-1} \begin{bmatrix} \boldsymbol{\Gamma}''^{\frac{1}{2}} & \mathbf{J}^\dagger \boldsymbol{\Gamma}'^{\frac{1}{2}} \end{bmatrix}. \end{aligned} \quad \text{(B.39a)}$$

Likewise, the vector $\boldsymbol{\sigma}$ is defined by

$$\begin{aligned} \boldsymbol{\sigma} = \begin{bmatrix} \boldsymbol{\sigma}'' \\ \boldsymbol{\sigma}' \end{bmatrix} &= \begin{bmatrix} -\sqrt{2} \boldsymbol{\Gamma}''^{\frac{1}{2}} \mathbf{G}^{-1} \mathbf{J}^\dagger \boldsymbol{\Gamma}'^{\frac{1}{2}} \boldsymbol{\Gamma}'^{\frac{1}{2}} \\ \sqrt{2}(\mathbb{1} - \boldsymbol{\Gamma}'^{\frac{1}{2}} \mathbf{J} \mathbf{G}^{-1} \mathbf{J}^\dagger \boldsymbol{\Gamma}'^{\frac{1}{2}}) \boldsymbol{\Gamma}'^{\frac{1}{2}} \end{bmatrix} \mathbf{K} \\ &= \sqrt{2} \begin{bmatrix} \mathbf{0} \\ \boldsymbol{\Gamma}'^{\frac{1}{2}} \mathbf{K} \end{bmatrix} - \sqrt{2} \begin{bmatrix} \boldsymbol{\Gamma}''^{\frac{1}{2}} \\ \boldsymbol{\Gamma}'^{\frac{1}{2}} \mathbf{J} \end{bmatrix} \mathbf{G}^{-1} \mathbf{J}^\dagger \boldsymbol{\Gamma}' \mathbf{K} \end{aligned} \quad \text{(B.39b)}$$

$$\mathbf{G} = \boldsymbol{\Gamma}'' + \mathbf{J}^\dagger \boldsymbol{\Gamma}' \mathbf{J} \quad \text{(B.39c)}$$

where $\boldsymbol{\Gamma}'$ and $\boldsymbol{\Gamma}''$ are the diagonal reduced frequency matrices defined in Equation B.29. Finally, the ground state overlap integral, I_0 is given by

$$I_0 = \langle \mathbf{0} | \mathbf{0} \rangle = \det(2\boldsymbol{\Gamma}'^{\frac{1}{2}} \mathbf{G}^{-1} \boldsymbol{\Gamma}''^{\frac{1}{2}})^{\frac{1}{2}} \times \exp\left(-\frac{1}{2} \mathbf{K}^\dagger \boldsymbol{\Gamma}'^{\frac{1}{2}} (\mathbb{1} - \boldsymbol{\Gamma}'^{\frac{1}{2}} \mathbf{J} \mathbf{G}^{-1} \mathbf{J}^\dagger \boldsymbol{\Gamma}'^{\frac{1}{2}}) \boldsymbol{\Gamma}'^{\frac{1}{2}} \mathbf{K} \right). \quad \text{(B.40)}$$

The derivation of the Franck-Condon factor recursion relation and a pseudocode implementation of the Franck-Condon integral calculation are given in appendix B.5.

Finally, the Herzberg-Teller (HT) vibronic coupling matrix elements can be calculated directly from the Franck-Condon integrals using the Hermite polynomial recursion relations. The HT vibronic coupling matrix element for an arbitrary vibronic transition is defined by

$$\langle \mathbf{v}' | q_k'' | \mathbf{v}'' \rangle = \langle \mathbf{v}' | \, q_k'' \left(\prod_l | v_l'' \rangle \right) = \langle \mathbf{v}' | \left(\prod_{l \neq k} | v_l'' \rangle \right) \times q_k'' \, | v_k'' \rangle \, . \tag{B.41}$$

The right hand side of the equation takes advantage of the fact that the vibrational modes are uncoupled and only mode k is affected by the q_k'' operator. The q_k'' operator is applied to the $|v_k''\rangle$ ket, resulting in the final expression

$$\begin{aligned} \langle \mathbf{v}' | q_k'' | \mathbf{v}'' \rangle &= \langle \mathbf{v}' | \left(\prod_{l \neq k} | v_l'' \rangle \right) \left[\sqrt{\frac{v_k''}{2}} \, | v_k'' - 1 \rangle + \sqrt{\frac{v_k'' + 1}{2}} \, | v_k'' + 1 \rangle \right] \\ &= \sqrt{\frac{v_k''}{2}} \, \langle \mathbf{v}' | v_0'' \cdots v_k'' - 1 \cdots v_N'' \rangle + \sqrt{\frac{v_k'' + 1}{2}} \, \langle \mathbf{v}' | v_0'' \cdots v_k'' + 1 \cdots v_N'' \rangle \, . \end{aligned} \tag{B.42}$$

The term in brackets on the top line of Equation B.42 follows directly from the Hermite polynomial recursion relations. The HT matrix elements can thus be calculated directly from the FCFs independent of the transformation between the ground and excited state coordinates.

The Symmetric Double-Well Potential

The presence of anharmonicity can quickly invalidate the previous analysis. This is particularly true of excited states of planar molecules such as formaldehyde, ammonia/ND_3, cyclopentene, and others. The excited states of these molecules have been shown to be significantly bent out of plane, leading to significant anharmonicity. The potential energy surfaces of these molecules have two equally probable minima on either side of the planar configuration. An example calculation of the potential energy curves for formaldehyde is shown in Figure B.1 demonstrating the appearance of the double well in the $\tilde{A}\,{}^1A_2$ state. Note that the energy scales of the upper and lower portion of the figure are vastly different; the anharmonic perturbation in the excited state is actually of relatively low energy. However, it does have a significant impact on energy levels, and as a result the vibrational wavefunctions. Experimental studies have measured energy levels of some of the lower vibrationally excited states of formaldehyde's v_4 mode, and have shown it is consistent with inversion through a low potential barrier [195] lending further evidence to the double-well potential description.

Coon, Naugle, and McKenzie [76] conveniently were able to find a method for determining state vectors and energy levels for the double-well potential as observed in formaldehyde. The proposed solution solved the Schroedinger equation variationally by finding a decomposition of the perturbed

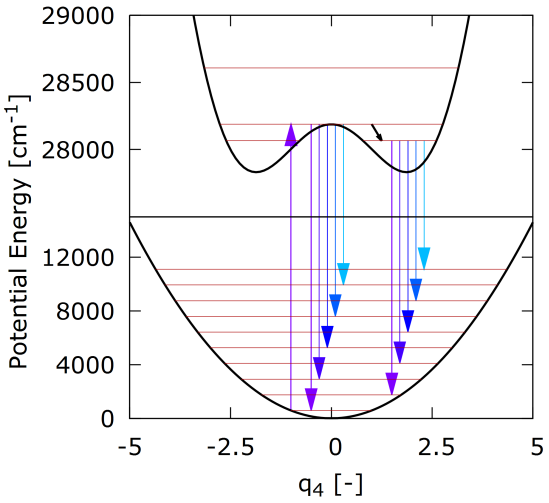

Figure B.1: Projection of formaldehyde's potential energy surface along v_4 (out-of-plane bending mode), calculated using the fit parameters from [171]. Horizontal red lines indicate vibrational energy levels, and vertical arrows indicated allowed absorption and fluorescence transitions.

potential (in this case a harmonic potential with a Gaussian perturbation) in the harmonic oscillator basis set. The energy levels and state vectors are then given simply by a sum over the basis vectors.

The perturbed Hamiltonian is given by Equation B.43, where the subscript v_0 represents the harmonic oscillator limit, and the subscript v' indicates the perturbed Hamiltonian. The Hamiltonian and resulting values are expressed in terms of mass-weighted normal coordinates, Q (as opposed to Cartesian coordinates x and dimensionless normal coordinates q).

$$\mathcal{H}_v = \frac{\partial^2}{\partial Q^2} + \frac{\omega^2 Q^2}{2} + Ae^{-a^2Q^2} = \mathcal{H}_{v_0} + \mathcal{H}_{v'} \qquad \mathcal{H}_{v'} = Ae^{-a^2Q^2} \tag{B.43}$$

The solution arises by decomposition of the perturbation in the harmonic oscillator basis set. Mathematically, the matrix H'_{ij} is built up recursively from the definitions

$$H'_{i,j} = \langle \Phi_{0,i} | Ae^{-a^2Q^2} | \Phi_{0,j} \rangle = \sqrt{\frac{i-1}{i}}(\beta^2 - 1)H'_{i-2,j} + \sqrt{\frac{j}{i}}\beta^2 H'_{i-1,j-1} \tag{B.44a}$$

$$H'_{i,0} = \sqrt{\frac{i-1}{i}}(\beta^2 - 1)H'_{i-2,0} \tag{B.44b}$$

$$H'_{0,0} = \hbar\omega K\beta \qquad H'_{1,1} = \hbar\omega K\beta^3 \tag{B.44c}$$

where the eigenstate $|\Phi_{0,j}\rangle$ is the harmonic oscillator eigenstate with vibrational quantum number j. The parameters β and K are dimensionless, and are determined from the barrier shape parameter, ρ,

and barrier height, B using the expressions

$$\beta = \sqrt{\frac{2B}{2B + e^{\rho} - \rho - 1}} \qquad K = \frac{Be^{\rho}}{e^{\rho} - \rho - 1} \tag{B.45a}$$

$$\rho = \ln\left(\frac{2Aa^2}{\omega^2}\right) \qquad B = \frac{A}{\hbar\omega}\frac{e^{\rho} - \rho - 1}{e^{\rho}}. \tag{B.45b}$$

Several sets of values have been reported as a solution for $\tilde{A}\ ^1A_2$ formaldehyde. Coon *et al.*, originally reported $\rho = 0.6$ and $B = 0.562$ for $\omega = 18.65$ THz (622 cm^{-1}). However, this study was restricted to $\rho = 0.6$ to simplify the curve fitting procedure. More recently, Lin *et al.* [171] found values of $\rho = 0.5$, $B = 0.5175$, and $\omega = 20.65$ THz (688.9 cm^{-1}) based on a series of *ab initio* calculations of the potential energy surface.

Once the Hamiltonian matrix is constructed, a solution is found by diagonalization of the matrix. In particular, a set of eigenvectors C_{ij} is found such that the following properties exist.

$$H_{m,n} = H_{0_{m,n}} + H'_{m,n} = C\mathcal{G}C^{\dagger} \qquad \Longrightarrow \qquad |\Phi_i\rangle = \sum_j C_{ij}\,|\Phi_{0,j}\rangle \tag{B.46}$$

where $C_{i,j}$ is the eigenvector matrix that diagonalizes the Hamiltonian and $\mathcal{G}$ is the diagonal energy matrix (with diagonal energies corresponding to the anharmonic energy levels), and $|\Phi_i\rangle$ is the anharmonic oscillator eigenstate with quantum number i.

Knowledge of the correct anharmonic energy levels are necessary for this calculation, but perhaps more important is the vibrational contribution to line strength. Lin [196] shows a simple method for calculating Franck-Condon factors, or vibrational overlap integrals, using the same decomposition used above. Since vibrational states can be written as a linear combination of harmonic oscillator states, the overlap integral can be calculated by summing over the individual harmonic oscillator components of both the initial and final states, or

$$\langle v'|v''\rangle = \left(\sum_i C'_{v',i}\,\langle i'|\right)\left(\sum_i C''_{v'',i}\,|i''\rangle\right) = \sum_i\sum_j C'_{v',i}C''_{v'',j}\,\langle i'|j''\rangle\,. \tag{B.47}$$

For a multidimensional system, this can be expanded in a straightforward manner as follows. If a mode is not being expanded in this manner, a sum does not need to be performed over it (*i.e.*, $C_{v,i} \to \delta_{v,i}$). In general, the anharmonic overlap integral is given by

$$\begin{aligned}\langle \mathbf{v}'|\mathbf{v}''\rangle &= \prod_i \left(\sum_j \sum_k C'^{(i)}_{v'_i,j} \langle j^{(i)}| \, C''^{(i)}_{v''_i,k} \, |k^{(i)}\rangle \right) \\ &= \sum_{\mathbf{n}',\mathbf{n}''} \left(\prod_i C^{(i)}_{v'_i,n'_i} C^{(i)}_{v''_i,n''_i} \langle \mathbf{n}'|\mathbf{n}''\rangle_0 \right).\end{aligned} \tag{B.48}$$

More explicitly, this double sum product can be calculated as follows. For every anharmonic overlap integral, a sum over all calculated harmonic overlap integrals is performed, and each term is weighted by the product of the appropriate elements of the the $2N$ eigenvector matrices for each anharmonic vibrational mode. Thus, in the general case the complexity of the algorithm scales as $O(K^2)$ for K total overlap integrals. For the harmonic overlap integrals, the calculation scales closer to $O(KM)$ where M is the highest vibrational quantum number considered per mode (and hence $\prod_i M_i = K$), and the Herzberg-Teller corrections scale as $O(KN)$.

B.4 Nonradiative Deactivation Theory

Similar to a radiative transition, the probability of a nonradiative transition is also given by Fermi's Golden Rule, with two differences. First, the perturbing Hamiltonian is a generally a result of non-Born-Oppenheimer terms that were originally ignored in the molecular Hamiltonian. However, second order coupling terms similar to the Herzberg-Teller mechanism can also induce non-radiative transitions [197]. The internal conversion process is typically attributed to nuclear kinetic energy terms which will be considered here. Further, as the intersystem crossing mechanism has not been ruled out completely for formaldehyde [198], this mechanism will be discussed as well.

The second difference between radiative and nonradiative transition rates is the energy conservation condition. Any non-radiative transitions from $i \rightarrow j$ must conserve energy, and hence ω is no longer a free parameter. The remainder of this section will describe quantitatively the theory of nonradiative transition rates, and in particular intersystem crossing and internal conversion.

B.4.1 Internal Conversion

The first nonradiative deactivation mechanism, and likely the most prominent one in formaldehyde is internal conversion. Internal conversion is the process in which an excited electronic state is deactivated through the excitation of a high-energy vibrational mode of the ground electronic state. This process is typically thought to occur as a result of non-Born-Oppenheimer terms in the molecular Hamiltonian, specifically resulting from the nuclear kinetic energy operator. The nuclear kinetic energy operator is

$$\mathcal{T}_N = \sum_I \frac{\hbar^2}{2M_I} \nabla^2_{\vec{\mathbf{R}}_I} = \sum_i \frac{\hbar^2}{2} \frac{\partial^2}{\partial Q_i^2} = \sum_i \frac{\hbar\omega_i}{2} \frac{\partial^2}{\partial q_i^2} \tag{B.49}$$

where the subscript I represents a sum over all atoms, with atomic coordinate $\vec{\boldsymbol{R}}_I$, and the subscript i sums over all normal modes. As before, Q_i is a mass-weighted normal coordinate, whereas q_i is a dimensionless normal coordinate.

The internal conversion Hamiltonian is given by (following from [199, 200])

$$\begin{aligned} \mathcal{H}_{IC} \left|\psi_i\right\rangle \left|\Phi_i\right\rangle &= -\sum_l \hbar\omega_{i,l} \left(\frac{\partial \left|\psi_i\right\rangle}{\partial q_l} \frac{\partial \left|\Phi_i\right\rangle}{\partial q_l} + \frac{1}{2} \frac{\partial^2 \left|\psi_i\right\rangle}{\partial q_l^2} \left|\Phi_i\right\rangle + \frac{1}{2} \left|\psi_i\right\rangle \frac{\partial^2 \left|\Phi_i\right\rangle}{\partial q_l^2} \right) \\ &\approx -\sum_l \hbar\omega_{i,l} \frac{\partial \left|\psi_i\right\rangle}{\partial q_l} \frac{\partial \left|\Phi_i\right\rangle}{\partial q_l}. \end{aligned} \tag{B.50}$$

where the Laplace operator is distributed to the electronic and vibrational eigenstates and $\omega_{i,l}$ is the harmonic frequency of vibrational mode l of electronic state i. The second derivative terms are often neglected as they are typically small. This expression differs with those from [199, 200] since here it has been rewritten in terms of the dimensionless normal coordinates.

Fermi's Golden Rule can now be used to calculate a rate constant for internal conversion as

$$k_{ij}^{(\mathrm{IC})} = 2\pi\hbar \left| \sum_l \omega_{i,l} \left\langle \psi_i \right| \frac{\partial}{\partial q_l'} \left| \psi_j \right\rangle \left\langle \Phi_i \right| \frac{\partial}{\partial q_l'} \left| \Phi_j \right\rangle \right|^2 \delta(E_i - E_j). \tag{B.51}$$

The rate constant is expressed as the transition rate from state j to state i. If the initial state is chosen to be an excited state, then the rate constant corresponds to a non-radiative deactivation process. Note that no rotational transition rate contribution is included as rotational equilibrium is assumed.

The vibrational term can be rewritten as

$$\begin{aligned} \left\langle \mathbf{v}' \right| \frac{\partial}{\partial q_k'} \left| \mathbf{v}'' \right\rangle &= \left(\prod_l \left\langle v_l' \right| \right) \frac{\partial}{\partial q_k'} \left| \mathbf{v}'' \right\rangle = \left(\prod_{l \neq k} \left\langle v_l' \right| \right) \left(\left\langle v_k' \right| \frac{\partial}{\partial q_k'} \right) \left| \mathbf{v}'' \right\rangle \\ &= \left(\prod_{l \neq k} \left\langle v_l' \right| \right) \left[\sqrt{\frac{v_k'}{2}} \left\langle v_k' - 1 \right| - \sqrt{\frac{v_k' + 1}{2}} \left\langle v_k' + 1 \right| \right] \left| \mathbf{v}'' \right\rangle \\ &= \sqrt{\frac{v_k''}{2}} \left\langle v_0' \cdots v_k' - 1 \cdots v_N' | \mathbf{v}'' \right\rangle - \sqrt{\frac{v_k'' + 1}{2}} \left\langle v_0' \cdots v_k' + 1 \cdots v_N' | \mathbf{v}' \right\rangle. \end{aligned} \tag{B.52}$$

This calculation could also be performed for the second derivative if the second order vibrational term in the kinetic energy operator (Equation B.50) were kept.

Finally, the electronic matrix element can be rewritten using the commutation relation for the nuclear momentum and electron Hamiltonian operators ($[\frac{\partial}{\partial q_k}, \mathcal{H}_e] = \frac{\partial \mathcal{V}}{\partial q_k}$, where $\mathcal{V}$ is the electrostatic potential). This results in

$$\begin{aligned}\langle\psi_i|\left[\frac{\partial}{\partial q_k},\mathcal{H}_e\right]|\psi_j\rangle = \langle\psi_i|\frac{\partial\mathcal{V}}{\partial q_k}|\psi_j\rangle = T_j\,\langle\psi_i|\frac{\partial}{\partial q_k}|\psi_j\rangle - T_i\,\langle\psi_i|\frac{\partial}{\partial q_k}|\psi_j\rangle \\ \implies \langle\psi_i|\frac{\partial}{\partial q_k}|\psi_j\rangle = \frac{\langle\psi_i|\frac{\partial\hat{\mathcal{V}}}{\partial q_k}|\psi_j\rangle}{T_j - T_i}.\end{aligned} \tag{B.53}$$

This matrix element can thus be calculated directly from knowledge of the electronic energy levels ($T_{n''}$ and $T_{n'}$), as well as a one electron integral of the electrostatic potential energy derivative. This quantity represents an inter-atomic force; a thorough discussion of the calculation of this force and calculation of the electrostatic potential in terms of the electron density is given by Feynman [201]. In general, this calculation requires knowledge of electron density and molecular geometry of both states. All of this information is accessible from any excited state *ab initio* molecular orbital calculation, such as Density Function Theory and its extensions.

The total non-radiative transition rate is simply given by summing over all combinations of initial and final states, weighting by the population fraction of the initial state, and integrating over the transition energy. The integration is needed because the above rate constant expression is a differential rate constant in energy space as a result of the energy conservation condition, [*i.e.*, the factor of $\delta(E_i - E_j)$]. More realistically, the sharp energy conservation should be replaced with a pressure and temperature dependent line shape function similar to radiative transitions.

B.4.2 Intersystem Crossing

Intersystem crossing, similar to internal conversion, is the result of non-Born-Oppenheimer terms in the molecular Hamiltonian. In particular, intersystem crossing is the result of spin-orbit coupling, and as such is a relativistic effect. It was first described by Pauli [202] in a classical sense by assuming an electron is placed in an external electromagnetic field. The field is then assumed to be the result of the electrostatic (Coulombic) potential, and the magnetic field is a result of the intrinsic magnetic moment of the electron. The spin-orbit coupling Hamiltonian in this sense is called the Breit-Pauli Hamiltonian [203] and is given by

$$\mathcal{H}_{SO} = \frac{\alpha\hbar}{2m^2c}\sum_l\left[\sum_I \frac{Z_l\vec{\mathbf{r}}_{lI}\times\vec{\mathbf{p}}_l}{r_{lI}^3}\cdot\vec{\mathbf{s}}_l + \sum_k\frac{\vec{\mathbf{r}}_{lk}\times\vec{\mathbf{p}}_l}{r_{lk}^3}\cdot(\vec{\mathbf{s}}_l + 2\vec{\mathbf{s}}_k)\right]. \tag{B.54}$$

Here, the summations over l and k are to be taken over all electrons, the summation over I is to be taken over all atoms, and $\vec{\mathbf{s}}_l$ represents the intrinsic spin of electron l. The equation contains two terms; the first (lowest order) term is due to single electron spin-orbit interaction, whereas the second (higher order) term is the result of coupling between electrons. This expression varies slightly from [203] as SI

units are being used here. In atomic units ($\alpha \to c^{-1}$ and $\hbar \to 1$), this equation reduces that in [203]. The intersystem crossing Hamiltonian is only parametrically dependent on nuclear geometry, and hence can be used directly in the Franck-Condon or Herzberg-Teller schemes.

From Fermi's Golden Rule, the transition rates due to intersystem crossing are given by

$$k_{ij}^{(\mathrm{SO})} = \frac{\pi\alpha^2\hbar}{2m^4c^2}\left|\langle\psi_i|\sum_l\left(\sum_I \frac{Z_l\vec{\mathbf{r}}_{lI}\times\vec{\mathbf{p}}_l}{r_{lI}^3}\cdot\vec{\mathbf{s}}_l + \sum_k \frac{\vec{\mathbf{r}}_{lj}\times\vec{\mathbf{p}}_l}{r_{lk}^3}\cdot(\vec{\mathbf{s}}_l + 2\vec{\mathbf{s}}_k)\right)|\psi_j\rangle\right|^2 I_v\delta(E_i - E_j) \tag{B.55}$$

Similar to internal conversion, rotational transition rates are neglected as rotational equilibrium is assumed. Equation B.55 could easily be extended to second order, similar to the Herzberg-Teller scheme, where the derivative of the electronic transition strength with respect to nuclear coordinate induces a Herzberg-Teller-like vibrational transition, as shown in equation B.7. Similar to internal conversion and radiative dipole transitions, these electronic matrix elements require knowledge of the molecular electronic eigenstate for calculation. This calculation could be performed using an *ab initio* molecular structure package. Finally, as with internal conversion, the total non-radiative deactivation rate is given by a sum over all possible vibronic states, weighted by population fraction, and integrated over the transition energy space to enforce the energy conservation condition. The sharp energy cutoff in the above equation should be replaced with a more realistic lineshape function for more accurate calculations, as transitions that are not infinitely slow are thus not perfectly sharp in energy space. Unlike internal conversion, intersystem crossing generally is most prominent in single-triplet transitions, and is very unlikely to occur between two singlet states, at least to first order. In the context of formaldehyde PLIF in-cylinder, intersystem crossing is most likely to occur between the $\tilde{A}\ ^1A_2$ and $\tilde{a}\ ^3A_2$ states.

B.4.3 Temperature Dependence

In either process, the rate coefficient is temperature-independent. Thus, temperature-dependence in the non-radiative relaxation processes arise as a result of the population distribution. Following excitation, if the electron population reaches equilibrium before spontaneous emission occurs, then the total non-radiative deactivation can be written as

$$k_{nr} = \sum_i \frac{e^{-E_i/k_BT}}{Z}\sum_j \left(k_{ij}^{(SO)} + k_{ij}^{(IC)}\right), \tag{B.56}$$

where Z is the partition function, i iterates over the vibrational levels of the excited electronic state, and j iterates over all other electronic states and the vibrational levels within those states.

For thermographic phosphors, the non-radiative deactivation typically is dominated by a single initial energy level i, and k_{nr} can be simplified to

$$k_{nr} = k_{nr,0}\frac{e^{-E_0/k_BT}}{Z(T)}, \tag{B.57}$$

where $k_{nr,0}$ is an effective non-radiative attempt rate, and E_0 is an effective energy gap. For a large energy gap relative to the vibrational energy level spacing, the partition function changes slowly relative to the exponential factor and is approximately constant over a modest temperature range, leading to the well known expression

$$k_{nr} = k_{nr,0}e^{-E_0/k_BT} \tag{B.58}$$

as in Equation 2.74 of [204] (Chapter 2).

B.5 Derivation of Recursion Relation

Calculation of Franck-Condon factors (FCFs) in the Duschinsky approximation are very well suited to recursive calculations. Beginning with equation B.37, an arbitrary FCF in the Duschinsky approximation is given by

$$\langle \mathbf{v}'|\mathbf{v}''\rangle = I_0\left[\prod_{j=1}^{N}\frac{(-1)^{v_j''+v_j'}}{\sqrt{v_j''!v_j'!}}\right]e^{\boldsymbol{\sigma}^\dagger\mathbf{M}\boldsymbol{\sigma}}\frac{\partial^{v_1''+\cdots+v_N''+v_1'+\cdots+v_N'}}{\partial\sigma_{N+1}^{v_1'}\cdots\partial\sigma_{2N}^{v_N'}\partial\sigma_1^{v_1''}\cdots\partial\sigma_N^{v_N''}}e^{-\boldsymbol{\sigma}^\dagger\mathbf{M}\boldsymbol{\sigma}}. \tag{B.59}$$

This equation can be rewritten by combining the quantum number vectors into a single value, $\langle\mathbf{v}\rangle = \langle\mathbf{v}'|\mathbf{v}''\rangle$ and $\mathbf{v} = [\mathbf{v}'\ \mathbf{v}'']$, similar to how the block matrices σ and $\mathbf{M}$ were constructed. This gives the following expression

$$\langle v_1\cdots|\cdots v_{2N}\rangle = I_0\left[\prod_j\frac{(-1)^{v_j}}{\sqrt{v_j!}}\right]\times\ e^{-\sigma^\dagger\mathbf{M}\sigma}\frac{\partial^{v_1\cdots v_{2N}}}{\partial\sigma_1^{v_1}\cdots\partial\sigma_{2N}^{v_{2N}}}e^{\sigma^\dagger\mathbf{M}\sigma}. \tag{B.60}$$

Now, a single entry in $\mathbf{v}$ is incremented by one (*i.e.*, $v_k \to v_k + 1$). The new Franck-Condon factor is now

$$\begin{aligned}\langle v_1\cdots v_{k+1}\cdots v_{2N}\rangle &= I_0\left[\prod_j\frac{(-1)^{v_j}}{\sqrt{v_j!}}\right]\times\ e^{-g}\frac{\partial^{v_1\cdots v_{2N}}}{\partial\sigma_1^{v_1}\cdots\partial\sigma_{2N}^{v_{2N}}}\frac{\partial}{\partial\sigma_k}e^{g}\\ &= I_0\left[\prod_j\frac{(-1)^{v_j}}{\sqrt{v_j!}}\right]\times\ e^{-g}\frac{\partial^{v_1\cdots v_{2N}}}{\partial\sigma_1^{v_1}\cdots\partial\sigma_{2N}^{v_{2N}}}\left[\frac{\partial g}{\partial\sigma_k}e^{g}\right].\end{aligned} \tag{B.61}$$

A recursion relation can be found through induction by distributing the partial derivatives in Equation

B.61 with respect to each variable, σ_i. Distributing the derivatives with respect to σ_i results in the expression

$$\frac{\partial^{v_i}}{\partial\sigma_i^{v_i}}\left[\frac{\partial g}{\partial\sigma_k}e^g\right] = \frac{\partial g}{\partial\sigma_k}\frac{\partial^{v_i}e^g}{\partial\sigma_i^{v_i}} + v_i\frac{\partial^{v_i-1}e^g}{\partial\sigma_i^{v_i-1}}\frac{\partial^2 g}{\partial\sigma_i\partial\sigma_k}. \tag{B.62}$$

Again, carrying through a derivative with respect to σ_j results in

$$\frac{\partial^{v_i+v_j}}{\partial\sigma_i^{v_i}\partial\sigma_j^{v_j}}\left[\frac{\partial g}{\partial\sigma_k}e^g\right] = \frac{\partial g}{\partial\sigma_k}\frac{\partial^{v_i+v_j}e^g}{\partial\sigma_i^{v_i}\partial\sigma_j^{v_j}} + v_i\frac{\partial^{v_i-1+v_j}e^g}{\partial\sigma_i^{v_i-1}\partial\sigma_j^{v_j}}\frac{\partial^2 g}{\partial\sigma_i\partial\sigma_k} + v_j\frac{\partial^{v_i+v_j-1}e^g}{\partial\sigma_i^{v_i}\partial\sigma_j^{v_j-1}}\frac{\partial^2 g}{\partial\sigma_j\partial\sigma_k}. \tag{B.63}$$

In this manner, the derivatives with respect to each variable, σ_i can be distributed. From the previous two equations, each new partial derivative adds a term to the resulting equation.

For an arbitrary number of derivatives, the expression can be rewritten as

$$\frac{\partial^{v_1\cdots v_{2N}}}{\partial\sigma_1^{v_1}\cdots\partial\sigma_{2N}^{v_{2N}}}\frac{\partial}{\partial\sigma_k}e^g = \frac{\partial g}{\partial\sigma_k}\frac{\partial^{v_1\cdots v_{2N}}}{\partial\sigma_1^{v_1}\cdots\partial\sigma_{2N}^{v_{2N}}}e^g + \sum_{j=1}^{2N} v_j\frac{\partial^2 g}{\partial\sigma_k\partial\sigma_j}\frac{\partial^{v_1\cdots(v_j-1)\cdots v_{2N}}}{\partial\sigma_1^{v_1}\cdots\partial\sigma_j^{v_j-1}\partial\sigma_{2N}^{v_{2N}}}e^g. \tag{B.64}$$

Note that any third or higher order derivatives of g are zero. As such, only two terms remain in equation B.62. The recursion relation follows from substitution into the above derivative equations. The recursion expression is identical to that given in chapter 3, and is as follows.

$$\langle v_1\cdots v_{k+1}\cdots v_{2N}\rangle = \sqrt{\frac{1}{v_k+1}}(\mathbf{T}\sigma)_k\langle v_1\cdots v_k\cdots v_{2N}\rangle + \sum_{j=1}^{2N}\sqrt{\frac{v_j}{v_k+1}}\mathbf{T}_{j,k}\langle v_1\cdots v_k\cdots v_{j-1}\cdots v_{2N}\rangle \tag{B.65}$$

B.5.1 Franck-Condon Factor Implementation

The following algorithm was implemented in Matlab to calculate FCFs recursively using the expression from the previous section. The algorithm loops through all vibrational transitions beginning at $\mathbf{v}' = \mathbf{v}'' = \mathbf{0}$, such that the current FCF depends only on those already calculated. The calculation is straightforward. Each FCF is defined by an index in the array, as well as a set of $2N$ vibrational quantum numbers (N for the excited state and N for the ground state). For each FCF, the index, k, of the last nonzero quantum number is found. The FCF is then calculated from the two terms in equation B.65 by first decrementing quantum number k by one, and adding the scaled FCF corresponding to the

new vector of quantum numbers. Then, each index up to (and including) k is decremented in a similar fashion as described in the equation above. Algorithm 1 describes a straightforward implementation.

Algorithm 1: Implementation of Franck-Condon Factor calculation

input : $1D$ array v ($2N \times 1$ array of highest vibrational quantum number per mode),
$2D$ array T ($2N \times 2N$ T matrix),
$1D$ array $T\sigma$ (product of $2N \times 2N$ T matrix and $2N \times 1$ σ vector)

output: $1D$ array S (list of all calculated FCFs, length $\prod(v_i + 1)$)

$S[1] \leftarrow 1$ // Set the 0-0 transition to unity. Scaling will be done later.
for $i = 2 \cdots \text{length}(S)$ **do**
  // Loop over all FCFs except the first one, since that was set above.
  $W \leftarrow \text{getSubscripts}(i, v)$ // Get the quantum number vector for this transition
  $k \leftarrow \text{getLastIndex}(W)$ // Find the last non-zero entry in W
  $W[k] \leftarrow W[k] - 1$ // Decrement last entry to access $v_k - 1$
  $l \leftarrow \text{getIndex}(W, v)$ // Find the index l corresponding to W
  $S[i] \leftarrow S[l] \times T\sigma[k]/\sqrt{v[k]}$ // Calculate first term in equation B.65
  // Loop over all modes up to k since $W[i > k] = 0$
  for $j = 1 \cdots k$ **do**
    if *W[j] = 0* **then**
      continue // If $W[j] = 0$, skip because we can't decrement it
    $W[j] \leftarrow W[j] - 1$ // Decrement current index
    $l \leftarrow \text{getIndex}(W, v)$ // Find the index l corresponding to the new W
    $S[i] \leftarrow S[i] + \sqrt{W[j]/W[k]} \times T[j][k] \times S[l]$ // Calculate second term of equation B.65
    $W[j] \leftarrow W[j] + 1$ // Restore previous index
  end
end

Appendix C

Spectroscopic Data for Formaldehyde

A complete spectroscopic dataset for formaldehyde was collected from literature and supplemented with the results of several *ab initio* calculations. The *ab initio* calculations used the Density Functional Theory (DFT; see, *e.g.*, [205] for a thorough discussion of DFT) with the Becke 3-parameter, Lee-Yang-Parr function (B3LYP; Becke 1988 [206] and Lee, Yang & Parr 1988 [207]) using the Alhrich's style triple-zeta valence basis set (Def2-TZVP) [208]. All calculations are performed using the Orca DFT software package [209].

Geometry optimization and frequency analysis of the ground state is done initially using the plain DFT calculation with the B3LYP functional. This finds the minimum energy structure of the ground state, and calculates the normal mode vectors associated with this structure. Although DFT is not expected to provide the most correct answer with respect to electronic properties, the B3LYP functional (and other hybrid functionals) have been recommended for use in vibration analysis of small molecules due to its computational simplicity and relative accuracy for harmonic [210] and anharmonic [211] analysis. However, since none of the methods used here can be expected to be exact, experimental vibratonal properties from literature will be included. In particular, harmonic frequencies should be taken from literature where available, as these values determine the location of spectral features. Dipole moments, derivatives, normal mode vectors, and several other properties are necessarily calculated using DFT.

Structural data for the formaldehyde molecule in each of it's electronic states was determined via the geometry optimization procedure. The ground state data was calculated as described above. The excited

Parameter	$\tilde{X}\ ^1A_1$	$\tilde{a}\ ^3A_2$	$\tilde{A}\ ^1A_2$	Units
r_{CO}	1.199	1.300	1.297	Å
r_{CH}	1.108	1.084	1.088	Å
$\measuredangle HCH$	122.0	119.0	119.0	°
ρ	0	0	0	°
a	9.482	9.310	9.229	cm^{-1}
b	1.306	1.153	1.158	cm^{-1}
c	1.148	1.025	1.029	cm^{-1}
$\mathcal{T}$	0	28,430	31,460	cm^{-1}

Table C.1: Calculated formaldehyde structure in its ground state ($\tilde{X}\ ^1A_1$) and first two excited states ($\tilde{a}\ ^3A_2$ and $\tilde{A}\ ^1A_2$). ρ represents the dihedral or out-of-plane bending angle. The spectroscopic constants show the correct trends, but a in particular is larger than experiments suggest for the excited states.

state structure was calculated using the time-dependent DFT (TD-DFT) approach. The structure of the ground and excited states are calculated separately. The geometry is summarized in Table C.1. Note that in the table, in all three states the out-of-plane bending angle is 0 (*i.e.*, the structures are planar); this is because the out-of-plane bending motion is captured by the anharmonic double-well potential, and the equilibrium configuration with this potential is planar. The geometry calculated here is consistent (although not identical to) previously reported data [77]. Spectroscopic rotational constants are calculated directly from the molecular geometry and are also reported in Table C.1.

A multi-reference configuration interaction (MRCI) calculation is also done to include the effect of double excitations using a complete active space with two electrons and two orbitals, CAS(2,2). The MRCI calculation uses the DFT result as a reference wavefunction. The MRCI calculation provides an improved estimate of electronic energy levels and dipole moments. The calculated electronic energy levels $\mathcal{T}$ are also included in Table C.1.

Next, vibrational analysis is performed on each of the optimized structures. As before, TD-DFT is used to determine the excited state vibrational frequencies and normal mode vectors. The calculated vibrational normal mode vectors (and associated harmonic frequencies) are tabulated in Table C.2, while the experimental vibrational frequencies are given in Table C.3. Table C.3 also contains experimental rotational constants. The experimental frequencies and rotational constants should be used to determine line locations as opposed to the calculation results, as even the relatively small errors in these *ab initio* methods are enough to alter the resulting spectra.

		$\tilde{X}\ ^1A_1$						$\tilde{a}\ ^3A_2$						$\tilde{A}\ ^1A_2$					
		v_1	v_2	v_3	v_4	v_5	v_6	v_1	v_2	v_3	v_4	v_5	v_6	v_1	v_2	v_3	v_4	v_5	v_6
	$\hat{x}$	0	0	0	0.17	0	0	0	0	0	0.16	0	0	0	0	0	0.16	0	0
C	$\hat{y}$	0	0	0	0	0.15	0.10	0	0	0	0	0.14	0.10	0	0	0	0	0.14	0.10
	$\hat{z}$	-0.06	0.59	-0.01	0	0	0	-0.05	0.34	-0.10	0	0	0	-0.05	0.36	-0.09	0	0	0
	$\hat{x}$	0	0	0	-0.04	0	0	0	0	0	-0.04	0	0	0	0	0	-0.04	0	0
O	$\hat{y}$	0	0	0	0	-0.08	0	0	0	0	0	-0.07	0	0	0	0	0	-0.07	0
	$\hat{z}$	0	-0.41	-0.08	0	0	0	0	-0.19	0.15	0	0	0	0	-0.21	0.14	0	0	0
	$\hat{x}$	0	0	0	-0.70	0	0	0	0	0	-0.70	0	0	0	0	0	-0.70	0	0
H	$\hat{y}$	0.61	0.44	-0.35	0	-0.25	-0.60	0.62	0.43	0.29	0	-0.25	-0.60	0.62	0.43	0.29	0	-0.25	-0.61
	$\hat{z}$	0.35	-0.22	0.61	0	0.65	-0.37	0.33	-0.49	-0.63	0	0.65	-0.36	0.33	-0.48	-0.63	0	0.65	-0.36
	$\hat{x}$	0	0	0	-0.70	0	0	0	0	0	-0.70	0	0	0	0	0	-0.70	0	0
H	$\hat{y}$	-0.61	-0.44	0.35	0	-0.25	-0.60	-0.62	-0.43	-0.29	0	-0.25	-0.60	-0.62	-0.43	-0.29	0	-0.25	-0.61
	$\hat{z}$	0.35	-0.22	-0.61	0	-0.65	0.37	0.33	-0.49	-0.63	0	-0.65	0.36	0.33	-0.48	-0.63	0	-0.65	0.36
	ω	2876	1820	1534	1201	1265	2930	3087	1372	1307	$988i$	880	3200	3058	1375	1301	$443i$	882	3169

Table C.2: Calculated formaldehyde normal mode vectors and harmonic frequencies for the three lowest energy states. The $\tilde{A}\ ^1A_2$ state is assumed to be planar. The out-of-plane bending mode frequencies for the excited states are imaginary because they are actually saddle points on the potential energy surface.

	$\tilde{X}\ ^1A_1$	$\tilde{a}\ ^3A_2$	$\tilde{A}\ ^1A_2$
ω_1	2782		2846
ω_2	1746	1283	1183
ω_3	1500		1293
ω_4	1167	-	-
ω_5	1249		2968
ω_6	2843		904
a_0	9.406	8.673	8.752*
b_0	1.295	1.156	1.125*
c_0	1.134	1.042	1.011*

v_4	$\tilde{X}\ ^1A_1$	$\tilde{a}\ ^3A_2$	$\tilde{A}\ ^1A_2$
0	0	0	0
1	1167.3‡	36	124.5
2	2327.1‡	538	542.3
3		777	947.9
4	4629.8‡	1175	1429.3
5		1573†	1949.8†

*Specifically taken for the 4_0^1 band of the $\tilde{A}\ ^1A_2 \rightarrow \tilde{X}\ ^1A_1$ transition.
†From [212]. Calculated (not observed) using a double-well potential.
‡From Reisner[213] via stimulated emission spectroscopy.

Table C.3: Vibrational and ($\mathbf{v} = \mathbf{0}$) rotational spectroscopic constants for formaldehyde. Left: harmonic and asymmetric rotor constants for all states. Right: vibrational energies of the out-of-plane bending mode overtones. All quantities are in units of cm^{-1}.

The normal mode vectors can be used to determine the Duschinsky shift and rotation parameters. These parameters are calculated as follows [214] with the equations:

$$\mathbf{J} = \mathbf{L'}^T\mathbf{B}^{-1}\mathbf{L''} \tag{C.1a}$$

and

$$\mathbf{K} = \mathbf{\Gamma}^{1/2}\mathbf{L'}^T\mathbf{M}^{1/2}(\mathbf{B}^{-1}\mathbf{x''}_0 - \mathbf{x'}_0) \tag{C.1b}$$

where $\mathbf{L}$ is the $(3N) \times (3N-6)$ normal coordinate matrix in Cartesian space, $\mathbf{x_0}$ is the vector of atomic coordinates (length $3N$) at the equilibrium location, and$\mathbf{M}$ is a diagonal mass matrix such that each entry $M_{i,i}$ is the atomic mass of the atom corresponding to coordinate x_i. The double prime notation ($''$) indicates the initial state and the single prime ($'$) indicates the upper state. In calculating the Duschinsky shift vector, the quantity $\mathbf{\Gamma}$ ($\Gamma_i = \omega_i/\hbar$) is the reduced frequency vector, and is needed to convert the vector from mass-weighted normal coordinates to dimensionless normal coordinates. $\mathbf{B}$ is a block-diagonal matrix describing axis switching effects. If axis switching effects are not significant, then $\mathbf{B} \rightarrow \mathbb{1}$. The calculated parameters $\boldsymbol{J}$ and $\boldsymbol{K}$ are shown in Tables C.4 assuming $\mathbf{B} \rightarrow \mathbb{1}$.

The Duschinsky matrices show that there is little coupling between the formaldehyde vibrational modes, and the out-of-plane bending mode (v_4) in particular does not couple to any other mode. Modes v_1, v_2 and v_3 do couple slightly, but only to a very small degree.

		v_1	v_2	v_3	v_4	v_5	v_6	
Transition				***J***				***K***
	v_1	0.9994	0.3673	-0.0336	0	0	0	-0.22
	v_2	0.1717	0.8883	-0.8660	0	0	0	1.85
$\tilde{X}\ ^1A_1$	v_3	-0.0806	0.4274	-0.9911	0	0	0	0.27
$\rightarrow$	v_4	0	0	0	-1	0	0	0
$\tilde{A}\ ^1A_2$	v_5	0	0	0	0	-1	0.1638	0
	v_6	0	0	0	0	-0.1489	0.9998	0
	v_1	0.9995	0.3642	-0.0302	0	0	0	-0.27
	v_2	0.1719	0.8750	-0.8804	0	0	0	1.91
$\tilde{X}\ ^1A_1$	v_3	-0.0878	0.4124	-0.9888	0	0	0	0.31
$\rightarrow$	v_4	0	0	0	-1	0	0	0
$\tilde{a}\ ^3A_2$	v_5	0	0	0	0	1	0.1623	0
	v_6	0	0	0	0	-0.1499	1	0
	v_1	1	0.1994	-0.0498	0	0	0	-0.01
	v_2	0.204	0.9995	0.8116	0	0	0	-0.02
$\tilde{A}\ ^1A_2$	v_3	-0.0539	0.7842	1	0	0	0	-0.05
$\rightarrow$	v_4	0	0	0	1	0	0	0
$\tilde{a}\ ^3A_2$	v_5	0	0	0	0	1	0.1465	0
	v_6	0	0	0	0	0.1491	1	0

Table C.4: Duschinsky transformation parameters for transitions between formaldehyde's three lowest electronic states

i	$\tilde{X}\ ^1A_1$		$\tilde{A}\ ^1A_2$	
j	$\tilde{X}\ ^1A_1$	$\tilde{A}\ ^1A_2$	$\tilde{X}\ ^1A_1$	$\tilde{A}\ ^1A_2$
μ	2.33	0	0	1.212
$\frac{\partial\mu}{\partial q_1}$	-0.138	0	0	0.263
$\frac{\partial\mu}{\partial q_2}$	0.224	0	0	-0.236
$\frac{\partial\mu}{\partial q_3}$	0.072	0	0	-0.274
$\frac{\partial\mu}{\partial q_4}$	0	0.170	0.199	0
$\frac{\partial\mu}{\partial q_5}$	0	0.009	0.042	0
$\frac{\partial\mu}{\partial q_6}$	0	0.001	0.062	0
$\lvert Q\rvert$	8.77	0.374	0.242	-
$\frac{\partial\lvert Q\rvert}{\partial q_1}$	0.108	0.042	0.026	-
$\frac{\partial\lvert Q\rvert}{\partial q_2}$	-0.029	-0.080	-0.058	-
$\frac{\partial\lvert Q\rvert}{\partial q_3}$	0.009	-0.008	0.025	-
$\frac{\partial\lvert Q\rvert}{\partial q_4}$	0	0	0	-
$\frac{\partial\lvert Q\rvert}{\partial q_5}$	0	0	0	-
$\frac{\partial\lvert Q\rvert}{\partial q_6}$	0	0	0	-

i	$\tilde{X}\ ^1A_1$	$\tilde{A}\ ^1A_2$
j	$\tilde{A}\ ^1A_2$	$\tilde{X}\ ^1A_1$
$\lvert M\rvert$	0.152	0.134
$\frac{\partial\lvert M\rvert}{\partial q_1}$	0.003	0.002
$\frac{\partial\lvert M\rvert}{\partial q_2}$	-0.009	-0.009
$\frac{\partial\lvert M\rvert}{\partial q_3}$	-0.002	0.005
$\frac{\partial\lvert M\rvert}{\partial q_4}$	0	0
$\frac{\partial\lvert M\rvert}{\partial q_5}$	0	0
$\frac{\partial\lvert M\rvert}{\partial q_6}$	0	0

Table C.5: Electronic matrix elements for formaldehyde. Note that transitions are from $i \rightarrow j$, and are assumed to be vertical. As a result, $M_{ij} \neq M_{ji}$ in general since the initial geometries are different. μ is the transition dipole moment operator, and is expressed in units of Debye (derivatives are also expressed in Debye). Q is the transition electric quadrupole moment, and is expressed in atomic units (electron charge $\times$ Bohr radius-squared, ea_0^2). The magnetic dipole transition moment M is also shown (with derivatives) on the right, in atomic units ($e\hbar/m_e$).

The final set of data required is the electronic matrix elements for the transitions, along with their derivatives with respect to normal coordinates. These are calculated by sweeping molecular geometry in a small range around the equilibrium state, and calculating the transition dipole and quadrupole moments between each state. Note that quantities entered as a dash (-) were not calculated.

The transition dipole moment table shows the symmetry of the molecule. Dipole transitions between the ground and first excited singlet state are allowed through vibronic interaction with vibrational modes v_4, v_5, and v_6. The electronic transition is also quadrupole and magnetic dipole allowed, although both of these transitions are much weaker than the vibrationally-induced dipole transitions.

Appendix D

Additional Multiple Scattering Considerations

D.1 Analytic Solution for Isotropic Single-Scattering

An additional feature of the method of successive orders is that it can be used to calculate the contribution of each scattering order analytically. Although the calculations are in general very difficult to perform, the solution for first-order isotropic scattering is relatively straightforward and will be presented here in support of the more detailed calculations discussed earlier in this section. This calculation is provided to show in detail an example of the method of successive orders, and to provide some analytical justification for the numeric results presented in the previous sections.

The initial source function is assumed to be a uniform source sheet, which corresponds to *e.g.*, excited phosphor particles in a thin layer within the cylinder. The zero order source function is thus $J_0(\tau', \mu, \phi) = J_0\delta(\tau' - \tau_s)/2$, where $\delta(z)$ is the Dirac-δ function. Carrying out the integral in Equation 6.31, the incident intensity is thus

$$I_0(\tau', \mu, \phi) = \frac{J_0}{2\mu} e^{-(\tau' - \tau_s)/\mu}. \tag{D.1}$$

This is exactly the Beer-Lambert attenuated source sheet, where the additional factor of μ in the exponential indicates the additional attenuation along paths that do not exit the cylinder at normal incidence. The factor of μ in the denominator is the result of integrating over the polar angle (wrapping around

the τ'-axis). The 1$^{\text{st}}$-order source function (J_1) is calculated by integrating I_0 over μ', leading to

$$J_1(\tau', \mu, \phi) = \frac{J_0}{4} \int_{-1}^{1} d\mu' \, \frac{e^{-(\tau' - \tau_s)/\mu'}}{\mu'} = \frac{J_0}{4} E_1(|\tau' - \tau_s|) \tag{D.2}$$

where

$$E_1(z) = \int_z^{\infty} \frac{e^{-t}}{t} dt \tag{D.3}$$

is the exponential integral function. Note that the source function is defined for both positive and negative arguments of $\tau' - \tau_s$; the integral is calculated by considering the flux either above or below the sheet (see Van de Hulst [134] for more detail). Finally, the first-order scattering intensity is calculated by integrating J_1 (with the appropriate Beer-Lambert attenuation and symmetry arguments included) over the optical depth τ''. For simplicity, we'll consider only the normal-incidence flux out of the cylinder ($\mu \to 1$), evaluated at the exit aperture. The first-order scattering intensity is thus

$$I_1(\tau_0, 1, \phi) = \frac{J_0}{4} e^{-\tau_0} \int_0^{\tau_0} E_1(|\tau'' - \tau_s|) e^{\tau''} \, d\tau''. \tag{D.4}$$

The relative increase in signal, relative to the Beer-Lambert attenuated zero-order signal, is then

$$\frac{I_1(\tau_0, 1, \phi)}{I_0(\tau_0, 1, \phi)} = \frac{e^{\tau_s}}{2} \int_0^{\tau_0} E_1(|\tau'' - \tau_s|) e^{\tau''} \, d\tau''. \tag{D.5}$$

Changing the integration variable such that $\nu = \tau'' - \tau_s$, and assuming the laser sheet is in the center of the cylinder ($\tau_s = \tau_0/2$), the integral can be rewritten as

$$\frac{I_1(\tau_0, 1, \phi)}{I_0(\tau_0, 1, \phi)} = \frac{e^{\tau_0}}{2} \int_{-\tau_0/2}^{\tau_0/2} E_1(|\nu|) e^{\nu} \, d\nu. \tag{D.6}$$

It is not immediately obvious whether this equation can be integrated analytically. However, in the small τ_0 limit, the series expansion can be used where $E_1(|\nu|) \approx -\ln|x|$ (neglecting a constant term that drops out following integration) and $e^{\nu} \approx 1$. Then the integral is approximately

$$\frac{I_1(\tau_0, 1, \phi)}{I_0(\tau_0, 1, \phi)} \approx \frac{e^{\tau_0}}{2} \int_{-\tau_0/2}^{\tau_0/2} -\ln|\nu| \, d\nu = e^{\tau_0} \int_0^{\tau_0/2} -\ln \nu \, d\nu = \frac{e^{\tau_0} \tau_0}{2} \left(1 - \ln\left(\frac{\tau_0}{2}\right)\right). \tag{D.7}$$

This approximation matches the numeric solution within 5-10% at τ_0 as large as 0.01, and is consistent with the values plotted in Figure 6.10.

D.2 Scattering Phase Function

The discussion so far has neglected the details of the scattering processes particularly as they relate to the scattering phase function. For calculations that assume small angle scattering, including the upcoming analysis of beam spreading or resolution changes, a more detailed investigation of the scattering phase function is warranted. A simple approximation of the Mie scattering phase function, the Henyey-Greenstein function, was assumed earlier. However, the Henyey-Greenstein function is insufficient for precisely capturing angle-resolved behaviors [215]. In particular, the mean-squared scattering angle $\langle\theta^2\rangle$ as calculated from the Henyey-Greenstein function diverges [216]. Mie scattering theory [217] provides an exact solution of far-field scattering behavior of electromagnetic plane waves incident on a perfect uncharged sphere of any diameter, and can be used to calculate $\langle\theta^2\rangle$. Mie theory has been described in detail in several books (*e.g.*, [140, 218, 219]), so the mathematical details will not be repeated here for brevity. The Mie phase function can be determined from Mie theory as [220]

$$P(\cos\theta) = \frac{1}{Q_s}\frac{\partial Q_s}{\partial \theta}, \tag{D.8}$$

where Q_s is the scattering efficiency and $\partial Q_s/\partial\theta$ is the angle-resolved scattering efficiency. This expression is normalized such that

$$\int_0^1 P(\cos\theta)\ \cos(\theta)\ d(\cos\theta) = g \tag{D.9}$$

and

$$\int_0^1 P(\cos\theta)\ \cos(\theta)\ d(\cos\theta) = \langle\theta^2\rangle. \tag{D.10}$$

All of the parameters that are necessary to investigate multiple scattering effects (specifically the mean-squared scattering angle $\langle\theta^2\rangle$ and the anisotropy parameter g) can thus be calculated directly from Mie theory. However, for large indices of refraction typical of the ceramic host materials used for phosphors ($M > 1.5$), there is a significant backscatter peak. In extreme cases the phase function contains two narrow peaks centered at $\theta = 0$ and $\theta = \pi$. Thus, for the discussion of small angle scattering, only forward scattering will be used to estimate $\langle\theta^2\rangle$, such that the average is only taken over forward-scattering angles $0 \leq \theta \leq \pi/2$. Alternatively, the approximation $\langle\theta^2\rangle = 2(1-g)$ has been suggested as well [216]. Figure D.1 shows plots of the anisotropy parameter g and scattering efficiency Q_s as a function of the scattering parameter x for several refractive indices. Similarly, Figure D.2 shows the mean-square scattering angle calculated from the Mie scattering cross-section (using only forward-scattered light), and the estimate $\langle\theta^2\rangle = 2(1-g)$ for comparison. Scattering parameters encountered

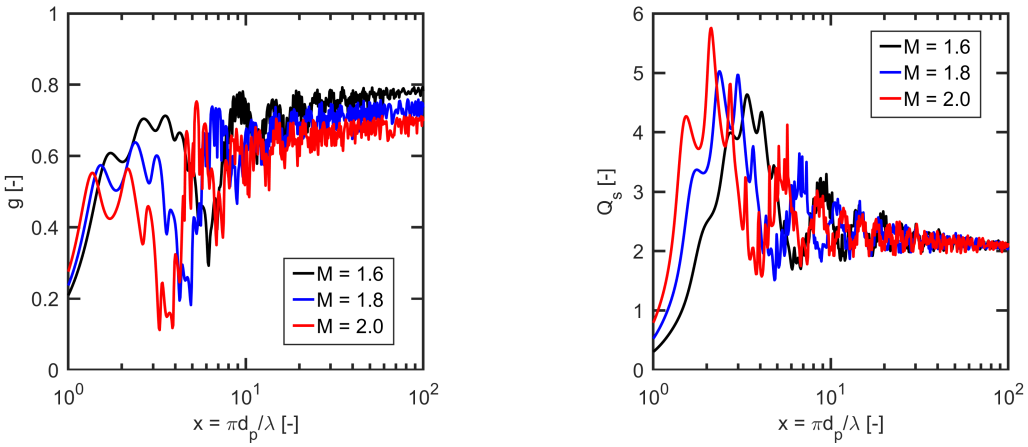

(a) Scattering anisotropy

(b) Scattering efficiency

Figure D.1: Scattering anisotropy and efficiency predicted by Mie scattering theory for several refractive indices (M).

in this work are on the order of 3 - 6, which puts the scattering anisotropy on the order of $g \approx 0.5$, mean-squared scattering angle around $\langle \theta^2 \rangle \approx 0.4$, and $Q_s \approx 2 - 5$. From Figure D.2, the mean-squared scattering angle is relatively large such that the small-angle scattering estimates of beam spreading may be incorrect.

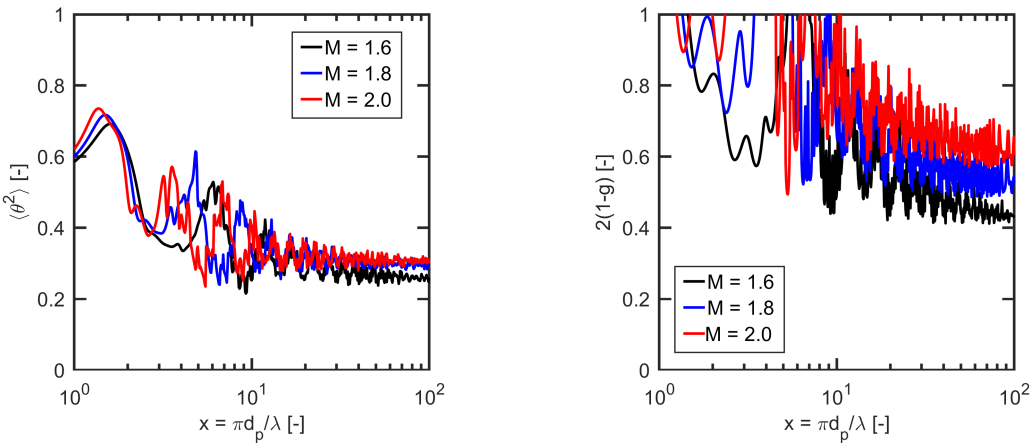

(a) Mie theory

(b) Approximation

Figure D.2: Mean-squared scattering angle calculated from forward-scattering peak of Mie theory and estimated as $\langle\theta^2\rangle \approx 2(1-g)$ for several values of refractive index (M).

Appendix E

Sensor Characterization

The proposed engine experiment makes use of several different cameras for temperature and concentration imaging. To estimate diagnostic performance adequately, detailed information regarding sensor linearity and noise characteristics is needed. Although the manufacturer provides some information on the upper bound of noise and nonlinearity, it often is not sufficient for performance prediction. Instead, several cameras were characterized experimentally, including 2 high-speed cameras (Vision Research Phantom V1211, and Vision Research Phantom V1840) and two ICCD cameras (Princeton Instruments PI-MAX4 1024i-HB-FG-18-P46, and Princeton Instruments PI-MAX2 7489-0022). The camera specifications are outlined in Table E.1, and quantum efficiency is plotted in Figure E.1 as a function of wavelength.

To provide a better understanding of noise properties, a camera characterization experiment was performed in a light box. The light box is an enclosed, dark box with an array of LEDs inside to provide a uniform light field. The cameras are placed in front of an aperture without a lens to illuminate the sensor uniformly. The current applied to the LEDs is varied to sweep the LED emission intensity to cover

Table E.1: Manufacturer provided specifications for tested cameras

Parameter	**PI-MAX4**	**PI-MAX2**	**Phantom V1840**	**Phantom V1211**	**Units**
Technology	ICCD	ICCD	CMOS	CMOS	-
Sensor Size	1024x1024	1024x1024	2048x1952	1280x800	pixels
Pixel Size	12.8	12.8	13.5	28	µm
Min. Exposure	0.5	0.5	142	500	ns
Max. Quantum Eff.	0.45	0.27	0.6	0.5	-
Full-Frame Speed	∼10	∼10	3,300	12,700	Hz

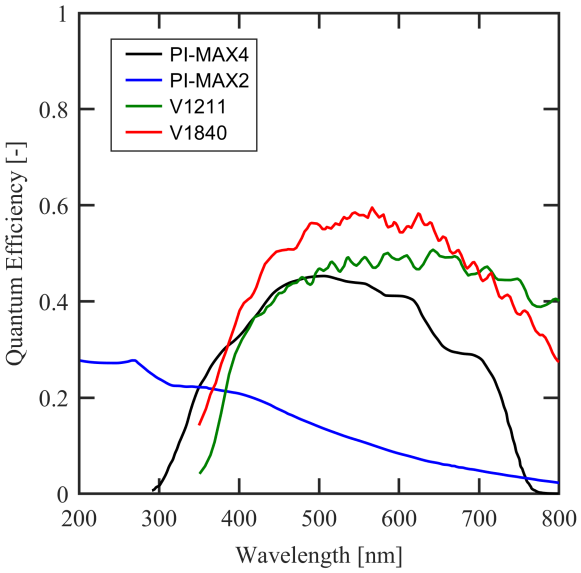

Figure E.1: Quantum efficiency for each camera as provided by the manufacturer.

the full range of the sensor. An experimental setup diagram is shown in Figure E.2. Two photodiodes are used to measure the intensity of the emitted light, and to provide a linear reference for the light intensity. The linearity of the photodiodes with respect to each other was verified; from this it is assumed that the photodiodes are linear with respect to photon flux.

At each intensity or exposure, a series of several hundred images are taken, and a small region in the center of the image stack (a 50x50 pixel square) is used to calculate the average signal (in counts), as well as the noise magnitude in both the temporal and spatial domains. A background subtraction is performed for each image set before analysis using an average background image that is acquired with the LEDs off. The results of the analysis are presented in the following subsections.

E.1 High-Speed Camera Noise & Linearity

The measured noise and linearity as a function of exposure is plotted in Figures E.3 and E.4, respectively, for each camera and operating mode. The Phantom V1840 has 5 operating modes, and each mode is tested independently, while the V1211 has only a single operating mode. The data presented here was taken at a frame rate of 2000 Hz for the V1211, 1000 Hz for the V1840 in high-speed and high-speed binned operation, and 100 Hz for all other modes. The sensor temperature was monitored and remained within 1°C throughout each experiment. Exposure duration was also held constant for a given condition, but was varied from 360 to 800 µs to match the dynamic range of the different camera modes with one

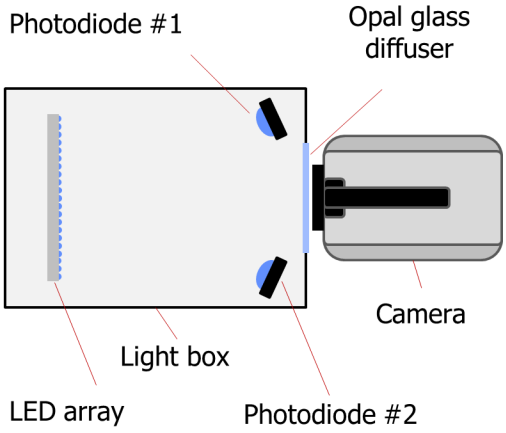

Figure E.2: Experimental setup diagram for light-box testing.

exception; the V1840 Brightfield mode required an exposure of 3500 µs.

The exposure, measured in electrons per pixel N_e, is calculated based on the measured photon flux using the expression

$$N_e = \dot{\phi}'' A t \eta_{QE}, \tag{E.1}$$

where $\dot{\phi}''$ is the photon flux, A is the pixel area, t is the exposure duration, η_{QE} is the quantum efficiency of the detector, and C_{AD} is the analog-to-digital controller (ADC) gain. The measured photodiode voltage is calibrated to photon flux using the same expression for a camera with a manufacturer-provided calibration (Princeton Instruments, PI-MAX4 1024i-HB-FG-18-P46). The sensor area, quantum efficiency, and ADC gain are provided by the manufacturer.

Figure E.3 only plots the temporal noise. In the spatial domain, there is an additional noise term due to variation in gain across each pixel, but otherwise should be identical. This additional spatial noise term is usually referred to as fixed-pattern noise. In principal, fixed-pattern noise can be removed by an appropriate flatfield and background correction. In the high-exposure limit, the noise curve trends towards a line. This is indicative of the shot-noise limit, where the mean-squared noise is proportional to signal. In the low signal-limit, the noise approaches a constant: the read-noise. The read-noise combines various thermal and flicker noise sources. Finally, near saturation, the mean-squared noise tends to increase slower than linear with exposure. This may be a result of saturation, where addition of electrons has a reduced impact on the measured signal. The sensor noise is fit to the form

$$s_e^2 = c_0^2 + \kappa N_e (1 - \alpha N_e)^2, \tag{E.2}$$

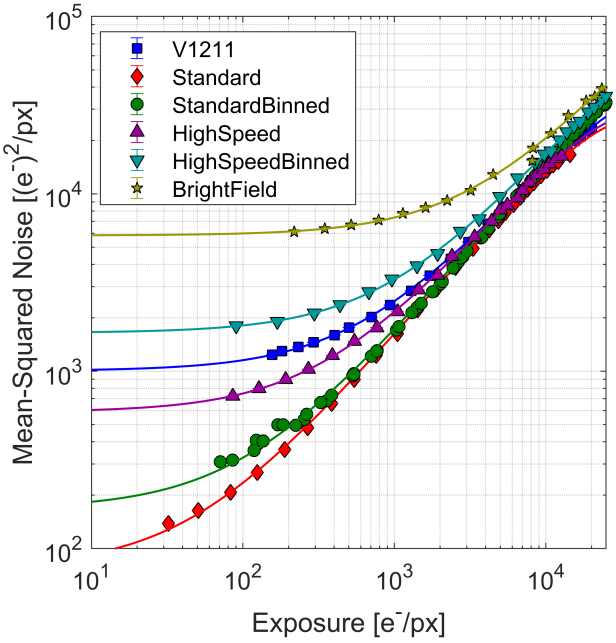

Figure E.3: Measured squared noise (or signal variance) as a function of exposure for high-speed cameras. Only one data series is shown for the V1211 as it has only a single operating mode. The remaining data series belong to the five different operating modes of the V1840.

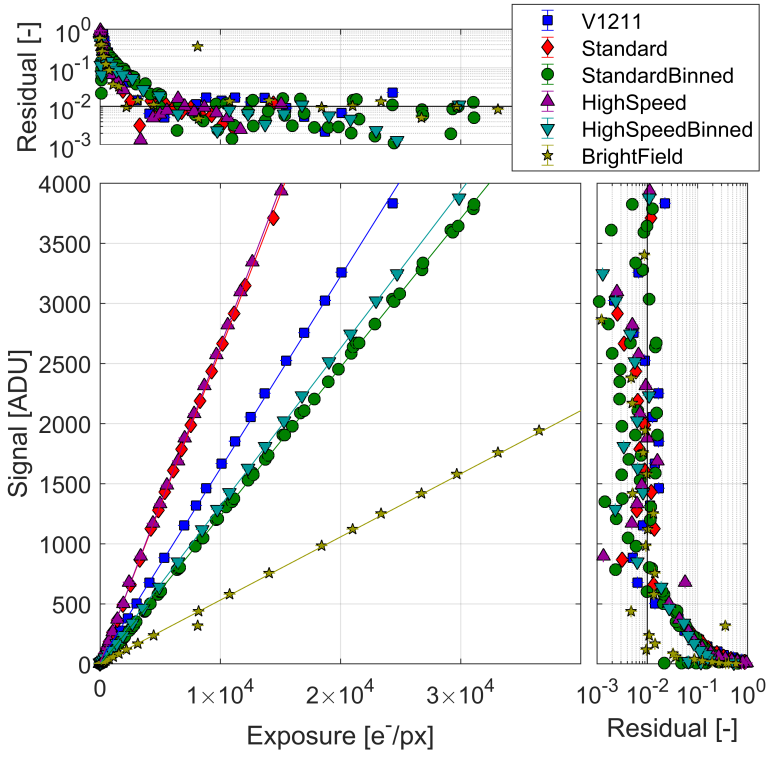

Figure E.4: Camera response as a function of exposure for high-speed cameras. Fractional residuals are plotted above and to the right. The V1840 Brightfield mode has a single apparent outlier near 8000 e⁻/px exposure; this is likely a result of experimental error.

Table E.2: Best-fit noise parameters for high-speed Phantom cameras based on light-box testing. The manufacturer-specified read noise is provided in parentheses for comparison. C_{AD} is the measured ADC gain, which is calculated as the inverse slope of the signal vs. exposure plot in Figure E.4.

Camera	c_0 [e$^-$]	κ [-]	α [10^{-6}]	C_{AD} [e$^-$/ADU]
V1211	31.7 (27)	1.5	6.6	2.73
V1840 Standard	8.8 (7.2)	1.58	9.0	1.99
V1840 Binned	13.0 (11.9)	1.57	4.0	4.18
V1840 High-Speed	24.2 (18.8)	1.61	8.7	1.96
V1840 HS Binned	40.6 (29.7)	1.65	3.8	3.95
V1840 Bright-Field	76.3 (58)	1.53	1.6	9.84

where c_0 represents the total thermal or offset noise, κ is a scale factor for the shot-noise resulting from non-ideal behavior in the circuit (or error in the exposure calibration), and α represents the non-linearity of the sensor [221, 222]. The results of the fits are presented in Table E.2. Table E.2 also includes the measured ADC gain, C_{AD}, which is calculated as the inverse of the slope of the signal vs. exposure plots in Figure E.4.

Figure E.4 shows the camera response as a function of a linear input exposure, corrected for quantum efficiency. From the plot, the Phantom V1840 in binned mode has the highest sensitivity, followed by the V1211. Both cameras (and in every mode for the V1840) exhibit strong non-linearity at low exposures. Comparing the two residual plots, non-linearity appears to be primarily a function of exposure and is not strongly dependent on camera parameters; the residual collapses when plotted against exposure, but does not collapse when plotted against signal. The residual is less than 1% for exposures above around 5,000 electrons per pixel for both cameras. Similarly, above 500 ADU the residuals are typically less than 1%, although the precise cutoff depends on the camera and operating mode.

Two additional measures of noise, the autocorrelation function and the power spectral density, were calculated from the data and are shown in Figures E.5 and E.6 for the spatial and temporal behavior, respectively. The power spectral density describes the bandwidth of the noise, while the autocorrelation function is used to determine whether there is a relationship between noise at different times or spatial locations. The spatial noise in Figure E.5 appears to be relatively strongly correlated, particularly for the V1211, and may be a result of the structure of the readout circuitry. In particular, there is modest correlation between measurements that are 8 pixels apart, and some correlation exists up to a distance of almost 50 pixels. The temporal behavior is much improved over the spatial behavior. Temporal noise has almost no correlation at the frame rates used here (the slightly non-zero correlation at long times is believed to be a result of the imperfect background subtraction process).

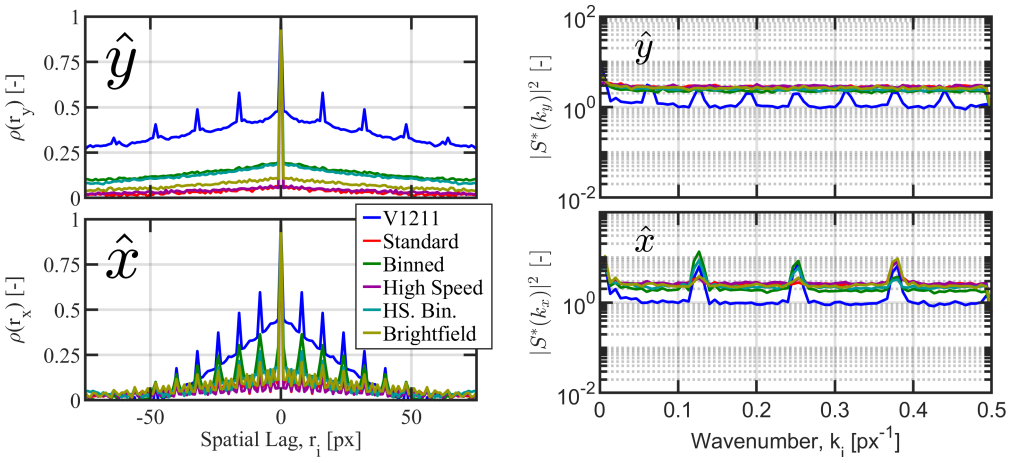

Figure E.5: Spatial autocorrelation (left) and power spectral density (right) of sensor noise for high speed cameras. In both plots, the vertical direction is shown on the top axes, and the horizontal direction on the bottom axes.

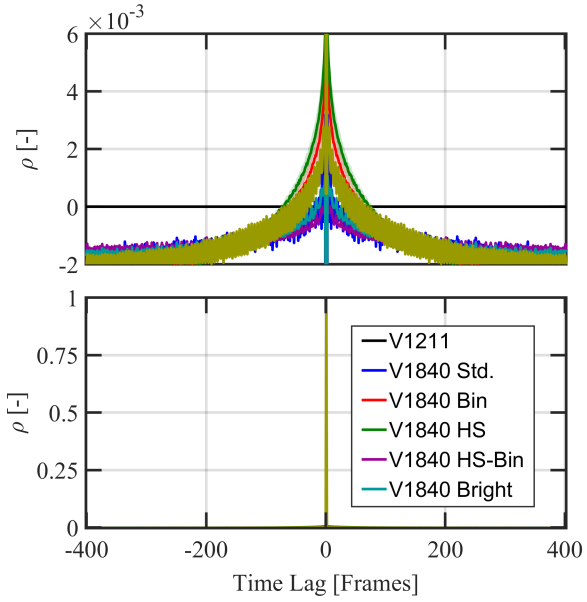

Figure E.6: Temporal autocorrelation of sensor noise for high speed cameras. The power spectral density is excluded because it is flat. This can be seen from the autocorrelation function, which is by definition the Fourier transform of the power spectral density. At late times the autocorrelation does not exactly approach zero; this is believed to be a result of the non-perfect background subtraction process.

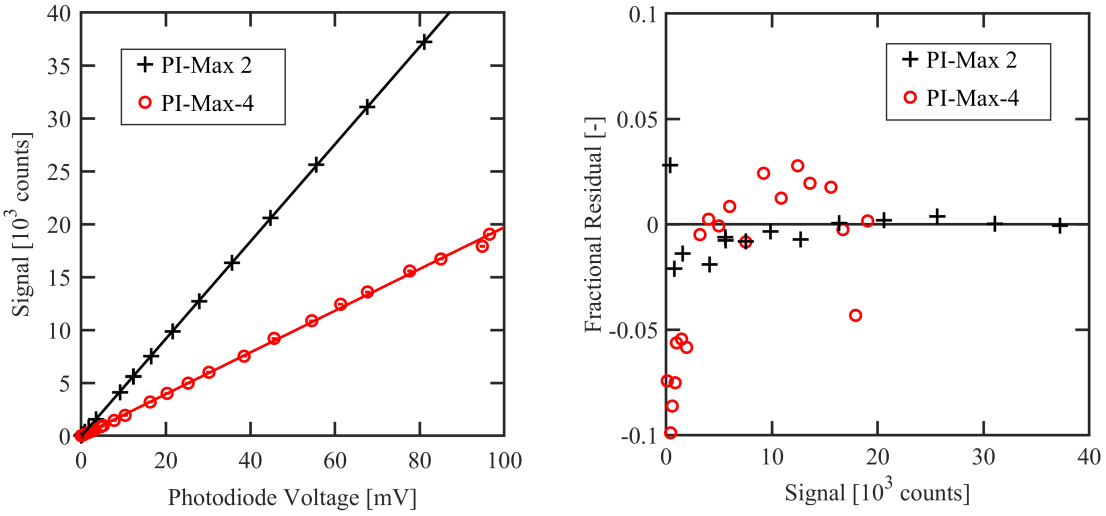

Figure E.7: Measured camera signal for the PI-Max2 and PI-Max4 as a function of exposure (Left) and the fractional residual from a linear fit (Right). Several measurements below 500 counts on either camera are excluded from the plot with residuals on the order of 100%.

E.2 Intensified CCD Camera Noise & Linearity

A similar analysis was performed for two intensified cameras as well: the Princeton Instruments PI-Max 4, and the Princeton Instruments PI-Max 2. Both cameras are run at a fixed gain, exposure, and frame rate. The PI-Max 4 is run at a gain of 20% of its maximum value, with a 30 µs exposure at 10 Hz operation. The PI-Max 4 is unbinned. The PI-Max 2 is run binned 2x2, with an exposure of 100 µs, and a gain of 50 (out of 255, on an exponential scale). The PI-Max 2 is assumed to be binned 2x2 for all measurements because significant nonlinearity was observed in the sensor response when unbinned.

Results for the intensified cameras are shown in Figures E.7 and E.8. Figure E.7 plots the signal measured on the camera as a function of the (linear) photodiode voltage. The cameras appear quite linear, but a significant residual from the linear fit appears at relatively low signals, particularly below 3000 counts on either camera. Above this threshold, the residuals are typically smaller and within the manufactuer specification. It is worth noting that the PI-Max 4 appears to be less linear than the PI-Max 2 with the settings tested here. The non-linearity observed in this data is a result of the CCD sensor, and is dominant at low signal levels. At high exposures, the intensifier can become nonlinear as well (see [223]; this study uses a similar intensifier and camera).

The noise measurements are likewise shown in Figure E.8. The noise power is again fit to a polynomial with the constant term representing the combined read noise and dark noise, the linear term representing

shot-noise, and the quadratic term representing fixed-pattern noise (spatial noise only), or

$$s_e^2 = c_0 + \kappa S + \gamma S^2. \tag{E.3}$$

In this case, the magnitude of the linear term (κ) is the microchannel plate noise factor. Since the microchannel plate is a non-ideal amplifier, shot-noise is scaled by a constant factor, typically on the order of 2 to 4 [224]. The noise factor is given by the square-root of the linear term in the polynomial fit, and is around 3.5 for both cameras at the specified gain. In general, the noise factor should be reduced at higher gain; typical values of the noise factor for filmed Gen. III intensifiers are between 2 and 3.5 [225], although for the filmless intensifier used here typical values are expected to be slightly improved. The PI-Max 2 appears to have less fixed-pattern noise than the PI-Max 4; this is likely in part due to the hardware binning used for the PI-Max 2 (which acts as a 4×4 moving average filter and reduces the spatial variation in gain on the sensor) but not on the PI-Max 4.

For diagnostic performance estimates, the noise in the ICCD measurement is given by

$$s_e^2 = c_0 + \kappa G^2 S, \tag{E.4}$$

where c_0 is the again fixed read noise and dark noise, G is the intensifier gain, κ is again the noise factor squared, and S_e is the signal in units of captured electrons. The gain factor is squared because the shot-noise occurs outside of the intensifier. The data in Figure E.8 was taken at $G = 60$, and the noise factor was found to be $\sqrt{\kappa} \approx 3.5$. For performance predictions, this value will be scaled to a gain of 300 and the noise factor will be estimated at 2.0 ($\kappa = 4.0$), as the noise factor is expected to decrease significantly at higher gain.

Finally, the autocorrelation functions, both spatial and temporal, are plotted in Figure E.9 for both cameras. The noise is largely temporally uncorrelated for both cameras. However, for the PI-Max 4, there is a moderate correlation for a significant number of frames. Noise is very slightly spatially correlated on both sensors as well; the autocorrelation peaks have a full-width at half maximum of 2 pixels.

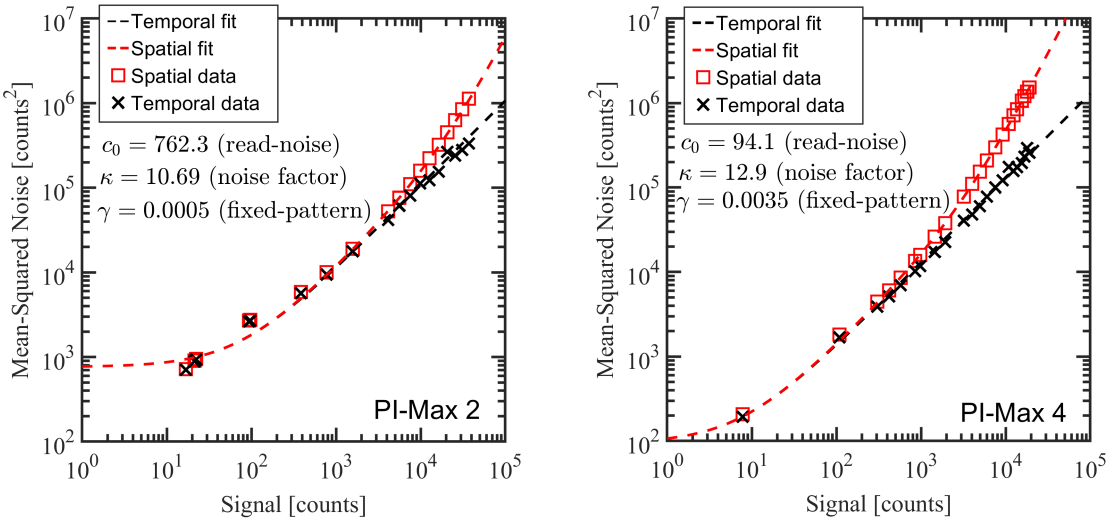

Figure E.8: Measured noise as a function of exposure for the PI-Max 2 and PI-Max 4

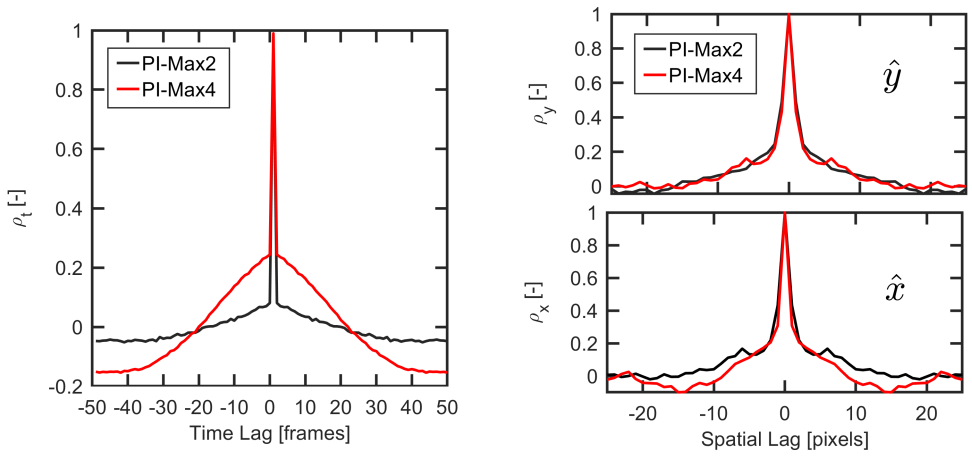

Figure E.9: Temporal (Left) and spatial (Right) noise autocorrelation functions calculated for the PI-Max 2 and PI-Max 4. The spatial autocorrelation function is shown in both the vertical (top) and horizontal directions (bottom).

Bibliography

[1] Chun Sang Yoo, Tianfeng Lu, Jacqueline H Chen, and Chung K Law. Direct numerical simulations of ignition of a lean n-heptane/air mixture with temperature inhomogeneities at constant volume: Parametric study. *Combustion and Flame*, 158(9):1727–1741, 2011.

[2] Chun Sang Yoo, Zhaoyu Luo, Tianfeng Lu, Hongjip Kim, and Jacqueline H Chen. A DNS study of ignition characteristics of a lean iso-octane/air mixture under HCCI and SACI conditions. *Proceedings of the Combustion Institute*, 34(2):2985–2993, 2013.

[3] Scott A Skeen, Julien Manin, and Lyle M Pickett. Simultaneous formaldehyde PLIF and high-speed schlieren imaging for ignition visualization in high-pressure spray flames. *Proceedings of the Combustion Institute*, 35(3):3167–3174, 2015.

[4] Rainer N Dahms, Günter A Paczko, Scott A Skeen, and Lyle M Pickett. Understanding the ignition mechanism of high-pressure spray flames. *Proceedings of the Combustion Institute*, 36(2): 2615–2623, 2017.

[5] Hiroyuki Yamada, Kotaro Suzaki, Hideki Sakanashi, Namil Choi, and Atsumu Tezaki. Kinetic measurements in homogeneous charge compression of dimethyl ether: role of intermediate formaldehyde controlling chain branching in the low-temperature oxidation mechanism. *Combustion and Flame*, 140(1-2):24–33, 2005.

[6] Christian Brackmann, Jenny Nygren, Xiao Bai, Zhongshan Li, Henrik Bladh, Boman Axelsson, Ingemar Denbratt, Lucien Koopmans, Per Erik Bengtsson, and Marcus Aldén. Laser-induced fluorescence of formaldehyde in combustion using third harmonic Nd:YAG laser excitation. *Spectrochimica Acta - Part A: Molecular and Biomolecular Spectroscopy*, 2003. ISSN 13861425. doi: 10.1016/S1386-1425(03)00163-X.

[7] Nicole Graf, Joachim Gronki, Christof Schulz, Thierry Baritaud, Jerôme Cherel, Pierre Duret, and Jacques Lavy. In-cylinder combustion visualization in an auto-igniting gasoline engine using fuel tracer-and formaldehyde-LIF imaging. Technical report, SAE Technical paper, 2001.

[8] Peter M Lillo, Lyle M Pickett, Helena Persson, Oivind Andersson, and Sanghoon Kook. Diesel spray ignition detection and spatial/temporal correction. *SAE International Journal of Engines*, 5(3):1330–1346, 2012.

[9] Christopher J Polonowski, Vivek K Mathur, Jeffrey Naber, and Jason R Blough. Accelerometer based sensing of combustion in a high speed HPCR diesel engine. Technical report, SAE Technical Paper, 2007.

[10] Chao F Daniels, Guoming G Zhu, and James Winkelman. Inaudible knock and partial-burn detection using in-cylinder ionization signal. Technical report, SAE Technical Paper, 2003.

[11] John E Dec and Christoph Espey. Chemiluminescence imaging of autoignition in a DI diesel engine. Technical report, SAE technical Paper, 1998.

[12] Brian Higgins, Dennis Siebers, and Allen Aradi. Diesel-spray ignition and premixed-burn behavior. *SAE transactions*, pages 961–984, 2000.

[13] PRN Childs, JR Greenwood, and CA Long. Review of temperature measurement. *Review of scientific instruments*, 71(8):2959–2978, 2000.

[14] Terrill A Cool, Andrew McIlroy, Fei Qi, Phillip R Westmoreland, Lionel Poisson, Darcy S Peterka, and Musahid Ahmed. Photoionization mass spectrometer for studies of flame chemistry with a synchrotron light source. *Review of scientific instruments*, 76(9):094102, 2005.

[15] Nils Hansen, Terrill A Cool, Phillip R Westmoreland, and Katharina Kohse-Höinghaus. Recent contributions of flame-sampling molecular-beam mass spectrometry to a fundamental understanding of combustion chemistry. *Progress in Energy and Combustion Science*, 35(2):168–191, 2009.

[16] Scott T Sanders, Jian Wang, Jay B Jeffries, and Ronald K Hanson. Diode-laser absorption sensor for line-of-sight gas temperature distributions. *Applied Optics*, 40(24):4404–4415, 2001.

[17] Xiang Liu, Jay B Jeffries, and Ronald K Hanson. Measurement of non-uniform temperature distributions using line-of-sight absorption spectroscopy. *AIAA journal*, 45(2):411–419, 2007.

[18] Christopher S Goldenstein, R Mitchell Spearrin, Jay B Jeffries, and Ronald K Hanson. Infrared laser-absorption sensing for combustion gases. *Progress in Energy and Combustion Science*, 60: 132–176, 2017.

[19] Ze Wang, Scott T Sanders, and Michael A Robinson. Spatially resolved concentration measurements based on backscatter absorption spectroscopy. *Applied Physics B*, 122(6):176, 2016.

[20] Francis P Hindle, Steve J Carey, Krikor B Ozanyan, Desmond E Winterbone, Eric Clough, and Hugh McCann. Measurement of gaseous hydrocarbon distribution by a near-infrared absorption tomography system. *Journal of Electronic Imaging*, 10(3):593–601, 2001.

[21] Joseph D Miller, Mikhail N Slipchenko, Terrence R Meyer, Hans U Stauffer, and James R Gord. Hybrid femtosecond/picosecond coherent anti-Stokes Raman scattering for high-speed gas-phase thermometry. *Optics letters*, 35(14):2430–2432, 2010.

[22] WD Kulatilaka, HU Stauffer, JR Gord, and S Roy. One-dimensional single-shot thermometry in flames using femtosecond-CARS line imaging. *Optics letters*, 36(21):4182–4184, 2011.

[23] Alexis Bohlin and Christopher J Kliewer. Communication: Two-dimensional gas-phase coherent anti-Stokes Raman spectroscopy (2D-CARS): Simultaneous planar imaging and multiplex spectroscopy in a single laser shot. *The Journal of Chemical Physics*, 138, 2013.

[24] Richard B Miles, Walter R Lempert, and Joseph N Forkey. Laser rayleigh scattering. *Measurement Science and Technology*, 12(5):R33, 2001.

[25] Martin Hof. Basics of optical spectroscopy. *Handbook of Spectroscopy*, pages 37–47, 2003.

[26] Matthew K Blessinger. *An Investigation of Low-Temperature Combustion Front Propagation Mechanisms*. PhD thesis, The University of Wisconsin-Madison, 2015.

[27] Christoph Espey, John E Dec, Thomas A Litzinger, and Domenic A Santavicca. Planar laser Rayleigh scattering for quantitative vapor-fuel imaging in a diesel jet. *Combustion and flame*, 109 (1-2):65–86, 1997.

[28] Alan C Eckbreth. *Laser diagnostics for combustion temperature and species*, volume 3. CRC press, 1996.

[29] R Miles and W Lempert. Two-dimensional measurement of density, velocity, and temperature in turbulent high-speed air flows by UV Rayleigh scattering. *Applied Physics B*, 51(1):1–7, 1990.

[30] D Hoffman, K-U Münch, and A Leipertz. Two-dimensional temperature determination in sooting flames by filtered Rayleigh scattering. *Optics letters*, 21(7):525–527, 1996.

[31] Gregory S Elliott, Nick Glumac, and Campbell D Carter. Molecular filtered Rayleigh scattering applied to combustion. *Measurement Science and Technology*, 12(4):452, 2001.

[32] Patton M Allison, Thomas A McManus, and Jeffrey A Sutton. Quantitative fuel vapor/air mixing imaging in droplet/gas regions of an evaporating spray flow using filtered Rayleigh scattering. *Optics letters*, 41(6):1074–1077, 2016.

[33] Gregory S Elliott and Mo Samimy. Rayleigh scattering technique for simultaneous measurements of velocity and thermodynamic properties. *AIAA journal*, 34(11):2346–2352, 1996.

[34] Christof Schulz and Volker Sick. Tracer-lif diagnostics: quantitative measurement of fuel concentration, temperature and fuel/air ratio in practical combustion systems. *Progress in Energy and Combustion Science*, 31(1):75–121, 2005.

[35] Nicholas James Neal, Jonny Jordan, and David A. Rothamer. Simultaneous measurements of in-cylinder temperature and velocity distribution in a small-bore diesel engine using thermographic phosphors. *SAE International*, 6(1):300–318, 2013. ISSN 19463936. doi: 10.4271/2013-01-0562. URL `http://saeeng.saejournals.org/content/6/1/300.short`.

[36] Benoit Fond, Christopher Abram, and Frank Beyrau. Characterisation of the luminescence properties of BAM:Eu^{2+} particles as a tracer for thermographic particle image velocimetry. *Applied Physics B*, 121(4):495–509, 2015.

[37] Dustin Witkowski and David A Rothamer. Emission properties and temperature quenching mechanisms of rare-earth elements doped in garnet hosts. *Journal of Luminescence*, 192:1250–1263, 2017.

[38] Dustin Witkowski and David A Rothamer. A novel strategy to improve the sensitivity of aerosol phosphor thermometry using co-doped phosphors. *Proceedings of the Combustion Institute*, 2018.

[39] Ronald K Hanson, R Mitchell Spearrin, and Christopher S Goldenstein. *Spectroscopy and optical diagnostics for gases*. Springer, 2016.

[40] Patrick Oßwald, Hanna Güldenberg, Katharina Kohse-Höinghaus, Bin Yang, Tao Yuan, and Fei Qi. Combustion of butanol isomers–a detailed molecular beam mass spectrometry investigation of their flame chemistry. *Combustion and Flame*, 158(1):2–15, 2011.

[41] Mattias Richter, Robert Collin, Jenny Nygren, Marcus Aldén, Leif Hildingsson, and Bengt Johansson. Studies of the combustion process with simultaneous formaldehyde and OH PLIF in a direct-injected HCCI engine. *JSME International Journal Series B Fluids and Thermal Engineering*, 48(4):701–707, 2005.

[42] M Mehl, WJ Pitz, M Sjöberg, and John E Dec. Detailed kinetic modeling of low-temperature heat release for PRF fuels in an HCCI engine. Technical report, SAE Technical Paper, 2009.

[43] Marco Mehl, William J Pitz, Charles K Westbrook, and Henry J Curran. Kinetic modeling of gasoline surrogate components and mixtures under engine conditions. *Proceedings of the Combustion Institute*, 33(1):193–200, 2011.

[44] I.E. Gordon, L.S. Rothman, C. Hill, R.V. Kochanov, Y. Tan, P.F. Bernath, M. Birk, V. Boudon, A. Campargue, K.V. Chance, B.J. Drouin, J.-M. Flaud, R.R. Gamache, J.T. Hodges, D. Jacquemart, V.I. Perevalov, A. Perrin, K.P. Shine, M.-A.H. Smith, J. Tennyson, G.C. Toon, H. Tran, V.G. Tyuterev, A. Barbe, A.G. Csaszar, V.M. Devi, T. Furtenbacher, J.J. Harrison, J.-M. Hartmann, T.J. Johnson A. Jolly, T. Karman, I. Kleiner, A.A. Kyuberis, J. Loos, O.M. Lyulin, S.T. Massie, S.N. Mikhailenko, N. Moazzen-Ahmadi, H.S.P. Muller, O.V. Naumenko, A.V. Nikitin, O.L. Polyansky, M. Rey, M. Rotger, S.W. Sharpe, K. Sung, E. Starikova, S.A. Tashkun, J. Vander Auwera, G. Wagner, J. Wilzewski, P. Wcislo, S. Yu, and E.J. Zak. The HITRAN2016 molecular spectroscopic database. *Journal of Quantitative Spectroscopy and Radiative Transfer*, 2017. doi: 10.1016/j.jqsrt.2017.06.038.

[45] K. Chance and J. Orphal. Revised ultraviolet absorption cross sections of H_2CO for the HITRAN database. *Journal of Quantitative Spectroscopy and Radiative Transfer*, 112:1509–1510, 2011. doi: 10.1016/j.jqsrt.2011.02.002.

[46] DC Moule and AD Walsh. Ultraviolet spectra and excited states of formaldehyde. *Chemical Reviews*, 75(1):67–84, 1975.

[47] Thomas Metz, Xiao Bai, Frederik Ossler, and Marcus Aldén. Fluorescence lifetimes of formaldehyde (H_2CO) in the $\tilde{A}1a2 \rightarrow \tilde{X}1a1$ band system at elevated temperatures and pressures. *Spectrochimica Acta - Part A: Molecular and Biomolecular Spectroscopy*, 2004. ISSN 13861425. doi: 10.1016/S1386-1425(03)00335-4.

[48] Y Yamasaki and A Tezaki. Non-linear pressure dependence of A-state fluorescence lifetime of formaldehyde. *Applied Physics B*, 80(7):791–795, 2005.

[49] Cherian A. Idicheria and Lyle M. Pickett. Effect of EGR on diesel premixed-burn equivalence ratio. *Proceedings of the Combustion Institute*, 2007. ISSN 15407489. doi: 10.1016/j.proci.2006.08.022.

[50] Joel E. Harrington and Kermit C. Smyth. Laser-induced fluorescence measurements of formaldehyde in a methane/air diffusion flame. *Chemical Physics Letters*, 1993. ISSN 00092614. doi: 10.1016/0009-2614(93)85265-P.

[51] Robert JH Klein-Douwel, Jorge Luque, Jay B Jeffries, Gregory P Smith, and David R Crosley. Laser-induced fluorescence of formaldehyde hot bands in flames. *Applied optics*, 39(21):3712–3715, 2000.

[52] Phillip H Paul and Habib N Najm. Planar laser-induced fluorescence imaging of flame heat release rate. *Symposium (International) on Combustion*, 27:43–50, 1998.

[53] C Bradley Moore and JC Weisshaar. Formaldehyde photochemistry. *Annual Review of Physical Chemistry*, 34(1):525–555, 1983.

[54] PC Bakker, Noud Maes, and Nico Dam. The potential of on-and off-resonant formaldehyde imaging combined with bootstrapping in diesel sprays. *Combustion and Flame*, 182:20–27, 2017.

[55] Jan Egermann, Thomas Seeger, and Alfred Leipertz. Application of 266-nm and 355-nm Nd:YAG laser radiation for the investigation of fuel-rich sooting hydrocarbon flames by Raman scattering. *Applied optics*, 43(29):5564–5574, 2004.

[56] Hendrik Thering, Lars Beckmann, Christian Jördens, Markus Röder, Thomas Dreier, and Christof Schulz. Formaldehyde laser-induced fluorescence imaging with a multi-band transmission filter. *Optics Letters*, 2014. ISSN 1539-4794. doi: 10.1364/OL.39.001873.

[57] Cherian A Idicheria and Lyle M Pickett. Formaldehyde visualization near lift-off location in a diesel jet. Technical report, SAE Technical Paper, 2006.

[58] Thierry Lachaux and Mark P B Musculus. In-cylinder unburned hydrocarbon visualization during low-temperature compression-ignition engine combustion using formaldehyde PLIF. *Proceedings of the Combustion Institute*, 2007. ISSN 15407489. doi: 10.1016/j.proci.2006.07.044.

[59] DS Hamilton, SK Gayen, GJ Pogatshnik, RD Ghen, and WJ Miniscalco. Optical-absorption and photoionization measurements from the excited states of Ce^{3+}:$Y_3Al_5O_{12}$. *Physical Review B*, 39 (13):8807, 1989.

[60] JK Lawson and Stephen A Payne. Excited-state absorption of Eu^{2+}-doped materials. *Physical Review B*, 47(21):14003, 1993.

[61] Benoit Fond, Christopher Abram, Andrew L Heyes, Andreas M Kempf, and Frank Beyrau. Simultaneous temperature, mixture fraction and velocity imaging in turbulent flows using thermographic phosphor tracer particles. *Optics express*, 20(20):22118–22133, 2012.

[62] Jonathan Jordan and David A Rothamer. Pr:YAG temperature imaging in gas-phase flows. *Applied Physics B*, 110(3):285–291, 2013.

[63] P Schreivogel, C Abram, B Fond, M Straußwald, F Beyrau, and M Pfitzner. Simultaneous kHz-rate temperature and velocity field measurements in the flow emanating from angled and trenched film cooling holes. *International Journal of Heat and Mass Transfer*, 103:390–400, 2016.

[64] JPJ Van Lipzig, M Yu, NJ Dam, CCM Luijten, and LPH de Goey. Gas-phase thermometry in a high-pressure cell using $BaMgAl_{10}O_{17}$:Eu as a thermographic phosphor. *Applied Physics B*, 111 (3):469–481, 2013.

[65] Hyunchang Lee, Benjamin Böhm, Amsini Sadiki, and Andreas Dreizler. Turbulent heat flux measurement in a non-reacting round jet, using $BaMgAl_{10}O_{17}$:Eu^{2+} phosphor thermography and particle image velocimetry. *Applied Physics B*, 122(7):209, 2016.

[66] Anthony O Ojo, Benoit Fond, Christopher Abram, Berend GM Van Wachem, Andrew L Heyes, and Frank Beyrau. Thermographic laser doppler velocimetry using the phase-shifted luminescence of BAM:Eu^{2+} phosphor particles for thermometry. *Optics Express*, 25(10):11833–11843, 2017.

[67] Michael Stephan, Florian Zentgraf, Edouard Berrocal, Barbara Albert, Benjamin Böhm, and Andreas Dreizler. Multiple scattering reduction in instantaneous gas phase phosphor thermometry: applications with dispersed seeding. *Measurement Science and Technology*, 30(5):054003, 2019.

[68] Zhiyao Yin, Benoit Fond, Georg Eckel, Christopher Abram, Wolfgang Meier, Isaac Boxx, and Frank Beyrau. Investigation of BAM:Eu^{2+} particles as a tracer for temperature imaging in flames. *Combustion and Flame*, 184:249–251, 2017.

[69] Christopher Abram, Benoit Fond, and Frank Beyrau. High-precision flow temperature imaging using ZnO thermographic phosphor tracer particles. *Optics express*, 23(15):19453–19468, 2015.

[70] Christopher Abram, Miriam Pougin, and Frank Beyrau. Temperature field measurements in liquids using ZnO thermographic phosphor tracer particles. *Experiments in Fluids*, 57(7):115, 2016.

[71] Luming Fan, Y Gao, A Hayakawa, and Simone Hochgreb. Simultaneous, two-camera, 2D gas-phase temperature and velocity measurements by thermographic particle image velocimetry with ZnO tracers. *Experiments in Fluids*, 58(4):34, 2017.

[72] Christopher Abram, Benoît Fond, and Frank Beyrau. Temperature measurement techniques for gas and liquid flows using thermographic phosphor tracer particles. *Progress in Energy and Combustion Science*, 64:93–156, 2018.

[73] Dustin Witkowski and David A. Rothamer. Scattering referenced aerosol phosphor thermometry, 2018.

[74] Pieter Dorenbos. Thermal quenching of Eu^{2+} 5d–4f luminescence in inorganic compounds. *Journal of Physics: Condensed Matter*, 17(50):8103, 2005.

[75] Helmut Hönl and Fritz London. Über die intensitäten der bandenlinien. *Zeitschrift für Physik*, 33 (1):803–809, 1925.

[76] J. B. Coon, N. W. Naugle, and R. D. McKenzie. The investigation of double-minimum potentials in molecules. *Journal of Molecular Spectroscopy*, pages 107–129, 1966.

[77] DJ Clouthier and DA Ramsay. The spectroscopy of formaldehyde and thioformaldehyde. *Annual Review of Physical Chemistry*, 34(1):31–58, 1983.

[78] Dick T Co, Thomas F Hanisco, James G Anderson, and Frank N Keutsch. Rotationally resolved absorption cross sections of formaldehyde in the 28100-28500 cm^{-1} (351-356 nm) spectral region: Implications for *in situ* LIF measurements. *The Journal of Physical Chemistry A*, 109(47):10675–10682, 2005.

[79] Martin B Crow, Alex Gilchrist, Gus Hancock, Rob Peverall, Graham Richmond, Grant AD Ritchie, and Sarah R Taylor. High-resolution absorption studies of the $\tilde{a}1a2$- $\tilde{x}1a1$ $2^0_2 4^0_1$ band of formaldehyde. *The Journal of Physical Chemistry A*, 113(24):6689–6696, 2009.

[80] Dimitrios C Kyritsis, Vito S Santoro, and Alessandro Gomez. The effect of temperature correction on the measured thickness of formaldehyde zones in diffusion flames for 355 nm excitation. *Experiments in fluids*, 37(5):769–772, 2004.

[81] Richard G Miller and Edward KC Lee. Single vibronic level photochemistry of formaldehydes in the $\tilde{A}\ ^1A_2$ state: Radiative and nonradiative processes in H_2CO, HDCO, and D_2CO. *The Journal of Chemical Physics*, 68(10):4448–4464, 1978.

[82] SJ Strickler and RJ Barnhart. Absolute vibronic intensities in the $^1\tilde{A}_2 \leftarrow {}^1\tilde{A}_1$ absorption spectrum of formaldehyde. *The Journal of Physical Chemistry*, 86(4):448–455, 1982.

[83] Joshua M Herzog, Dustin Witkowski, and David A Rothamer. Characterization of the Ce,Pr:LuAG phosphor for co-doped aerosol phosphor thermometry. *Journal of Luminescence*, 229:117665, 2020.

[84] Joshua M. Herzog, Dustin Witkowski, and David A. Rothamer. Comparison and combination of scattering-referenced and co-doped aerosol phosphor thermometry techniques using the ce,pr:luag phosphor. *in preparation*, 2021.

[85] Dustin Witkowski and David A Rothamer. Scattering referenced aerosol phosphor thermometry. *Measurement Science and Technology*, 30(4):044003, 2019.

[86] D Ragni, F Schrijer, BW Van Oudheusden, and F Scarano. Particle tracer response across shocks measured by PIV. *Experiments in fluids*, 50(1):53–64, 2011.

[87] Peter F DeCarlo, Jay G Slowik, Douglas R Worsnop, Paul Davidovits, and Jose L Jimenez. Particle morphology and density characterization by combined mobility and aerodynamic diameter measurements. part 1: Theory. *Aerosol Science and Technology*, 38(12):1185–1205, 2004.

[88] Walter A Harrison. *Solid state theory*. Courier Corporation, 1980.

[89] Alois Schauer. Thermal expansion, grueneisen parameter, and temperature dependence of lattice vibration frequencies of aluminum oxide. *Canadian Journal of Physics*, 43(4):523–531, 1965.

[90] Martin Lawrence, Hua Zhao, and Lionel Ganippa. Gas phase thermometry of hot turbulent jets using laser induced phosphorescence. *Optics express*, 21(10):12260–12281, 2013.

[91] Orson L Anderson. A simplified method for calculating the debye temperature from elastic constants. *Journal of Physics and Chemistry of Solids*, 24(7):909–917, 1963.

[92] Mahdi Amachraa, Zhenbin Wang, Chi Chen, Shruti Hariyani, Hanmei Tang, Jakoah Brgoch, and Shyue Ping Ong. Predicting thermal quenching in inorganic phosphors. *Chemistry of Materials*, 32(14):6256–6265, 2020.

[93] Pieter Dorenbos. The nephelauxetic effect on the electron binding energy in the $4f^q$ ground state of lanthanides in compounds. *Journal of Luminescence*, 214:116536, 2019.

[94] Pieter Dorenbos. Improved parameters for the lanthanide $4f^q$ and $4f^{q-1}5d$ curves in HRBE and VRBE schemes that takes the nephelauxetic effect into account. *Journal of Luminescence*, page 117164, 2020.

[95] Suchinder K Sharma, Yuan-Chih Lin, Irene Carrasco, Tobias Tingberg, Marco Bettinelli, and Maths Karlsson. Weak thermal quenching of the luminescence in the $Ca_3Sc_2Si_3O_{12}$:Ce^{3+} garnet phosphor. *Journal of Materials Chemistry C*, 6(33):8923–8933, 2018.

[96] P Dorenbos. Energy of the first $4f^7 \rightarrow 4f^6 5d$ transition of Eu^{2+} in inorganic compounds. *Journal of luminescence*, 104(4):239–260, 2003.

[97] Thomas Jüstel, Helmut Bechtel, Walter Mayr, and Detlef U Wiechert. Blue emitting $BaMgAl_{10}O_{17}$:Eu with a blue body color. *Journal of luminescence*, 104(1-2):137–143, 2003.

[98] JL Sommerdijk and ALN Stevels. Behavior of phosphors with aluminate host lattices. *Philips Tech. Rev*, 37(9-10):221–233, 1977.

[99] WT Carnall, GL Goodman, K Rajnak, and RS Rana. A systematic analysis of the spectra of the lanthanides doped into single crystal LaF_3. *The Journal of Chemical Physics*, 90(7):3443–3457, 1989.

[100] Dustin Witkowski and David A Rothamer. A methodology for identifying thermographic phosphors suitable for high-temperature gas thermometry: application to Ce^{3+} and Pr^{3+} doped oxide hosts. *Applied Physics B*, 123(8):226, 2017.

[101] Aleksander Zych, Matthijs de Lange, Celso de Mello Donegá, and Andries Meijerink. Analysis of the radiative lifetime of Pr^{3+} df emission. *Journal of Applied Physics*, 112(1):013536, 2012.

[102] Gustaf Särner, Mattias Richter, and Marcus Aldén. Investigations of blue emitting phosphors for thermometry. *Measurement Science and Technology*, 19(12):125304, 2008.

[103] M Laroche, S Girard, J Margerie, R Moncorgé, M Bettinelli, and E Cavalli. Experimental and theoretical investigation of the $4f^n \leftrightarrow 4f^{n-1}5d$ transitions in YPO_4:Pr^{3+} and YPO_4:Pr^{3+}, Ce^{3+}. *Journal of Physics: Condensed Matter*, 13(4):765, 2001.

[104] Alan Lenef, John Kelso, Yi Zheng, and Maxim Tchoul. Radiance limits of ceramic phosphors under high excitation fluxes. In *Current Developments in Lens Design and Optical Engineering XIV*, volume 8841, page 884107. International Society for Optics and Photonics, 2013.

[105] A Lenef, M Raukas, J Wang, and C Li. Phosphor performance under high intensity excitation by ingan laser diodes. *ECS Journal of Solid State Science and Technology*, 9(1):016019, 2020.

[106] Benoit Fond, Christopher Abram, and Frank Beyrau. On the characterisation of tracer particles for thermographic particle image velocimetry. *Applied Physics B*, 118(3):393–399, 2015.

[107] KV Ivanovskikh, A Meijerink, F Piccinelli, A Speghini, EI Zinin, C Ronda, and M Bettinelli. Optical spectroscopy of $Ca_3Sc_2Si_3O_{12}$, $Ca_3Y_2Si_3O_{12}$ and $Ca_3Lu_2Si_3O_{12}$ doped with Pr^{3+}. *Journal of luminescence*, 130(5):893–901, 2010.

[108] Joshua M Herzog, Dustin Witkowski, and David A Rothamer. Combustion-relevant aerosol phosphor thermometry imaging using Ce,Pr:LuAG, Ce:$GdPO_4$, and Ce:CSSO. *Proceedings of the Combustion Institute*, 2020.

[109] John Mandel. *The statistical analysis of experimental data*. Courier Corporation, 2012.

[110] DQ Nagasawa, N Mondrik, JL Marshall, DL DePoy, L Schmidt, B Hill, L Turner, and JP Rheault. Throughput of commercial photographic camera lenses for use in astronomical systems. In *Ground-based and Airborne Instrumentation for Astronomy VI*, volume 9908, page 99085C. International Society for Optics and Photonics, 2016.

[111] Nobuyuki Otsu. A threshold selection method from gray-level histograms. *IEEE transactions on systems, man, and cybernetics*, 9(1):62–66, 1979.

[112] MD Dramićanin, Ž Antić, Sanja Ćulubrk, Scott Phillip Ahrenkiel, and JM Nedeljković. Self-referenced luminescence thermometry with Sm^{3+} doped TiO_2 nanoparticles. *Nanotechnology*, 25 (48):485501, 2014.

[113] V Hindasageri, RP Vedula, and SV Prabhu. Thermocouple error correction for measuring the flame temperature with determination of emissivity and heat transfer coefficient. *Rev. Sci. Instrum.*, 84 (2):024902, 2013.

[114] Elisabeth Guazzelli and Jeffrey F Morris. *A physical introduction to suspension dynamics*. Cambridge University Press, 2011.

[115] Alla Zelenyuk, Yong Cai, and Dan Imre. From agglomerates of spheres to irregularly shaped particles: Determination of dynamic shape factors from measurements of mobility and vacuum aerodynamic diameters. *Aerosol Science and Technology*, 40(3):197–217, 2006.

[116] Daniel J Rader. Momentum slip correction factor for small particles in nine common gases. *Journal of aerosol science*, 21(2):161–168, 1990.

[117] E Loth. Drag of non-spherical solid particles of regular and irregular shape. *Powder Technology*, 182(3):342–353, 2008.

[118] Yung-Sung Cheng, Hsu-Chi Yeh, and Michael D Allen. Dynamic shape factor of a plate-like particle. *Aerosol science and technology*, 8(2):109–123, 1988.

[119] Christopher KW Tam. The drag on a cloud of spherical particles in low reynolds number flow. *Journal of Fluid Mechanics*, 38(3):537–546, 1969.

[120] A Melling. Tracer particles and seeding for particle image velocimetry. *Measurement science and technology*, 8(12):1406, 1997.

[121] M Samimy and SK Lele. Motion of particles with inertia in a compressible free shear layer. *Physics of Fluids A: Fluid Dynamics*, 3(8):1915–1923, 1991.

[122] Stephen B Pope. *Turbulent flows*. IOP Publishing, 2001.

[123] Kyle D Squires and John K Eaton. Particle response and turbulence modification in isotropic turbulence. *Physics of Fluids A: Fluid Dynamics*, 2(7):1191–1203, 1990.

[124] N Konopliv and Ephraim M Sparrow. Transient heat conduction in non-homogeneous spherical systems. *Wärme-und Stoffübertragung*, 3(4):197–210, 1970.

[125] William B Krantz. *Scaling analysis in modeling transport and reaction processes: a systematic approach to model building and the art of approximation*. John Wiley & Sons, 2007.

[126] Florian Zentgraf, Michael Stephan, Edouard Berrocal, Barbara Albert, Benjamin Böhm, and Andreas Dreizler. Application of structured illumination to gas phase thermometry using thermographic phosphor particles: a study for averaged imaging. *Experiments in Fluids*, 58(7):82, 2017.

[127] Luming Fan and Simone Hochgreb. Uncertainty analysis in structured laser illumination planar imaging (SLIPI) applied to non-linear signals: gas-phase phosphor thermometry. *Measurement Science and Technology*, 30(8):084003, 2019.

[128] Lihong V Wang and Hsin-i Wu. *Biomedical optics: principles and imaging*. John Wiley & Sons, 2012.

[129] James E Hansen and Larry D Travis. Light scattering in planetary atmospheres. *Space science reviews*, 16(4):527–610, 1974.

[130] Edouard Berrocal, Elias Kristensson, Mattias Richter, Mark Linne, and Marcus Aldén. Application of structured illumination for multiple scattering suppression in planar laser imaging of dense sprays. *Optics express*, 16(22):17870–17881, 2008.

[131] Edouard Berrocal. *Multiple scattering of light in optical diagnostics of dense sprays and other complex turbid media*. PhD thesis, Cranfield University, 2006.

[132] AA Kokhanovsky. Analytical solutions of multiple light scattering problems: a review. *Measurement Science and Technology*, 13(3):233, 2002.

[133] Lihong Wang, Steven L Jacques, and Liqiong Zheng. MCML—Monte Carlo modeling of light transport in multi-layered tissues. *Computer methods and programs in biomedicine*, 47(2):131–146, 1995.

[134] H C Van de Hulst. *Multiple light scattering: tables, formulas, and applications*. Elsevier, 1980.

[135] Louis G Henyey and Jesse L Greenstein. Diffuse radiation in the galaxy. *The Astrophysical Journal*, 93:70–83, 1941.

[136] John W McLean, Jonathan D Freeman, and Ronald E Walker. Beam spread function with time dispersion. *Applied Optics*, 37(21):4701–4711, 1998.

[137] Simon Premože, Michael Ashikhmin, Jerry Tessendorf, Ravi Ramamoorthi, and Shree Nayar. Practical rendering of multiple scattering effects in participating media. In *Proceedings of the Fifteenth Eurographics conference on Rendering Techniques*, pages 363–374. Citeseer, 2004.

[138] Jerry Tessendorf. Radiative transfer as a sum over paths. *Physical review A*, 35(2):872, 1987.

[139] Andrew Zardecki, Siegfried AW Gerstl, and Janon F Embury. Multiple scattering effects in spatial frequency filtering. *Applied optics*, 23(22):4124–4131, 1984.

[140] Craig F Bohren and Donald R Huffman. *Absorption and scattering of light by small particles*. John Wiley & Sons, 2008.

[141] Alex Krisman, Evatt R Hawkes, Mohsen Talei, Ankit Bhagatwala, and Jacqueline H Chen. A direct numerical simulation of cool-flame affected autoignition in diesel engine-relevant conditions. *Proceedings of the Combustion Institute*, 36(3):3567–3575, 2017.

[142] Irvin Glassman, Richard A Yetter, and Nick G Glumac. *Combustion*. Academic press, 2014.

[143] Judit Zádor, Craig A Taatjes, and Ravi X Fernandes. Kinetics of elementary reactions in low-temperature autoignition chemistry. *Progress in energy and combustion science*, 37(4):371–421, 2011.

[144] Hai Wang and David A Sheen. Combustion kinetic model uncertainty quantification, propagation and minimization. *Progress in Energy and Combustion Science*, 47:1–31, 2015.

[145] Jose M Desantes, Jean Arregle, J Javier Lopez, and Andreas Cronhjort. Scaling laws for free turbulent gas jets and diesel-like sprays. *Atomization and Sprays*, 16(4), 2006.

[146] Jose Maria Desantes, Raul Payri, Francisco Javier Salvador, and Antonio Gil. Development and validation of a theoretical model for diesel spray penetration. *Fuel*, 85(7-8):910–917, 2006.

[147] Dennis Siebers and Brian Higgins. Flame lift-off on direct-injection diesel sprays under quiescent conditions. *SAE Transactions*, pages 400–421, 2001.

[148] Dennis Siebers, Brian Higgins, and Lyle Pickett. Flame lift-off on direct-injection diesel fuel jets: oxygen concentration effects. *Sae Transactions*, pages 1490–1509, 2002.

[149] Lyle M Pickett and Dennis L Siebers. Soot in diesel fuel jets: effects of ambient temperature, ambient density, and injection pressure. *Combustion and Flame*, 138(1-2):114–135, 2004.

[150] Claude Elwood Shannon. Communication in the presence of noise. *Proceedings of the IRE*, 37(1): 10–21, 1949.

[151] Georges M Quénot, Jaroslaw Pakleza, and Tomasz A Kowalewski. Particle image velocimetry with optical flow. *Experiments in fluids*, 25(3):177–189, 1998.

[152] Richard D Keane and Ronald J Adrian. Optimization of particle image velocimeters. i. double pulsed systems. *Measurement science and technology*, 1(11):1202, 1990.

[153] Eric W Lemmon and Richard T Jacobsen. Viscosity and thermal conductivity equations for nitrogen, oxygen, argon, and air. *International Journal of Thermophysics*, 25(1):21–69, 2004.

[154] John H Clark, C Bradley Moore, and Nicholas S Nogar. The photochemistry of formaldehyde: Absolute quantum yields, radical reactions, and no reactions. *The Journal of Chemical Physics*, 68(3):1264–1271, 1978.

[155] Steven E Moran, Bobby Lee Ulich, William P Elkins, Richard J Strittmatter, and Michael James DeWeert. Intensified ccd (iccd) dynamic range and noise performance. In *Ultrahigh-and High-Speed Photography and Image-based Motion Measurement*, volume 3173, pages 430–457. International Society for Optics and Photonics, 1997.

[156] Haiqiao Wei, Wanhui Zhao, Zhen Lu, and Lei Zhou. Effects of oxygen concentrations on the ignition and quasi-steady processes of n-heptane spray flames using large eddy simulation. *Fuel*, 241:786–801, 2019.

[157] D L Dexter and James H Schulman. Theory of concentration quenching in inorganic phosphors. *The Journal of Chemical Physics*, 22(6):1063–1070, 1954.

[158] Charles Percy Snow. *The two cultures*. Cambridge University Press, 2012.

[159] American Physical Society. 07.1 climate change, 2007. URL `www.aps.org/policy/statements/07_1.cfm`.

[160] Stephanie C Herring, Nikolaos Christidis, Andrew Hoell, James P Kossin, Carl J Schreck III, and Peter A Stott. Explaining extreme events of 2016 from a climate perspective. *Bulletin of the American Meteorological Society*, 99(1):S1–S157, 2018.

[161] RD Reitz, H Ogawa, R Payri, T Fansler, S Kokjohn, Y Moriyoshi, AK Agarwal, D Arcoumanis, D Assanis, C Bae, et al. IJER editorial: The future of the internal combustion engine, 2020.

[162] American Chemical Society. Climate science toolkit, 2020. URL `https://www.acs.org/content/acs/en/climatescience.html`.

[163] Jan Faye. Copenhagen Interpretation of Quantum Mechanics. In Edward N. Zalta, editor, *The Stanford Encyclopedia of Philosophy*. Metaphysics Research Lab, Stanford University, winter 2019 edition, 2019.

[164] Gordon W. F. Drake and Mark M. Cassar, editors. *Springer Handbook of Atomic, Molecular, and Optical Physics*. Springer, 2006. ISBN 978-0-387-20802-2.

[165] Walter S Struve. *Fundamentals of Molecular Spectroscopy*. Wiley New York, 1989. ISBN 9780471854241.

[166] J.J. Sakurai and J. Napolitano. *Modern Quantum Mechanics*. Addison-Wesley, 2011. ISBN 9780805382914. URL `https://books.google.com/books?id=N4I-AQAACAAJ`.

[167] JA Pople and JW Sidman. Intensity of the symmetry-forbidden electronic absorption band of formaldehyde. *The Journal of Chemical Physics*, 27(6):1270–1277, 1957.

[168] G Orlandi and W Siebrand. Theory of vibronic intensity borrowing. comparison of Herzberg-Teller and Born-Oppenheimer coupling. *The Journal of Chemical Physics*, 58(10):4513–4523, 1973.

[169] Lev Davidovich Landau and Evgenii Mikhailovich Lifshitz. *Quantum mechanics: non-relativistic theory*, volume 3. Elsevier, 2013.

[170] Henry Eyring, John Walter, and George E Kimball. *Quantum chemistry*. Wiley, 1944.

[171] Chih-Kai Lin, Ming-Chung Li, Masahiro Yamaki, Michitoshi Hayashi, and Sheng Hsien Lin. A theoretical study on the spectroscopy and the radiative and non-radiative relaxation rate constants of the S_0 $^1A_1$ - S_1 $^1A_2$ vibronic transitions of formaldehyde. *Physical Chemistry Chemical Physics*, 12:11432–11444, 2010. doi: 10.1039/c004493h.

[172] SH Lin, LJ Colangelo, and H Erying. Theoretical analysis of emission spectra of electronic transitions of molecules in dense media. *Proceedings of the National Academy of Sciences*, 68(9): 2135–2140, 1971.

[173] Gilbert W King, R M Hainer, and Paul C Cross. The asymmetric rotor i. calculation and symmetry classification of energy levels. *The Journal of Chemical Physics*, 11(11), 1943. doi: 10.1063/1.1723778. URL http://dx.doi.org/10.1063/1.1723778.

[174] Paul C. Cross, R. M. Hainer, and Gilbert W. King. The asymmetric rotor ii. calculation of dipole intensities and line classification. *The Journal of Chemical Physics*, 12(6):210, 1944. ISSN 00219606. doi: 10.1063/1.1723935. URL http://scitation.aip.org/content/aip/journal/jcp/12/6/10.1063/1.1723935.

[175] Gilbert W King, Paul C Cross, and George B Thomas. The asymmetric rotor iii. punched-card methods of constructing band spectra. *The Journal of Chemical Physics*, 14(1):35–42, 1946.

[176] Gilbert W King. The asymmetric rotor. iv. an analysis of the 8.5-μ band of D_2O by punched-card techniques. *The Journal of Chemical Physics*, 15(2), 1947. doi: 10.1063/1.1746431. URL http://dx.doi.org/10.1063/1.1746431.

[177] R M Hainer and Gilbert W King. The asymmetric rotor v. an analysis of the 3.7-μ band of H_2S by punched-card techniques. *The Journal of Chemical Physics*, 15(2):1–147, 1947. doi: 10.1063/1.1746433. URL http://dx.doi.org/10.1063/1.1746433.

[178] Gilbert W King. The asymmetric rotor. vi. calculation of higher energy levels by means of the correspondence principle. *The Journal of Chemical Physics*, 15(11), 1947. doi: 10.1063/1.1746344. URL http://dx.doi.org/10.1063/1.1746344.

[179] R M Hainer, Paul C Cross, and Gilbert W King. The asymmetric rotor. vii. extension of the calculation of energy levels. *The Journal of Chemical Physics*, 17(17), 1949. doi: 10.1063/1.1723778. URL http://dx.doi.org/10.1063/1.1747406.

[180] Richard Henry Schwendeman. Tables for the rigid asymmetric rotor: Transformation coefficients from symmetric to asymmetric bases and expectation values of p2 (z), p4 (z), and p6 (z). Technical report, National Standard Reference Data System, 1968.

[181] Clasine Van Winter. The asymmetric rotator in quantum mechanics. *Physica*, 20(1-6):274–292, 1954.

[182] James K.G. Watson. Simplification of the molecular vibration-rotation hamiltonian. *Molecular Physics*, 15(5):479–490, 1968. doi: 10.1080/00268976800101381. URL https://doi.org/10.1080/00268976800101381.

[183] S C Wang. On the asymmetrical top in quantum mechanics. *Physical Review*, 34:243–252, 1929.

[184] James E. Wollrab. *Rotational Spectra and Molecular Structure*. Academic Press Inc., New York, 1967.

[185] Gerhard Herzberg. *Molecular spectra and molecular structure*. D. van Nostrand, 1966.

[186] JT Hougen and JKG Watson. Anomalous rotational line intensities in electronic transitions of polyatomic molecules: Axis-switching. *Canadian Journal of Physics*, 43(2):298–320, 1965.

[187] Lawrence Christian Biedenharn and James D Louck. *Angular momentum in quantum physics: theory and application*. Addison-Wesley, 1981.

[188] V. S. Vasan and R. J. Cross. Matrix elements for Morse oscillators. *The Journal of Chemical Physics*, 1983. ISSN 0021-9606. doi: 10.1063/1.445164.

[189] T E Sharp and H M Rosenstock. Franck—Condon factors for polyatomic molecules. *The Journal of Chemical Physics*, 41(11), 1964. doi: 10.1063/1.1725748. URL `http://dx.doi.org/10.1063/1.1725748`.

[190] R Islampour, M Dehestani, and S H Lin. A new expression for multidimensional Franck–Condon integrals. *Journal of Molecular Spectroscopy*, 194:179–184, 1999.

[191] Edgar Bright Wilson, John Courtney Decius, and Paul C Cross. *Molecular vibrations: the theory of infrared and Raman vibrational spectra*. Courier Corporation, 1980.

[192] F. Duschinsky. The importance of the electron spectrum in multi atomic molecules. concerning the Franck-Condon principle. *Acta Physicochimica URSS*, 7:551–566, 1937.

[193] Ilker Özkan. Franck-Condon principle for polyatomic molecules: Axis-switching effects and transformation of normal coordinates. *Journal of Molecular Spectroscopy*, 1990. ISSN 1096083X. doi: 10.1016/0022-2852(90)90247-N.

[194] C Manneback. Computation of the intensities of vibrational spectra of electronic bands in diatomic molecules. *Physica*, 17(11-12):1001–1010, 1951.

[195] G Wilse Robinson and V Erdmanis DiGiorgio. The nature of formaldehyde in its low-lying excited states. *Canadian Journal of Chemistry*, 36(1):31–38, 1958.

[196] Chih Kai Lin, Huan Cheng Chang, and S. H. Lin. Symmetric double-well potential model and its application to vibronic spectra: Studies of inversion modes of ammonia and nitrogen-vacancy defect centers in diamond. *Journal of Physical Chemistry A*, 2007. doi: 10.1021/jp073838i.

[197] DM Burland and GW Robinson. Is the breakdown of the born-oppenheimer approximation responsible for internal conversion in large molecules? *Proceedings of the National Academy of Sciences*, 66(2):257–264, 1970.

[198] Richard G Miller and Edward KC Lee. Intersystem crossing of triplet formaldehyde. *Chemical Physics Letters*, 27(4):475–478, 1974.

[199] Qian Peng, Yuanping Yi, Zhigang Shuai, and Jiushu Shao. Excited state radiationless decay process with Duschinsky rotation effect: Formalism and implementation. *The Journal of chemical physics*, 126(11):114302, 2007.

[200] M Hayashi, AM Mebel, KK Liang, and SH Lin. Ab initio calculations of radiationless transitions between excited and ground singlet electronic states of ethylene. *The Journal of chemical physics*, 108(5):2044–2055, 1998.

[201] Richard Phillips Feynman. Forces in molecules. *Physical Review*, 56(4):340, 1939.

[202] Wolfgang Pauli. Zur quantenmechanik des magnetischen elektrons. In *Wolfgang Pauli*, pages 282–305. Springer, 1988.

[203] Christel M Marian. Spin–orbit coupling and intersystem crossing in molecules. *Wiley Interdisciplinary Reviews: Computational Molecular Science*, 2(2):187–203, 2012.

[204] Shigeo Shionoya, William M Yen, and Hajime Yamamoto. *Phosphor handbook*. CRC press, 2018.

[205] Wolfram Koch and Max C Holthausen. *A chemist's guide to density functional theory*. John Wiley & Sons, 2015.

[206] A. D. Becke. Density-functional exchange-energy approximation with correct asymptotic behavior. *Physical Review A*, 38(6):3098–3100, 1988.

[207] Chengteh Lee, Weitao Yang, and Robert G Parr. Development of the Colle-Salvetti correlation-energy formula into a functional of the electron density. *Physical review B*, 37(2):785, 1988.

[208] Florian Weigend and Reinhart Ahlrichs. Balanced basis sets of split valence, triple zeta valence and quadruple zeta valence quality for H to Rn: Design and assessment of accuracy. *Physical Chemistry Chemical Physics*, 7(18):3297–3305, 2005.

[209] Frank Neese. The ORCA program system. *Wiley Interdisciplinary Reviews: Computational Molecular Science*, 2(1):73–78, 2012.

[210] Philippe Carbonniere, Tecla Lucca, Claude Pouchan, Nadia Rega, and Vincenzo Barone. Vibrational computations beyond the harmonic approximation: Performances of the B3LYP density functional for semirigid molecules. *Journal of computational chemistry*, 26(4):384–388, 2005.

[211] Johannes Neugebauer and Bernd A Hess. Fundamental vibrational frequencies of small polyatomic molecules from density-functional calculations and vibrational perturbation theory. *The Journal of chemical physics*, 118(16):7215–7225, 2003.

[212] Per Jensen and PR Bunker. The geometry and the inversion potential function of formaldehyde in the $\tilde{A}^1A_2$ and $\tilde{a}^3A_2$ electronic states. *Journal of Molecular Spectroscopy*, 94(1):114–125, 1982.

[213] David E. Reisner, Robert W. Field, James L. Kinsey, and Hai-Lung Dai. Stimulated emission spectroscpy: A complete set of vibrational constants for X^1A_1 formaldehyde. *The Journal of Chemical Physics*, 80(12):5968–5978, 1984. doi: 10.1063/1.446677. URL `http://dx.doi.org/10.1063/1.446677`.

[214] Gerald M Sando and Kenneth G Spears. Ab initio computation of the Duschinsky mixing of vibrations and nonlinear effects. *The Journal of Physical Chemistry A*, 105(22):5326–5333, 2001.

[215] Dominique Toublanc. Henyey–Greenstein and Mie phase functions in Monte Carlo radiative transfer computations. *Applied optics*, 35(18):3270–3274, 1996.

[216] HC Van de Hulst and George W Kattawar. Exact spread function for a pulsed collimated beam in a medium with small-angle scattering. *Applied optics*, 33(24):5820–5829, 1994.

[217] Gustav Mie. Pioneering mathematical description of scattering by spheres. *Ann. Phys*, 25(337): 0003–3804, 1908.

[218] Hendrik Christoffel van de Hulst. *Light scattering by small particles*. Courier Corporation, 1981.

[219] Michael I Mishchenko, Larry D Travis, and Andrew A Lacis. *Scattering, absorption, and emission of light by small particles*. Cambridge university press, 2002.

[220] Rudolf Penndorf. Angular Mie scattering. *JOSA*, 52(4):402–408, 1962.

[221] Hui Tian. *Noise analysis in CMOS image sensors*. PhD thesis, Stanford University, 2000.

[222] Hui Tian, Boyd Fowler, and Abbas E Gamal. Analysis of temporal noise in CMOS photodiode active pixel sensor. *IEEE Journal of Solid-State Circuits*, 36(1):92–101, 2001.

[223] Timothy C Williams and Christopher R Shaddix. Simultaneous correction of flat field and nonlinearity response of intensified charge-coupled devices. *Review of Scientific Instruments*, 78(12): 123702, 2007.

[224] DA Rothamer and JB Ghandhi. On the calibration of single-shot planar laser imaging techniques in engines. *SAE Transactions*, pages 1286–1303, 2002.

[225] Mark Stanford Robbins and Benjamin James Hadwen. The noise performance of electron multiplying charge-coupled devices. *IEEE transactions on electron devices*, 50(5):1227–1232, 2003.